PERFORMANCE OF HIGH-STRENGTH CONCRETE COMPOSITE COLUMNS SUBJECT TO EARTHQUAKE LOADING CONDITIONS

A Thesis Submitted to the University of Dublin for the Degree of Doctor of Philosophy in the Faculty of Engineering and System Sciences

by

John Edmond Deenihan B.A., B.A.I.

October 2010

Department of Civil, Structural and Environmental Engineering
University of Dublin
Trinity College
Dublin

To Nana

Thinking of you every day

DECLARATION

The author hereby declares that this thesis, in whole or in part, has not been submitted to any other university as an exercise for a degree. Except where reference has been given in the text, it is entirely the author's own work.

The author confirms that the Library may lend or copy the thesis upon request, for academic purpose.

ACKNOWLEDGEMENTS

Firstly, I would like to thank my supervisor Professor Brian Broderick for his continued guidance and support throughout the thesis. Your knowledge appears to have no limits. I would also like to thank Dr. Roger West for his contribution into this research. The kind people of Fairyhouse Steel must also be appreciated for providing the reinforcement used in this project.

I really appreciate the inordinate amount of time the technical staff placed on this research; particular thanks go to Chris O' Donovan, Dave McAuley, Kevin Ryan, Barry 'Baz' McElhiney, Eoin Dunne, Mick Harris and Sean Downey. No doubt some of you will never want to have to put up with me again.

My gratitude also to the 'Red Brick Clan', William Forrest, Andrew Galbraith, Alan *'Al the Black'* Hunt and Daniel McCrum. Many a long nights spent researching the décor of Kennedy's Bar.

I wish to give a special thanks to Mr. Daniel McCrum who had the arduous task of proof reading this thesis; it's much appreciated and won't be forgotten.

My sincere thanks go to my family and friends whose support and drive and pushed me all the way, thank you. Finally, last but by no means least, thank you Edel for all the love and support over the years.

SUMMARY

Composite construction has been used in industry for decades due to superior load carrying capacity of the members compared with traditional reinforced concrete construction. A composite column is a structural member that uses a combination of concrete incorporating structural steel shapes, pipes or tubes with or without reinforcing steel to provide adequate load carrying capacity to axial loads or a combination of axial loads and bending moments. The interactive and integral behaviour between the concrete and structural steel makes the composite column a very cost effective and structurally efficient member.

Modern design codes for the earthquake-resistant design of structures rely on the dissipation of seismic energy through the formation of pre-defined plastic hinge regions. Depending on the level of deformation required, a composite column must be adequately designed and detailed so that it possesses sufficient rotational capacity, without excessive deterioration. The European earthquake resistant design code, Eurocode 8, sets out specific design and detailing provisions for composite columns depending on the required level of dissipation assigned to the structural element.

Unfortunately, due to the highly brittle nature of high-strength concrete (HSC), Eurocode 8 states that a concrete strength greater $f_{ck} \geq 40$ N/mm^2 is outside the scope of the code for encased composite columns. HSC requires significantly more detailing to provide adequate confinement to the concrete, such that a suitable post-yield ductility can be achieved. Little work has been conducted to determine if the existing design provisions of Eurocode 8, can be used or modified to include the use of HSC for encased composite design.

An experimental programme is described in detail which compares the performance of HSC composite columns compared with traditional normal-strength concrete (NSC) composite columns. Six full-scale specimens were tested subject to a combination of constant axial load and varying lateral cyclic displacement, which is the conventional loading applied in seismic testing. All specimens possessed the same dimensions and quantities of steel, but differed with respect to the following three parameters: (i)

concrete compressive strength, (ii) level of applied axial load and, (iii) link spacing in the critical region of the specimen.

The experimental results are presented in terms of numerical results and visual observations. The results for the NSC composite columns illustrate that they possess excellent ductility and energy dissipation capacity at all levels of axial load. The NSC specimens display little to no sign of drops in resistance due to repeated cycles of identical displacement, thus the detailing provisions are adequate for this grade of concrete. The HSC specimen show severe deterioration to the concrete core at moderate levels of lateral displacement. The response of the HSC specimens with low levels of axial load was very similar to that recorded for the NSC specimens, suggesting that the detailing provisions of Eurocode 8 could effectively be used if a reduced limit on the applied axial load was implemented. It was observed that reduced link spacing could not effectively confine the concrete core nor could the specimen emulate the performance of a HSC specimen with low levels of axial load.

A numerical model was developed to predict the moment-displacement response of the column specimens and their strain capabilities. The numerical model was based on Mander's stress-strain model for confined concrete subject to uni-axial compression. The model was modified to incorporate a composite cross-section subject to combined axial and lateral cyclic loading. The model results show good correlation with the experimental data, but are less accurate for the HSC specimens. The strain energies in the transverse steel for different concrete strengths and axial loads are postulated.

A finite element model was further developed to predict the hysteretic response of the columns specimens using Zeus NonLinear (ZeusNL). The finite element model shows good correlation with the experimental data and provides a more accurate estimate of the maximum moment achieved by the HSC specimens as compared to the developed numerical model, but significantly over-estimates the yield stiffness of all specimens.

A parametric analysis was conducted using both models and it has been shown that both are sensitive to link spacing, axial load and concrete strength. The moment-displacement response predicted by both models are very similar, but diverge slightly when subject to large link spacings and high levels of axial load.

TABLE OF CONTENTS

LIST OF FIGURES

LIST OF TABLES

PRINCIPAL NOTATIONS

The following is a list of the principal notations. All of the following are defined in the text where they are used and solely listed here for clarity

Latin Upper Case Letters

Symbol	*Definition*
A_a	Area of steel section
A_c	Area of effectively confined concrete core
A_{cc}	Area of concrete core enclosed by the centreline of the perimeter link
$A_{cc(p)}$	Area of partially confined concrete
$A_{cc(h)}$	Area of highly confined concrete
A_s	Area of steel
A_{sp}	Area of transverse reinforcing bar
A_{sx}	Area of transverse reinforcing bar running in the x-direction
A_{sy}	Area of transverse reinforcing bar running in the x-direction
B	Section width
D	Section depth
E_a	Modulus of elasticity of steel section
E_c	Tangent modulus of elasticity of concrete
E_{cc}	Tangent modulus of elasticity of concrete
E_{ct}	Tangent modulus of elasticity of concrete in tension
E_s	Modulus of elasticity for the steel
E_{spy}	Steel post yield stiffness
I_a	Second moment of area of steel section
I_c	Second moment of area of un-cracked concrete in compression
I_s	Second moment of area of reinforcing steel
K_i	Initial stiffness
K_h	High confined concrete factor
K_p	Partially confined concrete factor
L	Length

L_{cr}	Effective length
M	Moment

Latin Upper Case Letters

Symbol	***Definition***
$M_{max,Rd}$	Maximum plastic moment of resistance of the structural cross section
M_u	Ultimate moment
M_y	Yield moment
$N_{b,Rd}$	Axial buckling capacity of a section
N_{cr}	Elastic critical buckling load
$N_{pl,Rd}$	Design plastic resistance of the gross cross-section
N_t	Limiting axial force
P	Axial load
P_c	Axial capacity of column cross section
p_g	Volumetric ratio
P_{oc}	Axial capacity of total concrete cross section
P_{occ}	Axial capacity of concrete core
P_{max}	Maximum applied load
P_y	Yield load
T_1	Fundamental period of vibration of a building
T_C	Upper limit of the period of the constant spectral acceleration branch
U_{cc}	Area under confined concrete stress-strain curve
U_{co}	Area under unconfined concrete stress-strain curve
U_{sc}	Energy to maintain yielding of the longitudinal steel in compression
U_{sf}	Strain energy of the transverse reinforcement up to the fracture
U_{sh}	Ultimate strain energy capacity of the confining reinforcement
V	Shear

Latin Lower Case Letters

Symbol	***Definition***
d_{bl}	Minimum longitudinal bar diameter
$d_{bL,max}$	Maximum diameter of longitudinal bars

d_{bw}	Transverse steel diameter
b_c	Width between centreline of links

Latin Lower Case Letters

Symbol	***Definition***
b_o	Minimum centre line dimension of lateral ties
d_c	Depth between centreline of links
d_s	Diameter of transverse link
f'_c	Uni-axial compressive strength of concrete
f'_{cc}	Confined concrete compressive strength
f'_{co}	Unconfined concrete compressive strength
f_{ck}	Characteristic concrete cylinder compressive strength at 28 days
f_{ck}	Concrete cube compressive strength at 28 days
f_l	Lateral pressure from the transverse reinforcement
f'_l	Effective lateral confining stress
f_c	Stress in the concrete
f_s	Stress in the transverse reinforcement
f_{ss}	Stress in the structural steel
f_{sk}	Reinforcing steel design yield strength
f_{sl}	Stress in the longitudinal reinforcement
f_t	Concrete tensile strength
f_u	Steel ultimate strength
f_y	Steel yield strength
f_{yd}	Structural steel yield strength
f_{yh}	Reinforcing steel yield strength
f_{ydL}	Design yield strength of longitudinal reinforcement
f_{ydw}	Design yield strength of transverse reinforcement
k_e	Confinement effectiveness coefficient
q	Structural behaviour factor
s	Transverse link spacing
s'	Clear vertical spacing between transverse links
w'	Distance between adjacent longitudinal bars
x	Neutral axis depth

Greek Upper Case Letters

Symbol	*Definition*
Δ	Displacement
Δ_{Ti}	Total displacement occurring between column tip and end
Δ_y	Yield displacement
χ	Slenderness reduction factor
θ	Rotation

Greek Lower Case Letters

Symbol	*Definition*
A	Imperfection constant
δ	Steel contribution ratio
γ_c	Partial safety factor for concrete
γ_s	Partial safety factor for reinforcing steel
γ_{Ma}	Partial safety factor for structural steel
λ	Slenderness factor
ε_c	Longitudinal concrete compressive strain
ε_{co}	Strain corresponding to maximum unconfined concrete strength
ε_{cc}	Strain corresponding to maximum confined concrete strength
$\varepsilon_{cc,p}$	Strain corresponding to yield stress of the partially confined concrete
ε_{cu}	Ultimate concrete compression strain
ε_s	Strain in transverse steel
ε_{sf}	Fracture strain in transverse steel
ε_{sp}	Spalling strain of the unconfined concrete
ε_u	Steel ultimate strain
ε_y	Steel yield strain
ε_{yr}	Longitudinal steel yield strain in compression
ε_{ys}	Structural steel yield strain in compression
ø_{min}	Longitudinal steel reinforcement diameter
ø	Curvature
ø_u	Measure of the ultimate curvature

Greek Lower Case Letters

Symbol	*Definition*
ϕ_u	Measure of the yield curvature
μ_ϕ	Curvature ductility factor
Δ_u	Measure of the ultimate displacement
Δ_y	Measure of the yield displacement
μ	Ductility
μ_Δ	Displacement ductility
ρ_{cc}	Ratio of area of longitudinal steel to the area of the concrete section
ρ_s	Transverse steel volumetric ratio
ρ_x	Ratio of transverse steel in the x-direction
ρ_y	Ratio of transverse steel in the y-direction
σ	Stress
σ_y	Steel yield stress
ψ	Rotation angle

Chapter 1

Introduction

Introduction

1.1 Preamble

The primary purpose of earthquake resistant design is to protect human life by avoiding structural collapse. Structural stability should be maintained at all times, thus adequate design and detailing must be provided to all structural elements so that the intended load paths are provided and shear, flexural and buckling failure are prevented.

The objective of this research is to determine if high-strength concrete (HSC) composite columns can achieve adequate displacement ductility to be incorporated in a highly dissipative composite moment resisting frame.

1.2 High Strength Concrete (HSC)

HSC has been available for some time but is infrequently used in earthquake regions as part of a dissipative structure due to the brittle nature of the concrete. HSC achieves higher compressive stress and strain values than normal-strength concrete (NSC) but unless adequately confined, the concrete may experience brittle failure with little prior transverse or longitudinal cracking in reinforced concrete members. Suitable reinforcement detailing can improve the resistance of the concrete core, providing additional load carrying capacity and improving post-yield performance.

HSC is frequently used in the United States in lower stories of skyscrapers as infill for circular hollow sections. The steel section provides adequate confinement to the concrete core and the concrete prevents the steel section from buckling at large lateral

displacements. The use of HSC for encased composite columns has been used far less in practice due to the difficulty and uncertainty of providing adequate confinement to the concrete at large displacements. Furthermore, it may not be cost effective to provide adequate confinement due to the volume of transverse steel required. However, if adequate confinement is provided, the concrete may resist loads well into the inelastic range of the materials and large lateral displacements can be achieved without excessive member deterioration or reduction in resistance.

HSC has a further advantage in that section sizes can be reduced due to the additional load carrying capacity of the high grade concrete. This can be of particularly useful for earthquake design as the seismic forces applied to a structure are determined from the ground conditions and the mass of a structure, thus a reduced mass due to smaller section sizes will reduce the earthquake loads which need to be resisted by the structure.

1.3 Capacity Design and Displacement Ductility

Capacity design is the design approach commonly employed by modern earthquake design codes. Capacity design implies that structures are designed to resist earthquakes through the development of plastic hinges at pre-defined locations. These plastic hinges are designed so that significant inelastic material behaviour can occur without loss of resistance, all the while ensuring that the magnitude of the inelastic deformations do not endanger the overall structural stability.

In capacity design, the yielding mode of the structure is pre-defined by the selection of those structural elements in the structural configuration which are allowed, and expected, to under-go inelastic deformation and dissipate energy during an earthquake. The plastic hinges are then detailed according to the required level of energy dissipation. All other elements are over-designed to remain elastic during earthquake excitation. Depending on the design energy dissipation level of the structure, design codes such as Eurocode 8, (CEN, 2004) specify a required displacement ductility capacity to be achieved by a plastic hinge. Thus, for higher levels of assumed energy dissipation, structural elements require more detailing to ensure sufficient plastic rotation without excessive deterioration to the core elements.

1.4 Scope and Objectives of Work

A large amount of research has been conducted into the seismic performance of composite columns, both encased and in-filled, but limited research has been conducted on the use of HSC in encased composite columns. This is due to the inherently brittle nature of HSC, and the associated difficulties in achieving adequate rotational ductilities. A critical aspect of capacity design is that pre-defined plastic hinges must be capable of achieving large significant inelastic deformations and energy dissipation: two properties which are especially difficult to achieve with high-strength concrete. As a result, suitable design and detailing of the reinforcement and structural steel is essential to confine the core concrete elements such that they achieve the required level of ductility during repeated cycles of cyclic loading.

The principle objective of this research was to investigate the inelastic performance of HSC and to determine if the existing design provisions in Eurocode 8, (CEN, 2004) could be used to design HSC encased columns for the displacement ductility required of a high ductility class (DCH) composite column within a moment resisting frame. Furthermore, the loading and confinement provisions were analysed with the intention of proposing code amendments that would improve the performance and resistance of the HSC specimens.

To examine the performance of both normal and high-strength concrete encased composite columns, an experimental programme of research was put in place with the aim of determining the displacement ductility and energy dissipation capacities of the representative composite columns. The experimental programme consisted of tests on six full-scale composite columns subjected to simultaneous axial and lateral cyclic loading, which is the conventional test loading applied in seismic testing. The results from these tests form the substantive part of this thesis. The test specimens possessed the same overall dimensions and steel contents but differed with respect to the following three parameters:

1. Concrete compressive strength
2. Level of applied axial load
3. Transverse link spacing

The results from each test were considered and compared to determine the effects of each parameter on both the normal and high-strength concrete specimens. The applied axial load was kept constant throughout each test, while displacement-controlled lateral cyclic loading was applied with increasing amplitude.

A numerical model was developed to represent the non-linear moment-displacement response of the specimens considered in the experimental programme. The model is based on Mander's stress-strain model for confined concrete (Mander *et al,* 1988) and was developed to capture the effects of combined axial and lateral loading on a composite cross section. Mander's energy balance approach to determine the strain energy in the transverse reinforcement at fracture was also extended to be applicable to composite cross-sections.

Finally, a finite element model was developed using Zeus NonLinear (ZeusNL) to simulate the load-deflection hysteretic performance of the specimens. The finite element model was compared with the numerical model and experimental results to validate the predictions and compare the accuracy of both model predictions.

The presentation of this work is outlined in the following section.

1.5 Organisation of the Thesis

Chapter 2 presents a literature review of previous research conducted on both composite and reinforced concrete members subject to earthquake loading conditions. The concepts of ductility and energy dissipation are introduced, as is the manner in which they are exploited by Eurocode 8, (CEN, 2004) using a capacity design approach. The bulk of the chapter deals with concrete confinement and how the various structural elements confine the core concrete and how they affect the ductility and energy dissipation of the members. While a considerable amount of research has been conducted on the performance of combined axial and cyclic loading of normal-strength composite columns, far less work has been conducted on high-strength concrete columns. This

chapter discusses the work previously undertaken, with particular focus on experimental work similar to the experimental programme undertaken as part of this research.

Chapter 3 and 4 are concerned with the experimental programme. Chapter 3 describes the test specimens and their production. A detailed analysis of the experimental set-up is also presented along with the associated capabilities and limitations of the experimental hardware. Chapter 4 considers the experimental test results. The experimental response of each specimen, subject to simultaneous axial and lateral cyclic loading, is presented. The specimens' responses are discussed in terms of both the numerical results obtained and the visual observations made during the test. Each specimen is reviewed in terms of ductility and energy dissipation capacity, and compared with similar specimens to determine the effects of varying key parameters on the performance of the HSC columns as a whole.

Chapter 6 presents the results of the numerical model as developed in Chapter 5 with the intention of predicting the response of the experimental columns, and to predict the energy and strains in the transverse reinforcement at fracture. Chapter 7 presents the results of a finite element model and a comparison between the finite element, numerical model and experimental results. Furthermore, Chapter 7 also presents a parametric study that investigates the effect of varying model parameters on the moment-displacement response of composite columns.

Finally, Chapter 8 summarises the work done, presents the principal conclusions reached and suggests some areas for further research.

Chapter 2

Literature Review

Literature Review

2.1 Introduction

The design of composite columns has been covered by British Standards for the last 50 years, whereby rudimentary measures were introduced into BS 449 (BSI 1969), to incorporate the combined benefits to concrete and steel. Since this, vast research has been undertaken to determine the performance of composite columns subject to uni-axial compressive loading and later into flexural and cyclic behaviour, ultimately leading to the current design standards for composite design and members subject to earthquake loading, Eurocode 4 (CEN, 2004) and Eurocode 8 (CEN, 2004), respectively. As this thesis concentrates on the performance of high strength concrete (HSC) subject to combined axial and cyclic bending, this chapter sets out the requirements for good earthquake resistance and describes the most relevant research and design developments in composite structures.

Section 2.2 introduces the requirements of structures to provide good earthquake resistance. Two of the most fundamental requirements of capacity design for composite construction are ductility and energy dissipation, which are described in Section 2.3. Since current design philosophies of moment resisting frames provide energy dissipation through post elastic deformations, it is essential that a designed dissipative member is capable of providing high levels of ductility to maximise the energy dissipation of the member and hence improve its performance.

The capacity design approach is introduced in Section 2.4 with respect to the design of composite members subject to earthquake conditions. Though it may not be viable to design structures to withstand severe ground shaking without any damage, a suitable

compromise must be established between allowable damage to a structure subject to an earthquake and the overall cost of the proposed design. At all times a structure must not fail, even if large deformations occur due to an earthquake of greater intensity than originally designed. This section discusses the factors influencing the above design approach.

The implementation of the capacity design approach as adopted in Eurocode 8 (CEN, 2004) is discussed in Section 2.5. This section analyses the fundamental requirements of the code and how varying levels of ductility and energy dissipation are achieved for various structures and how each is classified within the Eurocode. Composite columns achieve additional strength and resistance through adequately confined concrete, structural steel sections are an effective method of provide confinement, but varying shapes, steel yield strength and configuration of the longitudinal and transverse steel plays a significant role in effectively confining the concrete. Section 2.6 discusses the underlying factors influencing the concrete confinement.

As this research investigates the use of HSC, with strengths higher than the maximum permissible grade covered by Eurocode 8 (CEN, 2004), (i.e. $f_{ck} \geq 40$ N/mm^2), it is essential that an understanding of the characteristics and performance of HSC is conducted before being recommended for design. Section 2.6.2.8 investigates the performance of HSC and the implications if adopted in the design. Sections 2.7 and 2.8 discuss the behaviour of composite columns subject to varying levels of axial and combined axial and lateral loading. A literature review for material modelling is provided in Section 5.2

2.2 Earthquake Resistant Design

With an ever increasing surge in world population and demand for high rise construction in metropolitan areas, engineers face significantly challenging structural designs due to intricate architectural proposals. The complexity of designs are escalated when proposed structures are sited in earthquake prone regions. Even with an ever-increasing data base of knowledge in earthquake engineering, this act of nature continues to cause destruction and devastation over the world annually. Poorly designed structures, substandard

workmanship and departures from design codes are some of the main causes of structural collapse during and after earthquakes, Markovski (2010).

Structures designed sensibly and according to relevant codes have survived earthquakes of greater intensity than originally specified, even after members have undergone deformations far exceeding those tolerated under normal load combinations. Sensible planning and design has prevented multiple fatalities, thus it is evident that careful prior planning and adherence to earthquake resistant design codes can prevent structural collapse, and most importantly, prevent fatalities. Booth (1994) identifies the following characteristics, giving a broad outline of what is required for earthquake design:

- *Good Initial Planning*: at an early stage of planning it's essential to obtain data on the soil and rock conditions and groundwater levels at the site to estimate the site period, liquefaction potential and stability of slopes.
- *Structural Form*: careful consideration must be given to choose the optimal structural form (e.g. moment-resisting frame or shear walls) to resist an earthquake.
- *Structural Layout*: buildings that are well tied together and have well-defined and continuous load paths to the foundation perform better than structures lacking such features.
- *Ductility Responses*: a ductile response is essential to prohibit structural collapse in an extreme earthquake.
- *Detailing for Earthquake Response*: the reinforcement detailing in reinforced and composite construction is of utmost importance to prevent brittle failure, and to prevent buckling of the longitudinal steel.

The ductility response and detailing provisions are the two key parameters which shall be discussed in this research; these issues are directly related as good detailing improves the ductility performance of a member.

2.3 Ductility & Energy Dissipation

Ductility and energy dissipation are two of the most imperative criteria in seismic design. Current capacity based design philosophy for moment-resisting frames relies on the availability of ductility to enable the energy transferred into the structure from an earthquake to be dissipated through post elastic deformations of carefully designed seismic members. The ductility and energy dissipation capabilities of fully-encased composite members has been widely investigated and exploited particularly in Japan, Wakabayashi *et al,* (1974), Wakabayshi *et al,* (1987), and North America, Dierlin *et al,* (2000), Ricles *et al,* (1992) and Ricles *et al,* (1994) where they were established as an effective solution to earthquake resistance design. Energy dissipation is dependent on the availability of high levels of ductility, as good ductility ensures a large looped hysteresis response. The area within a hysteresis loop is a measure of the energy dissipation capacity of a member. All modern seismic design codes accept that high levels of ductility which provide a mechanism for energy dissipation, is the best method of preventing catastrophic collapse if an earthquake occurs.

2.3.1 Definitions of Ductility

In the context of structural frames, ductility is the ability of structural elements to rotate in the inelastic range so as to transfer the applied loads throughout the structure. Ductility serves as a shock absorber in a structure, for it reduces the transmitted force to one that is sustainable. When subject to static loading, if loaded to failure, the structure should under-go large deformations and show evident visual warnings of imminent collapse, and should under no circumstance behave in a brittle manner. When subject to earthquake or cyclic loading a ductile structure is one that can maintain its stability under repeated cyclic deformations considerable greater than its yield deflection.

Increased ductility provides ample warning of imminent collapse as large deformations prior to collapse are recognised, this increase in lateral deformation due to an improvement in ductility leads to an increased amount of energy being dissipated. Furthermore, an increase in ductility provides structural robustness, as adjacent local failure can be accommodated by specially designed seismic members (Hayes *et al.*). The

provision of ductility enables moment distribution in in-determinate structures near ultimate conditions.

Ductility is a non-dimensional factor equal to the ratio of ultimate deformation to yield deformation. For the purposes of this research, two forms of ductility are relevant and are defined as:

Curvature Ductility (μ_ϕ): This is the ratio of ultimate curvature (ϕ_u) to yield curvature (ϕ_y). It is referred to as 'section ductility' because it is dependent on material type, section shape and section properties. The curvature ductility can be determined from the moment-curvature curve.

Displacement Ductility (μ_Δ): This is the ratio of ultimate displacement (Δ_u) to yield displacement (Δ_y). Displacement ductility is the 'member' or 'structural' ductility since it is related to a whole structural member or system. Displacement ductility can be identified from the load-displacement curve.

2.3.2 Definition of Energy Dissipation

A single degree of freedom oscillator as illustrated in Figure 2.1 may be used to illustrate the inelastic behaviour on the response of a structure subject to severe earthquake motion Park *et al,* (1975). Figure 2.1 (a) illustrates the load deflection response for the oscillator within the elastic range, where point '*b*' is the maximum response. The shaded area within the curve *abc* is the potential energy stored at maximum deflection. As the oscillator returns to its initial position; the potential energy is converted to kinetic energy. If the oscillator is not strong enough to carry the full elastic response load a plastic hinge develops and a curve like that shown in Figure 2.1 (b) results. Once the plastic hinge develops the deflection response follows the line *de* with point *e* representing the maximum deflection. The potential energy stored is represented by the shaded area *adef.* However, unlike the elastic response, only a small proportion of this energy is converted into kinetic energy (i.e. the area within *egf*), whereas the remainder of the energy (i.e. area *adeg*) is dissipated by the plastic hinge, in the form of heat and other forms of irrecoverable energy, as the system undergoes irreparable damage. In

other words, in elastic structures all the potential energy stored in a cycle is returned in the form of velocity energy to the next cycle, whereas in elasto-plastic structures some of the stored energy is dissipated before entry into the next cycle.

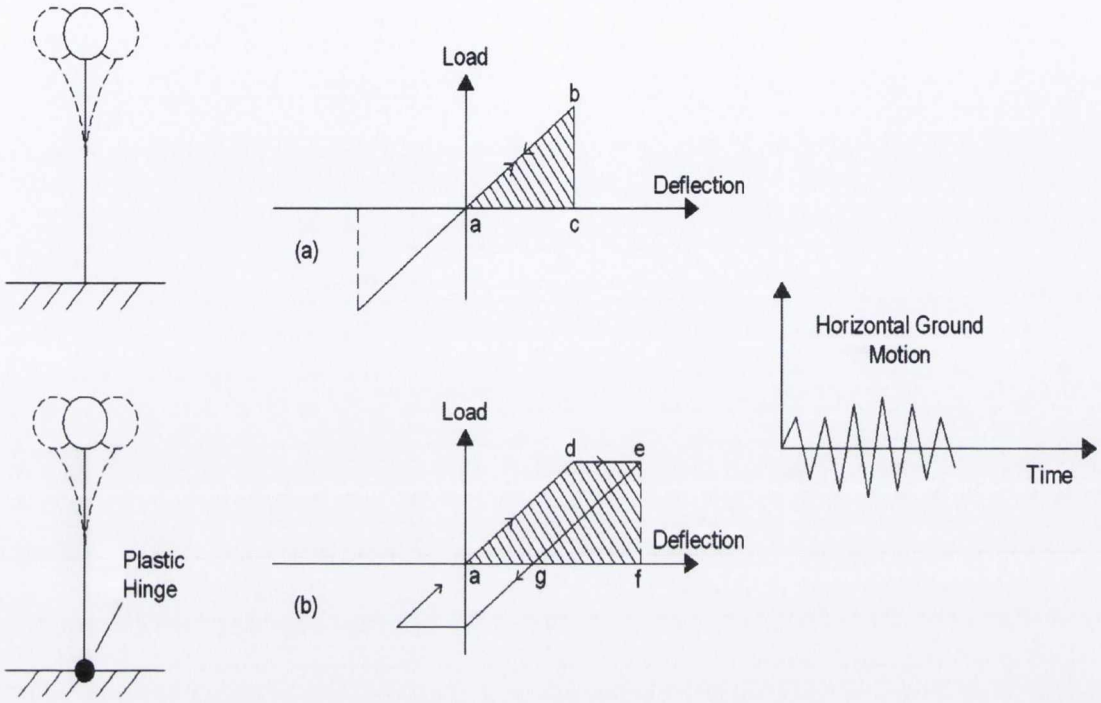

Figure 2.1: Response of Single Degree of Freedom Oscillator to Earthquake Motions, (a) Elastic Response, (b) Elasto-Plastic Response, Park *et al*, (1975).

2.4 Composite Construction for Earthquake Resistance

Under extreme loading situations, the performance of a structure is largely related to the inelastic behaviour of critical members and components. Structures subject to earthquake or other extreme conditions, i.e. severe impact, or explosions, are expected to undergo large deformations which are well in excess of those tolerated under normal loading conditions, all-the-while acting in a ductile rather than brittle manner, thus absorbing and dissipating the kinetic energy induced by the ground shaking via the formation of plastic hinges.

Concrete is a highly inelastic and non-linear material. It is not inherently ductile but instead acts in a brittle manner, providing little visual evidence before imminent failure, which is a direct contradiction to the requirements for a ductile structure suitable to resist earthquake loading. Mass concrete is hindered by its high mass-to-strength ratio

compared with steel. As earthquake loads arise from inertia effects, which are proportional to mass, bulky heavy members escalate the lateral loads applied to the structure.

Despite these disadvantages, if concrete is incorporated with steel sections and reinforcement to form a composite section, a highly ductile member with superior axial and bending capacity can be formed. The advantages of composite construction over reinforced concrete are as follows:

- Suitable detailed composite structures can possess superior ductility in bending, surpassing that of reinforced or mass concrete (Booth, 1994).
- Generally composite members have smaller cross-sections than alternative designs to sustain the same load, thus resulting in material savings and mass.
- Steel sections enhance confinement of concrete, and incorporated with properly detailed longitudinal and transverse reinforcement offer a section with good ductility in compression, with a lower tendency to buckling compared with a reinforced concrete section (Chen *et al,* 2004).
- Composite construction combines the formability and rigidity of reinforced concrete with the strength and speed of construction associated with structural steel to produce an economic structure (Griffis *et al,* 1986).
- Even after severe cracking of the concrete the steel section is capable of maintaining the applied loads, thus preventing sudden failure.
- The steel connections and members encased in concrete provide a monolithic structure that contributes to continuity of the structure, providing well defined and continuous load-paths, thus, increasing earthquake resistance (Booth, 1994).
- Concrete and steel are universally available and their construction technology is familiar. The steel can often also be used as permanent formwork and composite construction possesses good thermal and acoustic insulation and fireproof properties.

One noticeable disadvantage of composite construction is the need to provide shear connectors; this induces an additional material cost as well as necessitating the labour intensive process of welding the connectors.

2.4.1 Philosophy of Earthquake Resistance Design for Composite Structures

In order to minimise the risk of fatality in the event of an earthquake, structures may suffer structural damage but the prevention of structural collapse must be ensured. It is economically unfeasible to design a structure to withstand an earthquake without suffering post elastic damage (Housner *et al.*).

Seismic design philosophy sets out that the earthquake induced inertia loads for moderate earthquakes should not be so great so as to cause structural damage. Structures should behave in a elastic manner during moderate earthquakes, but are expected to suffer post-elastic deformations and damage when subject to severe earthquakes. The structure should be designed in such a manner that sufficient ductility is provided so as to prevent structural failure and loss of life even if the structure is damaged beyond its economic value.

Figure 2.2 illustrates the force required at identical deformations for an elastic and ductile member; it is evident that the development of plasticity in the ductile system limits the amount of force acting on the structure. Careful detailing is required to ensure the integrity of this system at large deformation.

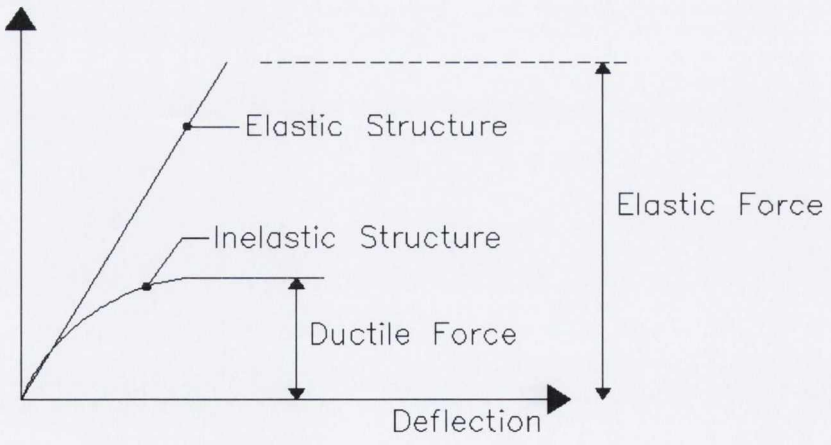

Figure 2.2: Forces in Ductile and Elastic Systems, Booth, (1994).

2.4.2 Capacity Design

The objective of capacity-based design is to create a load path, the strength of which is based on the strength that can be developed in the member or members from which post yield deformations are concentrated. A structural hierarchy of member strengths is adopted to ensure the development of the most appropriate plastic hinge mechanism in the event of a severe earthquake. The overriding objective in the design of frame columns is avoiding the formation of a storey mechanism. The most critical storey mechanism is the one created through the formation of plastic hinges in the top and bottom of all columns on a storey. The approaches to attaining this objective are many and still in, what might best be described as an evolving form. Eurocode 8, (CEN, 2004) adopts a capacity-based design approach, and it attempts to provide a reasonable safeguard against the formation of undesirable plastic hinges in the columns, as well as a methodology for avoiding unstable storey mechanisms.

The concept of '*capacity design*' was developed in New Zealand in the 1970s, (Mander *et al,* 1988), and since then has been adopted by design codes in many other seismic prone regions. Capacity design attempts to ensure a predictable structural response with inelastic deformations occurring at suitably designed members and member locations, all other members are over designed so as to concentrate the applied loads to the specifically designed members. Two sway-frame mechanisms exist, namely strong column/weak beam and weak column/strong beam. Both are compared to determine their merits when subject to seismic loading.

Strong column/weak beam methods over-design the vertical members (columns and walls) to remain elastic, with the exception of the base of the bottom storey. This method distributes all ductility demands to the beams. Both frame-mechanisms are illustrated in Figure 2.3. A '*weak storey*' frame-mechanism (Figure 2.3 (b)) suffers from a number of disadvantages which make it unsuitable for earthquake resistant design. In this mechanism the plastic hinges form in the columns and are formed in relatively few locations compared with the strong column/weak beam sway-mechanism, thus each hinge must dissipate a large amount of energy. This implies severe strength degradation of the columns and a reduction in their overall capacity to support gravity loads. In this mechanism $P - \Delta$ effects are also more severe.

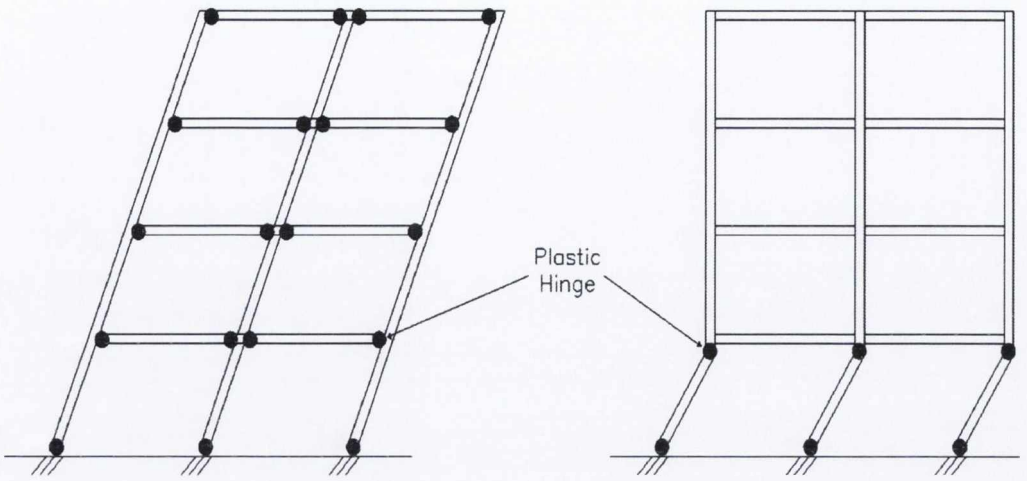

Strong Column/Weak Beam

Good Ductility

(a)

Weak Column/Strong Beam

("*Weak Storey*")

Poor Ductility

(b)

Figure 2.3: Multi-Storey Frames: (a) Strong Column/Weak Beam, (b) Weak Column/Strong Beam, Booth, (1994).

Beam failure is concentrated over a far less limited area due to the number of hinge locations, whereas column failure may be far more catastrophic resulting in subsequent loss of support to the floors above. Moreover, column failure is more likely to be governed by concrete strain than steel strain due to gravity-induced axial stresses. This is because columns experience compressive axial loads which results in columns having larger neutral axis depths than beams, which in turn means that the flexural capacity of the column is more dependent on the contribution of the concrete compressive stress distribution (Mander *et al,* 1988). Hence, the availability of rotational capacity is generally less (and brittleness greater) for this mechanism than for a strong column mechanism. This factor is more critical in reinforced concrete as the area of steel is significantly less than in composite cross sections, and in composite design the steel has a significant axial load capacity, often large enough carry the axial loads subsequent to concrete failure.

Plastic hinging of columns is inevitable during large earthquakes, particularly at the bases of columns in multi-storey frames. Often at this location plastic hinging is relied upon to permit energy dissipation (Park, 1992). Thus, the potential hinge regions in the

columns should be extensively detailed to enhance ductile behaviour. The detailing in the plastic hinge region is one of the key topics being researched in this thesis. Suitable detailing improves the ductility and energy dissipation of structural members, but the performance of confined HSC used in composite construction requires more research as with an increase in concrete strength an associated decrease in ductility is recorded. The ductility and detailing provisions of Eurocode 8, (CEN, 2004) are being assessed in this thesis incorporating normal and high-strength concrete (as additional detailing may be required to effectively confine the high-strength concrete).

Although based on a relatively straightforward philosophy, the application of capacity design is often complex and is made more complex when higher ductility capabilities are required. However, the fact that the design forces are almost inversely proportional to ductility is thought sufficient incentive for increasing ductility supply (Comité Euro-International du Béton, 1998). The advantages of limiting the magnitude of lateral forces are manifold:

- Foundation structures are lighter.
- Reduction of forces transmitted to the soil, thus reduces the likelihood of permanent soil deformations.
- The maximum response accelerations of the structure are reduced, thus minimising the potential damage to sensitive equipment mounted on the structure.

The "Comité Euro-International du Béton, (1998)" states that, *"ductility is the most effective defence against unanticipated and unfavourable characteristics of ground shaking"*.

Most modern design codes specify different combinations of strength and ductility based on prior experience and experimental research and testing. Four world regions, each with codes dealing with capacity design can be identified: Europe, America, Japan and New Zealand (EC8, 1998, ACI, 1992, AIJ, 1990 and NZ, 1995, respectively). The "Comité Euro-International du Béton, (1998)" declares that, the aim of these codes are *"to control the behaviour of a structure acted upon by a ground motion of very variable and*

unpredictable characteristics, intense enough to bring the structure close to, but not beyond, the exhaustion of its inelastic capacity".

All the codes adopt the capacity-based approach by ensuring adequate availability of ductility in specially designed members, thus ensuring sufficient energy dissipation. All other vertical members are suitably over-designed to ensure post-elastic yielding in the designated members and to avoid premature failure.

2.5 Eurocode 8

Eurocode 8, (CEN, 2004) applies to the design and construction of buildings and civil engineering works in seismic regions. Its purpose is to ensure that in the event of earthquakes:

- Human lives are protected.
- Damage is limited.
- Structures important for civil protection remain operational.

The research conducted within this thesis is confined by the design limitations of Eurocode 8, (CEN, 2004) and is primarily focused on determining the performance and damage experienced by HSC composite columns while subject to earthquakes.

2.5.1 Composite Construction Design Concepts

Eurocode 8 (CEN, 2004) defines capacity based design as *a "design method in which elements of the structural system are chosen and suitably designed and detailed for energy dissipation under severe deformations while all other structural elements are provided with sufficient strength so that the chosen means of energy dissipation can be maintained".*

Three design concepts are proposed by Eurocode 8, (CEN, 2004), all earthquake resistant composite buildings shall be designed in accordance with one of the following design concepts:

- *Concept 'A'*: Low-dissipative structural behaviour.
- *Concept 'B'*: Dissipative structural behaviour with composite dissipative zones;
- *Concept 'C'*: Dissipative structural behaviour with steel dissipative zones.

Table 1: Design Concepts, Structural Ductility Classes and Upper Limit of Reference Values of the Behaviour Factors Structural, Eurocode 8 (CEN, 2004).

Design Concept	*Structural Ductility Class*	*Range of the reference values of the behaviour factor, q*
Concept 'A': Low-dissipative structural behaviour	DCL (Low)	≤1.5 - 2
Concepts 'B' or 'C': Dissipative structural behaviour	DCM (Medium)	≤4 also limited by the values of Table 7.2, Eurocode 8, (CEN, 2004)
	DCH (High)	Only limited by the values of Table 7.2, Eurocode 8, (CEN, 2004)

Dissipate zones of a composite structure must be capable of resisting earthquake actions via large inelastic deformations at pre-defined plastic hinge locations. Concept 'A' specifies that the structure is to have low-dissipative behaviour, thus remain in the elastic range of the material properties, this is difficult and expensive to achieve thus it is rarely selected for a structure designed to resist earthquakes unless it is of significant importance (i.e. hospital) and has to remain functional at all times.

Concepts 'B' and 'C' rely on the development of reliable local plastic mechanisms (dissipative zones) in the structure such that as much energy as possible can be dissipated under the design earthquake action. Eurocode 8, (CEN, 2004) sets out specific rules for each ductility class so that each structural element relating to a specific design concept can adequately be designed to resist and dissipate the applied loads while avoiding ultimate failure at all times.

The design rules for concept 'B' are being used for the composite column design in this research. The aim is to determine if HSC can achieve the required displacement ductility set out by Eurocode 8, (CEN, 2004) for a highly dissipative structure. Furthermore, the research aims to determine if HSC can achieve a similar load-displacement response to

NSC using the existing design provisions, and if not, to suggest some recommendations to improve the response of a HSC composite column subject to combined axial and lateral cyclic loading.

Capacity design generally dominates the response of structures which rely heavily on the development of inelastic deformations to ensure a satisfactory seismic performance, thus is the case within Eurocode 8, (CEN, 2004) for highly ductile (DCH) frames. By contrast, structures designed for higher seismic forces, which are not required to develop significant inelastic deformations, are much less controlled by capacity design concepts; this is the case for low ductility (DCL) frames.

2.6 Concrete Confinement

Confinement is a means of increasing the maximum compressive strength of concrete by laterally restraining it from lateral expansion under compressive loading. This is achieved by imposing a lateral restraint in the form of a reinforcing cage, steel shell or fibre reinforced polymer (FRP) fabrics. This form of confinement is known as "passive confinement", the confining effect is initiated by the lateral expansion of the concrete and the confining pressure gradually increases as the concrete continues to expand.

Confinement, if suitably designed, prevents premature buckling of the compressed longitudinal reinforcement, acts as shear reinforcement and most importantly in the case of seismic design imparts additional ductile capacity to structural members.

2.6.1 Introduction

Unreinforced concrete behaves as a brittle material under loading, in essence the converse property required for seismic design, but adequately designed confining reinforcement improves the deformability of concrete. Confinement enables concrete to achieve a higher longitudinal strain at maximum compressive loading and can display a shallower post yield stress-strain slope, thus minimising strength decay after the concrete has achieved its maximum capacity. This is the quintessential requirement for seismic design as it prohibits brittle failure and unforeseen collapse.

Unreinforced concrete subject to longitudinal compressive loading is in a uni-axial state of stress. The compressive loading generates longitudinal strains that give rise to transverse tensile strains, which result in dilation of the concrete. As the compressive load increases towards the concretes maximum strength, the maximum longitudinal and transverse strains reach their limiting value and the concrete fails. However, much research has been conducted to prove that lateral confinement can greatly increase the ultimate strength and ductility of reinforced concrete subject to axial compressive loading.

Richart *et al,* (1929) concluded that laterally restrained concrete could achieve a noticeably higher strength than that of an unconfined specimen. He stated that the strength of the laterally confined concrete is the sum of the uni-axial compressive strength of concrete plus an added strength, which is a function of the lateral confinement. Richart *et al,* (1928) conducted a comprehensive series of experiments to determine the relationship between confinement and the additional strength achieved as a result. A fluid pressure was applied to the sides of the test cylinders to simulate confinement; an axial load was applied to the top of the specimen. The tests clearly identified an increase in ultimate strength and exhibited large deformations. Richart *et al,* (1928) adopted the following relationship,

$$f'_{cc} = f'_c + 4.1 f_l \tag{2.1}$$

Where:

f'_{cc} = The confined concrete compressive stress (N/mm^2).

f'_c = The uni-axial compressive strength of concrete (N/mm^2).

f'_l = The confining lateral stress applied to the concrete (N/mm^2).

The stress-strain curves for confined and unconfined curves are similar up until the cylinder strength is achieved, after this point the confined specimen exhibits a higher strain capacity, enhanced ultimate strength and shallower descending stress-strain slope. Figure 2.4 illustrates the stress-strain curves obtained by Lu *et al,* (2007), for a series of high-strength concrete cylinders confined by a range of lateral fluid pressures.

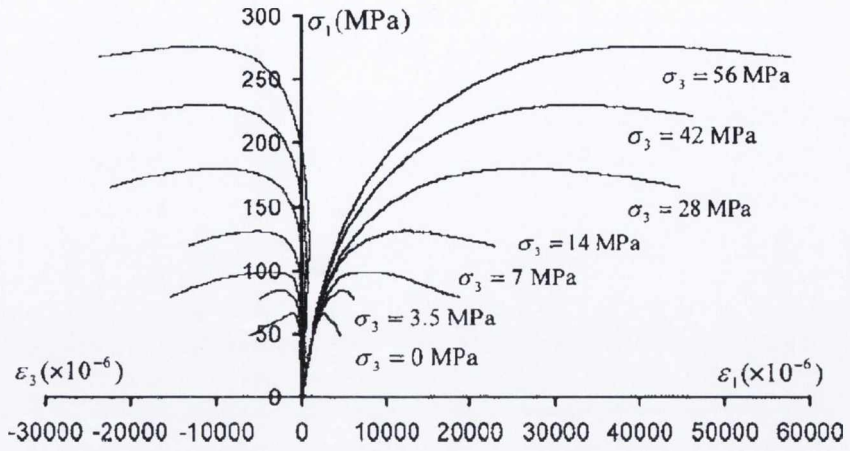

Figure 2.4: Axial Stress-Strain Curves from Tri-axial Compression Tests on Concrete Cylinders, Lu *et al,* (2007).

Early research on confined reinforced concrete behaviour was generally carried out on small scale concentrically loaded specimens, often with no cover or longitudinal reinforcement, at quasi-static rates of strain. Roy and Sozen's, (1964) tests indicated that no significant increase in concrete strength could be achieved by rectangular confining reinforcement, but a substantial increase in ductility could be achieved, i.e. a significant shift in the position of the longitudinal compressive strain at maximum compressive stress. Subsequent work conducted by Vallenas, Bertero and Popov, (1977), Sheikh and Uzumeri, (1980) and Scott, Park and Priestley, (1982) which tested more realistic specimens, based on those of scaled versions of actual building columns indicate that a noticeable increase in ultimate strength and ductility could be achieved by confining the specimens with rectilinear and octagonal shaped transverse reinforcement.

Reinforcement of this nature acts as "passive confinement", because it only becomes effective once the concrete approaches its unconfined compressive yield stress. At this point the internal stresses cause the concrete to crack internally and dilate, thus imposing a lateral force against the confining reinforcement. The transverse reinforcement reacts by imposing an inward confining force on the concrete.

A vast amount of research has been carried out to determine the most effective configuration of transverse steel in order to maximise the confining effect. Circular spirals are widely accepted as being the most effective method of confining concrete

(while still remaining practical), but despite their superior confinement effectiveness, rectilinear transverse links are still adopted, simply due to their ease of design, detailing and fabrication. Circular or curved structural sections require more detailing and are far more expensive to fabricate than squared sections, despite their advantages in relation to confinement. Simply put, the confinement and additional ductility achieved through rectilinear transverse reinforcement is substantial enough in terms of cost effectiveness to outweigh the additional benefits of adopting circular or spiralled reinforcement.

Booth, (1994) illustrates the confinement effect of circular and rectilinear transverse reinforcement in circular and rectangular columns respectively; the shaded area represents the confined concrete. Figure 2.5 shows how the location of the reinforcement effects the concrete confinement, the circular hoops are continually in a state of hoop tension, thus provide a constant confining pressure to all the internal concrete, at large transverse strains this approximates fluid confinement. The rectilinear link can only effectively confine the concrete at its corners, or locations of longitudinal steel (which restrain the link from arching out from the concrete core at this location). Between the corners the link has insufficient flexural stiffness to restrain the dilating concrete core. This causes the link to bend outwards (internal arching), thus rendering a large portion of the concrete cross-section unconfined, thus leaving only the central core and corners effectively confined as depicted in Sections A – A and B – B in Figure 2.5. The confining reaction from the rectilinear links comes from the longitudinal bars at positions where they are restrained by the links.

Some research has been conducted to determine the amount of arching occurring in order to determine the level of lost confinement and a number of models have been proposed. Experiments conducted by Sheikh and Uzumeri, (1980) and later refined by Mander *et al*, (1988) adopt a style of concrete arching in the form of a second-degree parabola with an initial slope of 45°. Experiments conducted by Campione, (2001) suggest that the presence of transverse reinforcement with rounded corners produces a further effective confinement area with respect to that of a perfectly square section. This is consistent with the model adopted by Booth, (1994) except for the exclusion of the longitudinal steel and adopted transverse steel with rounded corners, similar to Section A – A of Figure 2.5 for the rectangular column.

Mirza and Tikka, (1999) ignored parabolic arching between longitudinal bars for the purpose of modelling, but specified the boundary between the regions of highly and partially confined concrete; a parabolic arch was assumed to differentiate the boundary

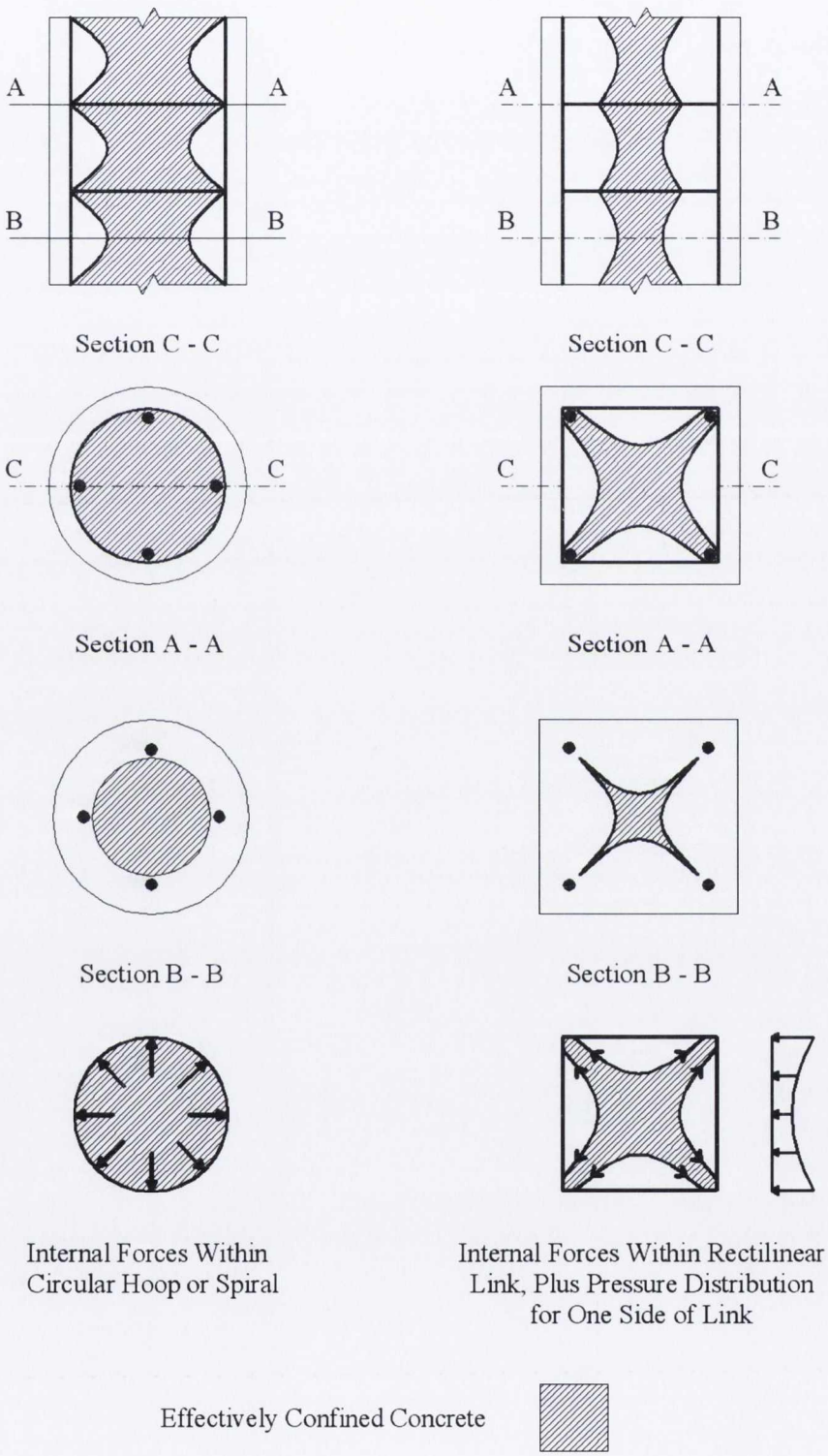

Figure 2.5: Circular and Rectilinear Sections Confined by Circular and Rectilinear Links Respectively – Areas of Effectively Confined Concrete and Internal Forces, Booth, (1994).

within the composite cross section. Chen and Lin, (2006) adopt Mander's, (Mander *et al,* 1988) parabolic arching approach for the partially and unconfined concrete interface and adopt a similar second-order parabolic arch for the highly and partially confined concrete interface. Minor adaptations and simplified versions of this form of arching have been implemented by Mirza and Skrabek, (1992) and El-Tawil and Deierlein, (1999).

2.6.2 Factors Influencing Confinement Effectiveness

Several variables effect concrete confinement, some of which are more prominent than others. The following is a list of such factors, which are separately analysed in the proceeding sections. As confinement from lateral reinforcement and structural sections only effectively takes place once the concrete approaches its yield strength, the concrete-strain curve displays little difference between the unconfined and confined ascending branch until the uni-axial compressive strength is approached, Figure 2.6 illustrates this phenomenon. Some of the factors below are more relevant for reinforced concrete sections rather than encased composite sections, due to the high quantity of structural steel compared to reinforcing steel in the composite members. Nevertheless, all factors shall be discusses in relation to a reinforced and encased composite cross section for completeness.

Factors Influencing Confinement Effectiveness:

- The ratio of the volume of transverse steel to the volume of the concrete core.
- Spacing of the transverse steel with respect to the dimensions of the concrete core.
- Reinforcement configuration.
- Yield strength of the transverse steel.
- Flexural stiffness of the transverse steel.
- Longitudinal steel behaviour.
- Yield strength of structural steel sections.
- Structural steel configuration.
- Concrete compressive strength, particularly with respect to HSC.
- Axial load level.
- Rate of loading.

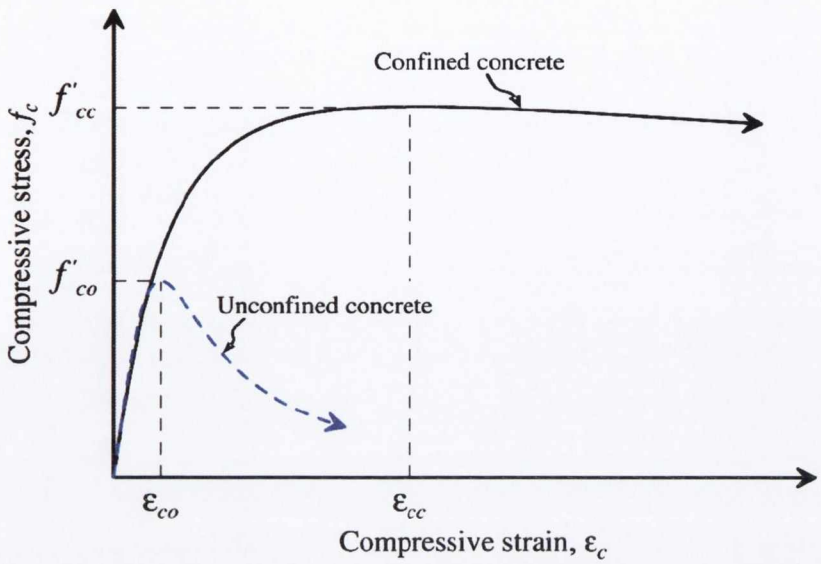

Figure 2.6: Confined and Unconfined Concrete Stress-Strain Curve, Chen *et al,* (2006).

2.6.2.1 Transverse Steel Content

For reinforced concrete sections this is the principal factor in determining the effectiveness of concrete confinement, once the transverse reinforcement is deemed to have failed, the confined core is free to further dilate and crush, thus failure of the member. For a composite member, failure of the transverse steel enables the partially confined concrete to fail but the inner core of the section enclosed by the structural steel is still effectively confined and capable of withstanding the applied loads up to a higher stress level. Thus, this parameter is not as crucial as the structural steel yield strength for composite cross sections.

Transverse confining steel can be considered in terms of (a) the volumetric ratio (the ratio of the volume of transverse steel to the volume of the confined concrete core) and (b) the transverse steel spacing. A close correlation exists between the two, but both need to be clearly distinguished for clarity. A high transverse volumetric ratio does not necessarily imply a close link spacing as it depends on the transverse bar diameter as well as the links spacing, as Equation (2.2) illustrates.

$$\rho_s = \frac{A_{sp}\,\pi\,d_s}{\pi/_4\; d_s^2 s} \tag{2.2}$$

Where:

A_{sp} = Area of transverse reinforcing bar (mm^2)

d_s = Diameter of transverse link (mm)

s = Transverse link spacing (mm)

High volumetric ratios imply an increase in the passive confinement pressure, thus increasing the strength of the confined concrete and overall ductility of the section. Close link spacing affects the confinement pressure distribution; closer link spacing confines a greater proportion of the enclosed concrete as smaller parabolic arching is achieved between the links, as discussed earlier in the chapter.

The effects of volumetric ratio and link spacing for reinforced concrete specimens is widely publicised and an agreement that both smaller link spacings and an increased volumetric ratio contribute to an increase in peak stress, strain at peak stress, fracture strain and a decrease in the descending slope of the stress-strain curve, (Mander *et al,* 1988, and Razvi *et al,* 1996). The above effects have also been scrutinised incorporating high strength concrete (HSC). Cusson *et al,* (1995) tested twenty seven full scale reinforced HSC specimens with a variety of reinforcement configurations and yield stresses, link spacings and volumetric ratios. The experimental programme supports the conclusions established from research with normal strength concrete (NSC) specimens.

Among the publicised findings for smaller tie spacings was the increase in confined concrete area and resulting confinement efficiency. Figure 2.7 illustrates the benefits of smaller link spacing in reinforced concrete cross sections subject to monotonic axial compression. The decreased tie spacing also increased the strain levels at which the longitudinal bars buckled. Cusson *et al,* (1995) noted that greater amounts of longitudinal reinforcement prevented premature buckling of the longitudinal reinforcement and certain reinforcement details enhance the potential strength and toughness gains for higher volumetric ratios as is shown in Figure 2.8.

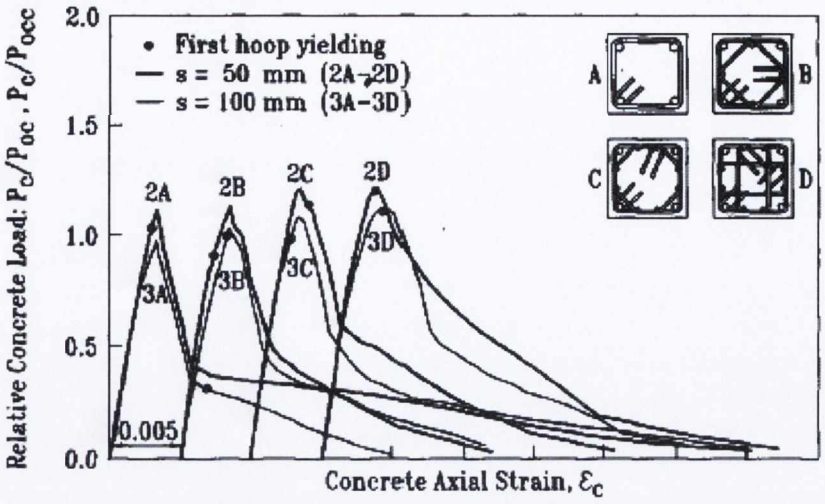

Figure 2.7: Effects of Tie Spacing for Reinforced Concrete Sections, Cusson *et al,* (1995).

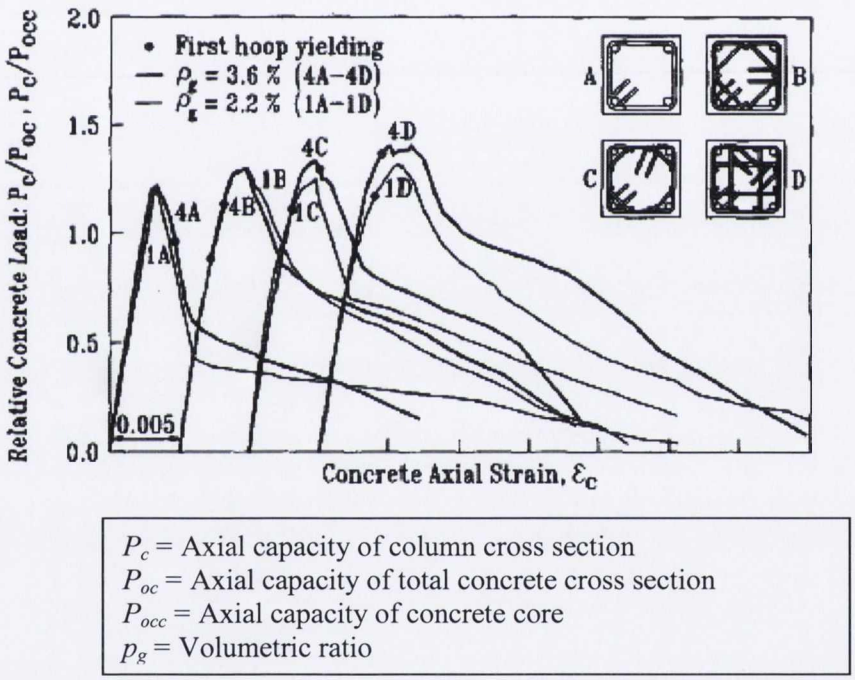

P_c = Axial capacity of column cross section
P_{oc} = Axial capacity of total concrete cross section
P_{occ} = Axial capacity of concrete core
p_g = Volumetric ratio

Figure 2.8: Effects of Volumetric Ratio for Reinforced Concrete Sections, Cusson *et al,* (1995).

Tie spacing and volumetric effects have been extensively researched for reinforced concrete sections while subject to axial compressive and flexural loading. Sheikh *et al,* (1994), Bayrak *et al,* (1998), Légeron *et al,* (2000) all examined the above effects. Sheikh *et al,* (1994) and Bayrak *et al,* (1998) both concluded that noticeable improvements in energy dissipation and ductility could be achieved due to an increase in

the transverse steel content. The research was conducted incorporating normal, high and ultra high strength concrete with all strength classes achieving the same conclusions.

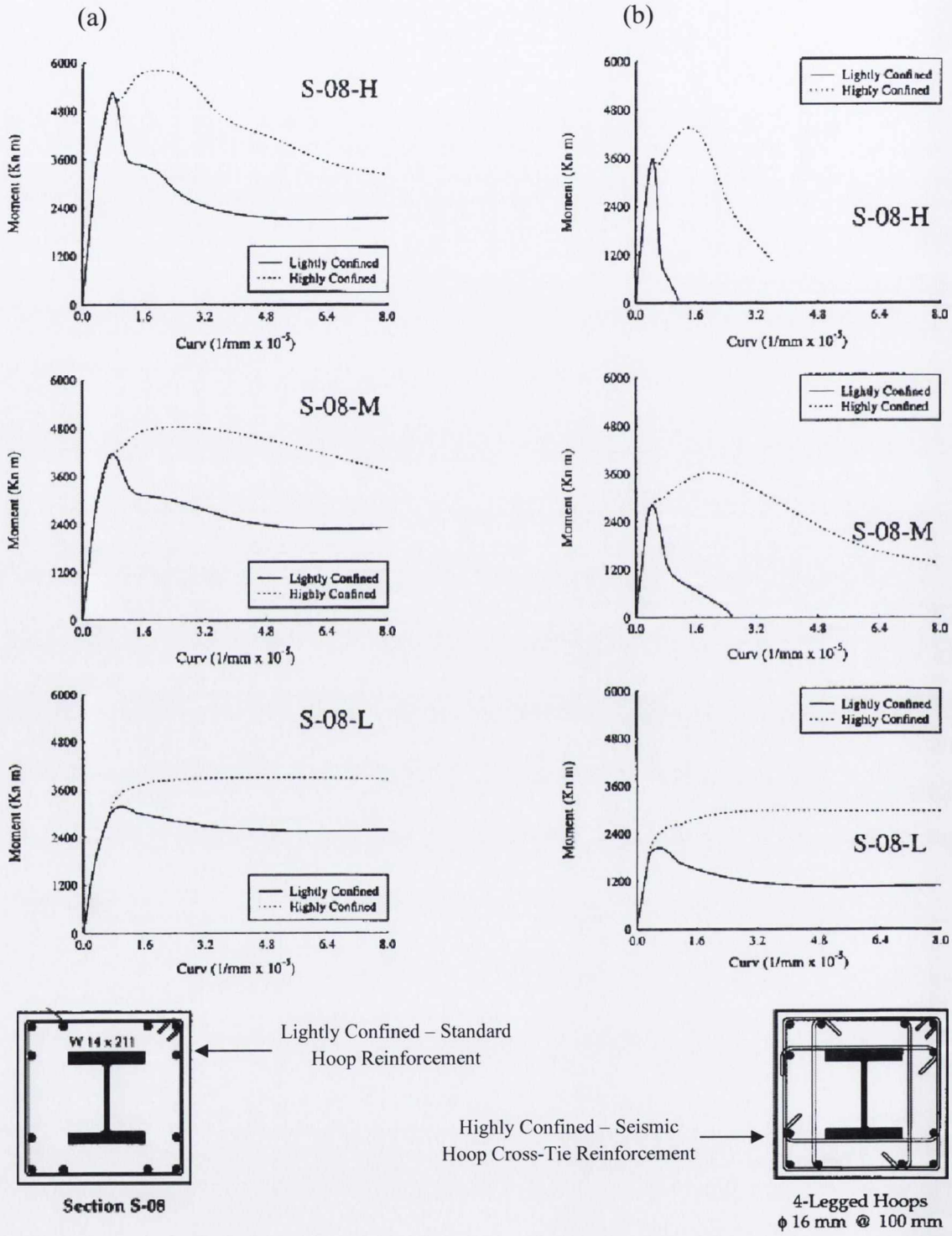

Figure 2.9: Influence of Steel Volumetric Ratio for Composite Columns Subject to Axial Load Levels of: (a) $0.3P_o$ and (b) $0.6P_o$, El-Tawil *et al,* (1999).

Légeron *et al,* (2000) concentrated on the volumetric ratio and axial effects on the cyclic behaviour of reinforced columns. The test series concluded that higher volumetric ratios enabled the formation of larger cyclic displacements in the inelastic range. They concluded that, while axial load is an important parameter, the volumetric ratio of confining steel is the main parameter in controlling the column response. A similar research programme was conducted by El-Tawil *et al,* (1999), except on composite cross sections.

The experimental work tested composite columns with standard reinforcement and seismic hoop reinforcement details. The hoops provide an increase in the volumetric ratio and provide additional confinement to the partially confined concrete. Figure 2.9 (a) clearly illustrates the benefits of an increased volumetric ratio compared with a standard composite reinforcement detail for high, medium and low strength concrete at an axial load level of 30% of the squash load. The tests conducted are also subject to a variety of axial loads; Figure 2.9 (b) shows the effects of identical sections subject to a far higher axial load (60% squash load). These tests furthermore prove the benefits of increased volumetric ratios at all concrete strength grades.

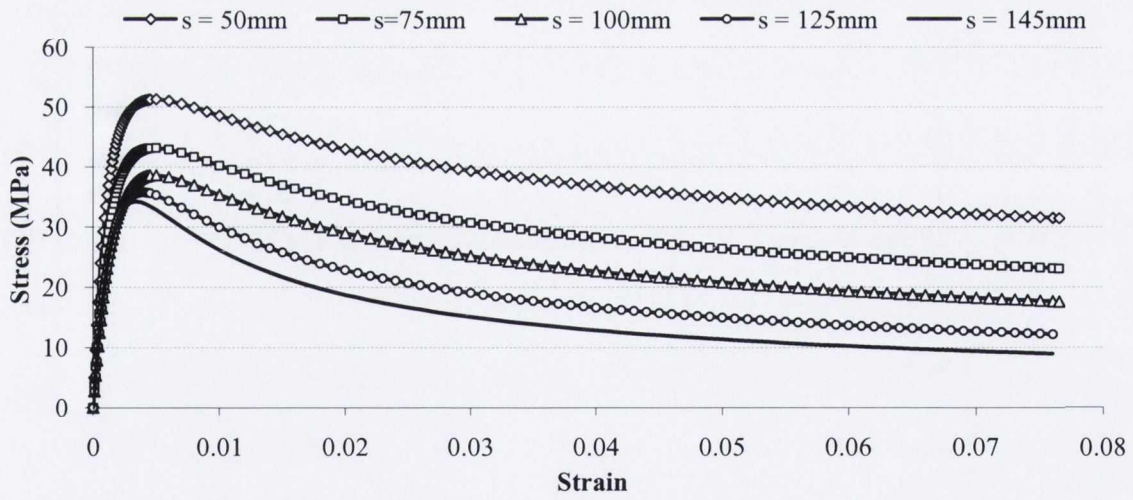

Figure 2.10: Stress-Strain Effects of Varied Link Spacing on Reinforced Concrete Columns Subject to Uni-Axial Compression.

Analysis conducted by the author as shown in Figure 2.10 illustrated the benefits of increased transverse steel content, in this case the link spacing has been reduced in order to provide enhanced confinement to the concrete core and prohibit the buckling of the longitudinal bars at higher strains. It is evident that minor reductions in link spacing can

lead to an increased confined concrete strength and shallower slope in the descending branch of the stress strain curve.

Sheikh *et al,* (1994) analysed the effects of varied transverse steel contents in HSC reinforced columns subject to cyclic loading conditions. Their conclusions were as evident as tests on uni-axial compressive tests. Figure 2.11 presents the load-displacement hysteresis curves for two near identical specimens with different volumetric ratios.

It is clear from the curves that the specimen with greater quantities of transverse reinforcement far out-performs the specimen with a lower volumetric ratio, larger areas within the hysteresis loops are evident as well as greater lateral displacement and peak values are achieved. Similar experimental conclusions could be drawn from that of composite specimens, but it may not be as evident, as the high quantity of steel in the encased section could make small volumetric changes to the transverse steel hard to differentiate in the hysteresis response.

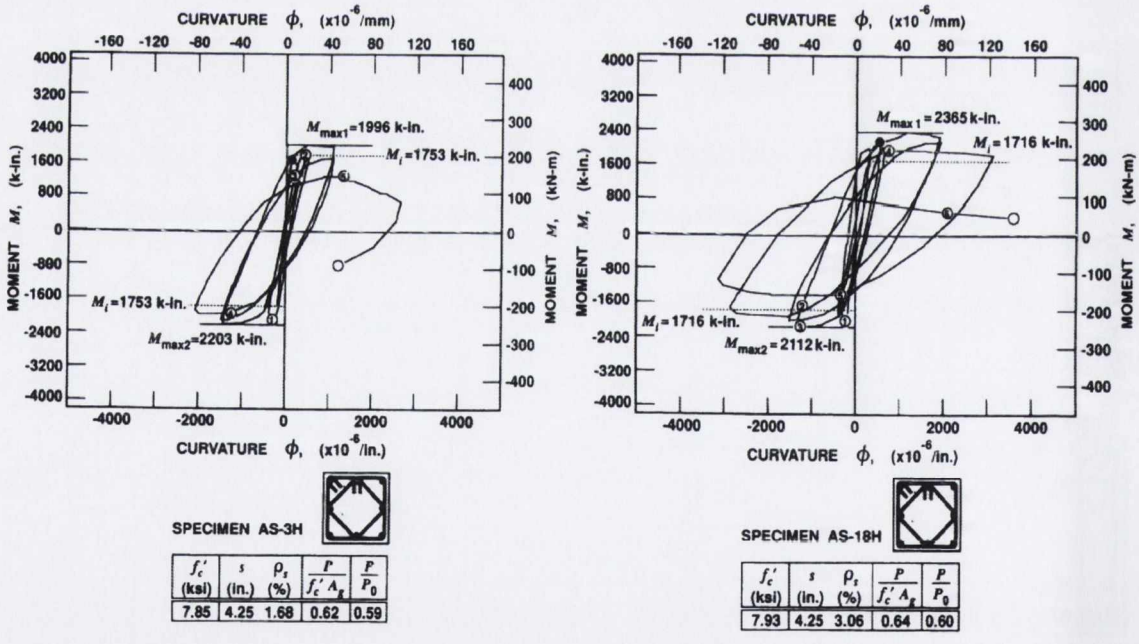

Figure 2.11: Reinforced Concrete Specimen Behaviour with Varied Volumetric Ratios, Sheikh *et al,* (1994).

Chen *et al,* (2006) conducted a series of experimental tests to determine the effects of varied link spacing and structural steel shapes on the confinement of concrete subject to

uni-axial compression. Figure 2.12 presents the experimental results from these tests, it is evident that the link spacing has little effect on the yield stress or strain of the section, but smaller spacings do lead to a significantly shallower post yield descending branch of the stress-strain curve.

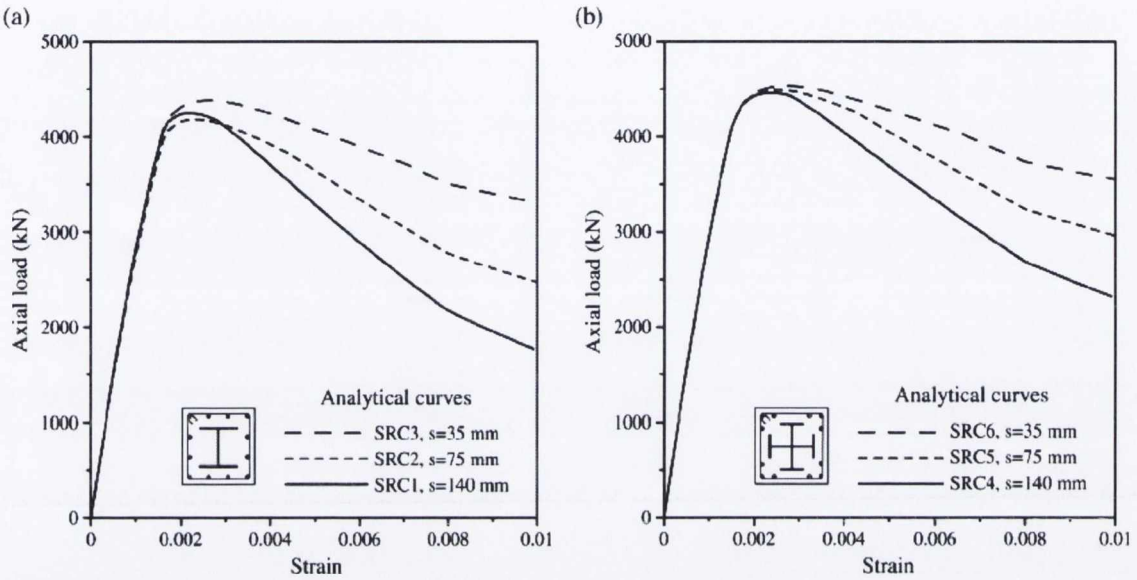

Figure 2.12: Effect of Tie Spacing on Axial Load–Strain Curves: (a) H-Shaped Steel Section; (b) Cross-Shaped Steel Section, Chen *et al,* (2006).

2.6.2.2 Reinforcement Configuration

Several reinforcement configurations have been proposed, tested and used in reinforced concrete columns. The primary function of the different configurations is to provide additional and prolonged confinement to the concrete core by means of effectively restraining the longitudinal steel from buckling prematurely. This is achieved by means of internal links, cross-ties, and hook angles. It is essential that these internal ties are effectively restrained and support the longitudinal steel to be effective. A vast amount of research has been conducted in this area (Sheikh *et al,* 1980, Cusson *et al,* 1995, Bayrak *et al,* 1998, and Razvi *et al,* 1996). All researchers conducted varied tests with different arrangements performing better than others. Ryan, (2001) reported in depth on their research (and others) and is a good reference for all their findings, as this is such a vast topic in its self and while not directly related to this research it shall not be discussed any further with respect to reinforced concrete sections.

Far less research has been carried out into the influence of reinforcement configurations in composite cross sections because the structural steel is far superior for confining the

inner concrete core and even after the lateral and longitudinal steel has failed, the steel section continues to confine the inner core to higher strains. Another major issue regarding the use of reinforcement configurations for composite sections is the general lack of free space within the cross section. Designers will tend to minimise the amount of cover concrete between the external face and steel flange extremes so as to maximise the work done by the steel section under lateral displacement, thus reducing the neutral axis depth and permitting the use of a smaller section. Cost and site fabrication and erection is another major issue and the benefits need to be carefully weighed up comparing the advantages of minor additional confinement against high potential erection costs. Figure 2.13 presents this phenomenon, where a large area of partially confined concrete is highly stressed. A larger steel section would reduce the neutral axis depth and place larger stresses into the steel which is generally superior at distributing the applied loads.

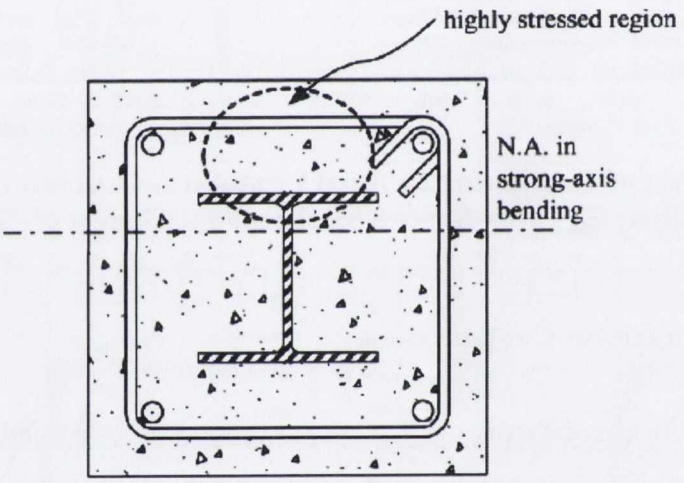

Figure 2.13 Typical Fully-Encased Composite Column Cross Section

Despite these issues some research has been conducted to assess the effectiveness of the layout of transverse reinforcement in order to confine the concrete core which confines the encased steel section, (Ricles *et al,* 1994 and El-Tawil *et al,* 1999). Figure 2.9 (a) and (b) clearly illustrates the advantage of cross tie reinforcement configurations at all levels of post sectional yielding. This configuration requires far more detailing and erection time than the octagonal configuration adopted by Ricles *et al,* (1994). This arrangement as illustrated in detail A and C in Figure 2.14 provides only minor additional confinement, concentrated primarily at the section corners. The major advantage of this configuration is the superior restraint provided to the longitudinal bars, the angular

restraint provided by the square and octagonal links prohibits rounding and buckling of intermediate longitudinal bars at higher strains compared with traditional rectilinear links alone.

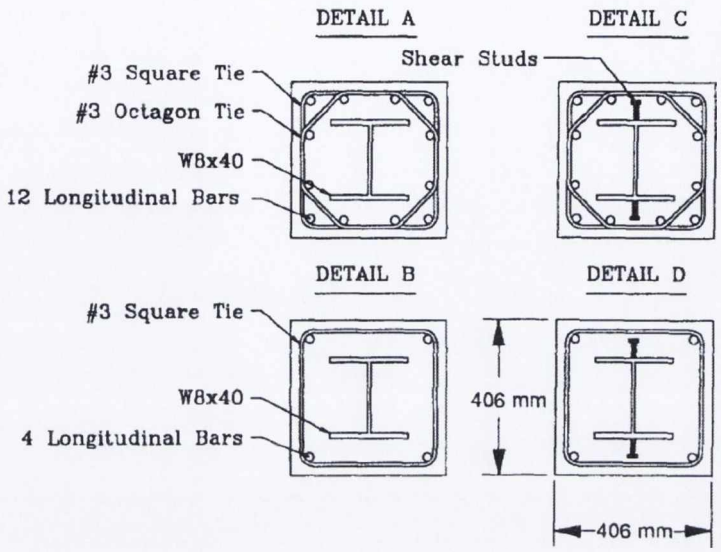

Figure 2.14: Cross-Section and Transverse Reinforcement Details, Ricles *et al,* (1994).

2.6.2.3 Transverse Steel Yield Strength

As previously discussed; transverse steel confines the core concrete, thus enabling it to achieve a higher compressive stress than unconfined concrete. The yield strength of the reinforcement is a critical factor as the higher the yield strength the greater the confinement pressure applied to the core and, hence, the higher the confinement efficiency. As with the transverse steel content and lateral steel configuration, the transverse steel yield strength is more critical in reinforced concrete sections than in composite sections as the steel section has load carrying and confinement capabilities beyond yielding of the transverse steel. In a reinforced section beyond the steel yield, the concrete core losses its confinement and the concrete is free to dilate and fail at lower compressive loads, thus failure of the section is reached.

Higher strength steel can be used as an alternative to a high volumetric ratio, without having a detrimental effect on the member behaviour. Hwang *et al,* (2004) conducted an experimental investigation to determine the behaviour of reinforced HSC columns with various volumetric ratios and varied transverse yield strength. The experimental results indicate that increasing the yield strength of the transverse reinforcement had little

influence on either the curvature ductility or the normalised dissipated energy. This is due to the fact that the yield stress was not achieved in the higher strength transverse reinforcement before longitudinal bar buckling, thus the higher strength steel becomes ineffective as the higher stresses cannot be achieved. Cusson *et al,* (1994) came to the same conclusion in their similar testing regime and Figure 2.15 clearly illustrates this phenomenon. Table 2 is an extract of the findings comparing the performance of both transverse steel grades.

Table 2: Effects of Transverse Steel Yield Strength, Hwang *et al,* (2004)

Group number	Specimen	S (mm)	Detail	$\frac{\rho_s}{\rho_{(ACI)}}$	f_{yh} (MPa)	Δ_2 (mm)	Φ_2 ($\times 10^{-4}$ rad/mm)	$\mu_{\Delta u} = \frac{\Delta_2}{\Delta_{yi}}$	$\mu_{\varphi u} = \frac{\Phi_2}{\Phi_{yi}}$	E_N
1	C-A	40	C	1.42	779	9.88	1.50	3.69	15.0	9.5
	L-C-S	40	C	1.00	549	9.66	1.96	3.64	14.7	10.0
2	D-A	46	D	1.42	779	12.07	2.38	4.38	17.8	9.6
	L-D-S	46	D	1.00	549	10.10	2.10	3.70	15.0	11.4

Hwang *et al,* (2004) also states that the use of high strength transverse steel could be used in HSC columns with larger link spacing. However, it is reported that one should be careful in using this approach as is evident in their experimental programme where one specimen with a smaller link spacing and lower transverse steel strength out-performed and produced a higher ductility than a specimen with higher yield strength and larger link spacing, it needs to be noted that both specimens had 100% of the required areas of transverse reinforcement, but the larger link spacing permitted the longitudinal bars to buckle prematurely.

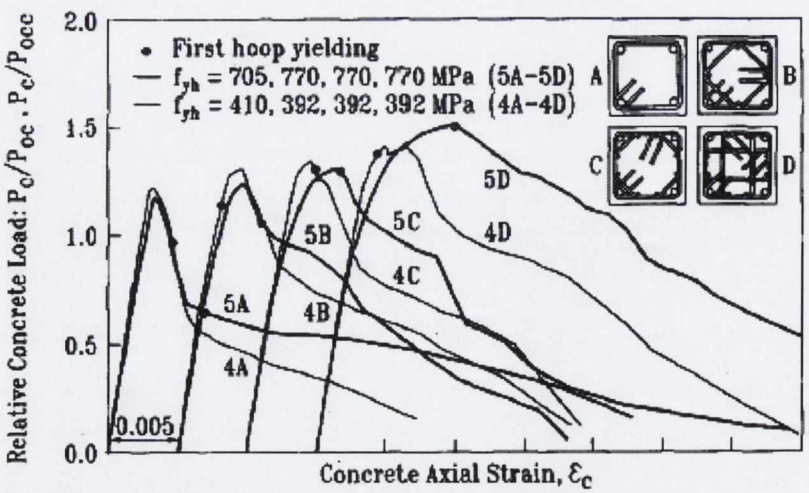

Figure 2.15: Effects of Transverse Steel Yield Strength, Cusson *et al,* (1994)

Cusson *et al,* (1994) reported that only in well confined columns with small link spacings, where the high strength transverse reinforcement was able to reach its yield strength, was a significant increase in strength and especially ductility achieved. This finding was supported by the experimental conclusions of Saatcioglu *et al,* (1998). Subsequent work conducted by Saatcioglu *et al,* (1999) on circular high strength concrete columns subject to simulated seismic loading proves that with careful detailing and small link spacing, high strength transverse reinforcement can significantly outperform a specimen with lower yield strength even if it has a higher volumetric ratio than the high strength specimen. Figure 2.16 is an extract of the load-displacement curves from this test regime.

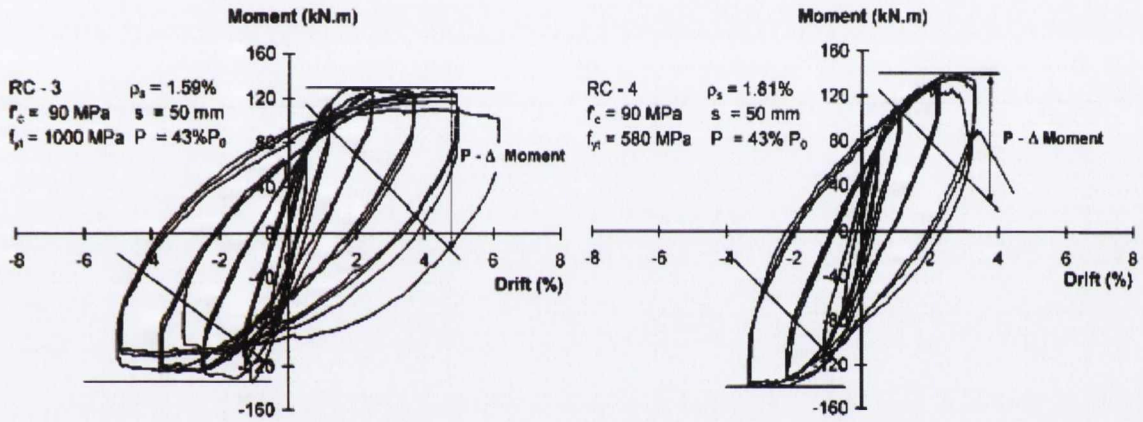

Figure 2.16: Influence of Well Confined High-Strength Transverse Reinforcement, Saatcioglu *et al,* (1998)

Hong *et al,* (2006) conducted similar tests on high strength concrete columns confined by low volumetric lateral ties. The study concludes that the upper limit of the lateral confining pressure applied to the concrete core can be determined using the yield strength of the lateral ties. Higher confining pressure applied to the concrete core would result in better confinement efficiency. However, for all specimens, no increase in strength enhancement or strain corresponding to the peak strength is displayed when the tie yield strength is increased from 379 MPa to 1420 MPa. This is because, when higher-grade ties are used, the stress in the lateral tie at the concrete peak strength is less than 50% of the tie yield strength. From this result, it is noted that an increase of lateral tie grade cannot compensate for the proportional reduction in the volumetric ratio for poorly confined columns such as the specimens used in this study. This is consistent with the

findings of Hwang *et al,* (2004) and Cusson *et al,* (1994). Figure 2.17 presents the findings of Hong *et al,* (2006).

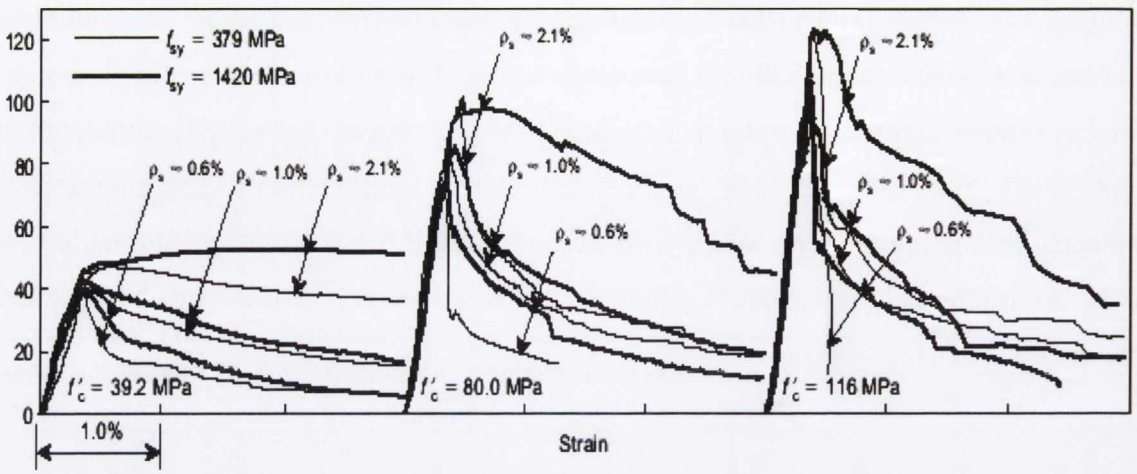

Figure 2.17: Effect of Tie Yield Strength, f_{sy} on the Stress–Strain Curve, Hong *et al,* (2006).

The reason that the confinement effect is not proportionally developed with increasing lateral tie yield strength can be explained by Figure 2.18, the experimental data from Hong, Han and Yi, (2006) is included in this graph for completeness. The graph presents the value $f_{s,exp} / f_{sy}$ as a function of the tie yield strength, where $f_{s,exp}$ is the stress in lateral ties at the concrete peak strength obtained using an average of measurements from strain gauges. It is evident that: (a) when f_{sy} is 317 and 379 MPa (with the exception of specimens having a concrete compressive strength of approximately 120 MPa), the lateral tie yields at the concrete peak strength or shortly after; and (b) when f_{sy} is 1028, 1288 and 1420 MPa, $f_{s,exp} / f_{sy}$ is lesser than or equal to 0.3 and the lateral tie does not yield in any of the specimen groups. It is evident from this graph that if the concrete confining pressure is calculated based on the tie yield strength for HSC it will be grossly overestimated, thus caution must be taken in this instance.

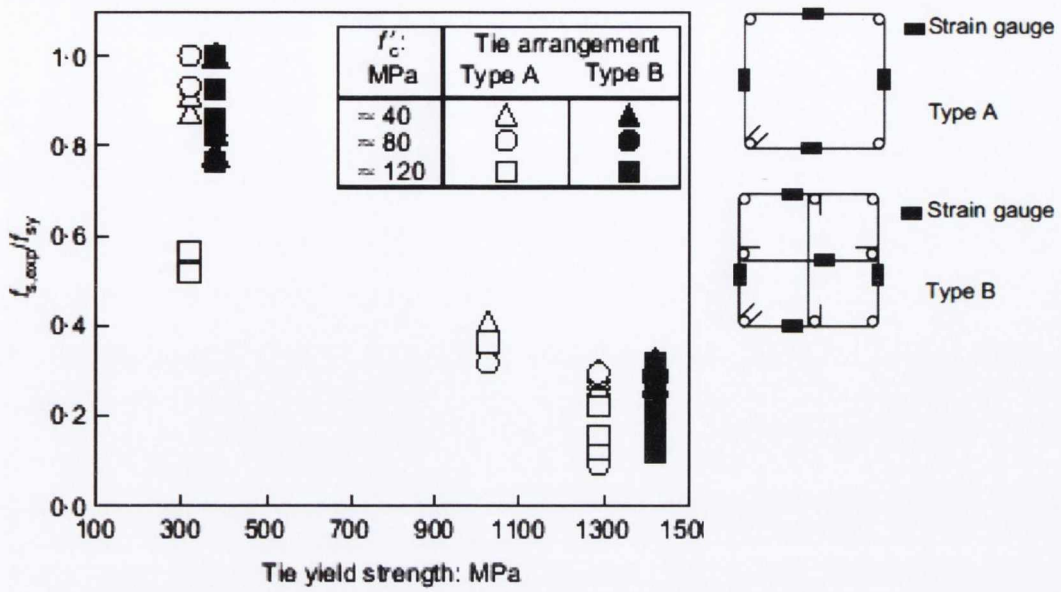

Figure 2.18: $f_{s,exp}$ / f_{sy} Versus Tie Yield Strength. f_{sy} in Lateral Ties at the Peak Strength, Hong *et al,* (2006).

More recent research was conducted by Ho *et al,* (2010) on the effectiveness of adding confinement for ductility improvement of high-strength concrete columns. It was concluded that although the addition of confining pressure is generally effective in improving the flexural ductility, its effectiveness rapidly decreases as the concrete strength or axial load level increases. This implies that the design of heavily loaded HSC columns to have at least the same level of flexural ductility that has been provided in the past to NSC columns can be quite difficult and may require an exceptionally large amount of confining reinforcement.

Little research is available into the effects of high strength lateral ties in composite cross sections as generally the confined concrete reaches its peak stress far in advance of the yield strength of the lateral ties. Furthermore, the core concrete confined within the flanges of the structural section is deemed sufficient along with the steel section to transfer loads at an ultimate limit condition, i.e. post yielding of lateral ties does not deem the specimen failed as it still has load carrying capabilities, even if beyond the serviceability and in the ultimate limit state conditions. The above research indicates that only in well confined composite columns can high strength lateral ties produce a significant improvement in the load carrying capacity, energy dissipation and ductility of composite members.

2.6.2.4 Flexural Stiffness of Reinforcing Steel

The flexural stiffness of reinforcing steel depends on bar diameter and unrestrained span. Clearly larger bar sizes and smaller link spacings will increase flexural rigidity but this is not always possible due to cost and fabrication time. Lower flexural stiffness of the transverse reinforcement permits arching of the lateral reinforcement (at unrestrained locations) when the confined concrete is stressed and begins to dilate. This arching effect renders some of the core concrete unconfined due to the inadequate flexural stiffness of the lateral steel. Figure 2.5 clearly identifies this phenomenon and illustrates the area of confined and unconfined concrete post lateral steel arching. Small ties lack the strength to resist the concrete expansion, thus either the diameter or distance between restraints need be carefully considered. Another effective alternative is the use of cross ties, as they reduce the unrestrained length between supports. This is a viable and effective method for reinforced columns and their merits were discussed previously.

For composite construction this is rarely feasible due to the limited space in the cross section, but welded link corners may prove an effective alternative as this would prohibit 'slipping' of the steel overlaps. Unfortunately no research is available to support this theory as yet for composite construction. The longitudinal steel is also prone to the same problems if the link spacing is too large. As a result the effective alternatives adopted by the European earthquake design code, Eurocode 8, (CEN, 2004) is to place limiting values on the lateral and longitudinal steel thickness and spacing. The limiting values for lateral tie spacing and thickness are given in the following expressions, respectively.

Lateral Tie Spacing Requirements

s = min($b_o/2$, 260, 9 d_{bl})mm, in ductility class DCM;

s = min($b_o/2$, 175, 8 d_{bl})mm, in ductility class DCH;

or at the lower part of the lower storey, in ductility class DCH:

s = min($b_o/2$, 150, 6 d_{bl})mm.

Lateral Tie Diameter Requirements

d_{bw} = 6mm in ductility class DCM

d_{bw} = max($0.35 d_{bL,max}[f_{ydL} / f_{ydw}]^{0.5}$, 6)mm, in ductility class DCH

Where:

s = *link spacing (mm)*

b_o = minimum centre line dimension of lateral ties (mm)

d_{bl} = minimum longitudinal bar diameter (mm)

d_{bw} = minimum diameter of links (mm)

$d_{bL,max}$ = maximum diameter of longitudinal bars (mm)

f_{ydL} = design yield strength of longitudinal reinforcement (N/mm^2)

f_{ydw} = design yield strength of transverse reinforcement (N/mm^2)

It is evident from the *'lateral tie diameter requirements'* that the longitudinal bar diameter is one of the primary limiting factors governing tie spacing, thus controlling the flexural stiffness of the section. The limiting values for restraint spacing of the longitudinal steel and diameter are given in the following expressions, which are set out in the European standard design guidelines of Eurocode 8 (CEN, 2004) and Eurocode 4 (CEN, 2004) respectively.

Longitudinal Steel Restraint Requirements

s = max(250mm in ductility class DCM, & 200mm in ductility class DCH) in critical zones.

Longitudinal Steel Diameter Requirements

$ø_{min}$ = 8mm

Where:

$ø_{min}$ = The longitudinal steel reinforcement diameter and in concrete-encased columns where it is allowed for in the resistance of the cross-section should not be less than 0.3% of the cross-section of the concrete.

It has been established in Sections 2.6.2.1 that the transverse steel content is a critical component in confining the core concrete, a significant amount of research has been conducted to determine the confining effects of various confinement reinforcement. But to date, little research exists to determine if the existing detailing provisions in Eurocode

8 would adequately confine HSC to achieve the displacement ductility required for a dissipative structural element.

2.6.2.5 Longitudinal Steel Behaviour

For effective capacity design, a reliable estimate of the ductility available in reinforced concrete members must be available. Thus, accurate models to predict the stress-strain behaviour of constituent materials must be available, or a range of reliable statistical data of the material characteristics must be on hand. For concrete, a thorough knowledge of confinement provided by reinforcement and structural steel sections is necessary; this is discussed in depth in Chapter 5.

For reinforcing steel, the yield and ultimate strengths and strains, strain hardening characteristics, and the effects of strain rate must all be given due consideration. As the actual yield strength of steel commonly exceeds the characteristic design strength of reinforcing steel, an increase in flexural strength will occur at plastic hinge locations. In general this may appear favourable as the design strength is conservative compared with the actual strength, but for capacity based design, it is of major concern as members are designed based on pre-defined plastic hinge locations, thus if member and connection strengths are exceeded in the preferred plastic hinge locations the structure may form undesirable plastic hinges and load paths. If plastic hinging does not occur at these locations, it may occur in undesirable locations, where careful detailing has not been provided, thus altering the pre-defined load paths and potentially creating a weak column/strong beam storey arrangement rather than a strong column/weak beam configuration, or vice versa, as discussed in Section 2.4.2.

Another major concern in capacity design is the increase in shear forces associated with an increase in flexural strength, which may lead to brittle shear failure. This is a more significant concern for reinforced concrete columns rather than composite columns due to the large quantity of steel in the latter, which can withstand the additional shear forces as its ratio of applied shear force to shear force capacity is generally low. An experimental and analytical programme conducted by Furakawa *et al,* (1996) found that

the use of high strength longitudinal steel in cantilever reinforced concrete beams subject to large inelastic rotations can lead to the tensile fracture of the longitudinal steel.

They considered the steel behaviour in terms of its yield strength ratio, which is defined as the ratio of ultimate strength to yield strength. The results from tests with a high yield strength ratio was of major concern for reinforced concrete structures subject to lateral cyclic displacements, as the specimens with a high yield strength ratio lead to a concentration of the strains at the hinge locations, which in turn leads to rupture of the reinforcing steel. Therefore, to avoid rupture of the reinforcing steel, Furakawa *et al,* (1996) recommended avoiding the use of longitudinal steel with a high yield strength ratio in the plastic hinge locations where large plastic rotation is expected. To date no specific tests have been conducted on the effects of this phenomenon for composite columns.

2.6.2.6 Yield Strength of Structural Steel Sections

The yield strength of the structural steel section is the predominant factor governing the confinement pressure of the highly confined concrete within a composite cross-section, as illustrated in Figure 2.19. The higher the steel strength, the higher the confinement pressure applied to the concrete core and, hence, the higher the confinement efficiency. The same principal applies for the partially confined concrete which is restrained by the lateral and longitudinal steel.

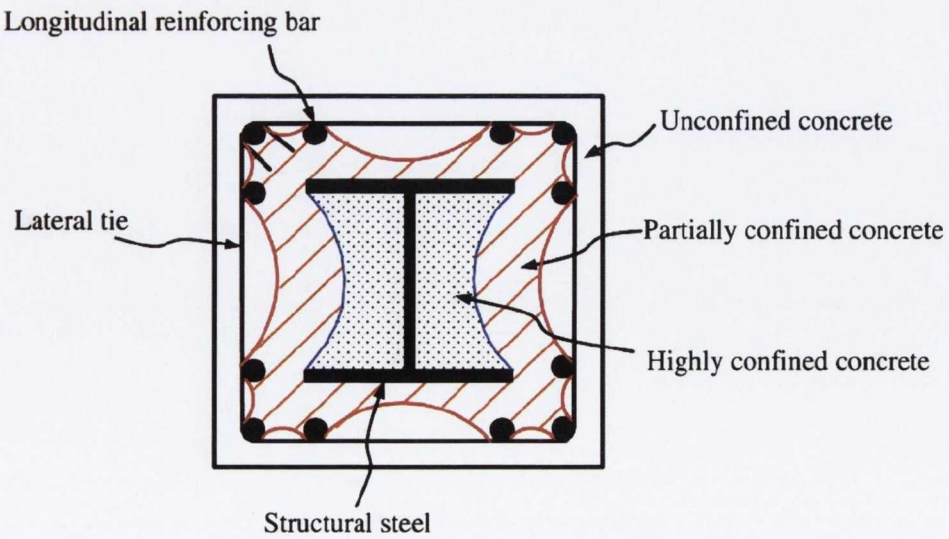

Figure 2.19: Confinement Zones within a Composite Column Cross-Section, Chen *et al,* (2006).

An increase in the yield strength of structural steel may be used to compensate for a reduction in the overall steel dimensions and volumetric ratio, even a reduction in the overall composite cross-section size. If the concrete reaches its maximum confined strength, f'_{cc} before the steel achieves its yield strength the core concrete will deteriorate

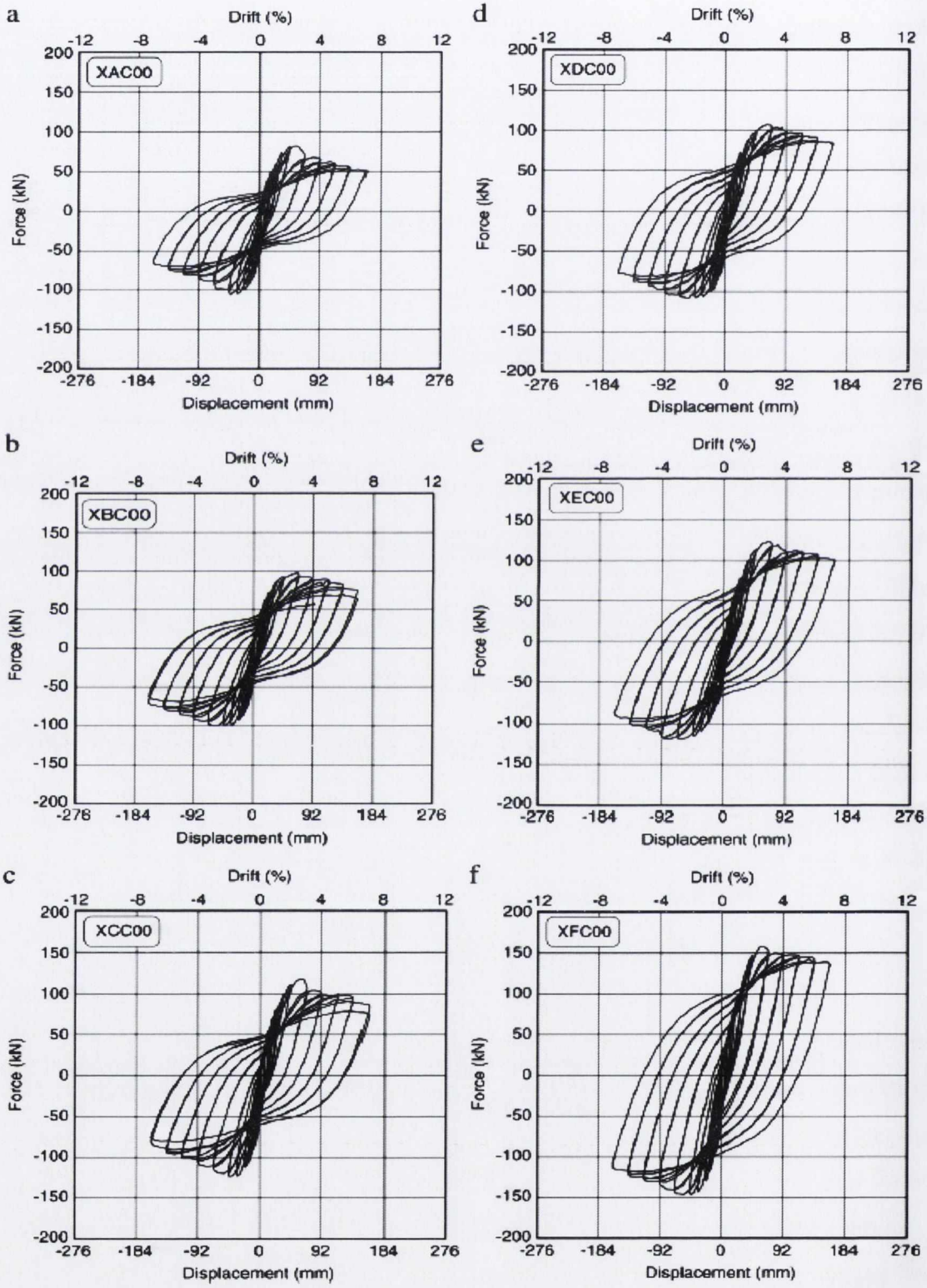

Figure 2.20: Effects of Increased Structural Steel Yield Strength, Hsu *et al,* (2009).

and reduce the local buckling capacity of the steel flange, due to the loss in additional confinement provided by the concrete. Thus caution must be used to determine what benefits may be gained by incorporating a high strength structural steel.

Where careful attention to detailing is provided, an increase in the structural steel yield strength can lead to a significant increase in the maximum moment achieved by a composite member subject to cyclic loading, as well as increased displacement ductility and energy dissipation performance of the section as is presented in Figure 2.20 (Hsu *et al,* 2009). The steel strength ratios (which are defined as the strength ratio between the structural steel section and the composite section) are: XAC00 (0.27), XBC00 (0.39), XDC00 (0.46), XCC00 (0.49), XEC00 (0.55) and XFC00 (0.67).

El-Tawil *et al,* (1999) propose that under severe seismic conditions, a possible collapse-avoidance design strategy could be to allow the concrete core to deteriorate and absorb energy, but to design and detail the steel core to resist the dead load of the structure and provide enough residual stiffness to minimise the risk of collapse. This concept is difficult to achieve for a capacity based design as an over-strength element in a plastic hinge location may cause yielding of adjacent members not specifically designed to incorporate plastic rotation, thus altering the load paths.

2.6.2.7 Structural Steel Shape & Configuration

Various configurations and layouts of confined steel exist even if the current design code, Eurocode 8, (CEN, 2004) does not elaborate on them. A series of encased I, H, T, cross and circular configurations all exist, each with their own unique properties and individual performance characteristics. Sakai *et al,* (2000) tested a series of composite columns with a variety of encased I, H and solid circular sections. The load-displacement hysteresis graphs for the test are presented in Figure 2.21.

Sakai *et al,* (2000) states that columns encased with core steel display larger earthquake resistant properties than those with usual reinforced configurations. The plots illustrate those specimens with the same quantity of core steel can display very different hysteretic responses. Specimens with encased I sections achieve a higher maximum yield load as

well as developing larger hysteretic loops (i.e. greater energy dissipation capabilities) and an increased yield ductility than a specimen with an encased H section. Two reasons for this are the larger area of confined concrete inside that of the I section, but more probably, the depth of the steel flanges from the neutral axis, allowing the I section to withstand higher strains before crushing of the concrete occurs.

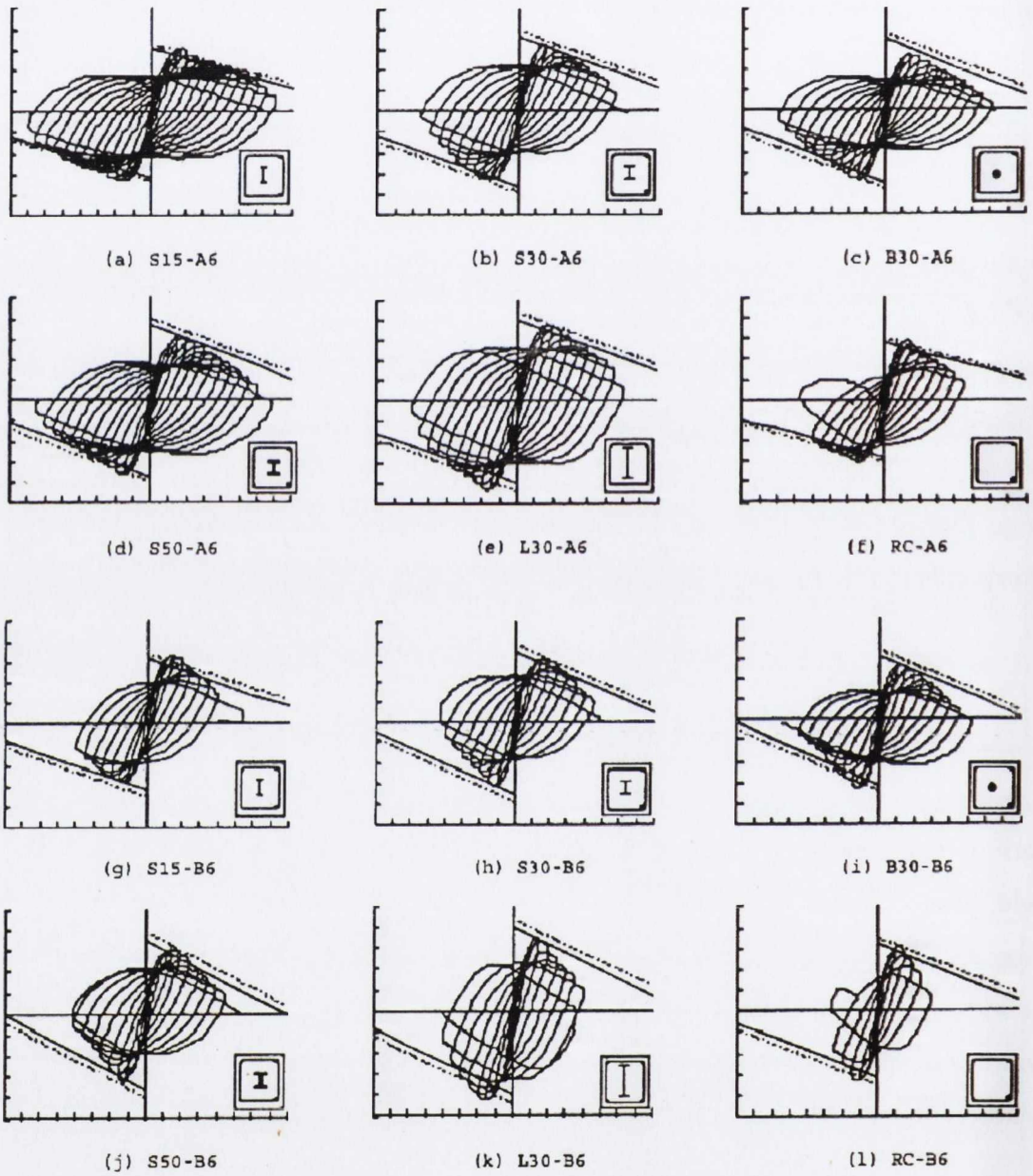

Figure 2.21: Hysteretic Responses for Various Confined Shapes, Sakai *et al,* (2000).

It should be noted that when identical specimens are subject to the limiting axial force prescribed by the design code, as presented in Equation (2.3), the I section again achieves a marginally higher yield load but fails to achieve a displacement ductility equal to that of an encased H section.

$$N_t = {}^1/_3 A_c f_c' + {}^2/_3 A_s f_y \tag{2.3}$$

Chen *et al,* (2006) conducted a series of tests on composite stub columns; one of the experimental parameters was to determine the effects that various steel shapes had on concrete confinement. The concrete confinement is confirmed from the comparisons of the predictions with experimental results. The tests indicate that cross-shaped steel sections lead to the highest confinement while the I-shaped section has the lowest. Figure 2.22 illustrates the theoretical regions for unconfined, partially and highly confined concrete in various composite cross sections.

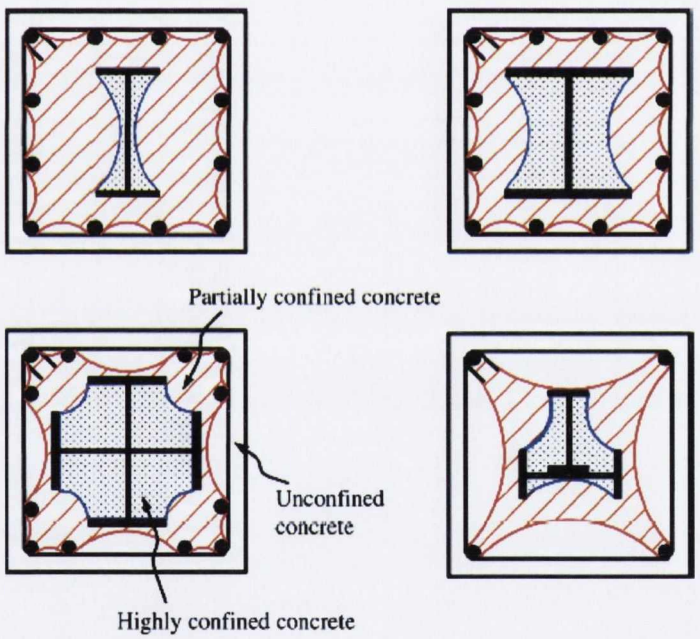

Figure 2.22: Regions for Unconfined, Partially and Highly Confined Concrete in Various Composite Cross-Sections, Chen *et al,* (2006).

Theoretical modelling, supported by experimental testing on the performance of stub columns subject to uni-axial compressive loading enabled Chen *et al,* (2006) to produce the concrete stress-strain curves presented in Figure 2.23 .The stress-strain curves clearly illustrate the benefits of high levels of confinement and present the effectiveness of

varied confined shapes on partially and highly confined concrete. The theoretical confined stress-strain curves were combined with the stress strain curves from coupon tests on the steel elements to produce a combined stress-strain curve for the composite section, the analytical and theoretical curves displayed strong agreement, thus validating the proposed confinement factors (as illustrated in Figure 2.28).

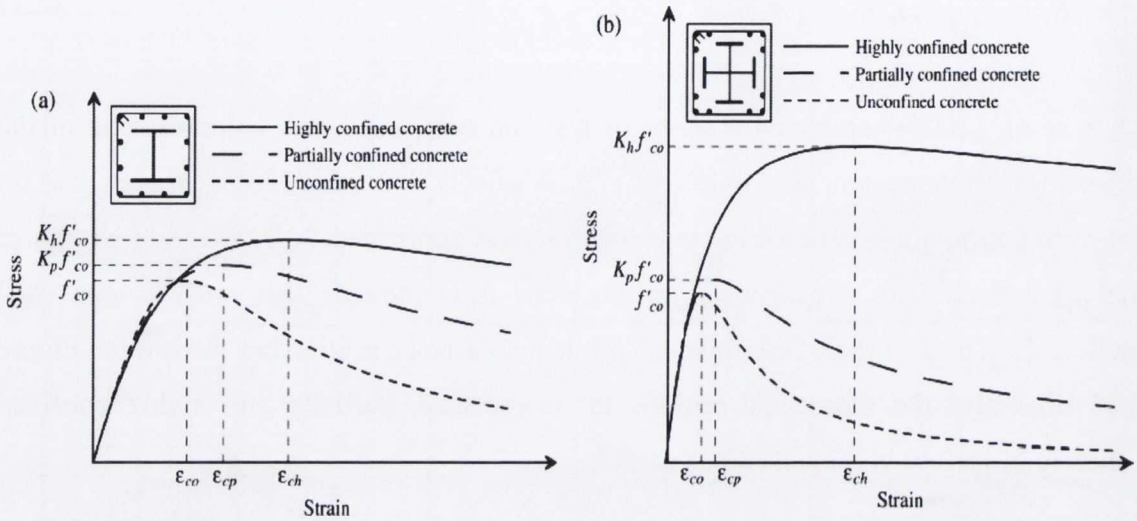

Figure 2.23: Stress-Strain Curves for Unconfined and Confined Concrete with Various Steel Configurations, Chen *et al,* (2006).

Inspection of Figure 2.22 would suggest that a cross section that has the highest area of confined concrete due to the high level of confining steel would also have the highest confining factor. Figure 2.24 confirms this theory, based on experimental work, backed up by analytical modelling, Chen *et al,* (2006) concludes that a cross shaped steel section provides greater levels of confinement for both the partially and highly confined concrete. Though the steel shape has no direct influence on the partially confined concrete, if suitably designed it confined a larger area of concrete than other configurations, thus leaving less concrete to be confined by the lateral ties and longitudinal steel, thus in turn minimising the work done by the lateral reinforcement.

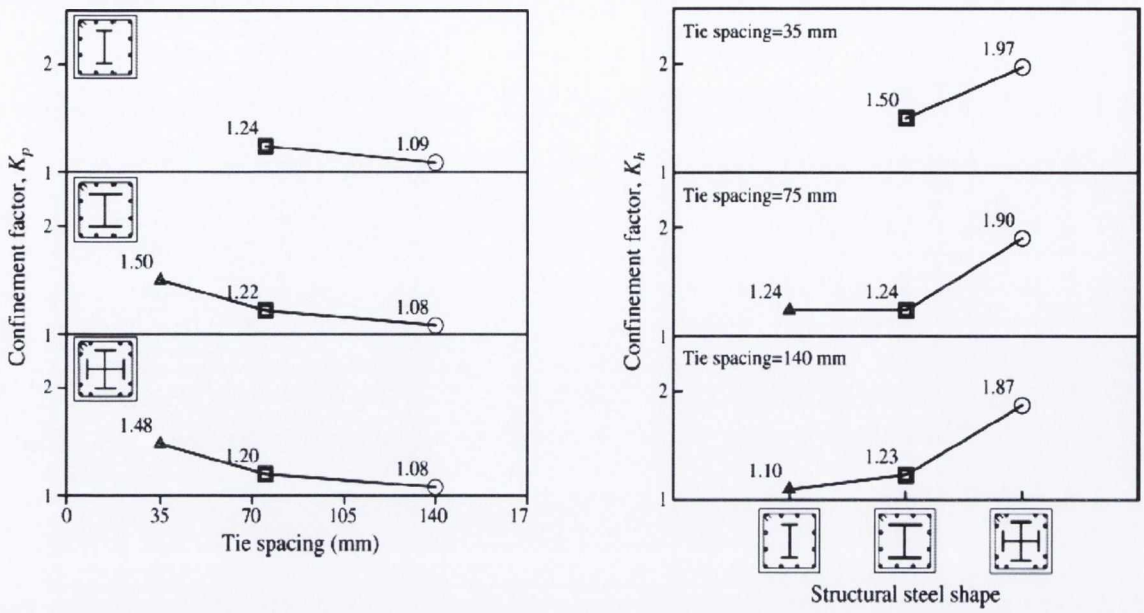

Figure 2.24: Confinement Factors for Partially and Highly Confined Concrete, Chen *et al*, (2006).

Where:

K_p = Partially confined concrete confinement factor

K_h = Highly confined concrete confinement factor

The partially confined concrete is defined as the area of concrete effectively confined by the transverse and longitudinal reinforcement less the concrete area confined by the structural steel section. The areas of confined concrete for various composite columns are illustrated in Figure 2.22. The equations relation to the calculation of the confined concrete areas and confinement factors are presented in Section 5.3.3.

2.6.2.8 High Strength Concrete

The use of high-strength concrete (HSC) has increased significantly in recent years due to its improved performance characteristics when compared with normal-strength concrete (NSC). Current seismic design codes, however, are predominantly based on data derived from tests on NSC. Furthermore, the extrapolation of NSC design rules to HSC is not always conservative and can lead to unsafe designs, (McFarlane, 2007).

HSC sometimes referred to as *high-performance concrete* (HPC) is designed to be more durable than NSC. The concrete is designed so that it meets significantly more stringent

criteria than those required for normal structural concrete (Nawy, 2000). HSC may be designed to achieve high workability, very high fluidity and minimum or negligible permeability. These characteristics are achieved by an increase in the cement content (or with the introduction of a cement like material, i.e. Ground Granulated Blast-furnace Slag (GGBS), A considerable reduction in the free water content will inherently increase the overall strength, but lead to a reduction in workability. The inclusion of a super-plasticiser will increase the workability without affecting the overall concrete strength significantly. HSC is more expensive to produce due to the additional mass of cement required and the associated costs with achieving the more stringent design and quality control criteria.

Nawy, (2000) states the additional material cost of using HSC can be balanced by the following major advantages associated with construction.

1. Reduction in member sizes, resulting in (a) increased internal floor dimension, and (b) reduction in the volume of produced concrete with an associated saving in construction time.
2. Reduction in the self-weight and superimposed dead load with the accompanying saving in smaller foundations.
3. Reduction in formwork area and cost with the accompanying reduction in shoring and stripping time due to high early-age gain in strength.
4. Longer spans and fewer beams required for the same magnitude of loading.
5. A reduction in axial shortening of compression supporting members.
6. Low creep and shrinkage properties.
7. Greater stiffness as a result of a higher modulus, E_c.
8. Higher resistance to freeze-thaw action, chemical attack, and significantly improved long-term durability and crack propagation.

However, not all of the concrete's properties are improved – HSC is significantly more brittle than NSC. HSC displays limited inelastic deformability compared with NSC when subject to earthquake loads; the stress-strain curve in Figure 2.25 (Mendis, 2001) presents a comparison of the post yield response of normal to very high strength concrete. It is evident from the graph that high strength concrete has little to no post

yield performance without the addition of confinement. HSC also displays "*early spalling*" when loaded in compression, Cusson *et al,* (1995).

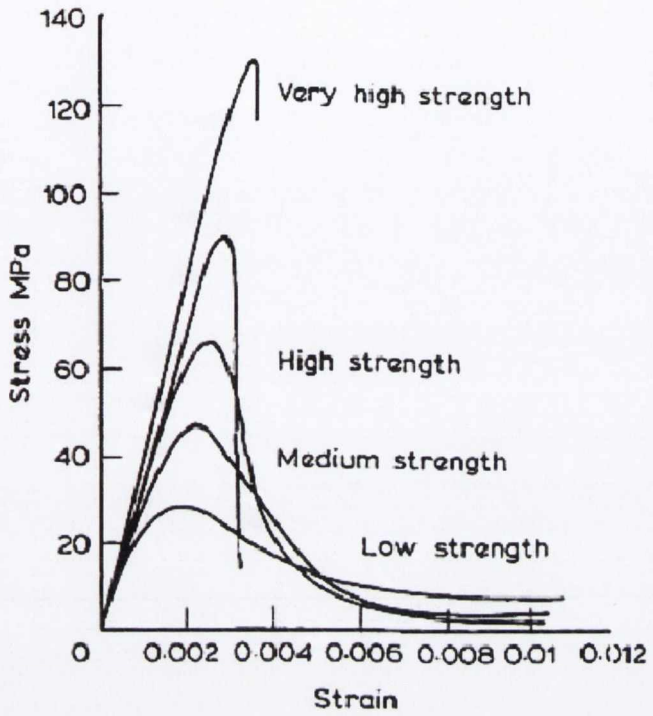

Figure 2.25: Stress-Strain Curves for Unconfined Concrete Cylinders with Varying Compressive Strengths, Mendis, (2001).

Typical stress–strain curves for various strengths of concrete are shown in Figure 2.25 and it is apparent that the behaviour of HSC differs significantly from NSC. These differences are characterised by Mendis, (2001) as follows:

- The strain at peak stress increases with increased strength, but the ultimate strain decreases.
- The elastic response of HSC is extended for a higher proportion of the ascending branch of the stress curve compared with NSC. Consequently, the curve remains approximately linear up to the peak stress.
- The post-peak descent becomes steeper with increased strength and the extensive ductility that is evident with NSC is not observed with HSC.

HSC becomes increasingly brittle as strength increases, as shown by the near-vertical descending branch of the stress–strain curve. This is a major concern for engineers as failure can be sudden, explosive and catastrophic, all undesirable characteristics for

capacity based seismic design in which the ductility of structural components is relied upon for the dissipation of earthquake-induced energy. It is clear that suitable detailing must be provided to HSC structural elements to improve their ductility and post yield performance. This is a major issue concerning HSC composite column performance and is one of the key issues being analysed throughout this research.

Figure 2.26 presents the axial load-displacement behaviour of HSC with various levels of confinement (McFarlane, 2007). It is apparent, that, as the specimen is loaded, the displacement increases in a linear manner up to the proportional limit. Loading beyond this point continues until the cover concrete spalls off (Point A). After the concrete cover shell spalls off, the remaining core of the column is required to provide the load bearing capacity that is lost by the spalling of the concrete cover (Point B). The ability of the column core to carry this load is dependent upon how well the core is confined by the reinforcement cage. In columns with low confinement, the dynamic effect created by the spalling of the concrete cover shell leads to a sudden failure of the column core. In well confined columns, expansion of the core activates the confinement provided by the links and catastrophic failure is prohibited. The column then carries load to a second peak which may be either higher or lower than the initial spalling load. The second peak capacity increases with the amount of confinement reinforcement as shown in the medium and high curves in Figure 2.26.

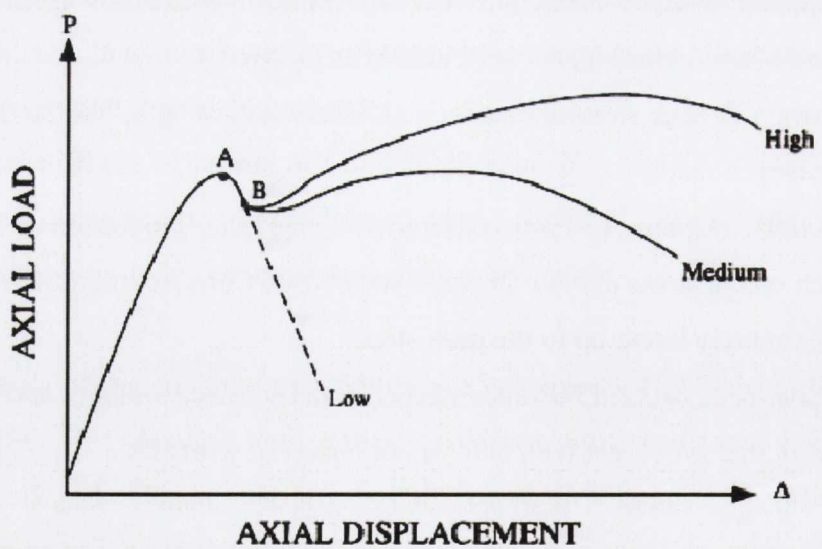

Figure 2.26: Typical Behaviour of HSC with Various Levels of Confinement, McFarlane, (2007).

A vast amount of research has been conducted into the confinement of HSC and it is widely accepted that careful detailing can improve the ductility of HSC specimens, although to a lesser degree than NSC. Razvi *et al,* (1994) conducted a large series of tests to determine the strength and deformability of confined high-strength concrete columns. The findings include the following:

- HSC columns exhibit extremely brittle behaviour unless confined by reinforcement. The primary parameters for confinement include volumetric ratio, spacing, arrangement, transverse steel yield strength, concrete strength and axial load.
- The lateral confining pressure required for high-strength concrete columns is significantly higher than that for normal strength concrete. This requirement may be met by either increasing the volumetric ratio or using higher grades of steel.
- High strength steel is fully effective in confining HSC columns. Columns with 86 to 116 MPa concrete, confined with 4.4 percent volumetric ratio of confining steel, exhibit approximately 250 percent increase in displacement ductility ratio when the yield steel strength is increased from 328 to 792 MPa.
- The deformability capacity of HSC columns decreases with axial compression. However, it is possible to obtain high deformability in highly compressed HSC columns, when either the volumetric ratio and/or the yield strength of confining reinforcement are increased.
- Cover concrete in HSC columns may fail prematurely due to instability of the shell under high compressive stresses, prior to attaining the crushing strength. This occurs when the closely spaced reinforcement creates a plane of separation between the cover and core concrete.

Cusson *et al,* (1994) examined the effects of HSC confined by rectangular links; it was deemed that HSC exhibits less lateral expansion under axial compression than NSC due to its higher modulus of elasticity and its lower internal micro cracking. Consequently, the confining reinforcement comes into play later in the process and the efficiency of passive confinement of high-strength concrete would be reduced. The test results confirm that significant strength and toughness enhancements can be achieved when lateral reinforcement is provided. However, greater strength and toughness gains are observed for specimens made with lower-strength concrete.

Cusson *et al,* (1994) found that the early spalling of the concrete cover results in a loss of axial capacity before any lateral confinement comes into effect. After the concrete cover had completely spalled off, important gains in strength, ductility, and toughness were recorded for the concrete core of well-confined specimens. Improvements in strength of approximately 50 and 100 percent, and in ductility of approximately 10 and 20 times greater than that of unconfined concrete were recorded for well-confined specimens made with 99.9 and 52.6 MPa concretes, respectively.

The performance of HSC in composite columns is similar to that in RC columns, except that as the area of partially confined concrete is far less than that of the core concrete area in reinforced specimens, the lateral reinforcement is subject to less lateral dilation from the expanding concrete, thus subject to smaller stresses. Encased steel sections provide excellent confinement for HSC due to the large quantity of steel and high loads required to cause local buckling.

Ricles *et al,* (1994) compared the seismic performance of steel encased composite columns; one of the varied parameters was the concrete strength. Identical sections with different unconfined compressive strengths (i.e. 30.9 and 62.9 MPa) achieved the same maximum displacement ductility of 6.0. However, during the subsequent second and third cycles of the displacement cycles the hysteresis loops for the HSC specimen showed a more pronounced (although not too significant) drop in capacity compared to the specimen with NSC.

This phenomenon was determined to be associated with a greater degree of concrete brittleness in the HSC, leading to a more pronounced spalling of its outer concrete core and micro cracking of its inner concrete core compared to the NSC specimen. Only a minor maximum load increase was recorded between the NSC and HSC specimens of 784.4 kN and 840.2 kN respectively.

2.6.2.9 Axial Load Level

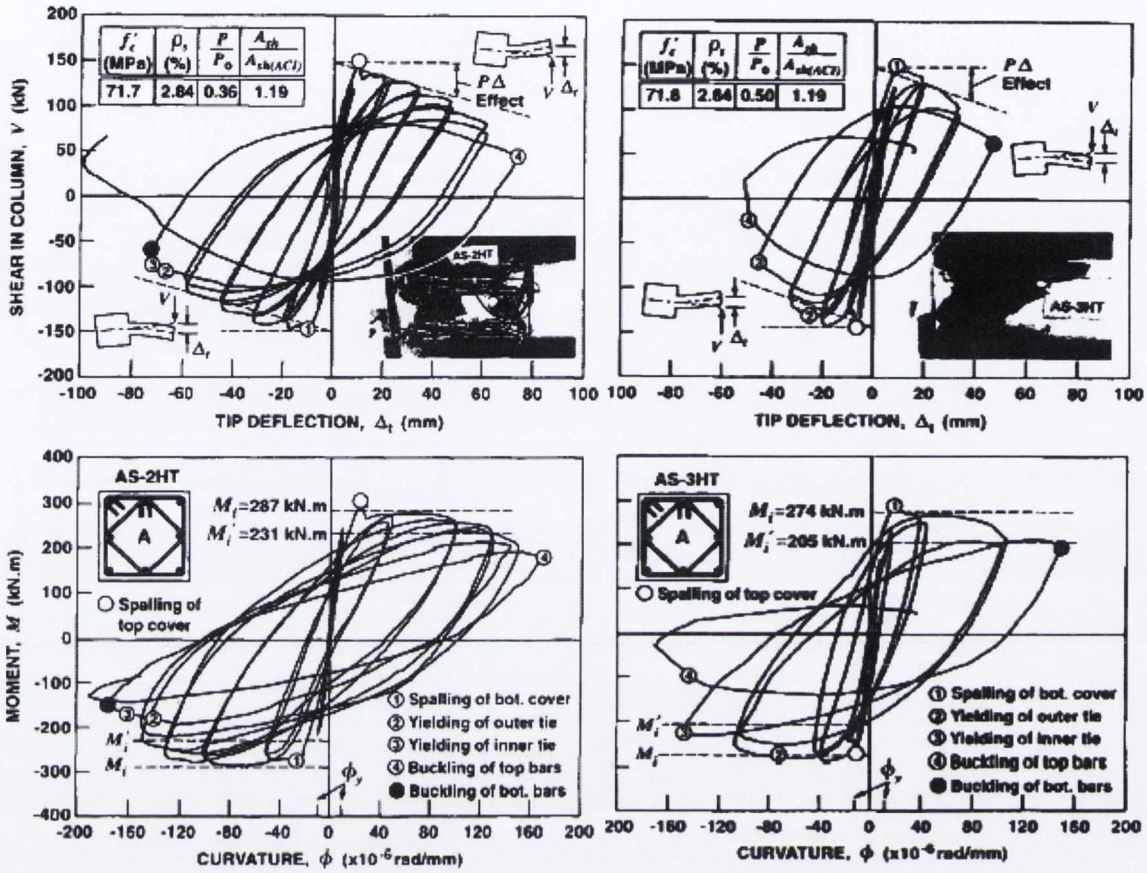

Figure 2.27: Moment Curvature Response Subject to Axial Load Levels: (a) 36% and (b) 50%, Bayrak *et al,* (1998).

Tests conducted by Bayrak *et al,* (1998) on the cyclic performance of reinforced concrete columns suggests that an increase in axial load reduces the column's deformability and ductility and accelerates strength and stiffness degradation with every cycle. To compensate for this, the authors suggest that, a larger amount of lateral reinforcement is required. It is suggested that, due to the substantial effect of axial load on sections performance, it should be incorporated as a design parameter in the design of confinement reinforcement.

Figure 2.27 presents two such identical specimens subject to axial load levels equivalent to 36 and 50% of the column compressive capabilities. The most notable difference is

the reduction in ductility capability for the specimen subject to 50% compressive capability, and, as a result a major reduction in energy dissipation capability.

Sakai *et al,* (2000) compared the earthquake resistance of varied confined shapes; among the experimental parameters was a varied axial load of (a) 30% of the ultimate compressive strength of the cross section, and (b) the limiting axial force, as per Equation (2.3). The hysteresis relationships illustrated in Figure 2.21 support the findings of Bayrak *et al,* (1998) as a noticeable decrease in deformability, ductility and energy dissipation capability is recorded for all confined shapes at a higher axial load level (i.e. at the limiting axial force)

2.7 Composite Members in Compression

There is very little research regarding the effect of various shapes of steel section on the axial compressive behaviour of concrete encased steel columns. The concrete confinement of composite columns with various shapes of steel section is not well understood yet, Chen *et al,* (2006). Several experimental programmes have examined the confinement effects in concrete-filled steel tube (CFT) composite columns, (Susantha *et al,* 2001, Han, 2002, O' Shea *et al,* 2000, Sakino *et al,* 2004, Giakoumelis *et al,* 2004, and Schneider, 1998). From previous work, it is clear that the steel tube, particularly the circular tube, can provide confinement of concrete and lead to the enhancement of strength and ductility of the CFT columns.

Chen *et al,* (2006) developed a model to predict the axial capacity of composite columns with varied confined shapes. Figure 2.28 presents the axial load-strain curves for selected specimens with the superimposed model predictions. It is evident a strong correlation exists between the experimental and analytical predictions, thus validating the proposed confined concrete stress-strain curves. The models maximum test loads were compared with those from the European composite design codes 'squash load' (Eurocode 4, (CEN, 2004), as defined by Equation (2.4). The test, model and design code predictions are all presented Table 3 for a numbers of researchers, along with the confidence ratio of the proposed model and code predictions compared with the test results. It should be noted that Table 3 only contains a select extract of results from this research but the complete

table is present in Chen *et al,* (2006). Table 3 contains experimental results from the following researchers, Chen and Yeh, (1996) for specimens SRC1 – SRC4, Tsai *et al,* (1996) for specimens src1 to src4 and Chen *et al,* (1999) for specimens CL-TE, CL-TO and CL-HO.

$$N_{pl.Rd} = A_a \frac{f_y}{\gamma_{Ma}} + A_c \left(\frac{0.85\, f_{ck}}{\gamma_c}\right) + A_s \frac{f_{sk}}{\gamma_s} \tag{2.4}$$

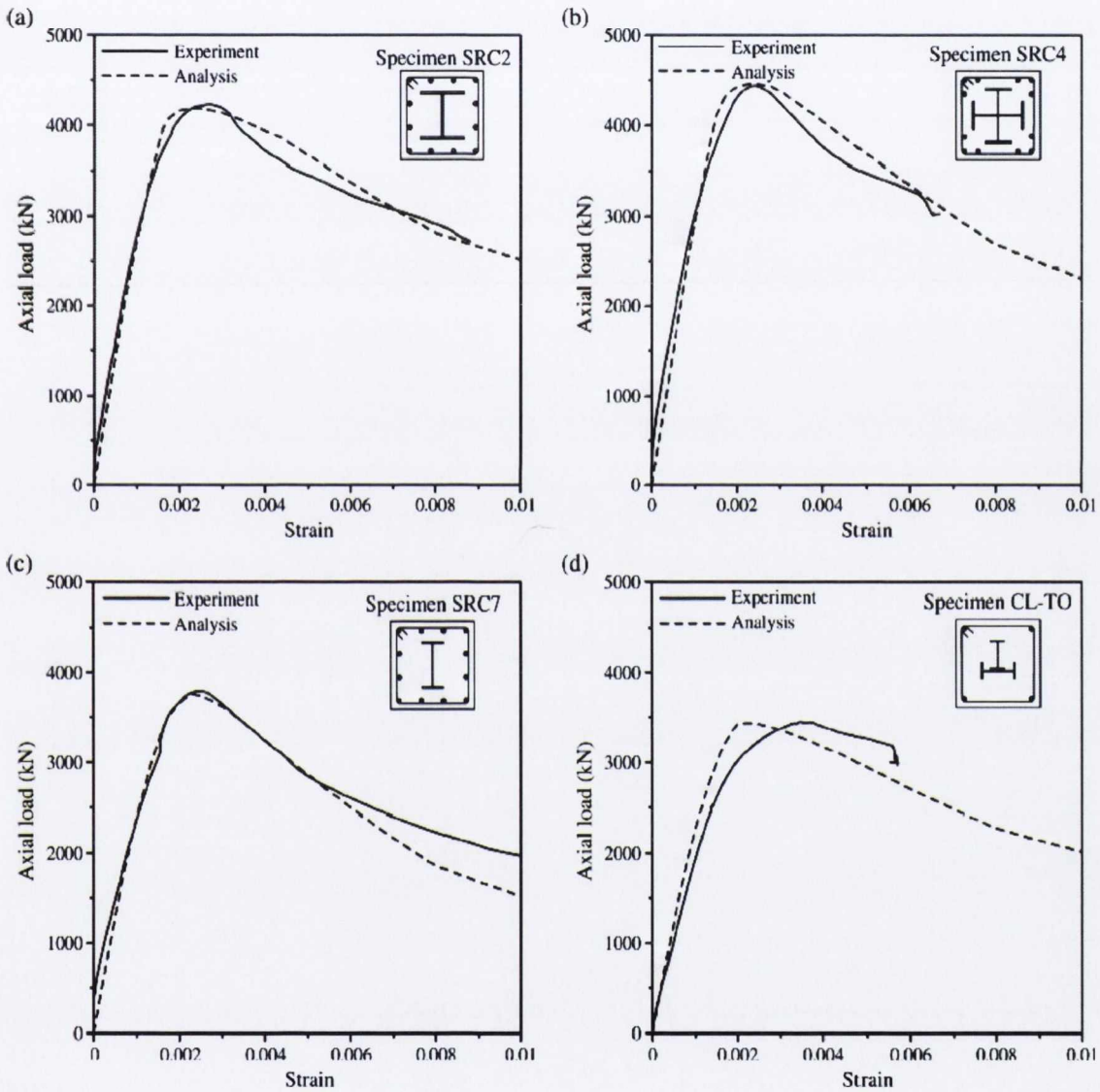

Figure 2.28: Comparison of Experimental and Analytical Axial Load-Strain Curves for Various Confined Steel Shapes, Chen *et al,* (2006).

By observation is it evident the model accurately predicts the maximum sectional axial compressive stress varying by a maximum of 10% but generally varying by between 0 –

4%. The 'squash load' as opposed varies between 90% and 124% of the maximum compressive test load. This method of predicting the maximum section compressive stress is clearly subject to considerable variation, particularly for encased I sections (i.e. SRC 7-10 in Chen *et al,* (2006)). Another major concern is the lack of consideration given to the level of confinement; this may seriously influence the overall values, particularly for specimens with either high levels of unconfined or highly confined concrete.

Table 3: Comparison between Experimental and Analytical Results

Specimen	Test P_{TEST} (kN)	$N_{pl,Rd}$ (kN)	Analysis P_{Analy}	$\frac{P_{TEST}}{N_{pl,Rd}}$	$\frac{P_{TEST}}{P_{Analy}}$
SRC1	4220	3920	4274	1.08	0.99
SRC2	4228	3835	4180	1.10	1.01
SRC3	4399	3939	4381	1.12	1.00
SRC4	4441	4242	4459	1.05	1.00
			Average	*1.13*	*1.01*
			Coefficient of Variation	*0.07*	*0.02*
src1	3602	3780	3486	0.95	1.03
src2	3502	3755	3462	0.93	1.01
src3	3836	4058	4062	0.95	0.94
src4	3854	4270	4304	0.90	0.90
			Average	*1.07*	*1.02*
			Coefficient of Variation	*0.09*	*0.06*
CL-TE	3452	3165	3433	1.09	1.01
CL-TO	3448	3165	3433	1.09	1.00
CL-HO	3514	3154	3428	1.11	1.03
			Average	*1.07*	*1.00*
			Coefficient of Variation	*0.05*	*0.02*

It was determined from the above results, conducted by several researchers on several cross-section sizes and shapes, that the 'squash load' is subject to high variation and a combined material stress-strain profile is a far more accurate predictor of the maximum sectional compressive stress. The 'squash load' can produce a vague estimate but unsuitable when an accurate prediction is required for capacity based design due to its failure to incorporate confinement in any form.

2.8 Composite Members in Combined Axial and Flexural Loading

Composite columns in seismic areas require careful detailing to resist combined axial and flexural loading, particularly for capacity based design an accurate understanding of the section behaviour is essential. Several research programmes have been conducted to verify the performance of composite columns subject to axial and flexural loading. From this research several analytical models have been developed to accurately predict the flexural performance of such specimens. Oh *et al,* (2006) concludes that composite column capacity can be determined, though conservatively using all modern design codes, (AISC-LRFD, 1993, ACI, 2005, AIJ, 1994 and Eurocode 4, CEN, 2004), however it was noticed that the AISC-LRFD, (1993) code provisions, for evaluating the load carrying capacity are too conservative, therefore it is desirable to use the Eurocode 4, (CEN, 2004) or AIJ, (1993) code provisions to evaluate the axial force-bending moment of steel-concrete composite columns.

Weng *et al,* (2002) compared the provisions of the ACI and AISC-LRFD codes for concrete encased composite column strength. The test results agree with the findings of Oh *et al,* (2006) It is stated that the ACI approach is a more accurate predictor of the capabilities of encased composite columns and that the column capabilities predicted using the ACI approach are less wide spread (i.e. smaller value of coefficient of variation) than those calculated using the AISC-LRFD approach. Figure 2.29 presents the P-M interaction curve for selected data within this study with the EC4 interaction curve superimposed on it. It is clear from the graph that the Eurocode approach is a more accurate predictor of sectional capacity for the results provided.

It is evident that all codes conservatively estimate the performance of composite columns subject to axial and flexural loading. As with members in pure compression, when part of a capacity based design, care needs to be taken to ensure that the member strength is not too conservatively estimated so as to prohibit the formation of plastic hinges in undesirable locations. A model shall be developed and discussed in later sections to effectively predict the performance of steel encased composite columns subject to combined axial and flexural loading.

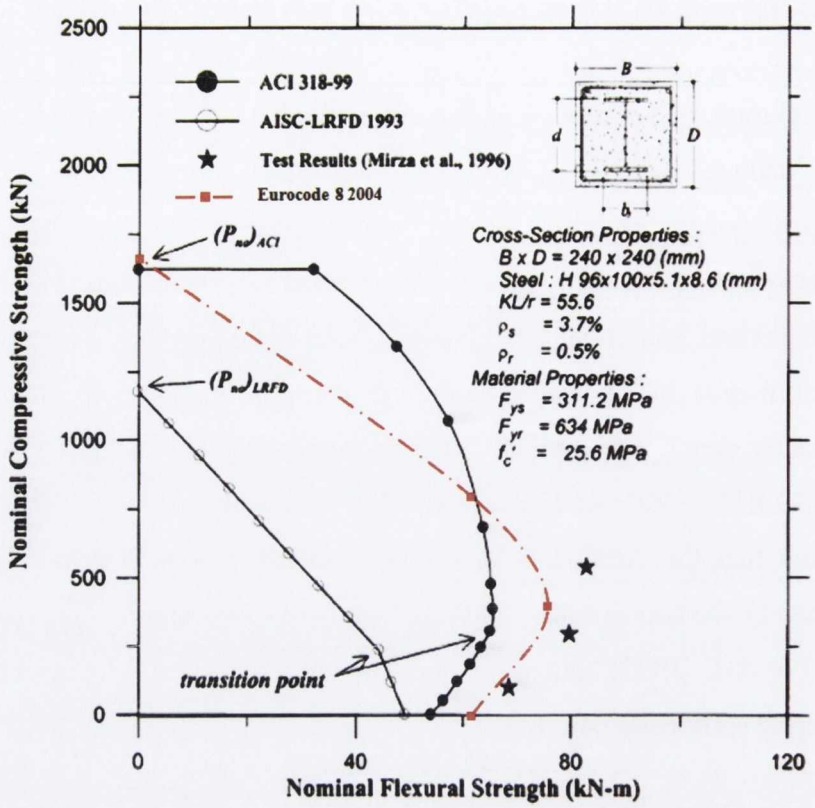

Figure 2.29: Comparison between Test Results and Nominal Strengths Predicted Using ACI, AISC-LRFD and Eurocode 4 Specification, Weng *et al,* (2002).

Vast amounts of research have been conducted on the behaviour of composite specimens subject to axial and lateral cyclic loading. Research conducted by Varma *et al,* (2002) on high-strength square concrete-filled steel tube columns indicates that cyclic loading does not have a significant influence on the flexural stiffness and moment capacity of CFT beam columns. However, the post peak moment resistance decreases more rapidly under cyclic loading. This is due to the failure of the concrete in tension which in unable to resist the applied loads in compression in load reversal. This is of particular interest when the concrete is unconfined or poorly confined by transverse and/or structural steel. Figure 2.26 presents the load-displacement response of HSC with varying levels of confinement.

Elghazouli *et al,* (2008) conducted research on the inelastic behaviour of composite members under combined bending and axial loading of partially encased composite columns. Some of the findings include that a significant increase in ultimate moment capacity can occur due to concrete confinement effects. The effectively confined concrete area close to the web and flanges of the cross-section has a significant influence

on the behaviour, particularly in the major axis direction. For major axis tests, it was demonstrated that the onset of local buckling resulted in a reduction in moment capacity, which was more pronounced in the presence of axial loading, largely due to the sudden release of confinement.

This is a critical factor for encased composite design as the steel section in the presence of axial load may be designed to resist the applied dead loads after the concrete elements have failed due to the applied earthquake loads. It is imperative that a suitable b/T ratio is selected if the design is to rely on the load carrying capacity of the steel section and confined core post seismic excitation.

Ballio, (1987) conducted a series of cyclic tests on partially encased composite columns with varying steel flange thickness to investigate the effects of concrete within the chambers of the partially encased section on the occurrence of local buckling. The results indicated that the concrete effectively restrained the web against rotation and buckling, furthermore, the steel flanges were prevented from deforming inwards, thus delayed the onset of local flange buckling.

Broderick, (1994) analysed the response of partially encased columns under earthquake loading, the results indicate that good energy dissipation and rotation ductility characteristics can be achieved even in the presence of high axial loads. It was noted that for axial loads in excess of 30% of the axial capacity of the member's cross-section, second-order effects reduced the ductility of the specimens somewhat. Broderick, (1994) also found that local buckling of the structural steel caused a reduction in the moment capacity of the section due to a loss of effectively confined section and a release in concrete confinement.

Early research was conducted by Wakabayashai *et al,* (1987) on the seismic performance of various forms of composite columns including the combined effects of combined axial compression and lateral cyclic displacements of fully encased composite columns. These experiments demonstrated that these members possess excellent local ductility and energy dissipation capacities in the presence of low to moderate axial load levels. But, when these loads exceed 30% of the axial capacity of the member, severe deterioration

to the core elements was observed, with an associated deterioration in hysteretic response.

El-Tawil *et al,* (1999) assessed the strength and ductility of concrete encased composite columns with an emphasis on seismic behaviour and the use of high-strength concrete. The results indicated that the AISC-LRFD, (1993) design provisions under-estimated the column strength prediction by 63% for a column with a steel core ratio 0f 0.04 and an unconfined concrete strength, f'_c of 110MPa.

El-Tawil *et al,* (1999) concludes that composite columns with medium to high-strength concrete (f'_c = 69 - 110MPa) and standard non-seismic reinforcement had low curvature ductilities on the order of μ_ϕ = 1 – 2 when subjected to intermediate to high axial load levels (P = 0.3 – 0.6P_o). This is contrasted to columns with normal-strength concrete (f'_c = 28 MPa) that had ductilities of (μ_ϕ = 4 – 12) under corresponding conditions. Ductility improved significantly when confinement steel was provided by the transverse hoop reinforcement specified in the AISC-LRFD, Seismic Provisions (1993) for composite columns. However, for high-strength concrete (f'_c = 69 - 110MPa) the resulting ductilities were still only about half of the μ_ϕ = 12 typically implied as a requirement for reinforced concrete frames in high seismic regions.

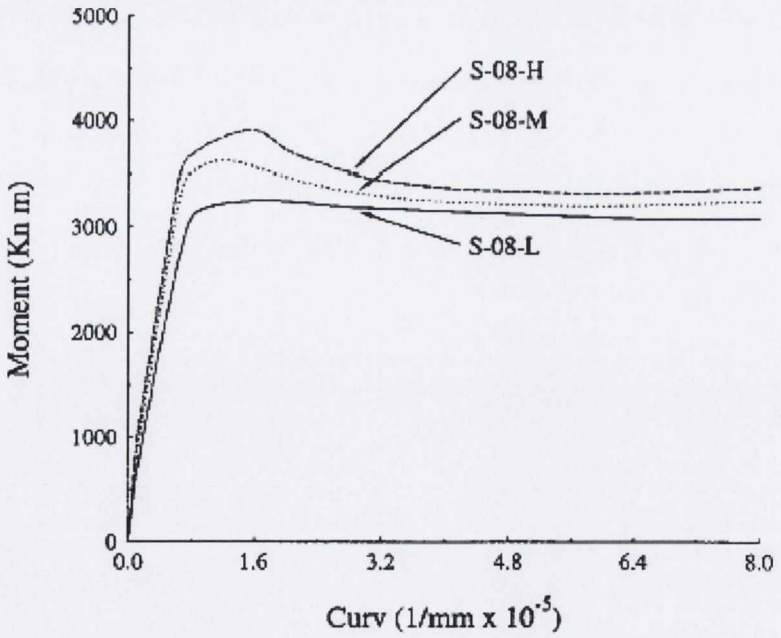

Figure 2.30: Moment versus Curvature Response as a Function of Concrete Strength, El-Tawil *et al,* (1999).

The moment versus curvature response for a composite section of varying concrete strength is illustrated in Figure 2.30. The plot indicates that for no applied axial load all grades of concrete (labelled L - f'_c = 28 MPa, M - f'_c = 69MPa and H - f'_c = 110MPa) achieve ductilities easily in excess of μ_ϕ = 12. There is a modest strength increase in the sections with higher-strength concrete; however this strength is lost as the extreme fibre of the high-strength concrete cover is crushed. Beyond the initial peak, the strength is maintained by the longitudinal reinforcement on the compression side of the member and the remaining concrete. Shin *et al,* (1989) and others noted similarly good ductility from experiments of reinforced concrete flexural members with high-strength concrete, and the same is expected for the other composite sections.

Figure 2.31 and Figure 2.32 present the response of medium and high-strength concrete composite columns, respectively, subject to axial loads corresponding to 30% of the sections axial capacity and flexural bending. The cross sections relating to the specific envelope curves are presented in Figure 2.33. Figure 2.31 and Figure 2.32 clearly show the large reduction in ductility due to the presence of axial compression (compared with Figure 2.30) where the nominal strength is dominated by concrete crushing above the balance point. Although the structural steel section is not effective in preventing the sharp drop in strength that occurs due to crushing of the concrete, the steel section does improve the post-peak ductility.

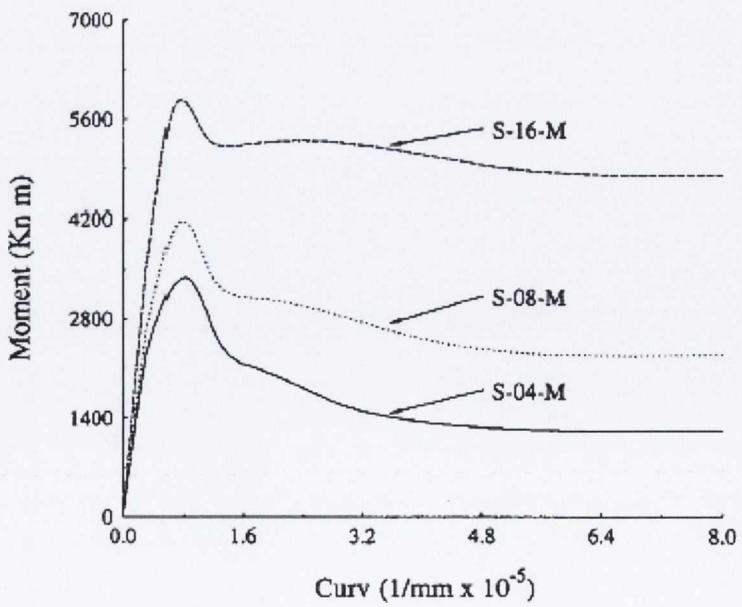

Figure 2.31: Response of Composite Section with Medium-Strength Concrete, $P = 0.3P_o$, El-Tawil *et al,* (1999).

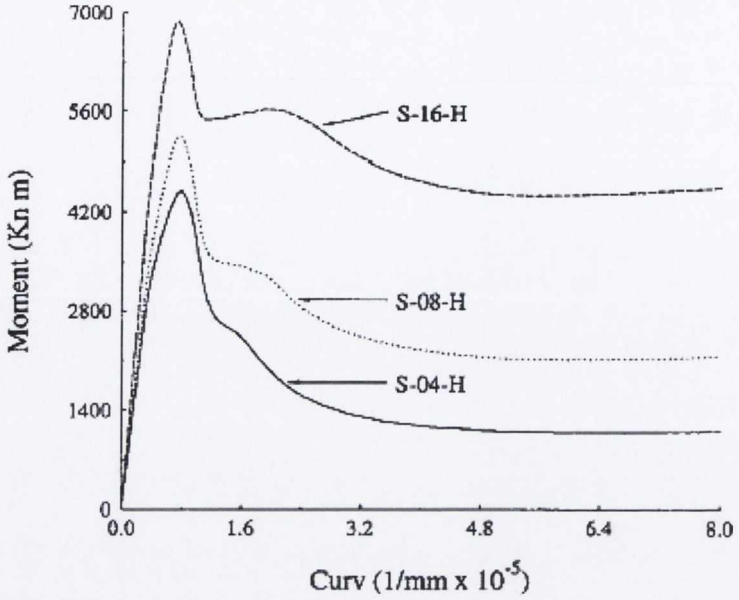

Figure 2.32: Response of Composite Section with High – Strength Concrete, $P = 0.3P_o$, El-Tawil *et al,* (1999).

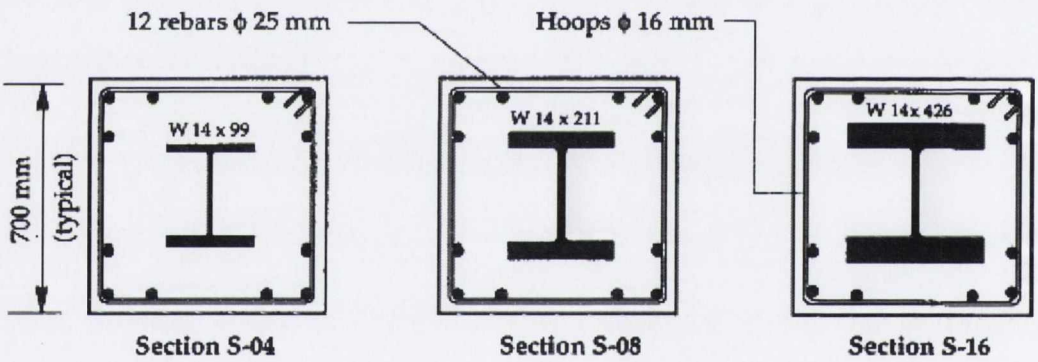

Figure 2.33: Composite Columns Tested by El-Tawil *et al,* (1999).

Finally, the curvature ductilities for the tested specimens are presented in Figure 2.34. It is clear that for moderate levels of axial load (i.e. $P = 0.3P_o$) neither the moderate or high strength concrete are capable of achieving a curvature ductility suitable for a moment resisting frame, unless seismic hoop reinforcement is introduced, as illustrated in Figure 2.35. No similar research has been conducted using the Eurocode 8 design provisions for HSC composite columns as of yet, but the values presented in Figure 2.34 illustrate that it is very difficult to achieve a suitable curvature ductility for HSC with moderate levels of axial load.

Section (1)	P/P_0 0 (2)	0.3 (3)	0.6 (4)
S-04-M	—	2	2
S-04-H	—	2	2
S-08-L	>12	>12 (>12)	4 (>12)
S-08-M	>12	2 (11)	2 (8)
S-08-H	>12	2 (6)	<2 (5)
S-16-M	—	>12	2
S-16-H	—	2–4	<2

Note: Values in parentheses are for sections with seismic hoop reinforcements.

Figure 2.34: Comparison of Curvature Ductilities, El-Tawil *et al,* (1999).

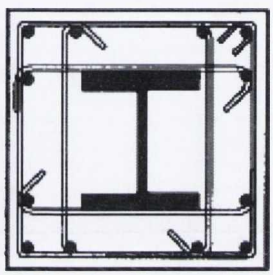

Figure 2.35: Details of Seismic Hoop Reinforcement for Specimen S-08, El-Tawil *et al,* (1999).

2.9 Conclusion

This chapter outlines the importance of detailing for composite design, with particular attention given to improving confinement. It is evident that suitable link spacing is a critical factor, particularly for HSC due to its inherent brittle nature. The chapter also outlines the need for significantly more research to be conducted into HSC composite columns subject to earthquake loading conditions. The requirements for capacity design are presented and some of the research conducted regarding HSC composite columns is discussed. It is clear from previous research that the design codes try to avoid the use of HSC, but it has been shown that with suitable detailing and axial load levels that HSC composite columns can achieve reasonable curvature ductility values. The literature review highlights a lack of research conducted in this area using the European design provisions (Eurocode 8, 2004), subsequent chapters try to deal with some of these issues.

Chapter 3

Experimental Programme

Experimental Programme

3.1 Introduction

The purpose of this chapter is to describe the testing materials, specimens, equipment and procedures used within the experimental programme. Section 3.2 initially presents, an in detailed description of the specimens examined in the tests, including dimensions and constituent materials. Subsequent sections deal with the reaction frame configuration followed by the material characteristics of the specimen constituents. The final sections deal with the specimen production process and finally a detailed description of the experimental equipment used throughout the testing programme.

3.2 Description of Tests

The experimental programme conducted an investigation of steel encased composite columns subject to combined axial and lateral cyclic loading , which is the conventional test loading applied in seismic testing. The primary objective of this investigation was to determine the effects of incorporating high strength concrete (HSC) into these columns and to determine if the current European earthquake design provisions, Eurocode 8 (CEN, 2004) can be implemented or modified to incorporate HSC.

The parameters varied in the tests are as follows:

- The concrete compressive strength, f'_c
- The level of applied axial load
- The link spacing in the critical region

Table 4 summarises the specimens tested in the study, identifying the concrete strength, link spacing and axial load level for each specimen. The number following 'JD' indicates

the order in which the specimen was tested and 'ID' number indicates the order in which the specimens were cast.

Table 4: Experimental Specimen Details

Specimen	Concrete Strength (N/mm^2)	Link Spacing (mm)	Axial Load (kN)	Nominal % of Axial Capacity
JD1 - ID2	25	72	900	30
JD2 - ID1	25	72	900	30
JD3 - ID3	25	72	1200	40
JD4 - ID5	85	72	1200	20
JD5 - ID6	85	72	2000	35
JD6 - ID4	85	50	2000	35

The actual concrete strength on the day of testing is provided in Table 15 for all specimens. The above specimen combinations were selected for a number of reasons. Primarily three normal and three high-strength specimens were selected to compare the performance of varying concrete compressive strength. Within these groups the level of applied axial load and link spacing was varied to extend the experimental results. The level of applied axial load was increased from 900kN – 1200kN for the NSC specimens to determine the effects of an increased axial load beyond the permissible axial load limit to be applied to composite columns. The same principle was adopted for the HSC specimens to facilitate a comparison between the normal and high-strength concrete.

The objective of this experimental programme is to determine the seismic resistance (particularly the ductility) of full scale HSC encased composite columns. The aim is to determine if HSC can be incorporated into encased composite column design using existing code provisions to match (or exceed) the performance of NSC composite columns, and, if not to determine suitable design alterations to improve the performance of the HSC specimens. The ductility requirements of Eurocode 8, (CEN, 2004) are discussed in detail for moment resisting frames (MRF's) in Section 3.2.7.4.

Six specimens were constructed with the aim of comparing five specimen groups, namely to determine (i) the effect of axial load level on HSC specimens, (ii) the effect of axial load on HSC specimens, (iii) comparing the behaviour between normal and high-

strength concrete, (iv) comparing the response of reduced link spacing for HSC specimens, and (v) to compare the behaviour of HSC specimens one having reduced levels of axial load and reduced link spacing. It was deemed unnecessary to review the NSC in terms of reduced link spacing and reduced levels of (maximum) applied lateral load as this research has been conducted previously and is already within the scope of Eurocode 8. The research within was conducted to broaden the scope of the Eurocode thus the above number of specimens and comparison groups were selected.

The link spacing was reduced for one of the HSC specimens to determine if an improved hysteretic performance could be achieved for a high level of applied axial load. HSC is more brittle than NSC thus the reduced link spacing (smaller than the minimum code provisions) was selected to improve the confinement of the core concrete. Specimen JD1 and JD2 were subject to identical testing conditions as Specimen JD1 was not restrained in the perpendicular direction to the applied lateral force, thus the specimen was subject to bi-axial buckling which affected the experimental results thus the test was repeated.

The grades of concrete selected were $25N/mm^2$ and $85N/mm^2$, the lower value was selected as it was well inside the scope of the maximum permissible strength of concrete in the Eurocodes. The higher value was selected as it is considerable outside the scope of the code, but is permissible within similar seismic design codes (i.e. the Japanese and American seismic design codes), thus this grade could be adopted into the Eurocode if suitable design and detailing rules were provided.

The hysteresis response along with the resistance ratio data and energy dissipation of all specimens shall be analysed in order to determine if HSC composite columns can achieve a displacement ductility equivalent to that of a highly ductile (DCH) composite column as part of a moment resisting frame, furthermore it shall be assessed if amendments to the design rules regarding the maximum level of applied axial load and maximum link spacing in the critical region of the column can improve the performance of HSC composite columns. These amendments aim to provide refined rules for the design of HSC composite columns on the basis of extending the maximum concrete grade used within the design code in the future.

3.2.1 Design Constraints

Selection of a suitable and realistic test specimen had to meet multiple design and practical constraints. The specimen had to adhere to all code requirements while remaining at a feasible section size so that the failure load and displacement could be achieved by the (MTS) actuator. The actuator (which is discussed in detail in Section 3.2.6.1) had a 150kN load capacity and ±125mm stroke. The maximum overall section length that could be placed into the test frame was limited to 3.5m; the lateral restraint and cross beams were of considerable size thus required ample room for movement and positioning, this was the primary limitation on the overall length of the test specimens.

Eurocode 8, (CEN, 2004) states that "for fully encased columns with composite behaviour, the minimum cross-sectional dimensions *b, h* or *d* should not be less than 250mm."

Eurocode 4, (CEN, 2004) requires that "the steel contribution ratio, δ should fulfil the following condition":

$$0.2 \leq \delta \leq 0.9 \tag{3.1}$$

Where:

$$\delta = \frac{A_a f_{yd}}{N_{pl,Rd}} \tag{3.2}$$

Where:

A_a = Area of steel section (mm^2)

f_{yd} = Yield strength of steel section (N/mm^2)

$N_{pl,Rd}$ = Plastic resistance to compression, defined in Section 3.2.7.2.

Furthermore, Eurocode 4, (CEN, 2004) states that "For a fully encased steel section, limits on the maximum thickness of concrete cover that may be used in calculation are":

$$\max c_z = 0.3h \;\; ; \;\; \max c_y = 0.4b$$

Where: c_z and c_y are defined in Figure 3.1.

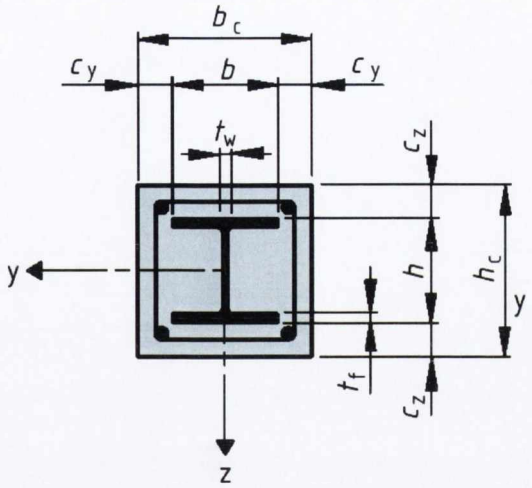

Figure 3.1: Typical Encased Composite Column Notation, Eurocode 4, (CEN, 2004)

"The longitudinal reinforcement that may be used in calculation should not exceed 6% of the concrete area".

Finally, Eurocode 4, (CEN, 2004) requires that "The concrete cover to a flange of a fully encased steel section should be not less than 40mm, or less than one-sixth of the breadth *b* of the flange".

The smallest universal column (UC) section size available, which adheres to the above criteria is a 203 x 46 kg/m^3 UC. Complying with the above concrete cover requirements a suitable overall section size of 300 x 300mm was adopted. The greatest design bending resistance moment is given by:

$$M_{max.Rd} = W_{pa}\frac{f_y}{\gamma_{Ma}} + W_{pc}\frac{\alpha f_{ck}}{2\gamma_c} + W_{ps}\frac{f_{sk}}{\gamma_s} \tag{3.3}$$

Note: the parameters for Equation (3.3) are given in Eurocode 4, (CEN, 2004).

For the specimen adopted in the experimental programme the maximum bending resistance, $M_{max,Rd}$ = 198kNm (for a 25N/mm^2 concrete compressive strength) and 303kNm (for a 85N/mm^2 concrete compressive strength). Adopting a column length of 2.5m, the lateral force required by the actuator corresponds to 79.2kN and 121.2kN, respectively. Both values are within the actuator force limits with an additional margin for material over-strength. The full M-N interaction curves are presented in detail in Section 4.2.3.

3.2.2 Specimen description

The experimental programme consisted of six fully encased composite columns, connected to a reinforced concrete base, representative of a foundation. Figure 3.2 illustrates the specimen dimension and detailing. All structural elements were designed according to Eurocode 8, (CEN, 2004) and other associated design codes, except for the welding of the column links, as described later. The specimens were 2750mm long from the top of the reinforced concrete base, with a 300 x 300mm cross-section. The cross section contains a centrally positioned 203 x 46kg universal column (UC) section which extends 250mm into the reinforced base.

The steel section extends 2600mm along the column length; the remaining 100mm consists of a reinforced concrete cross-section. The aim of this is to initially apply the axial load into the concrete and transfer the stresses into the steel section via shear connectors. The shear studs used were Grade 8.8 M22 bolts, these are not traditional shear studs but if welded on the shank with the hexagonal nut face facing out they act in an identical manner to traditional shear studs. These shear studs were welded to either sides of the web at 250mm centres, the aim of which was to ensure full interaction and load transfer between the steel and reinforced concrete elements.

The steel section is surrounded by a reinforcing cage consisting of 250 x 250mm, T8 bars, Grade S460 links with 90° hooks, shape code 51 conforming to BS 8666, (BSI, 2005). The link spacing in the critical region is presented in Table 4, beyond the critical region a common link spacing of 240mm applies throughout. The overlapped ends of the links were welded to prevent opening of the links at large strains, a phenomenon which results in loss of confinement to the partially confined concrete. There is no recommendation or provisions in the design code, Eurocode 4, (CEN, 2004) for welded links; it stipulates that links must contain 135° bent-in hooks.

This provision was not feasible for this experimental programme due to the limited cross-sectional space. Welding of steel alters the material properties and may cause the links to fracture at a reduced strain (thus reducing the ductility of the reinforcing steel). This was considered, but it did not have any effect on the experimental programme as throughout testing only one link fractured and this did not occur at a welded location, but

at a strain gauge location where the surface of the link was slightly ground down to accommodate the strain gauge.

Due to the practical size limitations of the composite column, the transverse reinforcement is spaced close to the steel section, as illustrated in section B – B of Figure 3.3 (all the minimum cover provisions are still adhered to). If 135° bent-in hooks were to be incorporated, the hooks would press against the steel flange and alter the square shape of the links. Welded 90° links are a suitable alternative as they provide additional confinement due to the lack of slip between overlaps at high strains. Longitudinal steel consisted of six T12 Grade S460 bars, four of which are located at the link corners, the other two located along the steel sections weak axis, thus providing additional moment resistance for major axis bending. The longitudinal steel was bent into the reinforced concrete base according to shape code 11, BS8666, (BSI, 2005).

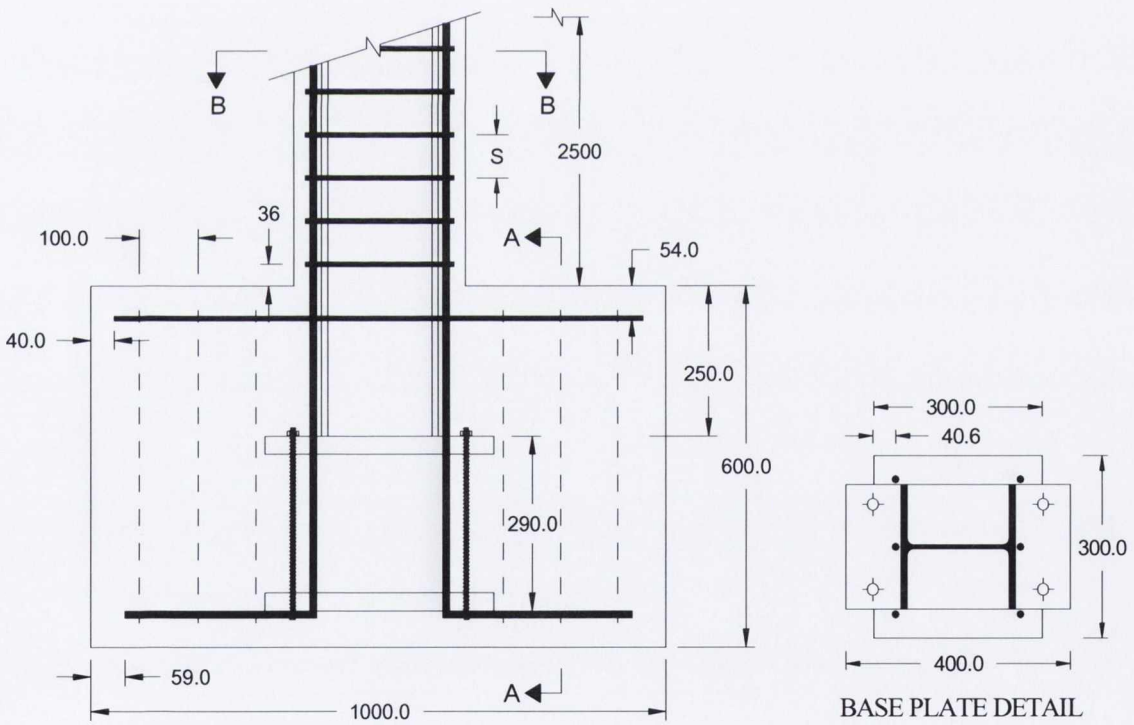

Figure 3.2: Composite Column Dimensions & Detailing

The footing was designed to resist the flexural and shear forces imposed on it by the capacity of the composite column. The base element was 1000mm long, 600mm x 600mm in breadth and width respectively with minimum 40mm cover to all steel. The base links consisted of T12 Grade S460 bars at 100mm spacings beyond the extremities of the anchor plates (Shape Code 51, BS8666, (BSI, 2005)). A base plate was welded to the end of the specimens, the details of which are provided in Figure 3.2.

The purpose of the base plate being welded to the column end was to provide additional interaction between the column and base element and to provide a connection mechanism for the anchor plate. The anchor plate was of identical size but was located 230mm below the base plate. The two plates were connected via four 20mm threaded bars, bolted at either side of both plates. The purpose of the anchor plate was to improve the interaction between the column and base element and to ensure that sufficient restraint was provided by the footing to enable the formation of a plastic hinge in the lower region of the composite column.

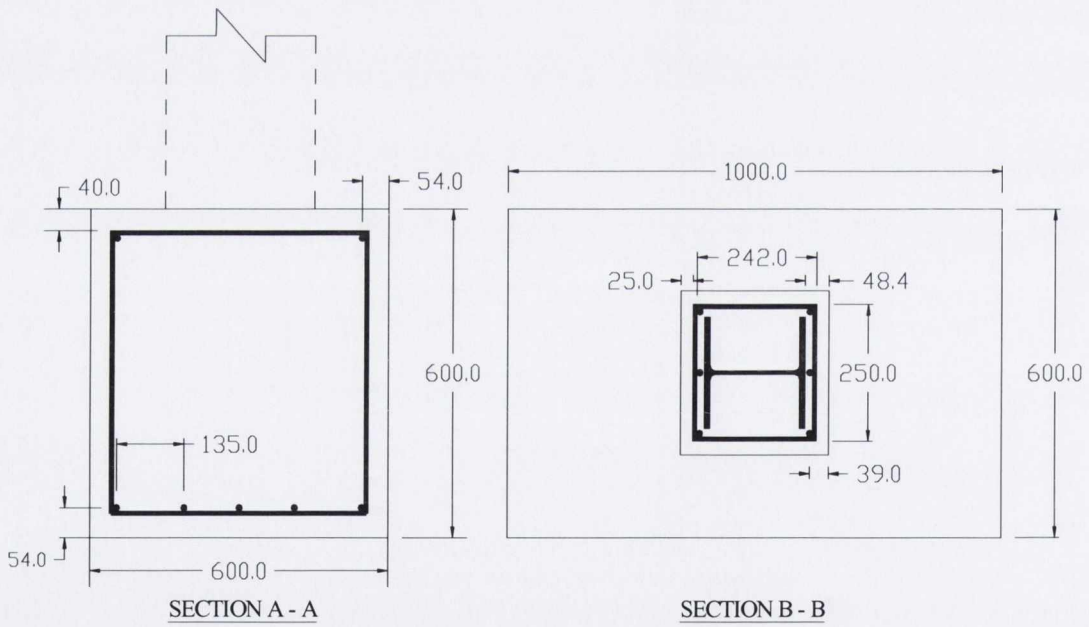

Figure 3.3: Specimen Section Details

In all of the test specimens the first link in the critical region is located 36mm above the interface between the column and base elements. 25mm cover is provided to all links in the column element along with approx 48mm cover to the extremities of the steel flange.

As detailed earlier, Eurocode 8, 2004 (CEN, 2004) stipulates that for fully encased columns with composite behaviour, the minimum cross section shall not be less than 250mm. Eurocode 4, (CEN, 2004) specifies a minimum cover of 40mm is required to steel flange elements of a composite column.

All structural and reinforcing steel was grade S275 and S460 respectively, the specific properties of which are provided in Section 3.2.4.2. The concrete material properties are presented in Section 3.2.4.1.

3.2.3 Reaction frame and test set-up

The test set-up as presented in Figure 3.4 was designed to apply a constant axial load to the specimen while the lateral load is displacement controlled via a 150kN MTS actuator. The specimen was tested on its side as head room was limited and it enabled a realistic section size to be analysed.

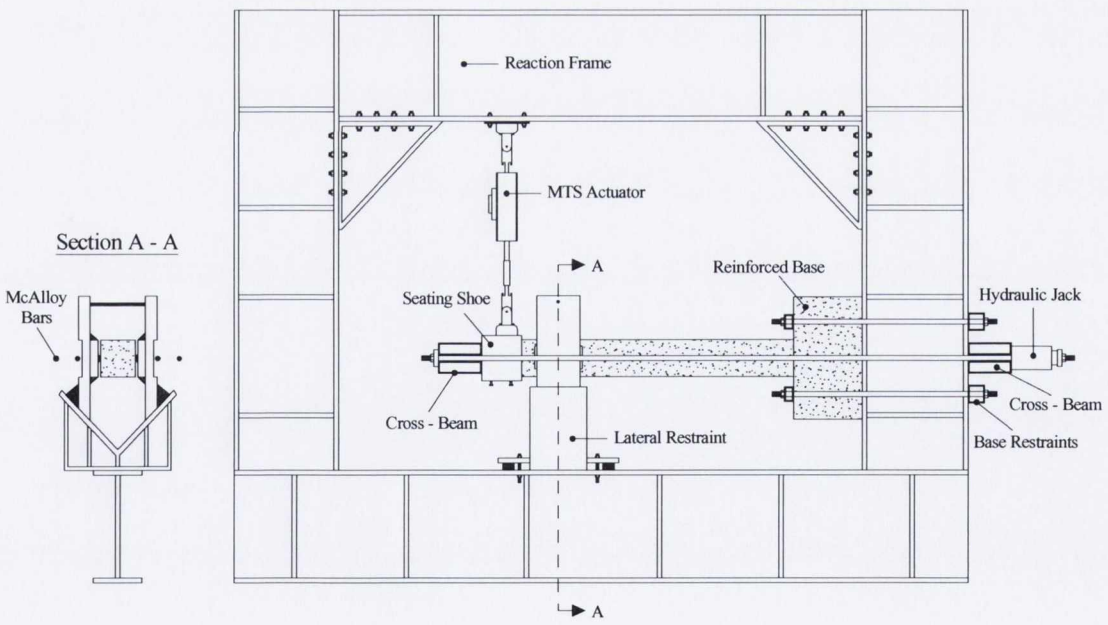

Figure 3.4: Reaction Frame and Test Set – Up

The axial load was applied by means of four No. 90 tonne jacks placed on an over-strength cross beam, which in turn was restrained by one end of the reaction frame. Four No. McAlloy bars ran through the cross beams and were bolted at the ends of each jack,

at the opposite end of the specimen an identical cross beam was used to distribute the applied axial load through the section and directly into the tip of the test specimen.

Figure 3.5 illustrates a more detailed representation of the applied loading and load transfer through the specimen and reaction frame. The cross beam was connected to the specimen by means of a seating shoe, which was placed over the specimen and clamped from below. The cross beam set-up provided lateral restraint to the jacks and ensured symmetrical loading of the specimen.

The force provided by the jacks placed the McAlloy bars in tension and transferred the loads through the far cross beam into the composite column, which in turn reacted against the test frame. Load cells were placed on two of the jacks, one on either side of the two McAlloy's running either side of the test specimen. The shoe had pre-drilled holes on its top face to facilitate connection of the MTS actuator at the desired distance from the column base. The other end of the actuator was bolted to the test frame thus providing a reaction mechanism for lateral loading.

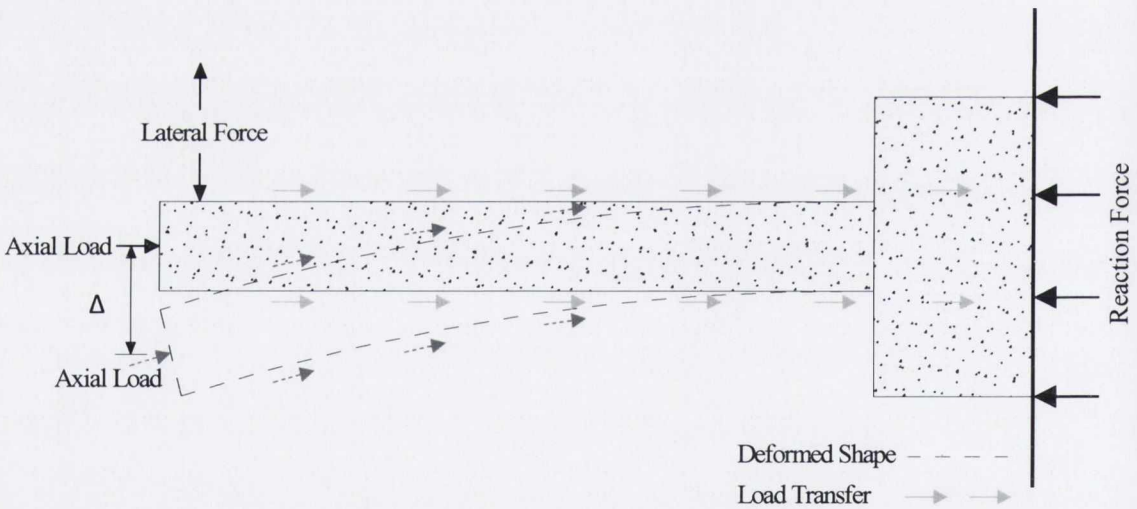

Figure 3.5: Schematic Representation of Applied Loads and Load Transfer

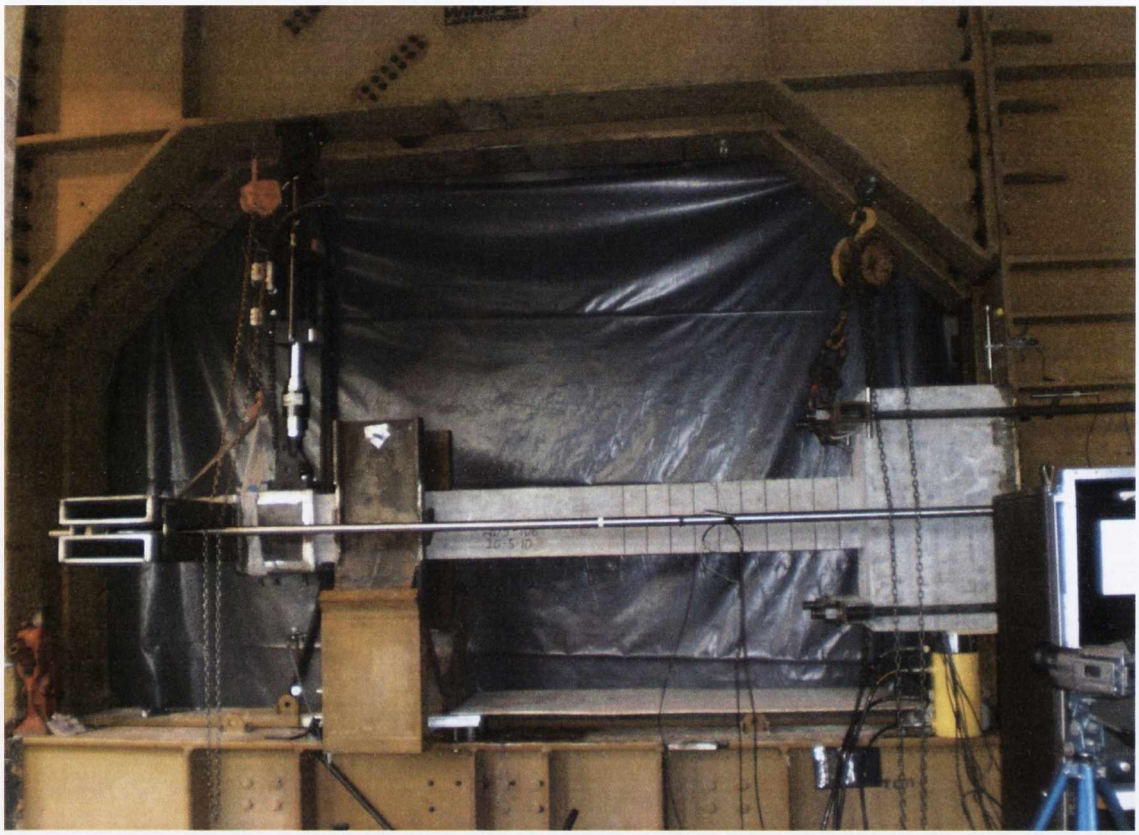

Figure 3.6: Reaction Frame and Specimen Alignment

The reinforced concrete base was held in position primarily by the compressive and frictional effects induced by the axial load, but additional clamps were placed on either end of the reinforced base, the clamps consisted of SHS cross beams connected via threaded McAlloy bars, which were post-tensioned subsequent to the application of axial load. These clamps provided additional restraint and prohibited any undesirable rotation of the base element during cyclical loading.

The specimen was restrained against out-of-plane movement by means of a roller restraint. Early tests proved that once the section had yielded, the column tended to buckle about both axes. This caused the column to move out of its original alignment and the axial load increased the moment about the tip due to its new geometry, thus inducing further 'out of plane' buckling. A roller restraint was designed to prevent this initial perpendicular movement. Figure 3.7 presents a photograph and detail of the roller restraint.

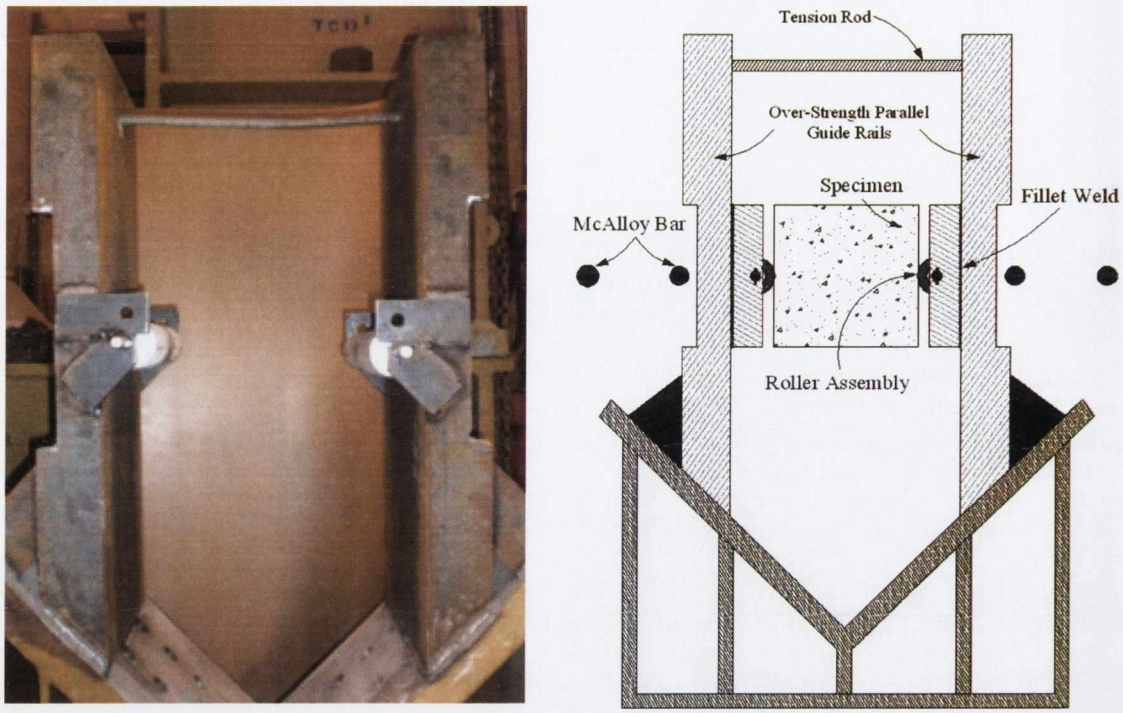

Figure 3.7: Roller Restraint Picture & Detail

The restraint consists of an over-strength steel section, bolted to the reaction frame with parallel channel sections providing the guide rails. A roller configuration was attached to the guide rails which rested on the vertical faces of the composite section. These rollers allowed for vertical displacement from the MTS actuator but prohibited perpendicular displacement.

3.2.4 Material properties

The following sections present the tested material properties for all constituent materials.

3.2.4.1 Concrete properties

Two different concrete mixes were used in the tests, one normal-strength (NSC) and one high-strength (HSC). The concrete was purchased off-site due to the quantity required and to remove variations between pours. Details of the concrete mix characteristics are provided in Table 5. A maximum aggregate size of 10mm is adopted throughout due to the density and limited room around the reinforcement. Table 6 presents the concrete

constituents and quantities for each mix. Every mix conformed to the production requirements of BS EN 206-1, (BSI, 2001) and associated codes.

Table 5: Concrete Mix Characteristics

Mix Property	*Normal-Strength Concrete*	*High-Strength Concrete*
f_{cu} (N/mm^2)	25	85
Slump (mm)	150	180
Water-cement ratio	0.60	0.35
Max. aggregate size (mm)	10	10
Admixture	NO	YES

A self-compacting admixture (ADVA Flow 411, of Grace Construction Products) was incorporated in the High-strength mix design to aid the workability of the mix. The aim was to reduce the water content thus maximising the potential 28 day concrete strength. It was deemed unnecessary to include an admixture in the normal strength mix. Both mixes incorporated grade 42.5 Normal Portland Cement, but the high-strength mix also incorporated ground granulated blast-furnace slag to improve workability and reduce the quantity of cement otherwise required to achieve a similar strength.

Table 6: Concrete Mix Quantities

Material	*NSC Mix (kg/m^3)*	*HSC Mix (kg/m^3)*
Cement	415	310
GGBS	N/A	210
10mm Aggregate	1075	900
Sand	460	544
Dust	200	231
Water	250	180
Admixture	N/A	4.16

3.2.4.2 Steel properties

Both reinforcing and structural steel coupons were tested according to BS 10002-1, (BSI, 2001). Table 7 and Table 8 present the average results for each sample with respect to

yield force (f_y), yield stress (σ_y), yield strain (ε_y), Young's Modulus (E_s), ultimate stress (f_u), ultimate stress (σ_u), extension at failure (mm) and ultimate strain (ε_u) for the reinforcing and structural steel respectively. A 500kN capacity Denison universal testing machine was used to load all samples to failure. Every sample contained a strain gauge at its mid-section to determine the elastic material properties, post yield strains caused these gauges to become detached, but using the recorded initial and final length of each sample, an ultimate strain value was measured. The yield and ultimate stresses are approximations as they are based on the original bar area and not on the reduced bar area at yield and ultimate strains. This applies for both round and flat samples.

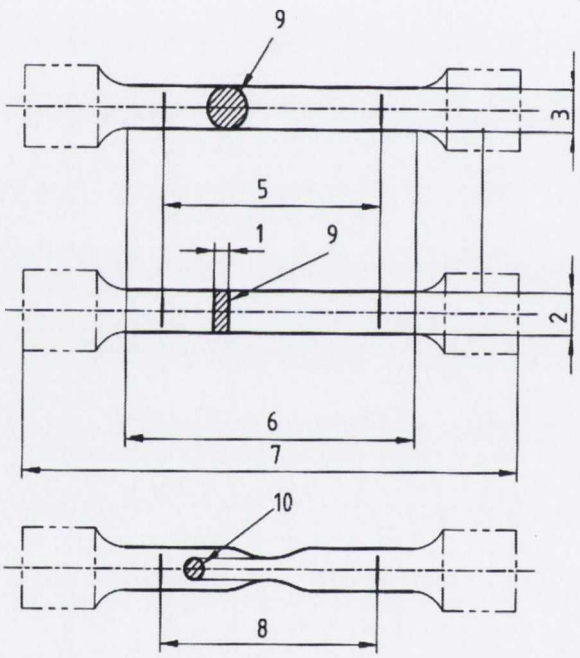

Reference Number	Designation
1	Wall thickness of tube or bar (mm)
2	Width of the parallel length of the longitudinal flat strip (mm)
3	Diameter of parallel length for circular test piece (mm)
5	Original gauge length (mm)
6	Parallel length (mm)
7	Total length of test piece (mm)
8	Final gauge length after fracture (mm)
9	Original cross-sectional area of gauge length (mm^2)
10	Minimum cross-sectional area after fracture (mm^2)

Figure 3.8: Shape and Definition of Steel Coupon Tests

Table 7: Steel Reinforcement Material Properties

Bar Size *(mm)*	f_y *(kN)*	σ_y *(N/mm^2)*	ε_y	E_s *(N/mm^2)*	f_u *(kN)*	σ_u *(N/mm^2)*	Extension at failure *(mm)*	ε_u
8	22.6	435	0.0021	207000	30.7	610	7.5	0.062
10	35.6	440	0.0021	209000	47.1	600	9	0.066
12	52	460	0.0022	210000	70.1	620	17	0.072

Table 8: Structural Steel Properties

Flat Bar Width *(mm)*	f_y *(kN)*	σ_y *(N/mm²)*	ε_y	E_s *(N/mm²)*	f_u *(kN)*	σ_u *(N/mm²)*	Extension at failure *(mm)*	ε_u
25	59.6	271	0.0014	187000	94.2	428	51	0.127
40	121	275	0.0015	183000	193.6	440	35	0.137

3.2.5 Specimen production

The first step in the fabrication was welding the shear connecters to both sides of the UC web; once this was complete the reinforced cage could be assembled around the steel section with welding of the links in the critical region. The final process was to secure the anchor plate and attach the relevant spacers to maintain the desired concrete cover to all exposed faces. Each base element contained four threaded lifting bolts which could incorporate lifting eyes once the concrete was cured. Each eye was secured to the base reinforcement and was sealed during the concrete pour.

Each specimen was extensively gauged at multiple locations on the steel flange, longitudinal bars, confining links and external concrete faces. The location and nature of these gauges are illustrated in Section 3.2.6. The specimens were cast using 19mm plywood formwork which was well cleaned and coated in a de-moulding agent to ease the stripping and re-use of the formwork. Each specimen was poured in two phases, the initial phase consisted of pouring the base element and vibrating to remove air voids (vibration only required for NSC as HSC contained self compacting admixture). The column element was poured approximately half an hour after, thus allowing the base sufficient time to settle and become adequately stiff, thus reducing the hydrostatic pressure imposed from the fluid concrete. Once final vibration was complete the exposed top face was smoothened with a steel trowel. The specimens remained in the formwork for three days before they were stripped and the formwork was cleaned and re-coated with de-moulding agent for the next pour. All specimens cured for a minimum of 28 days before they were tested

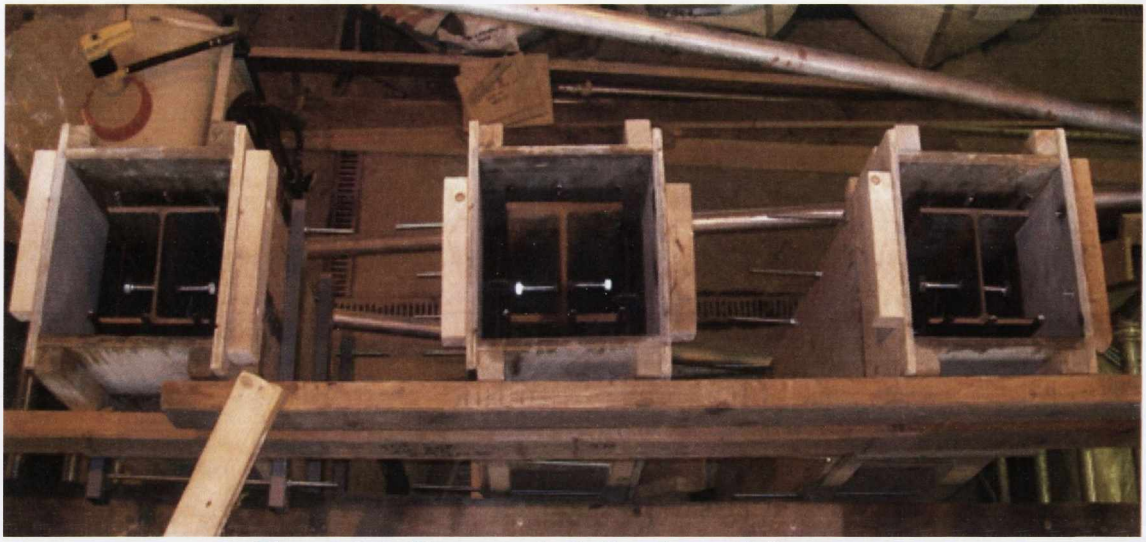

Figure 3.9: Formwork & Specimen Alignment

Figure 3.10: (A) & (B) Formwork Set-Up & Casting

3.2.6 Experimental equipment

The following section provides details of the experimental hardware and measurement instrumentation used during the experimental programme.

3.2.6.1 MTS actuator

The actuator used throughout testing was an MTS 150kN Fast Actuator. The stroke of the actuator was ±125mm. The MTS actuator is part of a real-time hybrid test system. The system has the capabilities of testing the critical parts of the structure (substructure) whilst simultaneously modelling the rest of the structure being considered. A numerical representation of a structure can be created in Mathworks Simulink on the Simulation PC and then downloaded onto the Target PC through fibre optic cables. The Target PC sends commands to the Structural Test System (STS) controller via the shared reflective memory called SCRAMNet (Shared Common RAM Network). The Test PC provides the user interface to the Servo-controller and allows tuning and control of the actuator through a Proportional-Integral-Derivative (PID) controller.

The command force/displacement is then sent from the Servo-controller to the MTS actuator. The measured force and displacement are sent back to the Servo-controller and then back to the Target PC, where the data is used to calculate the next time-step command displacement, making the process close-looped. The Real Time Hybrid Testing (RTHT) communication between the hardware and software is illustrated in Figure 3.11.

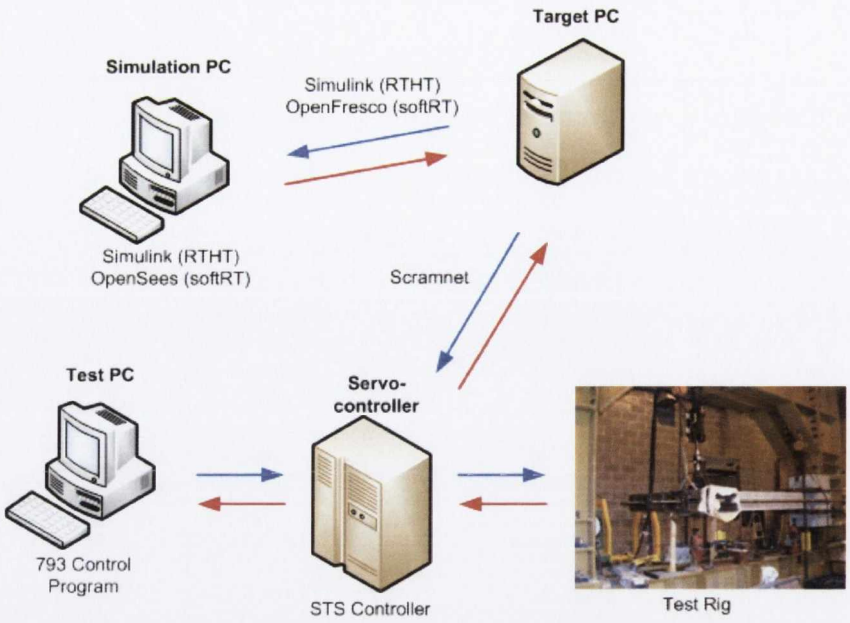

Figure 3.11: Schematic of the Hardware and Software for RTHT

The above described process is a considerably more complex process than was required for the experimental programme herein. For this research a predefined test-displacement history (as presented in Figure 3.17) was input into Test PC, the required displacements were sent from the STS controller to the MTS actuator. The measured force and displacement are sent back to the Servo-controller and then back to the Test PC and recorded. Figure 3.12 presents a schematic of the hardware and software used for the experimental programme.

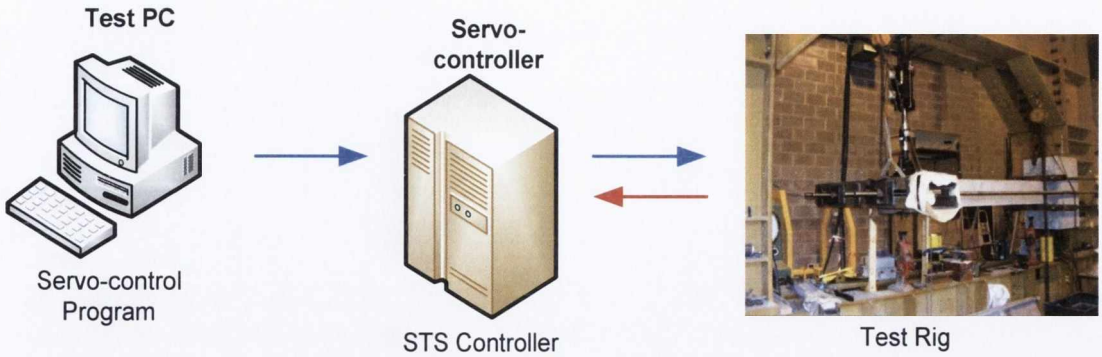

Figure 3.12: Schematic of the Hardware and Software for Experimental Programme

3.2.6.2 Strain gauges

All specimens were extensively gauged to measure the strain response of all composite elements at varying displacements. The strain gauges attached to reinforcing and structural steel were Radionics 120 Ohm, N11-MA5-120-11 gauges (5mm width and 120mm Gauge Length). Ribbed bars and flat steel were ground down to expose a flat smooth surface on which to attach the gauge. All steel surfaces were thoroughly cleaned and gauges were covered with a moisture proofing epoxy to prevent damage during the concrete pour.

Concrete (surface) gauges were attached at similar locations using TML 120 Ohm, PL-120 gauges. Table 9 and Table 10 present the location and reference annotation for all gauges; Figure 3.13 illustrates schematically the steel strain gauge locations. Figure 3.14 presents photographic images of both steel and concrete strain gauge location.

Table 9: Strain Gauge Reference and Location Specimens JD 1, 2 & 3

Gauge Reference	Gauge Location
SG 1	Longitudinal Bar, Face B-C, 600mm up from Base
SG 2	Longitudinal Bar, Face B, 600mm up from Base
SG 3	Longitudinal Bar, Face B-C, 600mm up from Base
SG 4	Steel Flange, Face B, 600mm up from Base
SG 5	Longitudinal Bar, Face B-C, 250mm up from Base
SG 6	Longitudinal Bar, Face B, 250mm up from Base
SG 7	Longitudinal Bar, Face B-C, 250mm up from Base
SG 8	Steel Flange, Face B, 250mm up from Base
SG 9	Longitudinal Bar, Face D-C, 600mm up from Base
SG 10	Longitudinal Bar, Face D, 600mm up from Base
SG 11	Longitudinal Bar, Face D-C, 600mm up from Base
SG 12	Steel Flange, Face D, 600mm up from Base
SG 13	Longitudinal Bar, Face D-C, 250mm up from Base
SG 14	Longitudinal Bar, Face D, 250mm up from Base
SG 15	Longitudinal Bar, Face D-C, 250mm up from Base
SG 16	Steel Flange, Face D, 250mm up from Base
SG 17	Transverse Link, Face A, 8^{th} link up from Base
SG 18	Transverse Link, Face A, 7^{th} link up from Base
SG 19	Transverse Link, Face A, 6^{th} link up from Base
SG 20	Transverse Link, Face A, 5^{th} link up from Base
SG 21	Transverse Link, Face A, 4^{th} link up from Base
SG 22	Transverse Link, Face A, 3^{rd} link up from Base
SG 23	Transverse Link, Face A, 2^{nd} link up from Base
SG 24	Transverse Link, Face C, 8^{th} link up from Base
SG 25	Transverse Link, Face C, 7^{th} link up from Base
SG 26	Transverse Link, Face C, 5^{th} link up from Base
SG 27	Transverse Link, Face C, 5^{th} link up from Base
SG 28	Transverse Link, Face C, 4^{th} link up from Base
SG 29	Transverse Link, Face C, 3^{rd} link up from Base
SG 30	Transverse Link, Face C, 2^{nd} link up from Base

Table 10: Strain Gauge Reference and Location Specimens JD 4, 5 & 6

Gauge Reference	Gauge Location
SG 1	Longitudinal Bar, Face B-C, 600mm up from Base
SG 2	Longitudinal Bar, Face B, 600mm up from Base
SG 3	Longitudinal Bar, Face B-C, 600mm up from Base
SG 4	Steel Flange, Face B, 600mm up from Base
SG 5	Longitudinal Bar, Face B-C, 250mm up from Base
SG 6	Longitudinal Bar, Face B, 250mm up from Base
SG 7	Longitudinal Bar, Face B-C, 250mm up from Base
SG 8	Steel Flange, Face B, 250mm up from Base
SG 9	Longitudinal Bar, Face D-C, 600mm up from Base
SG 10	Longitudinal Bar, Face D, 600mm up from Base
SG 11	Longitudinal Bar, Face D-C, 600mm up from Base
SG 12	Steel Flange, Face D, 600mm up from Base
SG 13	Longitudinal Bar, Face D-C, 250mm up from Base
SG 14	Longitudinal Bar, Face D, 250mm up from Base
SG 15	Longitudinal Bar, Face D-C, 250mm up from Base
SG 16	Steel Flange, Face D, 250mm up from Base
SG 17	Transverse Link, Face B, 6^{th} link up from Base
SG 18	Transverse Link, Face B, 5^{th} link up from Base
SG 19	Transverse Link, Face B, 4^{rd} link up from Base
SG 20	Transverse Link, Face B, 3^{rd} link up from Base
SG 21	Transverse Link, Face B, 2^{nd} link up from Base
SG 22	Transverse Link, Face D, 6^{th} link up from Base
SG 23	Transverse Link, Face D, 5^{th} link up from Base
SG 24	Transverse Link, Face D, 4^{rd} link up from Base
SG 25	Transverse Link, Face D, 3^{rd} link up from Base
SG 26	Transverse Link, Face D, 2^{nd} link up from Base
SG 27	Transverse Link, Face C, 6^{th} link up from Base
SG 28	Transverse Link, Face C, 4^{rd} link up from Base
SG 29	Transverse Link, Face A, 5^{th} link up from Base
SG 30	Transverse Link, Face A, 3^{nd} link up from Base

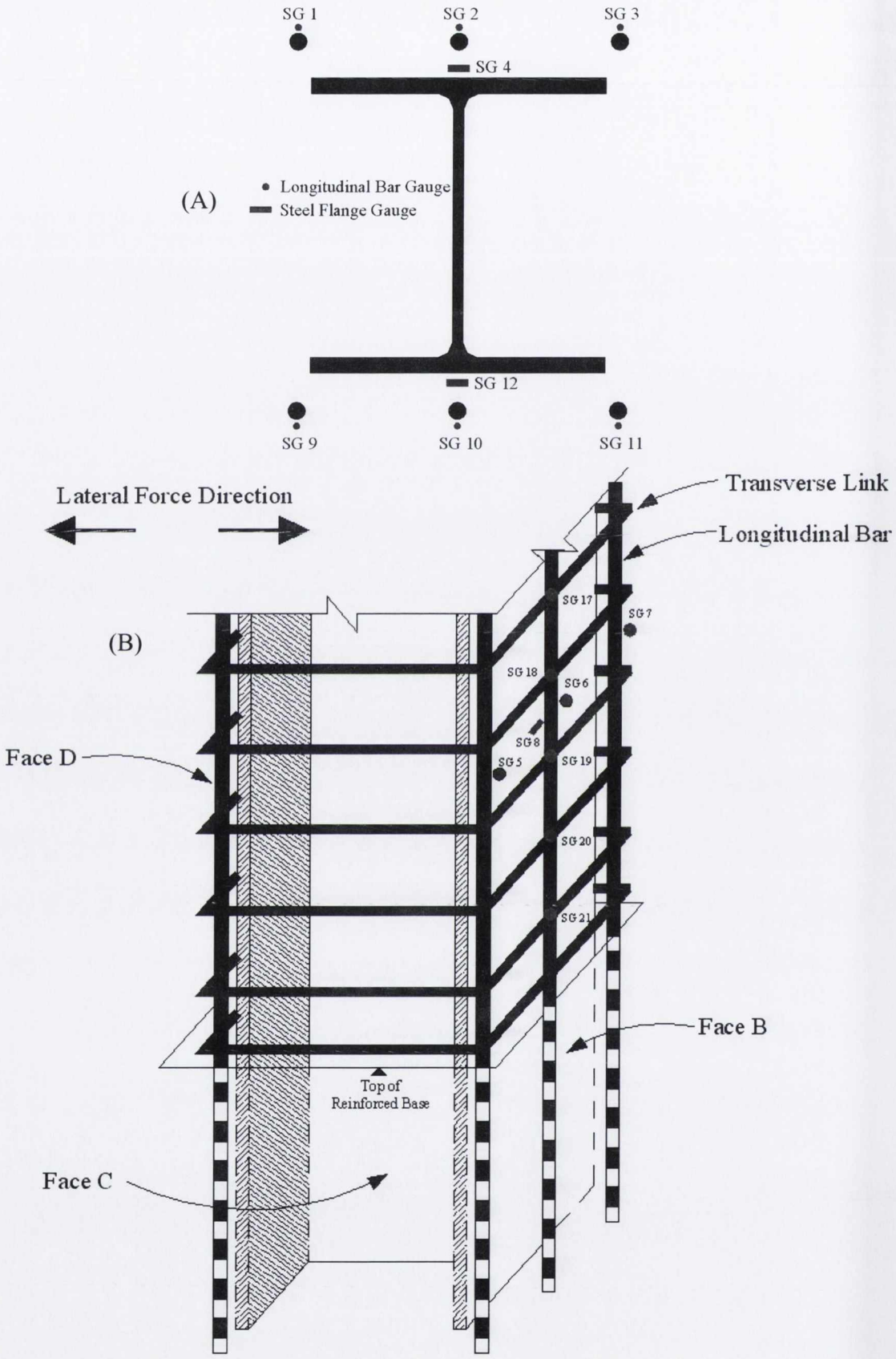

Figure 3.13: Strain Gauge Layout for Composite Column; (A) Layout at 600mm above Base Element; (B) Layout in Critical Region.

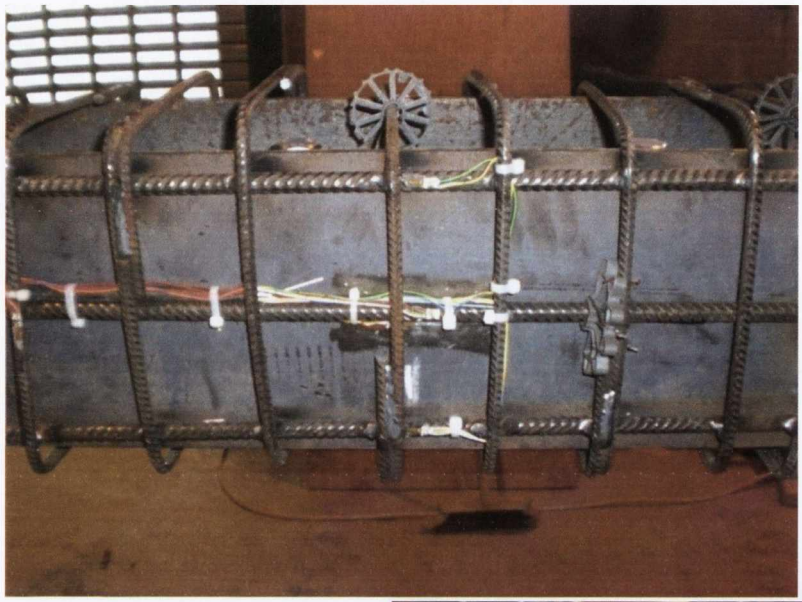

Figure 3.14: Steel and Concrete Strain Gauge Location and Connection Detail

3.2.6.3 LVDTs

Linear Variational Displacement Transformers (LVDTs) were fixed at a number of locations throughout the specimen to monitor undesirable specimen movement. An internal LVDT within the actuator was the primary mechanism for recording the displacement of the specimen, but an additional potentiometer (POT) was attached to the underside of the cross-beam seating shoe to measure the specimen displacement and record it on the System 5000. Table 11 identifies the referencing order of the LVDTs and specifies the displacement recorded by each. Figure 3.15 shows the locations of all LVDT instruments.

Table 11: LVDT Referencing and Location

LVDT Reference	Recording Displacement of the
LVDT 1	Restraint in Transverse Direction
LVDT 2	Restraint in Longitudinal Direction
LVDT 3	Reinforced Base (bottom corner)
LVDT 4	Reinforced Base (upper corner)
LVDT 5	Reinforced Base in Vertical Direction
POT	Composite Column at Lateral Loading Position

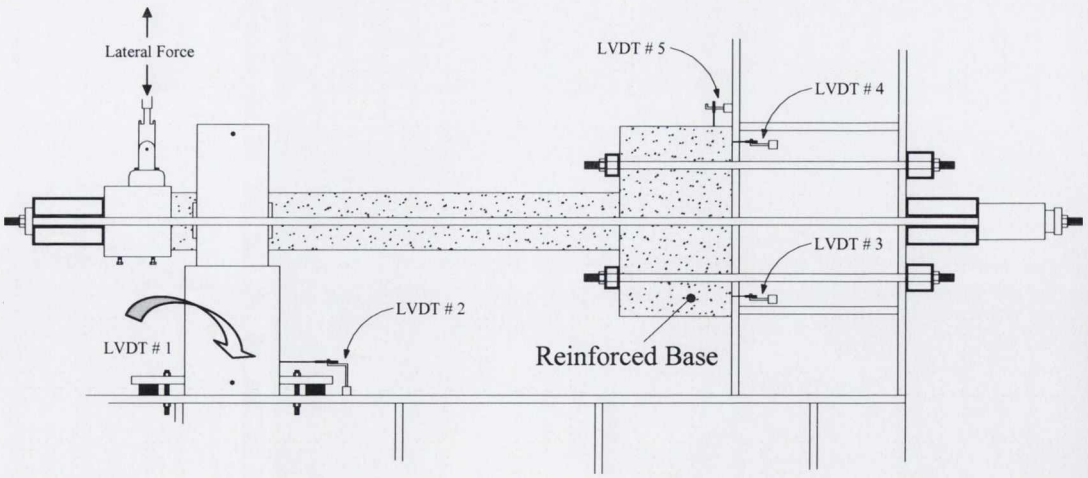

Figure 3.15: LVDT Locations

3.2.6.4 Data Acquisition

The hardware used to record the instrumentation attached to the test specimen was a StrainSmart® System 5000 Data Acquisition Unit. This unit is a specialist strain gauge and voltage logging system. This System 5000 recorded the strains of 30 No. internal steel gauges (locations of which are provided in Table 9 and Table 10), 4 No. external concrete gauges, 5 No. LVDT's, 1 No. Potentiometer and 2 No. load cells. A constant scan rate of 10 scans per second was adopted for all tests to allow for an accurate record of element strains.

3.2.7 Test procedure

3.2.7.1 Lateral loading

Specimens were subject to a constant axial compressive load while being displaced laterally by an MTS actuator. A shakedown test was performed prior to each major test to ensure all data acquisition units and instrumentation were recording correctly. This test also allowed the restraining clamps to be further tensioned post full axial load application. This removed any initial restraining forces and ensured the specimen was adequately clamped to the reaction frame. The shakedown test displaced the specimen at cycles significantly below their expected yield displacement. The shakedown test displacement history is presented in Figure 3.16.

For the main tests the specimens were subject to displacement cycles of multiples of 30mm. This value was selected to enable four full displacement cycles for all specimens (i.e. normal and high strength). Every specimen was subject to cycles of ¼, ½ and ¾ of this displacement, beyond this; all specimens were subject to three cycles of each displacement group corresponding to 30, 60, 90 and 120mm. The displacement history for the main test is presented in Figure 3.17.

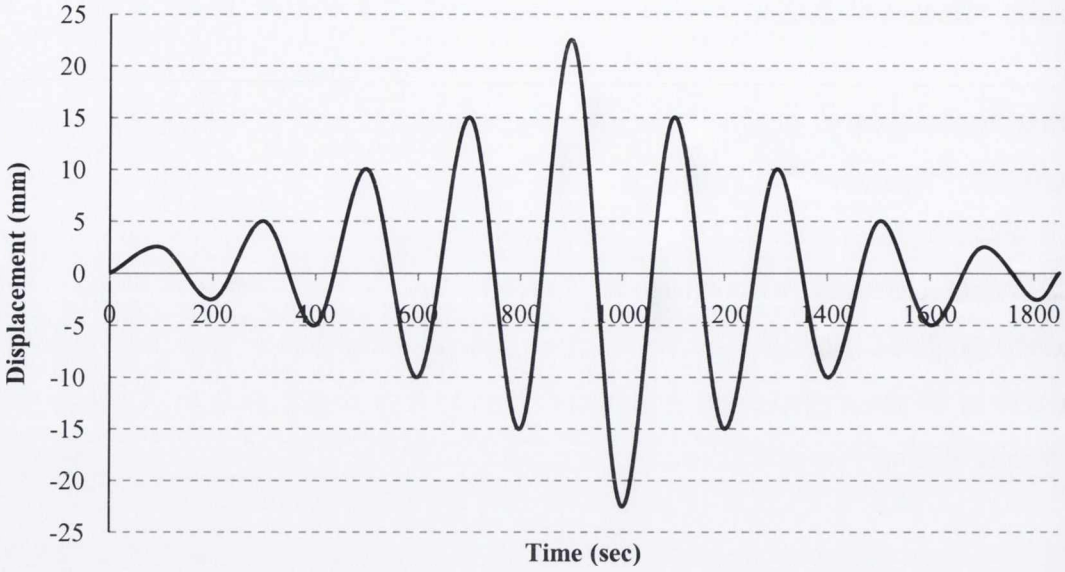

Figure 3.16: Shakedown Displacement History

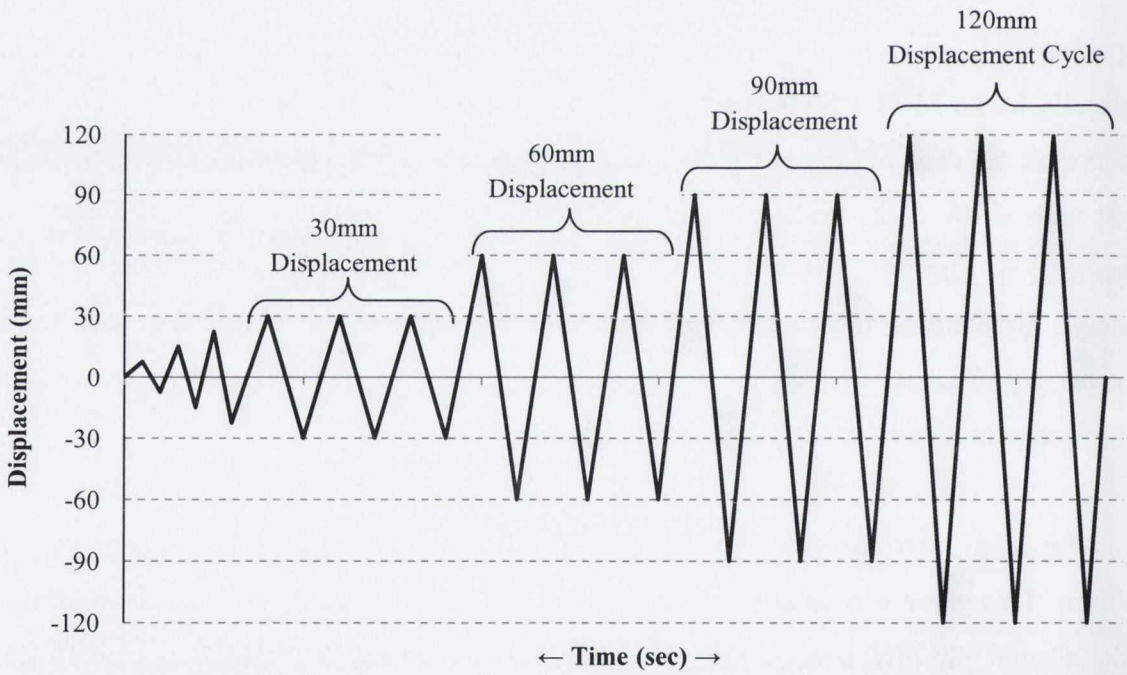

Figure 3.17: Main Test Displacement History

Note: Time scale not included in Figure 3.17 as minor variations were made in the test loading rate between tests due to practical limitations of the hydraulic oil cooling system. A rate of lateral displacement of approximately 2mm/second was adopted throughout.

3.2.7.2 Axial loading

Each specimen was subject to a constant axial load, specified as a proportion of the axial capacity of its cross-section, calculated using on the following expression from Eurocode 4, (CEN, 2004):

$$N_{pl.Rd} = A_a \frac{f_y}{\gamma M_a} + A_c \left(\frac{0.85\, f_{ck}}{\gamma_c}\right) + A_s \frac{f_{sk}}{\gamma_s} \tag{3.4}$$

Where:

$N_{pl,Rd}$ = Sectional axial compressive capacity

A_a = Area of steel section

A_c = Area of concrete

A_s = Area of longitudinal steel reinforcement

f_y = Yield stress of steel secton

f_{ck} = Compressive stress of the concrete

f_s = Yield stress of the longitudinal steel reinforcement

γ_{Ma} , γ_c and γ_s = Partial safety factors at ultimate limit state for the structural steel, concrete and longitudinal reinforcing steel.

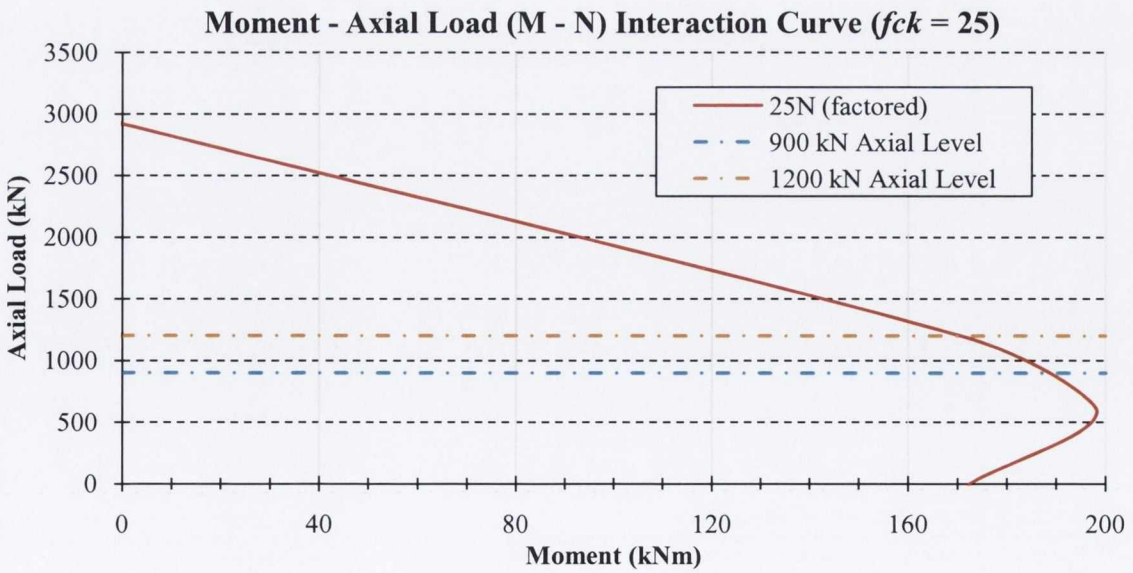

Figure 3.18: NSC Design M-N Interaction Curve

Figure 3.18 presents the design M-N interaction curve (based on Eurocode 4 (CEN, 2004) equations) for the NSC composite columns. From this interaction curve it is feasible to predict specimen bending capacity when subject to a specific constant axial compressive force, but it is shown in Chapter 4 that the M-N interaction curves underestimate the cross-sections' capacity due to the application of partial safety factors.

Table 4 (Section 3.2) presented the nominal percentage of axial load applied to each specimen based on their design axial capacity. The specimens are subject to different axial loads and the associated effects will be discussed in Chapter 4, of particular interest is the reduction in ductility expected in HSC specimens subjected to high axial loads.

Axial Buckling Capacity of Composite Columns

The axial capacity and the resistance to buckling of a composite member depends on a number of factors, primarily the level of axial load, the cross-section geometry, the material strengths, the member length and if any imperfections exist along the member length. A member may theoretically achieve its 'squash load' if restrained effectively but this is seldom possible, thus, a decrease in resistance is caused by the action of the applied compressive load, P.

Once the elastic critical buckling load, N_{cr} is reached the member will be prone to lateral buckling, thus preventing the ultimate axial capacity of the cross section being achieved. The elastic critical buckling load is a key value for design as a columns maximum design axial load must not exceed this value.

For lateral buckling of columns the design value of axial resistance, $N_{b,Rd}$ which must not be exceeded is given by:

$$N_{b,Rd} = \chi N_{pl,Rd} \tag{3.5}$$

Where:

χ = Slenderness reduction factor for the relevant buckling mode

$N_{pl,Rd}$ = Sectional axial compressive capacity, given in Equation (3.4).

χ is related to the non-dimensional slenderness ratio, λ and the imperfection constant, α by the following expression:

$$\chi = \{\phi + (\phi^2 - \lambda^2)^{0.5}\}^{-1} \quad \text{but} \chi \leq 1 \tag{3.6}$$

Where:

$$\phi = 0.5(1 + \alpha(\lambda - 0.2) + \lambda^2) \tag{3.7}$$

$$\lambda = \sqrt{\frac{N_{pl,Rd}}{N_{cr}}} \tag{3.8}$$

$\alpha = 0.34$ for a UC section (Grade S275, t_f <100mm, bending about the strong axis).

The elastic critical buckling load, N_{cr} for a concrete encased composite column of effective length L_{cr} is given by the Euler buckling strength with an effective rigidity $(EI)_e$.

$$N_{cr} = \frac{\pi^2(EI)_e}{(L_{cr})^2} = \frac{\pi^2(E_a I_a + 0.8E_{cd} I_c + E_s I_s)}{(L_{cr})^2} \tag{3.9}$$

Where:

I_a , I_c , and I_s = Second moment of area of the steel section, un-cracked concrete in compression and the longitudinal reinforcement about the axis of buckling.

E_a , E_{cd} , and E_s = The modulus of elasticity of the steel section, the concrete and the longitudinal reinforcement.

L_{cr} = 2.0L for a strut fixed at one end with a parallel load applied centrally to the other end.

For the two broad specimen groups discussed in this thesis, (i.e. the NSC and the HSC specimens) the following effective rigidities were calculated:

$(EI)_e = 2.1235E^{13}$ Nmm^2 (NSC specimen) and $(EI)_e = 2.5839E^{13}$ Nmm^2 (HSC specimen)

Using Equations (3.5) to (3.9), the following non-dimensional slenderness ratio, χ values were determined:

$\chi = 0.836$ (NSC specimens) and, $\chi = 0.813$ (HSC specimens)

This results in a design value of axial resistance, $N_{b,Rd}$ (which must not be exceeded) corresponding to:

$N_{b,Rd} = 2443$kN (for 25N/mm^2 specimens)

$N_{b,Rd} = 3336.4$kN (for 85N/mm^2 specimens)

3.2.7.3 P-Delta effects

P-Delta moments are additional moments imposed on a specimen due to the eccentricity between the line of the axial force and the longitudinal axis of the beam-column as the specimen displaces laterally. This is due to the specimen's rotation about a point some distance above the rotation point of the axial load apparatus. Therefore, specimens were subject to:

- A direct moment due to the applied lateral load at a fixed distance above the reinforced base.
- A moment due to the component of the axial load acting eccentrically (by a distance δ, as illustrated in Figure 3.19) to the specimen's longitudinal axis, or a 'P-Delta moment'.

The method of determining the P-Delta moment and the total moment acting on the specimen is set out in Equations (3.10) to (3.14).

$$\theta = Tan^{-1}(\Delta/4450) \tag{3.10}$$

$$\alpha = Tan^{-1}(\Delta/2550) \tag{3.11}$$

$$\gamma = \alpha - \theta \tag{3.12}$$

$$P_h = Pcos(90 - \gamma) \tag{3.13}$$

$$M = (F\ x\ 2550) + (P_h\ x\ 2700) \tag{3.14}$$

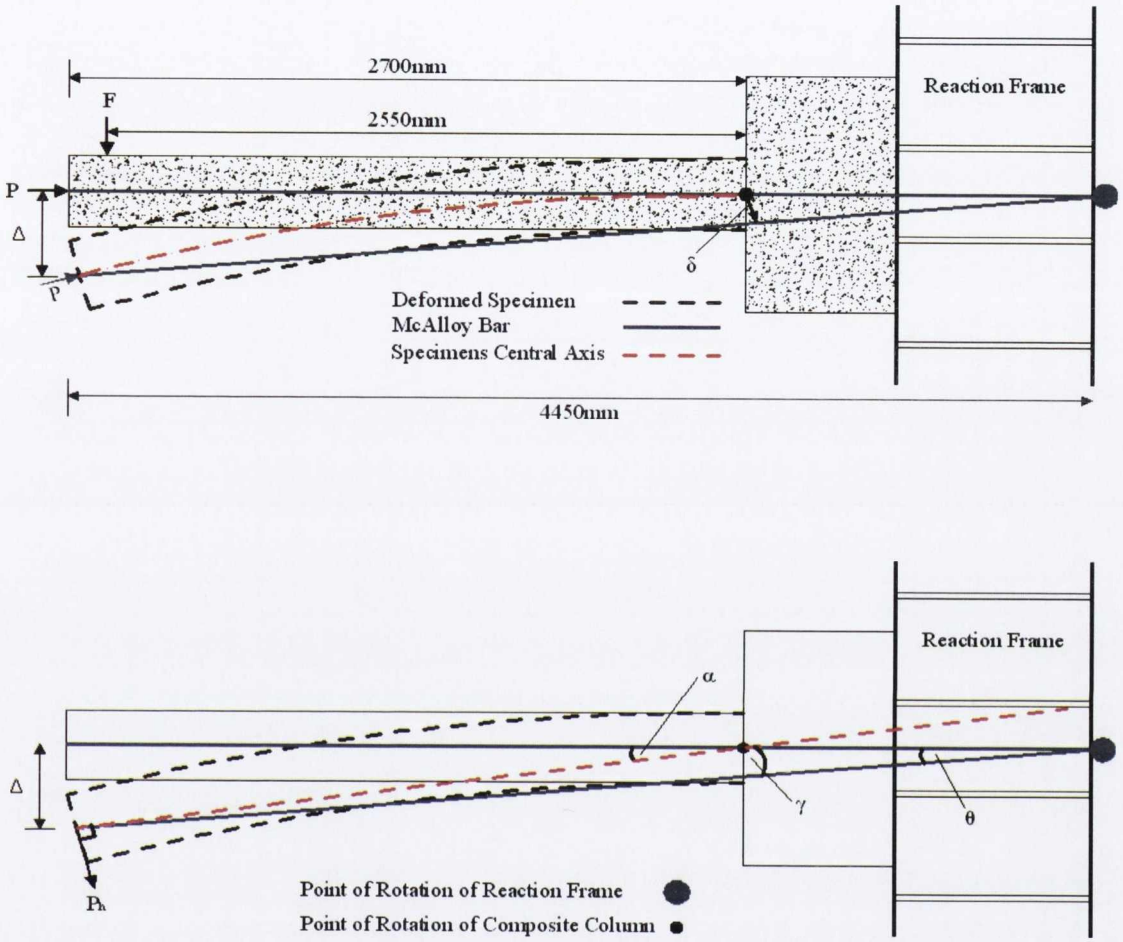

Figure 3.19: P-Delta Effects, Specimen Lengths, Loads and Relevant Angles

Where:

θ = Rotation angle of axial load apparatus central axis of the specimen

α = Rotation angle of central axis of specimen

γ = Angle between the specimens central axis and the McAlloy bar

P = The applied axial load (kN)

P_h = Component of 'P' causing P-Delta moment (kN)

Δ = The applied lateral displacement (mm)

F = The applied lateral load (kN)

M = Moment (kNm)

δ = Off-set of the axial load with respect to the point of rotation of the specimen (mm) = $\Delta(1750/4450)$, as per Figure 3.19.

3.2.7.4 Ductility Displacement Requirements

Eurocode 8, (CEN, 2004) sets out a required ductility displacement to be achieved by all structures depending on the level of energy dissipation required (i.e. 'Structural Behaviour Concept'). Depending on the design concept, structural configuration and section composition the elements are required to achieve a specific curvature ductility factor, μ_{ϕ}. The behaviour factors corresponding to each structural design concept are presented in Table 1 which is repeated below for convenience.

Eurocode 8 (CEN, 2004), stipulates that the overall ductility of the structure is achieved if the curvature ductility factor, μ_{ϕ} of a structural element achieves at least the following curvature ductilities:

$$\mu_{\varphi} = 2q - 1 \quad \text{if } T_1 \geq T_C \tag{3.15}$$

$$\mu_{\varphi} = 1 + 2(q - 1) \quad \text{if } T_1 < T_C \tag{3.16}$$

Where:

q = Structural behaviour factor, from Table 1

T_1 = Fundamental period of vibration of a building

T_C = Upper limit of the period of the constant spectral acceleration branch; (as specified by Eurocode 8 based on the ground conditions)

Table 1: Design Concepts, Structural Ductility Classes and Upper Limit of Reference Values of the Structural Behaviour Factors, Eurocode 8 (CEN, 2004).

Design Concept	*Structural Ductility Class*	*Range of the reference values of the behaviour factor, q*
Concept 'A': Low-dissipative structural behaviour	DCL (Low)	≤1.5 - 2
Concepts 'B' or 'C': Dissipative structural behaviour	DCM (Medium)	≤4 also limited by the values of Table 12
	DCH (High)	Only limited by the values of Table 12

The following relationship between displacement ductility, μ_Δ and structural behaviour factor, 'q' exists:

$$\mu_\Delta = q \tag{3.17}$$

The upper limit of reference values of behaviour factors, 'q' for structural systems regular in elevation, that are not specified in Table 1 are presented in Table 12.

Table 12: Reference Values of Behaviour Factors for Systems Regular in Elevation

STRUCTURAL TYPE	Ductility Class	
	DCM	DCH
Moment Resisting Frames	4	$5\alpha_u/\alpha_1$
Frame with Concentric Bracings		
Diagonal Bracing	4	4
V - Bracings	2	2.5
Frame with Eccentric Bracings	4	$5\alpha_u/\alpha_1$
Inverted Pendulum	2	$2\alpha_u/\alpha_1$
Moment Resisting Frame with Concentric Bracing	4	$4\alpha_u/\alpha_1$
Moment Resisting Frames with Infill's		
Unconnected Concrete or Masonry Infill's, in Contact with the Frame	2	2
Infill's Isolated from Moment Frame (see Moment Frames)	4	$5\alpha_u/\alpha_1$

Where: $(\alpha_u / \alpha_1) = 1.2$ & 1.3 for single & multi bay moment-resisting frame, respectively Thus, for a moment resisting frame, with fully encased composite column construction, the required displacement ductility, μ_Δ for the columns with medium and highly dissipative structural behaviour correspond to:

$\mu_\Delta = 4$ (for medium ductility class, DCM)
$\mu_\Delta = 6.5$ (for high ductility class, DCH)

The experimental load-deflection hysteresis plots presented in Chapter 4 need to achieve at least the values presented above to be considered as having adequate displacement ductility. As well as achieving adequate displacement ductility, the composite columns need to adhere to all other detailing provisions of Eurocode 8, (CEN, 2004).

Chapter 4

Experimental Results

Experimental Results

4.1 Introduction

An experimental investigation was conducted to compare the behaviour of composite columns using normal and high strength concrete. This chapter presents and analyses the results from six beam-column tests, each test applying a combination of lateral cyclic and constant axial compressive loading, representative of typical loading conditions used to simulate an earthquake. The only variables between tests were:

1. The unconfined concrete compressive strength
2. The axial load level
3. The link spacing in the critical region

The aim of these tests was to determine if HSC can be efficiently incorporated into composite column design based on Eurocode 8, (CEN, 2004) recommendations for NSC and if variations from the design provisions improve specimen performance. The observed specimen behaviour may also provide recommendations or improvements to be made to existing design rules to incorporate the use of HSC in earthquake-resistant composite column design.

This chapter is divided into several sections; Section 4.2 presents the specimen's initial stiffness, yield points, moment capacities, displacements and rotation capabilities. Section 4.3 provides the visual observations made throughout each test; Section 4.4 presents the specimen's hysteretic behaviour and moment-rotation curves. Section 4.5 discusses each specimen's energy dissipation and resistance, finally Section 4.6 compares the effects of link spacing, axial load and concrete strength on the specimens' ultimate displacement and total dissipated energy.

4.2 General results

Table 15 and Table 16 present the following measurement results for each specimen:

- Concrete compressive strength (f'_c)
- Yield load and displacement (P_y and Δ_y)
- Initial stiffness (K_i)
- Yield and ultimate moment (M_y and M_u)
- Ultimate displacement (Δ_u)
- Theoretical moment resistance from the M-N interaction curves (M_p)
- Displacement ductility (μ_Δ)

Table 15 presents the results for the six specimens in both the positive and negative displacements. Table 16 presents the average ultimate moments, ultimate to predicted moments and ductility ratios of both directions.

A noticeable difference between yield loads is evident from Table 15. This is attributable to a number of factors, primarily, once the concrete reaches its yield stress it cracks, thus reducing the area of concrete available to resist the applied stresses in subsequent cycles. Other factors causing variation could be due to minor variations in axial jack pressures and due to slight alignment errors during specimens casting and placement that must be expected in large scale tests of this nature.

4.2.1 Concrete compressive strengths

Two characteristic concrete compressive strengths (f_{ck}) were used throughout the test series (i.e. 25 N/mm^2 and 85 N/mm^2). Several cubes were taken from both concrete mixes to determine the compressive strength on the day of each specific test. Due to the turnover time of individual tests, the concrete had time to achieve minor additional strength gains relative to previous samples, thus Table 15 presents the average cube compressive strength ($f'_{ck,\ cube}$) on the day of each test.

4.2.2 Yield loads

Yielding is defined as the last point of linearity after which significant non-linear behaviour occurs. In terms of structural behaviour it refers to the point at which a specimen or material enters the post-elastic region and specimen deformation and irreparable damage is caused. As previously noted, a significant difference in yield loads was recorded in both directions, mainly due to concrete yielding on one face of the specimen, thus reducing the effective area of concrete for resistance in displacement cycles of opposing force. Other influencing factors are discussed in Section 4.5.

It can be seen from Table 15 for Specimen JD3 – ID3 that a difference in the yield load (P_y) in the positive and negative displacement is 73.0kN and 74.0kN, respectively. Similar variations are experienced by all other specimens. This effect can be contributed by any one or a combination of the above discrepancies.

Table 13 presents the experimental and theoretical yield loads. The average yield load (in both push and pull directions) is presented for specimens JD1, JD2, JD3 and JD4 but the yield load in only the push cycle is presented for JD5 and JD6 due to the level of damage experienced during the displacement cycle in which the yield load was recorded. The high level of damage altered the neutral axis depth and essentially meant that a different cross-section had to resist the lateral loads in subsequent displacement cycles, thus the yield load in the opposing direction would be significantly different to the push cycle yield load.

Table 13: Comparison between Experimental and Predicted Yield Loads

Specimen	P_y (kN) (factored)	P_y (kN) (un-factored)	P_y (kN) (proposed)	P_y (kN) (experimental)
JD1 – ID2	66.7	83.6	79.8	52
JD2 – ID1	66.7	83.6	79.8	76
JD3 – ID3	60.0	80.5	75.2	73.5
JD4 – ID5	99.9	117.9	112.9	98
JD5 – ID6	106.9	130.9	125.6	122
JD6 – ID4	106.9	130.9	125.6	128

It can be seen from Table 13 that the factored yield load predictions underestimate the yield resistance of the specimens (except for Specimens JD4 and JD1, but Specimen JD1 was subject to a level of bi-axial loading thus the yield results must be treated with caution). Likewise the un-factored predictions overestimate the yield loads, but overall are generally more accurate than the factored predictions. The proposed M-N interaction (which is discussed in Section 4.2.3) provides the most accurate prediction for the yield load (for most cases). It needs to be checked against a number of additional section sizes and results to be verified as an accurate predictor of the yield load. The methods by which the factored, un-factored and proposed yield loads are determined are described in Section 4.2.3.

It should be noted that the maximum experimental moment of Specimen JD4 lies on the factored M-N interaction curve; this is unexpected as the factored interaction curve is developed so a factor of safety will be incorporated into the design (i.e. the maximum moments will be in excess of the M-N predictions). Another influencing factor was that the actual concrete compressive strength ($f'_{ck,\ cube}$) for this specimen was 77.7N/mm^2, the tests are grouped into a characteristic strengths, so if the actual M-N interaction curve for this specimen was plotted, the experimental value would be underestimated by the theoretical curve. As a result the factored interaction curve provides the most accurate prediction of the yield load for this specimen.

4.2.3 Yield displacements

Yield displacement refers to the displacement just before the onset of non-elastic behaviour; it is the displacement corresponding to the yield load in the hysteretic response. The exact specimen yield displacement (Δ_y) is determined from the specimen load-displacement envelope curve. Δ_y is defined as the displacement of the intersection point of two lines: (a) a straight line that passes through the origin and $0.75P_{max}$ (i.e. the maximum load applied to the specimen) of the envelope curve, and (b) a horizontal line passing through P_{max}. Where a vertical line from this point crosses the envelope curve gives to the yield load (P_y). Figure 4.5 illustrates the above definition. Unfortunately a prior estimate of the yield displacement is required to determine the displacement history to be adopted throughout the testing programme (see Figure 3.17). A predicted yield

displacement can be calculated from Equation (4.1) for the tip displacement of a cantilever due to point loading at its free end:

$$\Delta_y = \frac{P_y L^3}{3EI} + \Delta_{P-\Delta} \tag{4.1}$$

Where:

Δ_y = yield displacement (mm)

P_y = yield load (N)

L = test span (mm)

E = modulus of elasticity (N/mm^2)

I = second moment of area (mm^4)

$\Delta_{P\text{-}\Delta}$ = Component of displacement due to axial load (mm)

$\Delta_{P\text{-}\Delta}$ was determined using a Finite Element Modelling Programme (ZeusNL), which is discussed in detail in Chapter 7. For any specific member a set of graphs can be established relating the members yield displacement and yield stiffness for any level of axial load. Figure 4.1 presents the yield stiffness of each specimen based on the level of applied axial load; it is clear from these plots that the yield stiffness increases with an increase in axial load, associated with a change in neutral axis depth. This was identified in the experimental results also (i.e. Comparison Group 2, Section 4.5.2). The yield stiffness is defined by the angle between the red superimposed line and the x –axis in Figure 4.5.

(a)

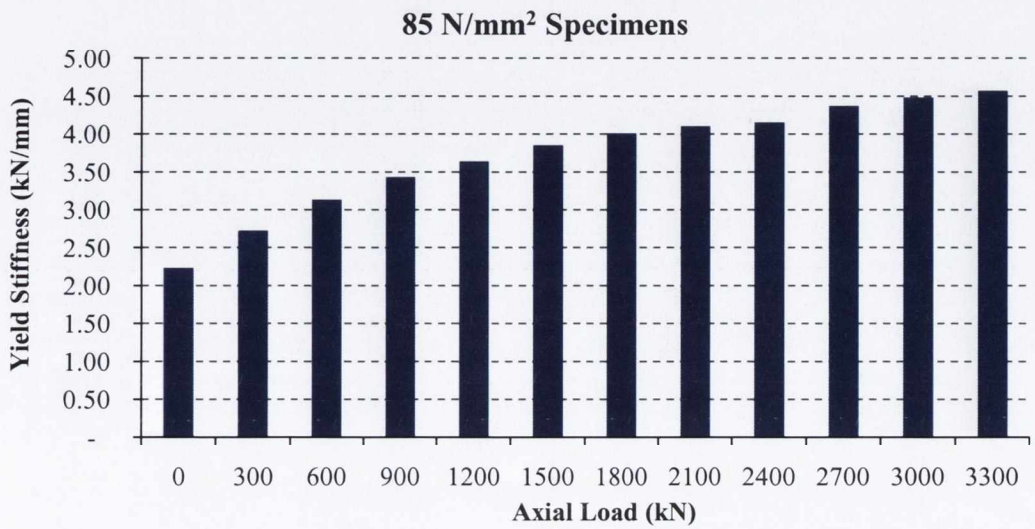

(b)

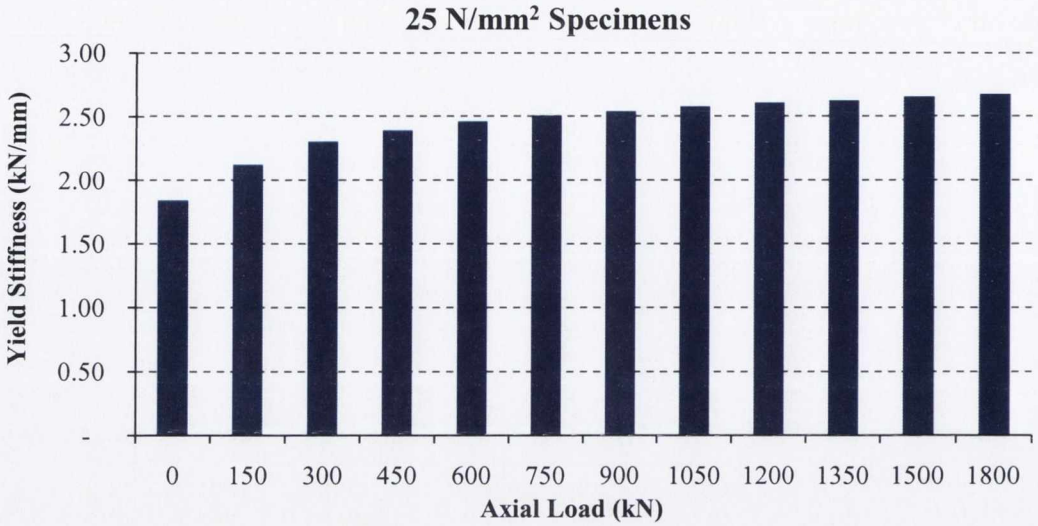

Figure 4.1: Specimen Yield Stiffness against Axial Load (a) 85 N/mm² (b) 25 N/mm²

An increase in yield stiffness would suggest that the yield displacement would be reduced as the specimens would achieve their maximum lateral resistance at a lower displacement than a similar specimen with lower stiffness, but the extra axial load will also contribute to an additional P – Δ induced displacement. Figure 4.2 (a) & (b) illustrate that for no applied axial load the maximum yield displacement is achieved, once some axial load is applied the increase in yield stiffness reduces the yield displacement and the additional displacement due to P – Δ effects is not significant enough to counteract the effects of the increase in stiffness, thus a minor fluctuation of the yield displacement occurs for any level of applied axial load.

(a)

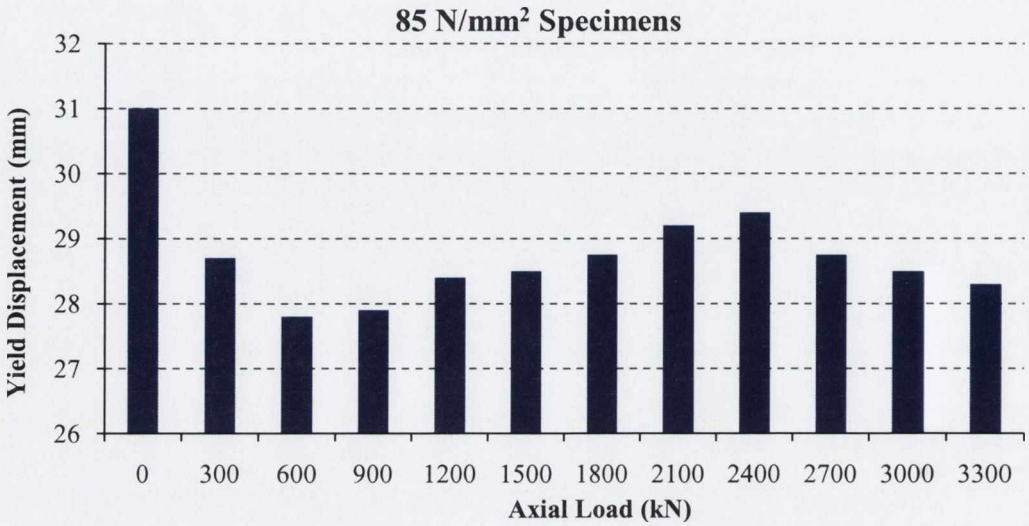

(b)

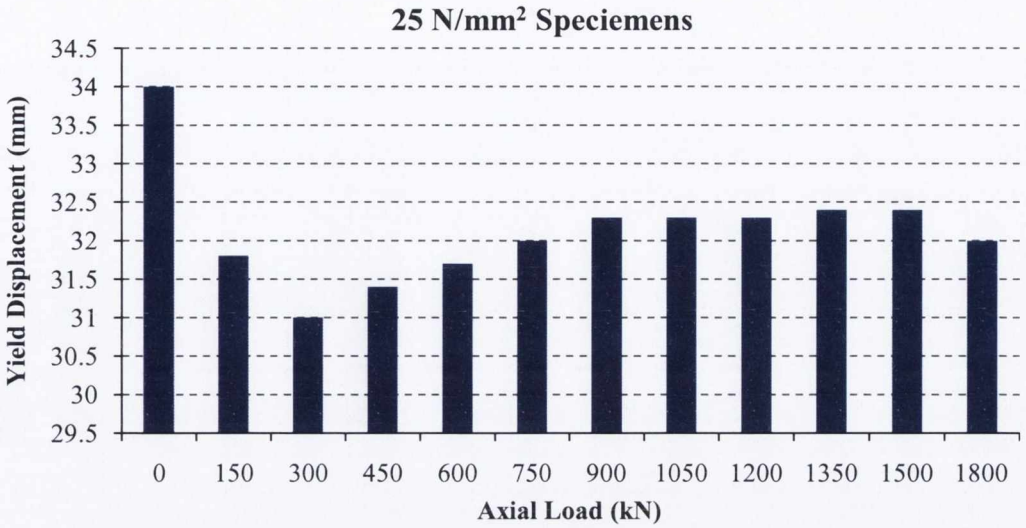

Figure 4.2: Yield Displacement against Axial Load (a) 85 N/mm^2 (b) 25 N/mm^2

The normalised yield stiffness and normalised yield displacement plots are presented in Figure 4.3 (a) & (b). The plots highlight the considerable fluctuation of the yield stiffness values compared with the yield displacement values thus highlighting that the stiffness is more susceptible to variations due to the level of applied axial load than the yield displacement. This would suggest that for any level of axial load the value of yield displacement should be reduced from that obtained if the specimen was subject to no axial load by a displacement correction value which is dependent on the level of applied axial load.

(a)

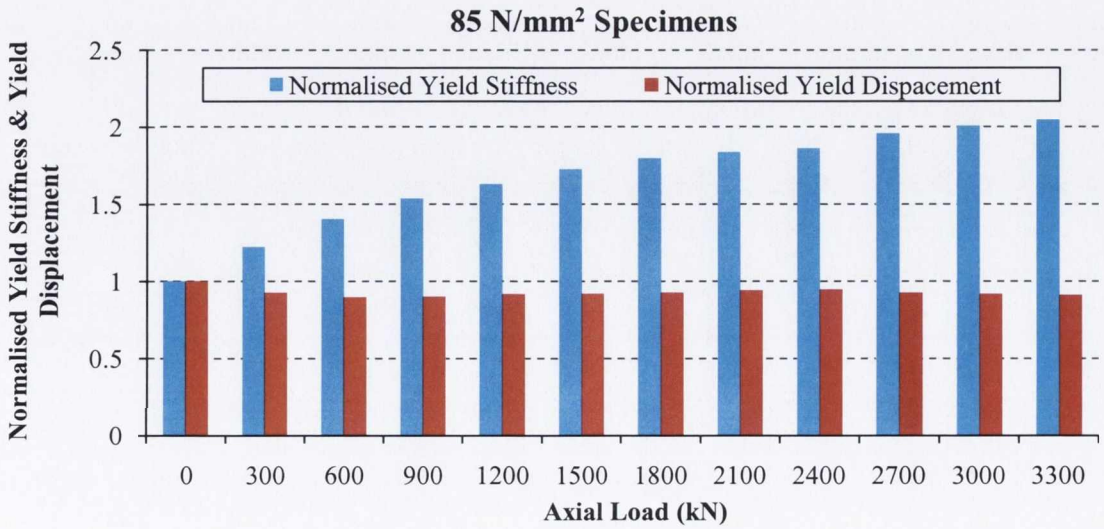

(b)

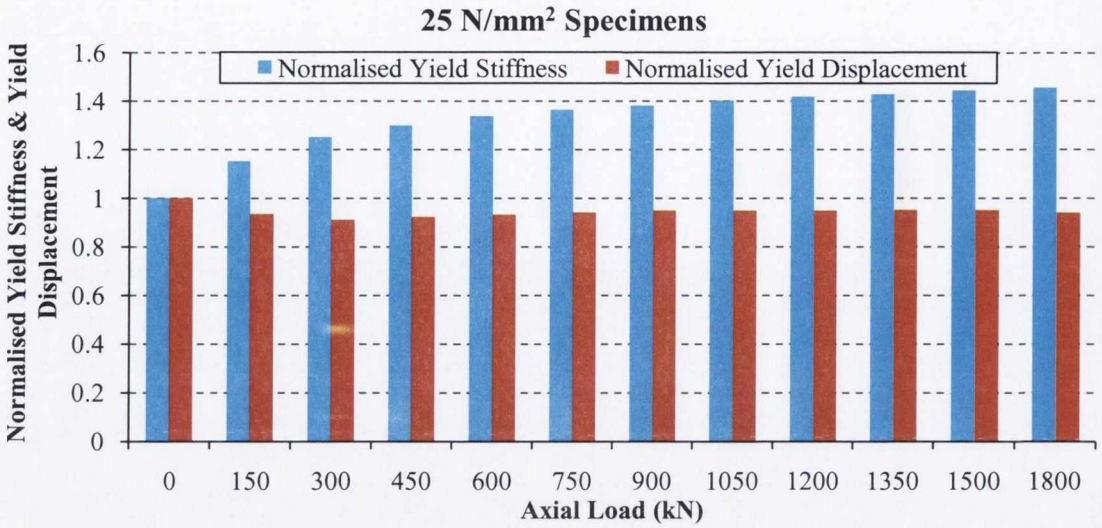

Figure 4.3: Normalised Yield Stiffness and Normalised Yield Displacement against Axial Load (a) 85 N/mm² (b) 25 N/mm²

Figure 4.4 (a) & (b) presents the correction contribution due to a given level of applied axial load, the value of $\Delta_{P-\Delta}$ in Equation (4.1) is determined from Figure 4.4 (a) & (b) for a given level of axial load. The value is negative as it has already been established that a reduced yield displacement will be recorded for a given level of axial load compared with the yield displacement recorded for a specimen subject to no axial load.

(a)

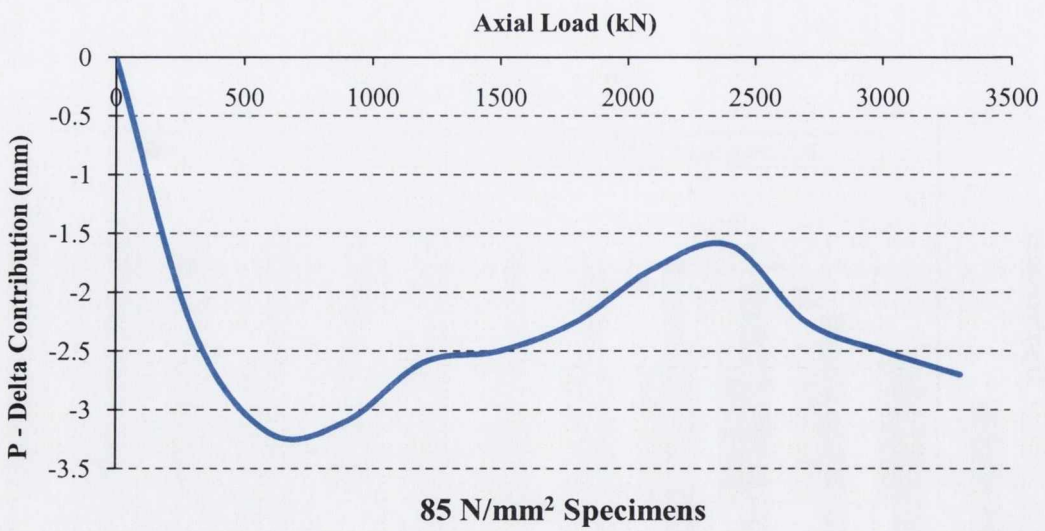

(b)

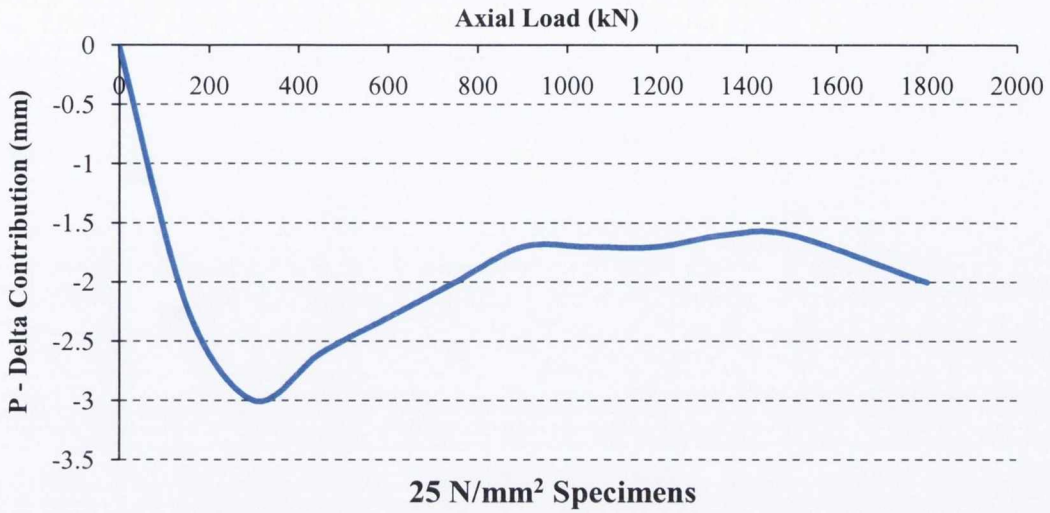

Figure 4.4: Displacement Correction Factor Due to Applied Axial Load (a) 85 N/mm² (b) 25 N/mm²

For typical levels of applied axial load i.e. 15 - 30% of the cross-sections axial capacity for both HSC and NSC specimens the variation in yield displacement (compared with a specimen subject to no axial load) equates to between -3 to -2mm for HSC and -2.6 to -1.7mm for NSC. As a percentage (using an average of the above values) based on the yield displacement recorded for a specimen with no axial load the values are approximately 8.7% and 7% for HSC and NSC respectively. The average value for any level of axial load equates to 7.9% and 6% for HSC and NSC respectively.

The yield load, P_y can be estimated by applying a factor of 0.9 to the load predicted by the cross-section M-N interaction curve for a specific axial load level. The multiplication factor of 0.9 is derived from Figure 4.5, where the vertical line representing the yield displacement crosses the envelope curve this has been found experimentally to occur at a load corresponding to 90 percent of the maximum lateral resistance (Shim *et al, 2006*), thus a conservative estimate of the yield load of a specimen can be determined by multiplying the maximum lateral resistance for a given axial load from the M-N interaction curve by a factor of 0.9.

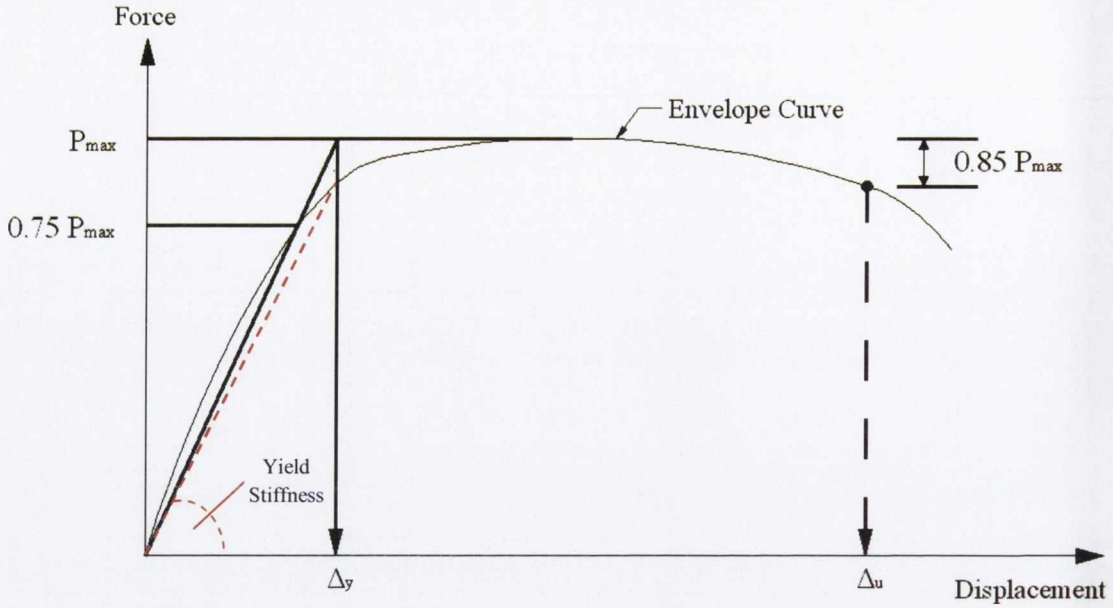

Figure 4.5: Definition of Yield and Ultimate Displacements

For the cross-section used in this experimental programme subject to 1200kN of axial load and incorporating 25N/mm^2 concrete cube strength (i.e. Specimen JD3 – ID3), the predicted yield displacement of 38.1mm is expected. This corresponds with actual yield displacements of 42 & -38.5mm in the push and pull directions, respectively. Table 14 presents the experimental and theoretical yield displacement values for all specimens.

Figure 4.6 and Figure 4.7 present the M-N interaction curves for both the 25 and 85 N/mm^2 specimens, respectively. Figure 4.6 and Figure 4.7 present the M-N interaction curves based on the equations provided in Eurocode 4, (CEN, 2004). The three curves are based on the formulae using factored and un-factored material safety multipliers and a proposed equation identical to that of the factored equation, with the removal of the reduction factor of 0.8 (which is dependent on the type of cross section).

This equation was selected to best fit the M-N interaction curve with the available test data. Experimental results are expected to lie outside the factored M-N interaction curve as it incorporates a factor of safety into the design. However, for capacity based design an accurate prediction of a member's performance is essential to ensure the formation of plastic hinges in the pre-designated locations.

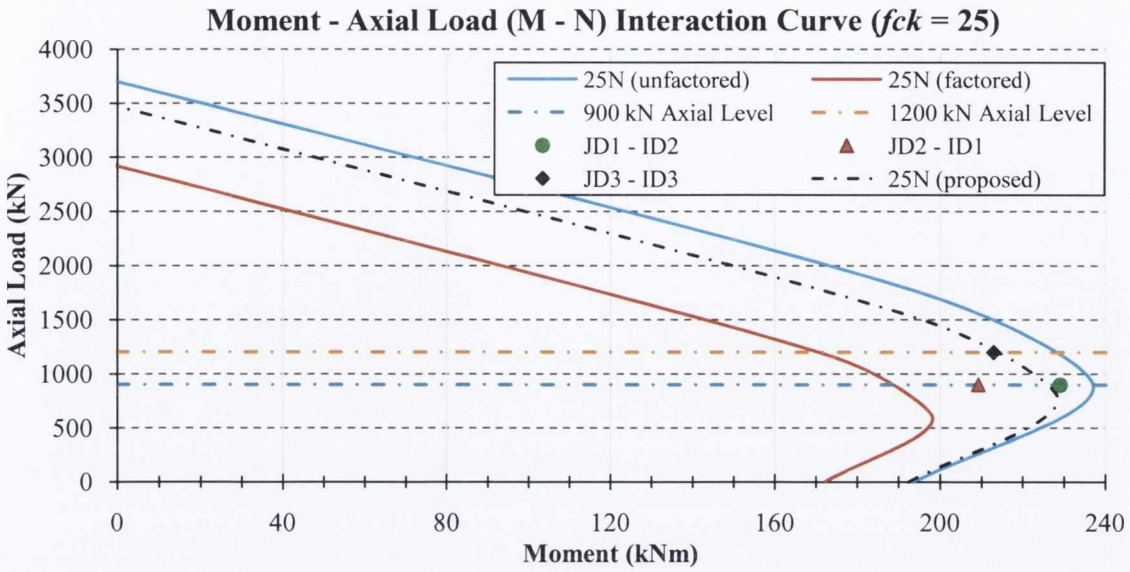

Figure 4.6: M - N Interaction Curve – NSC Specimens

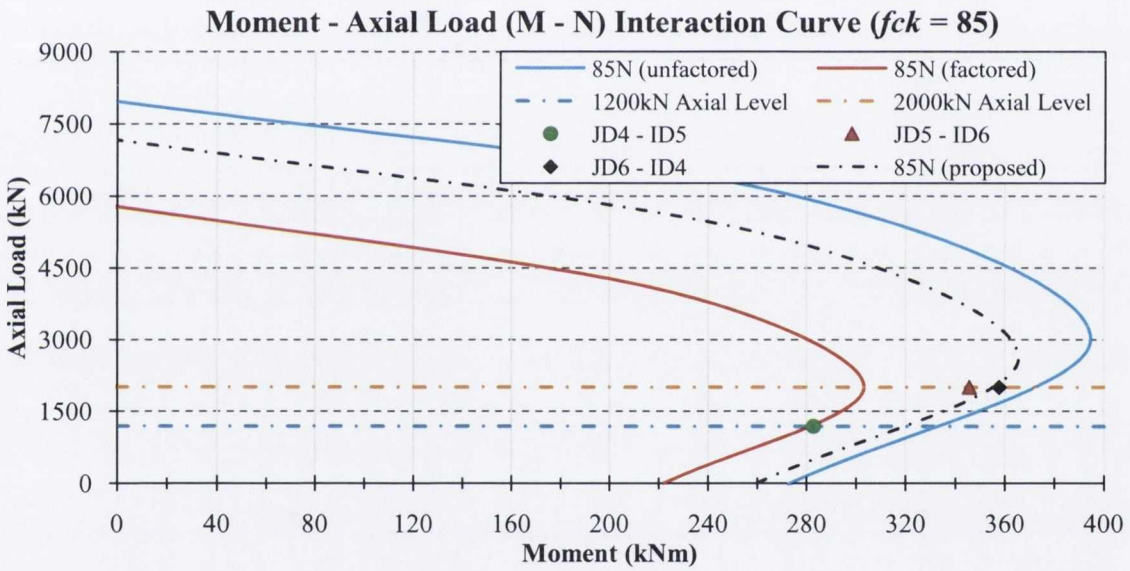

Figure 4.7: M - N Interaction Curve – HSC Specimens

Table 14: Comparison between Experimental and Predicted Yield Displacement

Specimen	$\Delta_{y,p}$ (mm) (factored)	$\Delta_{y,p}$ (mm) (un-factored)	$\Delta_{y,p}$ (mm) (proposed)	Δ_y (mm) (experimental)
JD1 – ID2	42.6	53.8	51.2	34
JD2 – ID1	42.6	53.8	51.2	34
JD3 – ID3	38.1	51.7	48.2	40
JD4 – ID5	51.9	61.7	59.0	45
JD5 – ID6	56.5	69.6	66.7	49.5
JD6 – ID4	56.5	69.6	66.7	40.5

The theoretical yield displacements provided in Table 14 illustrate that the factored M-N interaction predictions are the most accurate method of determining the actual yield displacement. However, it should be noted that the predictions are up to 39% over-estimated using Equation (4.1).The only specimen well predicted using this method is JD3 – ID3. It was determined in Section 4.2.2 that the proposed M-N interaction provided the most accurate prediction of the yield loads, but this translates into a poor prediction of the yield displacement using Equation (4.1).

4.2.4 Initial stiffness

Stiffness is the resistance of an elastic body to deformation by an applied force along a given degree of freedom when a set of loads and boundary conditions are prescribed on the elastic body. The initial stiffness is determined by calculating the slope of the first displacement cycles in both positive and negative directions. It was observed that the initial stiffness increased with concrete strength, regardless of the axial load level and this was consistent for both positive and negative stiffness (push and pull cycles), with the exception of the pull cycle of JD3 – ID3. For all specimens the stiffness recorded during the push cycles were lower than those recorded during the pull cycles. This is to be expected as a certain amount of damage will be experienced during the first displacement cycle, thus causing a certain amount of resistance to be lost on entering the opposed displacement direction.

4.2.5 Yield and ultimate moment capacities

The yield moments and maximum moments of resistance were determined by multiplying the yield and maximum loads by the lever arm. The lever arm length was determined to be 2.55m. The greatest moment is recorded at the furthest, unrestrained point from the lever arm; consequently, this is where the greatest level of damage is to be expected also. It was shown that the critically damaged area occurred approximately 100mm above this interface, due to the additional confinement provided by the reinforced base and the anchor system adopted. These visual observations are discussed in Section 4.3.1.

The ultimate load is only determined for one specimen (JD5 – ID6), all other specimens are capable of withstanding greater displacements, thus the values in Figure 4.8 must be used with caution as greater moments may be achieved by all other specimens. The ultimate moment values given in Figure 4.8 for all other specimens are the maximum moments achieved during the maximum displacement cycle achieved by the MTS actuator. The HSC specimens achieve higher ultimate moment than the NSC specimens but it must be noted that the specimens subject to high levels of axial load (i.e. 2000kN) were unable to maintain this level of moment resistance at subsequent cycles of similar displacement. This is evident from the resistance ratio plots presented in Section 4.6.1.

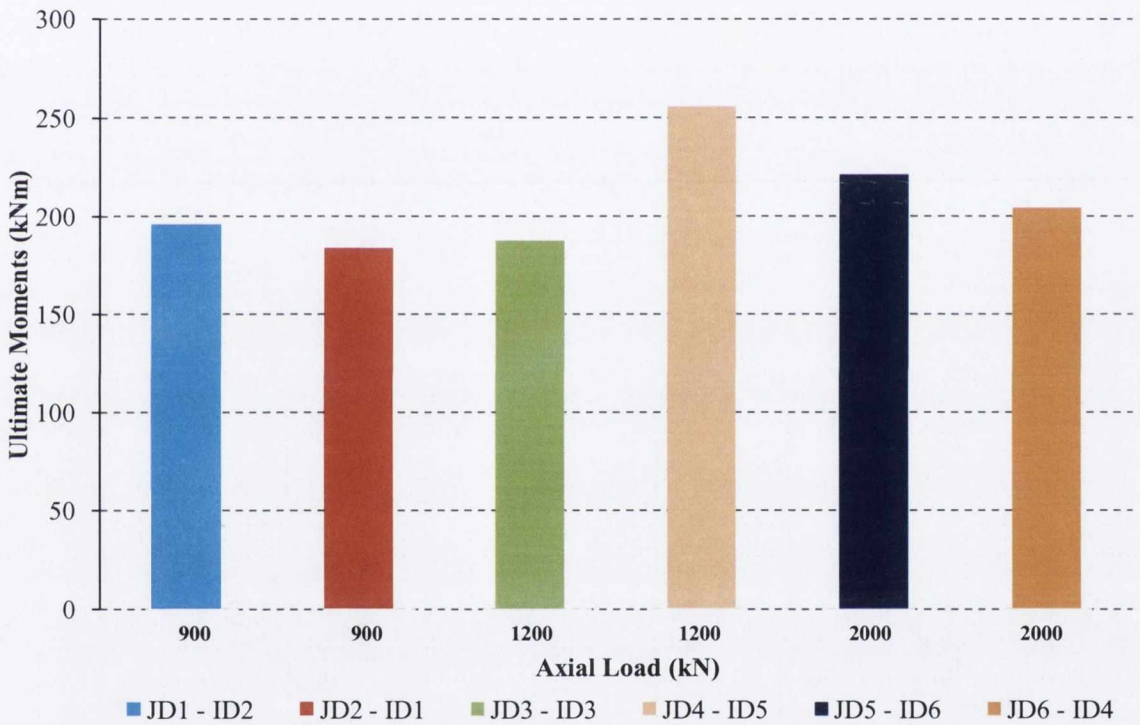

Figure 4.8: Ultimate Moments Achieved for Tested Specimens

The normal strength concrete specimens and specimens with lower percentages of axial load display little reduction in resistance drops at subsequent cycles of ultimate displacement. This suggests that these specimens would be capable of withstanding significantly greater displacements than Specimen JD6 – ID4 (this is the only high strength specimen with high levels of axial load not to collapse before the actuator stroke limit was reached) which displayed a significant drop in resistance during repeated cycles of 120mm displacement. The above mentioned specimens would thus record higher ultimate moments prior to collapse and increased ductility ratios. The ultimate

moment plot illustrates the advantage of lower axial load levels for HSC specimens and that reduced link spacing cannot effectively confine the concrete at high levels of axial load to mirror the performance of a lower axial load specimen.

Figure 4.9 presents the maximum moments achieved for all specimens. It is evident from this plot that the axial load has a significant effect on the strength of the HSC specimens. The reduced link spacing of JD6 compared with JD5 identifies only a marginal strength enhancement, but a significant post ultimate load performance is recorded, as detailed in Section 4.5.4. As is expected, the compressive strength of the concrete greatly influences the strength of the specimens. The maximum moments are superimposed on the predicted M-N interaction curves for both normal and high strength specimens in Figure 4.6 and Figure 4.7, respectively.

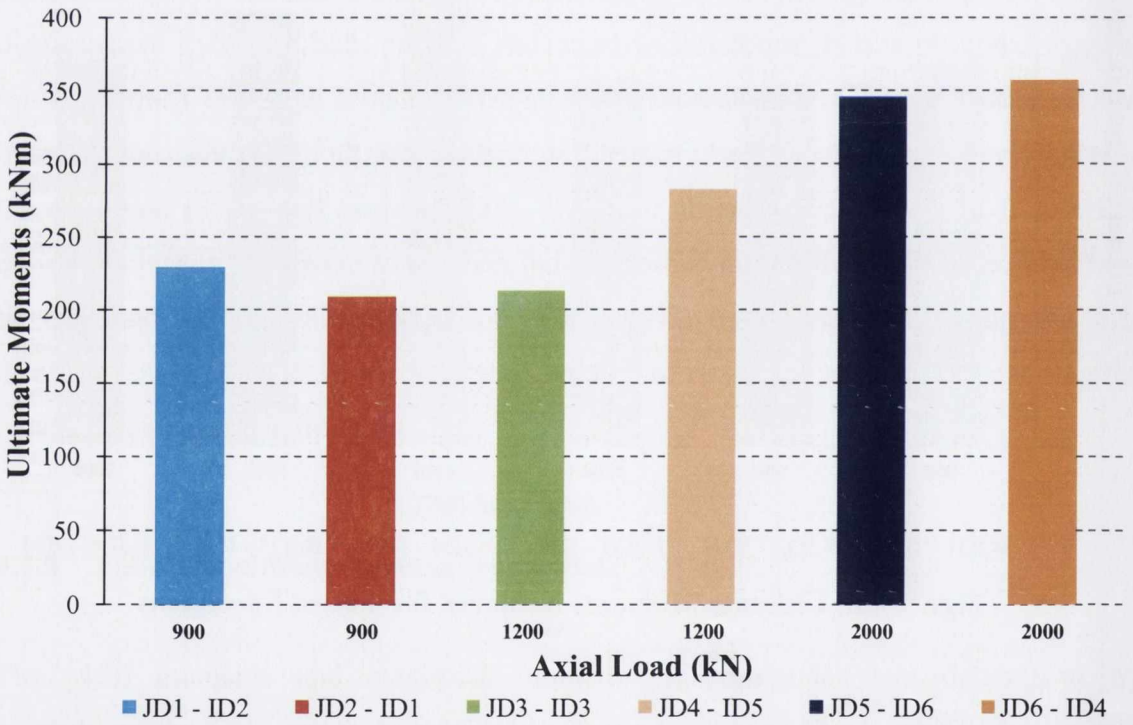

Figure 4.9: Maximum Moments Achieved for Tested Specimens

4.2.6 Displacement Ductility

Displacement ductility ratio, μ_Δ, is defined as the ratio of ultimate displacement to the yield displacement. The yield displacement refers to the displacement just before the onset of non-elastic behaviour, as defined in Section 4.2.3. The ultimate displacement is

defined at the point at which the specimens ultimately fail, due to the applied displacement history. As the displacement history was applied in multiples of 30mm, the accuracy of the quoted ultimate displacement values are limited. Two specimens that fail within a displacement group, i.e. 60mm will be deemed to have the same displacement ductility, though one specimen my fail at just over 30mm while the other may fail just before 60mm displacement.

The quoted values fail to quantify the specimens load carrying capacity subject to repeated cycles at a given displacement. This limitation is considered, with respect to the specimens' resistance drop ratio, in Section 4.6.1. A useful value in determining the actual displacement ductility ratio is to calculate the displacement ductility corresponding to a 15% drop in the maximum lateral load resistance from the specimen's load-deflection envelope curve. Another limitation was the ±125mm actuator stroke, this meant that the ultimate displacement of most specimens could not be reached, thus the ultimate displacement of these specimens is quoted as 120+mm.

4.2.7 Rotational Ductility

Rotational ductility, μ_ψ, is the ratio of ultimate rotation to the yield rotation. The values recorded for this research are identical to the displacement ductility values, as rotation (ψ) is the angle through which the specimen has deflected when subject to a lateral load. Rotational ductility is defined as:

$$\psi = \Delta/L \tag{4.2}$$

Where:

ψ = Rotation angle between vertical alignment and displaced centre-line.

L = Lever-arm length (mm)

Δ = Lateral displacement (mm)

The lever arm is assumed to be the distance from the point of lateral load application to the interface between the column and base elements. It shall be discussed in later sections that the actual plastic hinge location acts some distance above this interface due to the additional confinement provided by the base element.

Table 15 Test Results

Specimen	f_{ck} (N/mm^2)	K_i (kN/mm)	P_y (kN)	Δ_y (mm)	M_y (kNm)	Δ_u (mm)	M_u (kNm)	M_p (kNm)	M_u / M_p	μ_Δ	P (kN)	P / f_{ck} (A)
JD1 – ID2	24.5	2.54	52	28	132.6	120+	151	188	0.80	4.3+	900	40.8
		2.56	-82.5	-34	210.4		229		1.22	3.5+		
JD2 – ID1	25.2	2.64	73.5	33.5	187.4	120+	205.7	188	1.09	3.6+	900	39.7
		2.72	-78	-35	198.9		209.2		1.11	3.4+		
JD3 – ID3	25.8	2.79	73	42	186.2	120+	212.9	171	1.25	2.9+	1200	51.7
		2.29	-74	-38.5	188.7		194.8		1.14	3.1+		
JD4 – ID5	77.7	3.59	102.5	45.5	261.4	120+	282.7	282	1.00	2.6+	1200	17.2
		3.23	-94	-44	239.7		254		0.90	2.7+		
JD5 – ID6	84.5	3.72	122	49.5	311.1	60	345.6	303	1.14	1.8	2000	26.3
		3.25	105	-33.5	267.8		292.3		0.96	1.8		
JD6 – ID4	86.2	3.81	128	37	326.4	120+	357.7	303	1.18	3.2+	2000	25.8
		3.61	-107	-44.5	272.9		304.7		1.01	2.7+		

Table 16: Average Results from Positive and Negative Displacement Cycles

Specimen	P_y (kN)	M_y (kNm)	M_u (kNm)	M_u / M_p	μ_Δ
JD 1 – ID2	82.5	210.4	229	1.22	3.5+
JD 2 – ID1	75.5	192.5	207.5	1.10	3.5+
JD 3 – ID3	73.5	187.4	203.9	1.14	3.0+
JD 4 – ID5	98.5	251.2	268.4	0.95	2.65+
JD 5 – ID6	122	311.1	345.6	1.14	1.8+
JD 6 – ID4	128	326.4	357.7	1.18	3.2+

The values presented in Table 16 for Specimen JD1 are for the pull cycles only as the bi-axial buckling (discussed later in this chapter) caused a significant variation between the push and pull response. The values provided for JD5 and JD6 are for the push cycle only as the concrete cover spalled during the first 60mm push displacement cycle, thus causing a significant reduction in resistance for subsequent displacement cycles.

4.3 General observations

This section provides a detailed account of the visual observations made throughout the testing programme. Visual observations help identify particular discrepancies in the hysteretic behaviour that otherwise may be difficult to categorise, for example, a sudden drop in resistance in the hysteresis curve may be caused by the cover concrete spalling off or a slip of a restraint. Visual observations take note of these occurrences and enable an accurate assessment of the test and failure mechanisms to be achieved. Section 4.3.1 categorises the visual observations in terms of all specimens within a displacement cycle, while Section 4.3.2 discusses the visual observations contrasting similar specimens with varying concrete strengths, axial load levels and link spacing.

4.3.1 Visual observations

Due to the variations between specimens, i.e. concrete compressive strength, axial load level, link spacing, all specimens behaved differently but similarities exist between all specimens. A similar failure pattern is identified throughout and is presented in Table 18. Table 18 illustrates the form of degradation that occurred at a particular displacement cycle and the extent of the damage caused. Table 18 is divided into three columns; the first column identifies which displacement cycle the specimen is experiencing, the second column presents any visual degradation observed or any other important factor. The final column identifies specimens which have reached failure load (i.e. $0.85P_{max}$).

Photographs of specific specimens and degradation are presented in Figure 4.11 (A) to (Q), the photographs provide visual evidence of the damage recorded in the second column of Table 18 at a particular displacement. Figure 4.10 identifies the labelling system adopted throughout the tests clearly classifying each external concrete face. The steel flange is identified using the same label as the external face running parallel to it. The longitudinal reinforcement is identified similarly, except where the face is followed by a hyphen, which refers to the side on which the reinforcement lies, i.e. Bar B – C refers to a longitudinal bar on face 'B' of the specimen in the corner closest to face 'C'.

Table 17 summarises the behaviour of all composite columns observed and recorded (from the strain data in Appendix A) during the experiments. All the specimens displayed the flexural failure mode in which the longitudinal reinforcement buckled in the plastic region followed by local buckling of the steel flange. Initial flexural cracking occurred at a displacement of 7.5mm for all specimens. Vertical cracking (cracks propagating parallel to the line of axial load application) was evident during the 22.5mm displacement cycle for specimens JD1, JD2 and JD4, this demonstrates that a lower percentage of axial load leads to a delayed onset of vertical cracking, regardless of concrete strength as for all specimens with a higher percentage of axial load (i.e. JD3, JD5 and JD6) the vertical cracks were visible during the 15mm displacement cycle.

Table 17: Observed and Recorded Specimen Behaviour and Degradation

Specimen	**Displacement (mm)**							
Reference	7.5	15	22.5	30	30→60	60	90	120
JD1 – ID2	☼		۞	Ψ■		Φ	○□♦	×
JD2 – ID1	☼		۞	Ψ■		Φ○	□♦	×
JD3 – ID3	☼	۞		Φ■	Ψ	○	□♦	×
JD4 – ID5	☼		۞	Φ	Ψ	○■	□♦	×
JD5 – ID6	☼	۞			Ψ	Φ □♦○×■		
JD6 – ID4	☼	۞			Ψ	Φ □♦○■		×

☼: Initial flexural cracks, ۞: Vertical cracks, Φ: Spalling of concrete cover,
□: Rounding of transverse links, ♦: Buckling of reinforcement, ■: Yielding of steel flange,
○: Maximum lateral force, Ψ: Yield displacement, ×: Ultimate displacement

Yielding of the specimens occurred just after the 30mm displacement cycle for specimen's JD1 and JD2. For all other specimens yielding occurred between the 30 and 60mm displacement cycles. The exact values for specimen yielding are provided in Table 15. Major spalling of the cover concrete follows yielding and occurs corresponding to a displacement of 60mm for NSC specimens with low levels of axial load. HSC specimens with high levels of axial load also spalled at a displacement cycle of 60mm.

The maximum lateral load resistance was recorded at approximately 60mm for all specimens except for JD1. The maximum displacement of all specimens, except JD5 corresponds to the stroke limit of the actuator (i.e. 120mm). All other specimens were capable of resisting greater displacements. Specimen JD5 was terminated after the first 90mm displacement cycle as it became unable to resist the applied loads. The structural, longitudinal and transverse steel all yielded at varying displacements. Appendix A presents the strain versus scan plots for all the strain gauges attached to the steel and concrete elements.

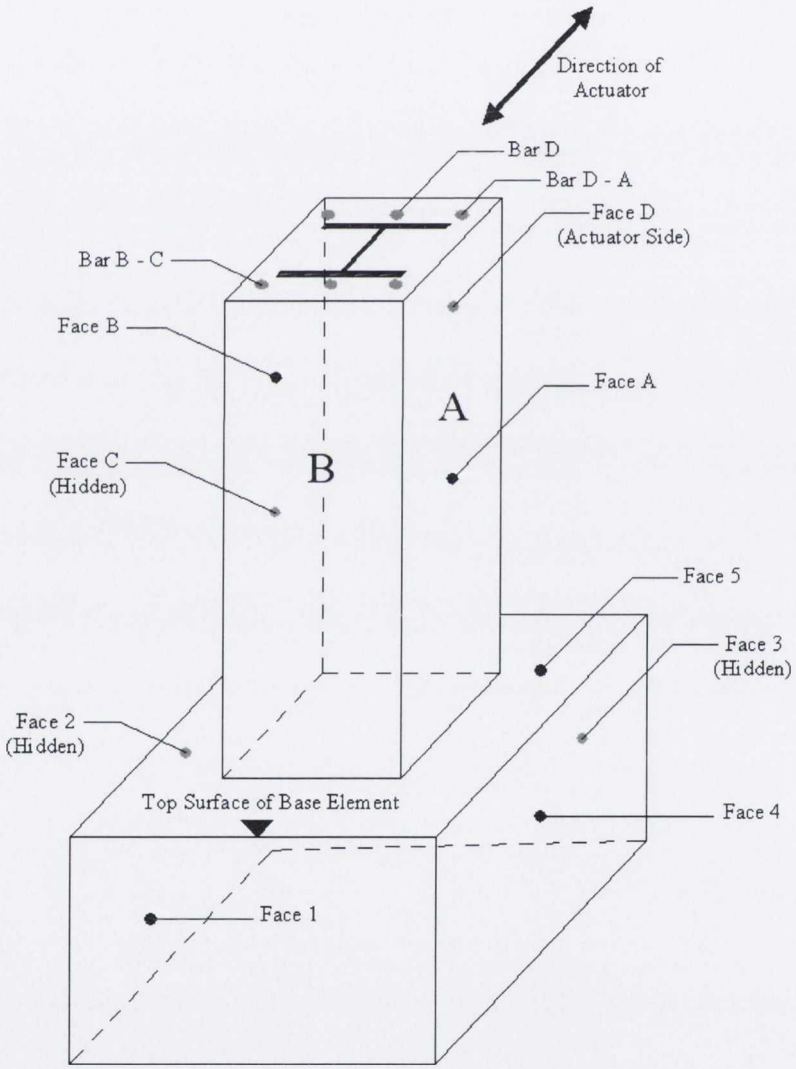

Figure 4.10: Specimen Labelling System

Note: When discussing the performance of the specimen and formation of cracks it shall be assumed that the specimens were tested in a vertical position, thus vertical cracks shall propagate in the direction of the base element towards the actuator.

Table 18: Visual Behaviour of Test Specimens

Loading History	Specimen Behaviour	Failed Specimen
Axial Load Application	• All specimens developed minor cracks in the base element due to 'bedding in' of the sample; minor cracks were visible in the connection point with the seating shoe due to the same phenomenon. No cracks developed any further during the test.	
Displacement Cycles – 7.5, 15 & 22.5mm	• Lateral cyclic loading was initiated immediately after axial load application. • Initial flexural cracking was evident (in the form of horizontal hairline cracks) in all specimens at a displacement of 7.5mm. • Vertical hairline cracks propagated from the horizontal cracks, developing particularly in the lower grade concrete, up to a height of 600mm from the base, only 100-200mm high in the HSC specimens. • Angular cracks developed in the base element at a displacement of 22.5mm for specimens JD3 – ID3, JD5 – ID6 & JD6 – ID4. The cracks were initially hairline but opened as the displacements increased, they were visible on Face 2 and Face 4. They originated from all corners of the column connection with the base, dissipating in an angular direction towards the bottom corners of the base.	
Displacement Cycles – 30mm	• Vertical cracks extended, up to 900mm in all specimens on Faces A & C. Horizontal crack opened slightly and developed up to 700mm in all specimens (Photo (A)). • All specimens experienced increased damage at 1st 30mm cycle • Base cracks opened to approximately 2mm for previously discussed specimens. • Minor spall from all HSC specimens, only 20-70mm flakes, gradually increasing in size with every cycle (Photo (B)). • Specimen JD3 – ID3 displayed marginally greater amounts of spall compared with the other NSC specimens, but was concentrated at the column – base interface. • Vertical cracks extended with repeated cycles of 30mm but tended to stay close to column corners in all specimens (Photo (C)).	

Loading History	Specimen Behaviour	Failed Specimen
	• Face B experienced the greatest degradation for all specimens. • HSC specimens suffered little damage at this displacement compared with to the NSC specimens, while specimens with higher axial loads displayed a slightly greater degradation than similar specimens with lower axial load levels.	
Displacement Cycle – 60mm (1) Push Cycle	• The first 60mm push cycle caused extensive damage to all specimens. All NSC specimens displayed spalling of the concrete cover. Pieces of concrete from 30-100mm in size detached from the column corners. • Specimen JD4 – ID6 developed major cracks to all faces, concrete approximately 100mm in size spalled from Face B&D • Vertical cracks widened on all specimens except for JD5 – ID6 and JD6 – ID4. Vertical cracks extended up to 500-700mm in all specimens (Photos (D) and (E)). • NSC specimens suffered extensive cracking to the plastic hinge region on Faces B & D, all cover concrete became loose and unable to sustain load (Photo (F)). Horizontal cracks developed on all faces, 900-1100mm up the column on all specimens. • Specimen JD5 – ID6 failed brittly on Face B at exactly 60mm displacement, this caused serious damage and a section of concrete 350mm long became loose, in repeated cycles it became detached and exposed the confining links and extremities of the steel flange. • The links on Face B displayed signs of yielding (and rounding). Face D was severely cracked up to a distance of 400mm from the base. • Specimen JD6 – ID4 yielded brittly (Face B) at a displacement of 51mm. As with Specimen JD5 – ID6 this caused a large section of concrete to spall from Face B (approximately 400mm long), when it fell off it exposed the links and steel extremities. The links had yielded and 'rounded' at this point due to the sudden failure and release of applied load. • The brittle failure of the specimens (JD5 and JD6) caused a major reduction in the lateral resistance as is depicted by the steep drop in the hysteresis plot for the respective specimens.	

Loading History	Specimen Behaviour	Failed Specimen
	• Specimen JD1 – ID2 developed a crack to its base, similar to previously discussed specimens (Photos (G) and (H)). The crack was visible on Faces 2 and 4. The crack opened to 3mm but did not extend further throughout the test. The base cracks were formed due to the force being transferred from the embedded steel section into the reinforced base. Once the steel yielded the forces transferred from the plastic hinge region were reduced thus no further expansion if the base cracks occurred.	
Displacement Cycle – 60mm (1) Pull Cycle	• All specimens degraded further, Specimen JD1 – ID2 was subject to increased spalling, particularly to Face B where the previously compressed concrete. Transverse links became exposed to Faces B and D. • Section of spall approximately 100-300mm detached from all specimens, primarily on Faces B & D, corners of all specimens displayed large cracks both horizontally and vertically at this point. • Specimen JD5 – ID6 achieved its maximum lateral force (in the negative displacement cycle) at 40mm displacement. From 40 – 60mm the specimen suffered extensive damage to the cover concrete at Face D and a noticeable drop in resistance was recorded (Photo (I)). • Specimen JD6 – ID4 failed brittly on Face D, a large section of spall removed from Face D (300mm long x 150mm wide). This caused another major drop in the load carrying capacity of the section which is illustrated in the hysteresis curve for this specimen. • Specimens JD5 – ID6 and JD6 – ID4 suffered the greatest damage at this displacement cycle due to the higher concrete strength (and associated increase in brittleness as a result) and higher levels of axial load (Photo (J)). • Specimens JD2 – ID1, JD3 – ID3 & JD4 – ID5 did not fail suddenly, but continued with an increasing level of damage throughout the cycle to all faces.	

Loading History	Specimen Behaviour	Failed Specimen
Displacement Cycle – 60mm (2 & 3) Push & Pull Cycles	• All specimens suffered exaggerated damage and spall during these cycles. Spalls of 50-300mm were recorded. • No specimen achieved as high a lateral load during repeated cycles this displacement as was recorded for the first cycle. • Specimens JD5 – ID6 and JD6 – ID4 experienced a higher degree of damage than other specimens (Photos (K) and (L)). • Links became partially visible in all other specimens.	
Displacement Cycle – 90mm	• Severe spall was experienced by all specimens, every face was cracked, majority of the cover concrete to all faces has been removed up to a height of 500mm from the base (Photo (M)). • Links and longitudinal steel was exposed to all specimens by this point, some specimens displayed steel flange extremities protruding (Photo (N)). • Specimen JD4 – ID5 achieved its maximum lateral force at approximately 70mm (in the 1st push cycle), at this point the concrete crushed and a drop in the load carrying capacity was recorded. Further cycles failed to achieve the same load. • Specimen JD5 – ID6 was terminated after the 1st push cycle of 90mm as the steel flange was evidently buckled and the specimen experienced a major drop in its load carrying capacity (Photo (O)). • By the end of the 90mm cycles it was evident that the longitudinal steel in all specimens had buckled to some degree. The partially confined concrete was crushed but still in place thus proving impossible to determine the point at which the steel flange buckled, but the strain data allowed the point of yielding to be determined.	JD5 – ID6
Displacement Cycle – 120mm	• All specimens except for JD5 – ID6 were subject to displacements up to the stroke limit of the actuator. Though some specimens had been deemed to have failed, the load was maintained to determine their performance at lower load carrying capacity. • All specimens experience severe cracking and spalling at this displacement (Photos (P) and (Q).	

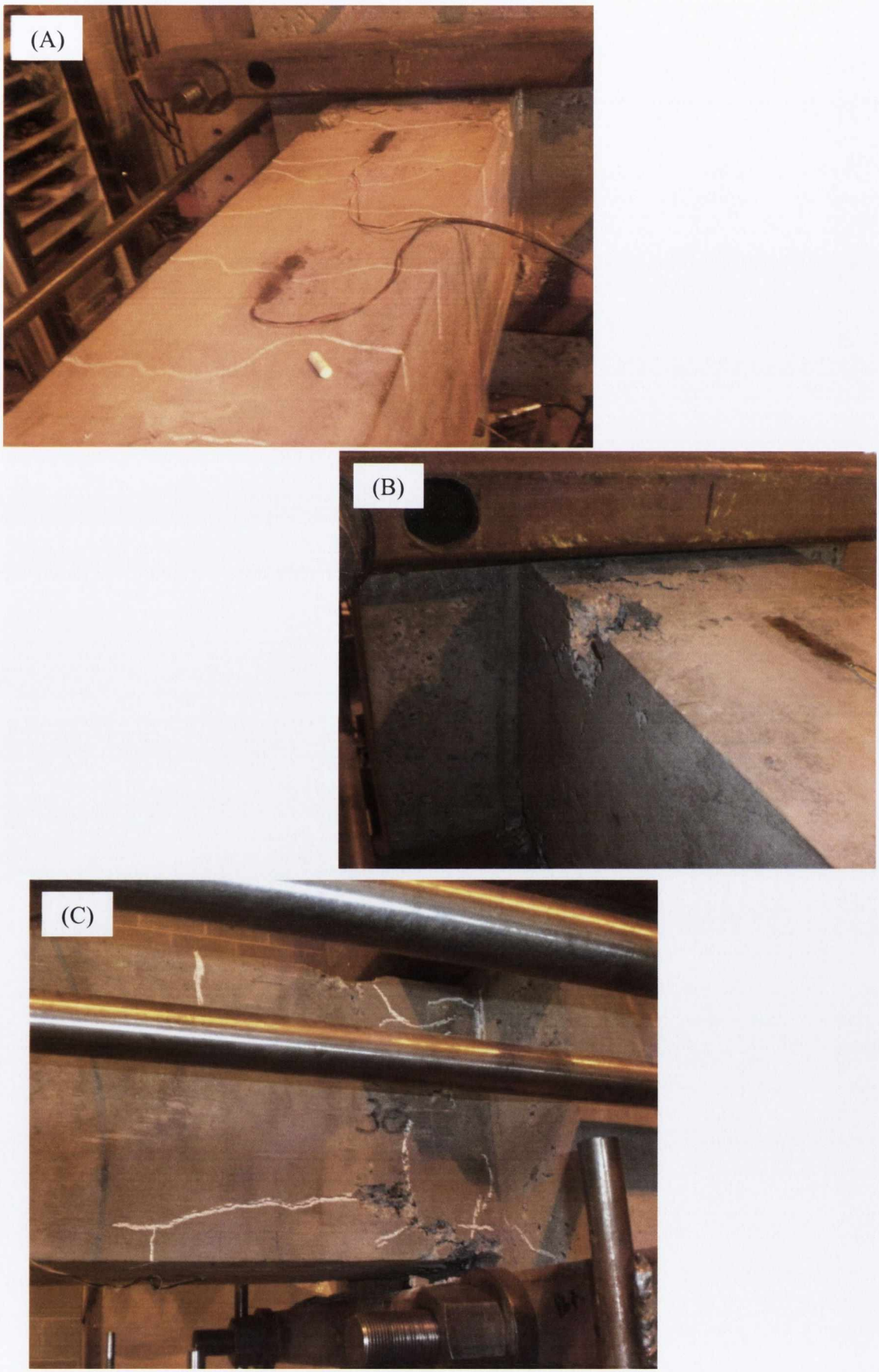

Figure 4.11: Photos: (A) – (C) Specimen JD1: Damage Post 30mm Displacement Cycle

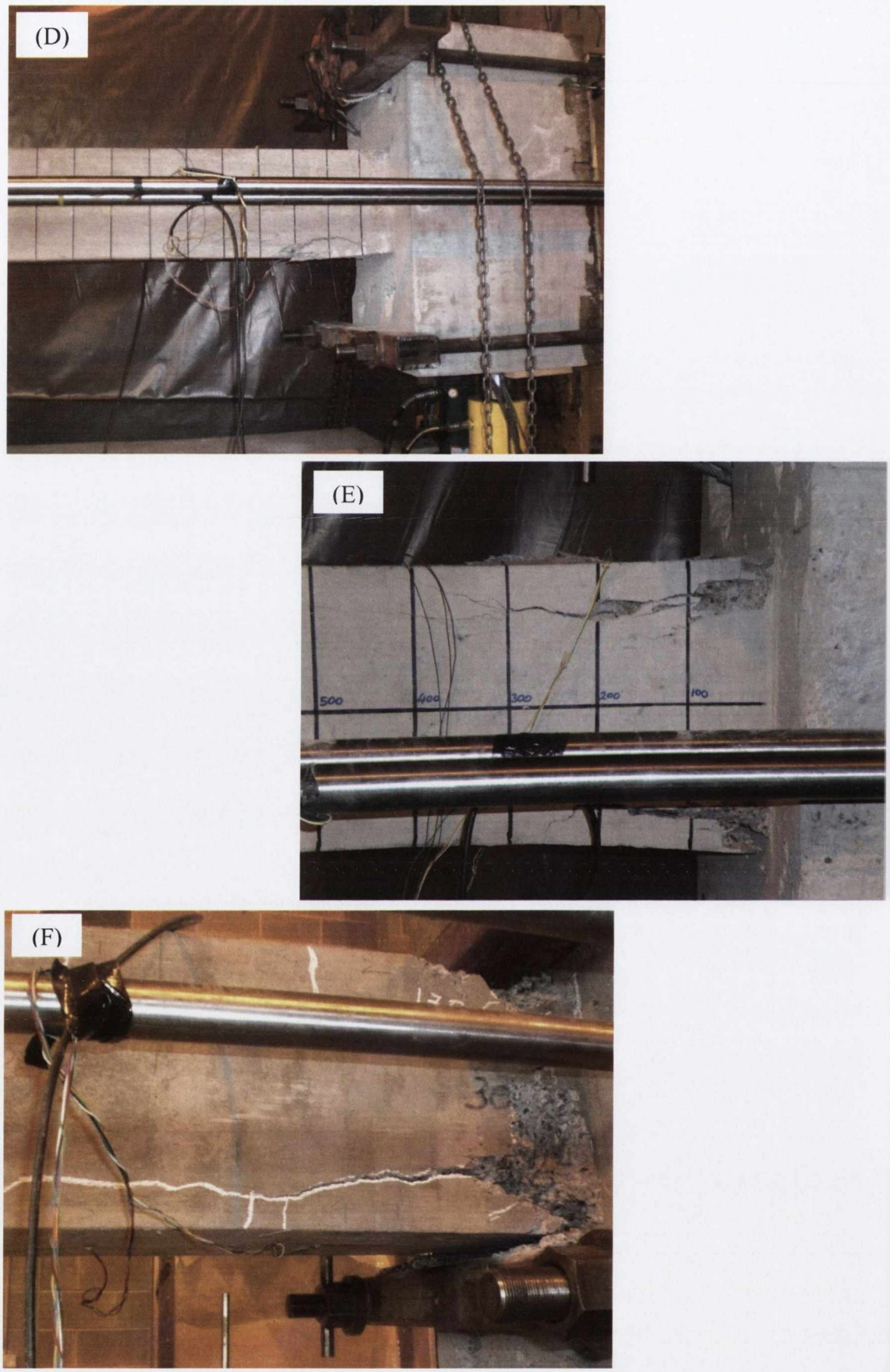

Figure 4.11: Photos: (D), (E) & (F) Specimen JD5, JD6 & JD1: Post 1st 60mm Displacement Cycle

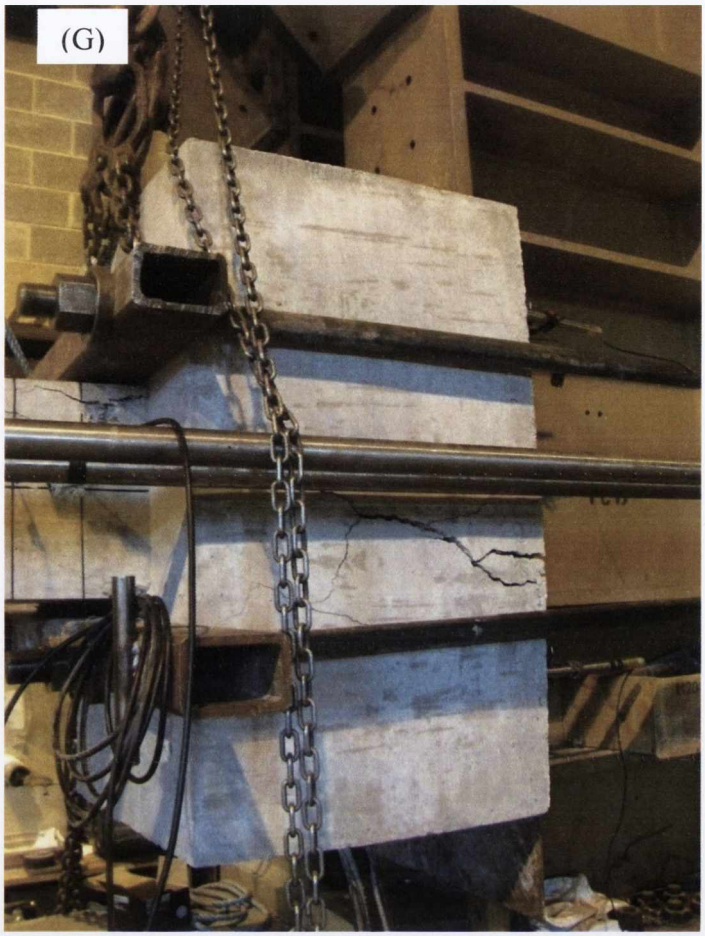

Figure 4.11: Photos: (G) & (H) Specimen JD5: Base Cracks, Face 4 & Face 2

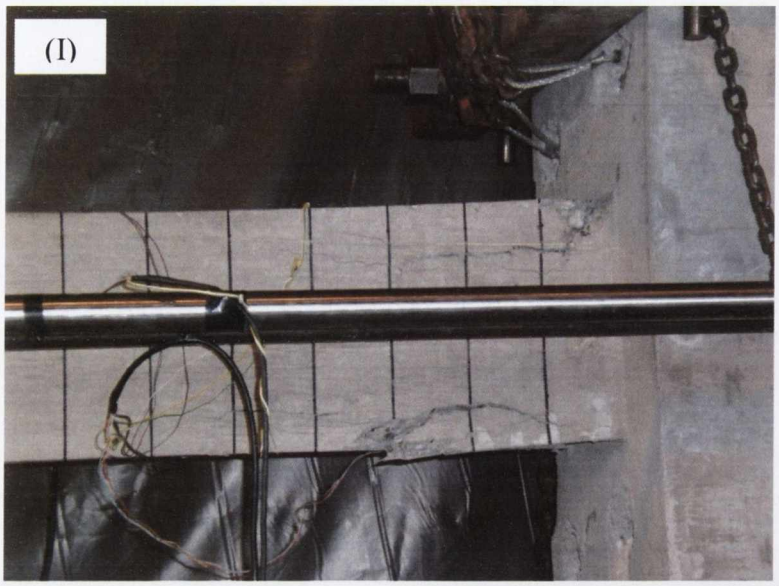

Figure 4.11: Photos: (I) & (J) Specimen JD5 & JD6 Post 1st 60mm displacement, (K) Specimen JD5 Post 2nd 60mm Displacement

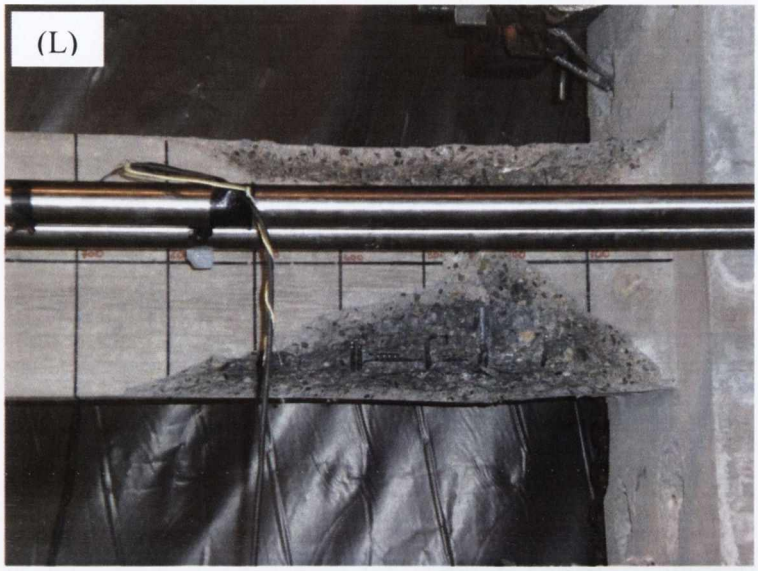

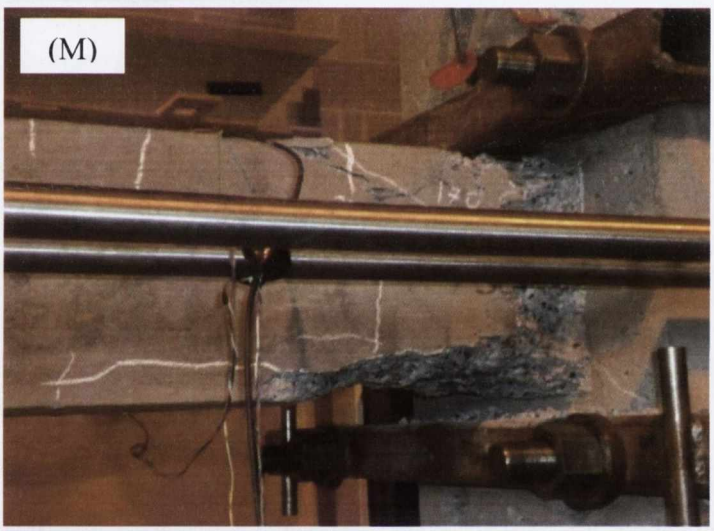

Figure 4.11: Photos: (L) Specimen JD5 Post 60mm Displacement Cycles, (M) Specimen JD1 Post 90mm Displacement Cycles, (N) Specimen JD5 Post 90mm Displacement Cycle

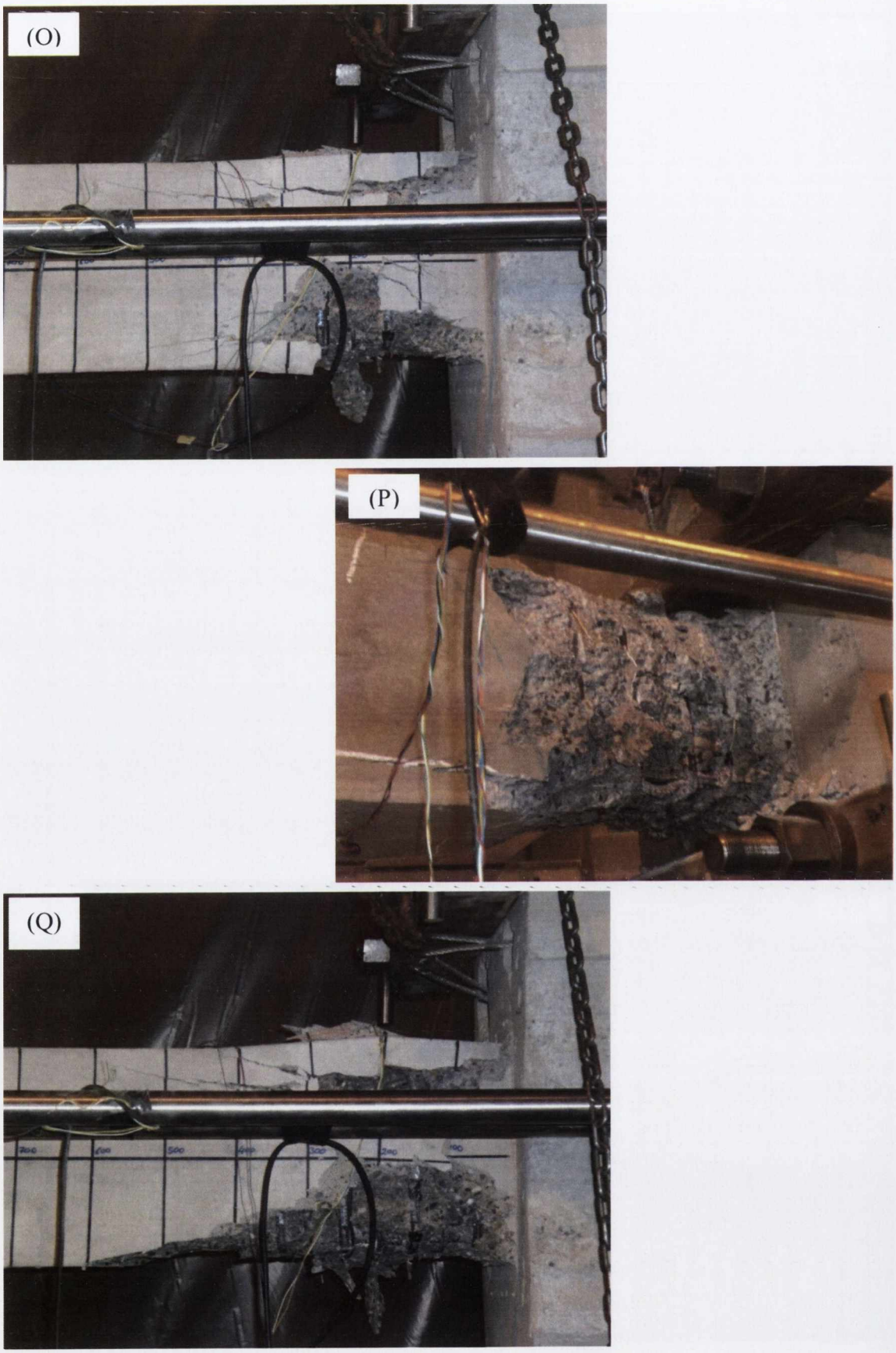

Figure 4.11: Photos: (O) Specimen JD6 Post 90mm Displacement Cycles, (P) & (Q) Specimen JD1 & JD6 Post 120mm Displacement Cycles

4.3.2 Failure comparisons

A similar failure process was identified from all specimens. All specimens initially displayed spalling of the cover concrete, further cyclic displacements caused degradation of the confined concrete core and bending of the transverse links. Subsequent transverse link yielding allowed the longitudinal steel to buckle at high displacements. Finally the flanges of the structural steel section buckled leading to a drop in the load carrying capacity of the section.

Table 19 presents a damage report recording of post testing damage observations for all specimens. The table is split into three sections; the first two columns identify the specimen being referred to, followed by the specific material in consideration. The final column provides a description of the damage incurred during the test, including the extent and location of the damage. Some of the damages recorded in Table 19 are presented in the photographs in Figure 4.11 (A) to (Q), these photographs are associated with specific damaged elements of the failed composite sections.

Table 19: Recorded Specimen Post-Test Damage

Specimen	Element	Description of Damage
JD1 – ID2	Longitudinal Bars	*Bar B – A*: Slightly buckled towards Face C by 4mm @ 60mm above the base. *Bar B*: Bar buckled out from Face B by 20mm @ 63mm above the base, just below the 2nd link up from the base interface. *Bar B – C*: Bar buckled out from Face B towards Face C by 25mm between 2nd and 3rd link (95mm along the column) *Bar D – A*: No evident buckling *Bar D*: Buckled out from Face D by 30mm between 3rd and 4th link, 180mm from interface. *Bar D – C*: Buckled by 35mm at the same location as Bar D.
	Steel Flange	*Face B*: Steel displayed no evident sign of local buckling to corner B – A, corner B – C was slightly buckled at a central distance of 110mm from the interface and over a length of 60mm *Face D*: Corner D – A remained unbuckled but Corner D – C was buckled over a length of 70mm at which the focus was 170mm from the column-base interface.

Specimen	Element	Description of Damage
	Transverse Links	*Face A*: No evident rounding of links. *Face B*: 2nd link from base interface bent outwards by 20mm, Link located 80mm up to column *Face C*: Slight rounding of 2nd and 3rd links. *Face D*: 3rd link bent outwards by 30mm, located 140mm along the column.
JD2 – ID1	Longitudinal Bars	*Bar B – A*: Bar slightly bent towards Face A by 5mm, located 200mm above the base. *Bar B*: Bent outwards by 14mm, buckled over a length of 135mm, centre-point located 195mm up the column. *Bar B – C*: No visible bar buckling. *Bar D – A*: Longitudinal bar bent towards Face A by 8mm @ a distance of 150mm up the column. *Bar D*: No visible buckling. *Bar D – C*: No visible buckling.
	Steel Flange	*Face B*: No visible buckling. *Face D*: No visible buckling.
	Transverse Links	*Face A*: No evident rounding of links. *Face B*: 3rd link bent outwards by 10mm, located 150mm above the base interface. *Face C*: No evident rounding of links. *Face D*: 2nd link bent by 4mm outwards, 90mm up from the base.
JD3 – ID3	Longitudinal Bars	*Bar B – A*: Bar buckled between 2nd & 3rd link by 5mm, located 125mm above the base. *Bar B*: Severely buckled outwards by 30mm @ 175mm above the interface between 3rd & 4th link. *Bar B – C*: Bent outwards by 15mm between 3rd & 4th link, 190mm from the base. *Bar D – A*: Bar bent outwards by 5mm @ 165mm up the column length, between 2nd & 3rd link. *Bar D*: Buckled by 20mm between 3rd & 4th link, concentrated at 180mm above the interface. *Bar D – C*: Severely buckled outwards by 26mm located between 2nd 3rd links.

Specimen	Element	Description of Damage
	Steel Flange	*Face B*: No visible local buckling to corner B – A, 120mm buckle to corner B – C centred at 180mm above the base interface. *Face D*: Slight buckle to corner D – A, 50mm long centred @ 265mm along the column, flange buckle at corner D – C, 120mm long, centred at 140mm above the base.
	Transverse Links	*Face A*: 3rd & 4th links slightly rounded. *Face B*: 2nd, 3rd & 4th links rounded by 5, 30 & 15mm respectively. *Face C*: Slight rounding of 2nd, 3rd, 4th & 5th links. *Face D*: 3rd link bent outwards by 20mm.
JD4 – ID5	Longitudinal Bars	*Bar B – A*: Slightly bent out from steel flange by 3mm @ 175mm from the base interface. *Bar B*: Buckled out by 10mm over a length of 50mm, centred at 160mm up to column face. *Bar B – C*: No evident signs of buckling. *Bar D – A*: Buckled outwards by 4mm @ 180mm from the base, also buckled towards Face A by 3mm. *Bar D*: Buckled by 12mm @ 160mm above the base. *Bar D – C*: Bent outwards by 3mm @ 180mm from the base, also buckled by 3mm towards Face C.
	Steel Flange	*Face B*: Steel buckled on both corners over a distance of 100-240mm from the base. *Face D*: Identical damage as Face B.
	Transverse Links	*Face A*: No evident link rounding. *Face B*: 3rd and 4th link bent upwards by 10 & 2mm at a distance of 150 & 222mm respectively. *Face C*: Only minor rounding of 3rd link. *Face D*: 3rd link buckled up by 12mm at 155mm above the base.
JD5 – ID6	Longitudinal Bars	*Bar B – A*: Minor buckle (2mm) recorded 170mm along the column. *Bar B*: Buckled by 10mm @ 220mm above the base. *Bar B – C*: No evident signs of buckling. *Bar D – A*: Bent up by 5mm @ 170mm above the base. *Bar D*: Bent up by 6mm @ 165mm above the base. *Bar D – C*: Buckled slightly by 2mm @ 165mm above the base.
	Steel Flange	*Face B*: Local buckling recorded to corner B – A over a distance of 250mm, starting 100mm above the base, no signs of buckling

Specimen	Element	Description of Damage
		to corner B – C. *Face D*: Buckling recorded to corner D – A initiating 130mm above the base over a length of 220mm, similar buckling at corner D – C.
	Transverse Links	*Face A*: No evident sign of link rounding. *Face B*: 2nd, 3rd & 4th links bent outwards by 3, 10 and 3mm respectively. Links located at 135, 220 & 295mm above the base interface respectively. *Face C*: No evident sign of link rounding. *Face D*: 2nd link bent upwards by 4mm, located 130mm up the column face.
JD6 – ID4	Longitudinal Bars	*Bar B – A*: Bent up by 3mm @ 165mm above the base. *Bar B*: Severely buckled by 20mm @ 165mm up the column face. *Bar B – C*: Buckled up by 5mm and towards Face C by 3mm. Buckled over a length of 90mm, centred @ 190mm above the base interface. *Bar D – A*: Buckled by 10mm towards Face A centred at 175mm up the column face. *Bar D*: Severely buckled by 30mm @ 185mm above the interface. *Bar D – C*: Severely buckled by 20mm @ 175mm above the interface.
	Steel Flange	*Face B*: Local buckling recorded at corner B – A, 3mm between 100-300mm above the interface, peaking at 170mm. Corner B – C severely buckled by 8mm @ 190mm from the base over a length of 100-350mm from the interface. *Face D*: Corner D – A buckled (similar to sine wave) by 5mm from 100-300mm up the column face. Corner D – C severely buckled by 15mm, centred @ 180mm above the interface.
	Transverse Links	*Face A*: Slight rounding of 4th, 5th & 6th links. *Face B*: 4th, 5th & 6th links bent outwards by 10, 20 & 5mm respectively. *Face C*: Slight rounding of 4th, 5th, 6th & 7th links. *Face D*: 4th & 6th links bent outwards by 5mm each, located @ 145 and 235mm from the base respectively. 5th link buckled severely by 30mm, located 190mm above the interface, link fractured at midpoint of Face D, 65mm above the steel flange.

Figure 4.12: Visual Post Test Specimen Damage

4.3.3 Influence of Axial Load

It was evident from even minor displacement cycles that specimens with high levels of axial loads suffered significantly more damage than specimens with low levels of axial load. Noticeable deterioration of the cover concrete began corresponding to a displacement of 15mm for all specimens with high axial load levels compared with 22.5mm displacements for all other specimens, irrespective of concrete strength. The axial load had less of an effect on the NSC specimens than observed on the HSC specimens; this is due to the inherent brittle nature of HSC, particularly at high axial loads. The low levels of axial load applied to Specimen JD4 caused a slow stable deterioration of the cover and core concrete, thus a stable resistance ratio was recorded (discussed in detail in Section 4.5). High levels of axial load caused severe damage to the HSC specimens as the cover concrete failed suddenly causing a severe reduction in resistance, leading to ultimate failure of Specimen JD5. Specimen JD5 and JD6 suffered significantly more deterioration to their concrete core and steel elements than all other specimens, thus it can be concluded that axial load levels (as a percentage of the axial capacity of the section) significantly affect HSC more than NSC specimens.

4.3.4 Influence of Concrete Strength

It has already been reported in Chapter 2 that HSC is more brittle than NSC and the experimental results support this. The NSC specimens deteriorated in a stable manner with continual small quantities of cover spall becoming detached from the specimens. At no point did sudden severe damage occur, unlike that recorded for the HSC specimens.

It is clear that the axial load level is very important in determining the response for composite specimens. Specimens with low axial load levels (i.e. Specimens JD2 and JD4) but different concrete strengths behave very similarly during testing, with similar amounts of spall and deterioration to the core being recorded. But for specimens with high levels of axial load, (i.e. JD3, JD5 and JD6) the HSC specimens suffered significantly more damage at all displacement cycles.

4.3.5 Influence of Link Spacing

Link spacing clearly affects the specimen's response as Specimen JD5 becomes unable to resist the applied loads once the cover concrete fails and buckling of the longitudinal steel is recorded. Specimen JD6 was identical but had a reduced link spacing compared to Specimen JD5. A similar sudden reduction in resistance was recorded once the cover concrete failed, but the reduced link spacing prevented the longitudinal steel from buckling at the same displacement as was observed for Specimen JD5. This enabled a subsequent stable resistance to be recorded for JD6 and prolonged resistance against the applied loads.

Due to the limited amount of partially confined concrete between the steel flanges and transverse links, it was impossible to determine visually if the reduced link spacing had any benefits in confining the core concrete, but the experimental data suggests that the reduced link spacing had significant benefits to the sections response and resistance.

4.3.6 Confining Influence of the Base Element

Visual inspection of the specimens showed that the maximum level of damage and deterioration of the core concrete occurred between 100 – 400mm above the base element. The first link is located 36mm above the base interface. The base element clearly provides additional confinement as the column element just above the interface is subjected to the greatest moments yet displays only minimal deterioration. The base element provides additional confinement to the column element just above the base, thus plastic hinging initially occurs above this region of additional confinement (i.e. approximately 100mm above the base interface). This phenomenon has been observed by several previous researchers (Paultre *et al,* 2001, Légeron *et al,* 2000, Bayrak *et al,* 1998, Sheikh *et al,* 1994 and Ryan, 2001).

4.4 Load-displacement and moment-rotation hysteretic behaviour

4.4.1 Introduction

This section outlines the load displacement hysteretic response of the six test specimens. The specimens are analysed by comparing their hysteresis responses with significant visual observations recorded during the test. Section 4.5 compares specimens in terms of energy dissipation, resistance and maximum applied load. This section also presents the moment rotation response of the test specimens, enabling the determination of the P – Δ effects experienced by the specimens.

4.4.2 Load-displacement hysteresis response

All the specimens display similar hysteresis curves. The hysteresis responses are all convex in shape in both directions from the origin, and are capable of supporting the applied loads post yielding (even if they are deemed to have failed). Figure 4.13 to Figure 4.18 present the load – displacement hysteresis response for specimens JD1 – ID2 through to JD6 – ID4, respectively. Despite the similarities in shape, the specimens

display several differences in terms of energy dissipation, maximum load achieved, post yielding response and slope of the ascending branches.

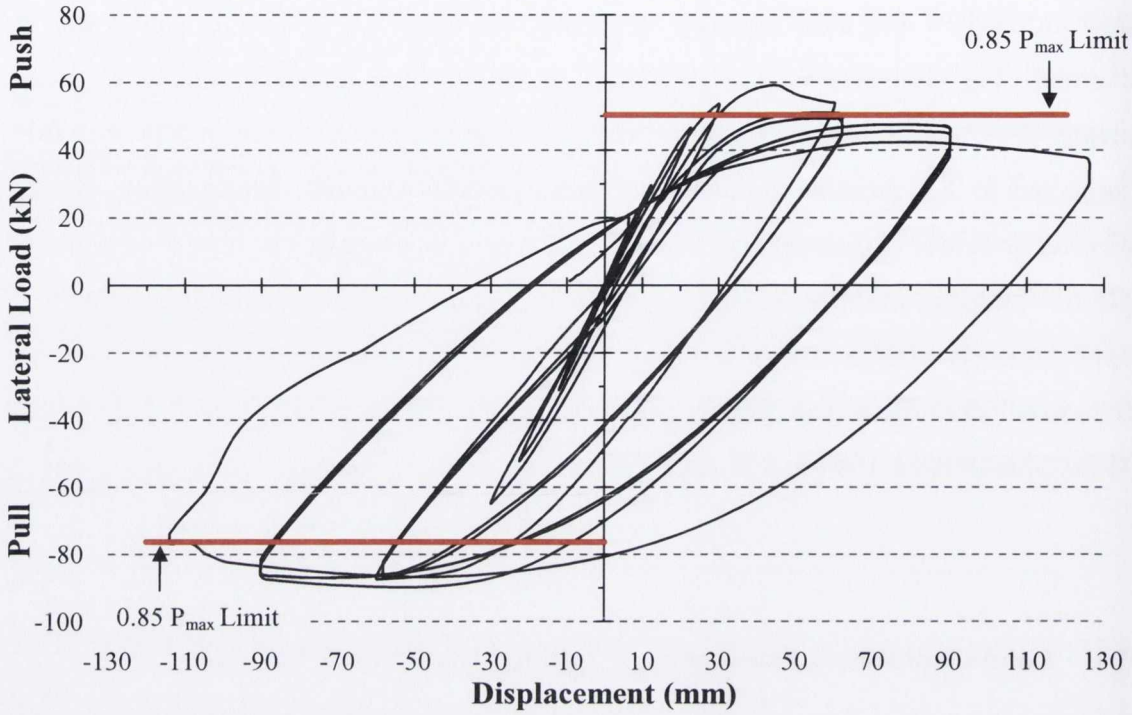

Figure 4.13: Hysteresis Response: Specimen JD1 – ID2

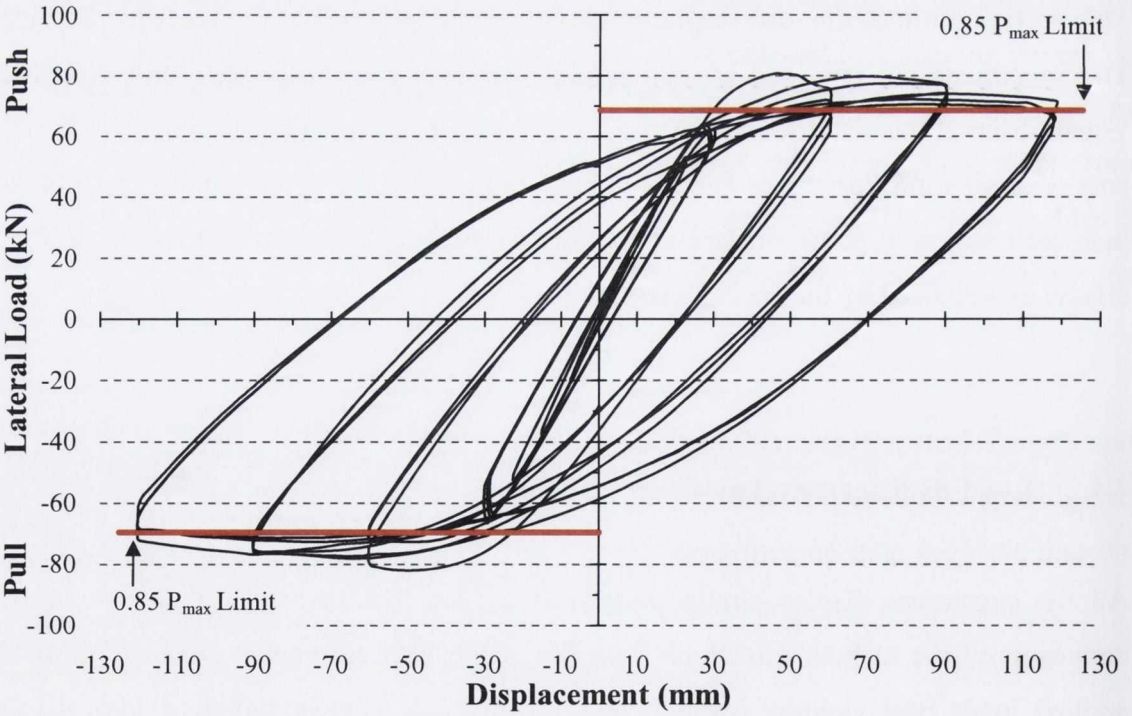

Figure 4.14: Hysteresis Response: Specimen JD2 – ID1

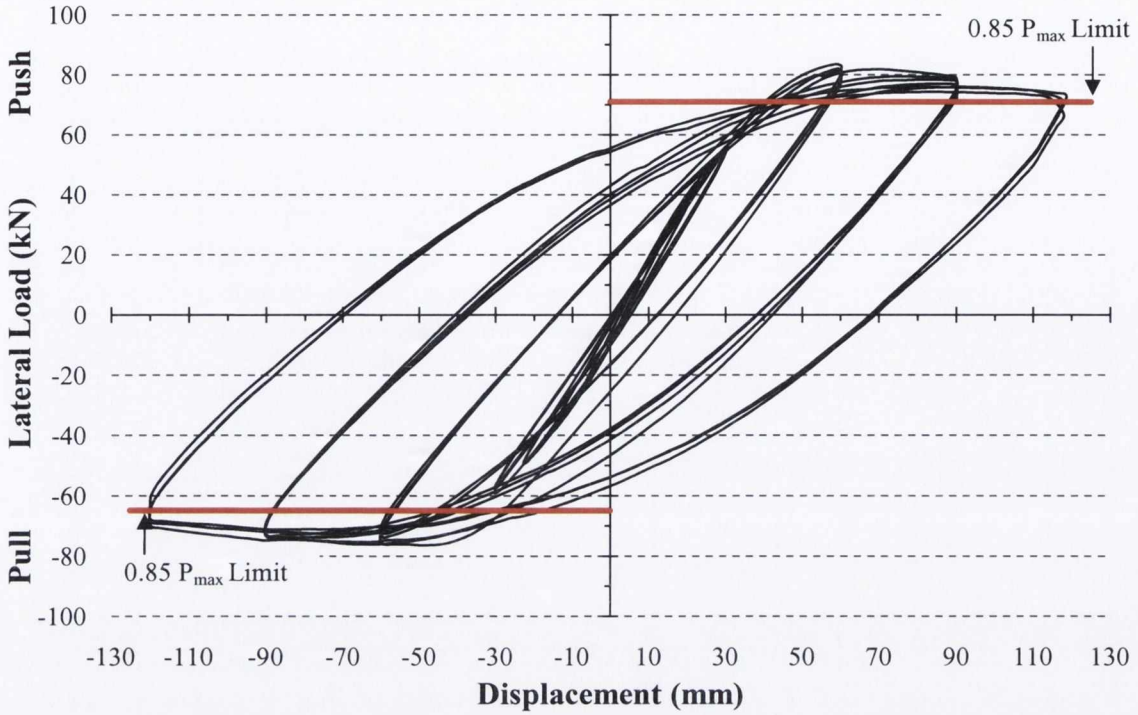

Figure 4.15: Hysteresis Response: Specimen JD3 – ID3

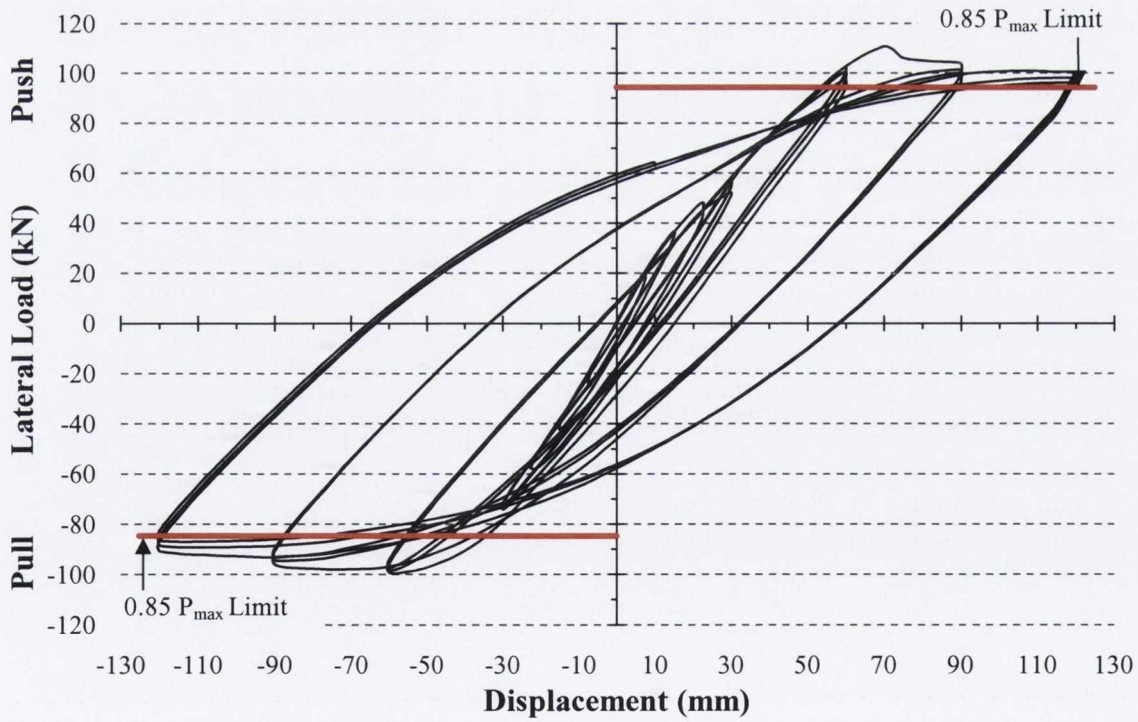

Figure 4.16: Hysteresis Response: Specimen JD4 – ID5

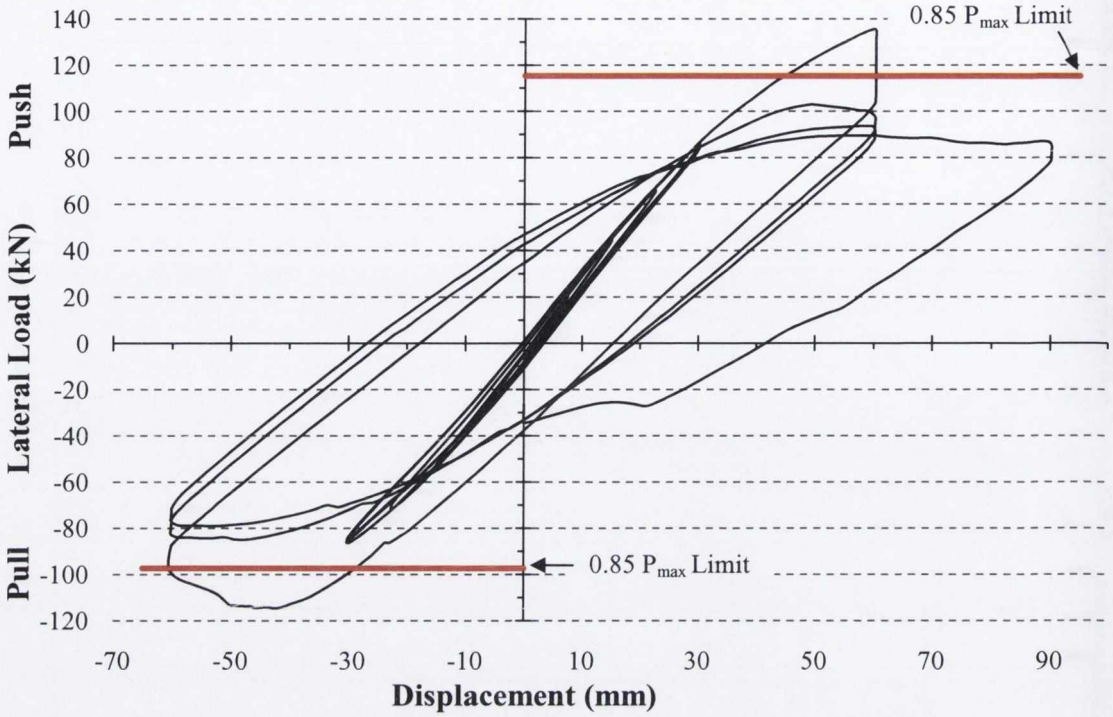

Figure 4.17: Hysteresis Response: Specimen JD5 – ID6

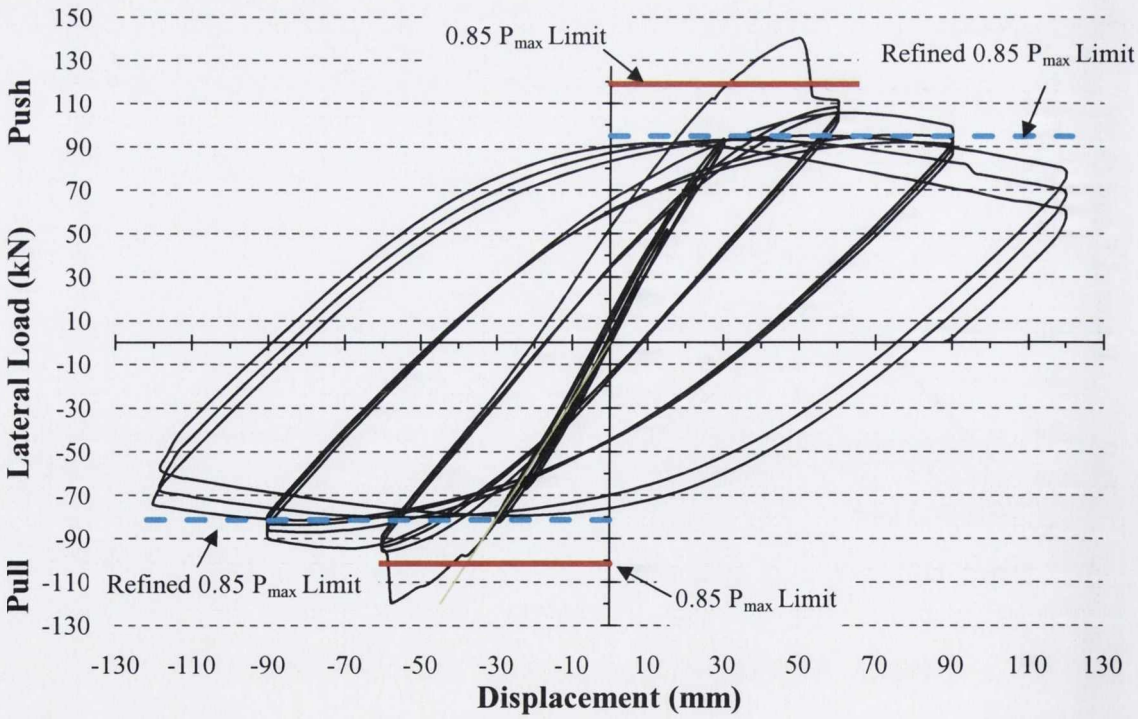

Figure 4.18: Hysteresis Response: Specimen JD6 – ID4

As the yield displacement is greater than 30mm for all specimens it is to be expected that a stable, linear response should be recorded by all specimens up to this displacement. Up to a displacement cycle of 30mm (and beyond in some cases) all specimens maintain their initial stiffness and only small hysteretic loops are evident, this is due to a lack of any steel yielding and the specimens being capable of storing the potential strain energy. This is consistent with the visual observations of Section 4.3.1. It is only when the concrete suffers a high degree of damage and spalling that the elastic energy is lost and a non-linear hysteretic behaviour is observed, thus inducing the large hysteresis loops.

Yielding occurred in all specimens during the 30 and 60mm displacement cycle, the visual observations support this as between these displacements the formation of major structural cracks was recorded and large quantities of spall initially occurred in this region. Post yielding response is reflected by a substantial increase of area enclosed within the hysteresis loops. All the specimens, except for JD3 – ID3 display a slight pinch in the hysteresis plots after the maximum positive lateral load was reached. This was due to the concrete cover suffering extensive cracking and losing all its load carrying capacity, thus reducing the overall sectional capacity. Specimen JD3 – ID3 did not experience this reduction in resistance as the maximum lateral load was achieved corresponding to a displacement of 30mm, thus the load was reversed before the resistance drop (and kink) could be recorded. All the specimens displayed evident signs of extensive yielding at the maximum lateral load where the specimens spalled large amounts of cover concrete and were subject to extensive cracking.

All specimens reached a positive and negative maximum lateral force (push and pull force) during the first cycle of 60mm displacement, except for the push cycle of Specimen JD4 – ID5, which occurred marginally after 60mm displacement. Subsequent cycles of 60mm displacement lead to a reduction in load carrying capacity and stiffness due to substantial concrete spall (both cover and core concrete) and buckling of the longitudinal and structural steel. Increased displacements caused similar but more severe damage, thus further reducing the resistance of the specimens. This is displayed by the large reduction in lateral load resistance for the 90 and 120mm displacement cycles.

Specimen JD1 – ID2 and Specimen JD2 – ID1 were subject to identical axial loads and had the same characteristic compressive strength and link spacing, but Specimen JD1 –

ID2 was not restrained laterally in position by the roller restraint. During this test, the specimen began to displace in a perpendicular direction to the applied lateral load, thus causing the specimen to yield and fail in a bi-axial manner. This caused one face to suffer extensively more damage than it's opposing one. As a result the values recorded must be used with caution. The maximum lateral loads between the specimens are similar and a noticeable reduction in load carrying capacity is recorded for both specimens' post 60mm displacement cycle.

Comparing Specimen JD2 – ID1 and Specimen JD3 – ID3 identifies the difference caused by an increase in axial load for NSC specimens; the specimens are subject to 30% and 40% of their axial capacity respectively. Similar maximum lateral loads, in both directions, are recorded for both specimens and the overall hysteresis response for both samples are very similar, except for two variations. Specimen JD2 encloses a larger area within its 30 and 60mm hysteresis loops, thus identifying that more substantial yielding has occurred in these cycles compared with the corresponding cycles of Specimen JD3. The maximum lateral load (push and pull) is achieved corresponding to a displacement of approximately 45mm for JD2 compared with 60mm and 45mm for Specimen JD3 (push and pull, respectively). A noticeable reduction in load carrying capacity was recorded for Specimen JD2 compared with Specimen JD3 due to the extensive cracking and spalling of the cover concrete. Specimen JD2 dissipates its elastic energy via this damage (as defined in Section 2.3.2) and subsequently produces larger loops than Specimen JD3. Overall little difference is recorded between both specimens and it can be deduced that for this concrete strength an increase in the axial load from 30-40% of the specimen's axial capacity is insignificant in terms of the specimen's performance and load carrying capacity. Both specimens suffered extensive concrete crushing and yielding of the transverse links and longitudinal steel, thus providing ample warning of imminent collapse.

Comparing Specimen JD3 – ID3 and Specimen JD4 – ID5 identifies the difference in behaviour for composite columns with both normal and high-strength concrete. The specimens have identical link spacing and axial load, thus a direct comparison of the merits of HSC can be deduced. Specimen JD4 achieves a maximum lateral resistance approximately 30% greater than that of the NSC specimen. Specimen JD4 achieves this force at displacements of 70mm and 60mm (push and pull, respectively) compared with

60mm and 45mm for Specimen JD3. A noticeable pinch in the hysteresis curve is recorded in the first 90mm cycle (at 70mm displacement) for Specimen JD4; this reduction in load is more significant than for NSC specimens due to the brittle nature of HSC. Visual observation showed that the concrete cover cracked suddenly and a reduction in lateral resistance was recorded as a result. Very similar descending slopes are recorded, thus a smaller area is enclosed within the HSC specimen near the origin, as the slope descent begins from a higher lateral load, Figure 4.19 presents this phenomenon. It can be seen that for lower applied lateral loads a larger area is enclosed within the hysteresis loops for the NSC specimen, but this is made up for in the additional area enclosed due to an increase in the maximum lateral load for the HSC specimen.

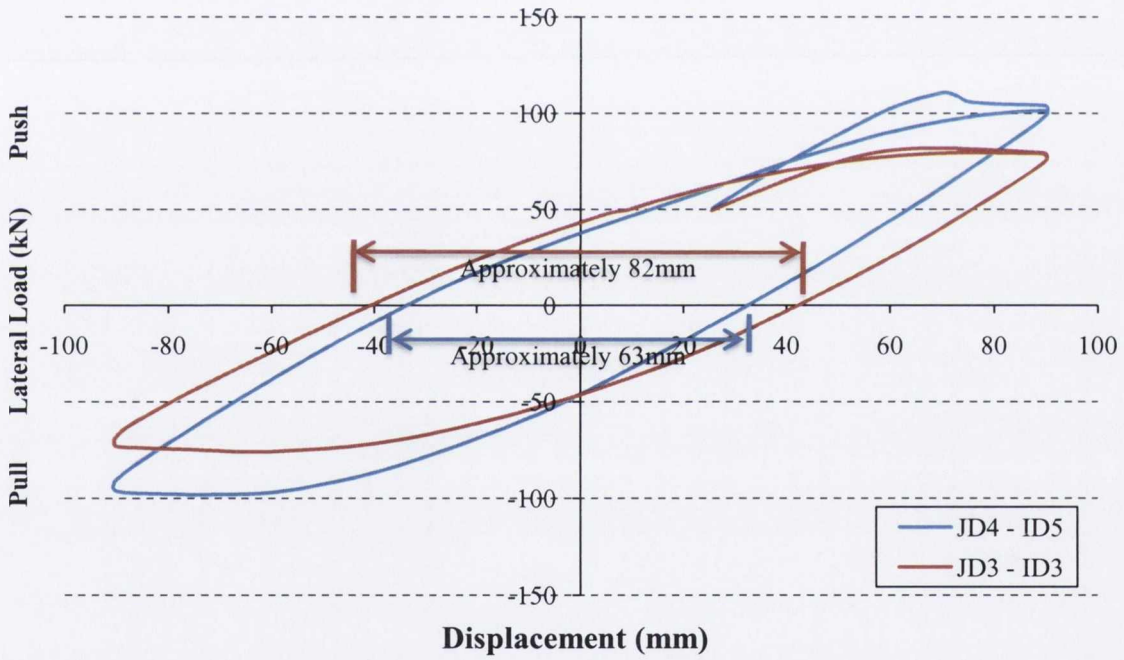

Figure 4.19: Area Enclosed within Hysteresis Loops

Figure 4.19 would suggest that a composite column with HSC can achieve a higher maximum lateral load but only achieve similar energy dissipation to that of an identical specimen with a far inferior concrete strength. Thus, unless the HSC is capable of withstanding large displacements, the benefits of the increased maximum lateral load may become irrelevant. A marginal increase in section size, using the NSC would

achieve the additional lateral load difference and significantly increase the potential energy dissipation.

Specimen JD4 – ID5 is identical to Specimen JD5 – ID4 except for the level of applied axial load throughout the test. Both possessed an identical characteristic cube strength ($f_{ck,\ cube}$ = 85N/mm^2) but were subject to 1200kN and 2000kN of constant axial load, respectively. Specimen JD5 produced a stable hysteresis curve up to the first displacement cycle of 60mm (in the push cycle), just as the specimen reached 60mm displacement a severe crack developed and a considerable reduction in load resistance was recorded, as depicted by its load-displacement hysteresis response. Specimen JD5 achieved a significantly higher maximum lateral load (135kN compared with 111kN), because moderate levels of compressive force increase the flexural capacity of composite members as is illustrated in a typical M-N interaction curve (Figure 3.18). A similar crack developed in the push cycle but with less severity (the crack did not develop so suddenly and the reduction in lateral load resistance was more prolonged).

Further cycles failed to achieve any similar lateral load, the specimen by this time had been deemed failed as the lateral load had dropped below 85% of the maximum lateral load achieved. The specimen tended to buckle perpendicular to the direction of lateral load application in the 90mm displacement cycle and produce a very unstable hysteresis curve with a further drop in resistance being recorded; the test was terminated at this point. Compared to Specimen JD4, Specimen JD5 enclosed a significantly greater area within the 60mm displacement cycles, but this is due to the large amount of elastic energy lost during the development of the major crack. Results indicate that Specimen JD5's details are unsuitable for dissipative earthquake resistant composite columns as it yields in such a brittle manner and is unable to maintain large lateral loads over high displacements. While HSC can be incorporated into composite column design, (as the stable hysteretic behaviour of JD4 suggest) high axial compressive forces combined with lateral bending tend to fail the specimen prematurely and result in an unsafe response providing little to no warning of failure. Improved provisions to confine the core concrete would appear to be required, thus improving the ductility of the member.

Specimen JD6 – ID4 contains a transverse link spacing of 50mm in the critical region, compared with 72mm for all other specimens. A direct contrast between Specimen JD5

and Specimen JD6 identifies the benefits of a reduced link spacing as all other specimen characteristics are identical. Specimen JD6 yields in a similar manner to Specimen JD5, with a sudden brittle failure of the concrete cover occurring on both faces perpendicular to the lateral load. This caused a major reduction in resistance, but unlike Specimen JD5, a stable hysteretic behaviour was achieved in subsequent cycles.

The concrete cover clearly resists a considerable percentage of the applied lateral force, the high-strength concrete failed to develop major longitudinal and transverse cracks prior to brittle failure (which would have altered the neutral axis depth gradually and transfer the applied stresses into the steel and confined concrete core elements). A stable cracking and spalling of the cover concrete would eliminate the large pinch in the hysteresis response thus avoiding a sudden reduction in load resistance of the specimen. The subsequent stable hysteresis behaviour suggests that the closely spaced transverse links adequately confined the concrete core and produced a more stable hysteresis curve (post concrete failure) compared with Specimen JD5.

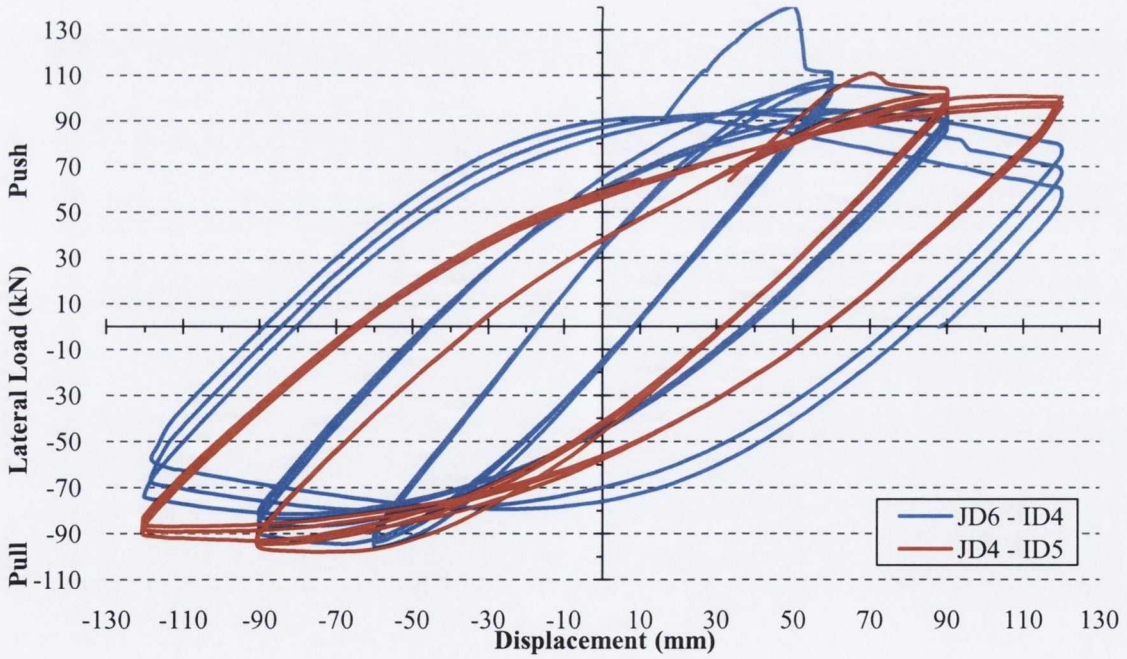

Figure 4.20: Hysteresis Comparison (Post Concrete Failure) for JD4 and JD6

Figure 4.20 presents the hysteresis response for Specimens JD4 and JD6 (post cover concrete failure). The 90mm displacement loops are very similar and the maximum loads

applied at these displacements are nearly identical. It is clear Figure 4.20 that the higher axial load (Specimen JD6) has caused the specimen to yield at a substantially lower displacement than the specimen with a lower axial load. Specimen JD4 is also subject to a larger link spacing in the critical region than Specimen JD6. It is evident that the increase in axial load and reduced link spacing increases the maximum lateral load attainable by the specimen, but when the cover concrete crushes this additional resistance is lost and the specimens behave similarly. The 120mm cycles indicate that Specimen JD4 out performs Specimen JD5 as it achieves a higher lateral load and suffers only a minor reduction in resistance from the previous displacement compared with a considerable drop recorded from Specimen JD6.

Specimen JD6 encloses considerably more area within its 120mm loop than Specimen JD4 (dissipating more energy), but the drop in resistance would suggest that the increase in axial load is more detrimental to the specimen than the advantages gained from a close link spacing. This would suggest that a limit on the maximum axial compressive force as well as a reduced link spacing should be applied if HSC is to be incorporated effectively into composite column design, as smaller link spacings cannot confine the inner concrete core sufficiently to counteract the detrimental effects of high compressive forces. The effects of link spacing and axial load shall be discussed in detail later in the chapter.

4.4.3 Moment-rotation hysteresis response

The moment-rotation responses for Specimen JD1 to JD6 are presented in Figure 4.21 to Figure 4.26, respectively. Rotation is defined in Equation (4.2), as the applied lateral displacement divided by the flexural length of the specimen. The moment adopted in these curves is a combination of the moment from the applied lateral force and the moment arising due to P-Delta effects. Section 3.2.7.3 discusses P-Delta effects in detail and the process by which this additional moment is formulated. Figure 4.21 to Figure 4.26 present the total combined moment, as well as a superimposed line representing the component due to P-Delta effects. The intention of these plots is to illustrate the increase in moment, due to P-Delta effects. These plots display similar characteristics to the load-deflection plots as the loops are of similar shape and reductions in resistance between

consecutive cycles of the same displacement are recognised. Beyond this section, the specimen response is considered in terms of load-displacement response only.

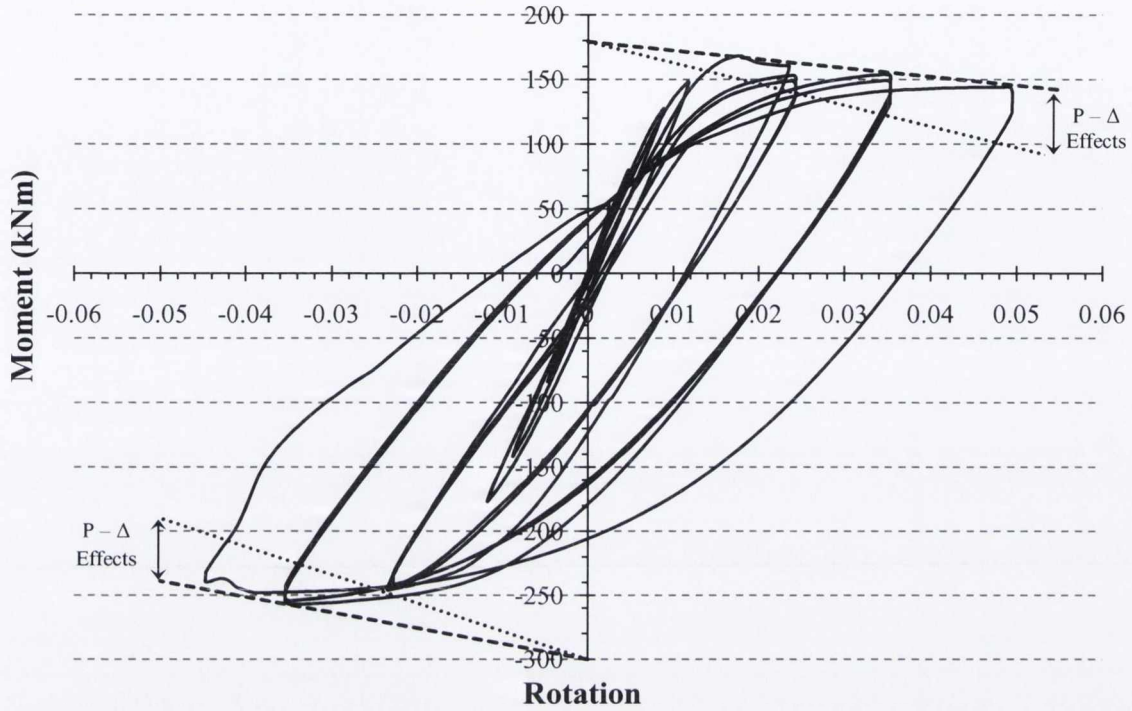

Figure 4.21: Moment Rotation Response: Specimen JD1 – ID2

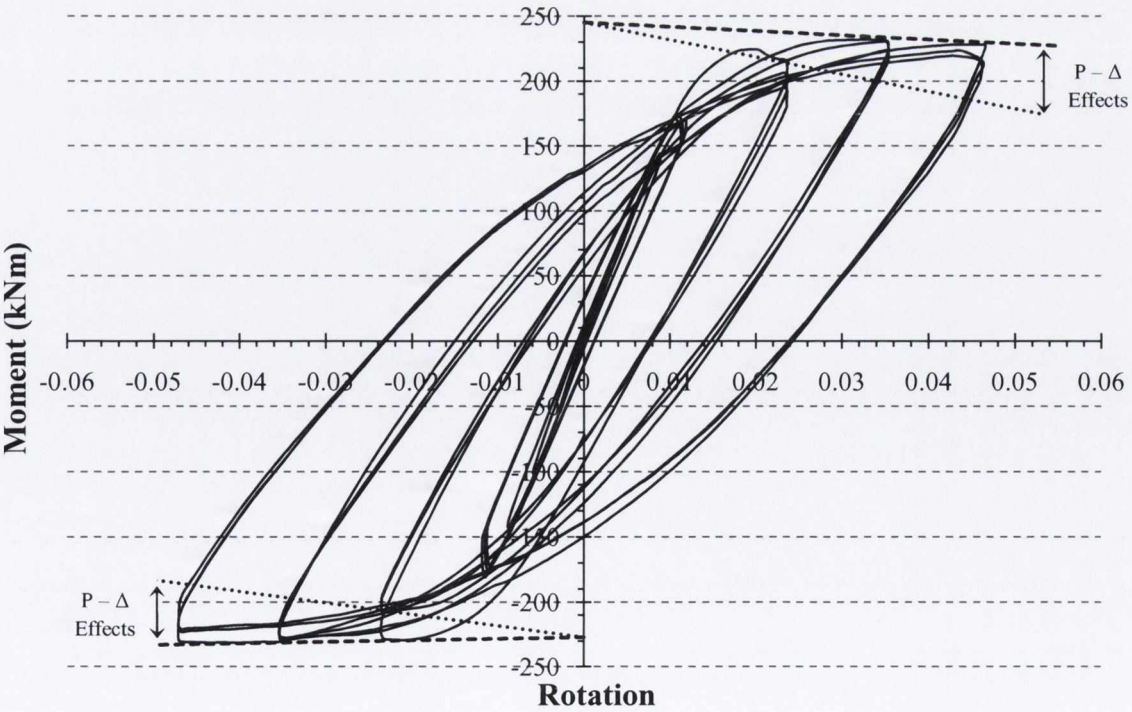

Figure 4.22: Moment Rotation Response: Specimen JD2 – ID1

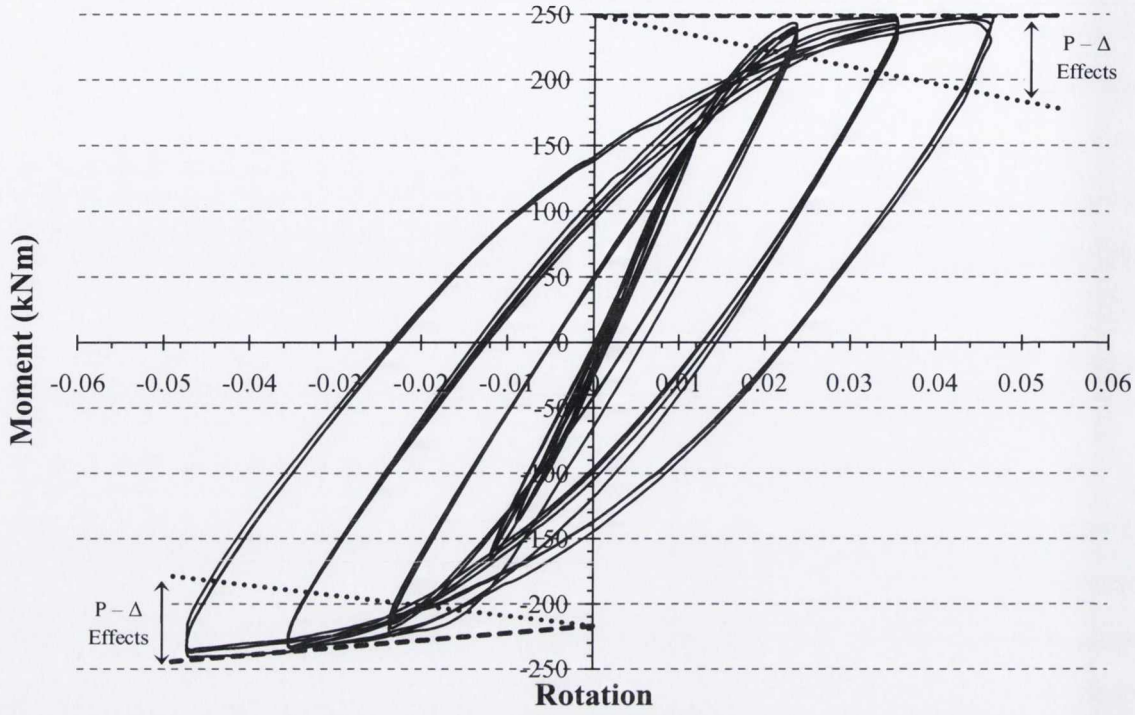

Figure 4.23: Moment Rotation Response: Specimen JD3 – ID3

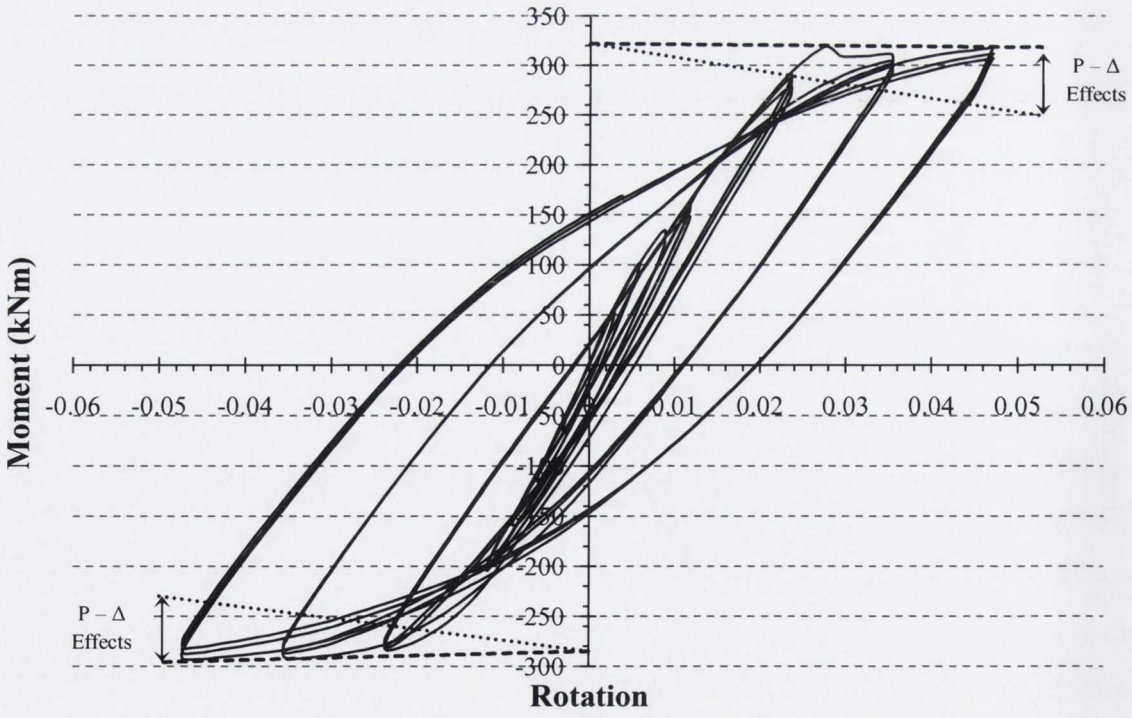

Figure 4.24: Moment Rotation Response: Specimen JD4 – ID5

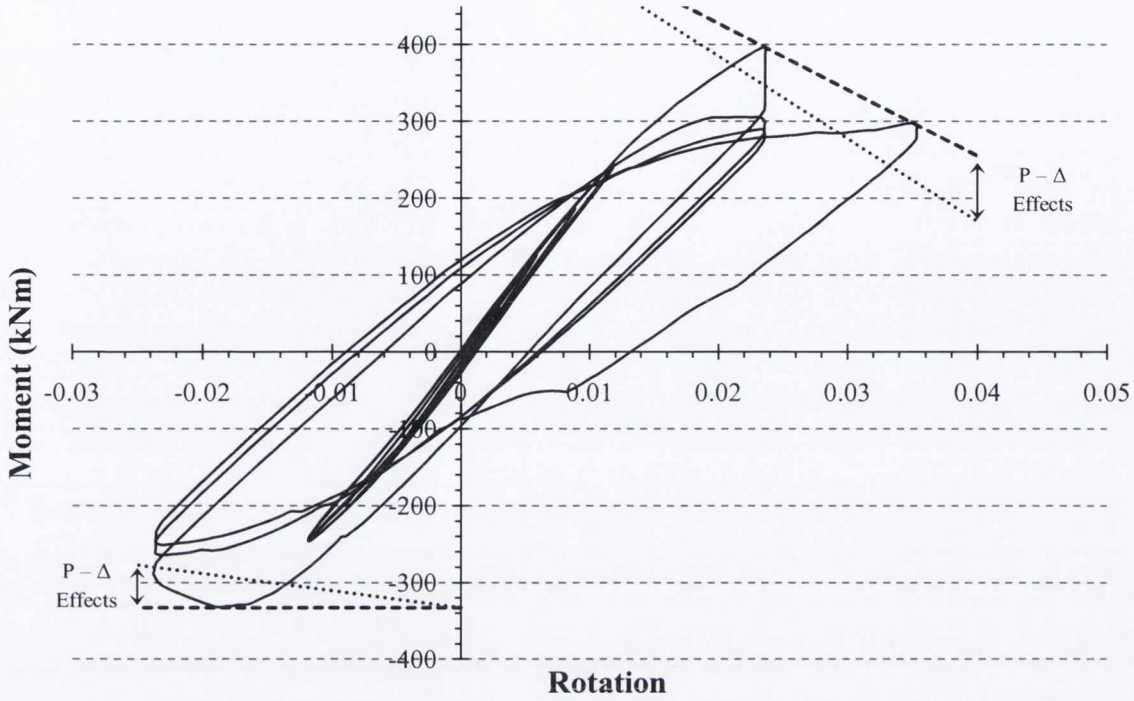

Figure 4.25: Moment Rotation Response: Specimen JD5 – ID6

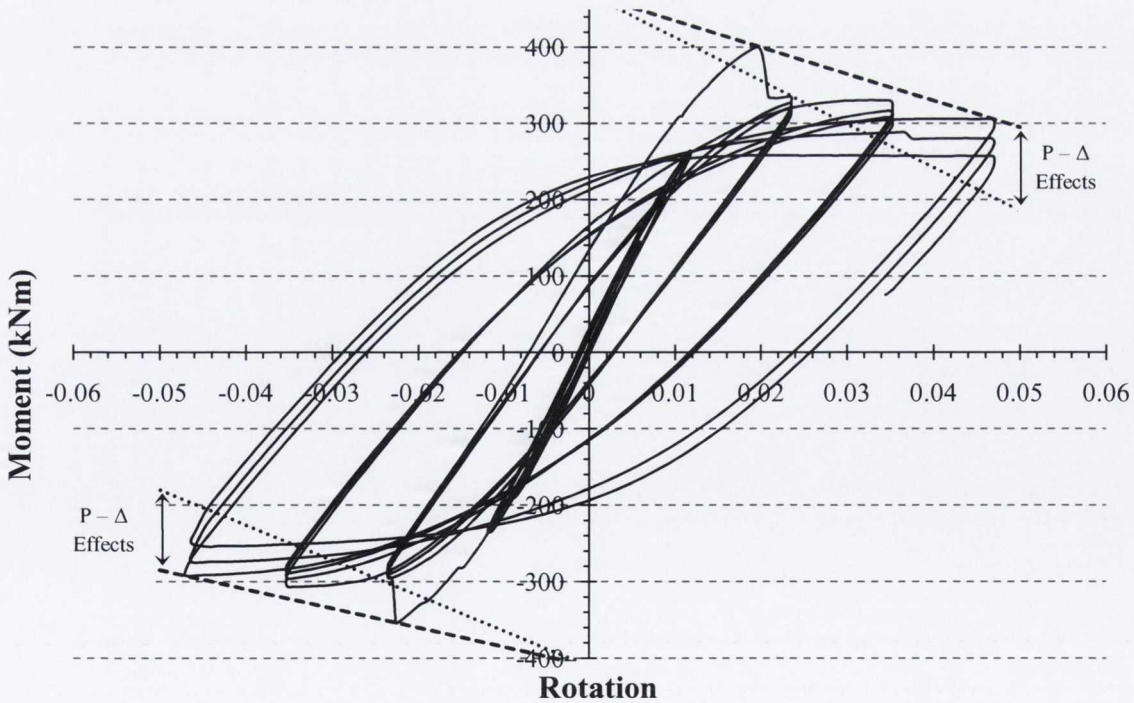

Figure 4.26: Moment Rotation Response: Specimen JD6 – ID4

4.5 Comparison groups

This section analyses in detail each specimen in terms of energy capacity and resistance, two key properties essential for earthquake resistance. Specimens are separated into comparison groups to determine the overall effects of concrete strength, axial load level and link spacing effects. The specimens are divided into groups as detailed in Table 20.

Table 20: Comparison Groups for Specimens

Group Number	Specimens	Reason for Comparison
1	JD1 – ID2 JD2 – ID1 JD3 – ID3	To determine the effects of an increased axial compressive load (30-40% of the specimens axial capacity) on NSC.
2	JD4 – ID5 JD5 – ID6	To determine the effects of an increased axial compressive load (20-35% of the specimens axial capacity) on HSC.
3	JD3 – ID3 JD4 – ID5	To determine the effects of an increased concrete compressive strength (from 25-85N/mm^2).
4	JD5 – ID6 JD6 – ID4	To determine the effects of a reduced link spacing in the critical region for HSC specimens.
5	JD4 – ID5 JD6 – ID4	To compare the effects of reduced link spacing and increased axial load.

Energy Dissipation

The amount of energy dissipated by a structure is determined by measuring the area within a hysteresis loop. Increased energy dissipation can be achieved by increasing the confinement of the concrete via reduced link spacing, additional longitudinal steel and greater quantities of structural steel (particularly increasing the amount of confined concrete between the steel flanges). From here on in, energy dissipation capacity shall be determined by plotting the area with each hysteresis loop against displacement cycle. The purpose of this is to determine the effects of the comparison variable in question and to determine what measures, if any, need to be implemented to incorporate HSC into composite column design.

Resistance

The cyclic resistance of a specimen is a measure of its ability to maintain load carrying capacity under cyclic loading. A specimen must be capable of maintaining the applied lateral load in subsequent cycles at a particular displacement, thus the resistance reflects the amount of degradation sustained by a specimen between subsequent cycles of similar displacement. Two evaluations of resistance are considered within this section, as follows:

- *Resistance Ratio:* This is the ratio of the maximum load attained in a cycle to the specimen yield load.

- *Minimum Resistance:* This is the minimum resistance attained in a group of cycles.

4.5.1 Group 1 (Specimens JD1, JD2 & JD3)

The three specimens considered in Group 1 are; JD1 – ID2, JD2 – ID1 and JD3 – ID3. The purpose of this comparison group was to determine the effects of increasing the axial compressive load from 30 to 40% of the section's plastic capacity. Specimens JD1 and JD2 were subject to axial loads equivalent to 30% of the section's compressive capacity, compared to JD3 which was subject to 40% axial capacity. Specimen JD1 was not restrained in direction perpendicular to lateral loading and as a result buckled in a bi-directional manner. The specimen primarily buckled bi-axially in the push cycle, only minor transverse displacement was recorded in the pull cycle. The hysteresis graphs for Specimens JD1, JD2 and JD3 are presented in Figure 4.13 to Figure 4.15, respectively. The visual aspects and reasons for the observed behaviour are discussed in Section 4.4.2. Figure 4.27 compares the experimental load-displacement envelopes (maximum load achieved per cycle) of the three specimens. The responses represent the average lateral load from both push and pull cycles over a given displacement, except for Specimen JD1, where only the pull cycle is considered due to the considerable reduction in lateral resistance experienced in the push cycle due to bi-axial buckling.

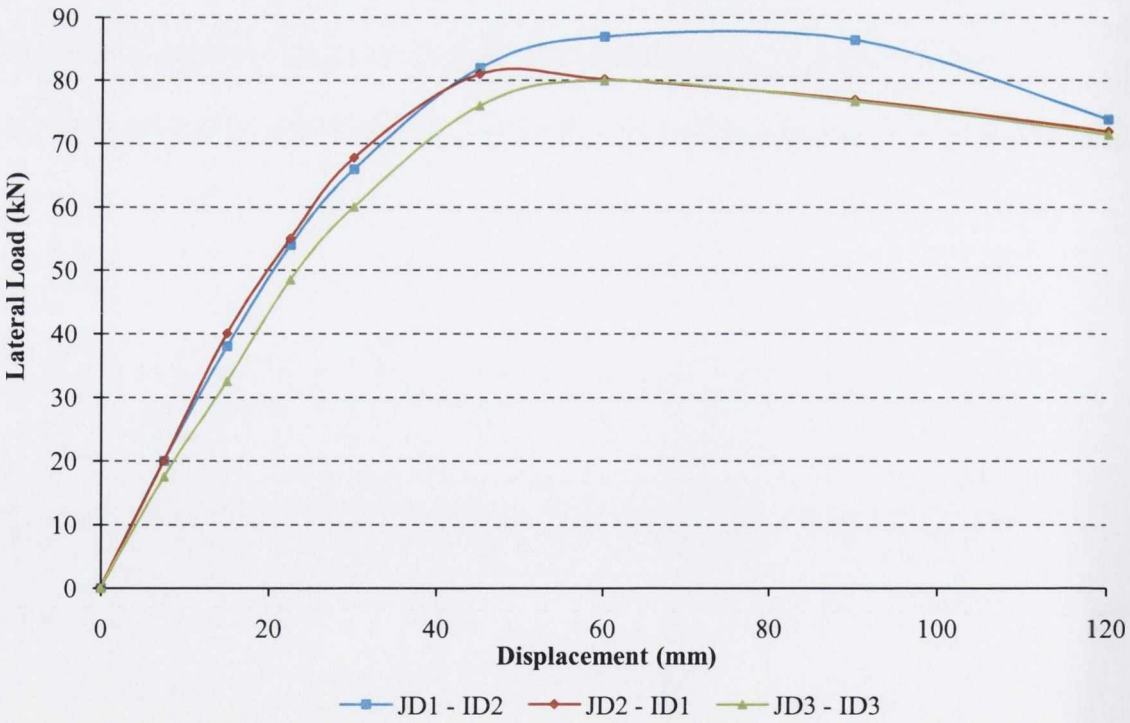

Figure 4.27: Load-Deflection Envelope Curves (Average in Both Directions); Specimens JD1, JD2 & JD3

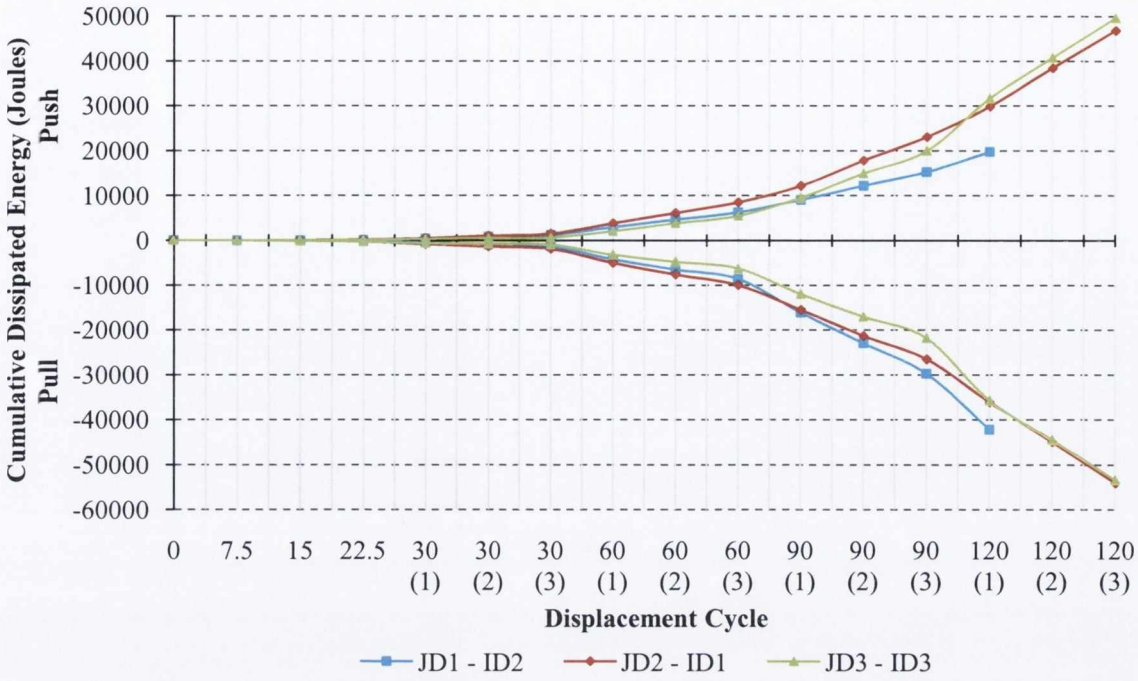

Figure 4.28: Dissipated Energy per Cycle (Comparison Group 1)

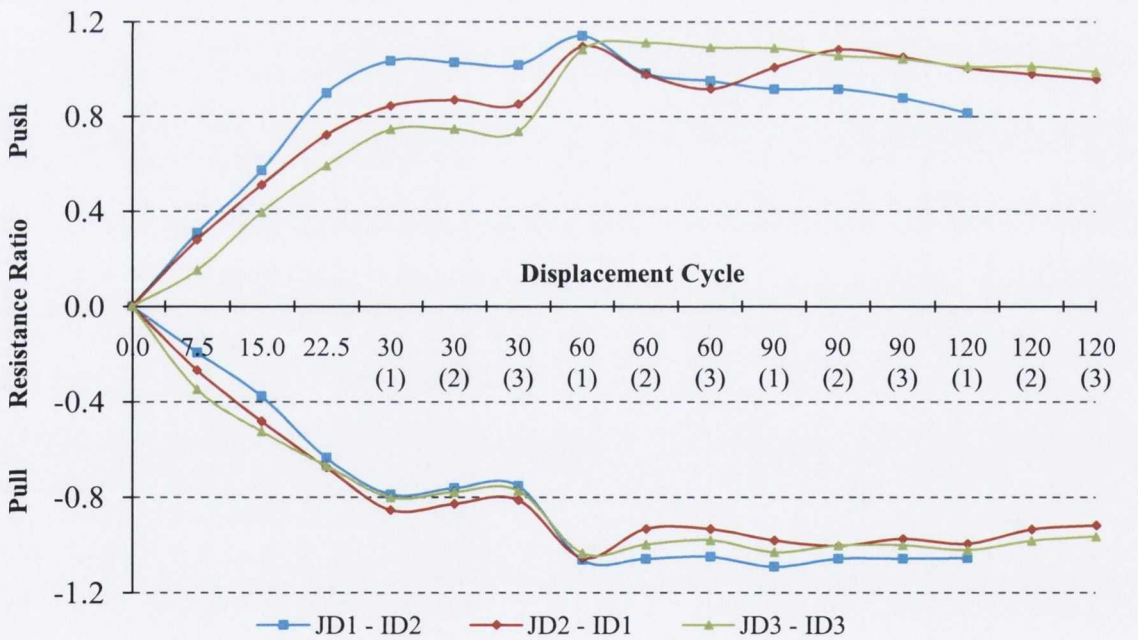

Figure 4.29: Group 1 - Resistance Ratio per Cycle

The most evident difference between the specimen responses is the greater maximum lateral load resisted by Specimen JD1, which may partially be due to the reduced axial

load level compared with Specimen JD3 but is also attributable to the bi-axial buckling, which altered the neutral axis depth and orientation, thus causing a larger quantity of steel to be concentrated in one side of the neutral axis and increasing its capacity. Due to its bi-axial response, Specimen JD1 is not discussed further as its results are not directly comparable with those of similar specimens; furthermore Specimen JD2 is identical to JD1 thus a comparison can be deduced from this specimen. The subsequent data includes the results of JD1 for completeness.

Two main variations exist between Specimen JD2 and Specimen JD3; the first being marginally the more stable resistance ratio of Specimen JD3, and secondly, the difference in displacement at the point of maximum lateral load. As Specimen JD2 achieves its maximum lateral load before Specimen JD3, an increased drop in the resistance of the specimen is recorded, thus increasing the energy dissipated by the specimen. The subsequent sections consider these effects quantitatively.

Energy Dissipation

Figure 4.28 presents the measured energy dissipation in each of the push and pull half cycles for the specimens in comparison Group 1. Only minor differences are observed between Specimens JD2 and JD3. Specimen JD2 has a marginally higher pre-yield stiffness and sustains slightly more damage up to the 90mm displacement cycles, represented by the increased energy dissipation in Figure 4.28. Both specimens behave very similarly in terms of average lateral load and energy dissipation from the first 90mm displacement cycle to the end of the test. Both specimens display a significant drop in the energy dissipated during the 60mm pull cycle, this is evident from the larger hysteresis loop for the first 60mm pull displacement cycle in Figure 4.14 and Figure 4.15. Subsequent loops are smaller due to the level of damage experience by the specimen and an inherent reduction in capacity as a result.

The increased axial load appears to have minimal negative effects up to a displacement of 120mm, beyond this the stroke limit of the actuator was reached and the test was terminated. All specimens experienced a marginal increase in energy dissipation in the 'pull' cycles of the experimental programme, this is attributable to the fact that 'Face B'

(i.e. the face furthest from actuator connection point and perpendicular to the lateral load direction) for all specimens suffered the highest level of deterioration, and, it is clear from all hysteresis curves that more of the displacement range occurs within the negative force range (i.e. pull cycles), thus increasing the energy dissipated.

Resistance

Specimen JD3 displays a smooth linear-like drop in resistance ratio in both the push and pull cycles, similar to the resistance drop of Specimen JD2 from the 90mm displacement cycles on. Specimen JD2 displays a significant drop in resistance during subsequent cycles of 60mm displacement as depicted in the load-displacement graph in Figure 4.14. This was due to the cover concrete experiencing increased spall during subsequent displacement cycles and an overall drop in the load carrying capacity of the section. This response was not experienced in the same degree by Specimen JD3. Overall both specimens have a stable resistance ratio and present no signs of immediate collapse or ultimate failure if subject to increased displacement cycles.

Figure 4.30 presents the minimum resistances of the specimens within each group for both push and pull displacements. The plots are a good indicator of how the stability of a specimen changes from one displacement to the next. The plots display an extremely stable behaviour of all specimens (including Specimens JD1 – ID2). Specimen JD2 displays a lower minimum resistance for the 60mm displacement cycles than the 90mm cycle due to the level of damage experience during the earlier cycles. Figure 4.30 further supports the theory that the specimens would not collapse suddenly if subject to further displacements as their behaviour remains stable and consistent.

(a)

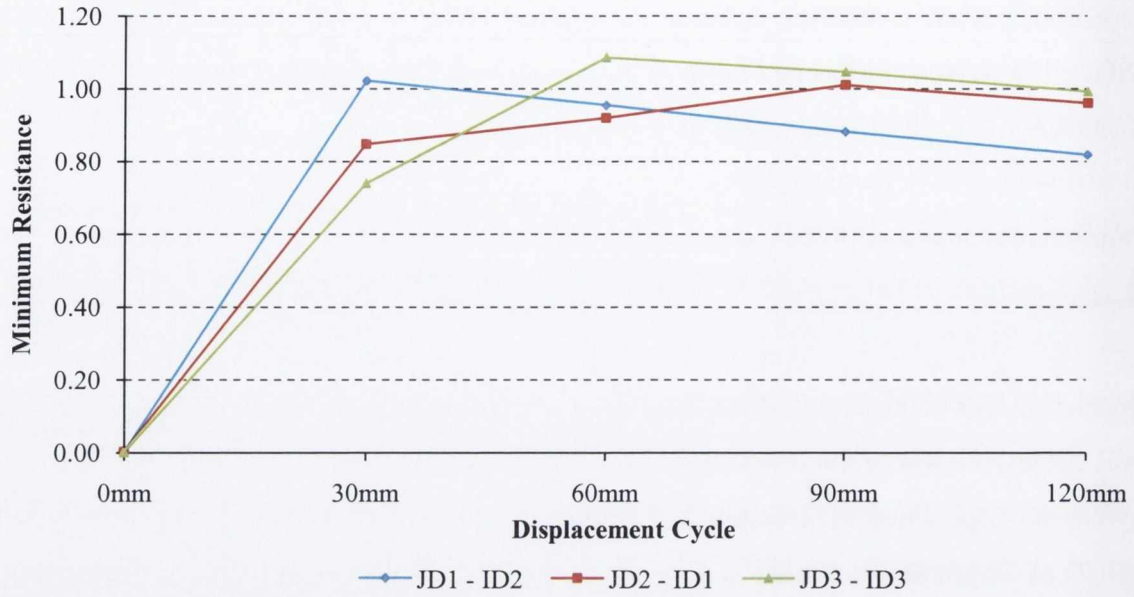

(b)

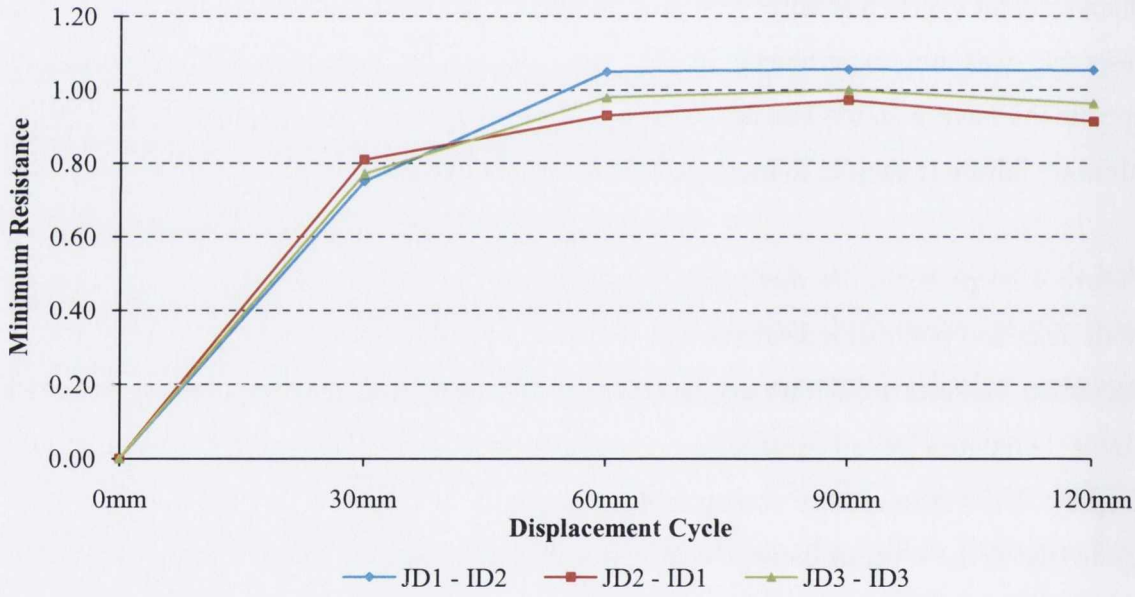

Figure 4.30: Group 1 - (a) Minimum Push Resistances, (b) Minimum Pull Resistances

4.5.2 Group 2 (Specimens JD4 & JD5)

Comparison Group 2 analyses the effects of an increased constant axial load on the performance of high-strength concrete (HSC). The two specimens compared are Specimen JD4 – ID5 and Specimen JD5 – ID6, both with characteristic concrete compressive cube strength of 85N/mm^2 and identical link spacing throughout. Figure

4.31 presents the load-deflection hysteresis response (average load in both directions) for both specimens. Major differences are evident between the performances of the specimens.

Specimen JD5 achieves a higher maximum lateral load resistance than Specimen JD4; this is consistent with the M-N interaction theory for these specimens (as illustrated in the M-N interaction plot in Figure 4.7), as an increased axial load (equivalent to that of Specimen JD5) will achieve a higher maximum lateral load resistance than Specimen JD4. Specimen JD5 also displays a higher pre-yield stiffness. Beyond the maximum lateral load resistance achieved, the specimens behave very differently. As previously discussed in the visual inspections of Section 4.3.1 Specimen JD5 cracked suddenly and severe spall and reinforcement buckling occurred at the first 60mm displacement cycle in the push direction. This caused a severe reduction in the resistance of the section and was repeated (to a lesser extent) in the first 60mm pull cycle. Subsequent cycles failed to achieve anywhere near as high a resistance and the specimen became unstable at which point the test was terminated after the first push cycle of 90mm displacement.

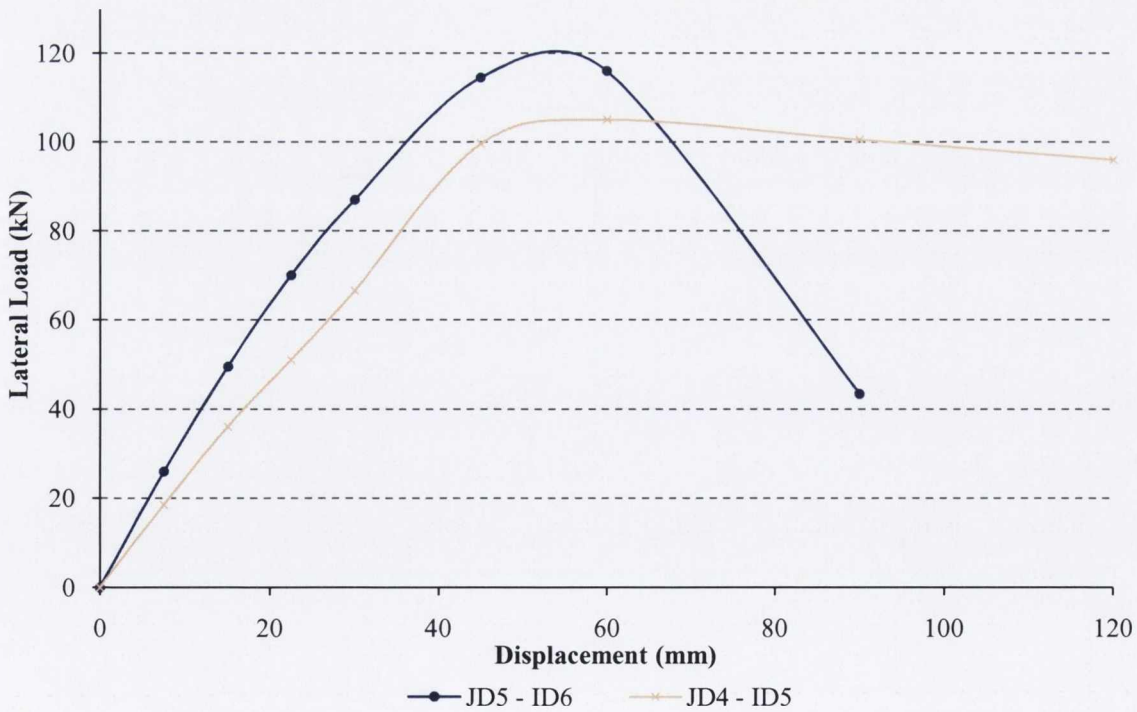

Figure 4.31: Load-Deflection Envelope Curves (Average in Both Directions); Specimens JD4 & JD5

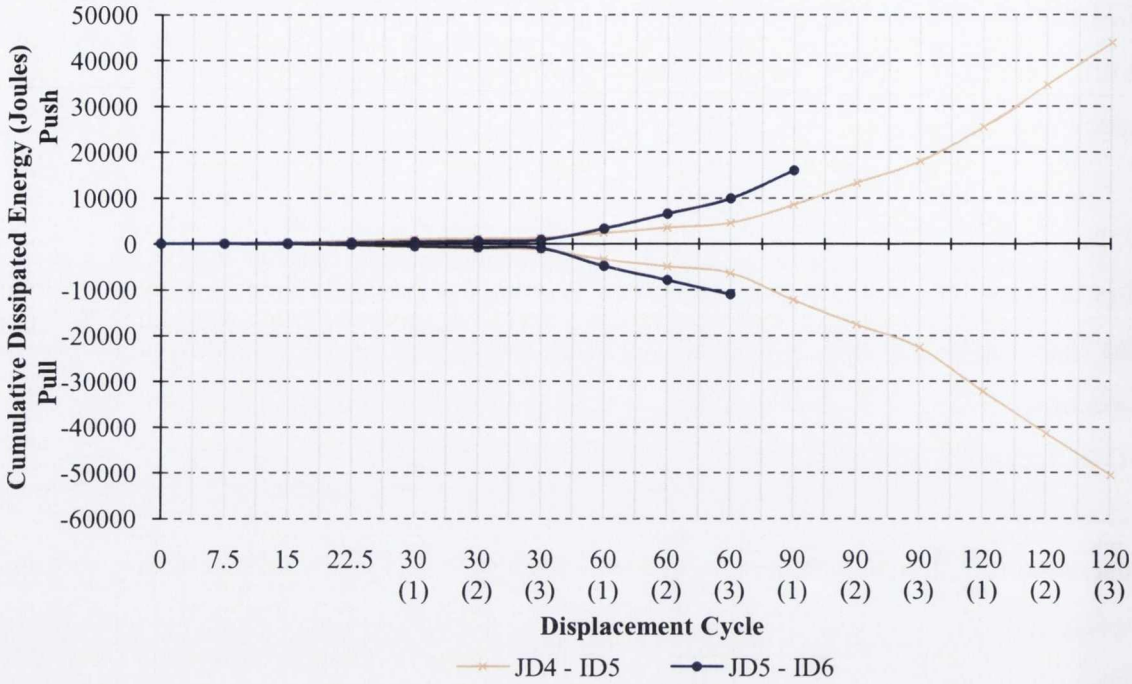

Figure 4.32: Dissipated Energy per Cycle (Comparison Group 2)

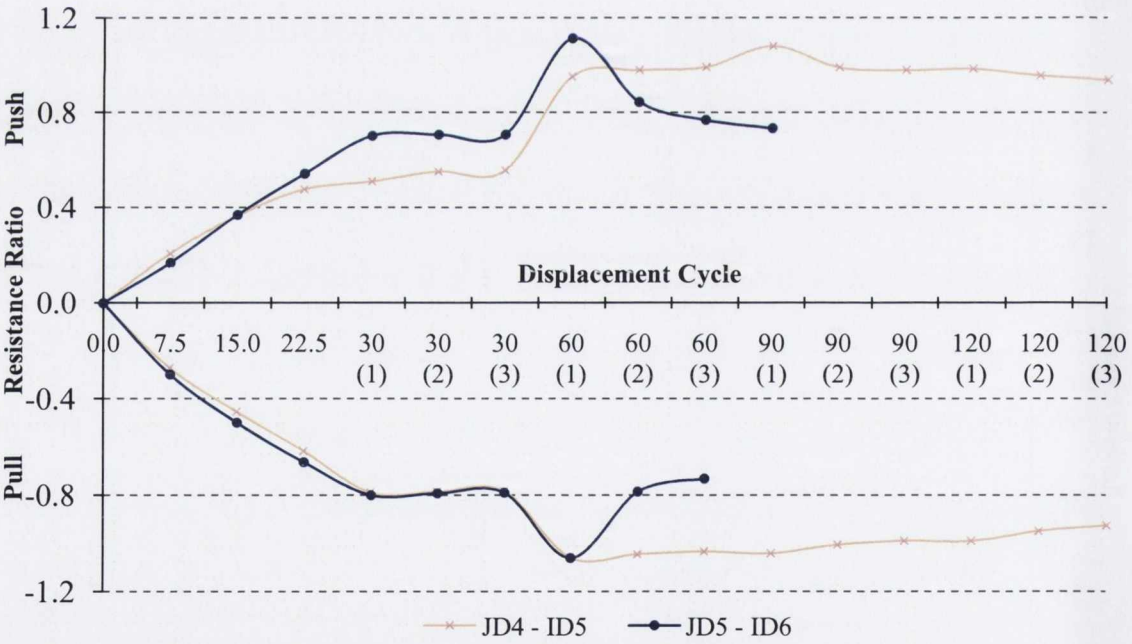

Figure 4.33: Group 2 - Resistance Ratio per Cycle

Specimen JD4 achieved its maximum resistance just after the 60mm push displacement cycles also but experienced only a minor drop in resistance thereafter. The load-deflection hysteresis plots for Specimen JD4 and Specimen JD5 are presented in Figure 4.16 and Figure 4.17, respectively, and illustrate the unstable resistance nature of

Specimen JD5. Subsequent displacement cycles for Specimen JD4 (post achieving its maximum lateral load resistance) present a stable hysteresis behaviour and consistent drop in resistance, consistent with the behaviour of a normal-strength concrete.

Energy Dissipation

Figure 4.32 presents the dissipated energy of the two specimens in the half cycles of each hysteresis loop. No noticeable difference in the energy dissipated is experienced until the 60mm displacement cycle, as prior to this the specimens are within their elastic range. During the 60mm cycles, Specimen JD4 experiences little degradation and little to no drop in resistance, thus only a small amount of energy is dissipated compared with Specimen JD5. The severe damage experienced by Specimen JD5 at this displacement dissipates a large amount of energy; this also alters the shape of subsequent hysteresis loops, evident from its load-deflection hysteresis curve (Figure 4.17). Specimen JD5 dissipates more energy than Specimen JD4 in all post yield cycles, but due to the significant drop in resistance and unstable nature the test was terminated after the first 90mm cycle.

Specimen JD4 continued with an increased level of energy dissipated per displacement cycle due to the increase in size of the hysteresis loops. The test was terminated after the stroke limit of the actuator was reached. The specimen displayed behaviour such that it could withstand further displacements without sudden collapse and drop in resistance.

Resistance

Figure 4.33 presents the resistance ratio per cycle for both Specimens JD4 and JD5. It is clear both specimens behave in a similar manner up to attaining their respective maximum lateral resistances, thereafter a substantial divergence occurs. Specimen JD5 experiences a significant drop in resistance, consistent with its hysteresis plot and the visual observations. The drop in resistance in considerable below the $0.85P_{max}$ limit line superimposed on the load-deflection hysteresis plot in Figure 4.17, the section is unable to resist the applied loads beyond this displacement cycle thus the section is deemed failed.

Stable hysteresis behaviour is desirable as it generally ensures imminent structural collapse is avoidable, but Specimen JD5 fails to achieve this post spalling of the cover concrete. This supports the theory that high levels of axial load are detrimental to the performance of HSC designed using existing design provisions.

Specimen JD4 experienced a stable reduction in resistance and was still above the $0.85P_{max}$ limit when the stroke limit of the actuator was reached. This indicates that this level of axial load ($\approx$ 20% axial capacity) is a suitable level to be placed on HSC composite columns. The resistance ratio indicates that this specimen could easily withstand higher displacements.

The minimum resistance ratios for the push and pull half cycles of each displacement group are presented in Figure 4.34. The plots confirm the superior performance of Specimen JD4; it illustrates the stable and consistent resistance drop of Specimen JD4 compared with the less stable performance of Specimen JD5 and its failure to achieve large displacement cycles.

(a)

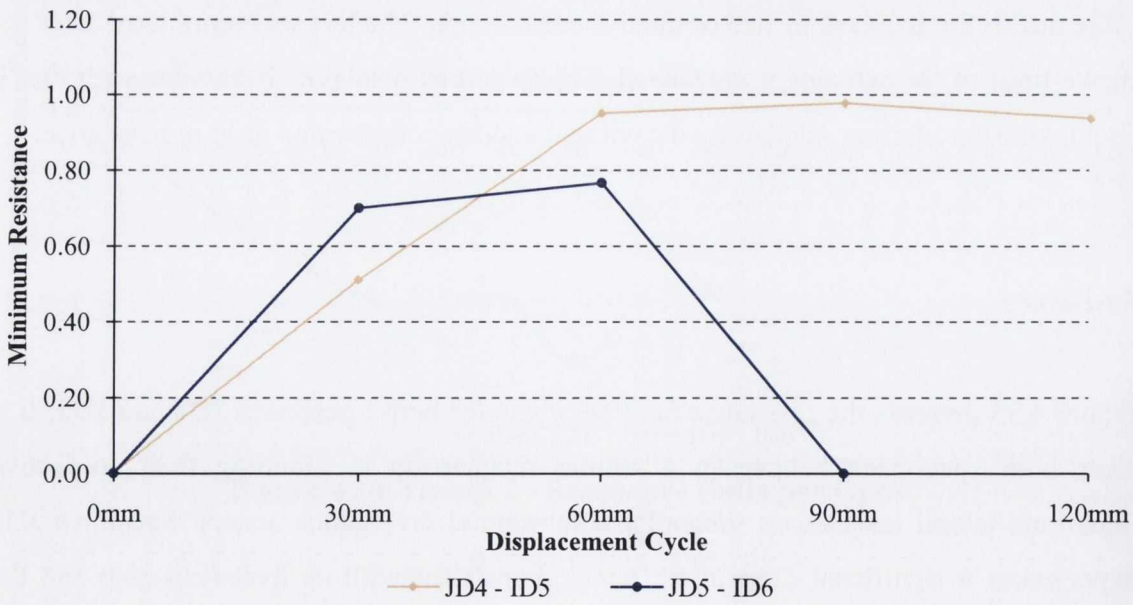

(b)

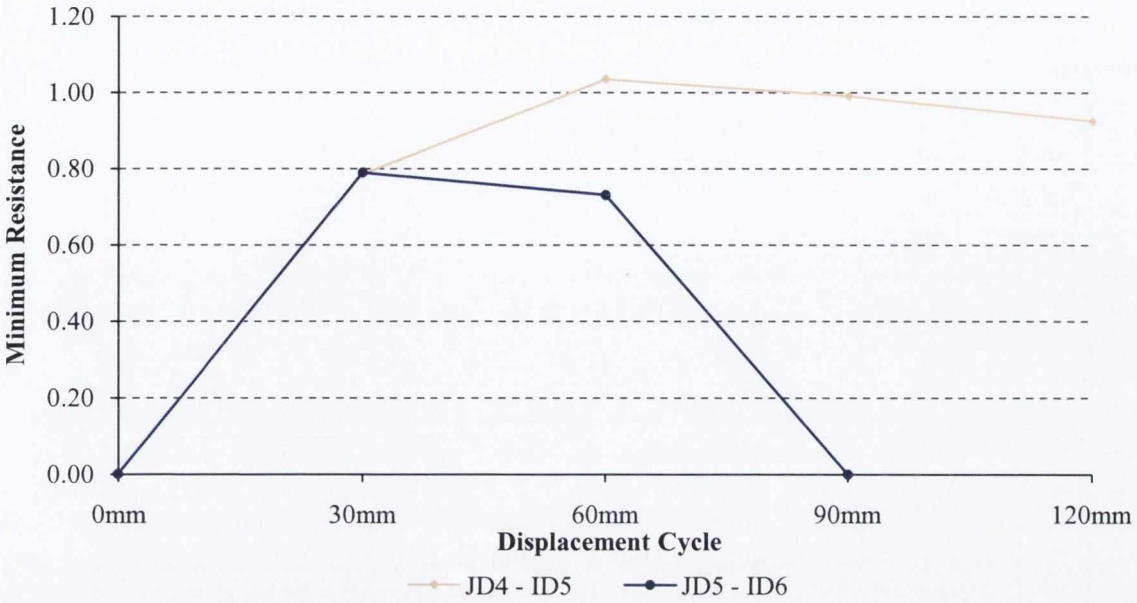

Figure 4.34: Group 2 - (a) Minimum Push Resistances, (b) Minimum Pull Resistances

4.5.3 Group 3 (Specimens JD3 & JD4)

The two specimens compared in Group 3 are; Specimen JD3 – ID3 and Specimen JD4 – ID5. The load-deflection hysteresis curve (average load in both directions) for both specimens is presented in Figure 4.35. The purpose of this comparison group is to determine the effects of an increased concrete strength from 25 – 85N/mm^2 (cube strength). Both specimens consisted of identical link spacing and were subject to an identical constant axial load (1200kN). This axial load is equivalent to approximately 40% and 20% of the section's axial capacities, respectively.

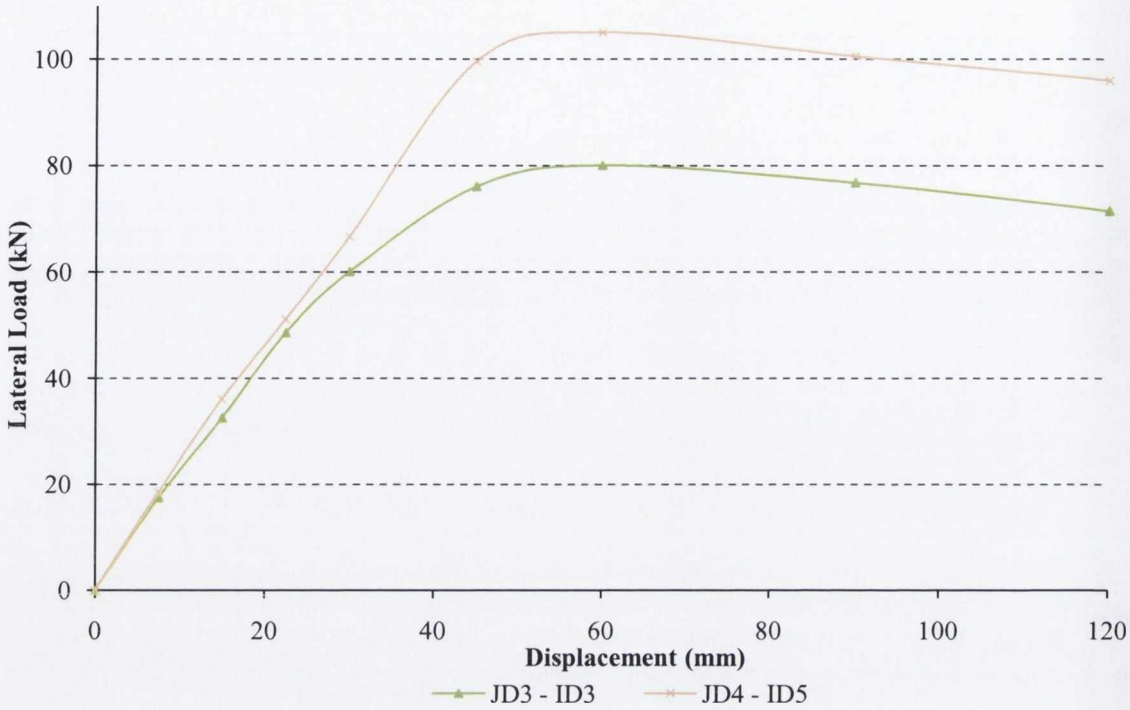

Figure 4.35: Load-Deflection Envelope Curves (Average in Both Directions); Specimens JD3 & JD4

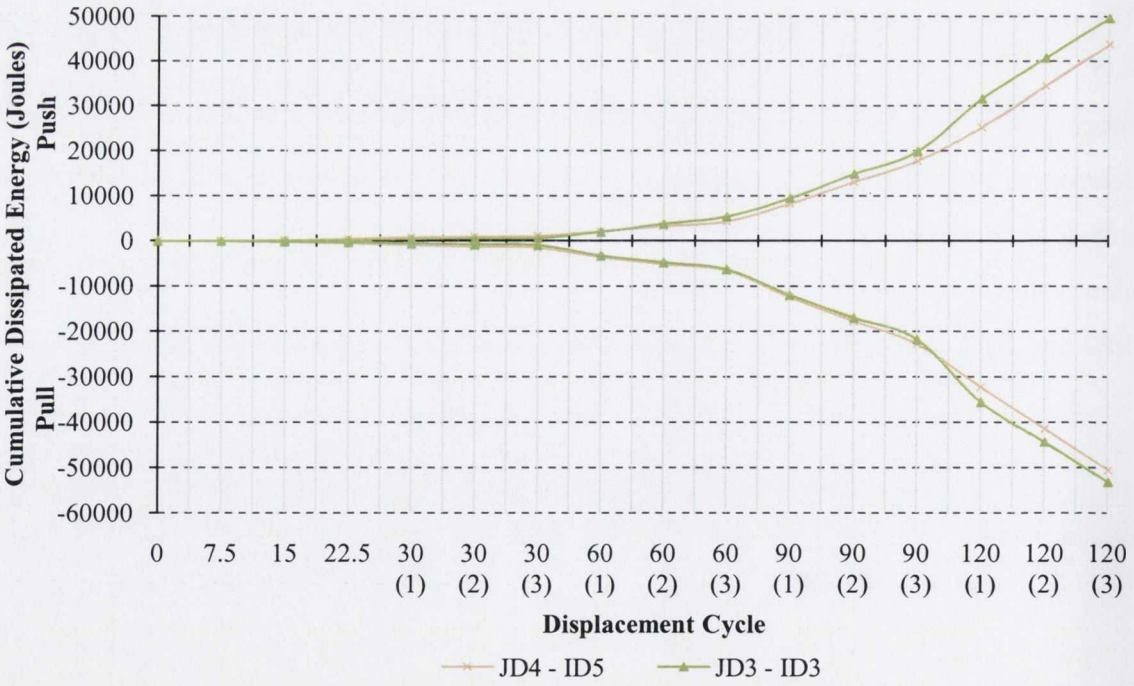

Figure 4.36: Dissipated Energy per Cycle (Comparison Group 3)

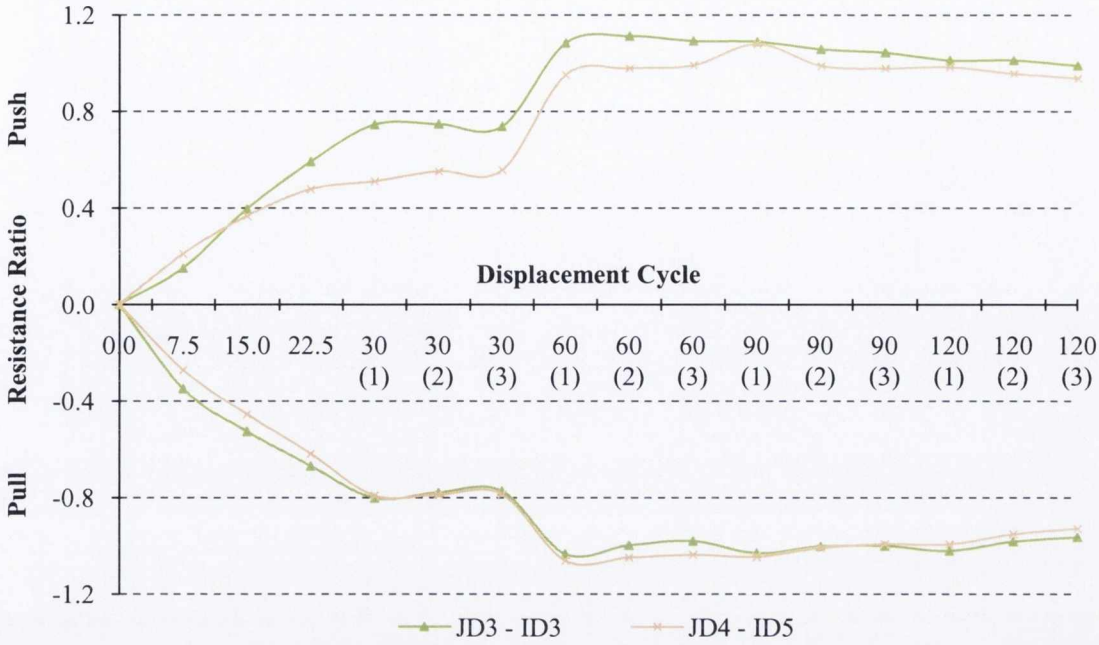

Figure 4.37: Group 3 - Resistance Ratio per Cycle

Both specimens display very similar pre-yield characteristics. Specimen JD4 achieves a significantly higher maximum lateral resistance (P_{max}) due to the higher concrete compressive strength. The performance of both specimens post P_{max} is very similar; they display a near identical load-displacement slope, representing the drop in resistance. When the stroke limit of the actuator was reached, both specimen's load carrying capacity was still above the $0.85P_{max}$ limit and both displayed every sign that they could withstand greater displacements without sudden collapse or drop in resistance.

Energy Dissipation

Figure 4.36 presents the energy dissipated per cycle for Specimens JD3 and JD4. The response of both specimens is very similar. The plots in Figure 4.36 are almost identical and display the same reductions in energy dissipated within displacement groups. Section 4.4.2 introduced the reason why the dissipated energy was similar, on analysing a typical hysteresis loop from each specimen, as is presented in Figure 4.19, it is clear that an additional area is contained within the HSC loop above the maximum lateral resistance of the NSC specimen. But, as the descending slopes of the curves are similar, the HSC curves crosses the x-axis at a lower displacement than the NSC specimen, thus the area between the two descending slopes counteracts the additional area due to the increase in the maximum lateral resistance and a similar energy dissipation is recorded.

As the envelope curves (post P_{max}) are similar, all values of energy dissipation are expected to be similar, as is the case here.

The brittle nature of HSC may tend to cause a reduction in lateral resistance at large ductility demands. However, this level of axial load has already been observed to be suitable for this grade of concrete. Both specimens seem capable of withstanding higher displacements as their reduction in load carrying resistance is subtle and stable.

Resistance

The resistance ratio per cycle for Specimen JD3 and Specimen JD4 is presented in Figure 4.37. The plot is similar to the energy dissipation plot and confirms the gradual reduction in load carrying capacity of the section. Specimen JD3 achieves a higher resistance during all displacement cycles in the push plane, the resistance response in the pull direction is almost identical for Specimens JD3 and JD4, the near identical behaviour recorded in the hysteresis graphs supports this finding (Figure 4.15 and Figure 4.16). Both specimens appear to be capable of withstanding higher displacements, beyond the stroke limit of the actuator. This is supported by the minimum push and pull resistances achieved per displacement cycle as illustrated in Figure 4.38.

(a)

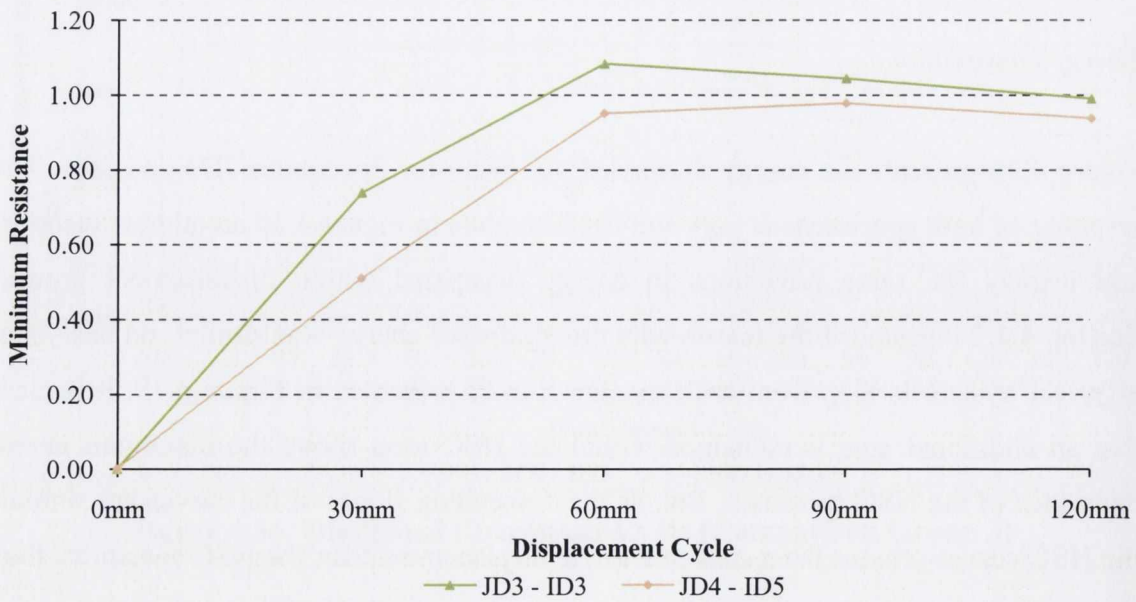

(b)

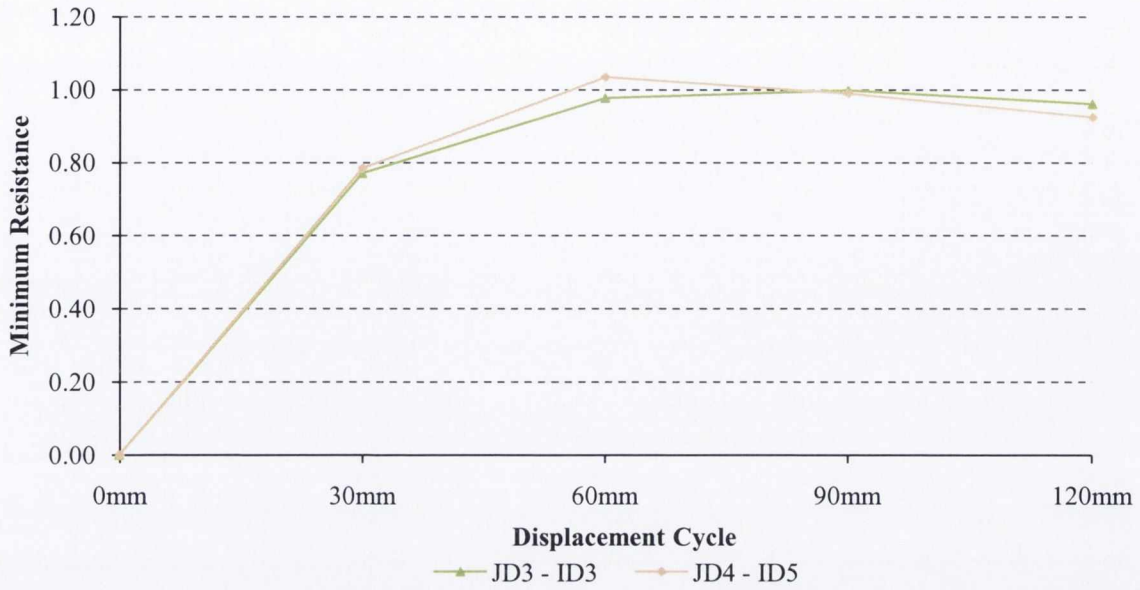

Figure 4.38: Group 3 - (a) Minimum Push Resistances, (b) Minimum Pull Resistances

4.5.4 Group 4 (Specimens JD5 & JD6)

Comparison Group 4 compares the response of two HSC specimens with high levels of axial load but with different link spacings in the critical region of the member. The two specimens compared are Specimen JD5 – ID6 and Specimen JD6 – ID4. Specimen JD5 contains transverse links at a spacing of 72mm within the critical region compared to 50mm for Specimen JD6. The axial load level corresponds to 40% of the specimen's axial capacity. It has already been shown that this level of axial load can be detrimental to the performance of HSC composite section (Comparison Group 2, i.e. Section 4.5.2).

The load-deflection envelope curve for the two specimens is presented in Figure 4.39. Both specimens have similar pre-yield stiffness; Specimen JD6 achieves a marginally higher maximum lateral resistance (P_{max}), as is to be expected due to the decreased link spacing. Past attaining P_{max}, both specimens experience a sharp reduction in lateral resistance. This has previously been observed at high axial loads, but here Specimen JD6 displays a much lower drop in resistance than Specimen JD5. This is attributable to the increased confinement from the decreased link spacing.

Unlike Specimen JD5, which became unstable after this drop in resistance, Specimen JD6 reached a plateau at which the load carrying capacity stabilised and normal hysteretic behaviour continued. Beyond this displacement, reasonable drops in resistance were recorded but stable hysteresis loops remained. Clearly the reduced link spacing benefited the specimen. The brittle nature of HSC caused the sudden crushing of the cover concrete and associated drop in resistance, if intermediate lateral displacements between the 30mm and 60mm cycles were incorporated in the test displacement history it is possible that the cover concrete would have spalled before the 60mm cycles, thus reducing the sudden reduction in resistance (possibly also reducing the maximum lateral resistance, P_{max}). This may have enabled the specimen's load carrying capacity to remain within the $0.85P_{max}$ limit beyond the 90mm displacement cycles. The load-deflection envelope curve (Figure 4.39) illustrates that a reduced link spacing does not achieve a high enough ductility displacement for a composite column, but it does indicate the benefits of a reduced link spacing for HSC.

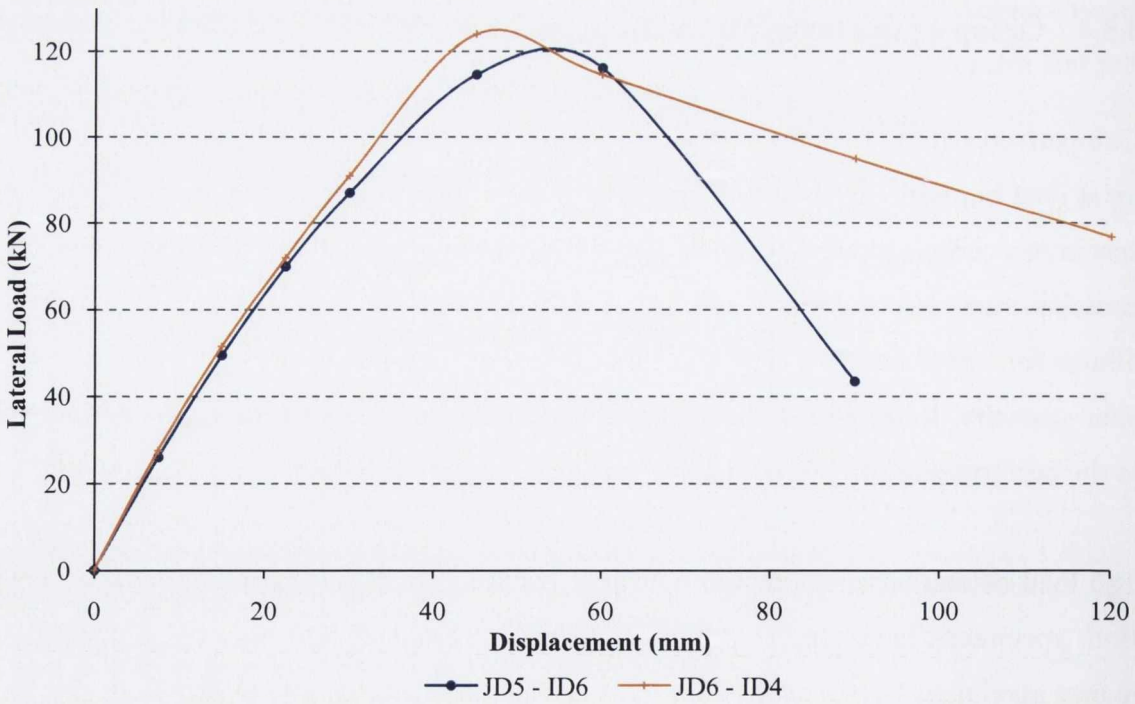

Figure 4.39: Load-Deflection Envelope Curves (Average in Both Directions); Specimens JD5 & JD6

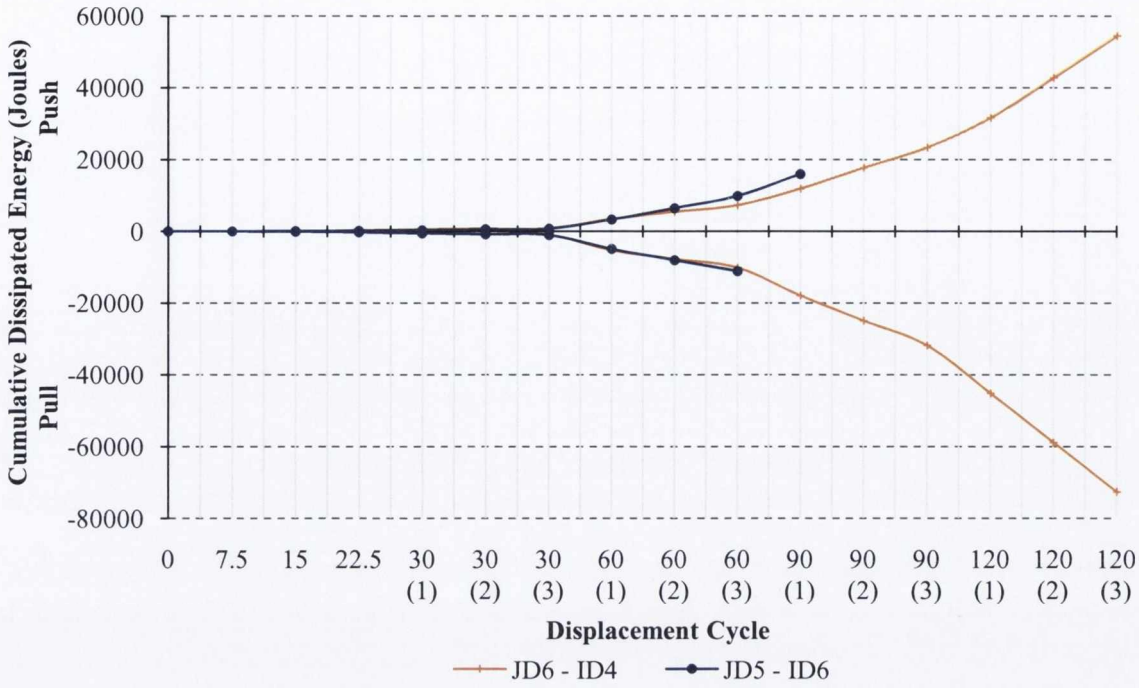

Figure 4.40: Dissipated Energy per Cycle (Comparison Group 4)

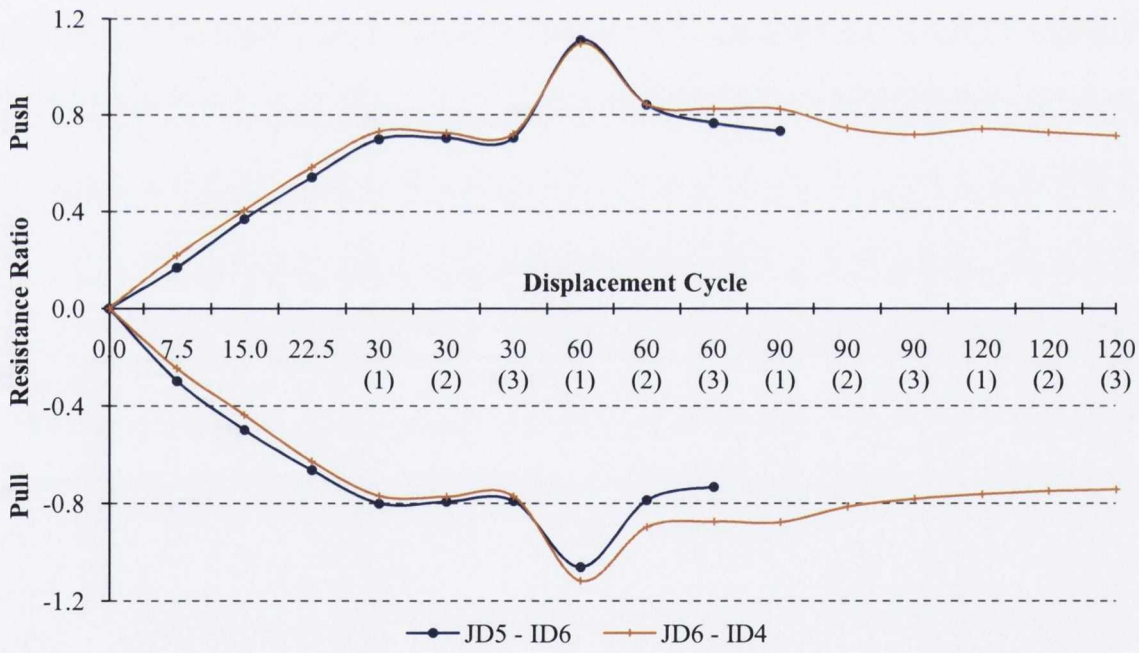

Figure 4.41: Group 4 - Resistance Ratio per Cycle

Energy Dissipation

The energy dissipated by Specimens JD5 and Specimen JD6 in each displacement cycle is presented in Figure 4.40. Both specimens display similar behaviour up to the end of

the first 60mm displacement cycle; beyond this the improved behaviour of Specimen JD6 is evident. Specimen JD6 is capable of dissipating energy well beyond the termination cycle of Specimen JD5. Specimen JD5 dissipates more energy from the first 60mm displacement cycle through to its termination point due to the extensive damage incurred at the point of maximum lateral load (P_{max}), as discussed previously.

Even though Specimen JD6 has improved energy dissipation capabilities it was still subject to extensive damage during the 60mm displacement cycles and dropped below the $0.85P_{max}$ limit. The specimen can be considered to have reached its useful deformation capacity, even though collapse was avoided and sufficient load carrying capacity was resumed post cover concrete crushing. However, the energy dissipation comparison shows that reduced link spacing at a high axial load level is beneficial in terms of performance and is a sensible option if incorporating HSC into composite column design, but it still lacks the ability to maintain high levels of lateral load over large displacements when subject to high levels of axial load. Comparison Group 5 looks at the performance of HSC with a lower axial load levels and larger link spacing compared with high axial load levels and smaller link spacing to determine which component is critical.

Resistance

The resistance plot for both specimens, as illustrated in Figure 4.41, is very similar up to the termination of Specimen JD5. Both specimens display a strong increase in resistance from the 30mm – 60mm displacement, at which point a sharp reduction in resistance (of almost equal quantities) is recorded for both specimens in either direction, i.e. push and pull displacements. Beyond this Specimen JD5 becomes unstable and the hysteretic loops become tighter and enclose a smaller area. It is evident that the resistance of the specimens has dropped below $0.85P_{max}$ for both specimens post 60mm displacement but Specimen JD6 regains load carrying capacity and is subject to only a shallow deprecation in resistance for the remainder of the test, thus indicating the benefits of reduced link spacing for HSC.

The minimum resistance ratio plots for the push and pull cycles (Figure 4.42) illustrate that all minimum resistances are well below the maximum resistance attained at a specific displacement cycle during the test. It further supports the superior performance of Specimen JD6 as for all displacements the minimum resistance is greater than that recorded by Specimen JD5 (except for the marginal increase during the 30mm pull cycle for Specimen JD5).

(a)

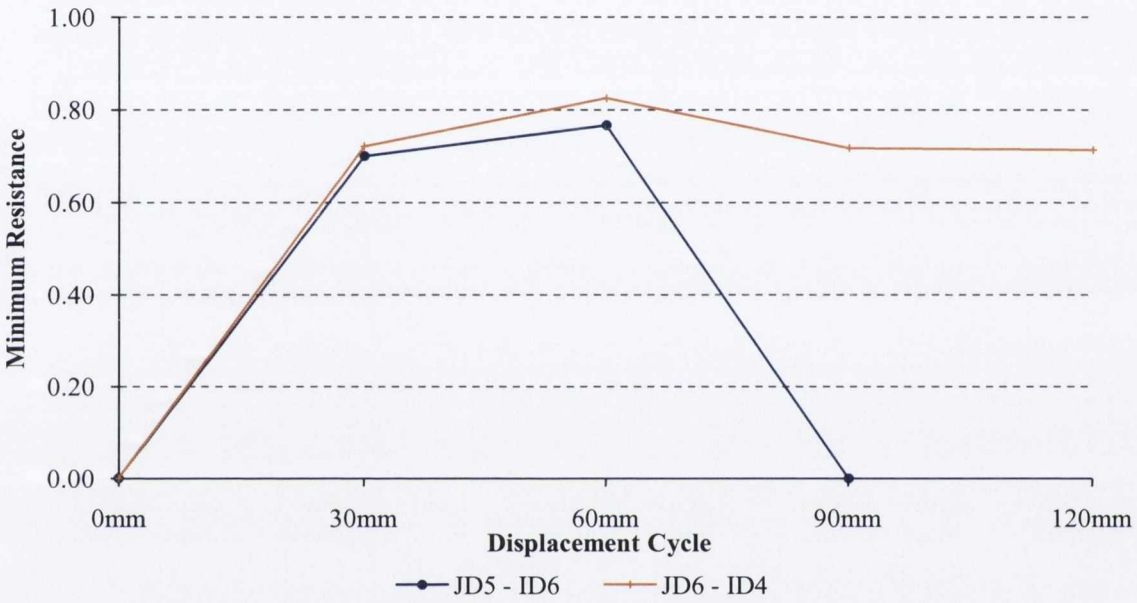

(b)

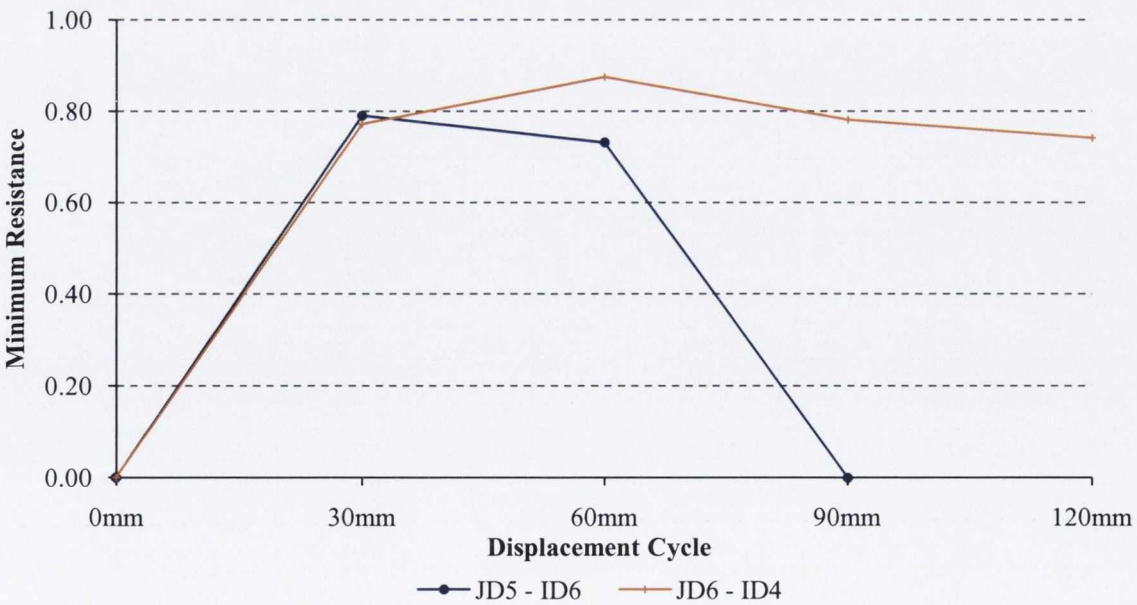

Figure 4.42: Group 4 - (a) Minimum Push Resistances, (b) Minimum Pull Resistances

Figure 4.43 presents the hysteresis curves for Specimens JD3 and JD6, to compare the difference in performance of the two specimens if the resistance of the cover concrete prior to spalling is removed from Specimen JD6. It is evident that on removal of the resistance contribution due to the concrete cover that a reasonable stable behaviour is recorded. Specimen JD6 achieves a higher maximum lateral load resistance (than Specimen JD3) but is subject to a steeper reduction in resistance at displacements beyond achieving its maximum resistance, this is due to the increase in concrete strength compared with Specimen JD3. HSC is more brittle than NSC, this accounts for the increased drop in load resistance of Specimen JD6.

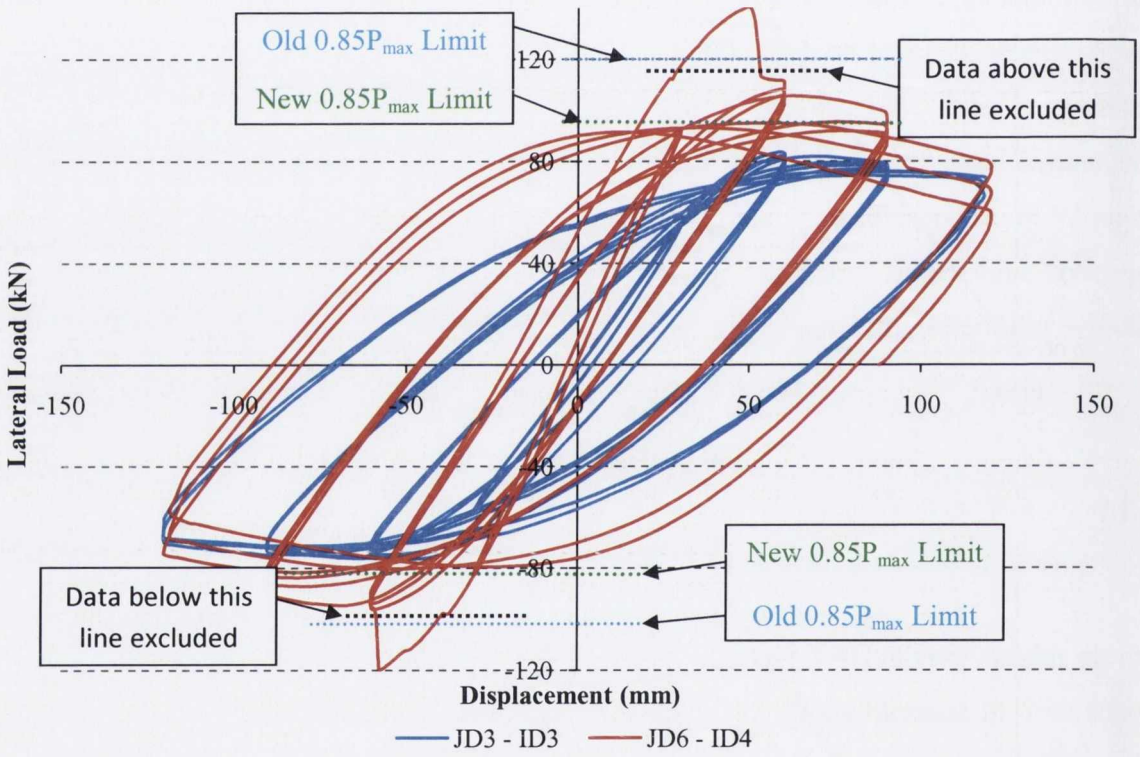

Figure 4.43: Hysteresis Plot Comparing JD3 and JD6

Referring to Figure 4.43, the 'old' $0.85P_{max}$ limit refers to a reduction in resistance corresponding to 85% of the maximum recorded lateral resistance. The 'new' $0.85P_{max}$ limit refers to a reduction in resistance corresponding to 85% of the adjusted maximum resistance. The adjusted maximum resistance corresponds to the superimposed line in Figure 4.43. This theoretical line is based on the assumption that if intermediate displacement cycles between 30mm and 60mm were introduced the cover concrete would spall earlier. Therefore, the additional resistance recorded by the cover concrete

would be removed from the hysteresis plot, and a response similar to the superimposed line in Figure 4.43 would be recoded.

The resistance plot for Specimen JD6 and the adjusted Specimen JD6 (with reduced P_{max}, due to removal of brittle concrete element) is presented in Figure 4.44. The plot demonstrates that if the cover concrete was to be prohibited from cracking so abruptly (and the associated loss of resistance removed) the specimen would behave in a very stable manner, similar to that of a NSC specimen. The above hysteresis plot demonstrates the location of the 'new' and 'old' $0.85P_{max}$ limits. These limits demonstrate that the original section is outside the failure criterion just after the crushing of the concrete cover during the first push and pull cycle of 60mm displacement.

The modified limits indicate that the section can withstand up to the first 120mm displacement in both the push and pull cycle before it is considered to have failed, it should be noted that the 120mm cycle achieves the failure limit load at a displacement of between 60mm and 90mm, but drops off again at higher displacements. As long as this load is achieved at any point during a displacement cycle the section is deemed to have achieved a displacement ductility corresponding to that displacement. This is not a sufficiently high displacement ductility for a highly ductile member but it does indicate that if the cover capacity and resistance loss is ignored the section can perform adequately well to high displacements and show ample signs of deterioration prior to imminent collapse. It remains to be seen if higher displacements can achieve the failure limit load, but on inspection the reduction in resistance between displacement groups would suggest the load will not be reached beyond the 120mm cycles.

As for the unadjusted Specimen JD6, the axial load level is critical as it degrades the specimen rapidly, thus dropping the resistance below the failure limit prematurely compared with a lower axial load level.

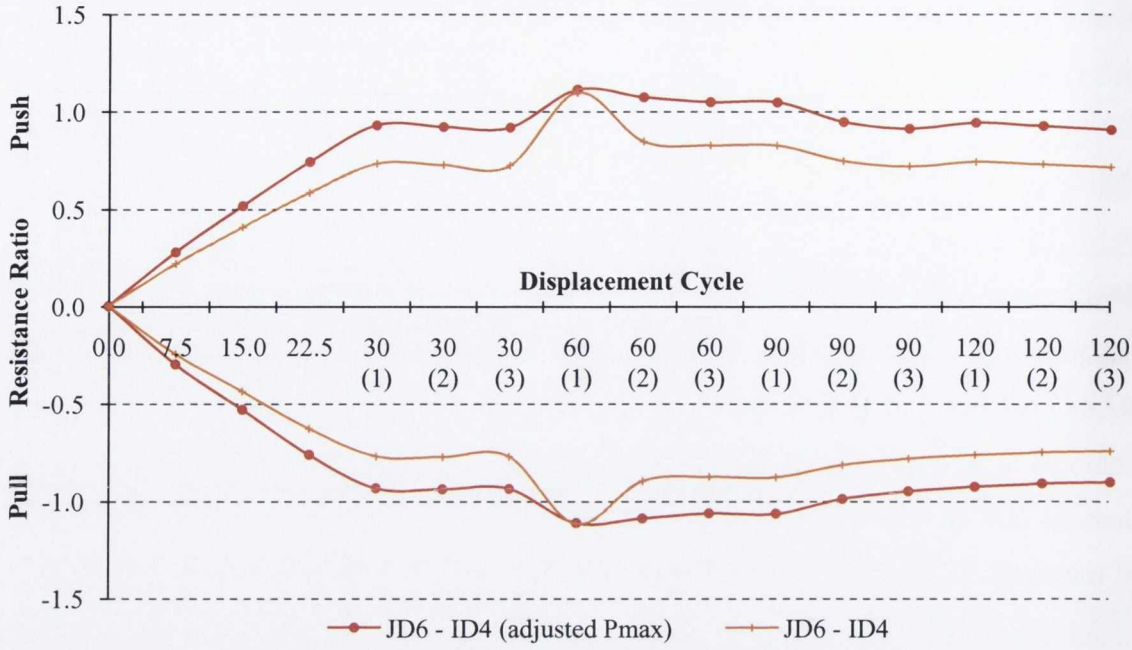

Figure 4.44: JD6 and Adjusted JD6 - Resistance Ratio per Cycle

4.5.5 Group 5 (Specimens JD4 & JD6)

The purpose of comparison Group 5 is to compare the performance of two HSC specimens, one of which possesses smaller link spacings, but is also subject to a higher axial load. The two specimens considered are Specimen JD4 – ID5 and Specimen JD6 – ID4. Specimen JD4 has a link spacing 144% greater than Specimen JD6 but is only subject to 60% of the axial load that is applied to Specimen JD6. Figure 4.45 compares the load-deflection envelope curves of the two specimens.

Specimen JD6 achieves a higher maximum lateral resistance and displays a steeper pre-yield stiffness; this is to be expected due to the increased axial load level and additional confinement provided by the reduced link spacing. Beyond the maximum lateral load the two specimens behave very differently. For Specimen JD6 the load resistance drops considerably, but Specimen JD4 displays a shallow and consistent reduction due to its limited degradation between displacement groups.

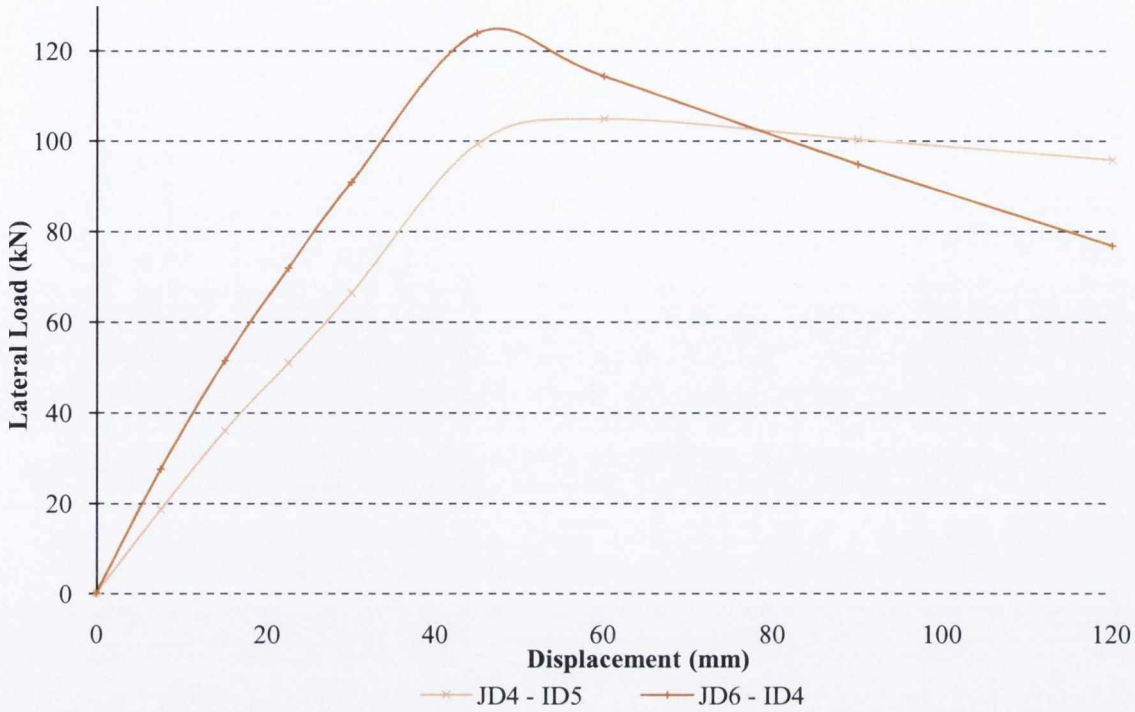

Figure 4.45: Load-Deflection Envelope Curves (Average in Both Directions); Specimens JD4 & JD6

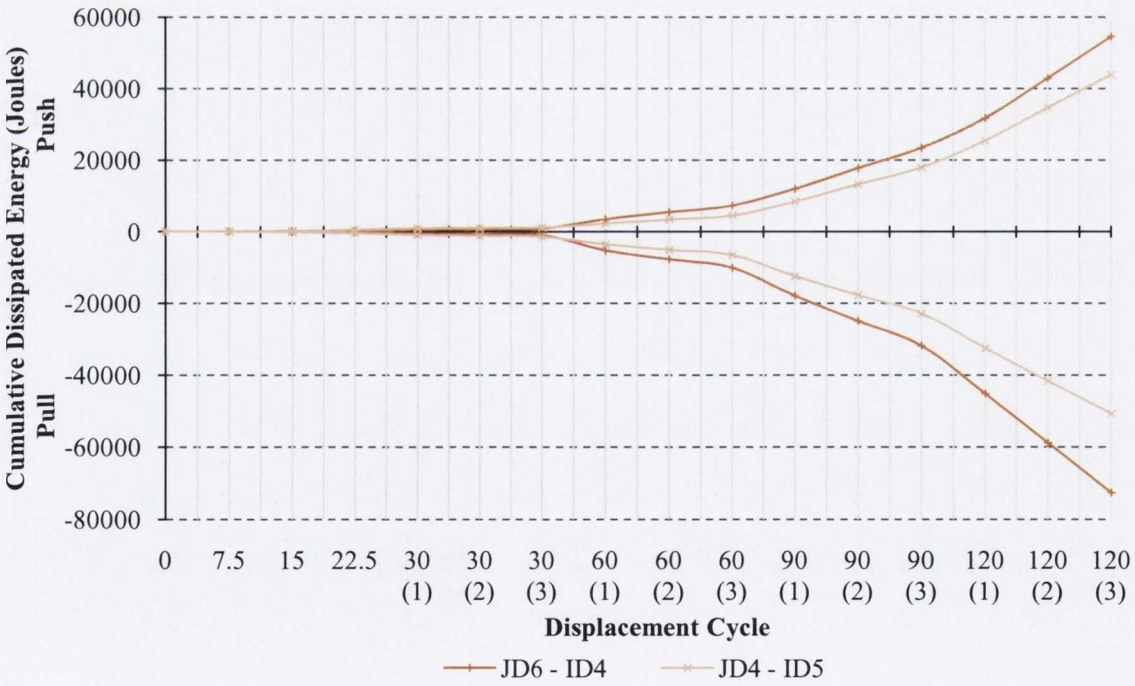

Figure 4.46: Dissipated Energy per Cycle (Comparison Group 5)

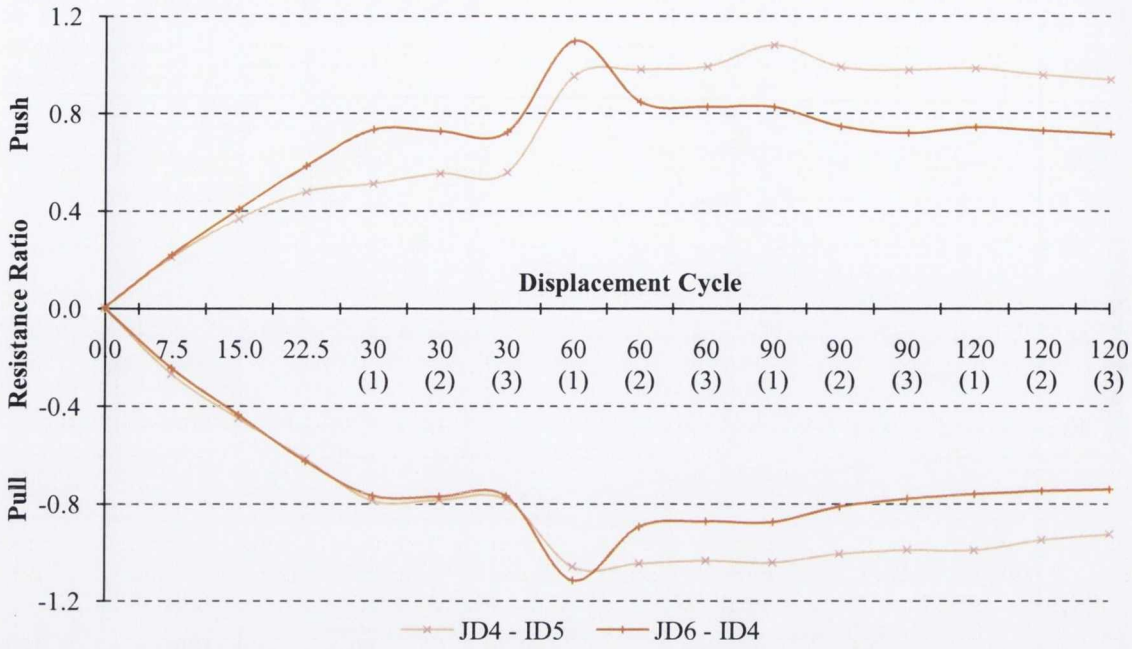

Figure 4.47: Group 5 - Resistance Ratio per Cycle

The envelope curve suggests that an increase in axial load is beneficial for increasing the overall lateral capacity of the specimen but if subject to a cyclic load, the high axial load has detrimental effects as it degrades the specimen at a significantly higher rate. Furthermore the reduced link spacing is unable to confine the concrete sufficiently to sustain the high lateral load resistances. As previously stated, the reduced link spacing is beneficial for improving the performance of a HSC composite column subject to high axial load levels, but the reduced spacing cannot outperform a specimen with lower axial load levels, even if the link spacing is increased.

Energy Dissipation

Figure 4.46 illustrates the energy dissipated by Specimens JD4 and JD6 in each half displacement cycle. Both specimens behave similarly; experiencing a reduced amount of energy dissipated for subsequent cycles at identical displacement. Specimen JD6 dissipated more energy from the 60mm cycle onwards, due to the extensive degradation of the specimen at this displacement, and the deterioration of the core concrete during subsequent cycles at higher displacements. Both specimens are capable of dissipating

high levels of energy and appear to behave suitably up to this displacement, even though the load-displacement plots present two very contrasting performances.

Resistance

Figure 4.47 compares the resistance ratio per cycle for Specimen JD4 and Specimen JD6. Similar to the load-deflection envelope curve the resistances vary significantly once the maximum resistance is reached. As previously discussed, Specimen JD6 displays an immediate drop in resistance compared with a gradual reduction from Specimen JD4. This demonstrates the improved performance of Specimen JD4 due to the lower axial load, even though it has a larger link spacing.

Using the reduced P_{max} limit as introduced in the previous comparison group, the variation between the resistance ratios per cycle plot becomes less skewed, as illustrated in Figure 4.48. In this instance once the maximum resistance is attained both specimens display similar deterioration characteristics, though Specimen JD6 still deteriorates marginally more than Specimen JD4. Caution must be taken when comparing these plots as Specimen JD6 achieves its maximum lateral load (for the 120mm displacement cycle) at a displacement between 10 – 20mm, while the corresponding maximum load is achieved by Specimen JD4 at 120mm displacement.

Beyond achieving this maximum load, Specimen JD6 loses resistance considerably up to the 120mm displacement, and subsequent cycles also display considerable drops in resistance compared with Specimen JD4. Figure 4.20 illustrates this phenomenon for both specimens. This indicates that increased displacement cycles will cause a significant drop in resistance of Specimen JD6 compared with Specimen JD4 as the section is becoming increasingly unstable and deteriorating considerably faster, the resistance ratio plot will become highly skewed as a result.

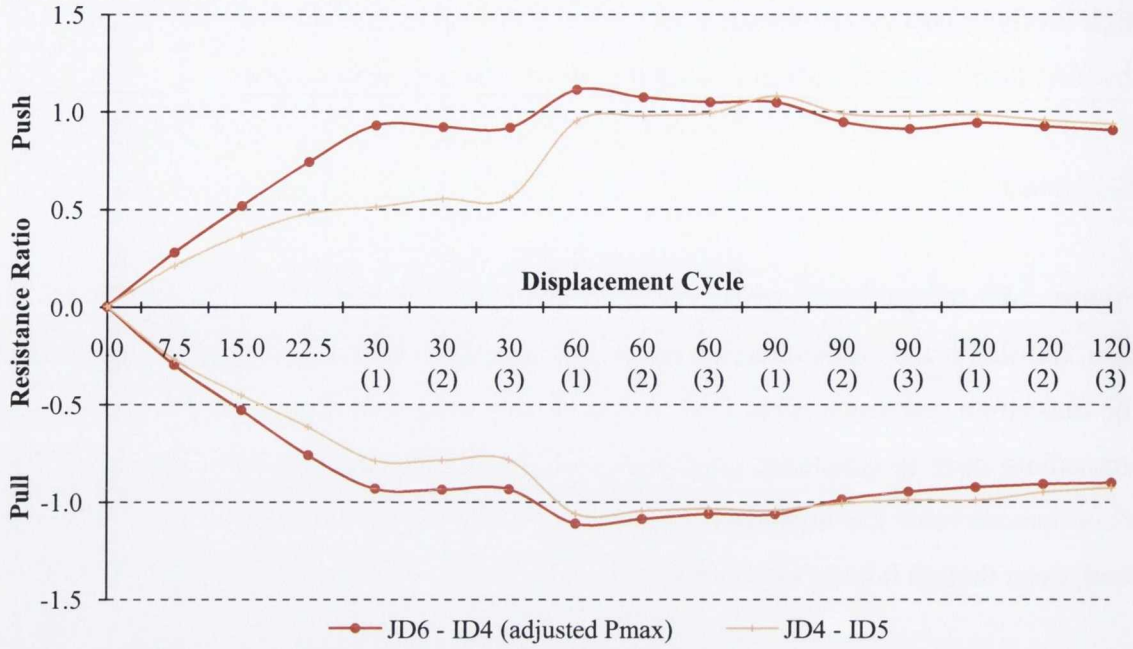

Figure 4.48: JD4 and Adjusted JD6 - Resistance Ratio per Cycle

Figure 4.49 shows the minimum resistance ratios for each push and pull displacement group. The plot identifies the clear reduction in resistance of Specimen JD6 compared with Specimen JD4, but proves that once the initial resistance drop has occurred, a subtle drop in resistance is maintained for the remainder of the test. Figure 4.49 clearly identifies the superior performance of JD4.

(a)

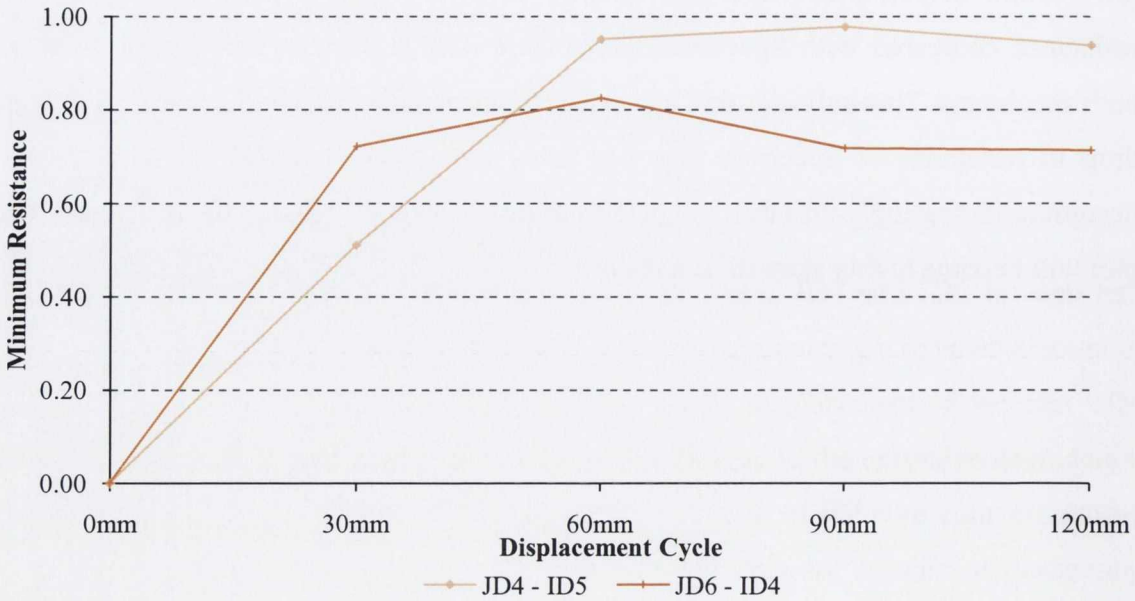

(b)

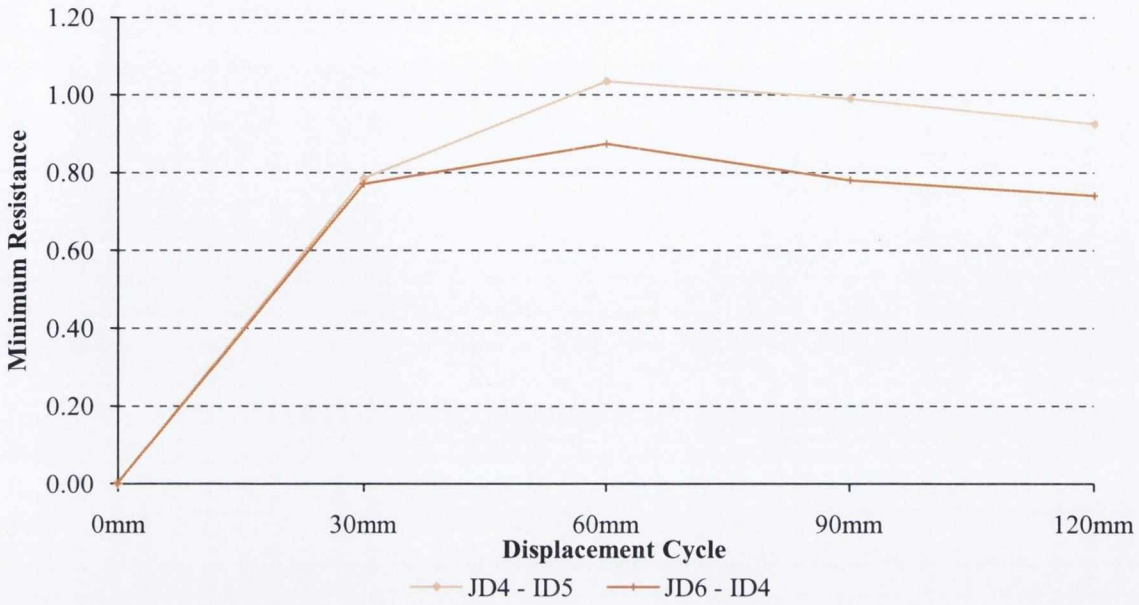

Figure 4.49: Group 5 - (a) Minimum Push Resistances, (b) Minimum Pull Resistances

4.6 Effects of concrete strength

4.6.1 Ultimate displacement and concrete strength

Figure 4.50 compares the ultimate displacement of all specimens in terms of concrete compressive strength and axial load level based on the $0.85P_{max}$ limits presented in the hysteresis plots. Three of the four specimens that reached the stroke limit of the actuator while remaining within the bounds of the $0.85P_{max}$ limits were NSC specimens, two of which were subject to a higher percentage of their axial capacity than the HSC specimens. The other specimen to reach the actuator stroke, within the resistance limits, was Specimen JD4. This specimen was only subject to 20% of its cross-sections axial capacity. Specimens JD5 and JD6 were subject to an equivalent of 35% of the axial capacity but Specimen JD6 has a reduced link spacing from 72mm – 50mm compared with all other specimens.

Due to the large increases in lateral displacement between consecutive displacement cycles in the adopted test-displacement history (as illustrated in Figure 3.17), the displacement ductility values have only a limited relevance. The reason for this is twofold; primarily the increase in lateral displacement between cycles is too large to determine the exact ultimate displacement and secondly only two specimens fail before the actuator stroke limit is reached. It is critical to determine the performance of all specimens within a displacement cycle, i.e. one specimen may be capable of resisting the 120mm displacement adequately, with only a minor drop in resistance while another may resist the displacement but display a large drop in resistance due to repeated displacement cycles. Resistance drop ratio plots provide invaluable data in order to distinguish between the varying capacities of specimens with the same displacements.

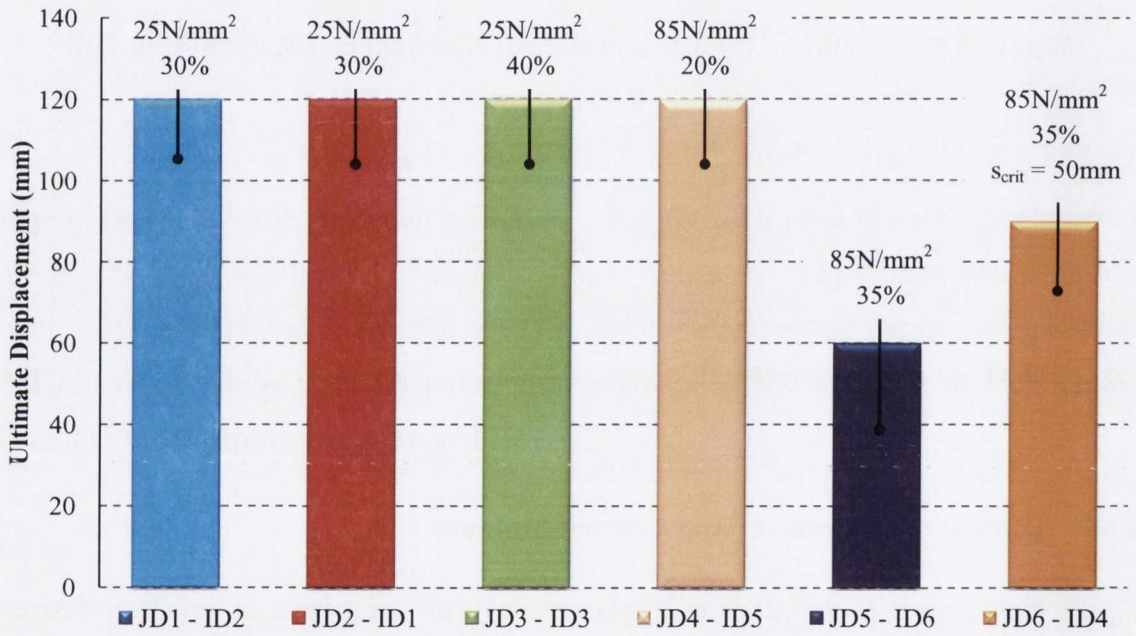

Figure 4.50: Ultimate Displacement versus Concrete Strength

Figure 4.51 to Figure 4.56 illustrate the resistance drop ratios of all specimens. The resistance drop ratio is the ratio of the load carrying capacity of a specimen at the end of a given displacement cycle relative to its load carrying capacity at the beginning of that cycle. The resistance drop ratio is measure of the damage incurred to a specimen during repeated cycles at a given displacement. The ratio determines the change in resistance and is a good indicator through which to compare specimens and determine which should be capable of withstanding the largest displacements.

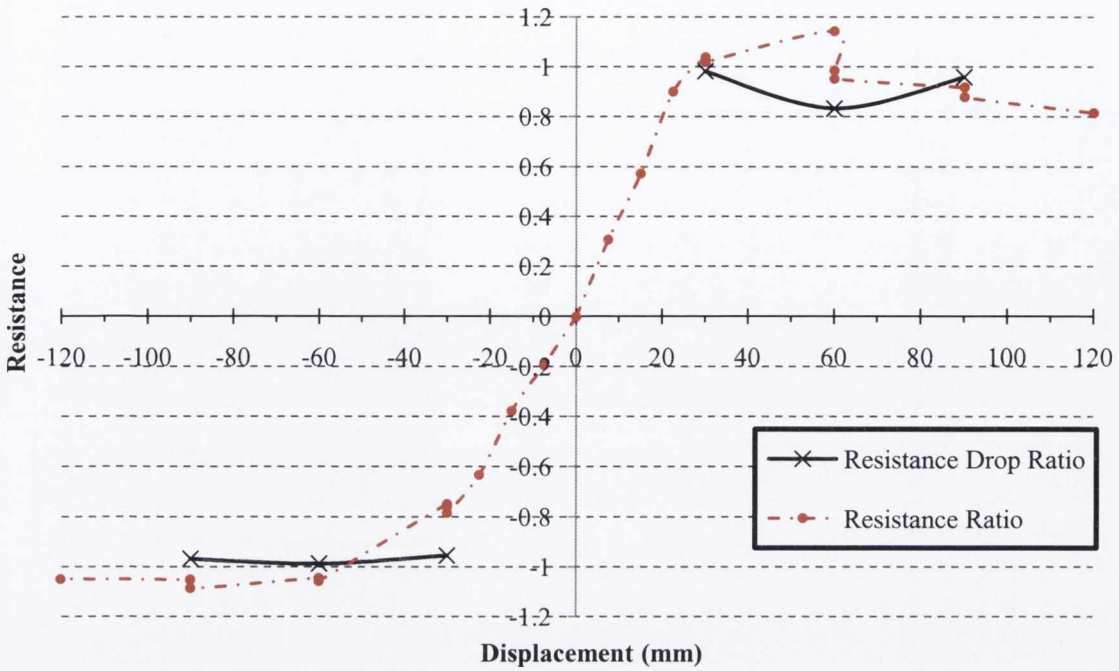

Figure 4.51: Resistance and Resistance Drop Ratios: Specimen JD1 – ID2

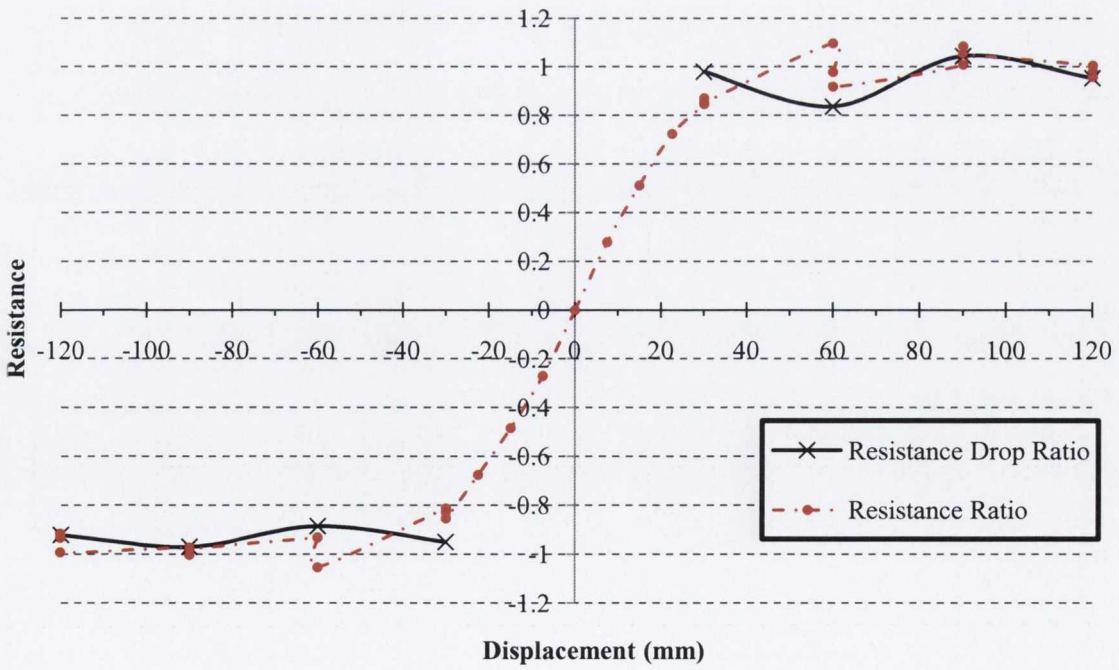

Figure 4.52: Resistance and Resistance Drop Ratios: Specimen JD2 – ID1

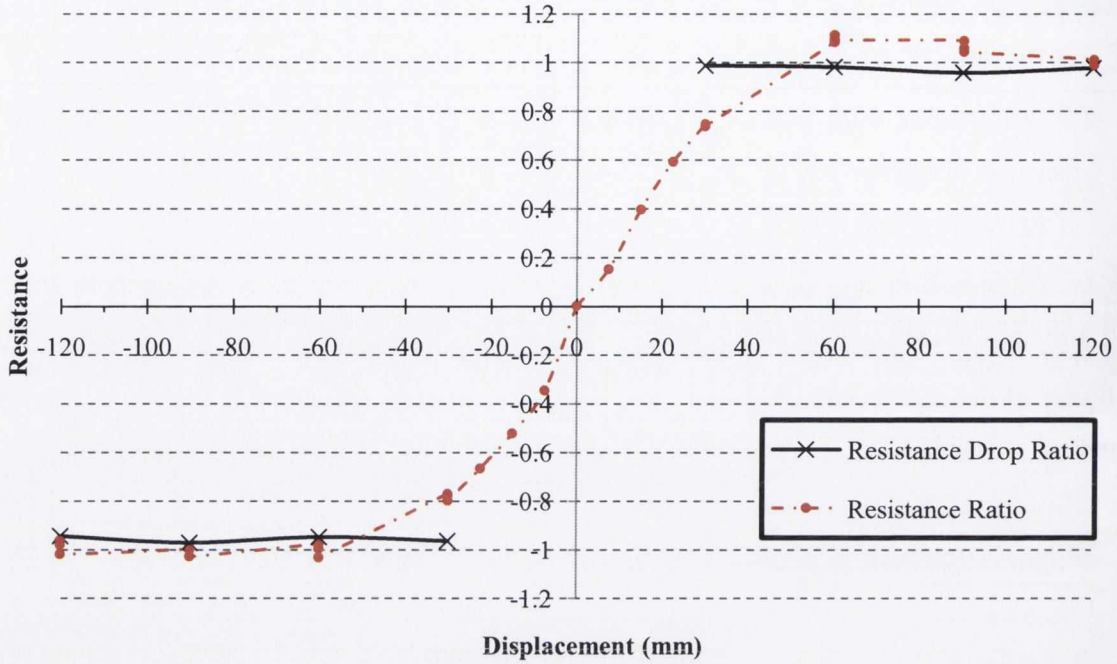

Figure 4.53: Resistance and Resistance Drop Ratios: Specimen JD3 – ID3

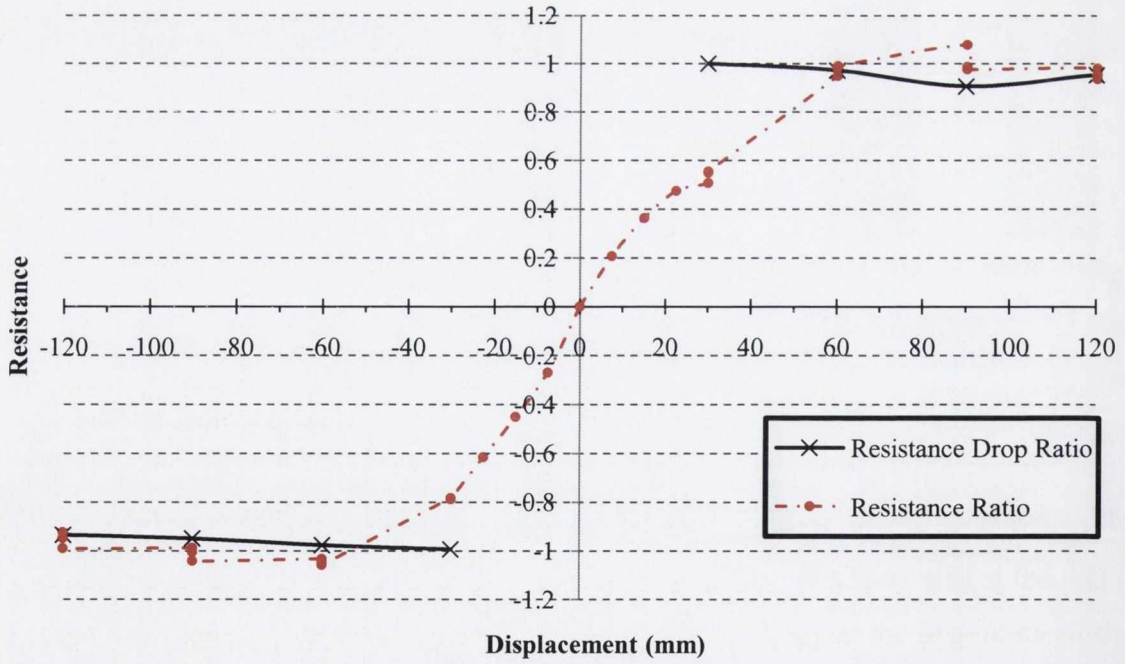

Figure 4.54: Resistance and Resistance Drop Ratios: Specimen JD4 – ID5

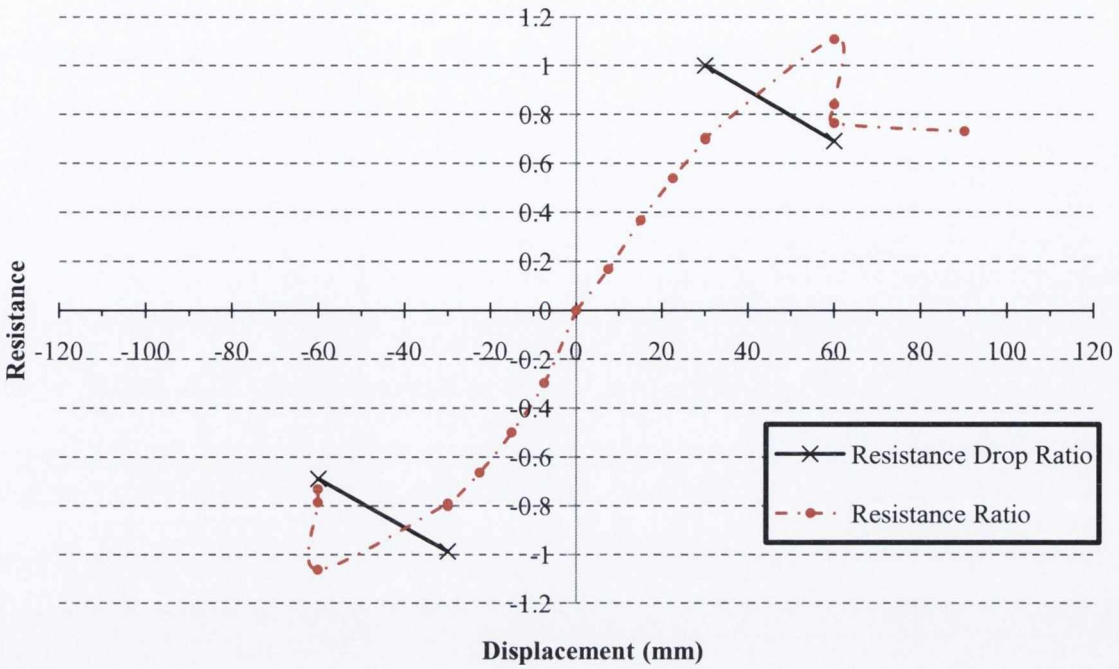

Figure 4.55: Resistance and Resistance Drop Ratios: Specimen JD5 – ID6

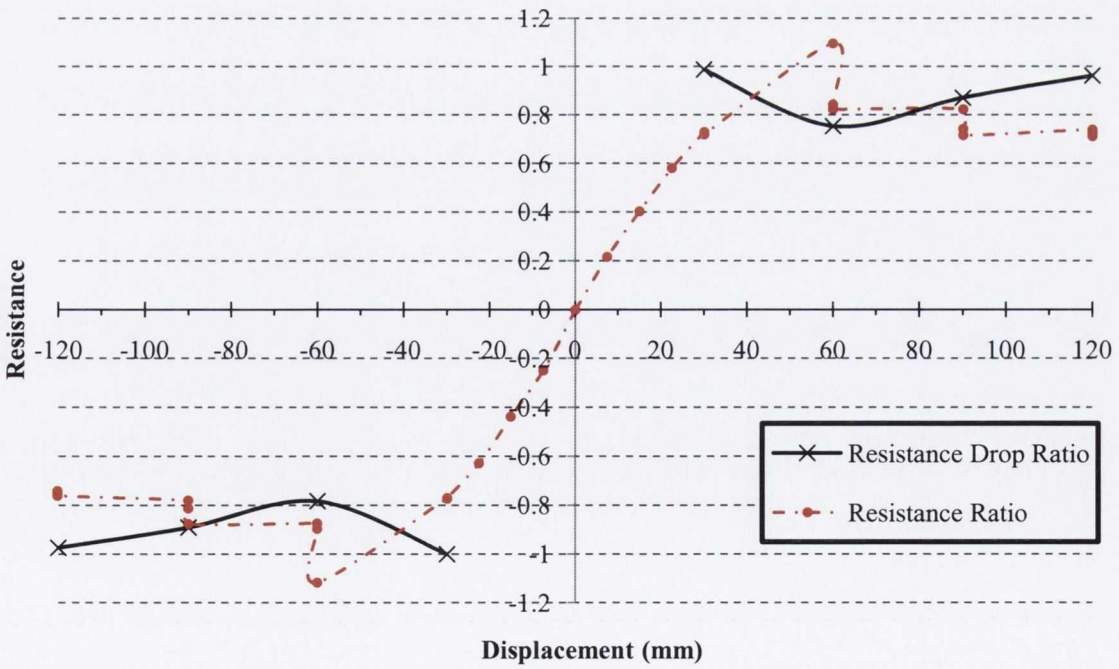

Figure 4.56: Resistance and Resistance Drop Ratios: Specimen JD6 – ID4

Figure 4.51 to Figure 4.56 indicate that a negligible resistance drop is experienced by all NSC specimens (a minor gain between displacement cycles is recorded in some cases) up to the stroke limit of the actuator. The same response is recoded for Specimen JD4 (HSC with low axial load specimen). The minor reduction in resistance drop ratios would suggest that these specimens can adequately resist greater displacements without experiencing ultimate failure in the fore coming displacement cycles.

Specimen JD5 (Figure 4.55) reached ultimate failure during the initial 90mm displacement cycle this explains the sharp reduction in resistance. Specimen JD6 (Figure 4.56) displays a sharp resistance drop during the 60mm displacement cycles but displays a stable increase in resistance up to the actuator stroke limit. This would suggest that this specimen can resist greater displacements but the fluctuations in the resistance drop ratio would suggest that the specimen is not as stable at the NSC specimens at 120mm displacement cycle.

4.7 Displacement Ductility

The displacement ductility requirements for a composite column as part of a moment resisting frame are presented in Section 3.2.7.4. The displacement ductility requirements are presented below for convenience:

$\mu_\Delta = 4$ (for medium ductility class, DCM)

$\mu_\Delta = 6.5$ (for high ductility class, DCH)

Thus, a required displacement (without ultimate failure) equivalent to $4\Delta_y$ and $6.5\Delta_y$ is required for a medium and highly dissipative fully encased composite, respectively.

Table 21 presents the values corresponding to the yield displacement, Δ_y for each tested specimen. The target and recoded ultimate displacements are also presented.

Table 21: Comparison between Required and Achieved Displacements

Specimen	Yield Displacement (mm)	DCM Required Displacement (mm)	DCH Required Displacement (mm)	Ultimate Displacement	Displacement Ductility Achieved
JD1 – ID2	34	136	221	120+	3.53+
JD2 – ID1	34	136	221	120+	3.53+
JD3 – ID3	40	160	260	120+	3.00+
JD4 – ID5	45	180	293	120+	2.60+
JD5 – ID6	49.5	198	322	60	1.21
JD6 – ID4	40.5	162	263	120+	2.96+

The values presented in Table 21 illustrate that all specimens when subject to a displacement of 120mm do not achieve the required displacement ductility required for a medium ductility class (DCM) composite column. It is important to note that only one specimen has ultimately failed by this point (i.e. Specimen JD5 – ID6), all other specimens are capable of resisting higher displacement (thus the ultimate and ductility displacement values are presented with a '+' symbol) and would as a result record an increased displacement ductility.

The presented values for all other specimens (except Specimen JD5) are reasonably close to the required displacement ductility required for a medium ductility class (DCM) composite column. The stable hysteretic behaviour presented in Figure 4.13 to Figure 4.18 (excluding Figure 4.17) at the stroke limit of the actuator indicate that all specimens (excluding Specimen JD5) would achieve, at least a displacement ductility factor of μ_Δ = 4. Further displacement cycles need to be conducted to prove that the un-failed specimens will be capable of achieving a displacement ductility factor corresponding to μ_Δ = 4, but on reviewing the hysteresis behaviour in conjunction with the stable resistance ratios, it is feasible to assume that the specimens will be capable of resisting greater displacements, particularly the NSC specimens and HSC specimens with low levels of applied axial load.

The normal strength concrete (NSC) composite columns show a more stable hysteretic response thus would be more likely to achieve a high ductility class than the HSC, due to

the severe level of deterioration of the concrete core at high axial load levels. HSC subject to low levels of axial load (i.e. Specimen JD4) displays a very stable hysteretic response, with little deterioration to the core concrete, further testing is required to determine if this level of axial load, applied to high-strength concrete could achieve the displacement ductility requirement of a highly ductile composite column.

It is worth noting that the yield displacements are subject to some interpretation as the optimum method to achieve the actual yield displacement is to subject the specimen to constant (not cyclic) lateral loading until failure, from this the actual yield displacement can be determined, as described in Section 4.2.3.

Finally, the results from the stable hysteretic response indicate that the NSC specimens and HSC specimens with lower axial load levels and HSC specimens with higher axial load levels and reduced link spacing should achieve at least the requirements of medium ductility class (DCM) composite column.

4.8 Strain Data

The location and reference notation for all strain gauges were presented in Section 3.2.6.2. The majority of the strains versus scan plots for the strain gauges are presented in Appendix A. Strain data is useful to explain particular deviations in linearity (generally in the inelastic response) recorded in load deflection hysteresis response of a specimen. Sudden reductions in resistance will generally be accompanied by 'spikes' in strain data for either and/or steel and concrete elements, representing yielding or possible fracture of these materials.

The strain plots can also be used to determine at exactly which point in displacement a particular material entered its inelastic response, and, can often be related back to the hysteresis response. Strain data is generally only usefully up to a certain displacement, because at a certain point the gauges will be detached and the recordings will be compromised, thus it is very difficult to record the exact material strains at high displacements.

Figure 4.57 presents the strain versus scan plot for Strain Gauge 6 of Specimen JD6 – ID4. This gauge is located on the middle longitudinal bar on Face B, located 250mm above the base interface. The red line superimposed on this plot represents the yield strain of the longitudinal steel, thus if the strain plot exceeds this value the reinforcement has entered the inelastic response.

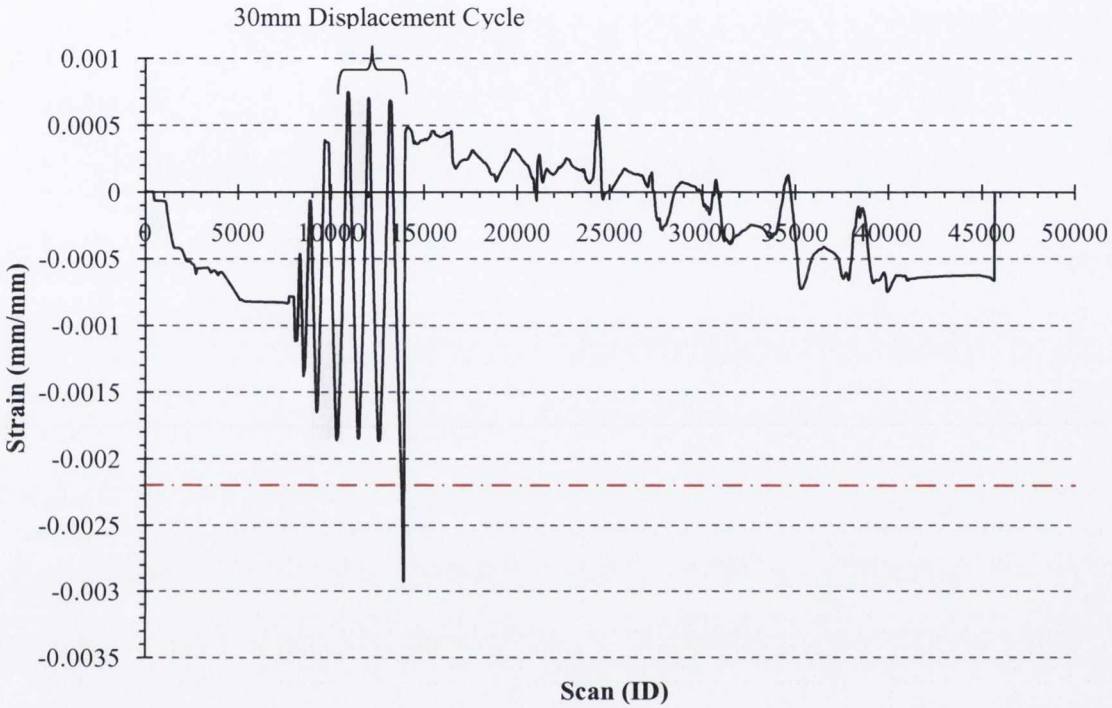

Figure 4.57: Strain vs. Scan Plot: Specimen JD6 – ID4 (Strain Gauge #6)

Figure 4.57 illustrates that the reinforcement enters the inelastic range during the first displacement of 60mm. The 30mm displacement cycles show no signs of inelastic behaviour. During load reversal of the first 60mm displacement cycle the strain response becomes unstable and no consistent behaviour is recorded for further displacements. At this point it can be seen that some external factor has affected the gauge. The main possibilities are that the gauge has become detached or the wires protruding from the gauge to the recording instrument have been compromised. To try and determine this, the strain versus scan plot for the external concrete on Face B at the same distance from the base is examined.

Figure 4.58 and Figure 4.59 present the strain versus scan data for two concrete gauges located 250mm above the base interface, attached to Face D and Face B, respectively.

The red superimposed line represents the yield strain of the unconfined concrete in compression.

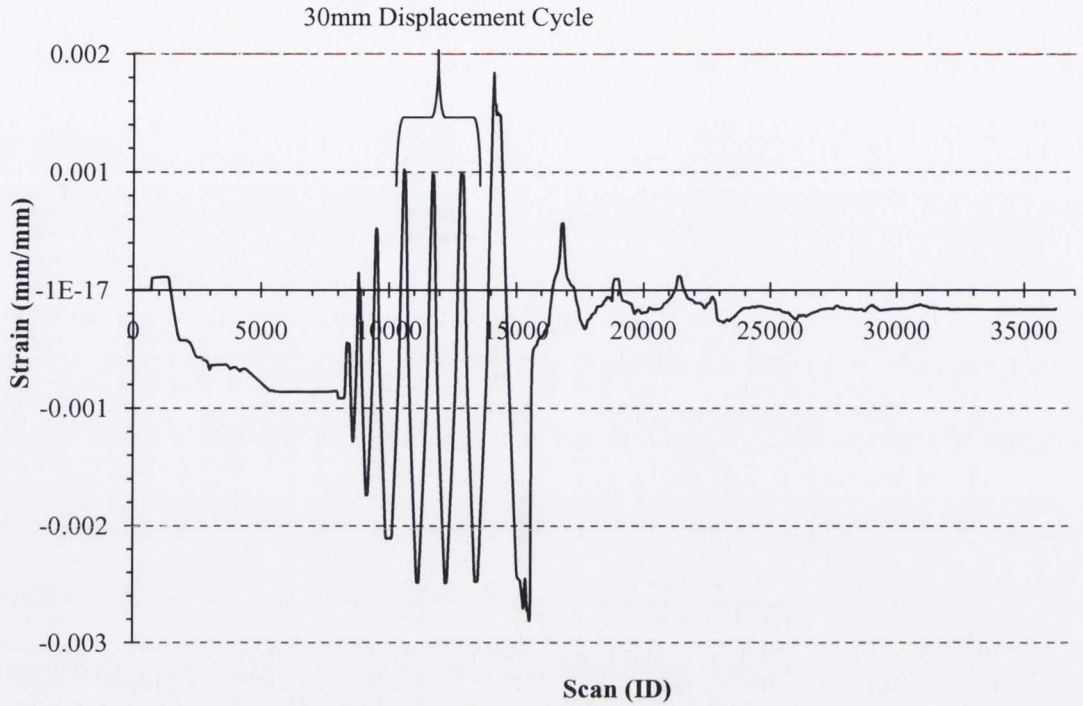

Figure 4.58: Strain vs. Scan Plot: Specimen JD6 – ID4

(Concrete Gauge: Face D, 250mm from Base)

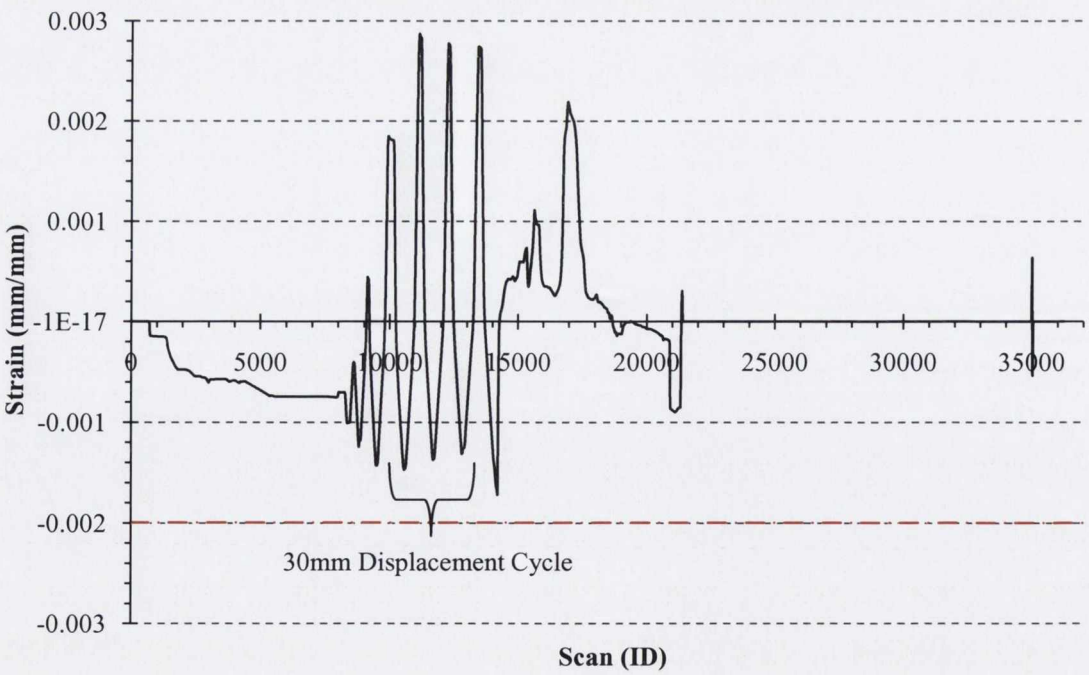

Figure 4.59: Strain vs. Scan Plot: Specimen JD6 – ID4

(Concrete Gauge: Face B, 250mm from Base)

The concrete strain plots provide a similar response to the steel strain plot, referring to Figure 4.59 it is clear that the cover concrete has not spalled until reaching the first 60mm displacement cycle. Beyond this point the concrete spalls and the strain recording are compromised. Face B was on the opposite side to the actuator connection and the actuator began the test with a push cycle, thus Face B recorded spalling of the cover concrete before Face D (thus the strain data for Face D recorded two strain peaks for the 60mm displacement cycle, one initially in tension, due to the push cycle and the second in compression due to the load reversal).

Figure 4.58 illustrates that after the first 60mm pull displacement cycle the concrete failed (and spalled), thus subsequent strain recording are compromised. Both concrete strain plots indicate that the concrete to either face (perpendicular to the axis of lateral loading) spalled during the first 60mm displacement cycle. This suggests that the wires protruding from the gauges may have become snagged, thus causing the steel strain reading to be compromised, as is evident from Figure 4.57.

The strain data can also be related to the hysteresis plot for this specimen (i.e. Figure 4.18). It is clear from the hysteresis plot that a considerable reduction in resistance is recorded during both push and pull loading for the first 60mm displacement cycle, this corresponds with the concrete strain plots (Figure 4.58 and Figure 4.59), where it has already been established that the cover concrete fails to both Face B and Face D during this displacement cycle, thus confirming the reason for a significant reduction in resistance.

4.9 Conclusions

NSC composite columns display very good ductility and energy dissipation capacity at all tested levels of axial load. It was observed visually that the NSC specimens suffered slower deterioration of the cover and core concrete elements at all post-yield displacements than the HSC specimens. The resistance ratio plots for the NSC specimens displayed little signs of a reduction in resistance at subsequent cycles of identical displacement, thus suggesting that increased displacement levels could be achieved while avoiding imminent collapse.

HSC composite columns with low levels of axial load displayed a very similar response to the NSC specimens; this suggests that the applied level of axial load (i.e. 20% of the section's axial capacity) is a suitable axial load level to be used for dissipative composite columns. HSC composite columns with high levels of axial load suffered severe reductions in resistance due to the brittle failure of the cover concrete. Subsequent ultimate failure of the HSC composite columns was recorded for specimens with larger link spacings.

Reduced link spacing failed to prevent the reduction in resistance due to the brittle failure of the concrete but they did enable to column to resist the applied loads during subsequent cycles of displacement and a stable resistance ratio plot was recorded thereafter. The specimen with reduced link spacing was unable to achieve a stable hysteresis response similar to a HSC specimen with low levels of axial load. Therefore, it is proposed that the maximum load than can be applied to a HSC composite column is reduced from the existing design provision of 30% of the sections axial capacity (Eurocode 8, (CEN, 2004)).

Only one specimen reached ultimate failure before the stroke limit of the actuator was reached, but reviewing the ductility displacements achieved by all specimens in Table 21 it is unlikely that any of the HSC specimens will achieve a displacement ductility required for a highly dissipative composite column (possibly with the exception of a column with a very low axial load). Further work is required in this area to validate this assumption. It is expected that all remaining HSC specimens would achieve a displacement ductility required by a member with medium dissipative capabilities (DCM) due to the stable hysteresis response and stable resistance ratios.

Chapter 5

Numerical Modelling

Numerical Modelling

5.1 Introduction

This chapter describes the development of a numerical model to represent the response of the test specimens described in previous chapters. The purpose of the numerical model is to examine if the behaviour of HSC composite columns can effectively be determined by simulating the performance of the tested specimens, and to allow the experimental results to be extended to incorporate a wider range of section sizes and material properties.

Section 5.2 provides a brief literature review, containing the progression of material modelling through to its application to modern composite and reinforced concrete modelling. The development of the member cross-section model is outlined in Section 5.3 followed by a description of the moment-curvature and moment-displacement response determination in Sections 5.4 and 5.5, respectively. The implementation of the model is presented in Section 5.6.

5.2 Modelling – Literature Review

Concrete Models

Reinforced concrete and composite stress-strain modelling has progressed over the decades through a host of material models refined and modified by numerous researchers. Richart *et al,* (1928) was one of the first to experiment with the confinement effects on normal strength concrete and concluded that lateral pressure greatly enhances the maximum concrete strength. They proposed the following relation for the maximum strength of confined concrete, f'_{cc}:

$$f'_{cc} = f'_{co} + 4.1f_l \tag{5.1}$$

Where:

f_{co} = The maximum strength of unconfined concrete

f_l = The equivalent uniform lateral pressure

Research on confined reinforced concrete proved that substantial gains in ductility could be achieved due to an increase in confinement, (Kent and Park, 1971). This research reported that no strength gains were achieved through confinement, which contradicted earlier research conducted by Roy and Sozen, (1964), which clearly illustrated that significant gains in both strength and ductility can be achieved through the use of confining reinforcement. Subsequent research confirmed that gains in both strength and ductility can be achieved due to rectangular and octagonal transverse reinforcement, but the resulting analytical models showed wide diverging opinions on the strength and ductility increase of confined reinforced concrete sections (Leslie, 1974, Desayi *et al*, 1978, Vallenas *et al*, 1977, Sheikh and Uzumeri, 1980, and Scott *et al*, 1982.). Modern stress-strain models for composite columns often incorporate the Mander *et al,* (1988) stress-strain model for confined concrete, as illustrated in Figure 5.1. (Chen *et al,* 2006, El-Tawil *et al,* 1999 and Ricles *et al,* 1994).

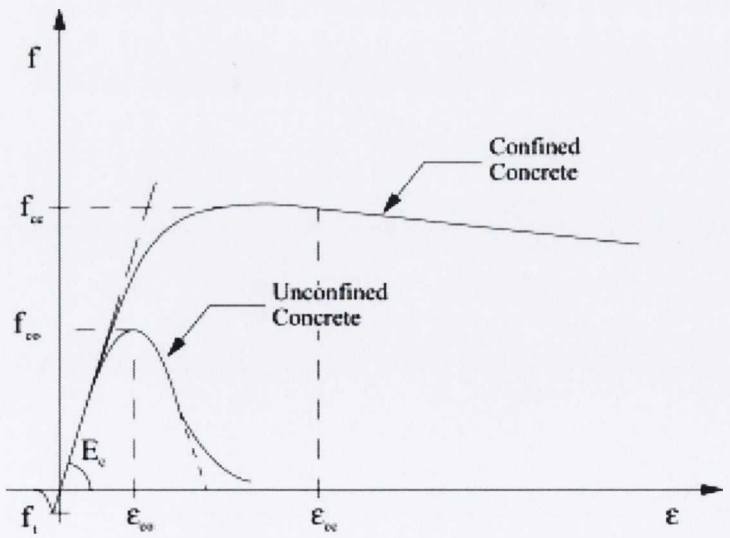

Figure 5.1: Stress-Strain Curve for Confined and Unconfined Concrete, Mander *et al,* (1988).

This model as previously stated was adopted by several other researchers and displayed good agreement with the experimental results, thus was also adopted for the development of the NSC composite column response model discussed later in this chapter.

Numerous stress-strain models have been proposed over the years for the compression zone of the concrete section, and mathematical expressions for some of these models are presented in Table 22. The parameters for each model can be found in the corresponding research papers. The purpose of presenting Table 22 is to illustrate some of the variation used to model the confinement effects of normal-strength concrete.

Table 22: Mathematical expressions for concrete stress-strain relations

Model	$0 \le \varepsilon_c \le \varepsilon_{co}$	$\varepsilon_{co} \le \varepsilon_c \le \varepsilon_{cu}$
Hognestad *et al.* (1955)	$\sigma_c = f_c\left[\frac{2\varepsilon_c}{\varepsilon_{co}} - \left(\frac{\varepsilon_c}{\varepsilon_{co}}\right)^2\right]$	$\sigma_c = f_c\left[1 - 0.15\left(\frac{\varepsilon_c - \varepsilon_{co}}{\varepsilon_{cu} - \varepsilon_{co}}\right)\right]$
Eurocode 2 (CEN, 2004)	$\sigma_c = f_c\left[1 - \left(1 - \frac{\varepsilon_c}{\varepsilon_{co}}\right)^n\right]$	$\sigma_c = f_c$
Kent *et al.* (1971) unconfined	$\sigma_c = f_c\left[\frac{2\varepsilon_c}{\varepsilon_{co}} - \left(\frac{\varepsilon_c}{\varepsilon_{co}}\right)^2\right]$	$\sigma_c = f_c\left[1 - Z_u(\varepsilon_c - \varepsilon_{co})\right]$
Kent *et al.* (1971) confined	$\sigma_c = f_{cc}\left[\frac{2\varepsilon_c}{\varepsilon_{coc}} - \left(\frac{\varepsilon_c}{\varepsilon_{coc}}\right)^2\right]$	$\sigma_c = f_{cc}\left[1 - Z_c(\varepsilon_c - \varepsilon_{coc})\right] \ge 0.2 f_{cc}$
Saatcioglu & Razvi (1998)	$\sigma_c = f_{cc}\left[\frac{2\varepsilon_c}{\varepsilon_{cc}} - \left(\frac{\varepsilon_c}{\varepsilon_{cc}}\right)^2\right]^{1/1+2K} \le f_{cc}$	$\sigma_c = f_{cc} + \left(\frac{f_{cc} - f_{85}}{\varepsilon_{cc} - \varepsilon_{85}}\right)(\varepsilon_c - \varepsilon_{cc}) \ge 0.2 f_{cc}$

* *For concrete of grade f_{ck} (MPa) ≤ 50*

[n] Dependent on grade of concrete ([n] = 2 for *grade $f_{ck} \le 50$, otherwise $n = 1.4 + 23.4[(90\text{-}f_{ck})/100]^4$*)

Where:

f_c = Unconfined concrete strength (N/mm^2)

f_{cc} = Confined Concrete Strength (N/mm^2)

ε_{co} = Strain corresponding to peak unconfined concrete stress

ε_{cu} = Ultimate concrete compression strain

ε_{cc} = Strain corresponding to peak confined concrete stress

ε_{coc} = Strain corresponding to peak confined concrete stress

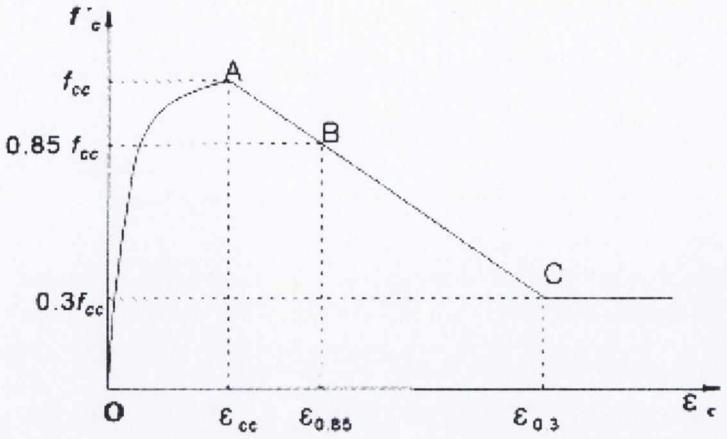

Figure 5.2: Concrete Stress-Strain Model Adopted by Chung *et al*, (2002).

More recently, Chung *et al*, (2002), proposed that the stress–strain curve for confined concrete can be predicted by the three coordinates, *A*, *B*, and *C* as illustrated by Figure 5.2. The coordinate *A* corresponds to the peak stress-strain (f_{cc}, ε_{cc}), B the stress-strain ($0.85f_{cc}$, $\varepsilon_{0.85}$), and *C* the stress-strain ($0.3f_{cc}$, $\varepsilon_{0.3}$). The coordinate *C* is located at the extension line to connect the coordinates *A* and *B*.

Reinforcing and Structural Steel Models

Stress-strain models for reinforcing and structural steel are far less complex than those proposed for concrete in compression. The stress-strain relationship for steel is widely known as the material behaves in a linear manner up to its yield point, followed by a plateau region and strain hardening up to its ultimate strain. This is significantly different to concrete as it experiences a drop in resistance based on the level of confinement. The idealised stress-strain behaviour for steel is presented in Figure 5.3.

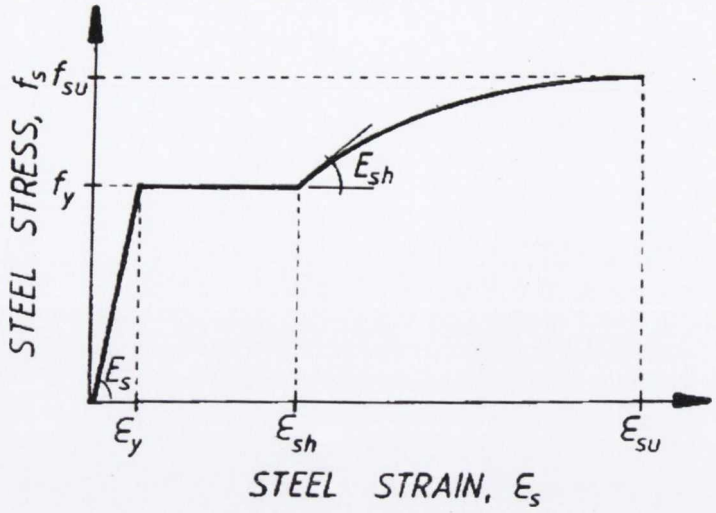

Figure 5.3: Idealised Stress-Strain Model for Reinforcing and Structural Steel.

Mander *et al*, (1988), provides a full literature review on the development of steel stress-strain models including modelling of the strain hardening branch and cyclic loading of the steel. The exact details of the adopted models for reinforcing and structural steel in tension are presented in Sections 5.3.7 and 5.3.8. In general, identical behaviour under tension and compression is assumed for modelling the longitudinal bars in the reinforced concrete or composite members subjected to flexural bending moment (Mirza *et al,* 1992, El-Tawil *et al,* 1999). However, buckling of the longitudinal bars occurs at large inelastic deformation when those members are subjected to axial compressive force. The buckling of the longitudinal bars greatly influences the strength and ductility of the member, as the load-carrying capacity and ductility of the bars decreases when they buckle. This behaviour has been observed in the tests of reinforcing bars by Bayrak and Sheikh, (1998). This suggests that a refined model is required to incorporate the buckling of the steel and the associated loss in resistance and confinement as a result. Figure 5.4 presents a simple constitutive model considering the inelastic buckling of the longitudinal bars in compression as adopted by Chen *et al*, (2006).

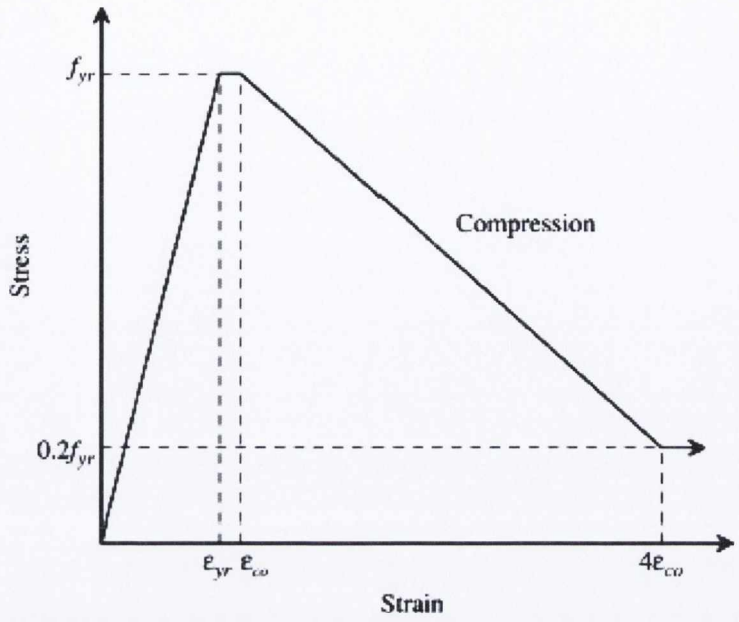

Figure 5.4: Stress-Strain Relationship for Longitudinal Steel in Compression, Chen *et al,* (2006).

The following assumptions are used by Chen *et al,* (2006) to generate the model. The longitudinal bar under compression will reach the yield strength with a yield plateau. The stress of the bar begins to degrade when the axial strain of the bar reaches the strain ε_{co}, corresponding to the peak compressive stress f'_{co} of the unconfined concrete. It is assumed that the bar will buckle following spalling of the concrete cover when the axial stress in the concrete cover reaches the peak strength. The stress in the bar is assumed to drop to 20% of its yield strength and remain constant afterwards.

A similar stress–strain relation as that adopted for the longitudinal bar is assumed for the structural steel section, as shown in Figure 5.5. Chen *et al,* (2006) predicts that local buckling of the elements, particularly the flanges, of the structural steel section is likely to occur after the crushing of the partially confined concrete. Therefore, stress degradation is assumed after the axial strain reaches the strain, $\varepsilon_{cc,p}$, representing the crushing of the partially confined concrete. Post-peak strength of 20% of the yield strength is assumed when the axial strain reaches four times the strain of $\varepsilon_{cc,p}$.

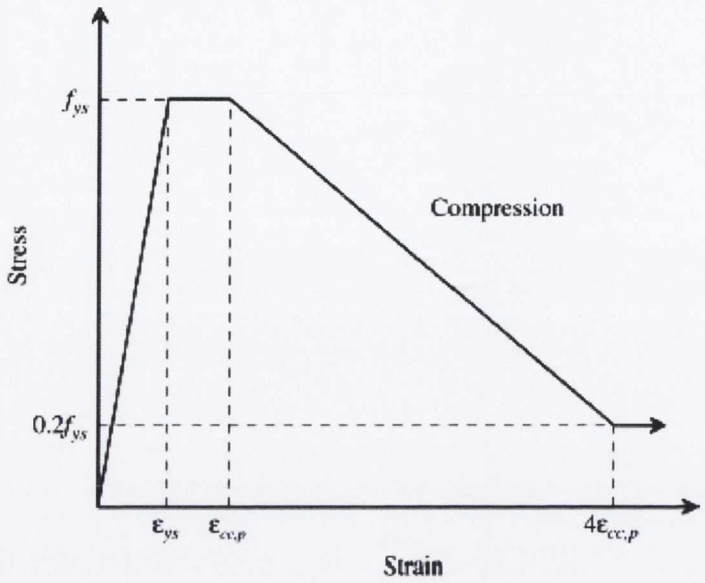

Figure 5.5: Stress-Strain Relationship for Structural Steel in Compression, Chen *et al,* (2006).

HSC Models

The use of HSC has become increasingly popular due to the advancements in material technology and a behaviour of the additives used to make the high performance concrete, i.e. Ground Granulated Blast-furnace Slag (GGBS). Unfortunately an increase in compressive strength leads to a decrease in ductility for concrete elements, thus refined stress-strain equations are required for modelling the performance of HSC. Figure 5.6 presents typical stress-strain curves for various concrete compressive strengths, (Mendis, 2001).

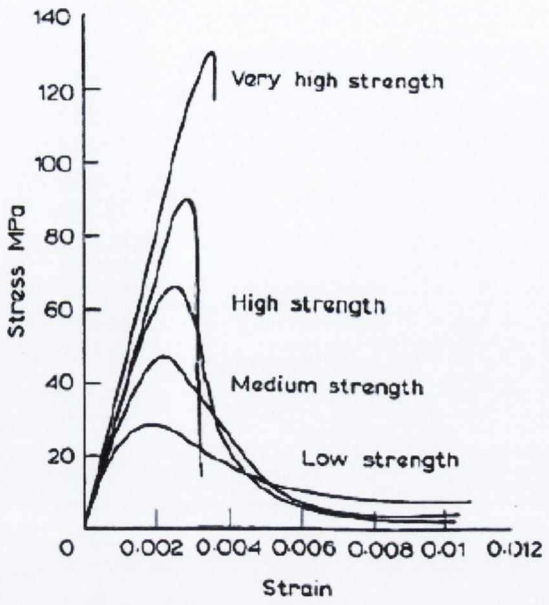

Figure 5.6: Stress-Strain Curves for Varying Concrete Compressive Strengths, Mendis, (2001).

Considerably less research has been conducted involving modelling of HSC compared with NSC. Several researchers have developed stress-strain models for HSC to predict the severe variation in post yield performance between NSC and HSC (as illustrated in Figure 5.6 above). Han *et al,* (2003) proposed a stress-strain model, as presented in Figure 5.7. The ascending part (OA) is adopted from a relationship originally proposed by Popovics, (1973), for concrete, and is written as:

$$f_c = \frac{f_{cc}^{'}\left(\frac{\varepsilon_c}{\varepsilon_{cc}}\right)\gamma}{\gamma - 1 + \left(\frac{\varepsilon_c}{\varepsilon_{cc}}\right)^{\gamma}}, \varepsilon_c \leq \varepsilon_{cc} \tag{5.2}$$

$$\gamma = \frac{E_c}{E_c - E_{sec}} \tag{5.3}$$

Where: γ controls the initial slope and the curvature of the ascending branch. The descending branch (ABC) of the stress–strain curve is linear and written as:

$$f_c = f_{cc}^{'}\left[0.85 - 0.5\left\{\frac{\varepsilon_c - \varepsilon_{c85c}}{\varepsilon_{c50c} - \varepsilon_{cc}}\right\}\right] \geq 0.3f_{cc}^{'} \tag{5.4}$$

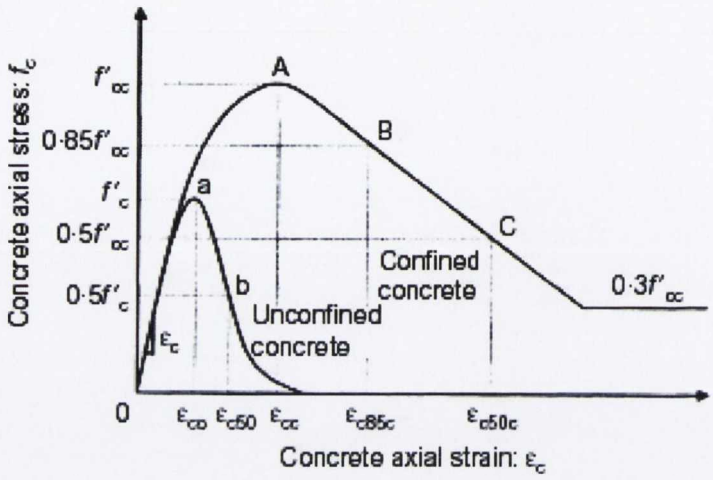

Figure 5.7: Stress-Strain Curve for Confined High-Strength Concrete, Han *et al*, (2003).

Bing *et al,* (2001), derived a similar stress-strain relationship as presented in Figure 5.8. A similar descending branch is evident with a marginally higher concrete stress at link fracture. In the case of this model, several branches defined by different functions are adopted; this is an easier method to adjust the model curve to experimental data because the characteristics of ascending and descending branches can be controlled independently. Hence, Bing *et al.,* (2001), decided to establish a model by modifying the model proposed by Muguruma and Watanabe, (1990), as shown as follows. The model consists of three branches expressed by Equations (5.5) to (5.8), and a tail with a constant stress of $0.4f'_{cc}$.

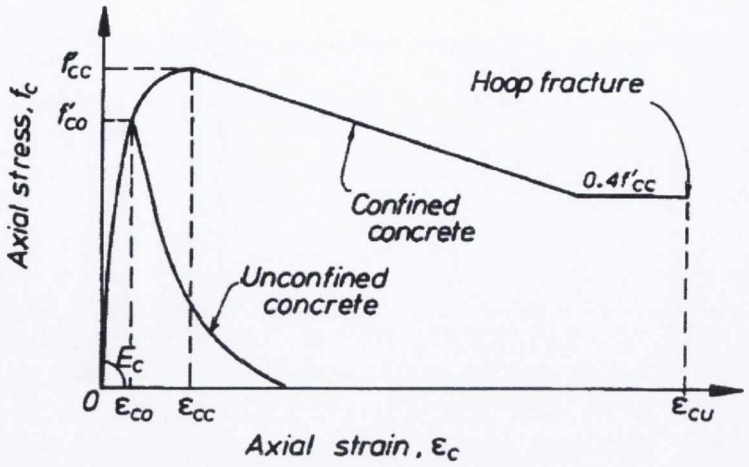

Figure 5.8 Proposed Stress-Strain Relationship for Confined HSC, Bing *et al*, (2001).

When $0 \leq \varepsilon_c \leq \varepsilon_{co}$

$$f_c = E_c\varepsilon_c + \frac{(f'_{co} - E_c\varepsilon_{co})}{\varepsilon_{co}^2}\,\varepsilon_c^2 \tag{5.5}$$

When $\varepsilon_{co} \leq \varepsilon_c \leq \varepsilon_{cc}$

$$f_c = f'_{cc} - \frac{(f'_{cc} - f'_{co})}{(\varepsilon_{cc} - \varepsilon_{co})^2}\,.(\varepsilon_c - \varepsilon_{cc})^2 \tag{5.6}$$

When $\varepsilon_c \geq \varepsilon_{cc}$

$$f_c = f_{cc} - \beta\left(\frac{f'_{cc}}{\varepsilon_{cc}}\right).(\varepsilon_c - \varepsilon_{cc}) \geq 0.4f'_{cc} \tag{5.7}$$

Where:

$$\beta = (0.048f'_{co} - 2.14) - (0.098f'_{co} - 4.57)\left(\frac{f'_l}{f'_{co}}\right)^{1/3} \tag{5.8}$$

When: $f_{yh} \leq 550$ MPa and $f'_{co} > 75$ MPa

Where:

f'_l = Lateral pressure from the transverse reinforcement

Both proposed models show reasonably good correlations with the tested stress-strain curves for HSC specimens, more recently, research conducted by Hong *et al,* (2006), developed a refined set of equations to produce a curved descending branch, as shown in Figure 5.9. A full set of corresponding equations can be found in the referred paper. The model reasonably predicts the experimental results for both NSC and HSC columns.

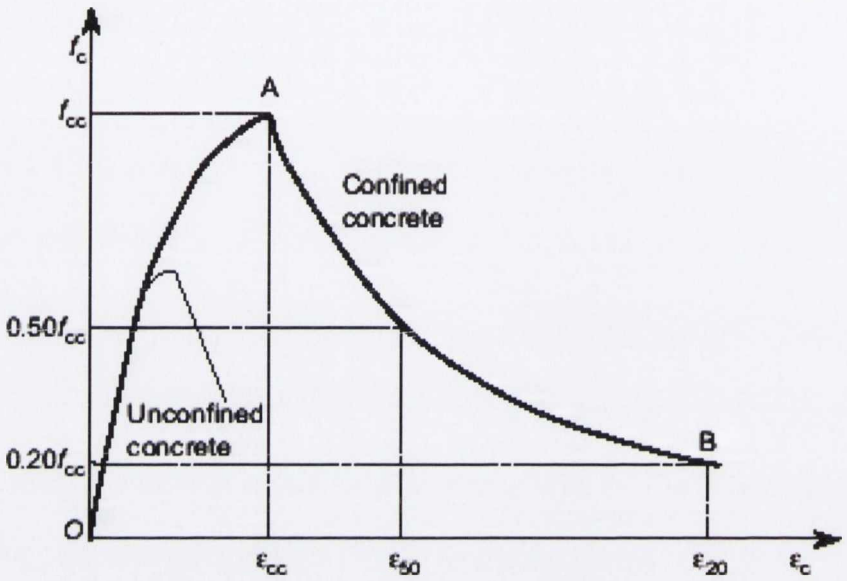

Figure 5.9: Proposed Stress-Strain Relationship for Confined HSC, Hong *et al,* (2006).

5.3 Material Models

The following section contains the models adopted and contains details of the model modifications used to develop the numerical model in this research.

The NSC material model used in this research is based on the work of Mander *et al,* (1988), who developed a theoretical stress-strain model for confined concrete members with either circular or rectangular sections subjected to static or dynamic axial compressive loading, either monotonically or cyclically applied. The concrete section may contain any general type of confinement with either spirals or circular hoops, or rectangular hoops with or without supplementary cross ties. Various levels of confinement are taken into account by defining an effective lateral confining stress,

which is dependent on the configuration of the transverse and longitudinal reinforcement.

The ultimate compressive concrete strain, ε_{cu}, defined as that strain at which first fracture of the transverse reinforcement occurred, was determined by equating the work done on the confined concrete and longitudinal reinforcement when deformed in compression to the available strain energy capacity of the transverse reinforcement when fracture occurred. The following sections discuss the modifications required to develop this model from a reinforced concrete section subject to axial loading to a composite section subject to lateral cyclic loading with a constant axial compressive force. Models for structural and reinforcing steel as well as HSC models are refined from the models presented in Section 5.2.

5.3.1 Confined Concrete in Compression

Mander *et al.* (1988), proposed a unified stress-strain approach for confined concrete for both rectangular and circular shaped transverse reinforcement. A detailed representation of this model is illustrated in Figure 5.10 and is based on an equation suggested by Popovics, (1973). For a slow (quasi-static) strain rate and monotonic loading, the longitudinal compressive concrete stress f_c is given by:

$$f_c = \frac{f'_{cc}\, x\, r}{r - 1 + x^r} \tag{5.9}$$

Where: f'_{cc} = the compressive strength of the confined concrete, (Section 5.3.2), and,

$$x = \frac{\varepsilon_c}{\varepsilon_{cc}} \tag{5.10}$$

Where: ε_c = Longitudinal compressive concrete strain.

$$r = \frac{E_c}{E_c - E_{sec}} \tag{5.11}$$

$$E_c = 5000\sqrt{f'_{co}} \tag{5.12}$$

$$E_{sec} = \frac{f'_{cc}}{\varepsilon_{cc}} \tag{5.13}$$

$$\varepsilon_{cc} = \varepsilon_{co}\left[1 + 5\left(\frac{f'_{cc}}{f'_{co}} - 1\right)\right] \tag{5.14}$$

As suggested by Richart *et al*, (1928), where f'_{co} and ε_{co} are the unconfined concrete strength and corresponding strain, respectively.

To define the stress-strain behaviour of the cover concrete (outside the confined core concrete) the part of the falling branch in the region where $\varepsilon_c > 2\varepsilon_{co}$ is assumed to be a straight line which reaches zero stress at the spalling strain, ε_{sp}.

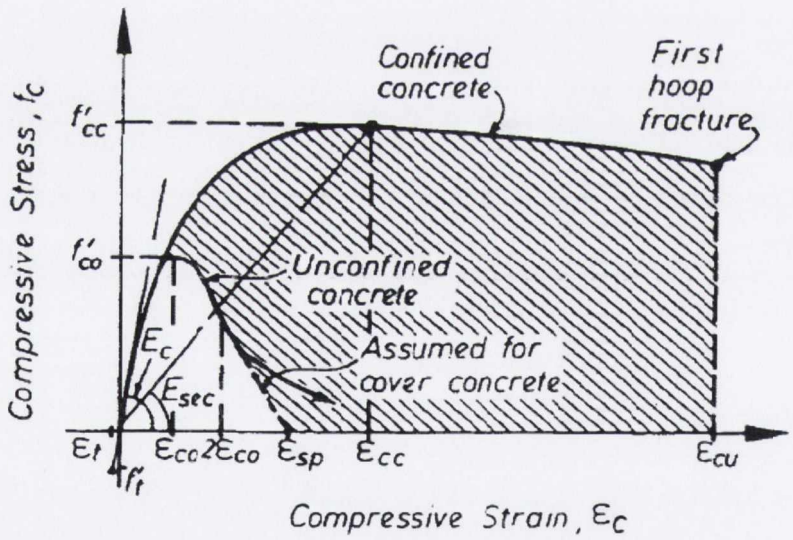

Figure 5.10: Detailed Stress-Strain Model for Monotonic Loading of Confined and Unconfined Concrete, Mander *et al*, (1988).

Mander adopted a similar approach to the one used by Sheikh and Uzumeri, (1980), to determine the effective lateral pressure on the concrete section. The maximum transverse pressure from the confining steel can only be exerted effectively on that part of the concrete core where the confining stress has fully developed due to arching action. Figure 5.12 shows the arching action that is assumed to occur between the levels of

rectangular hoop reinforcement. Midway between the levels of the transverse reinforcement, the area of ineffectively confined concrete will be largest and the area of effectively confined concrete core, A_e will be smallest.

When using the stress-strain relation (Equation (5.9)) for computing the strength and ductility of columns it is assumed for convenience that the area of the confined concrete is the area of the concrete within the centre lines of the transverse link, A_{cc}. In order to allow for the fact that $A_e < A_{cc}$, the effective lateral confining pressure, f'_l is given as:

$$f'_l = f_l \, k_e \tag{5.15}$$

Where:

f_l = Lateral pressure from the transverse reinforcement, assumed to be uniformly distributed over the surface of the concrete core, and,

$$k_e = \frac{A_e}{A_{cc}} \tag{5.16}$$

Where: k_e = confinement effectiveness coefficient, and,

$$A_{cc} = A_c \, (1 - \rho_{cc}) \tag{5.17}$$

Where: ρ_{cc} = ratio of area of longitudinal reinforcement to the area of the concrete section, and A_c = area of core of section enclosed by the centre line of the transverse link.

In rectangular sections, parabolic arching is assumed to act in the form of second degree parabolas with an initial tangent slope of 45°. Arching occurs along both principal plains, between adjacent layers of transverse reinforcement in the vertical direction and between longitudinal reinforcement in the horizontal direction as illustrated in Figure 5.11.

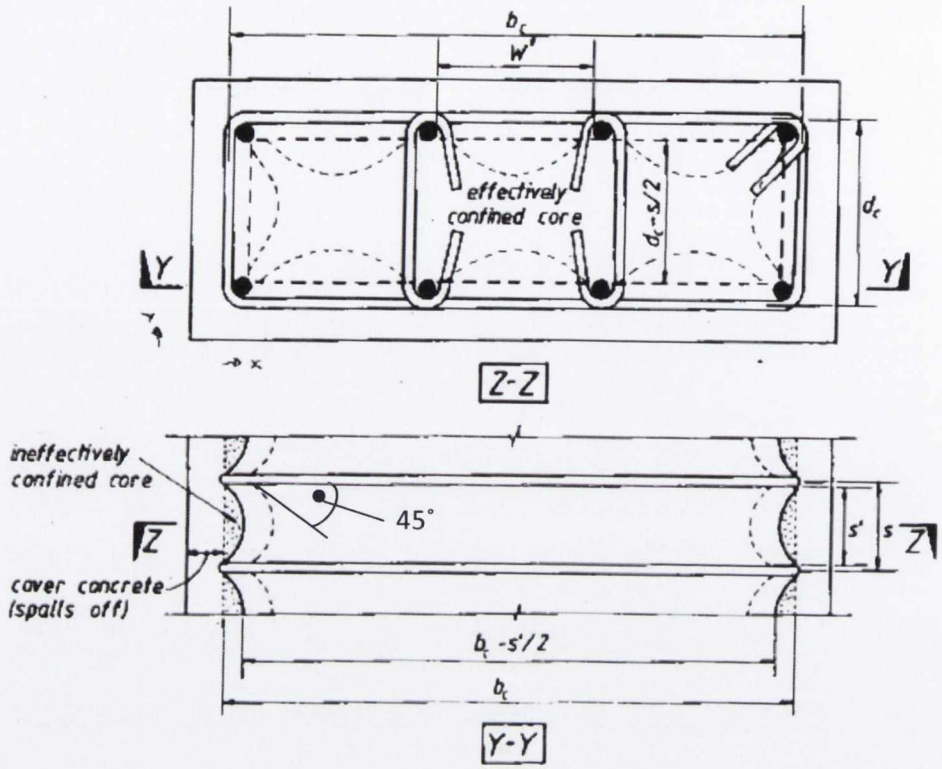

Figure 5.11: Effectively Confined Core for Rectangular Link Reinforcement, Mander *et al*, (1988).

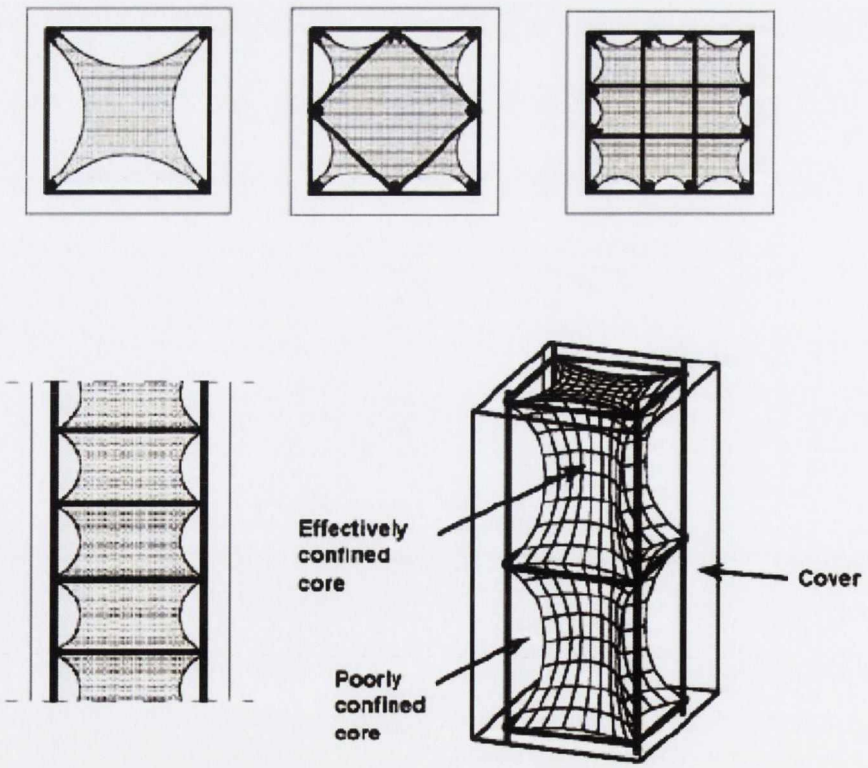

Figure 5.12: Effectively Confined Core for Rectangular Concrete Columns, Mendis, (2001).

Mander *et al*, (1988), found that the effectively confined area of concrete at link level is determined by subtracting the area of ineffectively confined concrete outside the second order parabola from the effectively confined concrete core at link level, A_c (i.e. the area enclosed by the centre line of the lateral link). For one parabola, the ineffective area (A) is:

$$A = \frac{(w_i')^2}{6} \tag{5.18}$$

Where, w_i' refers to the i^{th} clear distance between adjacent longitudinal bars.

Hence, the total plan area of ineffectively confined concrete at link level, for 'n' number of longitudinal bars is:

$$A_i = \sum_{i=1}^{n} \frac{(w_i')^2}{6} \tag{5.19}$$

Incorporating the influence of the ineffective area in plan (Figure 5.11, Section Y - Y), the area of effectively confined concrete core, A_e, midway between levels of lateral reinforcement is:

$$A_e = \left(b_c\, d_c - \sum_{i=1}^{n} \frac{(w_i')^2}{6}\right)\left(1 - \frac{s'}{2b_c}\right)\left(1 - \frac{s'}{2d_c}\right) \tag{5.20}$$

Where, b_c and d_c refer to the core dimensions between the centrelines of the perimeter links, in both the x and y directions, respectively. s' refers to the clear vertical spacing between lateral links.

Thus, rearranging Equation (5.16), it can be determined that the confinement effectiveness factor, k_e is:

$$k_e = \left(1 - \sum_{i=1}^{n} \frac{(w_i')^2}{6b_c d_c}\right)\left(1 - \frac{s'}{2b_c}\right)\left(1 - \frac{s'}{2d_c}\right)\Big/(1 - \rho_{cc}) \tag{5.21}$$

It is possible for rectangular reinforced concrete members to have different quantities of transverse confining steel in the x and y directions, these may be expressed as:

$$\rho_x = \frac{A_{sx}}{sd_c} \tag{5.22}$$

And,

$$\rho_y = \frac{A_{sy}}{sb_c} \tag{5.23}$$

Where: A_{sx} and A_{sy} = the total area of transverse bar running in the x and y direction, respectively.

The lateral confining stress on the concrete (total transverse link divided by the vertical area of confined concrete) is given in the x direction as:

$$f_{lx} = \left(\frac{A_{sx}}{sd_c}\right)(f_{yh}) = (\rho_x)(f_{yh}) \tag{5.24}$$

And in the y direction as:

$$f_{ly} = \left(\frac{A_{sy}}{sb_c}\right)(f_{yh}) = (\rho_y)(f_{yh}) \tag{5.25}$$

Where: f_{yh} = the yield strength of the transverse reinforcement.

Rearranging Equation (5.15), the effective lateral confining stresses in the x and y directions become:

$$f'_{lx} = k_e(\rho_x)(f_{yh}) \tag{5.26}$$

$$f'_{ly} = k_e(\rho_y)(f_{yh}) \tag{5.27}$$

5.3.2 Compressive Strength of Confined Concrete, f'_{cc}

Mander *et al,* (1988) provides a general solution for the multi-axial failure criterion in terms of the two lateral confining stresses; Figure 5.13 presents this general solution. When the confined concrete core is placed in tri-axial compression with equal effective lateral confining stresses, f'_l from spiral or rectilinear links, the confined concrete compressive strength, f'_{cc}, is given by:

$$f'_{cc} = f'_{co}\left(-1.254 + 2.254\sqrt{1 + \frac{7.94\,f'_l}{f'_{co}}} - 2\frac{f'_l}{f'_{co}}\right) \tag{5.28}$$

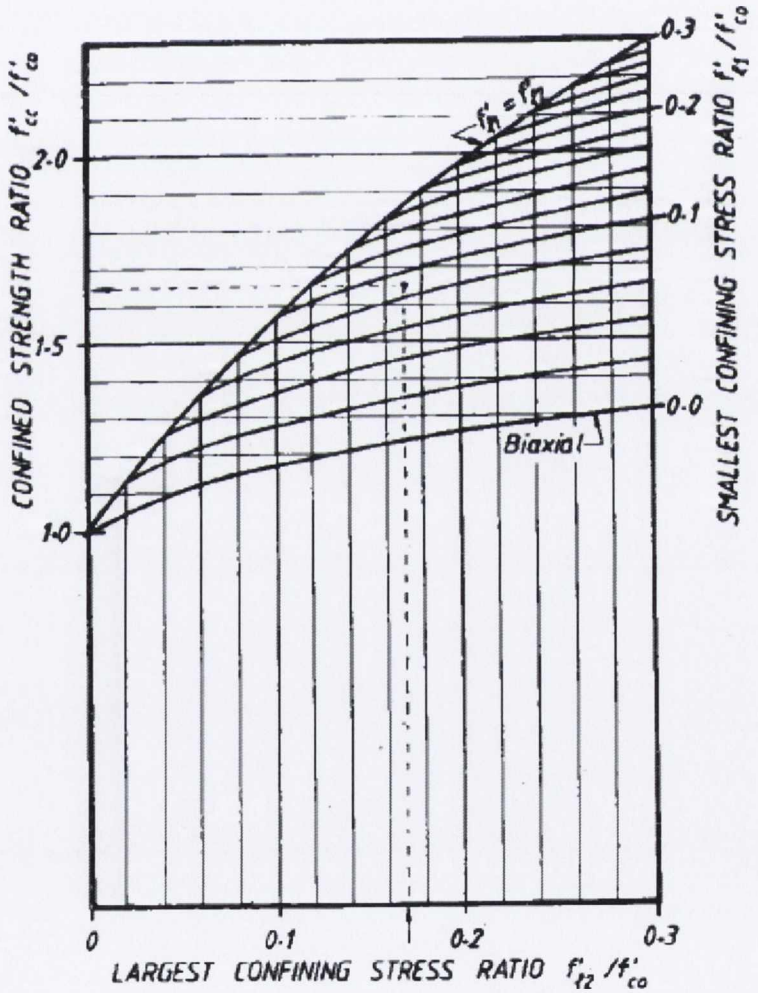

Figure 5.13: Confining Strength Determination from Lateral Confining Stresses for Rectangular Sections, Mander *et al,* (1988).

5.3.3 Confinement Factors for Encased Composite Columns

The theory presented in Sections 5.3.1 and 5.3.2 is developed for a reinforced concrete cross-section; the same principles can be adopted for a composite cross section as the longitudinal and transverse steel confine the concrete in an identical manner except for the additional confinement provided by the structural steel section. Thus, the core concrete is modelled as two parts, a partially confined element and highly confined element as presented in Figure 5.14.

The partial confinement factor, K_p is determined using the same process as discussed in Section 5.3.1 and Equation (5.28), Thus K_p is equivalent to:

$$K_p = \frac{f'_{cc}}{f'_{co}} \tag{5.29}$$

Where:

f'_{cc} = Confined concrete compressive strength, determined from Section 5.3.1

The area of concrete to which the confinement factor is applied, is determined from Equation (5.30). The area of structural steel and area of highly confined concrete is deducted from Equation (5.20) to produce a partially confined concrete area equivalent to:

$$A_{cc(p)} = \left(b_c\, d_c - \sum_{i=1}^{n} \frac{(w'_i)^2}{6}\right)\left(1 - \frac{s'}{2b_c}\right)\left(1 - \frac{s'}{2d_c}\right) - A_a - A_{cc(h)} \tag{5.30}$$

Where:

$A_{cc(p)}$ and $A_{cc(h)}$ = Area of partially and highly confined concrete (mm^2), respectively

A_a = Area of steel section

Parabolic arching identical to that assumed to act between the longitudinal bars was adopted to model the influence of the structural steel section, i.e. a second order parabola with an initial slope of 45° acting between the extremities of the steel flanges is

assumed to define the boundary between the highly and partially confined concrete, as illustrated in Figure 5.14.

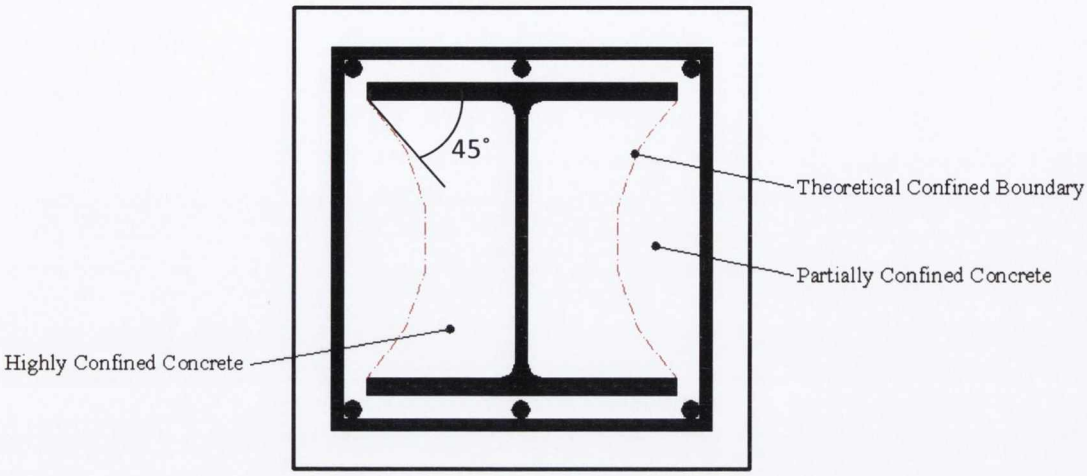

Figure 5.14: Theoretical Partial and Highly Confined Boundary

No widely accepted method of determining the confinement factor for highly confined concrete, K_h is available. The highly confined factor was determined analytically by varying the confinement factor to best-fit experimental values. A value of K_h = 1.3 was found to work with good accuracy for the NSC specimens. Due to the brittle nature of the HSC the confinement factor for the highly confined concrete was kept identical to that of the partially confined concrete which displayed good agreement with the experimental data. A more robust method to determine the highly confined confinement factor is required but would require a variety of cross sections and material properties to develop a universal formula.

5.3.4 Ultimate Concrete Compression Strain

The ability to determine the ultimate rotation capacity of a flexural plastic hinge is especially important for earthquake resistance and capacity design. To achieve this, it is essential to determine the ultimate concrete compressive strain, ε_{cu}, as illustrated in Figure 5.10. Scott *et al,* (1982) proposed that the ultimate concrete compressive strain can be defined as the longitudinal strain at which the first hoop fracture occurs, since this can be regarded as the end of the useful region of the stress-strain curve for the confined

concrete. Beyond this strain there is a loss of buckling restraint of the longitudinal reinforcement and a sudden drop in resistance.

Subsequently, Mander *et al.* (1988) proposed a rational method for predicting the longitudinal concrete compressive strain at first link fracture based on an energy balance approach. In this approach, the additional ductility available when concrete members are confined is considered to be due to the energy stored in the transverse reinforcement.

Referring to the stress-strain curves for unconfined and confined concrete as illustrated in Figure 5.10, the area under each curve represents the total strain energy per unit volume required to fail the concrete. The increase in strain energy at failure resulting from confinement can only be provided by the strain energy capacity of the confining reinforcement as it yields in tension. Thus, by equating the ultimate strain energy capacity of the confining reinforcement per unit volume of concrete core (U_{sh}) to the difference in area between the confined (U_{cc}) and the unconfined (U_{co}) concrete stress-strain curves, plus additional energy required to maintain yielding in the longitudinal steel in compression (U_{sc}), the longitudinal concrete compressive strain corresponding to hoop fracture can be calculated. Thus,

$$U_{sh} = U_{cc} + U_{sc} - U_{co} \tag{5.31}$$

Where:

U_{sh} = Ultimate strain energy capacity of the confining reinforcement

U_{cc} = Area under confined concrete stress-strain curve

U_{co} = Area under unconfined concrete stress-strain curve

U_{sc} = Energy required to maintain yielding of the longitudinal steel in compression

Expanding Equation (5.31), Mander obtains the following relationship:

$$\rho_s A_{cc} \int_0^{\varepsilon_{sf}} f_s \, \delta\varepsilon_s = A_{cc} \int_0^{\varepsilon_{cu}} f_c \, \delta\varepsilon_c + \rho_{cc} A_{cc} \int_0^{\varepsilon_{cu}} f_{sl} \, \delta\varepsilon_c - A_{cc} \int_0^{\varepsilon_{sp}} f_c \, \delta\varepsilon_c \tag{5.32}$$

Where:

ρ_s = Ratio of volume of transverse reinforcement to volume of concrete core

A_{cc} = Area of concrete core (mm^2)

f_s and ε_s = Stress (N/mm^2) and strain in the transverse reinforcement

ε_{sf} = Fracture strain of transverse reinforcement

ε_{cu} = Ultimate longitudinal compressive strain

ρ_{cc} = ratio of longitudinal reinforcement to volume of concrete core

f_{sl} = Stress in the longitudinal reinforcement (N/mm^2)

ε_{sp} = Spalling strain of the unconfined concrete

In other words, the strain energy capacity of the confining reinforcement per unit volume of concrete core is equal to the strain energy capacity of the confined concrete plus the strain energy capacity of the longitudinal steel less the strain energy capacity of the concrete in its unconfined state (i.e. the strain energy capacity that the concrete has when the concrete strains are so low that the transverse steel does not provide a confining pressure).

The first term on the left-hand side of Equation (5.32):

$$\int_0^{\varepsilon_{sf}} f_s \, \delta\varepsilon_s = U_{sf} \tag{5.33}$$

U_{sf} represents the strain energy (MJ/m^3) of the transverse reinforcement up to the fracture strain ε_{sf}. i.e. the area under the stress-strain curve up to the fracture strain.

Mander *et al,* (1988) conducted a series of tests on Grade 275 and 380 reinforcement of varying bar diameters. The results indicate that U_{sf} is effectively independent of bar size and yield strength, and may be takes as (within ± 10%):

$$U_{sf} = 110MJ/m^3 \tag{5.34}$$

For the steel considered, ε_{sf} ranged between 0.24 and 0.29.

For the last term on the right-hand side of Equation (5.32), the area under the stress-strain curve for unconfined concrete is required. Mander *et al,* (1988) found from analysis of measured data, from a range of plain concrete specimens that the area under the stress-strain curve for unconfined concrete may be approximated as:

$$\int_0^{\varepsilon_{sp}} f_c \, \delta\varepsilon_c = 0.017\sqrt{f'_{co}} \ (\mathrm{MJ/m^3}) \tag{5.35}$$

Where:

f'_{co} = unconfined concrete compressive strength ($\mathrm{N/mm^2}$)

5.3.4.1 Ultimate Strain in Composite Columns

The above theory is based on the assumptions that the ultimate failure occurs due to the fracture of a transverse link in a reinforced concrete specimen subject to uni-axial compressive loading. However, in this research the test specimens are composite columns subject to combined axial and lateral loading. Thus during the displacement cycles some of the core concrete and steel is in tension and the neutral axis depth varies with displacement.

It is realistic to define the ultimate strain of a composite column as the point at which the first link fractures, as this will inevitably occur at a large strain. Furthermore, if the link fractures, the partially confined concrete loses its confining pressure and fails, thus removing the confining pressure applied to the structural steel section. The loss of the additional confining pressure provided by the partially confined concrete will accelerate the resistance drop of the steel section which ultimately resists the remaining applied loads.

To account for the variable confinement levels provided by the longitudinal and structural steel, a new term is required to account for the structural steel section and the confinement provided by it, thus the confined concrete element needs to be split into two elements. The structural steel element becomes:

$$\int_0^{\varepsilon_{cu}} f_{ss}\, \delta\varepsilon_{ss} = U_{ss} \tag{5.36}$$

Where:

f_{ss} and ε_{ss} = Stress (N/mm^2) and strain in structural steel section, respectively

The confined core element is sub-divided into a partially and highly confined concrete core elements given by:

$$A_{cc(p)} \int_0^{\varepsilon_{cu}} f_{c(p)}\, \delta\varepsilon_{c(p)} + A_{cc(h)} \int_0^{\varepsilon_{cu}} f_{c(h)}\, \delta\varepsilon_{c(h)} \tag{5.37}$$

Where:

$f_{c(p)}$ and $f_{c(h)}$ = Stress in the partially and highly confined concrete, respectively (N/mm^2)

$\varepsilon_{c(p)}$ and $\varepsilon_{c(h)}$ = Strain in the partially and highly confined concrete, respectively

$A_{cc(p)}$ and $A_{cc(p)}$ = Area of the partially and highly confined concrete core elements, respectively

Thus, Equation (5.32) becomes:

$$\begin{aligned} \rho_s A_{cc} \int_0^{\varepsilon_{sf}} f_s\, \delta\varepsilon_s & \\ &= A_{cc(p)} \int_0^{\varepsilon_{cu}} f_{c(p)}\, \delta\varepsilon_{c(p)} \\ &+ A_{cc(h)} \int_0^{\varepsilon_{cu}} f_{c(h)}\, \delta\varepsilon_{c(h)} + \rho_{ss} A_{cc} \int_0^{\varepsilon_{cu}} f_{ss}\, \delta\varepsilon_{ss} \\ &+ \rho_{cc} A_{cc} \int_0^{\varepsilon_{cu}} f_{sl}\, \delta\varepsilon_c - A_{cc} \int_0^{\varepsilon_{sp}} f_c\, \delta\varepsilon_c \end{aligned} \tag{5.38}$$

Where:

ρ_{ss} = ratio of the volume of structural steel to volume of concrete

Equation (5.38) takes no account of the varying neutral axis and the varying area of core elements in compression, thus, the area A_{cc} in each of the terms on the right-hand side the Equation (5.38) should be replaced with the actual area of concrete core in compression.

Therefore, A_{cc} becomes dependent on the stress-state and the position of the neutral axis. Thus Equation (5.38) becomes:

$$\begin{aligned}
&\rho_s A_{cc} \int_0^{\varepsilon_{sf}} f_s \, \delta\varepsilon_s \\
&= \sum_{i=1}^{n} A_{i(p)} \int_0^{\varepsilon_{cu}} f_{ci(p)} \, \delta\varepsilon_{ci(p)} \\
&+ \sum_{i=1}^{n} A_{i(h)} \int_0^{\varepsilon_{cu}} f_{ci(h)} \, \delta\varepsilon_{ci(h)} + \rho_{ss} \sum_{i=1}^{n} A_i \int_0^{\varepsilon_{cu}} f_{ssi} \, \delta\varepsilon_{ssi} \\
&+ \rho_{cc} \sum_{i=1}^{n} A_i \int_0^{\varepsilon_{cu}} f_{sli} \, \delta\varepsilon_{ci} - \sum_{i=1}^{n} A_i \int_0^{\varepsilon_{sp}} f_{ci} \, \delta\varepsilon_{ci}
\end{aligned} \tag{5.39}$$

Finally, substituting in Equation (5.34) and Equation (5.35), Equation (5.39) becomes:

$$\begin{aligned}
&110\rho_s A_{cc} = \\
&\sum_{i=1}^{n} A_{i(p)} \int_0^{\varepsilon_{cu}} f_{ci(p)} \, \delta\varepsilon_{ci(p)} \\
&+ \sum_{i=1}^{n} A_{i(h)} \int_0^{\varepsilon_{cu}} f_{ci(h)} \, \delta\varepsilon_{ci(h)} + \rho_{ss} \sum_{i=1}^{n} A_i \int_0^{\varepsilon_{cu}} f_{ssi} \, \delta\varepsilon_{ssi} \\
&+ \rho_{cc} \sum_{i=1}^{n} A_i \int_0^{\varepsilon_{cu}} f_{sli} \, \delta\varepsilon_{ci} - 0.017\sqrt{f'_{co}}
\end{aligned} \tag{5.40}$$

With a knowledge of f_c, f_{ss} and f_{sl} from the pre-defined stress-strain curves, the longitudinal concrete compressive strain ε_{cu} at the stage of first fracture of the transverse reinforcement can be solved for numerically using Equation (5.40).

5.3.5 Concrete in Tension

Neville, (1995), provides the following relationship for concrete in tension up to the maximum tensile strength:

$$f_t = 0.12(f_{cu})^{0.7} \tag{5.41}$$

Where: f_t = concrete tensile strength (N/mm^2), and f_{cu} = concrete cube compressive strength (N/mm^2).

The concrete cover in tension reaches its maximum tensile strength, f_t, at a strain, ε_t. Hence, the elastic modulus in tension, E_{ct}, is:

$$E_{ct} = \frac{f_t}{\varepsilon_t} \tag{5.42}$$

Once the strain corresponding to the maximum tensile strength of concrete is reached, the tension cover is assumed to lose its strength instantaneously.

5.3.6 Unconfined Concrete in Compression

Unconfined concrete in compression behaves identically to confined concrete up to the unconfined concrete strength, f'_{co}, according to Mander's model for confined concrete. The maximum unconfined compressive stress occurs at a strain, ε_{co}, equivalent to a value of 0.002. Up to this point the stress-strain relationship is defined by Equation (5.9). Mander *et al.* (1988) defines a linear drop in the cover resistance to zero stress from 0.002 strain to ε_{sp}.

5.3.7 Reinforcing Steel

Reinforcing Steel in Tension

Reinforcing steel in tension is assumed to have a stress-strain profile corresponding to that presented in Figure 5.15. The curve is simplified from the actual stress-strain curve but agrees with the overall model adequately. The ascending branch represents the elastic region of the steel; subsequently the material enters the inelastic region of strain hardening up to the ultimate stress at fracture. The post yield stiffness was determined

from the yield and ultimate strains and stresses from steel coupon tests, the values of which are presented in Table 7.

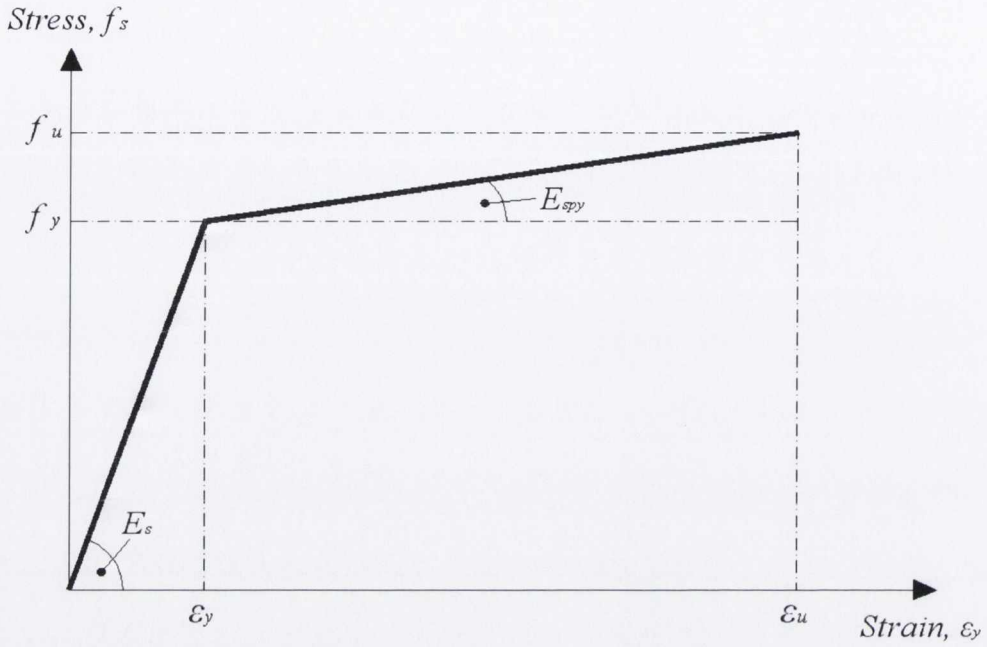

Figure 5.15: Reinforcing Steel Stress-Strain Curve in Tension

Where:

f_y , ε_y = steel yield stress (N/mm^2) and yield strain, respectively

f_u , ε_u = steel ultimate stress (N/mm^2) and ultimate strain, respectively

E_s = Young's Modulus of Elasticity (N/mm^2)

E_{spy} = Post-yield Stiffness (N/mm^2)

Reinforcing Steel in Compression

Reinforcing steel is assumed to behave in an identical manner when subjected to compressive and tensile forces if it is adequately restrained against buckling. Due to the space between lateral confining links and the loss of cover concrete following repeated cycles of lateral load, the steel loses its confinement thus altering the stress-strain profile. Figure 5.4 presents the adopted reinforcing steel stress-strain model in compression and Figure 5.16 presents the combined stress-strain curve for compression and tension.

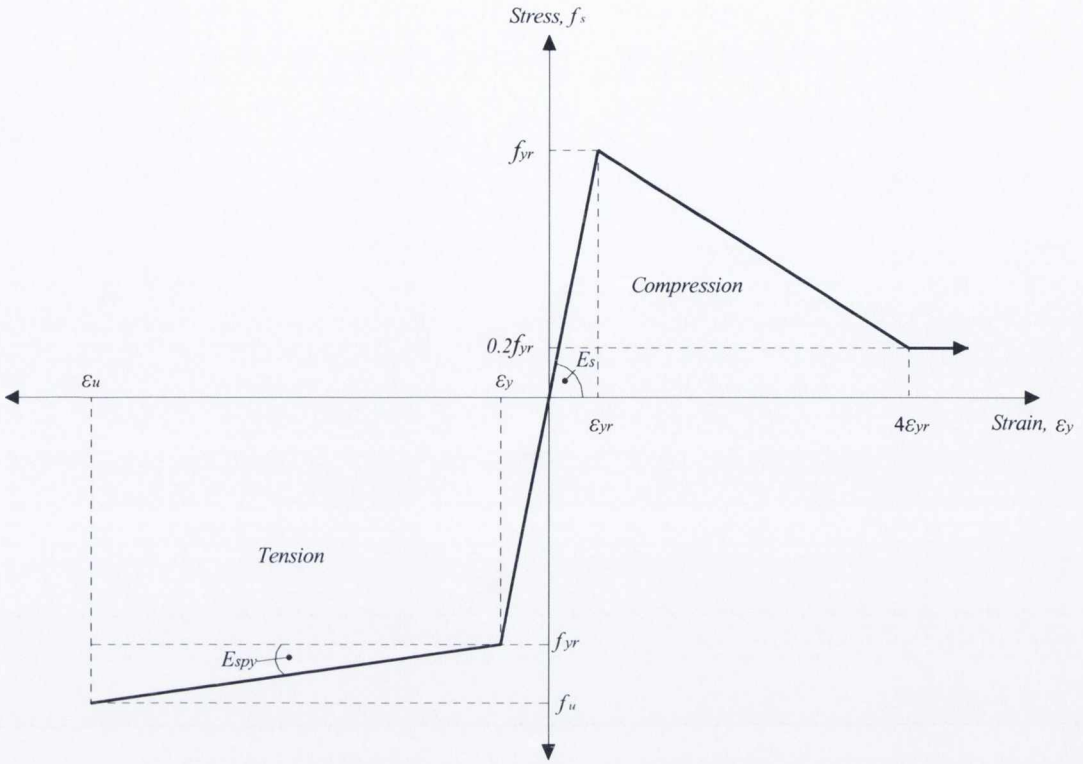

Figure 5.16: Combined Reinforcing Steel Stress-Strain Curve

Where:

f_{yr} , ε_{yr} = Reinforcing steel yield stress (N/mm^2) and yield strain, respectively

5.3.8 Structural Steel

The structural steel is assumed to behave in a similar manner to the reinforcing steel, the tensile stress-strain curve is assumed to correspond to Figure 5.15 while in the compression region the curve is identified by Figure 5.5. The combined stress strain curve in tension and compression is presented in Figure 5.17. The post yield plateau accounts for the sustained load resistance of the steel until the partially confined concrete adjacent to it reaches its yield strain, at which point the steel loses its confining stresses and a considerable drop in resistance is experienced for increasing strains. The resistance drop occurs due to local buckling of the steel flange within the inelastic range of the material. The b/T ratio of the steel section must be considered before adopting this stress-strain model as high b/T ratios may not experience inelastic buckling.

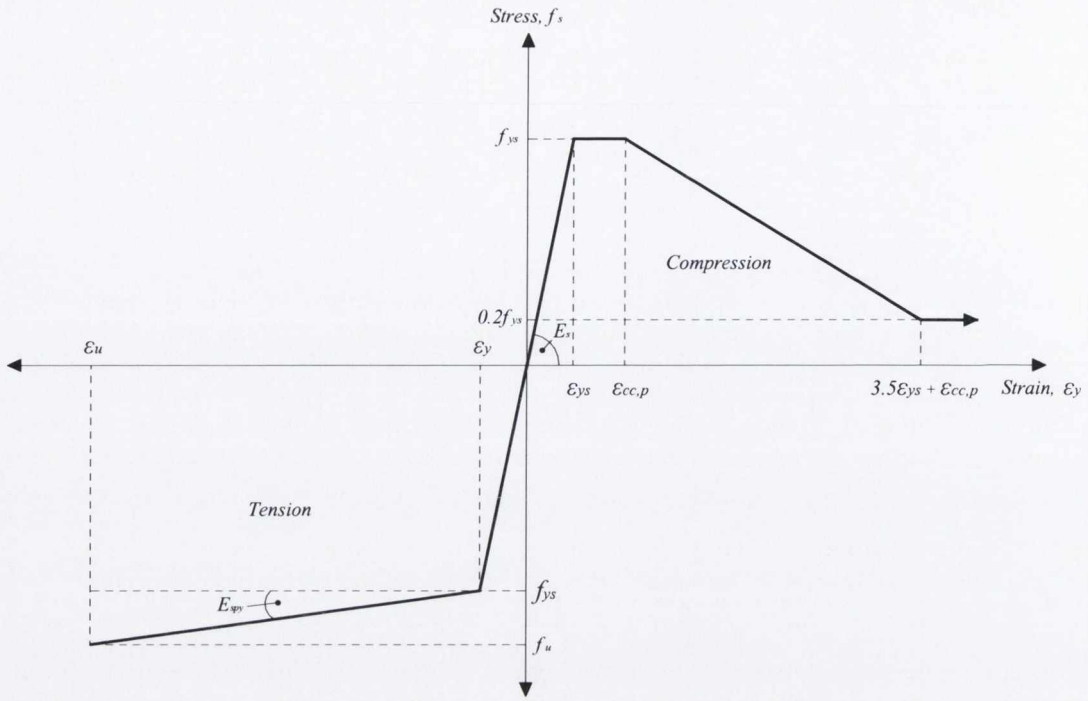

Figure 5.17: Combined Structural Steel Stress-Strain Curve

Where:

f_{ys} , ε_{ys} = Structural steel yield stress (N/mm^2) and yield strain, respectively

$\varepsilon_{cc,p}$ = Strain at maximum partially confined concrete stress

5.3.9 High-Strength Concrete

HSC is inherently more brittle than NSC, thus the analytical model needs to reflect this. The model adopted in this research was proposed by Hong *et al,* (2006), which is presented in Figure 5.9. This model was selected as it produced a sharp reduction in resistance of the confined concrete stress beyond the strain corresponding to the maximum confined concrete stress.

The stress-strain relationship is based on the following equations:

$$f_c = f_{cc}\left(1 - \left(1 - \frac{\varepsilon_c}{\varepsilon_{cc}}\right)^{\alpha}\right) \text{ Where: } (0 \leq \varepsilon_c \leq \varepsilon_{cc}) \tag{5.43}$$

$$f_{cc} = f_{co}\left[1.0 + 1.6\left(\frac{\rho_e}{f_{co}}\right)^{0.5}\right] \tag{5.44}$$

$$\alpha = E_c\frac{\varepsilon_{cc}}{f_{cc}} \tag{5.45}$$

$$E_c = 3320\sqrt{f_{co}} + 6900 \tag{5.46}$$

$$f_c = f_{cc}\,exp(k_3(\varepsilon_c - \varepsilon_{cc})^{k_4}) \text{ Where: } (\varepsilon_c \geq \varepsilon_{cc}) \tag{5.47}$$

$$k_3 = \frac{\ln 0.5}{(\varepsilon_{50} - \varepsilon_{cc})^{k_4}} \tag{5.48}$$

$$k_4 = 0.3 + 12\frac{k_2\rho_e}{f_{co}} \tag{5.49}$$

$$k_2 = 1 + k_e\frac{(f_{sy} - f_{s,cal})}{f_{sy}} \tag{5.50}$$

$$\rho_e = k_e\rho_w f_{s,cal} \tag{5.51}$$

k_e is the effective confinement coefficient, defined by Mander *et al,* (1988) provided in Equation (5.21).

$$f_{s,cal} = E_s\left[0.45\varepsilon_{co} + 6.8\left(\frac{k_e\rho_w}{f_{co}}\right)^{9/10}\right] \leq f_{sy} \tag{5.52}$$

$$\varepsilon_{co} = 0.0028 - 0.0008k_1 \tag{5.53}$$

$$k_1 = {}^{40}/_{f_{co}} \leq 1.0 \tag{5.54}$$

$$\varepsilon_{50} = \varepsilon_{50u} + 30\frac{k_2^2\rho_e}{f_{co}^2} \tag{5.55}$$

$$\varepsilon_{50u} = 0.0028 + 0.0007k_1 \tag{5.56}$$

$$f_{co} = 0.85f_c' \tag{5.57}$$

$$\varepsilon_{cc} = \varepsilon_{co} + 0.021\left(\frac{\rho_e}{f_{co}}\right)^{3/5} \tag{5.58}$$

5.4 Moment-Curvature Response

This section describes the process to determine the moment-curvature response of a given composite cross section. Figure 5.18 presents an arbitrary composite column cross-section, a typical member used to withstand combined flexural and axial loading. The section comprises the following material regions:

- Cover concrete
- Partially confined concrete
- Highly confined concrete
- Longitudinal reinforcing steel
- Structural steel

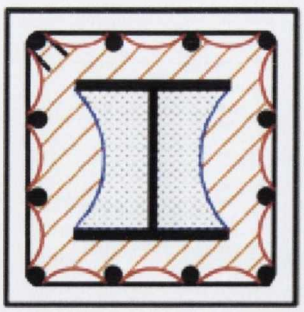

Figure 5.18: Composite Column of Arbitrary Cross Section

Figure 2.19 labels these individual regions in detail. To determine the moment-curvature response the normal assumptions for flexural analysis are made:

- The strain profile is linear at all stages of loading up to ultimate (i.e. the Navier-Bernoulli 'plane-sections remain plane' hypothesis holds).
- Steel and concrete strains at a given distance from the neutral axis are identical (i.e. perfect bond exists between concrete and steel elements).
- Concrete tensile strength is ignored.
- Axial force is applied at the section's centroid, thus eliminating any eccentricities.
- Concrete and steel non-linear stress-strain relationships are known:

$$f_{c(y)} = \Phi_c(\varepsilon_{c(y)}) = \Phi_c(\varepsilon_{(y)}) \tag{5.59}$$

$$f_{s(y)} = \Phi_s(\varepsilon_{s(y)}) = \Phi_s(\varepsilon_{(y)}) \tag{5.60}$$

Where:

Φ_c = Concrete stress-strain relationship

Φ_s = Steel stress-strain relationship

$f_{c(y)}$ & $f_{s(y)}$ = Concrete and steel stress for a given neutral axis depth, respectively

$\varepsilon_{c(y)}$ & $\varepsilon_{s(y)}$ = Concrete and steel strains for a given neutral axis depth, respectively

The material stress-strain models discussed previously shall be applied to the individual elements. The reason the tensile capacity of the concrete is ignored is twofold, firstly the section is designed to withstand reversed loading, typical of seismic actions, since the neutral axis will generally be in the compression side of the sections centroid, cracks under reversed loading will extend through the entire section. Thus on load reversal the compression zone will occur in a location previously cracked under the moment of opposite sign and no tensile capacity will exist as a result. Secondly, the contribution of the concrete's tensile strength is negligible compared with that of the steel elements.

Figure 5.19 presents a typical composite cross-section sub-divided into a number of elemental strips, containing one primary constituent material. The element height, D_n , varies and its depth below the extreme compression fibre is termed χ_n . Figure 5.20

provides an illustration for the definition of curvature and element strains. From this it can be deduced that the strain at the extreme compression fibre is:

$$\varepsilon_c = \emptyset x \tag{5.61}$$

Where:

ε_c = Strain in the extreme compression fibre

$\emptyset$ = Curvature (mm^{-1})

x = Neutral axis depth (mm)

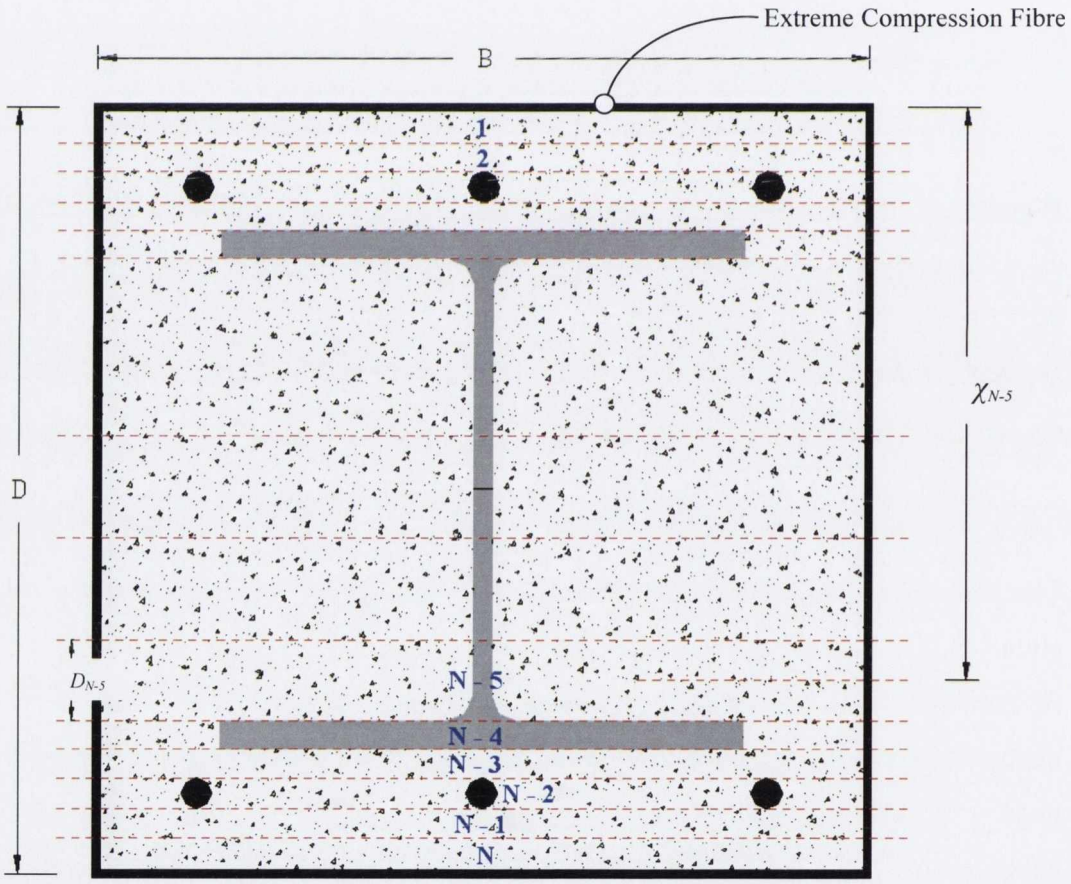

Figure 5.19: Composite Cross-Section Sub-Divided into N-Strip Elements

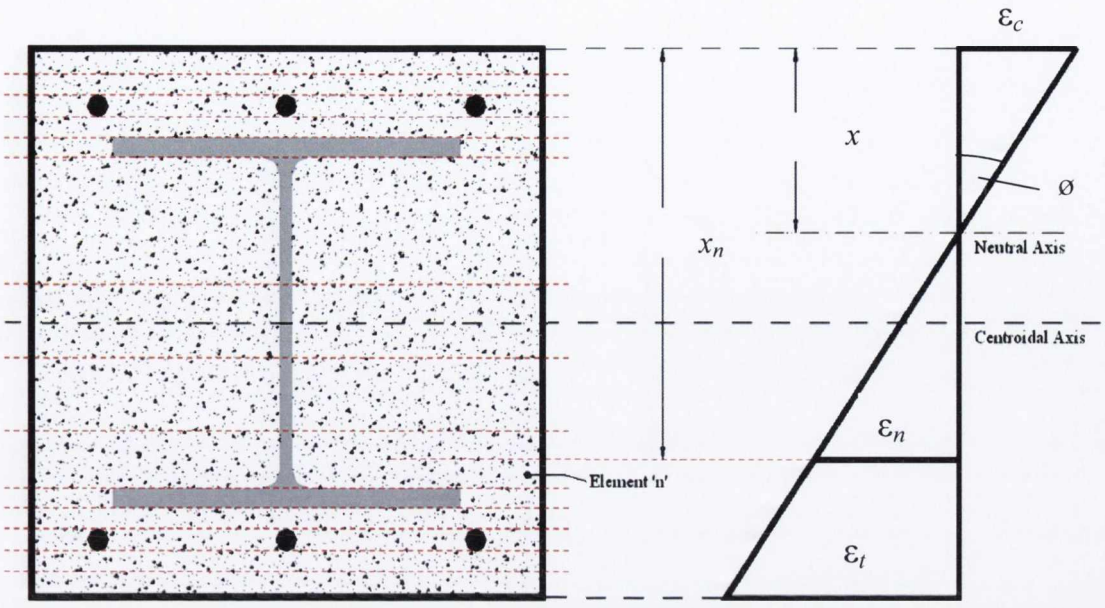

Figure 5.20: Definition of Curvature and element strain

Element Strains:

Hence, the strain in element 'n' is given by:

$$x_n < x : \varepsilon_n = \left(\frac{\varepsilon_c}{x}\right)(x - x_n) \tag{5.62}$$

$$x_n > x : \varepsilon_n = \left(\frac{\varepsilon_c}{x}\right)(x_n - x) \tag{5.63}$$

Where:

x_n = Distance from the extreme compression fibre to the centre of element 'n'

ε_n = Strain in element 'n'

Element Stresses:

The stresses in the unconfined normal-strength concrete elements in compression are:

$$\varepsilon_n < 0.002 : \sigma_n = f_c \text{ (from Equation (5.9))} \tag{5.64}$$

$$\varepsilon_n = 0.002 : \sigma_n = f_{co}^{'} \tag{5.65}$$

$$0.002 < \varepsilon_n < \varepsilon_{sp} : \sigma_n = \left(\frac{f_{co}^{'}}{\varepsilon_{sp} - 0.002} \right) (\varepsilon_{sp} - \varepsilon_n) \tag{5.66}$$

$$\varepsilon_{sp} \leq \varepsilon_n : \sigma_n = 0 \tag{5.67}$$

Where:

f_c = The longitudinal concrete compressive stress according to Mander's stress-strain model for confined concrete up to $\varepsilon_n = 0.002$.

The stresses in the unconfined concrete elements in tension are:

$$\varepsilon_n < \varepsilon_t : \sigma_n = (E_{ct})(\varepsilon_n) \tag{5.68}$$

$$\varepsilon_n = \varepsilon_t : \sigma_n = f_t \tag{5.69}$$

$$\varepsilon_n > \varepsilon_t : \sigma_n = 0 \tag{5.70}$$

Where:

ε_t = Strain corresponding to the tensile capacity of the concrete

E_{ct} = Concrete modulus in tension (N/mm^2)

f_t = Tensile strength of concrete, from Equation (5.41) (N/mm^2)

The stresses in the normal-strength concrete core are as follows:

$$x_n < x : \sigma_n = f_c \text{ (from Equation (5.9))} \tag{5.71}$$

$$x_n \geq x : \sigma_n = 0 \tag{5.72}$$

The stresses in the unconfined high-strength concrete elements in compression are:

$$\varepsilon_n < 0.002 : \sigma_n = f_c \text{ (from Equation (5.9))} \tag{5.73}$$

$$\varepsilon_n = 0.002 : \sigma_n = f_{co}^{'} \tag{5.74}$$

$$0.002 \leq \varepsilon_n : \sigma_n = 0 \tag{5.75}$$

The stresses in the high-strength concrete core are as follows:

$$0 \leq \varepsilon_n \leq \varepsilon_{cc} : \sigma_n = f_{cc}\left(1 - \left(1 - \frac{\varepsilon_c}{\varepsilon_{cc}}\right)^{\alpha}\right) \tag{5.76}$$

$$\varepsilon_{cc} \leq \varepsilon_n : \sigma_n = f_{cc}\, exp(k_3(\varepsilon_c - \varepsilon_{cc})^{k_4}) \tag{5.77}$$

Where:

α, k_3 and k_4 are defined in Section 5.3.9

The stresses in the longitudinal and structural steel in tension are:

$$\varepsilon_n < \varepsilon_y : \sigma_n = (E_s)(\varepsilon_n) \tag{5.78}$$

$$\varepsilon_y < \varepsilon_n < \varepsilon_u : \sigma_n = (E_s)(\varepsilon_n) + (E_{spy})(\varepsilon_n - \varepsilon_y) \tag{5.79}$$

$$\varepsilon_n > \varepsilon_u : \sigma_n = 0 \tag{5.80}$$

The stresses in the longitudinal steel in compression are:

$$\varepsilon_n < \varepsilon_{yr} : \sigma_n = (E_s)(\varepsilon_n) \tag{5.81}$$

$$\varepsilon_{yr} < \varepsilon_n \leq 4\varepsilon_{yr} : \sigma_n = (f_{yr}) - \left(\left\{\frac{0.8\, f_{yr}}{3\varepsilon_{yr}}\right\}\{\varepsilon_n - \varepsilon_{yr}\}\right) \tag{5.82}$$

$$\varepsilon_n > 4\varepsilon_{yr} : \sigma_n = 0.2 f_{yr} \tag{5.83}$$

The stresses in the structural steel in compression are:

$$\varepsilon_n < \varepsilon_{ys} : \sigma_n = (E_s)(\varepsilon_n) \tag{5.84}$$

$$\varepsilon_{ys} \leq \varepsilon_n \leq \varepsilon_{cc,p} : \sigma_n = f_{ys} \tag{5.85}$$

$$\varepsilon_{cc,p} < \varepsilon_n \leq (\varepsilon_{cc,p} + 3.5\varepsilon_{ys}) : \sigma_n = (f_{ys}) - \left(\left\{\frac{0.8\, f_{ys}}{3.5\varepsilon_{ys}}\right\}\{\varepsilon_n - \varepsilon_{ys}\}\right) \tag{5.86}$$

$$\varepsilon_n > (\varepsilon_{cc,p} + 3.5\varepsilon_{ys})\ \sigma_n = 0.2 f_{ys} \tag{5.87}$$

Element Forces:

Equations (5.88) and (5.89) are used to determine the force in each strip, by multiplying the element stress by its equivalent material area. The equations take into account the global position of the strip relative to the neutral axis location, thus the resultant forces have a positive sign convention for compression regions and are negative for tensile forces. Some strips contain both steel and concrete, in this instance both material elements are considered, unless the strip is in tension when the tensile resistance of the concrete is ignored.

$$x_n < x : F_n = (A_n)(\sigma_n) \tag{5.88}$$

$$x_n > x : F_n = -(A_n)(\sigma_n) \tag{5.89}$$

Where:

F_n = The force in element 'n' (N)

A_n = The area of element 'n' (mm^2)

Neutral Axis Depth:

The neutral axis depth, x, is measured from the extreme compression fibre, for a given value of curvature. It is determined iteratively when the following equation is satisfied:

$$\sum_{i=1}^{n} F_i + P = 0 \tag{5.90}$$

Where:

i = Element Number

P = Applied Axial Load (N)

Moments of Resistance:

The moment of resistance due to the force in each element is determined by evaluating:

$$M_n = (F_n)\left(\frac{D}{2} - x_n\right) \tag{5.91}$$

Where:

M_n = Moment due to the force in element 'n'

D/2 = Distance from the extreme compression fibre to the sections centroid

Equation (5.91) will result in a negative moment for elements where x_n is greater than D/2. Thus the total moment acting on the section is the sum of all these element moments, given by:

$$M = \sum_{n=1}^{N} M_n \tag{5.92}$$

Where:

M = Total Moment (Nmm)

The above procedure can be used for any input curvature value and a corresponding set of resistance moments may be calculated and the resulting moment-curvature responses can be plotted.

To summarise, the moment curvature analysis is executed in accordance with the following procedure:

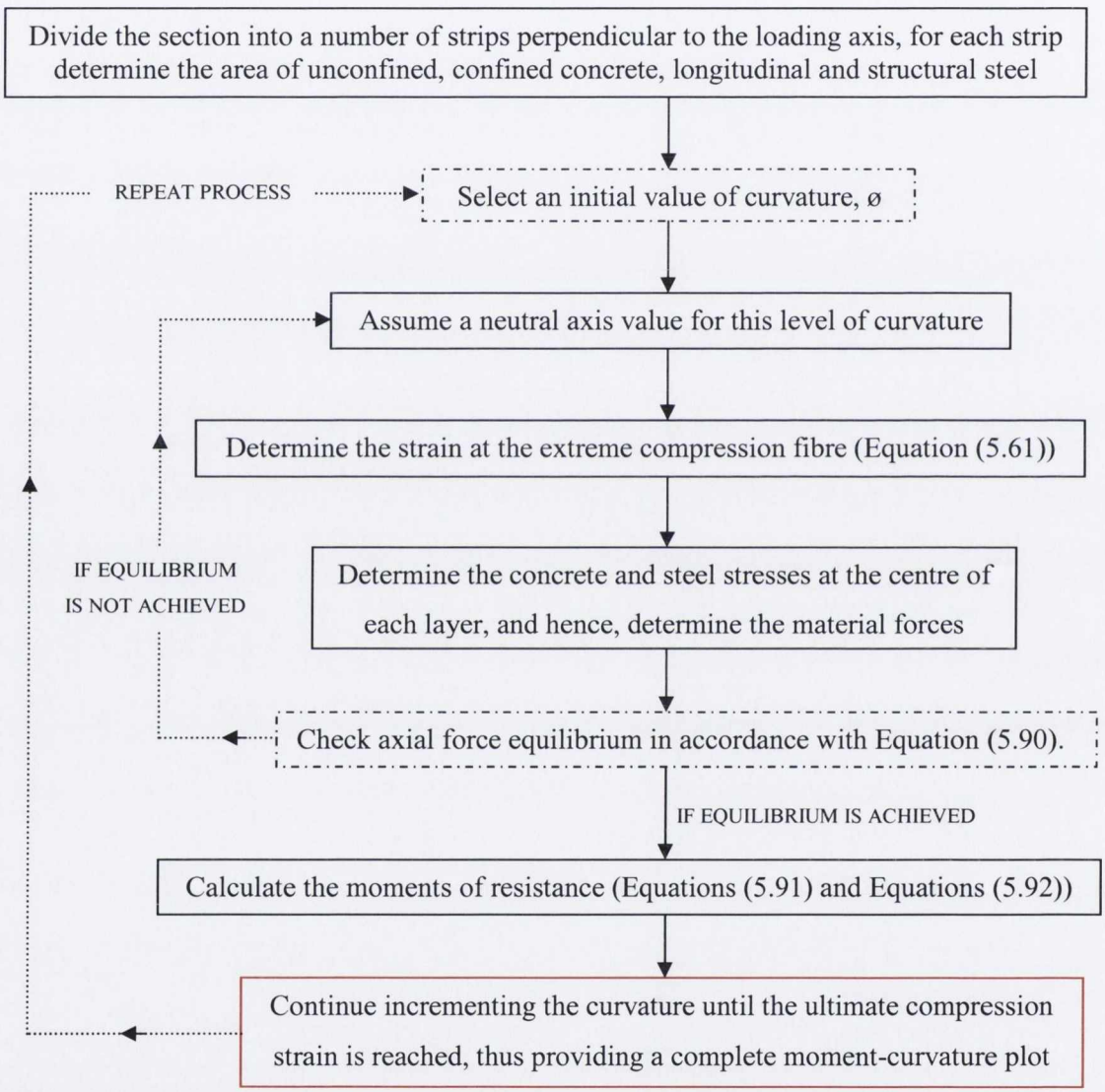

5.5 Moment-Displacement Response

This section describes how the moment-displacement response can be determined from the moment-curvature response, using the well-known relationships between member curvature, rotation and displacement.

5.5.1 Basic Equations

For a homogenous elastic column, the curvature can be determined from the following expression:

$$ø = \frac{M}{EI} \tag{5.93}$$

Where:

EI = Slope of the linear ascending branch of the moment curvature curve (Nmm^2).

This equation implies that for an elastic column, a linear change in moment along the column will cause a linear change in curvature, hence, the linear curvature profile of Figure 5.21 is observed.

The following well known relationships between displacement, rotation and curvature exist:

$$\Delta = y = displacement \tag{5.94}$$

$$\theta = \frac{dy}{dx} = rotation \tag{5.95}$$

$$ø = \frac{d^2y}{dx^2} = curvature\,, \qquad \text{(approximately)} \tag{5.96}$$

Similarly:

$$\theta = \int ø\, \delta x \tag{5.97}$$

$$\Delta = \int\int ø\, \delta x \tag{5.98}$$

Consider a homogenous elastic cantilever column as presented in Figure 5.21, the column is subject to a lateral load, P and axial compressive force, N. This induces a tip displacement, Δ, and rotation θ. Figure 5.21 (a) – (e) illustrate the deformed shape, moment, curvature, rotation and displacement profiles of the column in the elastic range. Equations (5.97) and (5.98) imply that the rotation and displacement of the column can be determined by equating the area under the curvature and rotation profiles, respectively. These relationships also hold equally well for an inelastic column (Figure 5.21 (f) – (h)).

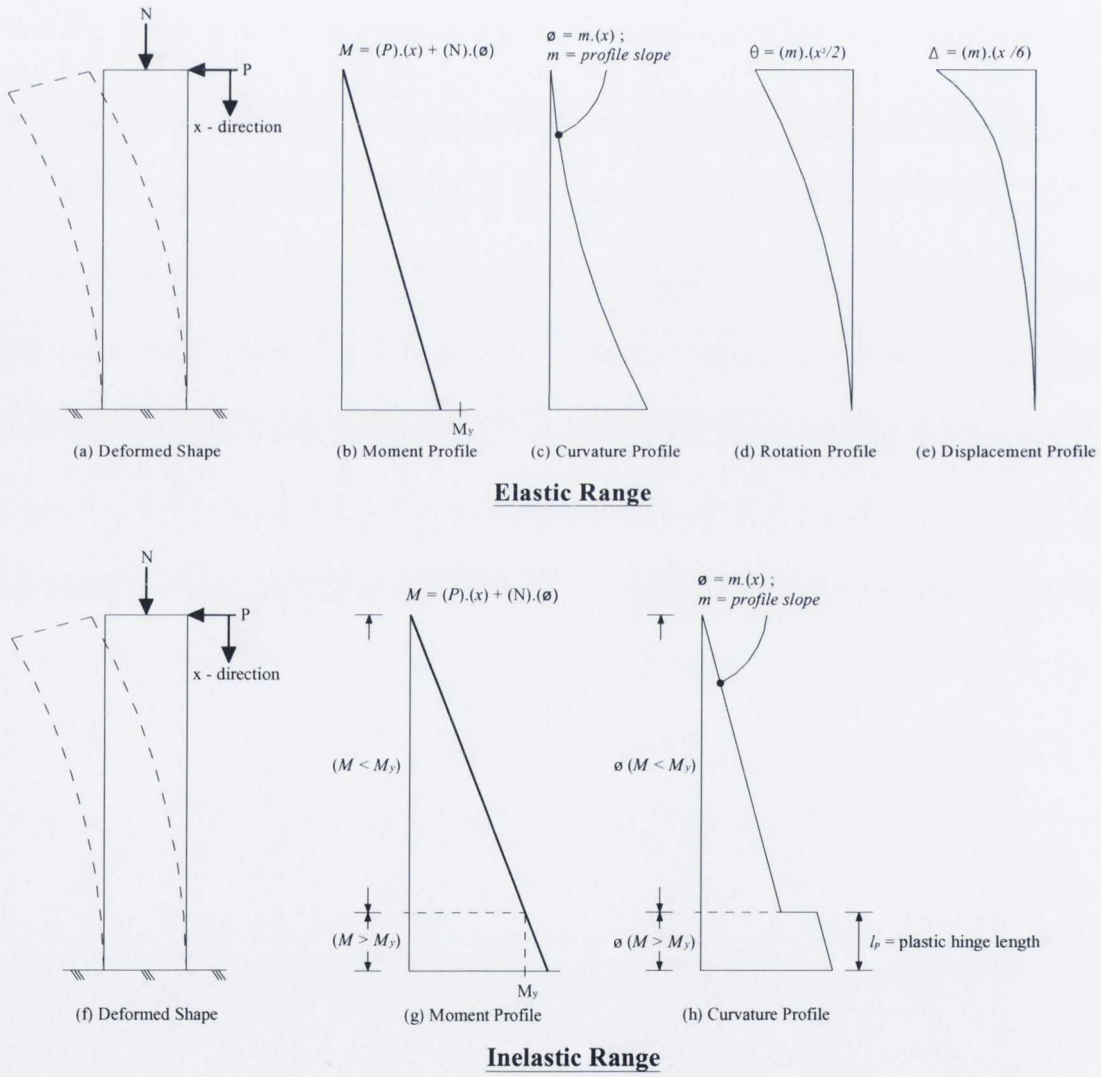

Figure 5.21: Cantilever Column, Elastic and Inelastic Profiles

5.5.2 Displacement Equations

Consider the cantilever column in Figure 5.22, which is subject to a lateral load, P, resulting in a deflection, Δ. The column is divided into a number of elements, where the element at the fixed end is referred to as the 'plastic hinge element', since this is the region where potential plastic deformation occurs. If the column remains elastic, the curvature profile will be linear, as per Figure 5.22 (c).

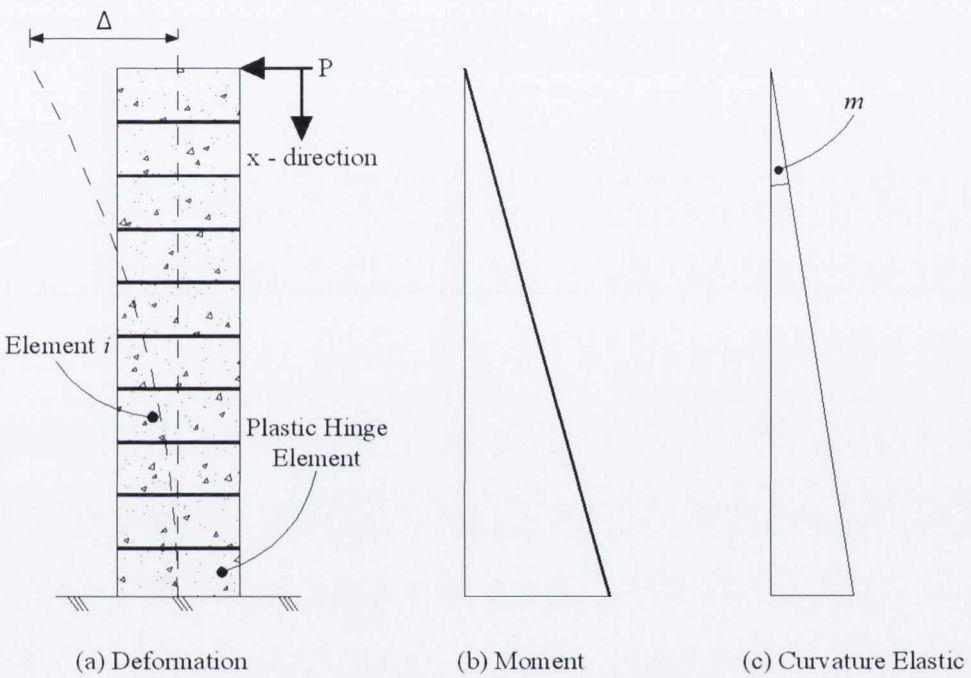

Figure 5.22: Elastic Curvature Profile for Cantilever Column

Therefore, for a homogenous elastic column, curvature along the member is defined as:

$$\phi = mx \tag{5.99}$$

Where:

m = Slope of the curvature profile (mm^{-2}), which can be determined if the curvature profile is known.

x = Distance along the column.

Substituting into Equation (5.98), the total displacement occurring between the column tip and element *'i'* is:

$$\Delta_{Ti} = \int_0^{x_i} \int \phi \, \delta x = \int_0^{x_i} \int mx \, \delta x = \frac{mx_i^3}{6} + C_1 x + C_2 \tag{5.100}$$

Where:

Δ_{Ti} = Total displacement occurring between column tip and element *'i'* (mm).

x_i = Distance from fixed end/plastic hinge (i.e. element *'i'*) to point of lateral load.

Thus, by solving the equation for the initial conditions at $x = 0$, $m = 0$ and $\Delta_{Ti} = 0$ (at distance x from the base) the constant of integration $C_2 = 0$.

Solving for the conditions at $x_i = x$, $m = m$, $C_2 = 0$ and $\Delta_{Ti} = \Delta$ (at distance x from the base) the constant of integration C_1 becomes:

$$\Delta = \frac{mx_i^3}{6} + C_1 x + 0 \quad thus \quad C_1 = \frac{\Delta}{x} - \frac{mx^2}{6} \tag{5.101}$$

Consider an inelastic column, as illustrated in Figure 5.23, with a corresponding curvature profile as illustrated in Figure 5.23 (c) or (d). For the curvature profile in Figure 5.23 (d), a 'curvature step' equal to a curvature increment of 'h' occurs at the change in profile slope. Equation (5.98) is still applicable to both these curvature profiles once the changes in profile slope are included. For both of the curvature profiles depicted in Figure 5.23 (c) and (d) the following conditions apply:

$$0 < x \leq x_p : \phi = m_1 x \tag{5.102}$$

$$x_p < x \leq L : \phi = m_1 x + m_2 (x - x_p) + h \tag{5.103}$$

Where:

x_p = Distance from column tip to the point at which the slope of the curvature profile changes (mm)

m_1 = Slope of curvature profile in the elastic region (mm^{-2})

m_2 = Second slope of curvature profile, i.e. in the plastic region (mm^{-2})

L = Column length (mm)

h = Curvature Step

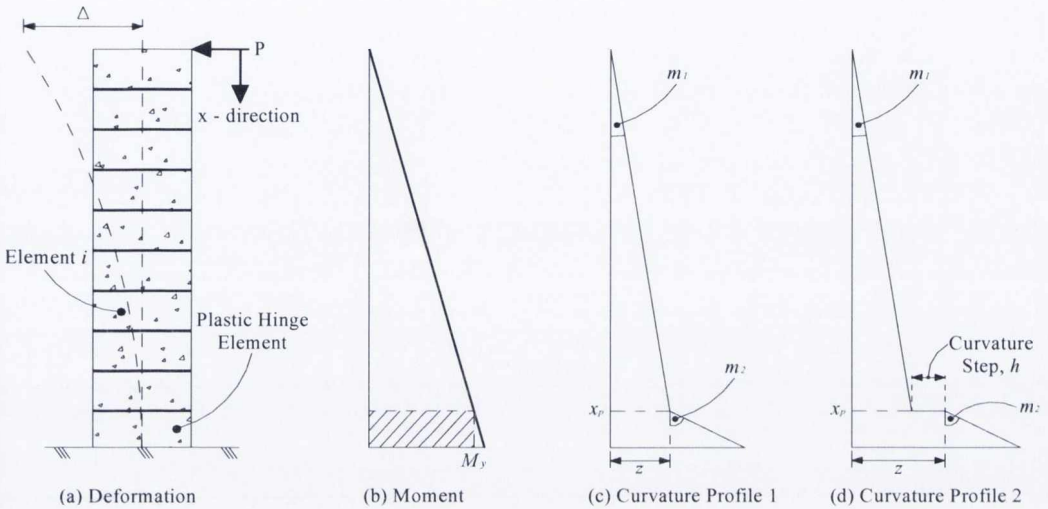

Figure 5.23: Inelastic Curvature Profiles

Note: The above curvature profiles are not consistent with the numerical profiles in Figure 6.1 to Figure 6.6, the above figures have been exaggerated for clarity. As the concrete spalls a reduction in the lateral resistance is recorded for increasing levels of curvature.

Hence, the total displacement occurring between the column tip and any point within the plastic hinge element is:

$$\Delta_{Ti\,ph} = \int_0^{x_p} \int m_1 x \; \delta x + \int_{x_p}^{x_i} \int m_2 (x - x_p) + h\delta x \qquad (5.104)$$

$\Delta_{Ti\,ph}$ = Total displacement between the column tip to some point *'i'* in the plastic hinge element (mm).

5.6 Implementation of Numerical Model

An EXCEL spreadsheet is used to implement the numerical models to determine the moment-curvature and moment-displacement responses for each of the test specimens discussed in previous chapters. Section 5.6.1 provides the specimen cross-section details

required to determine the moment-curvature response. Section 5.6.2 describes the transformation from moment-curvature to moment-displacement data, Finally Section 5.6.3 describes how the strain and strain energy corresponding to failure of the specimens are determined.

5.6.1 Moment-Curvature Response

A detailed specimen description is provided in Section 3.2.2, Table 23 provides details of the concrete characteristics including, confined factors for partially and highly confined concrete (K_p and K_h) and unconfined concrete strength (f'_{co}), compressive elastic modulus (E_c), tensile strength (f_t) and tensile elastic modulus (E_{ct}). Table 24 presents the characteristics for the reinforcing and structural steel in tension; further details have been provided in Section 5.3.7 and 5.3.8. The spalling strain, ε_{sp} is assumed to be 0.0035 for confined concrete, for the NSC and HSC the spalling strain of the cover concrete is assumed to correspond to 0.002 and 0.0024, respectively. Section 5.4 described how the cross-section is divided into a number of strips, and

Table 25 provides details of these strips in terms of constituent material, element depth, area, depth from the extreme compression fibre and lever arm length from the section centroid, $((D/2)-x_n)$.

Table 23: Concrete Characteristics

Specimen	f'_{co} (N/mm^2)	K_p	K_h	E_c (N/mm^2)	f_{ct} (N/mm^2)	E_t (N/mm^2)
JD1 – ID2	25	1.18	1.3	25000	1.14	1142.2
JD2 – ID1	25	1.18	1.3	25000	1.14	1142.2
JD3 – ID3	25	1.18	1.3	25000	1.14	1142.2
JD4 – ID5	77.7	1.06	1.06	33881	2.53	2530.0
JD5 – ID6	85	1.05	1.05	37509	2.69	2690.1
JD6 – ID4	85	1.09	1.09	37509	2.69	2690.1

Table 24: Reinforcing and Structural Steel Tensile Characteristics

Property	Reinforcing Steel	Structural Steel
Yield stress, f_y (N/mm^2)	460	275
Strain at yield, ε_y	0.0022	0.0015
Young's Modulus, E_s (N/mm^2)	210000	183000
Ultimate strength, f_u (N/mm^2)	610	440
Strain at ultimate, ε_u	0.072	0.137
Post-yield stiffness, E_{spy} (N/mm^2)	3410	1190

Table 25: Cross-Section Strip Details

Element Number	Constituent Material	D_n (mm)	Steel Area, A_n (mm^2)	Concrete Area, A_n (mm^2)	x_n (mm)	$(D/2) - x_n$ (mm)
1	C.Cover	9	0	2700	4.5	145.5
2	C.Cover	6	0	1800	12	138
6	C.R. & P.Conf.	6	170	1630	36	114
7	C.R. & P.Conf.	6	170	1460	42	108
8	P.Conf.	1.7	0	510	45.85	104.15
9	P.Conf.	1.7	0	510	47.55	102.45
10	C.F. & P.Conf.	0.5	101.8	48.2	48.65	101.35
11	C.F. & P.Conf.	0.5	101.8	48.2	49.15	100.85
32	H.C.C. & S.W.	4.6	34.96	1345.04	61.7	88.3
33	H.C.C. & S.W.	4	30.4	1169.6	66	84
75	H.C.C. & S.W.	4	30.4	1169.6	234	84
76	H.C.C. & S.W.	4.6	34.96	1345.04	238.3	88.3
97	T.F. & P.Conf.	0.5	101.8	48.2	250.85	100.85
98	T.F. & P.Conf.	0.5	101.8	48.2	251.35	101.35
99	P.Conf.	1.7	0	510	252.45	102.45
100	P.Conf.	1.7	0	510	254.25	104.15
101	T.R. & P.Conf.	6	170	1460	258	108
102	T.R. & P.Conf	6	170	1630	264	114
106	T.Cover	6	0	1800	288	138
107	T.Cover	9	0	2700	295.5	145.5

The notation used in Table 25 are as follows:

C.Cover, T.Cover = Compression cover and tension Cover, respectively

C.R. = Compression reinforcement

P.Conf = Partially confined concrete

C.F. = Compression flange

H.C.C. = Highly confined concrete

S.W. = Steel web

T.F. = Tension flange

T.R. = Tension reinforcement

5.6.2 Moment-Displacement Response

This section describes in detail the step-by-step process by which the moment curvature response in converted into the moment-displacement response. The member is divided into 13 No. longitudinal elements and all plastic hinging is assumed to occur in the element adjoining the base section, thus all other elements are assumed to remain elastic. This is a major assumption and is not necessarily true as the plastic hinge length will vary in depth with an increase in moment. Furthermore, the base will provide additional confinement to the column just above base interface. A more detailed prediction of the plastic hinge length may improve the accuracy of the proposed numerical model. Figure 5.24 presents the column longitudinal and plastic hinge elements.

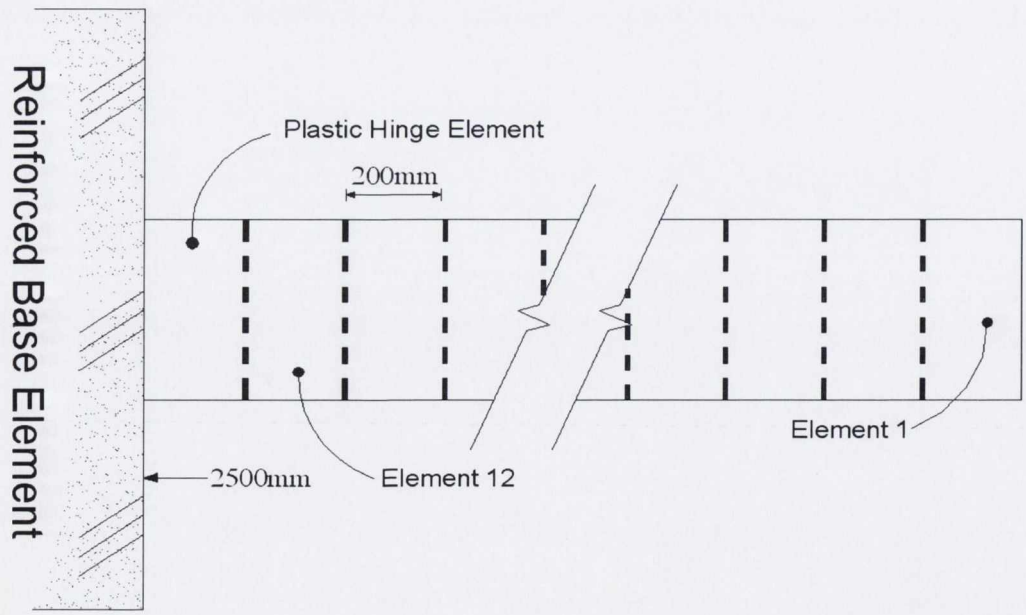

Figure 5.24: Column Divided into Longitudinal Elements

The moment-displacement response is determined as follows:

1. The moment curvature response is plotted using the procedure established in Sections 5.4 and 5.6.1.
2. A load is assumed to act laterally at the top of the specimen, as illustrated in Figure 5.23(a). For this load value the moment is calculated in each longitudinal element, with the exception of the plastic hinge element, thus providing a moment profile, (Figure 5.23 (b)).
3. For any element the corresponding curvature can be read from the moment-curvature profile to provide a curvature profile.
4. Assuming the h-value of Equation (5.104) as zero and that any plastic deformation occurs only in the plastic hinge element, Equation (5.104) becomes:

$$\Delta_T = \int_0^{x=2300} \int m_1 x \, \delta x + \int_{x=2300}^{x=2550} \int m_2 (x - 2300) \, \delta x \qquad (5.105)$$

Where:

Δ_T = Total column displacement

m_1 = Slope of curvature profile from column tip up to (but not including) plastic hinge element.

m_2 = Slope of curvature profile over the plastic hinge element.

The value m_2 is equal to the curvature gradient occurring over the plastic hinge element:

$$m_2 = \frac{\emptyset_{13} - \emptyset_{12}}{200} \qquad (5.106)$$

Where:

$\emptyset_{12}$ = Curvature from extreme top fibre of plastic hinge element to column tip (mm^{-1}), from curvature profile

$\emptyset_{13}$ = Curvature in plastic hinge element (mm^{-1})

200 = length of individual longitudinal element.

Hence, substituting Equation (5.106) into Equation (5.105), the curvature value of $\emptyset_{13}$ can be determined.

5. The moment corresponding to the curvature value ϕ_{13} is determined from the moment-curvature response. If this results in a different load acting on the beam as that assumed in step 2 a different load is assumed and an iterative process initiated until both loads converge (i.e. steps 2 to 5 repeated until both loads converge).

6. The moment displacement response is plotted.

5.6.3 Strain Energy and Strain in Transverse Steel

In order to compare the displacement capacity of the specimens, the strain energy and strains at failure are predicted using the procedure established in Section 5.3.4. It is evident from the experimental data that all specimens yield between the 30 and 60mm displacement cycle, thus for modelling purposes the specimens are assumed not to have yielded before or during the 30mm displacement cycle, but yield just after this displacement. The strain energy and strains are determined as follows:

The strain energy of the transverse steel (U_{sl}) for the peak moment of any displacement cycle is determined using Equation (5.40). The cover strain value ε_{sp} is assumed to be 0.002 and 0.0024 (for NSC and HSC, respectively) as this is the strain corresponding to peak unconfined concrete stress. It is assumed, for computational simplicity, that beyond this strain, the concrete loses strength instantaneously, also on load reversal the cover concrete in tension becomes cracked and loses its load carrying capacity. The strain energies are converted to strain values as follows:

Elastic Cycles (30mm Displacement)

For these cycles, the term on the left-hand side of Equation (5.40) becomes:

$$\int_0^{\varepsilon_s} f_s \, \delta\varepsilon_s = \int_0^{\varepsilon_s} E_s \varepsilon_s \, \delta\varepsilon_s = U_{sl} \tag{5.107}$$

Where:

U_{sl} = Strain energy in the link at the respective cycle (MJ/m^3)

With the exception of ε_s, all the parameters in Equation (5.107) are known, hence ε_s may be calculated.

Inelastic Cycles (60 – 120mm Displacements)

For the 60 – 120mm displacement cycles, the term on the left-hand side of Equation (5.40) becomes:

$$\int_0^{\varepsilon_s} f_s \, \delta\varepsilon_s = \int_0^{0.0022} E_s \varepsilon_s \, \delta\varepsilon_s + \int_{0.0022}^{\varepsilon_s} \left(0.0022 E_s + E_{spy}(\varepsilon_s - 0.0022)\right) \delta\varepsilon_s = U_{sl} \tag{5.108}$$

Again, with the exception of ε_s, all the parameters in Equation (5.108) are known, hence ε_s may be calculated.

5.7 Summary

This chapter describes a theory and implementation procedures for the prediction of the moment-displacement response of the composite columns considered in this research. A method is presented through which the strain energy and strain in the transverse steel may be predicted leading to the calculation of the ultimate deformation capacity. Chapter 6 presents the response of the column specimens predicted using these methods, and a comparison with the experimental results. The predicted strains in the transverse steel at failure are also presented.

Chapter 6

Model Predictions

Model Predictions

6.1 Introduction

This chapter presents the moment-curvature and moment displacement predictions using the model developed in Chapter 5. The model predictions are compared with the test results presented in Chapter 4.

Section 6.2 presents the predicted moment-curvature response and predicted curvature for a given neutral axis depth. Section 6.3 presents the moment-displacement response based on the procedure set out in Section 5.6.2. A parametric analysis of an identical section with a $40N/mm^2$ unconfined concrete strength is conducted in Section 6.4, the purpose of which is to determine if the model is capable of predicting variations in the moment-displacement response due to minor changes in the design and loading parameters. The predicted failure strains and strain energies are discussed in Section 6.5, followed by some conclusions in Section 6.6.

6.2 Moment-Curvature Response

The predicted moment-curvature responses of the test specimens are presented in Figure 6.1 to Figure 6.4. The moment-curvature response was determined using the defined stress strain models described in Chapter 5. Only four moment-curvature responses are presented as specimen pairs JD1 and JD2 and JD5 and JD6 have the same predicted response. The actual concrete strength during testing varies between these specimens but an exact non-destructive in-situ concrete strength is impossible to determine (as the sample concrete cubes were cured under optimum conditions), thus it is viable to assume

both have a similar concrete strength and use a moment-curvature response based on a characteristic concrete strength value.

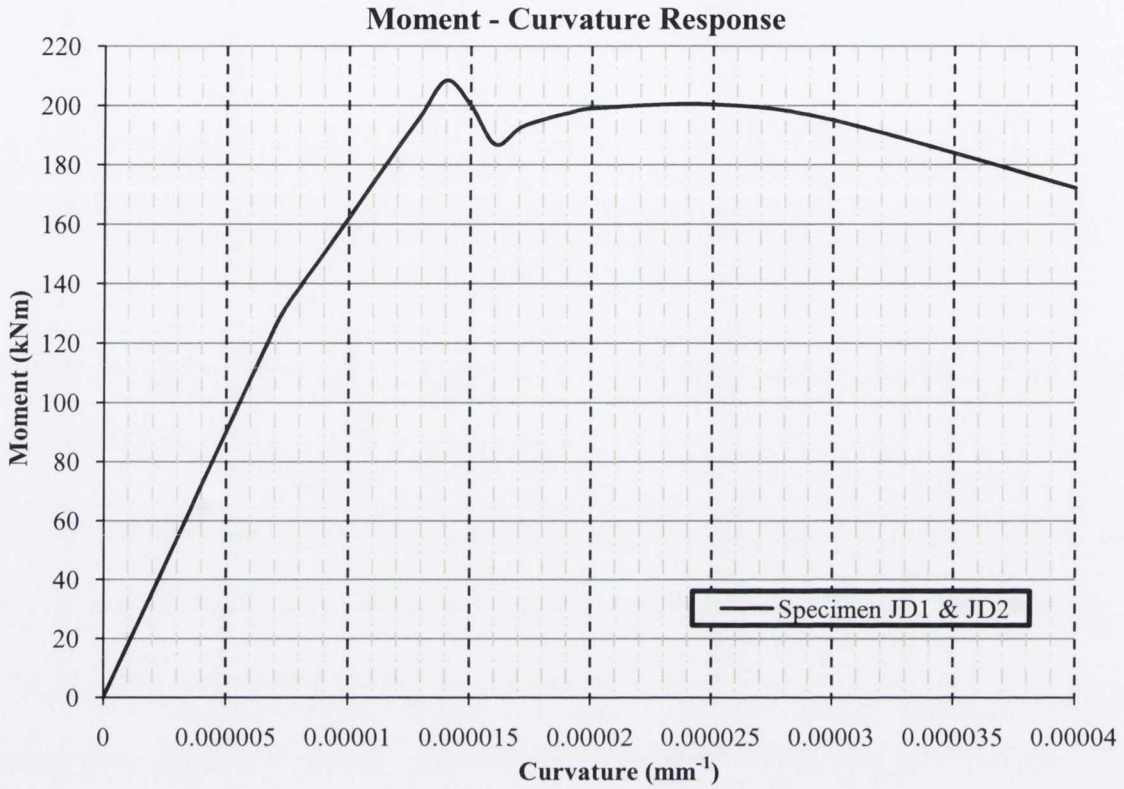

Figure 6.1: Predicted Moment Curvature Response, Specimens JD1 & JD2

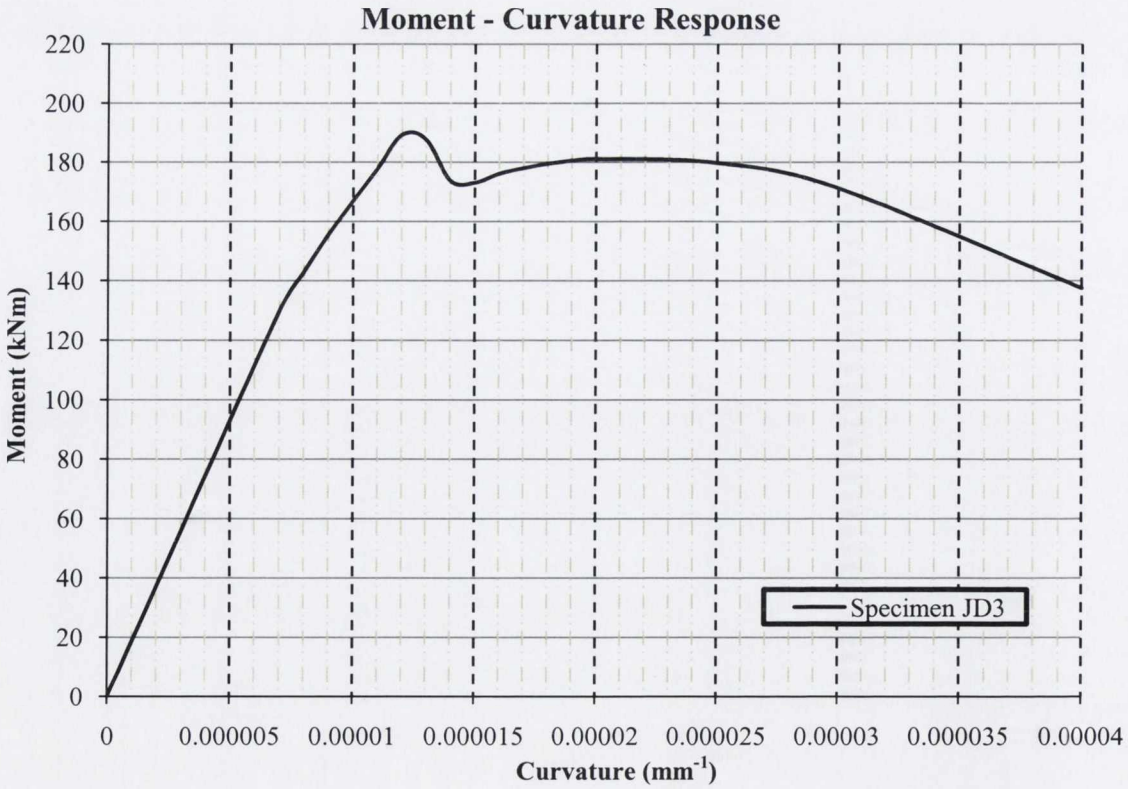

Figure 6.2: Predicted Moment Curvature Response, Specimen JD3

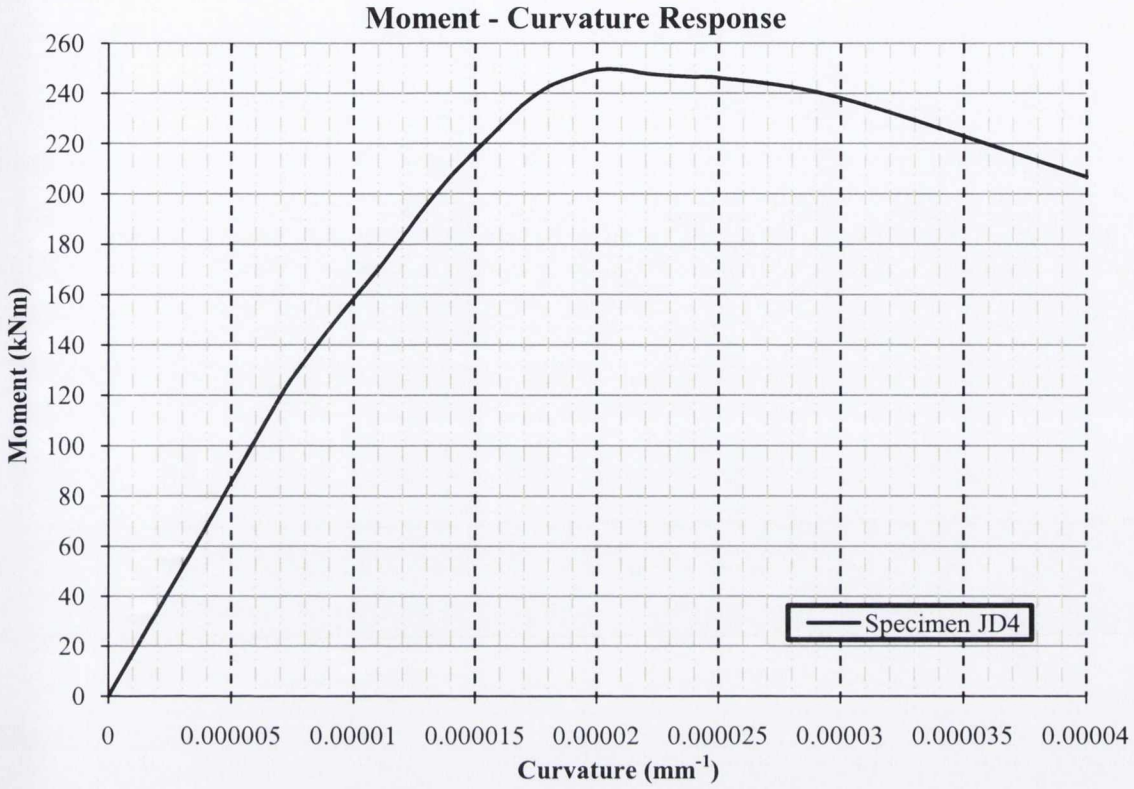

Figure 6.3: Predicted Moment Curvature Response, Specimen JD4

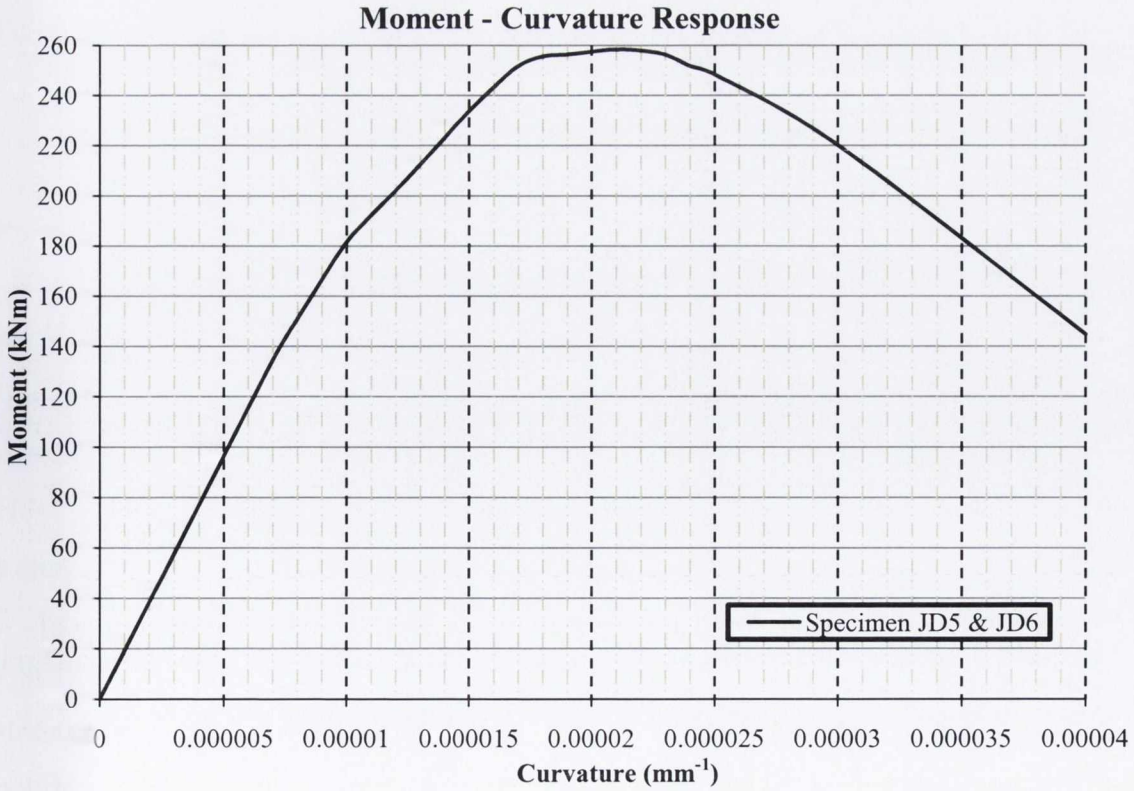

Figure 6.4: Predicted Moment Curvature Response, Specimens JD5 & JD6

Figure 6.5 and Figure 6.6 present the general moment curvature shapes displayed the NSC and HSC specimens, respectively. The specimens display similar characteristics but some obvious difference appear due to the different concrete stress-strain model used for the HSC specimens and the high levels of axial load applied. Critical points on these curves are marked and discussed individually.

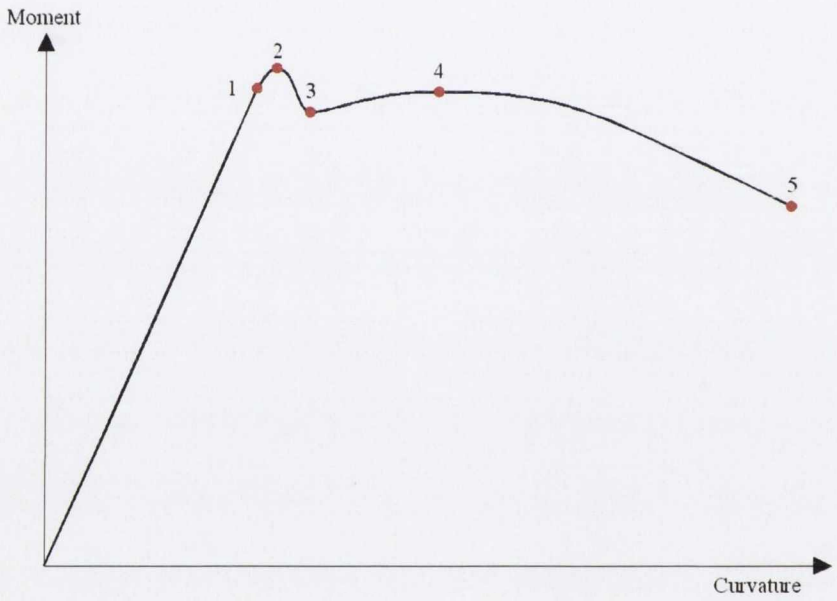

Figure 6.5: Moment Curvature Response, Shape 1 - NSC

Shape 1: NSC Specimens

Point 1: Compression cover concrete reaches its peak stress, thus leading to the onset of non-linear behaviour

Point 2: Structural steel section yields in compression and plateaus.

Point 3: Compression cover loses its strength and spalls off.

Point 4: Peak post-yield moment is reached, reduction in resistance of structural steel and longitudinal bars in compression.

Point 5: Moment of resistance is lost beyond this point.

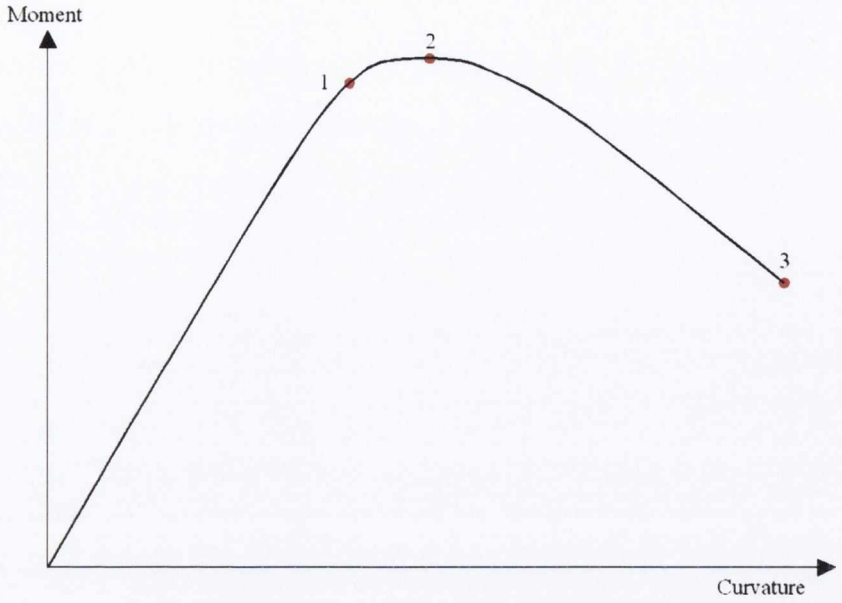

Figure 6.6: Moment Curvature Response, Shape 2 - HSC

Shape 2: HSC Specimens

Point 1: Yield of longitudinal bar in compression, plateau of structural steel in compression and spalling of compression cover.

Point 2: Peak moment is reached, reduction in resistance of structural steel and longitudinal bar in compression, and yielding of structural steel in tension is recorded beyond this point.

Point 3: Moment of resistance is lost beyond this point.

All of the predicted moment-curvature relationships behave in a linear-like manner up to 'Point1'. At 'Point 1' the compression cover reaches its peak stress for the NSC specimens and initial yielding of the longitudinal and structural steel is recorded for the HSC specimens. Beyond this, strength degradation of the cover concrete is recorded and a strength plateau is formed for the structural steel. The peak moment is reached at 'Point 2', beyond which the cover concrete is assumed to spall for the NSC specimens. For the HSC curves, a steady drop in resistance is recorded from 'Point 2' to 'Point 3' as the structural and longitudinal steel experience drops in resistance due to the loss in confinement.

The reduction in resistance is more pronounced for the specimens with higher axial loads, as they are required to withstand greater P – Δ moments due to the increased axial load level. The NSC curves experience a moment increase up to 'Point 4' due to the plateau of the structural steel combined with the post-yield strain hardening strength increase of the longitudinal steel in tension. Beyond 'Point 4' the structural and longitudinal steel in compression experience a reduction in resistance up to 'Point 5'. As with the HSC curves, the NSC curves experience a sharper reduction in resistance when subject to an increased axial load level.

The specimens subjected to higher axial load levels enter the non-linear response marginally before specimens with lower axial load levels, as material yield stresses are reached at lower curvatures. Beyond 'Point 5' and 'Point 3' (for the normal and high-strength curves, respectively) the moment resistance is lost.

Figure 6.7 to Figure 6.10 present the predicted variation in neutral axis depth with curvature. All curves bear distinct resemblance to an inverted moment curvature plot for the same specimen. These plots illustrate that the neutral axis decreases up to the point where the section reaches its maximum moment. Beyond this the neutral axis increases again up to the point of loss of resistance. This is due to the fact that beyond the point of maximum resistance, the model predicts that the specimen will experience severe spall and deterioration of the core concrete, as well as a reduction in the resistance of the steel elements in compression. If the core concrete loses its resistance capabilities, the neutral axis will have to increase in depth from the extreme compression fibre to enable the remaining core concrete and steel elements to resist the applied loads.

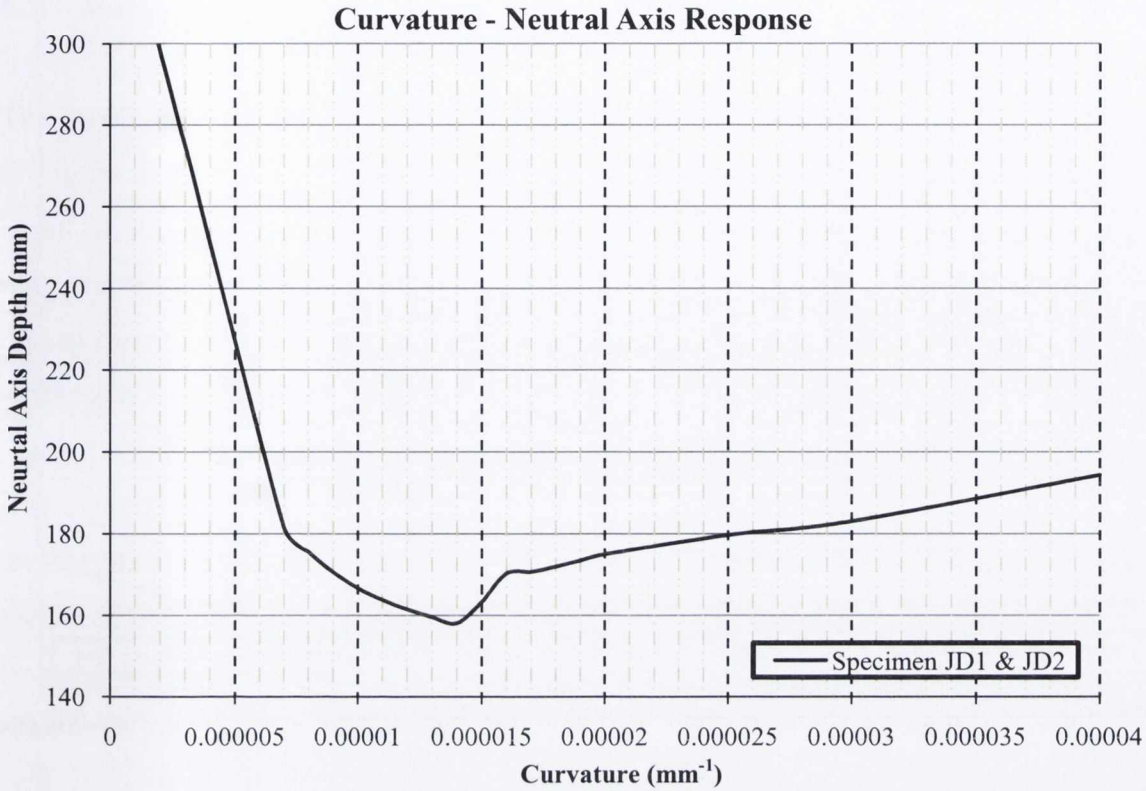

Figure 6.7: Neutral Axis Depth Variation with Curvature Response, Specimens JD1 & JD2

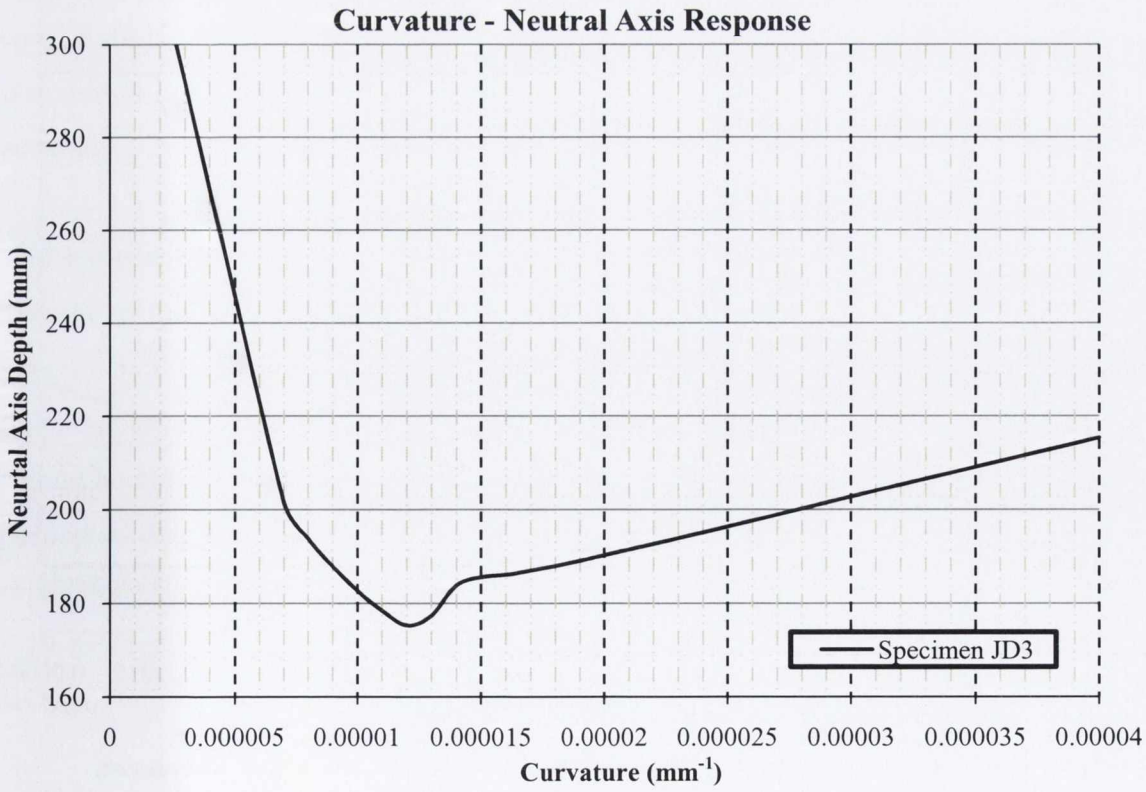

Figure 6.8: Neutral Axis Depth Variation with Curvature Response, Specimen JD3

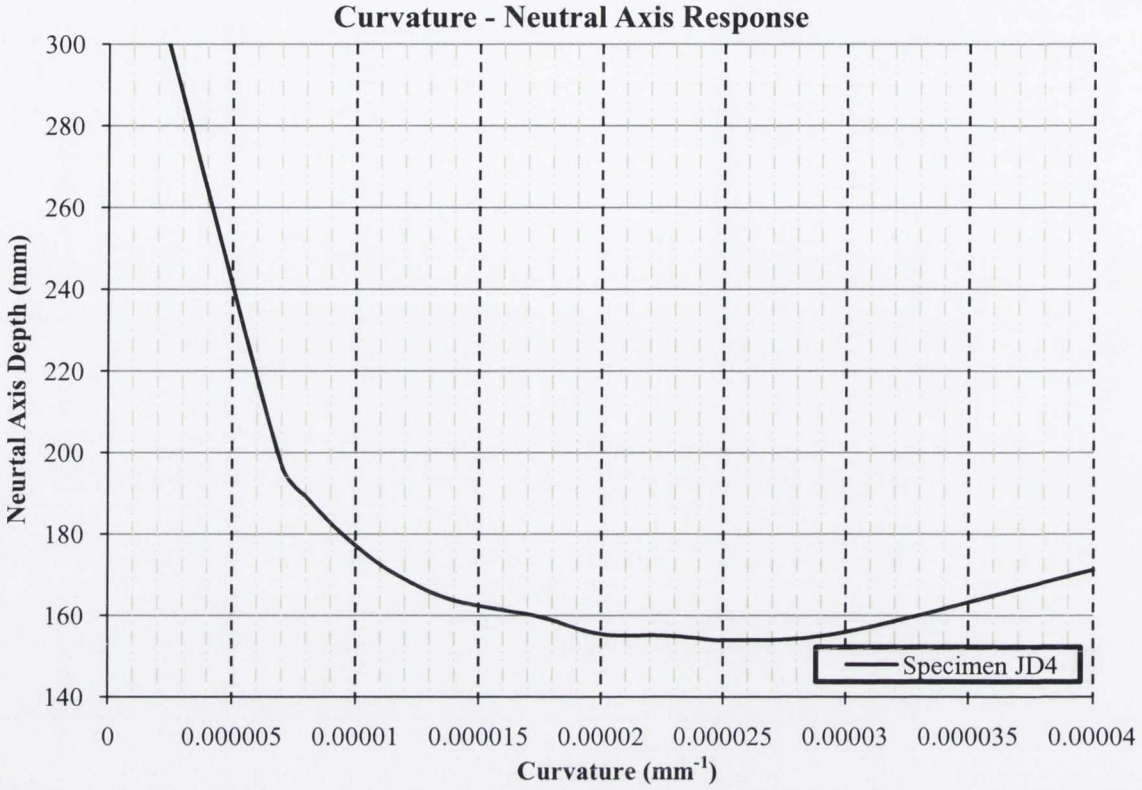

Figure 6.9: Neutral Axis Depth Variation with Curvature Response, Specimen JD4

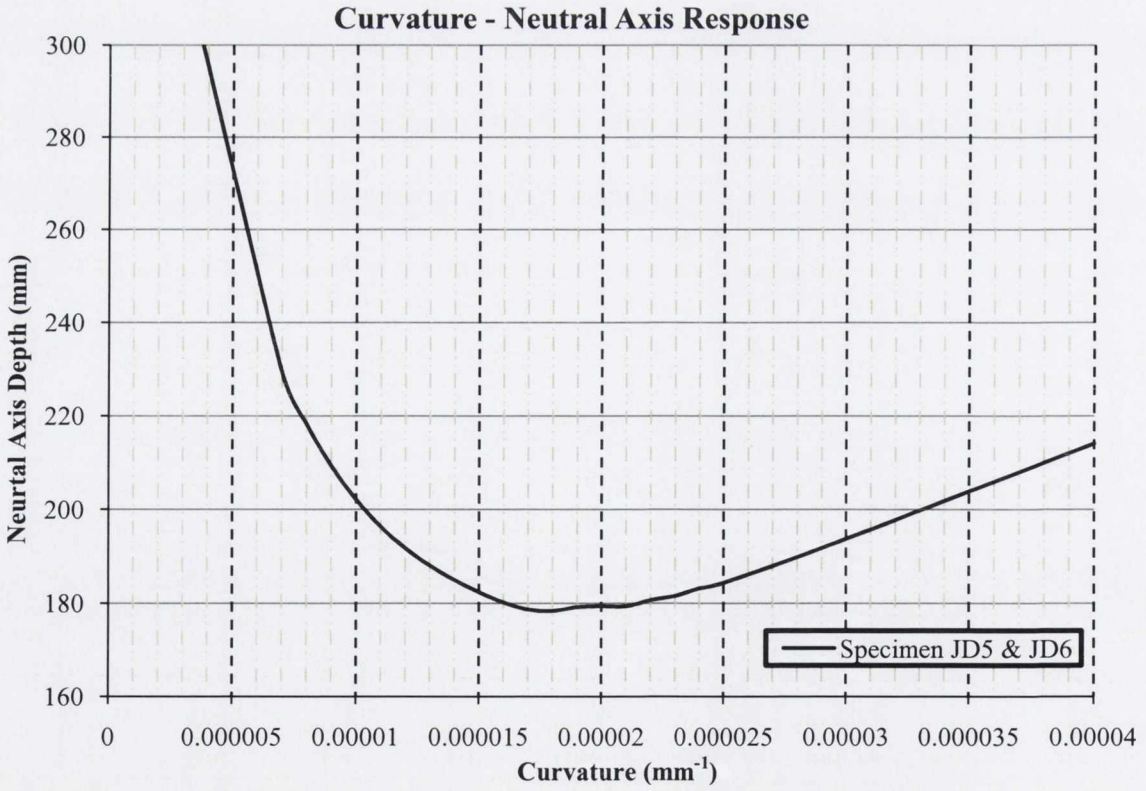

Figure 6.10: Neutral Axis Depth Variation with Curvature Response, Specimens JD5 & JD6

6.3 Moment-Displacement Response

The moment-displacement responses for the six specimens are presented in Figure 6.11 to Figure 6.16. The experimental curves presented in these graphs are envelope curves based on the maximum load achieved during a particular displacement cycle. Table 26 presents the ratio of the experimental to predicted analytical moments for each displacement cycle; the ratio of the predicted initial stiffness to the experimental initial stiffness is also presented.

It is evident from the moment-displacement response and the values presented in Table 26 that the analytical model predicts the sections performance reasonably well. The pre yield and initial stiffness values display are overestimated by the analytical model for all specimens. The post yield performance shows good correlation, especially for the NSC specimens and HSC specimens with low levels of axial load.

The quicker stiffness degradation and deterioration of the core concrete under the higher axial load levels is considerably more difficult to model. The concrete models were developed to predict the response of concrete under monotonic compression, not a combination of lateral cyclic and axial loading. The sudden deterioration of the cover concrete is difficult to model and is the primary reason for variation in the modelling accuracy.

The experimental curves presented in Figure 6.11 to Figure 6.16 are based on the average of the maximum resistances recorded in each direction (i.e. push and pull). The experimental results for Specimen JD1 is based on the recorded values for the pull cycle only, due to the bi-axial buckling observed during this test (as discussed in Chapter 4). It should be noted that the variation in maximum resistance observed during each cycle at a particular displacement is not recorded in the experimental curves, thus the model predictions have been superimposed onto the load-deflection hysteresis plots in Figure 6.19 to Figure 6.24. The visual observations of these plots are discussed later in the section.

The numerical model has been developed to predict the lateral load-displacement response of the section; the results can easily be converted to include $P - \Delta$ effects by

adding to the bending moment due to the eccentricity of the axial load during lateral loading. Section 3.2.7.3 described the process and formulae to predict this additional moment.

Fifteen of the seventeen predicted post-yield moment capacity values are within 10% of their corresponding experimental values, the two exceptions being the ultimate displacement of JD5 and the 60mm displacement of JD6. The case of Specimen JD5 shows that it is very difficult to predict the load-displacement response of a specimen at its ultimate displacement due to the rapid deterioration of the core elements. The model underestimates the maximum lateral resistance of the HSC specimens subject to high levels of axial load, as evident from the load-deflection plots for Specimen JD5 and JD6 (Figure 6.23 and Figure 6.24, respectively). The analytical model predicts that the cover concrete spalled prior to reaching the 60mm displacement cycle, thus it made no contribution to the specimen's resistance in subsequent model predictions.

However, from the visual observations presented in Section 4.3.1 it is clear that the cover concrete remained largely undamaged at this displacement, thus still contributing significantly to the moment of resistance of the section. Due to the depth of concrete cover (i.e. 40mm) and its distance from the neutral axis during loading, the additional contribution in moment resistance is significant, thus partially explaining the difference recorded between experimental and analytical values.

The brittle failure of the concrete produced a considerable reduction in the resistance recorded in load-deflection hysteresis plot for specimens JD5 and JD6. Beyond 60mm displacement cycle (for Specimen JD6) the experimental values coincide with good accuracy (within 10%) to the predicted model values. If each specimen was to be subject to several intermediate displacement cycles the cover concrete would have spalled and the resistance would have been reduced, thus preventing the kink and sharp drop in resistance evident from the hysteresis plots. Figure 6.17 and Figure 6.18 present the experimental and model predictions with the peak resistance removed, similar to that expected if the cover concrete had spalled prior reaching the 60mm displacement cycle. The altered experimental to model ratios are also presented in Table 26.

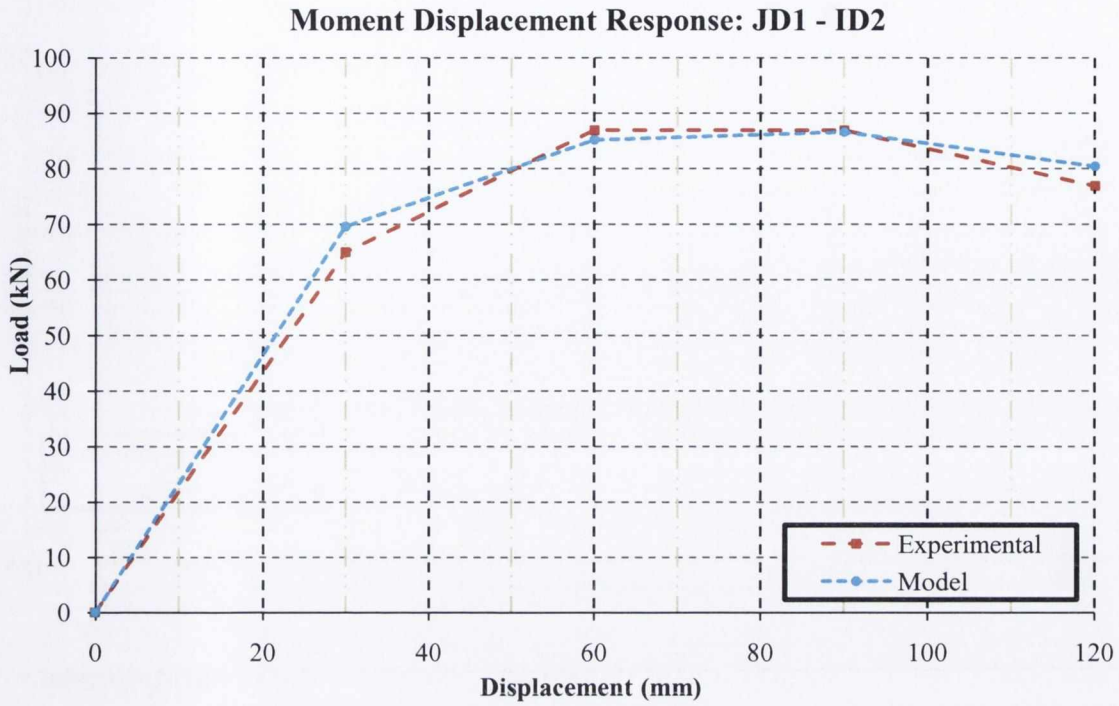

Figure 6.11: Experimental and Analytical Moment-Displacement Response, Specimen JD1 – ID2

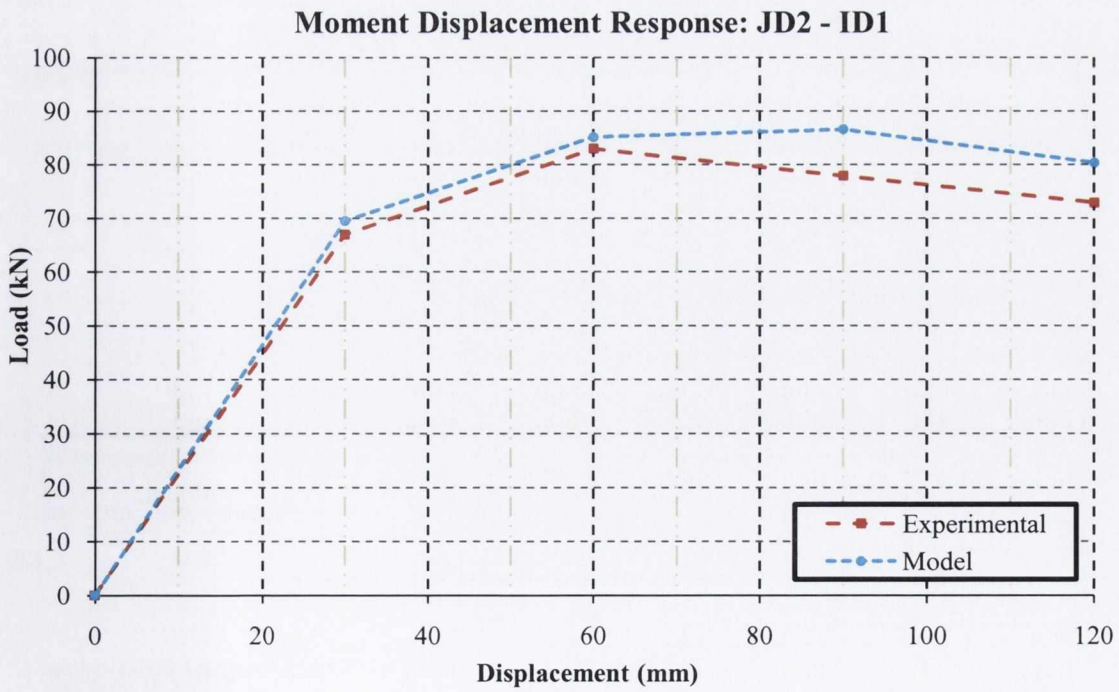

Figure 6.12: Experimental and Analytical Moment-Displacement Response, Specimen JD2 – ID1

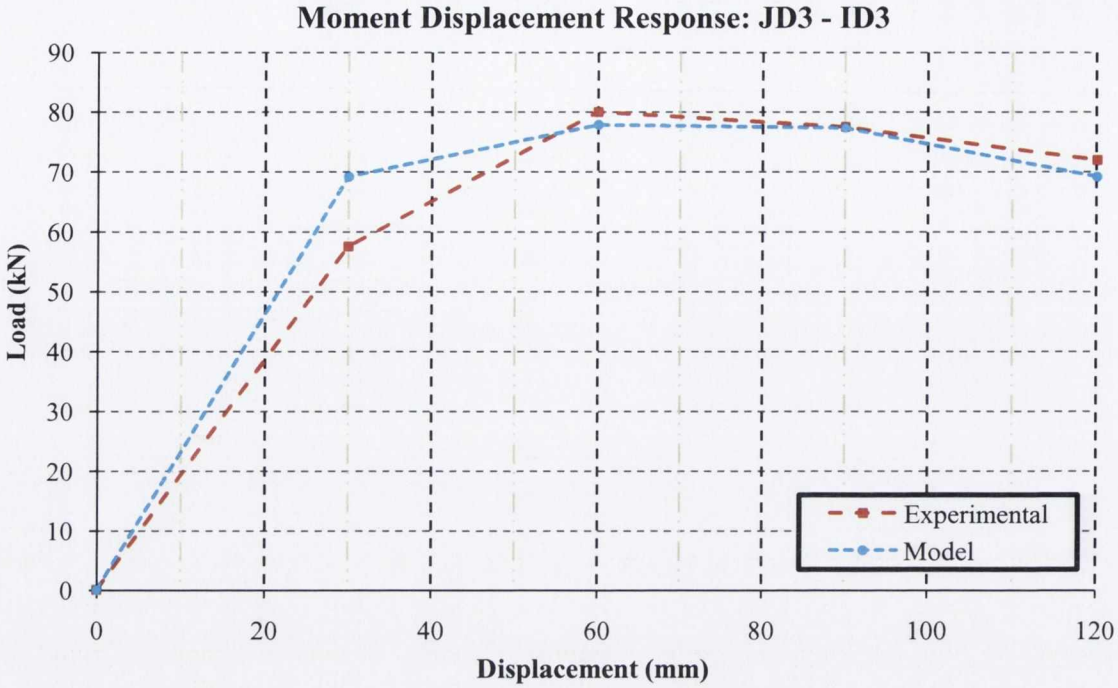

Figure 6.13: Experimental and Analytical Moment-Displacement Response, Specimen JD3 – ID3

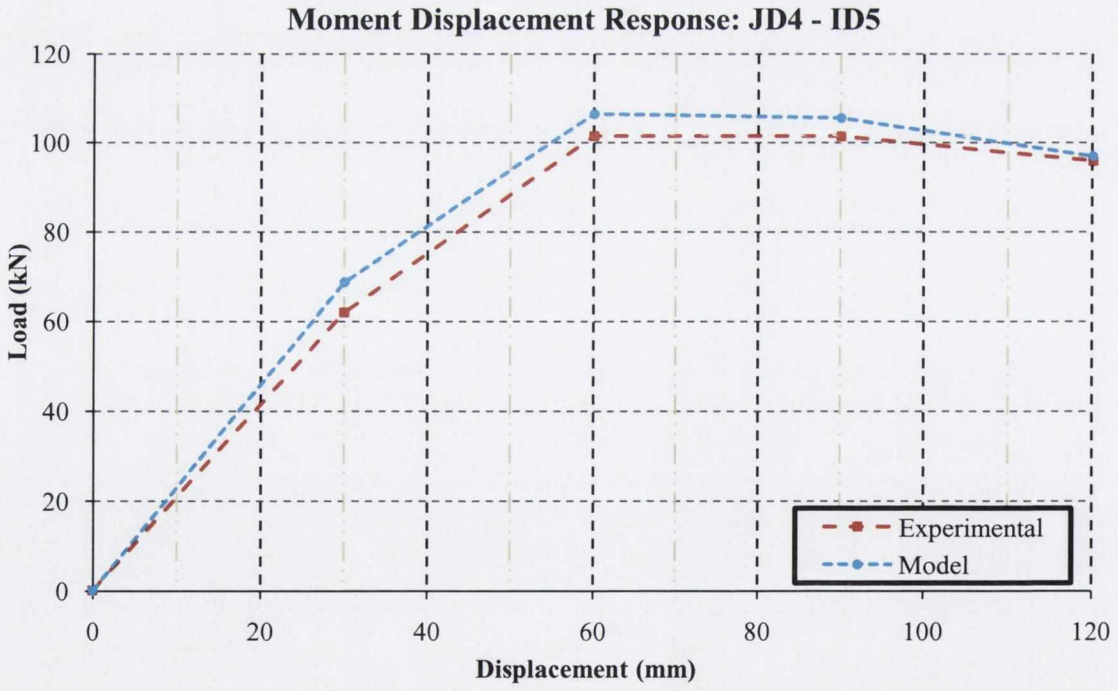

Figure 6.14: Experimental and Analytical Moment-Displacement Response, Specimen JD4 – ID5

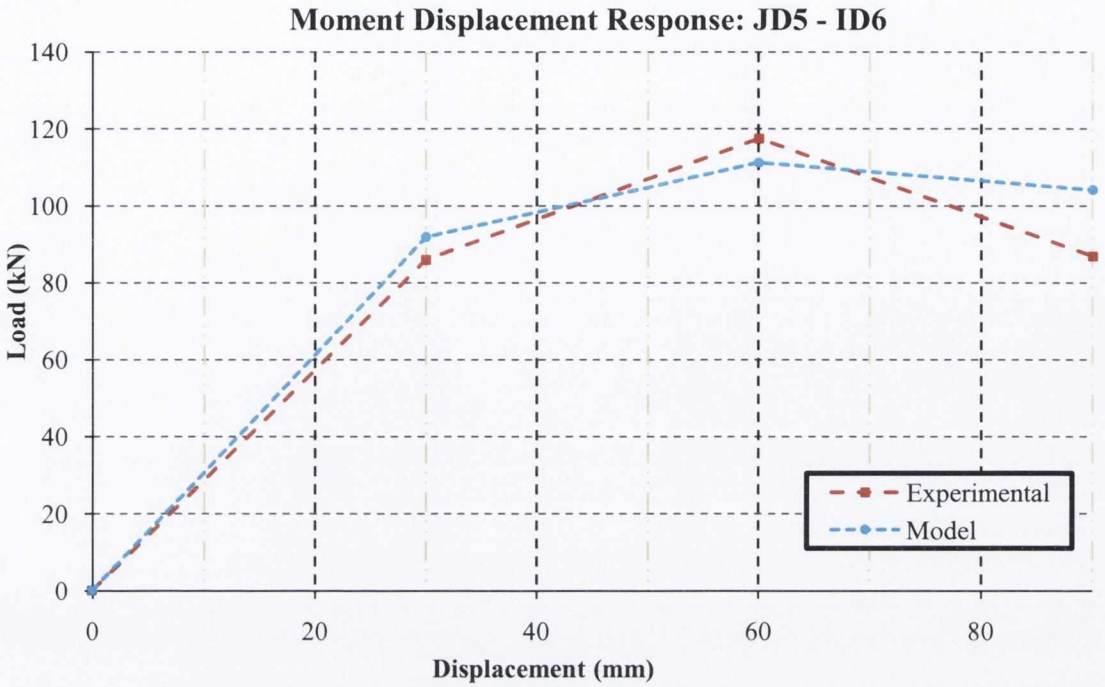

Figure 6.15: Experimental and Analytical Moment-Displacement Response, Specimen JD5 – ID6

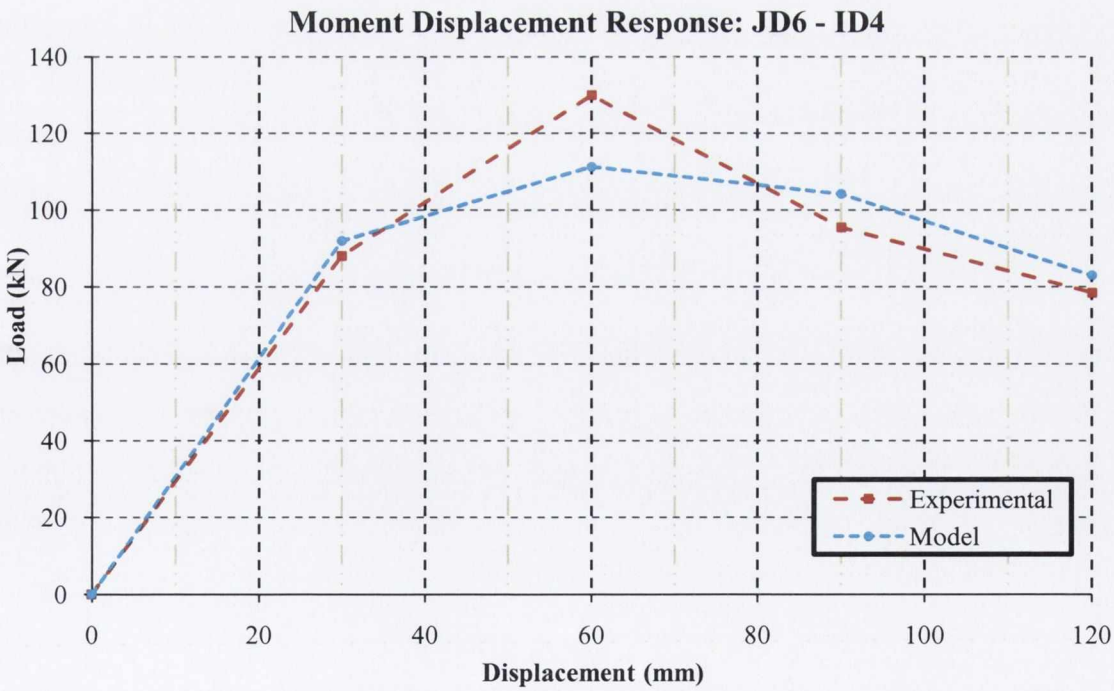

Figure 6.16: Experimental and Analytical Moment-Displacement Response, Specimen JD6 – ID4

Table 26: Model Accuracy: Percentage Error of Experimental to Analytical Moments.

	Displacement (mm)				
Specimen	**30**	**60**	**90**	**120**	**Initial Stiffness**
JD1 – ID2	6.60%	-2.06%	-0.36%	4.32%	10.36%
JD2 – ID1	5.88%	6.15%	9.45%	9.29%	15.53%
JD3 – ID3	16.84%	-2.81%	-0.21%	-4.05%	10.21%
JD4 – ID5	9.79%	4.66%	3.88%	1.02%	7.57%
JD5 – ID6	6.48%	-5.56%	16.56%	---	13.69%
JD6 – ID4	4.31%	-16.79%	8.41%	5.48%	21.03%
JD5 (altered)	6.48%	5.67%	16.56%	---	13.69%
JD6 (altered)	4.31%	5.67%	8.41%	5.48%	21.03%

Note: Negative values represent an under estimation of the analytical model compared with experimental values.

The initial stiffness errors presented in Table 26 vary between 7.6 and 21% of the observed experimental values. All analytical values overestimate the experimental values. The values are a reasonable estimation, the variation may be due to the material models adopted and the assumptions of the entire model, including that full interaction between the concrete and steel exists (due to the inclusion of shear connectors), this assumption in part may have created an idealised load displacement relationship compared with the actual specimen response, thus accounting for the variation in initial stiffness values recorded.

The values for JD5 and JD6 (altered) are based on the moment-displacement response curves presented in Figure 6.17 and Figure 6.18. The load-deflection hysteresis plots are presented to illustrate the complete model accuracy compared with the experimental values (Figure 6.19 to Figure 6.24). The superimposed red line represents the model predictions at each displacement.

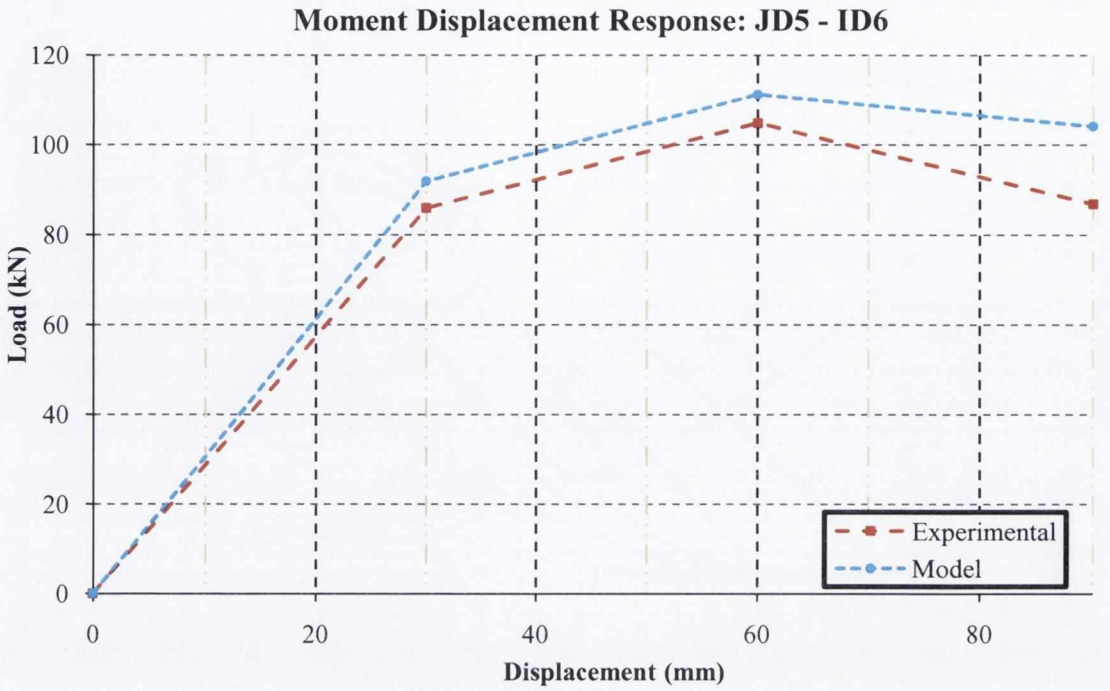

Figure 6.17: Alternative Experimental and Analytical Moment-Displacement Response, Specimen JD5 – ID6

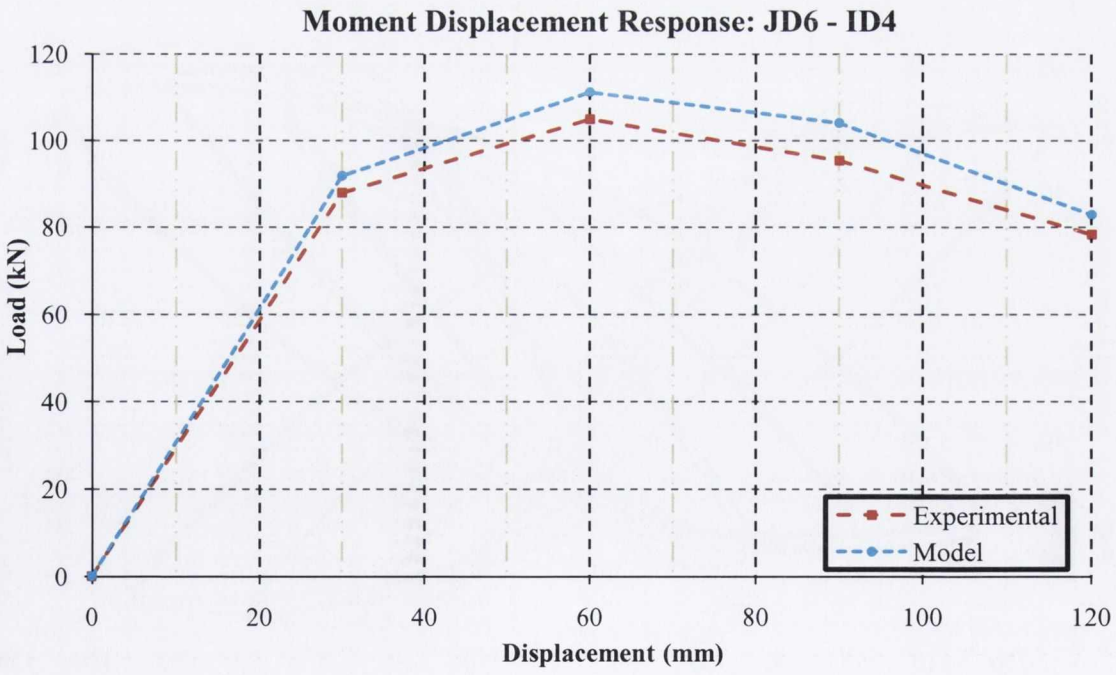

Figure 6.18: Alternative Experimental and Analytical Moment-Displacement Response, Specimen JD6 – ID4

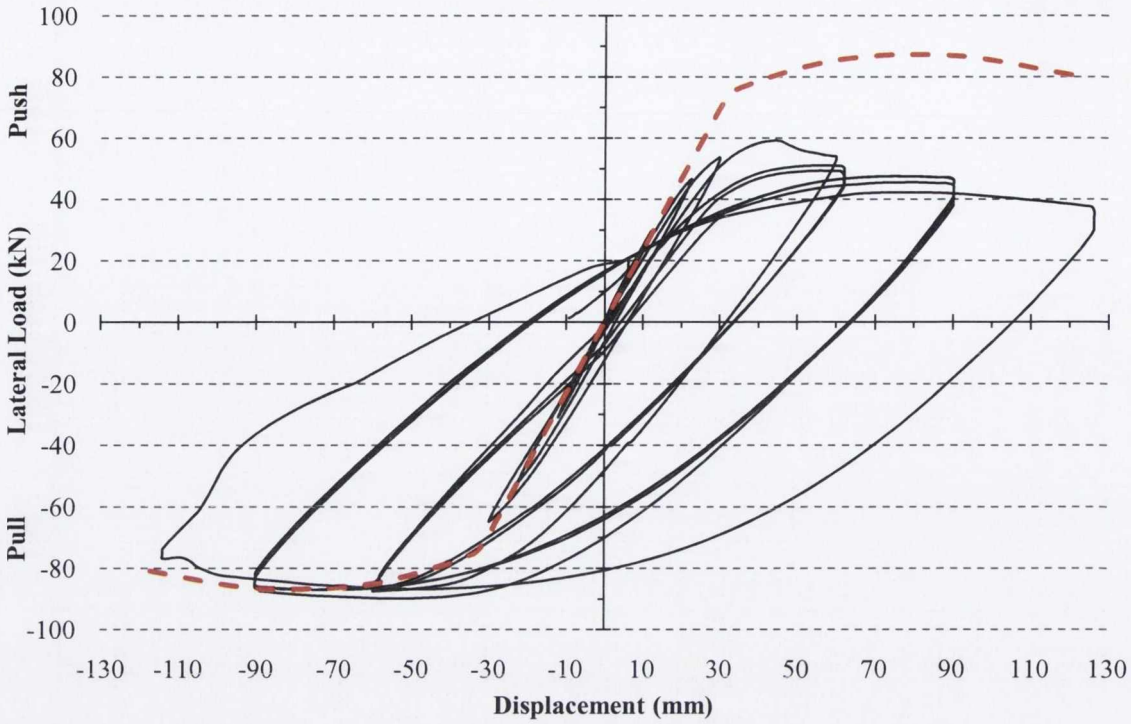

Figure 6.19: Hysteresis Plot and Model Predictions: Specimen JD1 – ID2

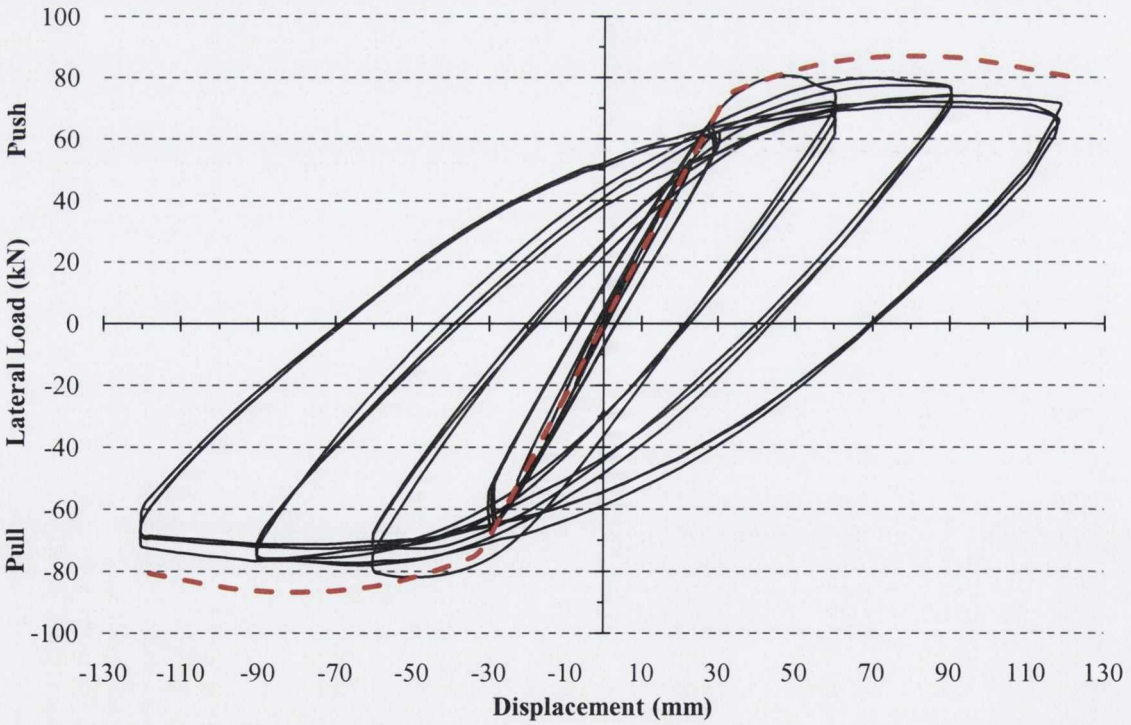

Figure 6.20: Hysteresis Plot and Model Predictions: Specimen JD2 – ID1

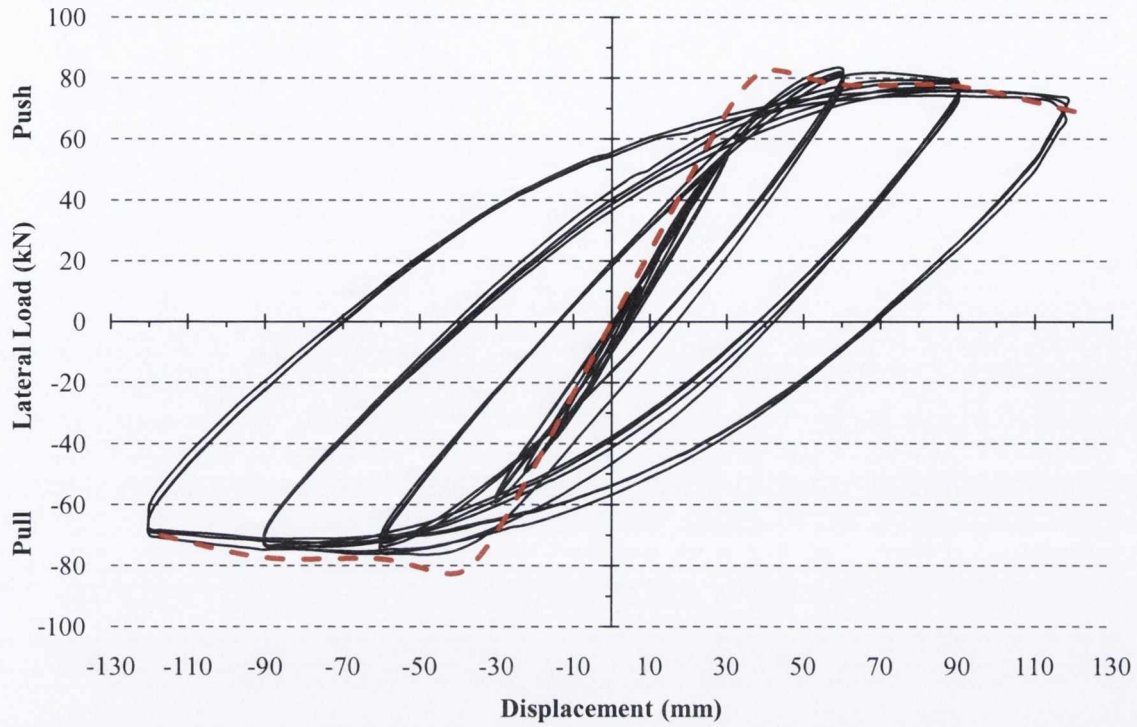

Figure 6.21: Hysteresis Plot and Model Predictions: Specimen JD3 – ID3

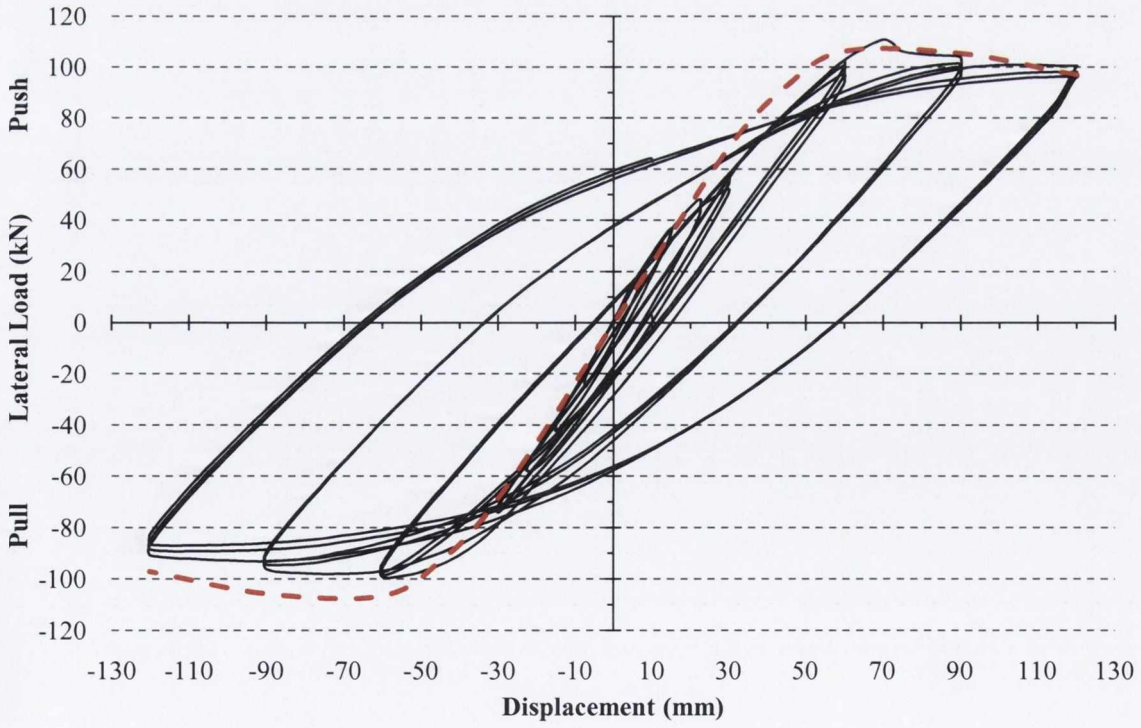

Figure 6.22: Hysteresis Plot and Model Predictions: Specimen JD4 – ID5

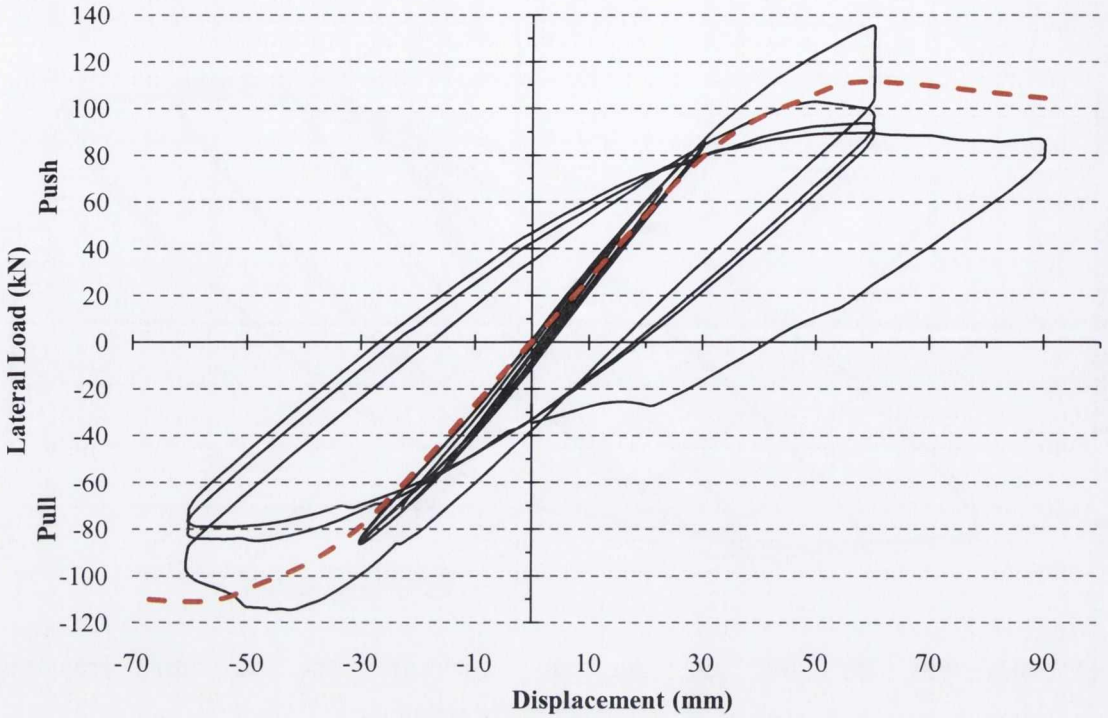

Figure 6.23: Hysteresis Plot and Model Predictions: Specimen JD5 – ID6

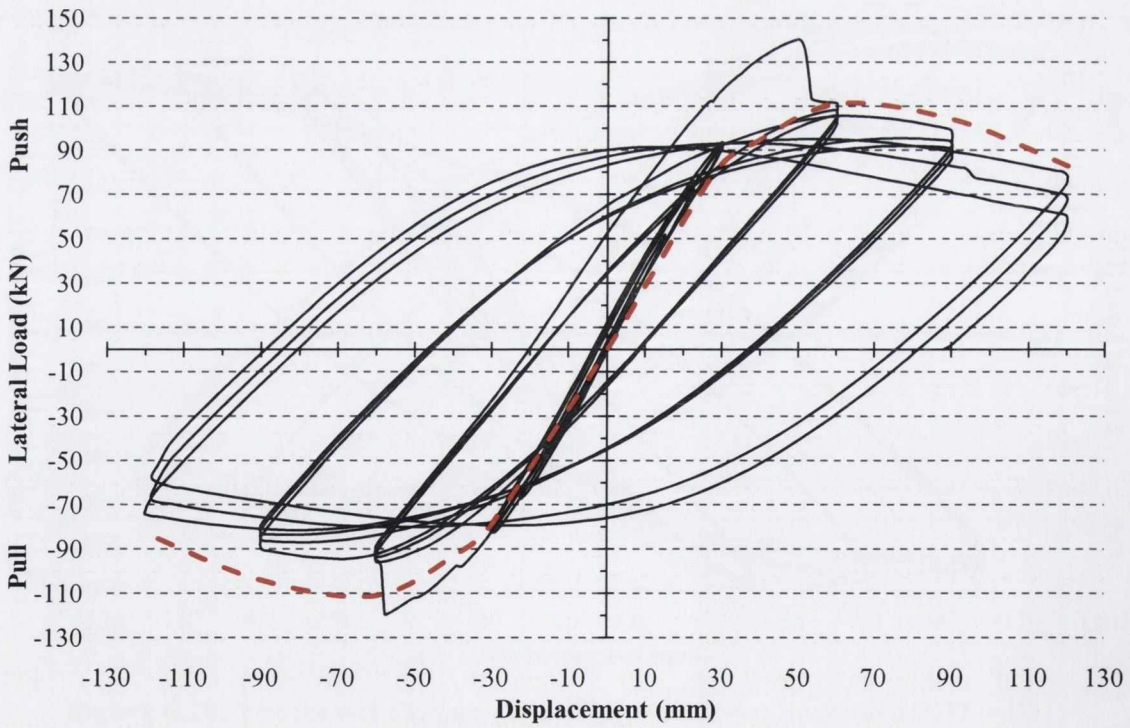

Figure 6.24: Hysteresis Plot and Model Predictions: Specimen JD6 – ID4

6.4 Parametric Analysis

This section sets out the results using the proposed model of a theoretical cross-section of identical specification to the tested specimens except incorporating an unconfined concrete compressive strength of 40N/mm^2. The purpose of this is to illustrate that the proposed model is sensitive enough to pick up small variations in the following parameters, namely; link spacing and axial load. The predicted moment-curvature response for an identical cross-section as described in Chapter 3 with the exception of an unconfined concrete compressive strength of 40N/mm^2 is presented in Figure 6.25. The variation in neutral axis depth with curvature plot is presented in Figure 6.26. Finally the predicted moment-displacement response is shown in Figure 6.27.

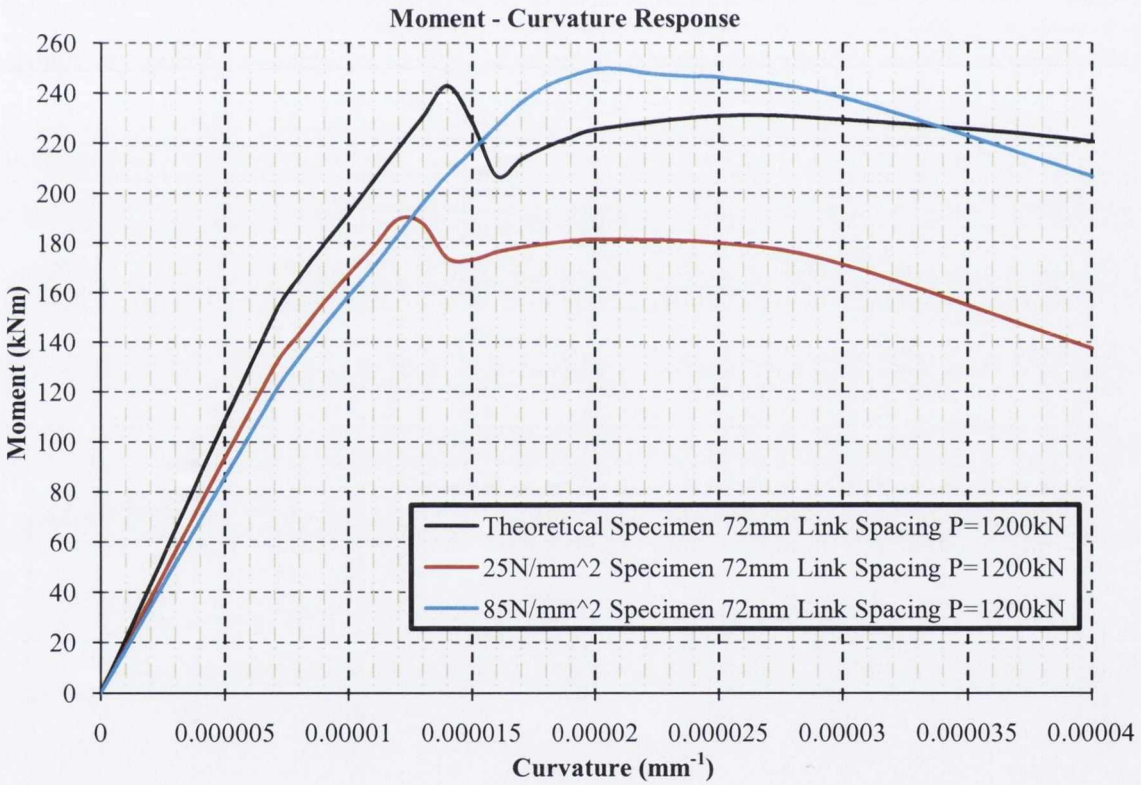

Figure 6.25: Predicted Moment Curvature Response, Theoretical Specimen

The moment curvature response in Figure 6.25 is similar to that of the other NSC moment-curvature responses. A steep initial slope is recorded up to the yield curvature followed by a sudden reduction in lateral resistance, thereafter a brief resistance gain is experienced before a reduction in resistance up to the strain corresponding to loss of resistance.

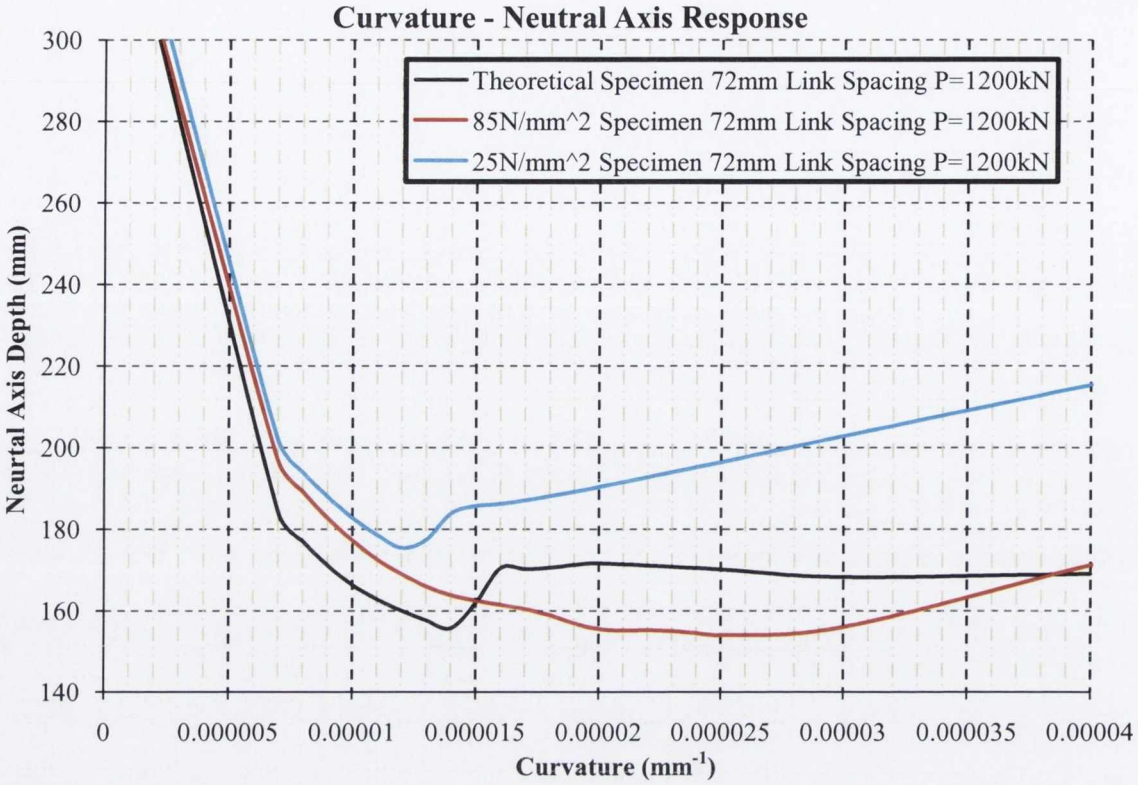

Figure 6.26: Neutral Axis Depth Variation with Curvature Response, Theoretical Specimen

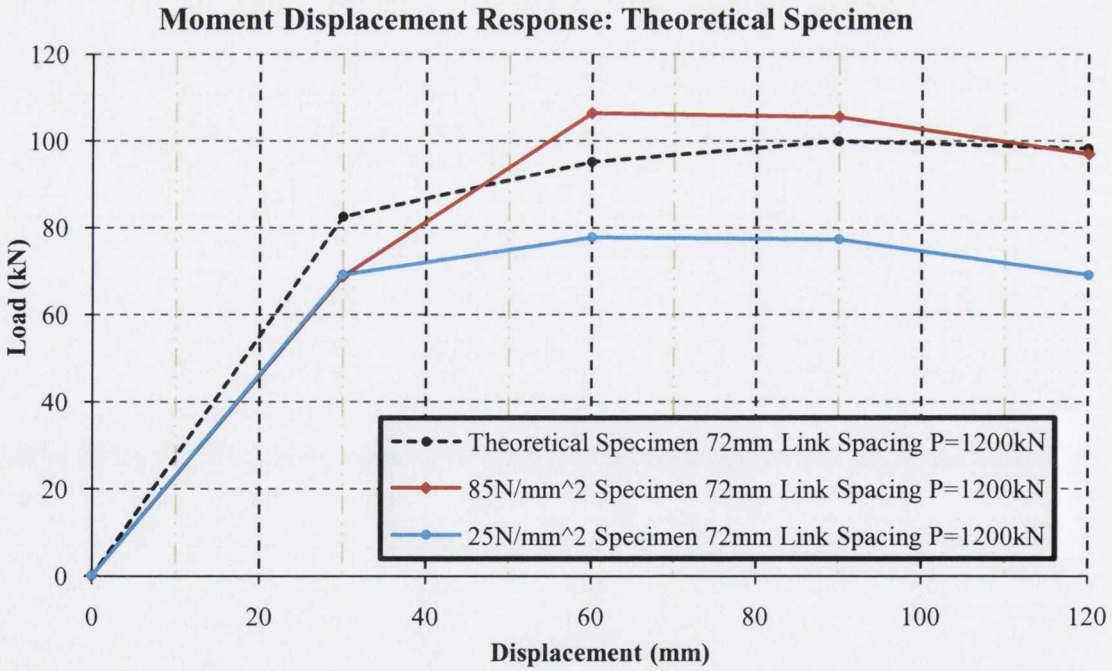

Figure 6.27: Analytical Moment-Displacement Response: Theoretical Specimen

Parameter Variations

Figure 6.28 presents the theoretical response of a identical specimen as described in Chapter 3, but with a few minor variations. Each specimen has one varying parameter, such as an increase in link spacing, a minor increase in axial load and a major increase in axial load. The variation in neutral axis depth with curvature is presented in Figure 6.29.

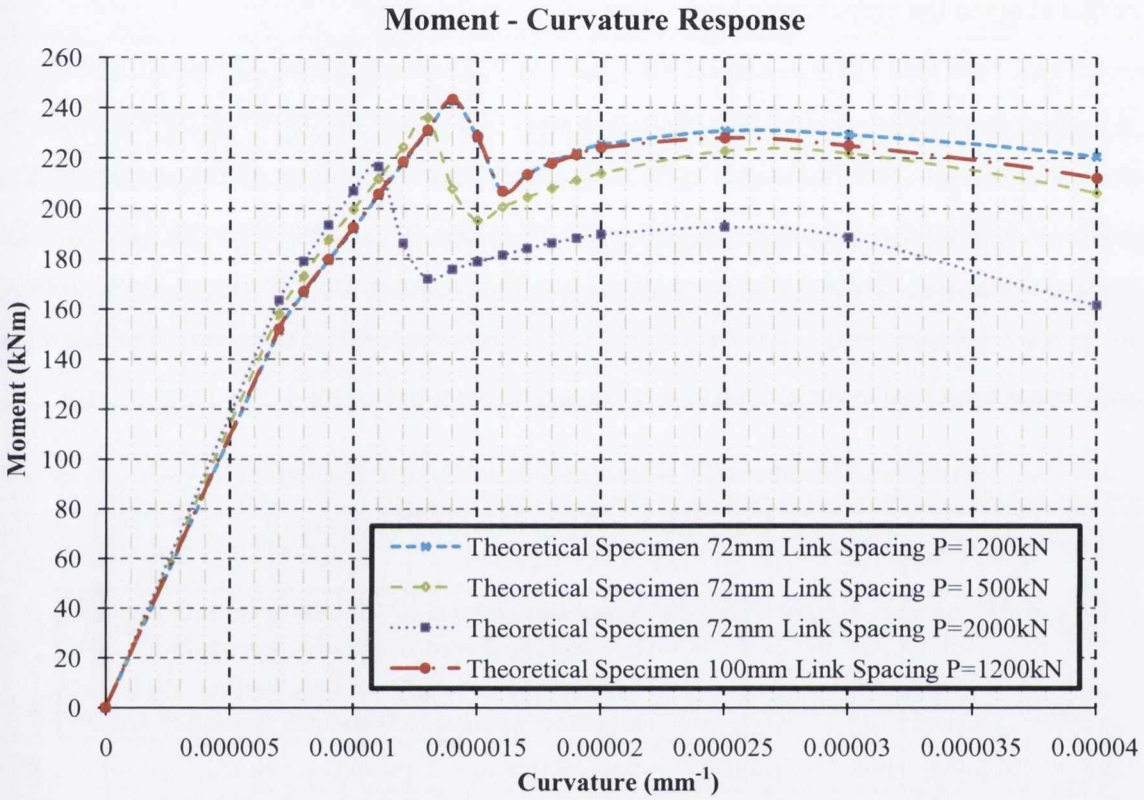

Figure 6.28: Predicted Moment Curvature Response, Varied Parameters

Little difference in the moment-curvature response is evident between specimens with identical axial loads but different link spacing. This is due to the limited area of partially confined concrete in the member's cross section as there is limited room between the transverse links and the steel section. The longitudinal and transverse steel provide the primary mechanism through which the partially confined concrete is confined, thus unless a large area of this concrete exists, little variation in the moment-curvature response will be evident unless a very large increase/decrease in link spacing is proposed. Be as it may, a minor variation exists between the two lines from a curvature of $2.0e^{-5}$ onwards. This illustrates that the proposed model is capable of predicting variations in the moment-curvature response from increased confinement levels due to a change in link spacing.

It should be noted that for specimens with similar axial load levels, little to no variation in the moment-curvature response will exist up to a curvature value of approximately $1.6.e^{-5}$. This lack of variation is due to the fact that the confined and unconfined concrete have not reached their maximum compressive stress at this curvature level, and thus the additional compressive strength gains due to improved confinement cannot be observed at this stage in the response.

It is clear from Figure 6.28 that a change in axial load level is effectively captured by the proposed model. The increased axial load level caused yielding of the specimen at a lower displacement than a specimen with an axial load equivalent to 1200kN. An increase in initial stiffness is also recorded for an increased axial load level. An increase in initial stiffness was also recorded in the experimental programme for identical specimens with higher axial load levels, as can be seen in Figure 4.31.

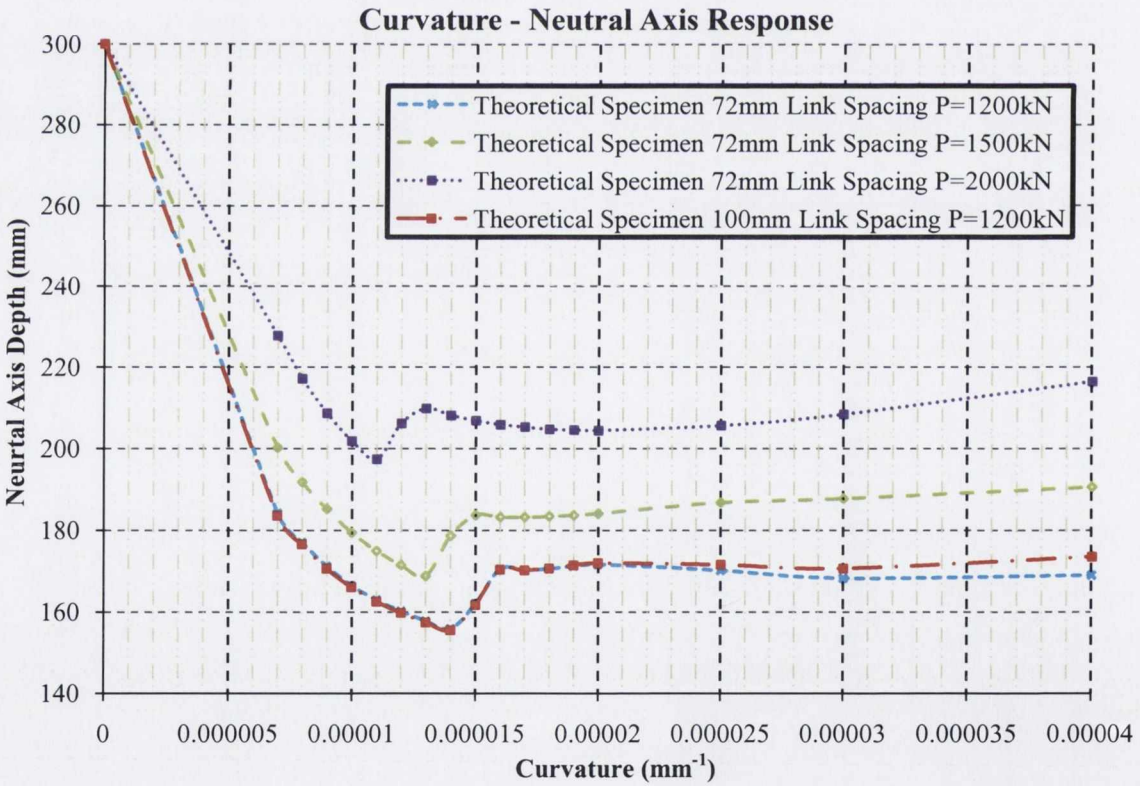

Figure 6.29: Neutral Axis Depth Variation with Curvature Response, Varied Parameters

The predicted moment-displacement responses of the theoretical specimens are presented in Figure 6.30. It is clear that little variation in the moment-displacement

response exists for specimens with varied link spacing and minor changes in axial load levels. It has already been determined that the minimal area of partially confined concrete will lead to little variation between specimens with varied link spacing. To determine why little variation exists in the moment-displacement response due to a minor change in axial load level the M-N interaction curve for this specimen must be analysed, which is presented in Figure 6.31.

The M-N interaction curve illustrates that even with an increase in axial load level from 1200kN to 1500kN, the specimen is expected to achieve a similar maximum moment, thus illustrating why a similar pre-yield response is recorded. If the specimens were subjected to increased displacements the two responses would diverge as the increased axial load would cause the concrete core to degrade at a faster rate. An initial divergence is illustrated in Figure 6.30 for these two specimens at displacements above 60mm.

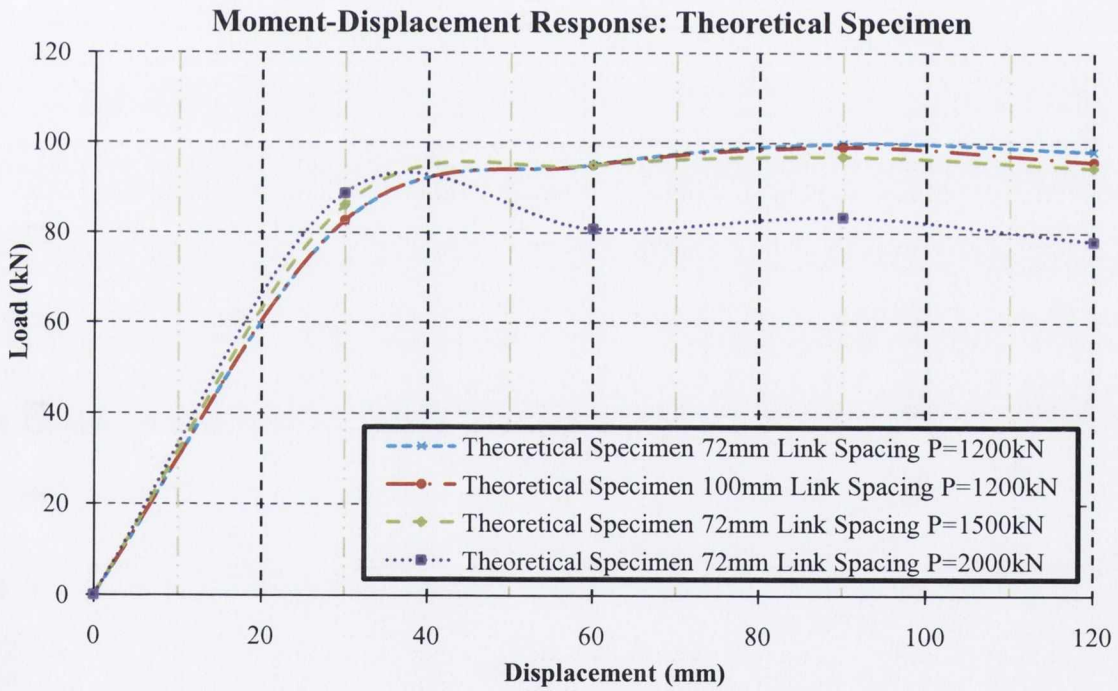

Figure 6.30: Predicted Moment-Displacement Response: Varied Parameters

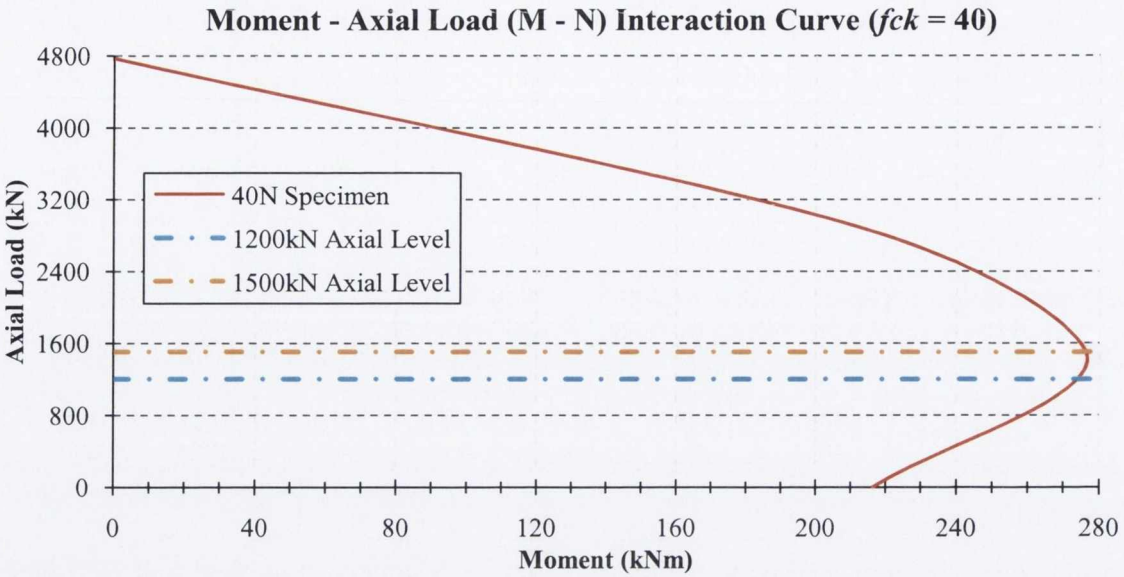

Figure 6.31: M-N Interaction Curve: 40N/mm^2 Specimen 72mm Link Spacing

Overall the proposed model is capable of predicting a change in the moment-displacement response due to minor variations in link spacing, axial load level and concrete strength.

6.5 Strain and Strain Energies

The strains and strain energies in the transverse steel were predicted using the theory established in Chapter 5. The predicted strains in the transverse steel with respect to displacement cycle are presented in Figure 6.32 and Figure 6.33.

These plots display similar characteristics; all display a shallow initial slope (up to 30mm displacement), with all specimens yielding in the 60mm displacement cycles. During this cycle, yielding of the structural and longitudinal steel occurs. The increased axial load level between Specimen JD1 and JD3 results in an increase in the transverse steel strain at all displacements. This is supported by the HSC specimens where a significant increase in transverse strain is recorded between Specimen JD4 and JD5. The reduced link spacing of JD6 increases the volumetric ratio of the confining reinforcement, thus evidently a reduction in the transverse steel strain is recorded for the same axial load level (i.e. Specimen JD6 compared with JD5).

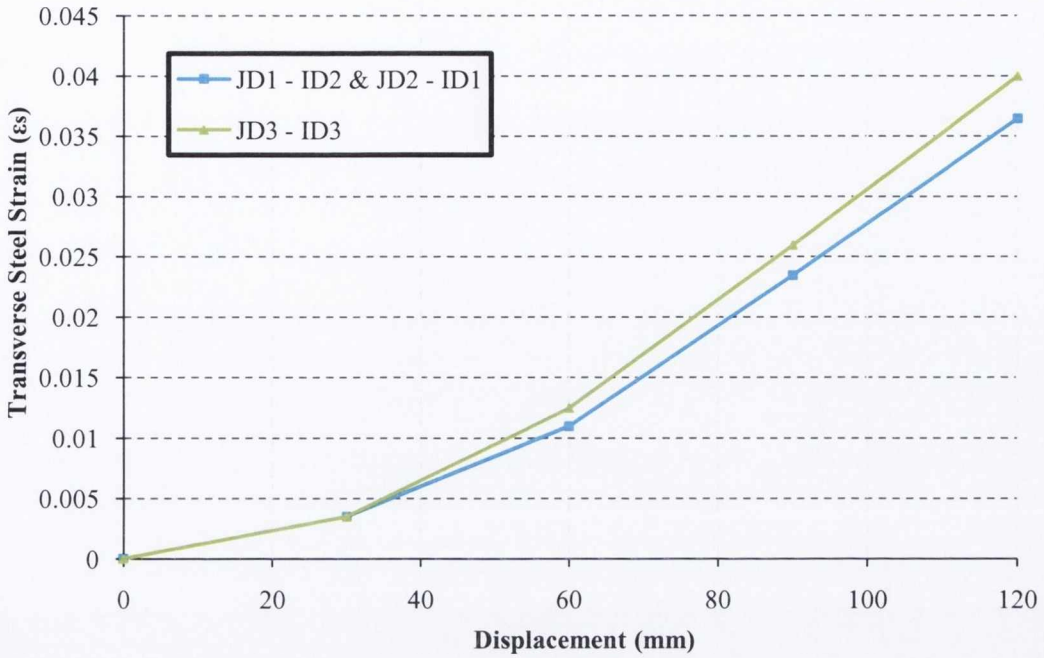

Figure 6.32: Transverse Steel Strain per Displacement Cycle: NSC Specimens

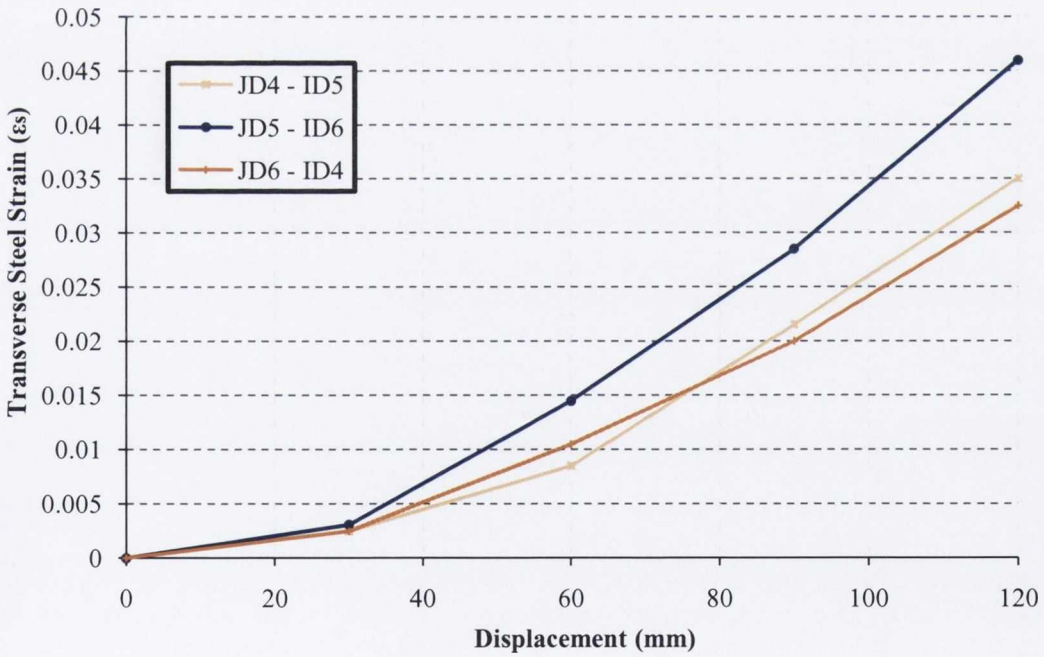

Figure 6.33: Transverse Steel Strain per Displacement Cycle: HSC Specimens

Table 27: Strain and Strain Energy at Link Opening

Specimen	Strain in Transverse Steel, ε_s	Strain Energy at Link Fracture ($MJ/m^{3)}$
JD1 – ID2	0.037	19.63+
JD2 – ID1	0.037	19.63+
JD3 – ID3	0.0401	21.45+
JD4 – ID5	0.03515	18.56+
JD5 – ID6	0.04625	25.16+
JD6 – ID4	0.0326	17.11+

Table 27 presents the predicted transverse steel strains and strain energies in all specimens at a displacement corresponding to the termination point of the tests. As the links did not fracture, the strain energy values provided in the table include a '+' value to indicate that higher transverse strains are required to fracture the links. It is important to note that all values are significantly less than the quoted value of $110MJ/m^3$, from Equation (5.34) as cited by Mander *et al,* (1988). This is expected as none of the links fractured during the test, thus strain values predicted by the model at the termination displacement are all below the ultimate strain values of the transverse links. Furthermore, the equations developed by Mander *et al,* (1988) were for reinforced concrete subject to uni-axial compression thus may not be entirely suitable for a composite column subject to axial and cyclic lateral loading.

Further work is required to determine if the stated values hold for a composite cross-section subject to a combination of axial and lateral cyclic loading. Additional tests are also required to determine whether welding the transverse links reduces their fracture strain, thus reducing the strain energy at which the section ultimately fails. The values in Table 27 indicate the model is capable of predicting an increase in strain energy due to an increase in axial load (i.e. Specimen JD1 compared with JD3 and Specimen JD4 compared with JD5).

The model further indicates that a reduction in strain energy is recorded for an increase in concrete strength at identical axial loads, i.e. Specimen JD3 compared with JD4. This result can be deceiving as it presents that an increased concrete strength reduces the

strain energy in the link at an identical displacement, but the specimens are subjected to different levels of axial load, i.e. 40 % and 20% of the sections axial capacity for Specimens JD3 and JD4, respectively. If two specimens with similar axial load levels were compared (i.e. JD3 and JD5, subjected to 40% and 35% of their axial capacity, respectively), the results indicate that the increase in concrete strength leads to an increase in strain energy for a given displacement.

6.6 Conclusions

The results of the numerical model presented in this chapter show good correlation with the experimental results presented in Chapter 4. It has been identified that the proposed model predicts the post yield response for each specimen at all level of displacement, with the exception of two values for the HSC specimens, the reasons of which were discussed earlier. It is clear that the model is capable of predicting the moment curvature and moment displacement response envelope of the test specimens. The model is also capable of determining the variation in transverse strain demands between specimens with different grades of concrete, levels of axial load and variations in link spacing; this is a key requirement in determining the ductility capacity of composite columns.

The moment-curvature response is sensitive to levels of axial load and link spacing. The moment-displacement response shows good correlation with the experimental results post yield but overestimates the initial stiffness by between 7 – 21% for all specimens. The variation between these values may be due to the material models adopted and the assumption of full interaction between steel and concrete elements, thus predicting an idealised composite stress-strain relationship. The parametric analysis illustrates that the model is receptive to minor variations in link spacing, concrete strength and axial load.

The obtained results show that the model, modified from a reinforced concrete model subject to uni-axial compression can predict the behaviour of a composite column subject to combined axial and lateral loading. Furthermore, the model is capable of determining the strain energy of the specimens at varying displacements, though additional work is required to verify if the ultimate values quoted by Mander *et al,* (1988) hold for a composite cross-section subject to cyclic loading conditions.

Chapter 7

Finite Element Modelling

Finite Element Modelling

7.1 Introduction

Further to the development of the numerical model presented in Chapters 5 and 6, a finite element programme was used to predict the capacity and performance of the specimens described in Chapter 3. The finite element package used was Zeus Nonlinear (ZeusNL), which can be used to predict the displacement behaviour of plane and space frames under static or dynamic loading, taking into account both geometric and material nonlinear behaviour, it employs the fibre cross-section modelling technique of the numerical model Section 7.2 briefly introduces the method and material stress-strain response employed in the prediction of member moment capacity, followed by a comparison between the predicted and experimental load-deflection hysteresis plots in Section 7.3. A comparison of the predictions of the model developed in Chapter 5 and the ZeusNL model are discussed in Section 7.4, followed by a parametric study for the proposed members from Section 6.4 is presented in Section 7.5. Finally, conclusions on the ZeusNL models are presented in Section 7.6.

7.2 Model Development

The dynamic analysis programme 'ZeusNL' has been developed to predict the displacement behaviour of two- and three-dimensional frame structures under static and transient dynamic loading, taking into account geometric nonlinearities and the effects of material plasticity. A variety of elements may be used, ranging from the ideal plastic hinge element to the exact elastoplastic cubic formulation, accounting for the spread of inelastic behaviour across the section and along the member length. A detailed description of all available elements and material models in 'ZeusNL' is beyond the

scope of this research. Herein, only the elastoplastic cubic element (by which the cross section is monitored), is discussed and the process involved in defining the specimen and loading history.

The Elastoplastic Cubic Element

The model element assumes a cubic shape function in the chord system, monitoring stresses and strains at various points across two Gaussian sections. This gives the possibility of a spread of inelastic behaviour throughout the cross-section. Two nodes define the element, each of them having three degrees of freedom in 2-D analysis, as shown in Figure 7.1. For the evaluation of the element forces, numerical integration is performed at the two Gauss points. For this purpose, the section at each Gauss point is divided into a number of monitoring points (monitoring areas), similar to the sub-division of the cross-section adopted for the proposed numerical model in Chapter 5.

Note: Nodes (1) and (2) are the end-nodes of the element. The element local x-axis lies on the line defined by them.

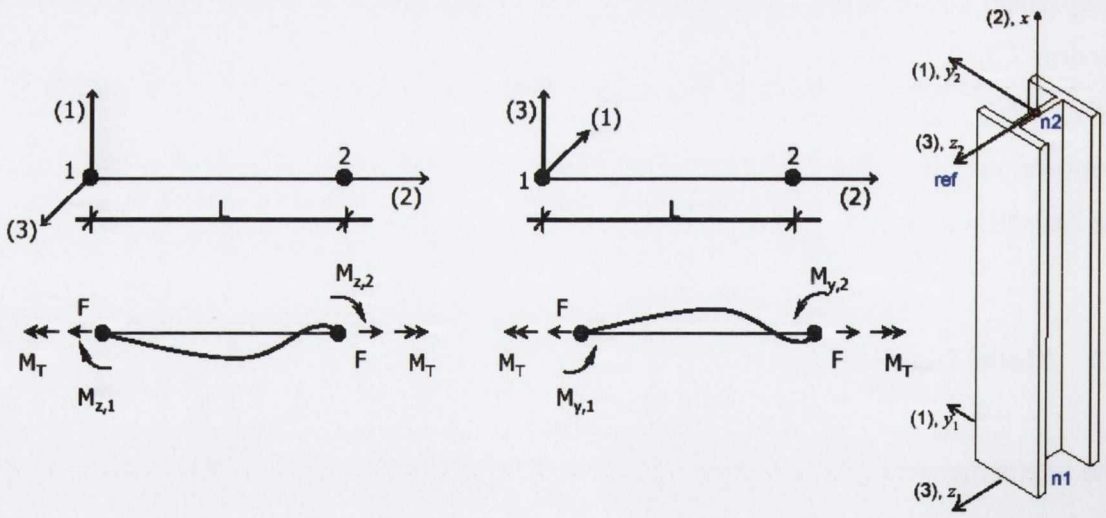

Figure 7.1: Chord Freedoms of the Cubic Formulation, ZeusNL

The global response of the cubic element is obtained by transformations from the chord to the global system. For the calculation of normal stresses at the monitoring areas, increments of strain are calculated from the last equilibrium state.

Specimen Development

The analysis performed was a static time-history analysis, typical of a simulation used to determine the performance of individually tested specimens. The first process is to define the material stress-strain characteristics for the constituent materials. All material values are determined from material tests and are presented in Chapter 5. Figure 7.2 presents a typical ZeusNL interface for specifying the material stress-strain characteristics.

A non-linear constant confinement model was selected to represent the unconfined and highly confined concrete while a non-linear variable confinement model was used to represent the confining effects of the longitudinal and transverse steel on the partially confined concrete; furthermore this was the only stress-strain model which allowed the transverse steel dimensions, stresses and strains to be incorporated into the design. The Sheikh and Uzumeri concrete model was used to represent the behaviour of the HSC as it predicts the sudden drop in resistance beyond the strain corresponding to the maximum confined stress. A comparison of the concrete stress-strain predictions using the model adopted by ZeusNL and for the numerical model developed in Chapter 5 is presented in Figure 7.3.

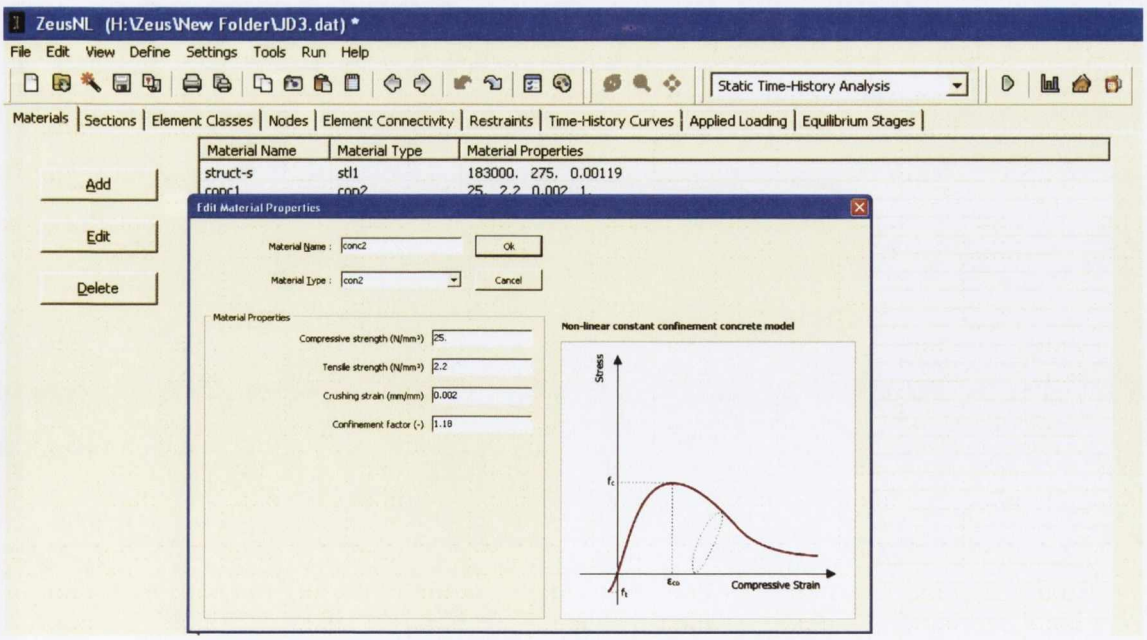

Figure 7.2: ZeusNL Interface: Material Stress-Strain Properties

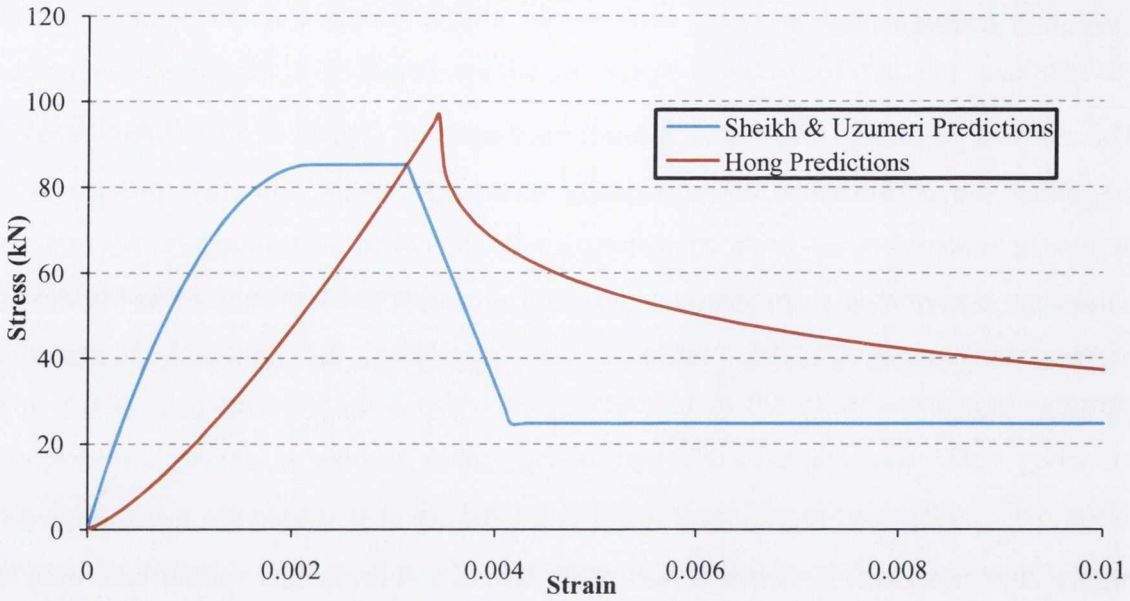

Figure 7.3: ZeusNL & Numerical Concrete Stress – Strain Model Curves

The stress-strain curve adopted by ZeusNL, which is based on the equations and published work of Sheikh and Uzumeri, 1980. This model was developed for NSC, thus the equations for determining the strain corresponding to the maximum concrete compressive strength will be lower than that expected for a HSC. It has already been shown that HSC achieves a higher stress at peak confined concrete strength (i.e. Section 2.6.2.8). this is illustrated above as the stress-strain curves display very different responses.

The Sheikh and Uzumeri model predicts a higher stiffness prior to yielding; this is a major factor which causes the ZeusNL envelope predictions to be stiffer than the predictions using the numerical model developed in Chapter 5, this shall be discussed later in the chapter. The model also predicts a considerable reduction in resistance after the maximum lateral resistance was achieved; the response is similar to that using the HSC stress-strain equations (Hong *et al.*). It was necessary to emulate this type of response so that the ZeusNL model could accurately predict the point at which the cover concrete spalled, thus reducing the lateral resistance of the specimen.

Once the material properties are established, the specific cross-section type and details need to be specified. Figure 7.4 presents the specimen's cross-section properties interface. After defining the section properties the elemental nodes need to be established, as presented in Figure 7.5, furthermore the elemental connectivity, restraints and number of monitoring points need to be established. The final process is to define the applied loading acting on the specimen; the lateral load is defined by a time-history curve, identical to the main test displacement-history curve presented in Figure 3.17.

Finally an integrity check is conducted on the frame before the analysis is conducted. Once the analysis is complete, the results can be plotted comparing the following variables: nodal displacement, nodal rotation, inter-storey drift, support force, support moment, element force / moment, element shear, element curvature and time. A typical nodal displacement versus support moment plot is presented in Figure 7.6.

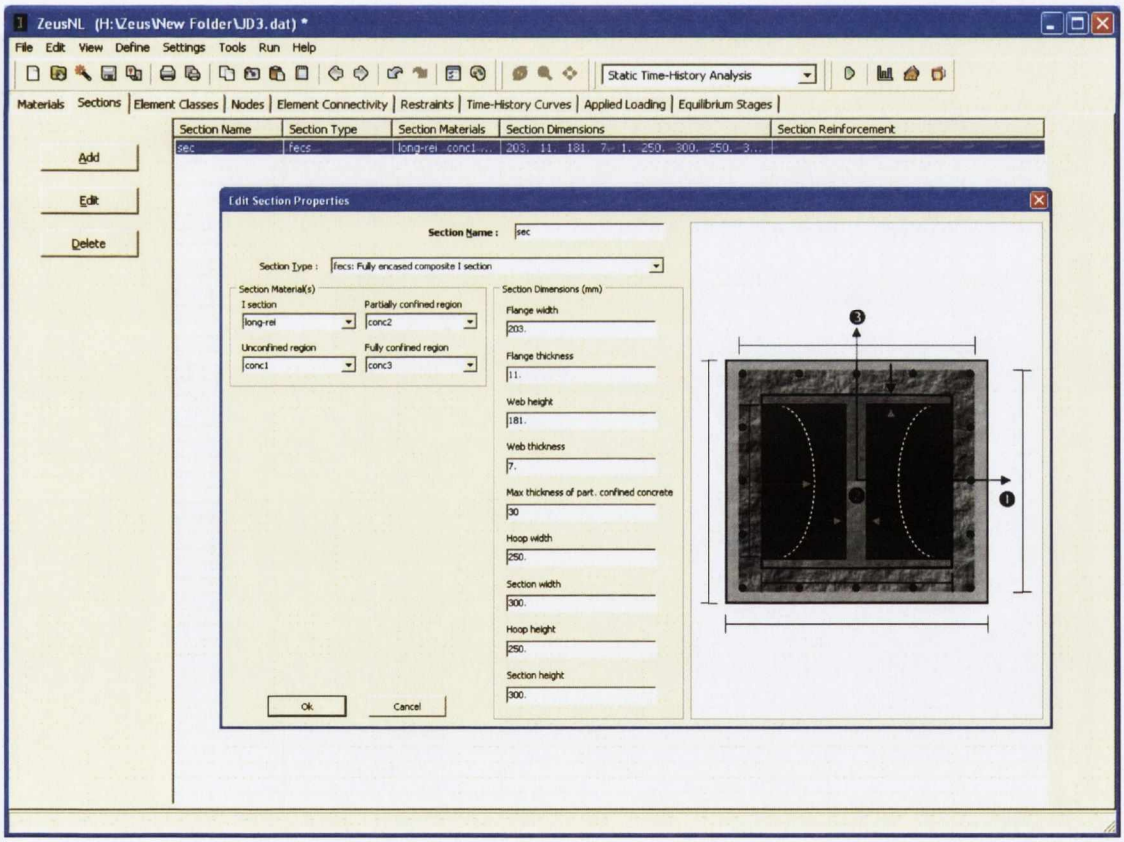

Figure 7.4: ZeusNL Interface: Cross-Section Properties Interface

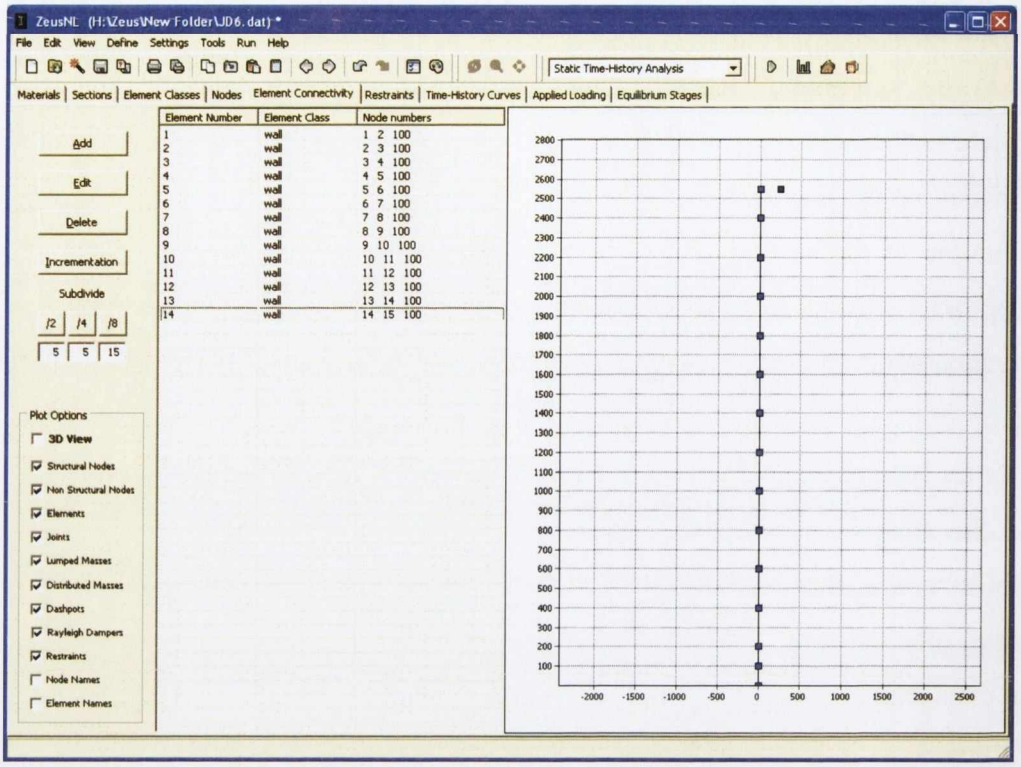

Figure 7.5: ZeusNL Interface: Elemental Connectivity Interface

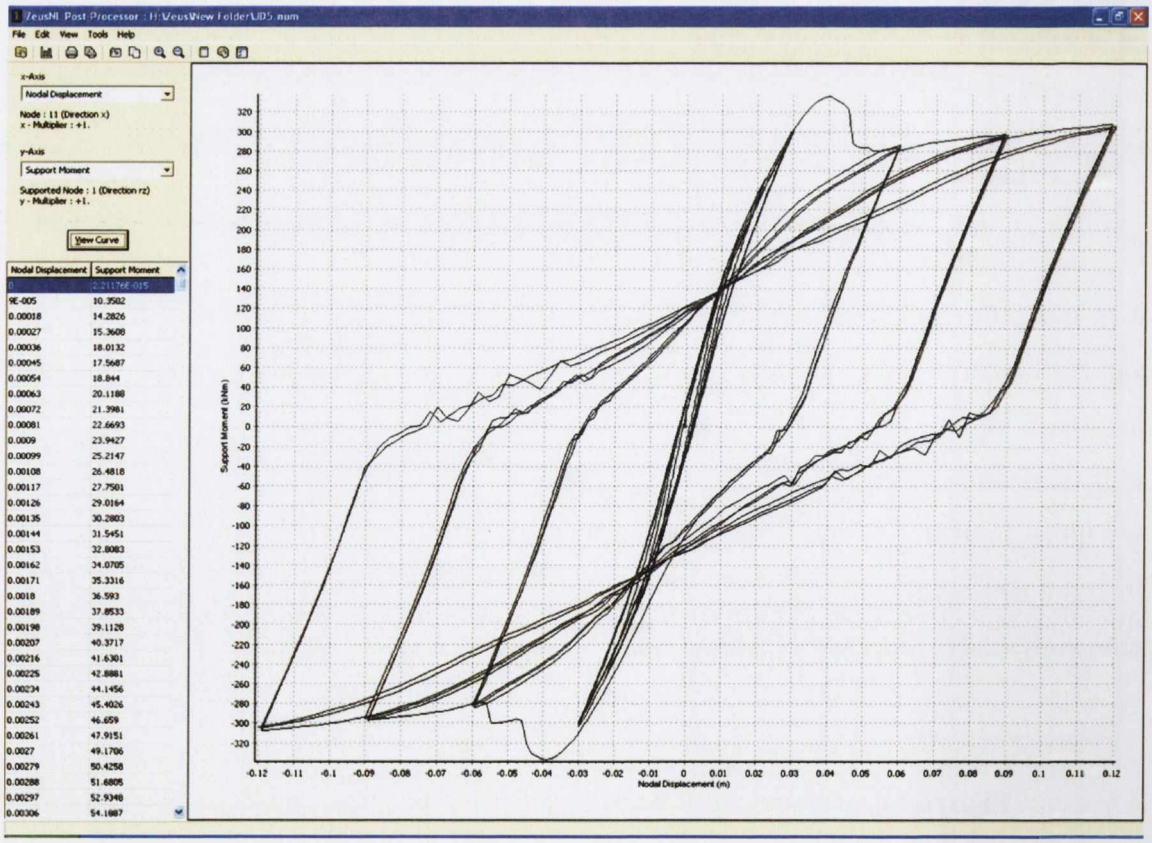

Figure 7.6: ZeusNL Interface: Predicted Results – Displacement vs. Moment

7.3 Model Predictions

The FEM predictions are compared with the experimental results in Figure 7.7 to Figure 7.12. The FEM predictions show good correlation with the experimental results, particularly for the NSC specimens. The FEM underestimates the performance of Specimen JD1 in the pull cycles but it overestimates the response by over 30% in the push cycles. This is due to the lack of a lateral restraint during this test, thus a certain degree of bi-axial buckling occurred, as discussed in previous chapters. The unloading branch for all specimens is significantly different to the actual specimen response, which would lead to an error in the estimate of the energy dissipated. Once the section re-enters the loading phase, the FEM predictions match the experimental hysteretic behaviour with good accuracy, especially for the NSC specimens (as illustrated in Figure 7.7 to Figure 7.12).

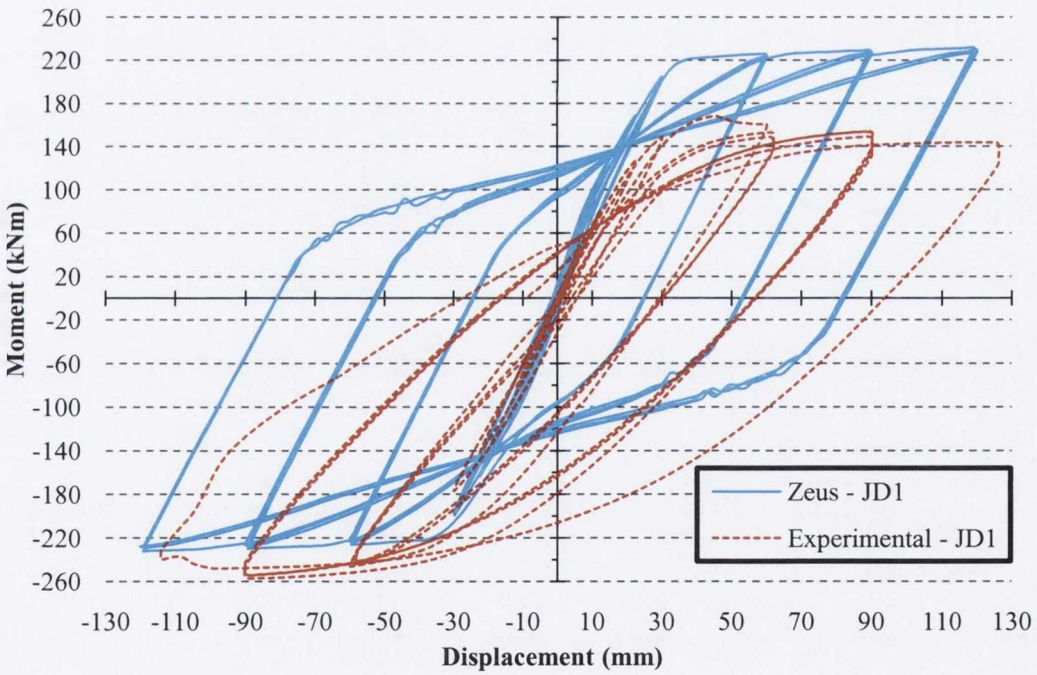

Figure 7.7: Zeus Prediction Versus Experimental Results: JD1 – ID2

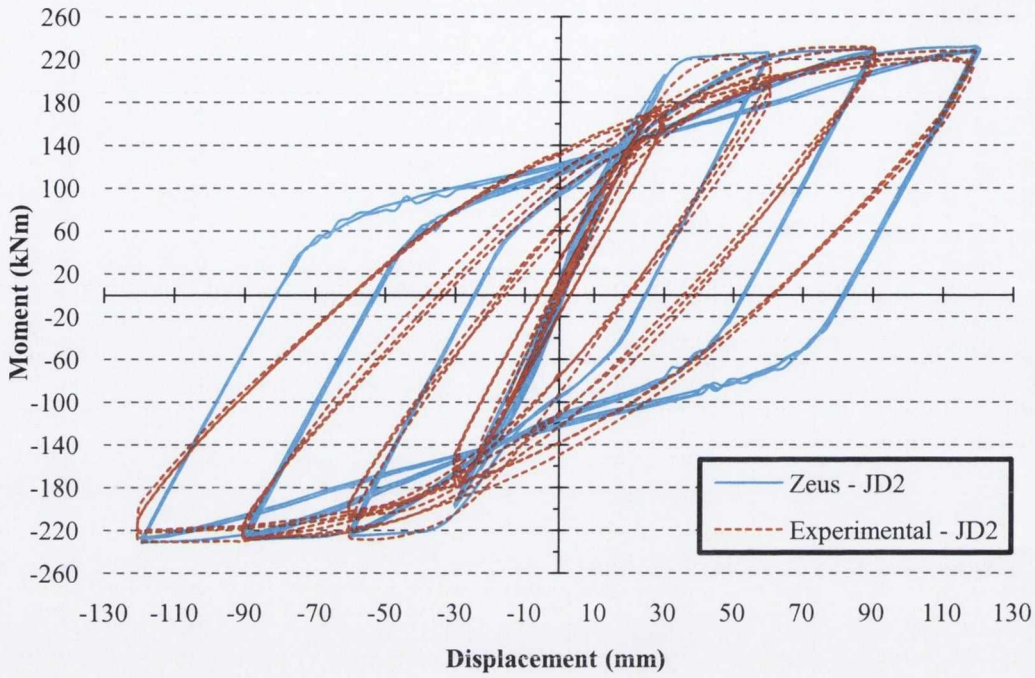

Figure 7.8: Zeus Prediction Versus Experimental Results: JD2 – ID1

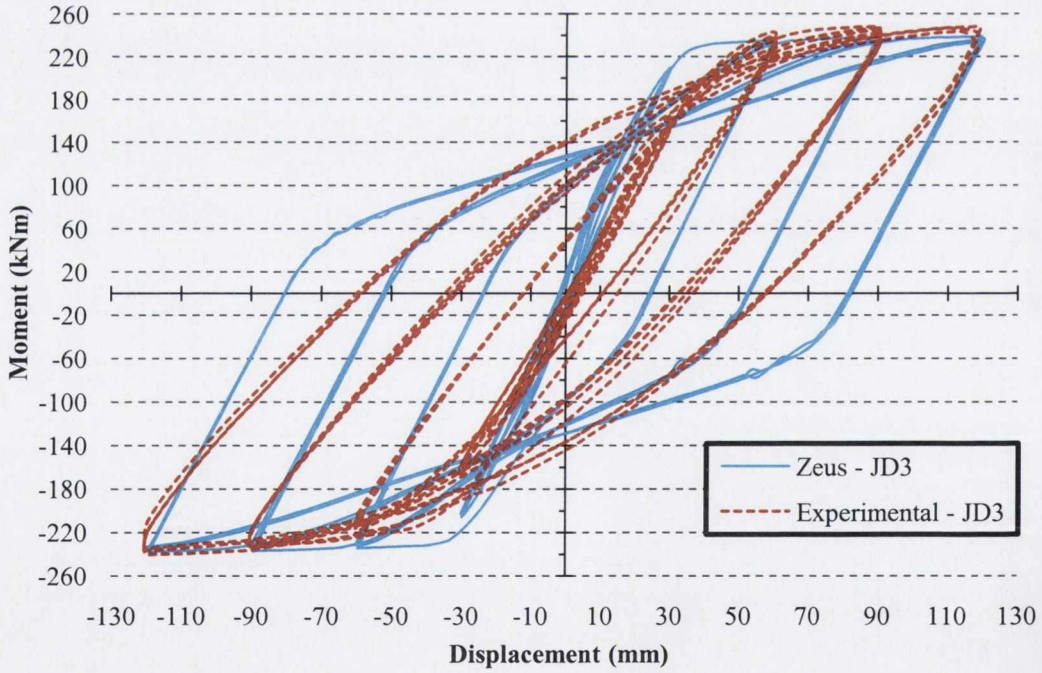

Figure 7.9: Zeus Prediction Versus Experimental Results: JD3 – ID3

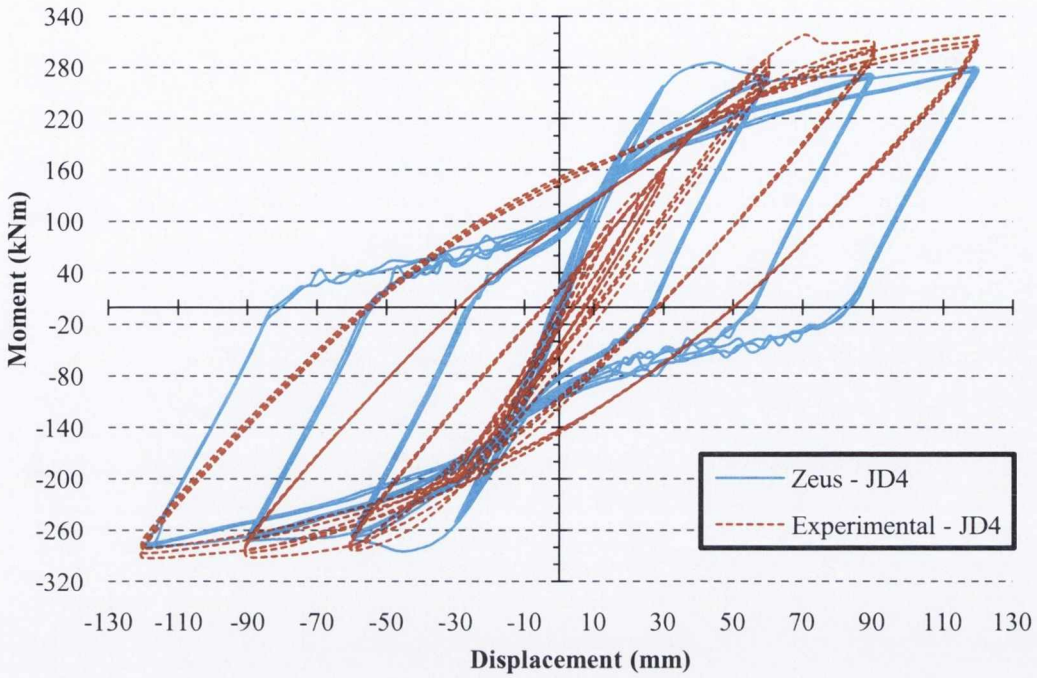

Figure 7.10: Zeus Prediction Versus Experimental Results: JD4 – ID5

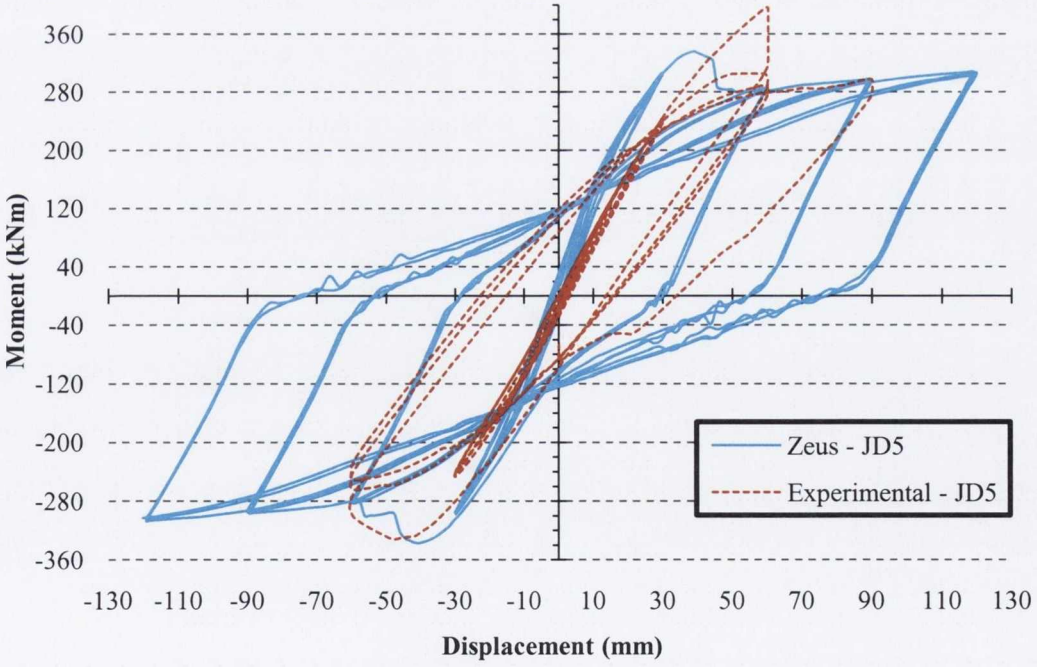

Figure 7.11: Zeus Prediction Versus Experimental Results: JD5 – ID6

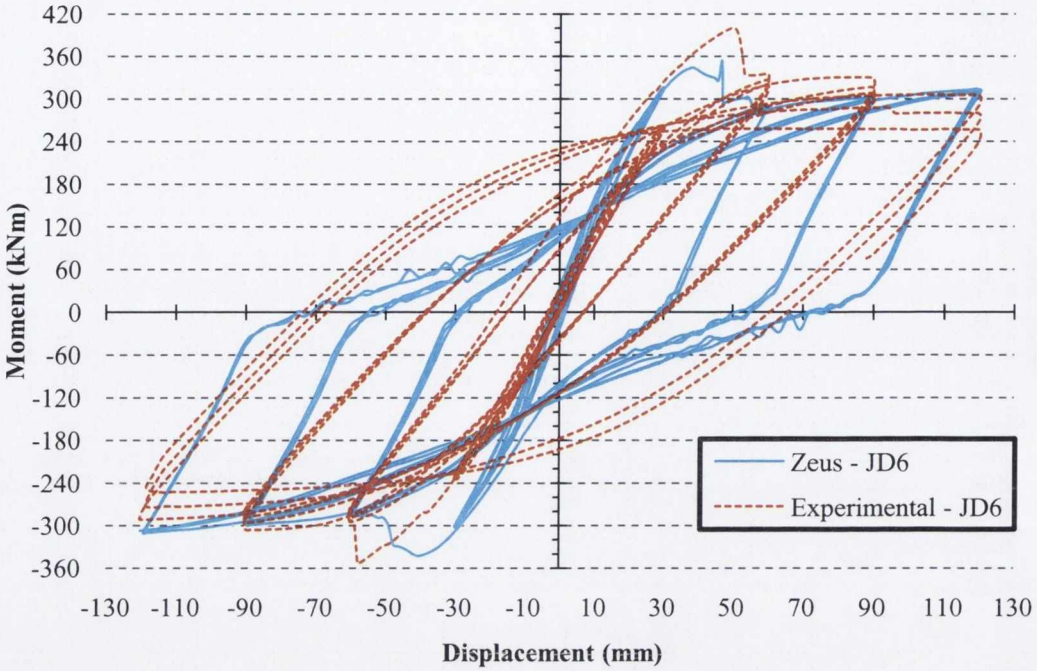

Figure 7.12: Zeus Prediction Versus Experimental Results: JD6 – ID4

The HSC specimen predictions are less accurate than those for the NSC specimens. This is due to the difficulty in accurately predicting the brittle nature of HSC. Furthermore, the FEM has only four stress-strain curves available for concrete, none of which are fully suited to model HSC, thus the initial yield and spalling of the concrete is difficult to simulate. One notable variation between the experimental and FEM predictions for the HSC specimens is that the FEM predicts yielding and spalling of the cover concrete at a lower displacement than was recorded by the experimental tests.

Beyond the displacement corresponding to concrete spalling, a good correlation exists. The experimental results display a drop in resistance at subsequent cycles of identical displacement, but the FEM predicts that a similar resistance is reached at all subsequent cycles. This is unrealistic, as for post-yield displacements the cover and core concrete will suffer some level of damage and the overall resistance will be reduced.

The FEM underestimates the maximum resistance of the HSC specimens, but for all axial load levels (especially the specimens with high axial loads) a reduction in resistance is recorded due to the predicted spalling of the cover concrete and deterioration of the core concrete. Finally, the FEM overestimates the initial stiffness of

all specimens, thus leading to a premature yield displacement compared with the experimental results.

7.4 Model Comparisons

Figure 7.13 to Figure 7.18 present the moment-displacement envelope curves for the experimental, ZeusNL and proposed models. The moment-displacement plots allow for the P-Delta effects due to the axial load. The purpose of this section is to examine the merits of either model through comparison with the experimental data. It is clear from all plots that both models predict the moment-displacement relationship well, especially for the normal strength concrete specimens. It was established in Table 26 that the proposed numerical model overestimated the initial stiffness of all specimens, but it is clear that the ZeusNL predictions severely overestimate the initial stiffness of all specimens, particularly the HSC specimens.

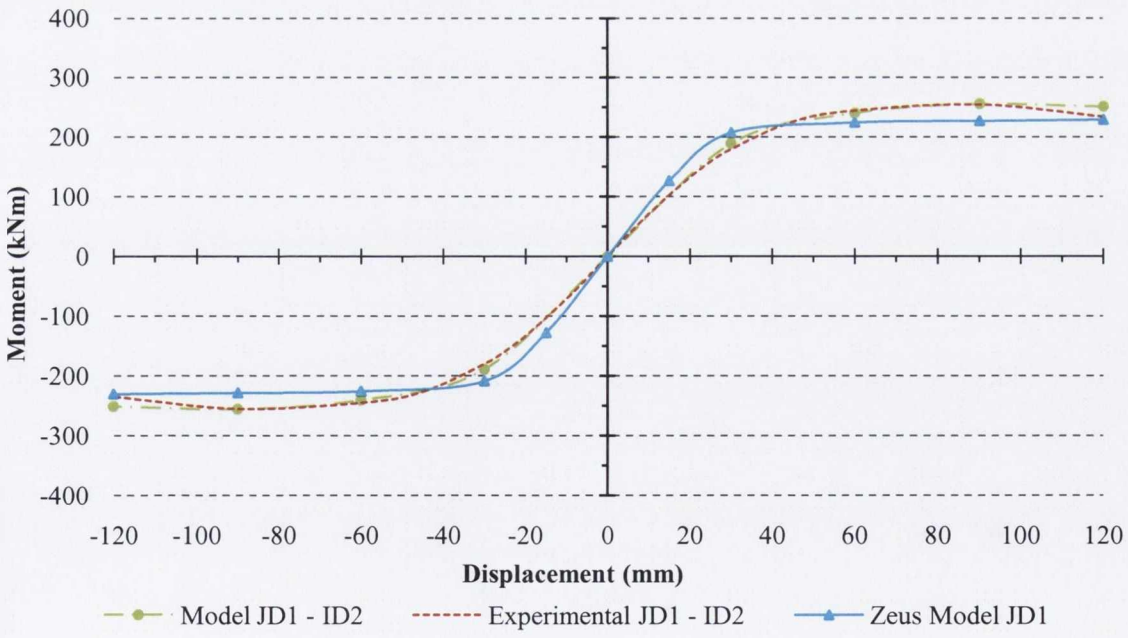

Figure 7.13: Model and Experimental Envelope Curves: JD1 – ID2

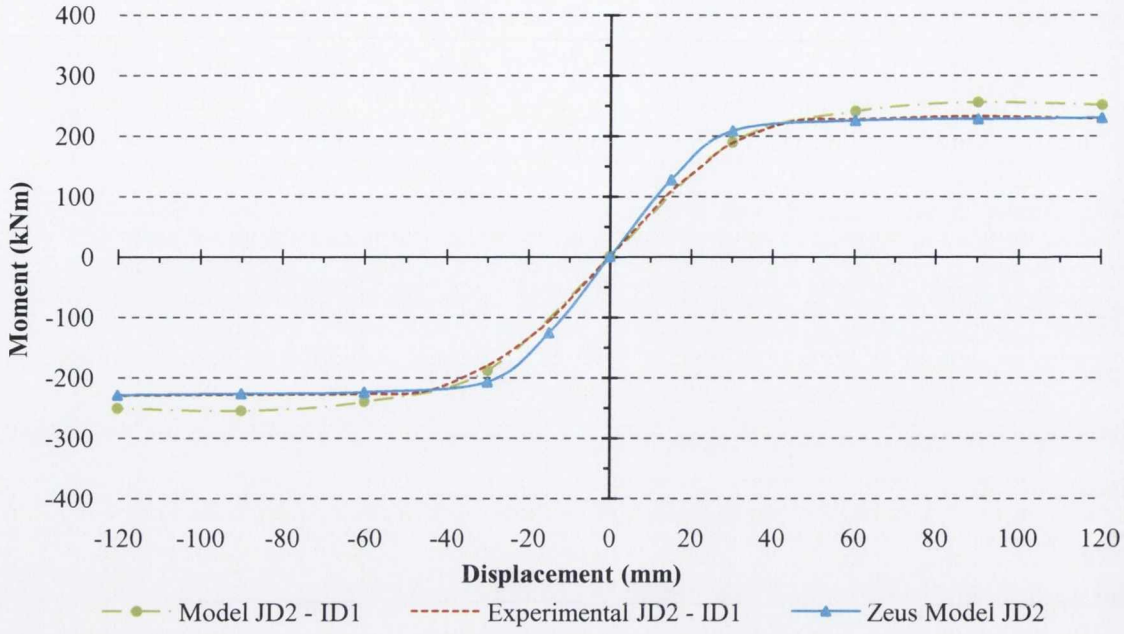

Figure 7.14: Model and Experimental Envelope Curves: JD2 – ID1

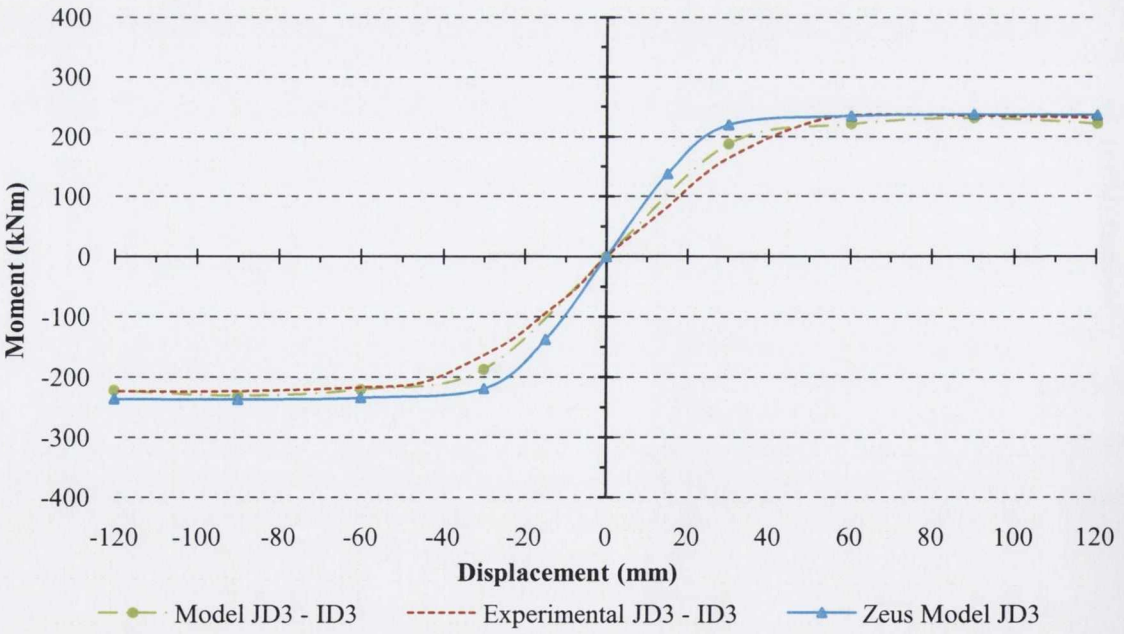

Figure 7.15: Model and Experimental Envelope Curves: JD3 – ID3

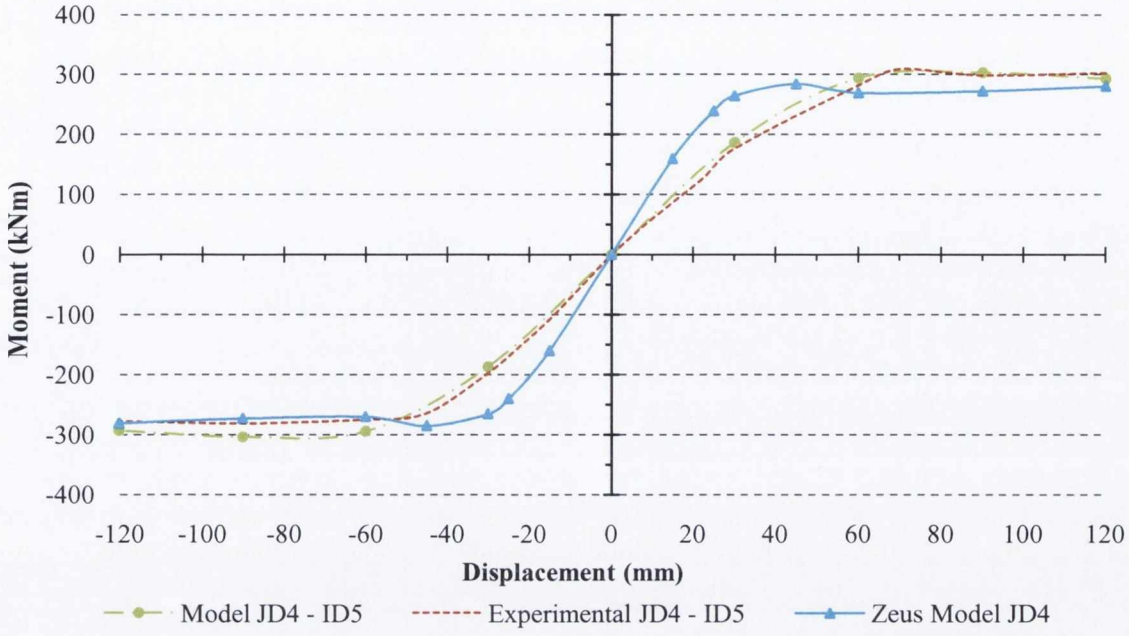

Figure 7.16: Model and Experimental Envelope Curves: JD4 – ID5

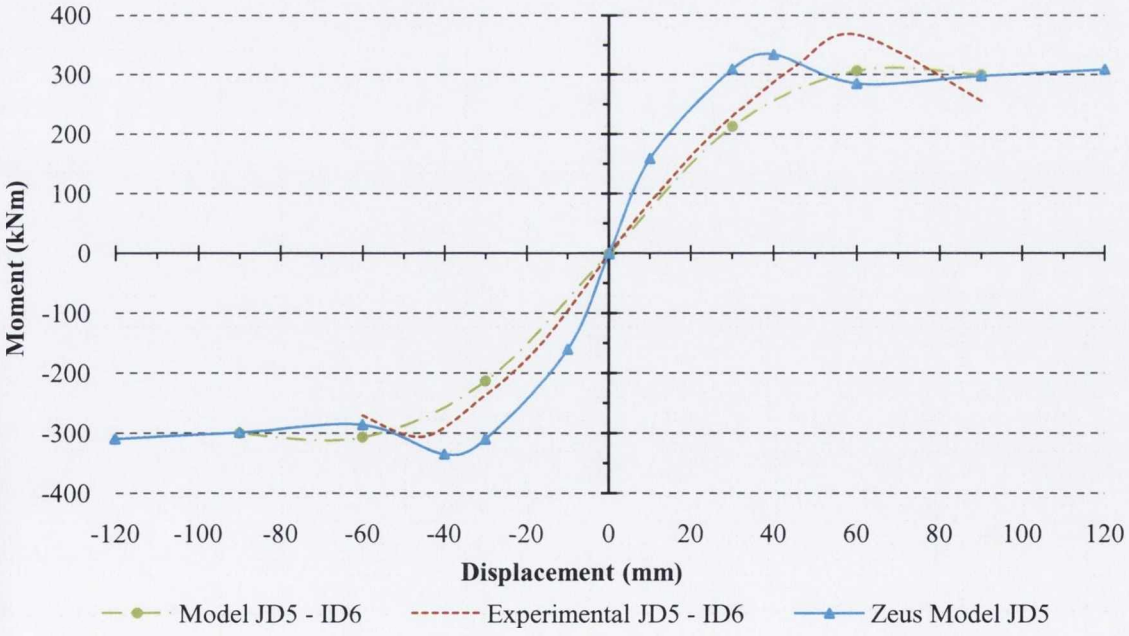

Figure 7.17: Model and Experimental Envelope Curves: JD5 – ID6

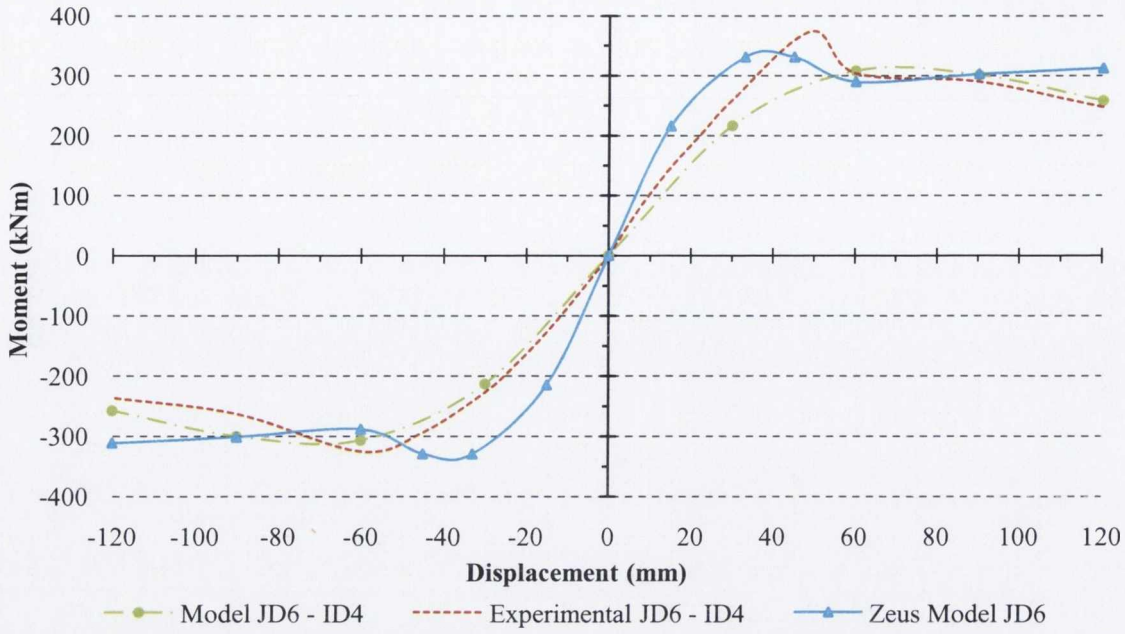

Figure 7.18: Model and Experimental Envelope Curves: JD6 – ID4

In the case of the NSC specimens, neither model establishes dominance in performance as both match the predicted moment-displacement very well. Both models are clearly suitable for predicting the performance of NSC specimens with low axial load levels. The level of uncertainty in response increases with an increase in axial load and increase in concrete strength as the materials behave in a more brittle manner and the point at which non-linear behaviour occurs is accelerated. This causes problems for any model as it becomes increasingly difficult to model the behaviour of a deteriorating concrete core. The only clear benefit of the proposed model is that it predicts the initial stiffness of a normal strength concrete with higher axial load levels (i.e. JD3 – ID3) more accurately, but the ZeusNL model predicts the post yield response very well compared to the experimental results.

A more significant deviation from the experimental results is evident for the HSC predictions. Both the proposed and ZeusNL models predict the response of a specimen with HSC and low axial loads well (i.e. JD4 – ID5), but the ZeusNL model tends to underestimate the displacement at which yielding occurs. This is the case for all specimens and is due to its over-estimation of the initial and yield stiffness. It has already been established that the primary reason for this over-estimation of pre-yield stiffness is due to the concrete stress-strain model adopted. The model adopted was developed for

NSC, thus the strain corresponding to maximum confined concrete stress will be lower than the strain obtained using a suitable HSC stress-strain model. This invariably will cause the hysteresis response to be stiffer than the experimental results as is evident from the HSC model and envelope curves (i.e. Figure 7.16 to Figure 7.18).

The proposed model underestimates the maximum resistance of JD5 – ID6 (i.e. HSC specimen with high axial load levels and 72mm link spacing), the ZeusNL model accurately predicts this maximum resistance but due to the significant over-estimation of stiffness this resistance occurs at a significantly lower displacement than recorded experimentally. Beyond the maximum resistance and spalling of the cover concrete both model display very similar responses but predict a continued stable resistance of the section, whereas the experimental results show a significant drop in resistance followed by an inability of the section to resist the applied axial loads and ultimately failure is recorded. This illustrates the difficulty for analytical models to accurately predict the response of HSC specimens with high axial loads.

A similar pre-maximum resistance response is predicted by both models for a HSC specimen with high axial loads and reduced link spacing (i.e. JD6 – ID4), but the proposed model predicts the inelastic response of this specimen to a greater degree of accuracy than the ZeusNL model.

Overall both models provide a reasonable estimate of the maximum resistance and post yield response of all specimens, each with its merits and flaws. Either model could be used with a degree of confidence to predict the moment-displacement relationship of a normal or high strength concrete composite cross-section, but it must be noted (using the ZeusNL model) that the predicted response of the HSC specimens subject to high levels of axial loads begin to deviate from the experimental results from the 90mm displacement cycle onwards.

7.5 Parametric Comparisons

Figure 7.19 presents the results of a parametric study using ZeusNL conducted on a 40N/mm^2 composite cross section of identical dimensions to that described in Chapter 3. The varied parameters were identical to those varied in the parametric study in Section 6.4. The predictions are very similar to those presented for the proposed model in Figure 6.30 with the exception of the specimen subject to an axial load of 2000kN. All curves include P-Delta effects and the comparison curves between the proposed and ZeusNL model are presented in Figure 7.20 to Figure 7.23. Referring to Figure 7.19 the Zeus model predicts that a resistance gain will be achieved by the theoretical specimen with an increase in axial load from 1200 – 1500kN, the proposed model predicts a minor decrease in post-yield resistance.

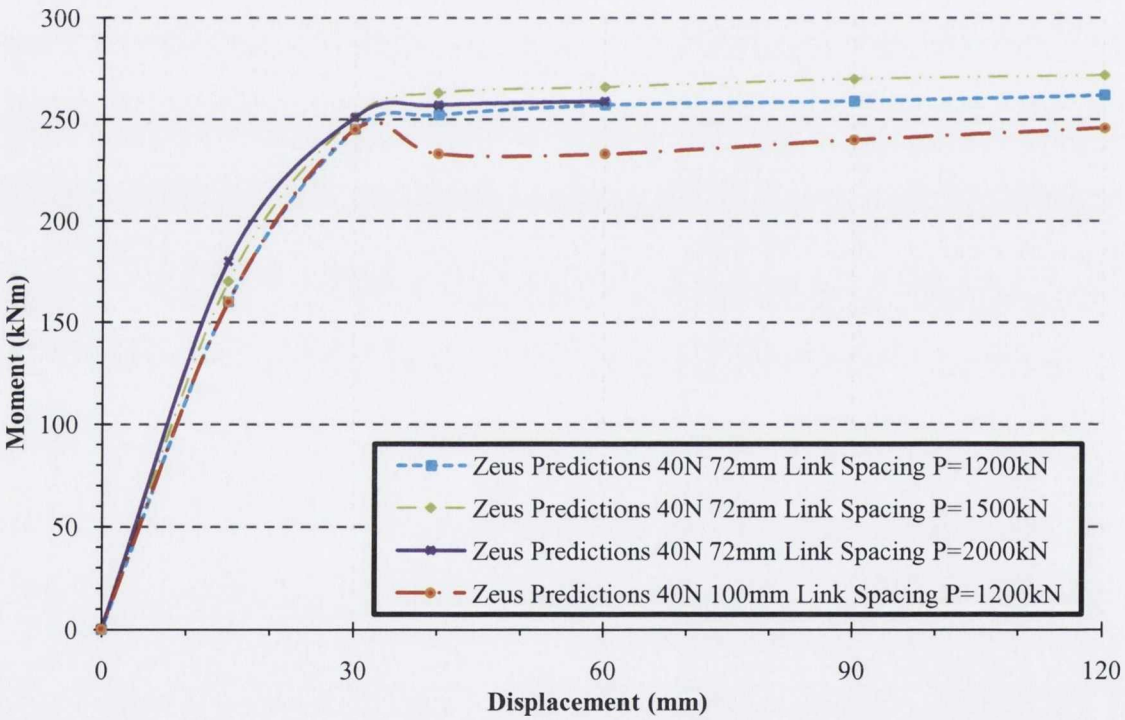

Figure 7.19: ZeusNL Predicted Moment-Displacement Response: Theoretical Specimen

Furthermore, the proposed model predicts that a negligible reduction in resistance will be experienced due to an increase in link spacing from 72 – 100mm, the Zeus model

predicts that a sudden reduction in resistance will occur (primarily due to yielding of the partially confined concrete) followed by a stable (yet shallow slope) increase in resistance up to 120mm displacement. The most significant deviation between the models is for the specimen subject to a high axial load level of 2000kN. The proposed model illustrates a reduction in resistance (approximately 15%) post achieving its maximum resistance; a subsequent stable resistance is recorded up to a displacement of 90mm followed by a shallow reduction in resistance up to 120mm lateral displacement. By contrast, the ZeusNL predicts a stable resistance up to a displacement of 60mm, but on load reversal the section is unable to resist the applied loads and ultimately fails (this is presented more clearly in the predicted moment-displacement hysteresis plots for the ZeusNL model in Figure 7.26). For completeness the ZeusNL predicted moment-displacement relationships for all theoretical models are presented in Figure 7.24 to Figure. Overall the both models differ in their predictions but it is evident that both are capable of presenting varied moment-displacement responses due to slight changes in concrete strength, link spacing and axial load level.

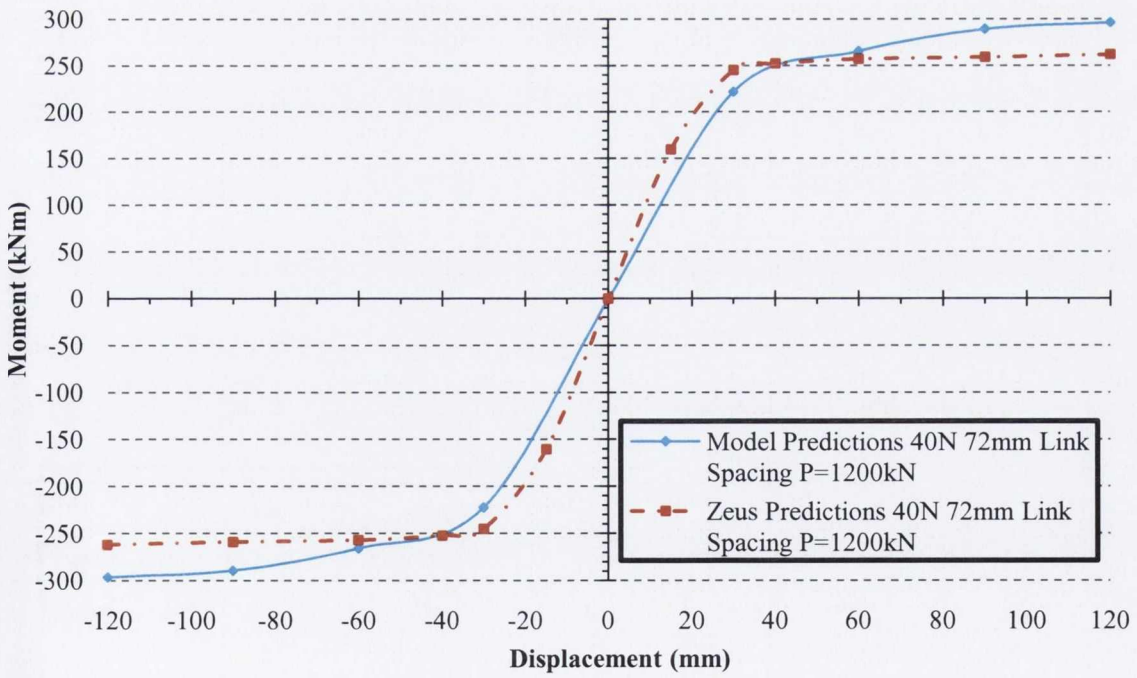

Figure 7.20: Zeus and Proposed Model Predictions: Theoretical Specimen – 72mm Link Spacing & P = 1200kN

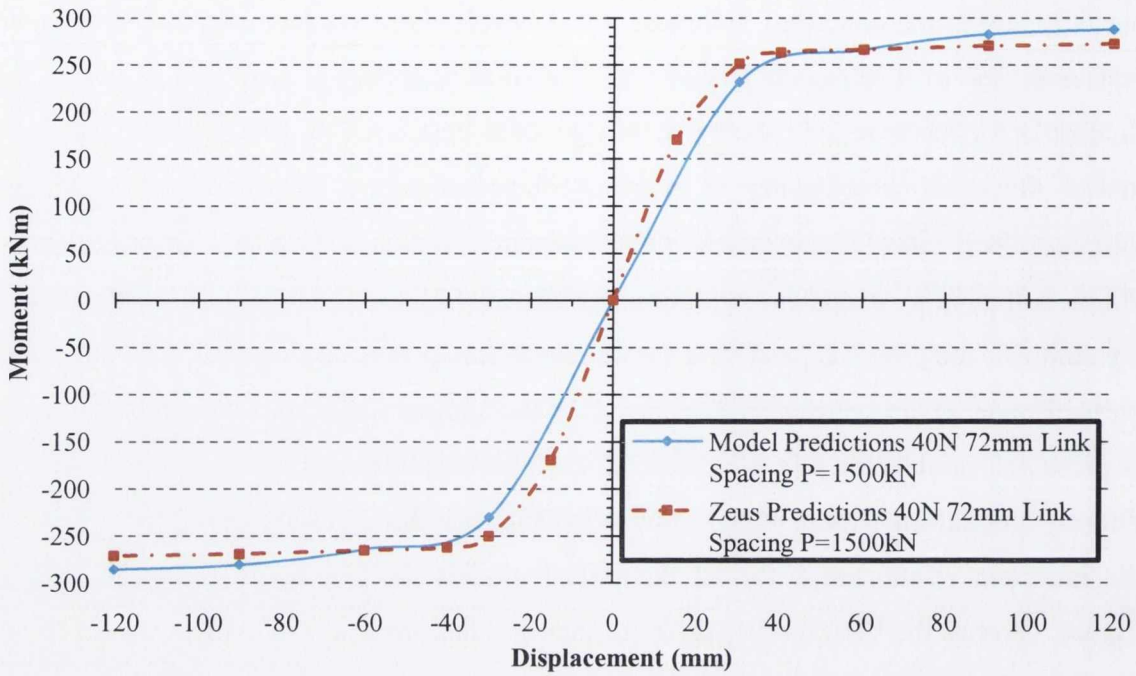

Figure 7.21: Zeus and Proposed Model Predictions: Theoretical Specimen – 72mm Link Spacing & P = 1500kN

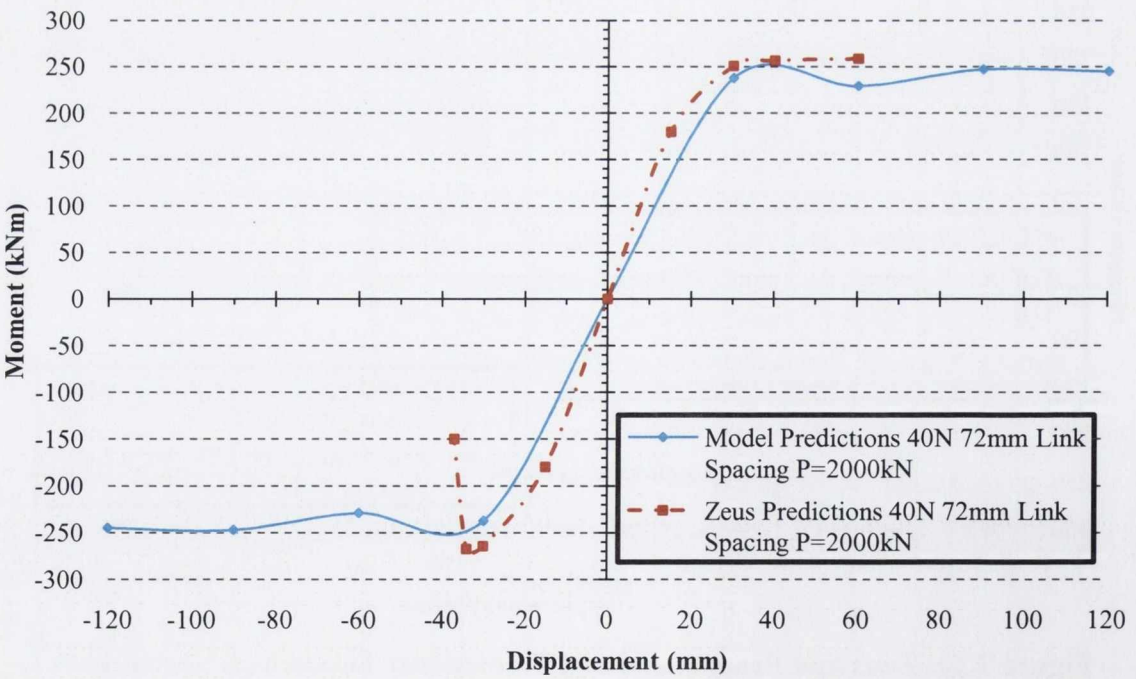

Figure 7.22: Zeus and Proposed Model Predictions: Theoretical Specimen – 72mm Link Spacing & P = 2000kN

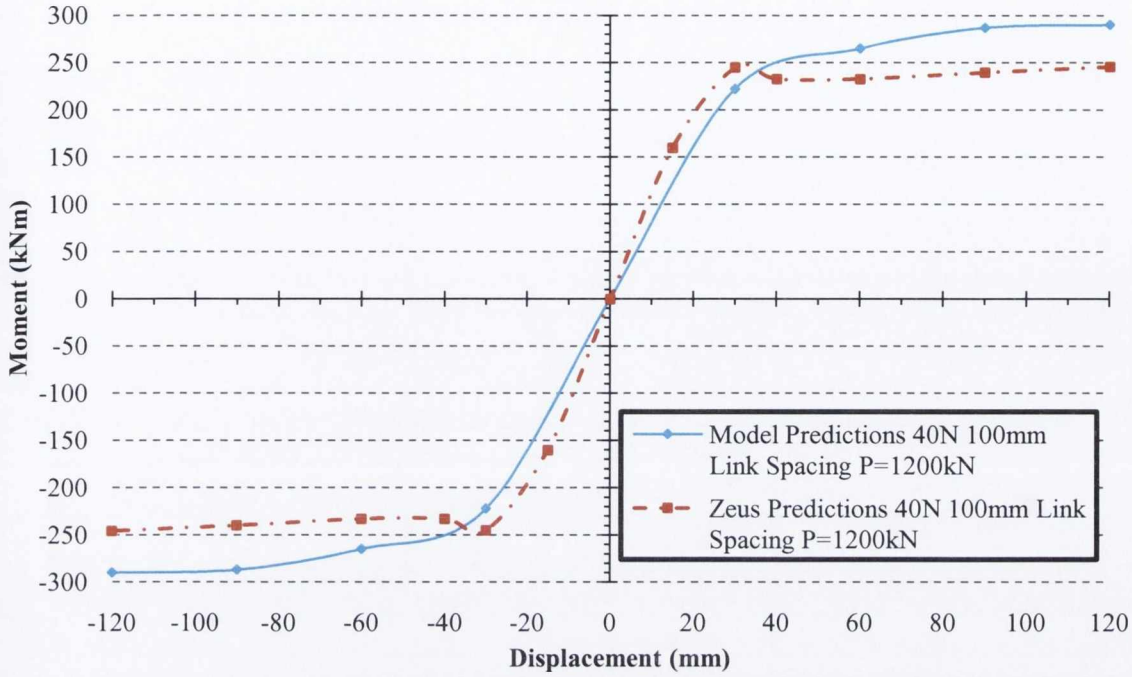

Figure 7.23: Zeus and Proposed Model Predictions: Theoretical Specimen – 100mm Link Spacing & P = 1200kN

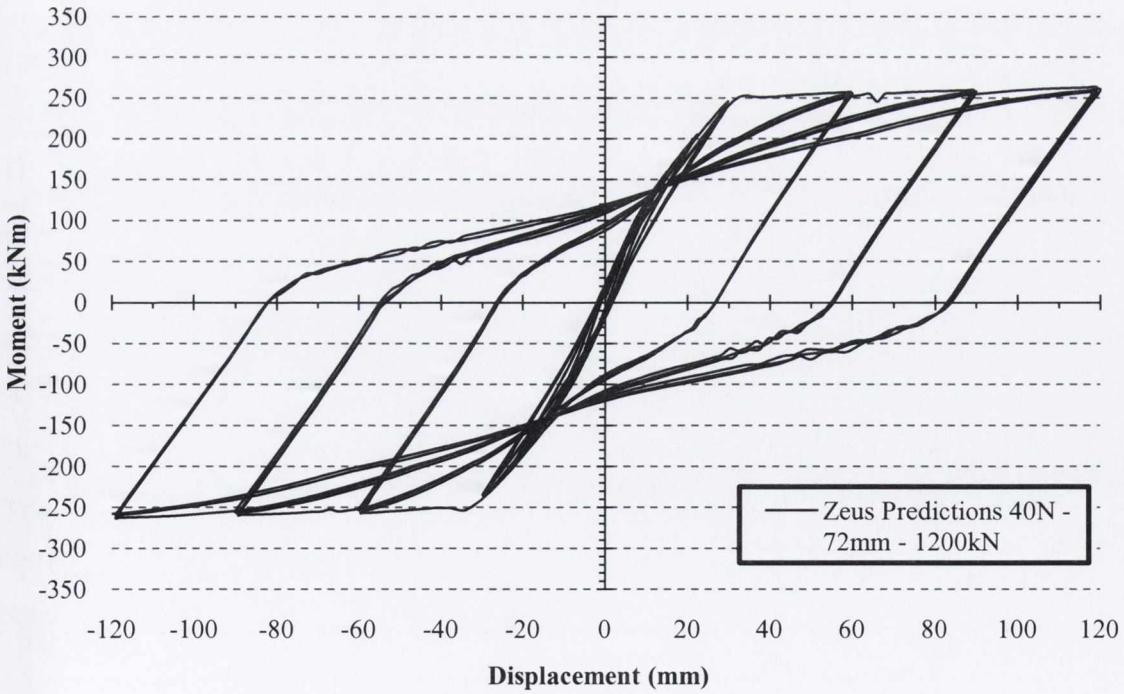

Figure 7.24: Zeus Hysteresis Predictions: Theoretical Specimen – 72mm Link Spacing & P = 1200kN

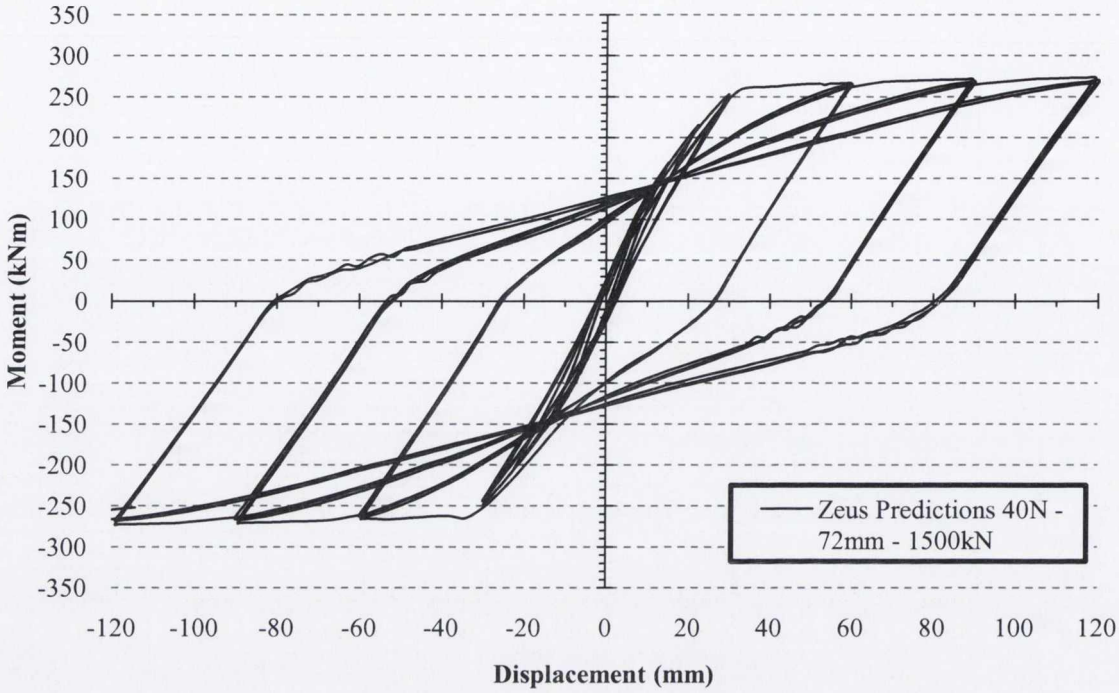

Figure 7.25: Zeus Hysteresis Predictions: Theoretical Specimen – 72mm Link Spacing & P = 1500kN

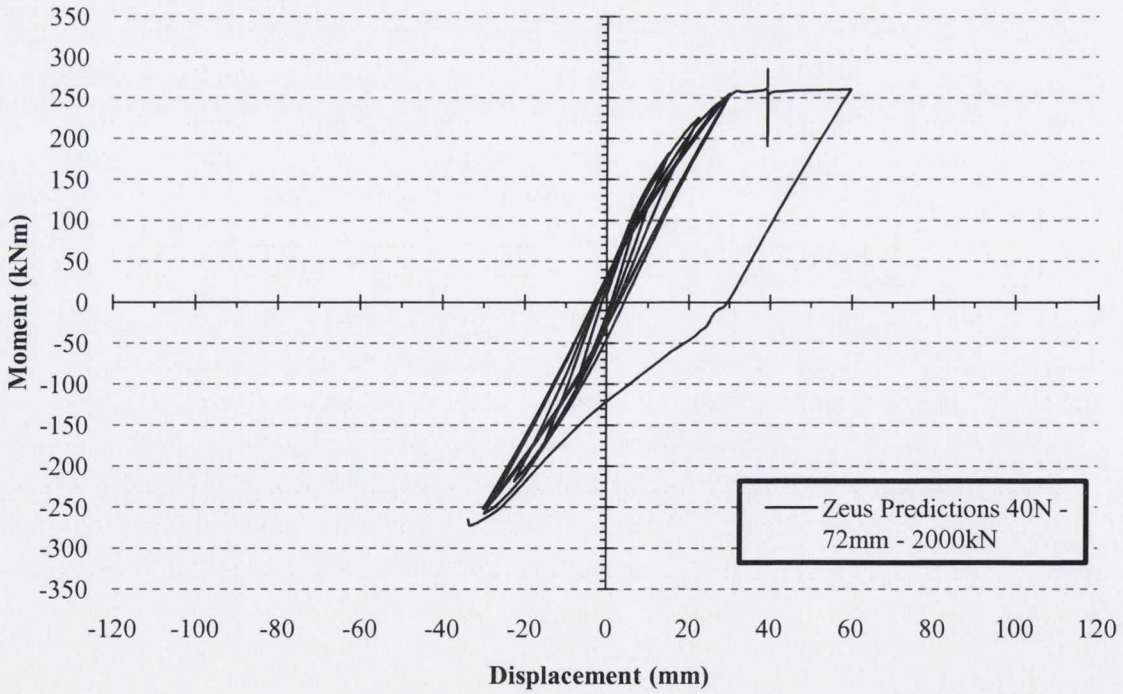

Figure 7.26: Zeus Hysteresis Predictions: Theoretical Specimen – 72mm Link Spacing & P = 2000kN

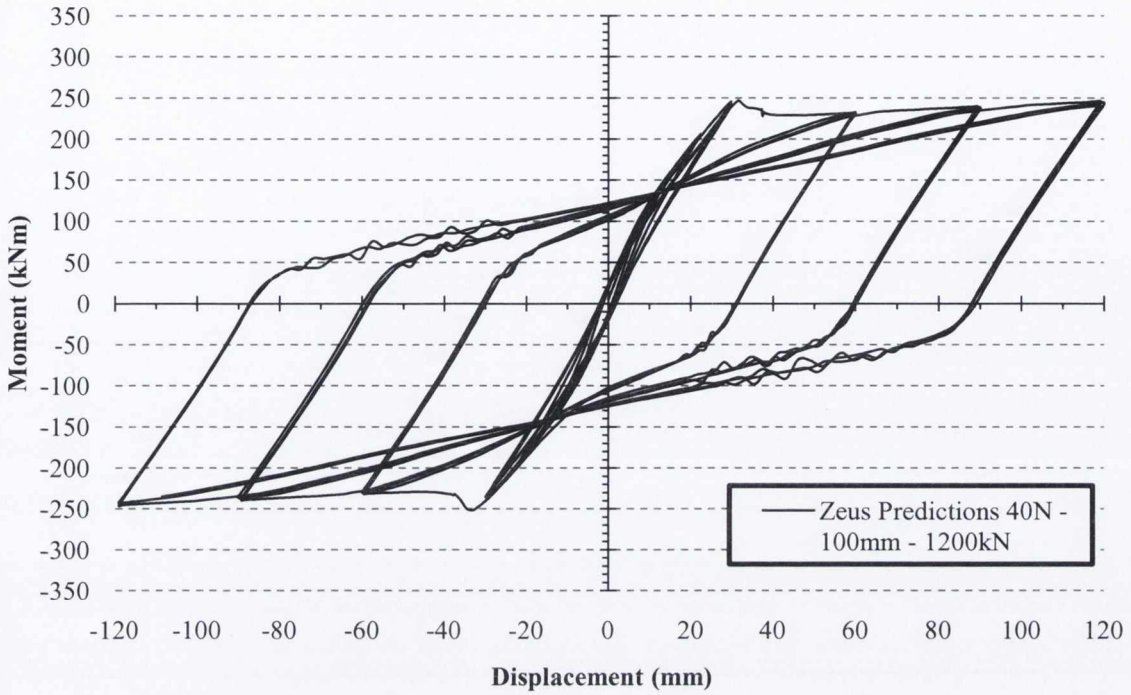

Figure 7.27: Zeus Hysteresis Predictions: Theoretical Specimen – 100mm Link Spacing & P = 1200kN

7.6 Conclusions

The finite element model (FEM) predicts the post yield behaviour of all specimens with good accuracy but overestimates the initial stiffness and underestimates the yield displacement for all specimens. The FEM fails to predict a drop in resistance at subsequent cycles of similar displacement. Furthermore the unloading branch of the predicted hysteretic behaviour was considerably different to the actual behaviour. This is important if an accurate estimate of the energy dissipation capability of the section is required. Overall the model provides a good indication of the performance of the composite column and could safely be used to accurately estimate of the load-deflection behaviour of both normal and high-strength concrete specimens.

Both the proposed and ZeusNL models predict the response of both normal and high-strength concrete composite columns with a reasonable degree of accuracy. Neither model displays superior accuracy over the other as the proposed model underestimates

the maximum resistance of the HSC specimens but the ZeusNL predicts the maximum resistance accurately but at a significantly lower displacement due to its over-estimation of the sections initial and yield stiffness. Both models could be used with confidence to predict the response of any normal strength composite column based on the results recorded in this chapter but care must be used in relation to prediction on HSC specimens with high axial load levels.

The parametric analysis indicates that the ZeusNL model (like the proposed model) is capable of predicting a change to the moment-displacement response of a section due to minor variations in concrete strength, link spacing and axial load levels. The Zeus model predicts a higher yield stiffness compared with the proposed model but predicts a lower resistance post yield than the proposed model.

Chapter 8

Conclusions

Conclusions

8.1 Introduction

The objective of this research was to determine if high-strength concrete (HSC) composite columns could achieve adequate ductility displacement capacities, similar to that of normal-strength concrete (NSC) composite columns subject to earthquake loading conditions, using the existing design and detailing provisions specified by Eurocode 8, (CEN, 2004). Furthermore, these detailing and loading provisions were analysed with a view to improving the ductility performance of HSC composite columns.

The experimental results indicate that HSC specimens subject to high levels of axial load are unable to resist the necessary displacements expected to be applied to a structure of medium ductility class during an earthquake. It was further found that a HSC member with reduced levels of axial load could attain the displacement ductility requirements of a medium ductility class member (DCM). Further tests would be required to determine the ultimate displacement ductility of these columns.

Experimental studies were conducted to determine the load-deflection hysteretic performance of representative NSC composite columns suitable for use within a dissipative composite structure. Subsequent experimental tests were conducted on HSC composite columns to determine if similar or improved hysteretic performance could be achieved using identical or improved detailing and loading provisions. A numerical model was developed to predict the moment-displacement response of the composite columns. A finite element package (ZeusNL) was also used to predict the load-displacement hysteresis performance of all specimens.

8.2 Experimental Studies

A series of six full-scale columns specimens were considered in the experimental programme. All specimens complied with the loading and detailing provisions of Eurocode 8, except for one HSC specimen which employed a reduced link spacing. The columns were subject to a combination of axial and lateral cyclic loading, which is the conventional loading applied in seismic testing. In each test the axial load was kept constant, while displacement-controlled lateral cyclic loading was applied with increasing amplitude. The parameters varied between the tests were (i) concrete compressive strength, (ii) level of axial load, and (iii) link spacing. The two characteristic concrete compressive strengths tested were 25N/mm^2 and 85N/mm^2. The applied axial loading levels varied from 20 – 40% of the specimen's cross-sectional axial capacity. The link spacing in the critical region of the column was 72mm, except for Specimen JD6 in which it was reduced to 50mm.

It was concluded from the tests that:

- The experimental observations and results indicated that composite columns possess good cyclic strength and ductility if adequately confined.

- Minor increases in the level of axial load (from 30 to 40% of axial capacity) had little effect on the hysteretic performance of NSC columns.

- An increase in the level of axial load (from 20 – 35% of axial capacity) had detrimental effects on the hysteretic performance of HSC columns. The HSC tends to fail suddenly, without excessive spalling prior to failure.

- For HSC composite columns, the increased level of axial load leads to a severe reduction in resistance following spalling of the cover concrete. Subsequent ultimate failure is recorded shortly thereafter, at a displacement ductility below that observed in a specimen with reduced levels of axial load.

- HSC composite columns with low levels of axial load (i.e. 20% of axial capacity) display hysteretic and resistance ratio properties that are similar to the NSC composite columns. This suggests that HSC can achieve displacement ductility

capacities comparable to those of NSC specimens if the maximum axial load is limited, possible by the implementation of a rule within the design code (Eurocode 8, (CEN,2004)).

- A reduced link spacing significantly improves the hysteretic performance of HSC, but sudden failure of the cover concrete is still recorded. The reduced link spacing prevents the specimen from ultimately failing as a subsequent stable hysteresis and resistance ratio plot is recorded. This suggests that a reduced link spacing should be incorporated into Eurocode 8, (CEN, 2004), for the detailing of HSC composite columns.

- A reduced link spacing in HSC specimens subjected to high axial loads does not achieve the stable hysteretic response displayed by HSC specimens subject to low levels of axial load (i.e. 20% of axial capacity). This suggests that for HSC composite columns the critical parameter for design is the level of applied axial load, as it causes undesirable brittle failure of the HSC, rather than the link spacing in critical zones.

- Though no specimens (excluding Specimen JD5) reached ultimate failure, it can be concluded that HSC specimens can only achieve the displacement ductility required of a highly dissipative member when the level of applied axial load is very low. However, it has been observed that HSC specimens with reduced link spacing and/or reduced levels of axial load are expected to achieve a displacement ductility capacity corresponding to that required in a moment resisting structure of medium dissipative capabilities (DCM).

8.3 Numerical Model

A numerical model, based on Mander's theoretical stress-strain model for confined concrete (Mander *et al.* 1988), was developed. The numerical model was developed to incorporate normal or high-strength concrete subject to constant axial load and varying cross-section curvature. The model is capable of predicting the moment-curvature and moment-displacement response of the column specimens considered in this research.

It was concluded from the numerical model that:

- The moment-displacement response of the NSC composite columns can be adequately determined, notably in the post-yield range of the response.

- The moment-displacement response of the HSC composite columns can also be adequately determined using the numerical model, but for increased levels of axial load, the numerical model tends to underestimate the maximum resistance of the specimen.

- The numerical model fails to predict the sudden drop in resistance displayed by HSC composite columns subject to high axial load levels upon spalling of the cover concrete. The model predicts a reduction in resistance at this point but continued stable reduction in resistance is recorded thereafter.

- The numerical model overestimates the initial stiffness of all specimens; this may be due to the assumption of full interaction between steel and concrete elements and an idealised concrete stress-strain relationship, thus overestimating the pre-yield stiffness response.

Mander's approach to the prediction of the fracture strain in transverse reinforcement in reinforced concrete columns was extended to cover composite column cross-sections. The predicted fracture strains indicate that for a given axial load and lateral displacement, a higher strain is predicted in the NSC specimens compared to the HSC specimens. But, if the axial load is varied so that NSC and HSC columns are subject to the same percentage of the cross-section's axial capacity the model predicts that the HSC specimens will experience the greater transverse steel strains. In either case, the

differences are not great, and it can be concluded that transverse link fracture is no more likely to occur in HSC columns than in NSC columns.

8.4 Finite Element Model

The Zeus Nonlinear (ZeusNL) finite element package was used to further predict the load-displacement hysteresis response of the column specimens considered in this research.

It was concluded from the finite element model that:

- The Zeus model was capable of adequately predicting the hysteresis response of all NSC specimens.

- The Zeus model predicted the HSC specimens reasonably well, but it predicted that the yield displacement occurred at significantly lower displacements than recorded experimentally, this was due to the considerable over-estimation of the initial and yield stiffness of the specimen.

- In HSC specimens, Zeus predicts a sudden drop in resistance due to brittle failure of the cover concrete, but as with the proposed numerical model, the maximum resistance of the specimen was underestimated.

Comparing both model predictions against the experimental result it was concluded that:

- Neither model provided superior accuracy, as the proposed numerical model underestimates the maximum resistance of the HSC specimens to a greater degree than the Zeus model.

- The proposed numerical model also fails to predict the sudden drop in resistance recorded due to brittle failure of the cover concrete, but it does provide a more accurate prediction of the initial and yield stiffness of the specimen and a more reliable estimate of the yield displacement of the section as a result.

8.5 Parametric Analysis

A parametric analysis was conducted using both models to determine if both were capable of predicting variations in the moment-displacement response due to minor changes in link spacing and axial load levels. It was determined from the analysis that:

- Both models displayed changes in the moment-displacement response due to minor alterations in link spacing and axial load levels.

- Both models displayed similar responses for minor increases in axial load level, but the Zeus model predicts that increased deterioration of the specimen will be experienced at higher levels of axial load and increased link spacing, compared with the proposed numerical model predictions.

- The Zeus model predicts a greater initial and yield stiffness than the proposed numerical model. The proposed numerical model is expected to provide a more accurate estimate of yield stiffness, as determined from a comparison with experimental results.

8.6 Further Work

This study investigated the performance of HSC composite columns compared with NSC composite specimens with a view to establishing their earthquake resistance properties and displacement ductility capabilities. Numerical and finite element models were also developed to predict the moment-displacement response of the tested specimens. However, while many issues have been addressed, the application of HSC composite columns in earthquake resistant structures still requires further research. Some of the areas which should be investigated are:

- Though a variety of columns were tested with various compressive strengths, axial load levels and link spacings, tests on an extended range of section sizes with different concrete strengths and axial loads are required to provide full insight into the seismic performance of HSC composite columns.

- Considerably more work is required to determine a suitable limit on the axial load to be applied to a HSC composite column.

- Tests on HSC composite columns that impose greater displacements than were possible within the scope of this research are required to achieve an accurate prediction of their displacement ductility, and to determine if HSC composite columns can achieve a displacement ductility corresponding to a highly dissipative moment resisting frame.

- The performance of welded transverse links compared with traditional 135° bent in hooks needs to be further considered, to assess whether welded links fracture prematurely, preventing high lateral displacements being achieved.

- The proposed numerical model has shown that Mander's approach to the prediction of failure strain in reinforced concrete may be extended to predict failure strains in composite cross-sections. However, a more accurate estimate of the strain energy at link fracture is required for a composite cross-section, particularity if welded links are used.

- One of the major assumptions employed in the numerical model is that all the plastic hinging occurs in a single longitudinal element of specified length. A more accurate prediction of the plastic hinge length is required and the form of the curvature profile within the plastic hinge needs to be defined to make the model more applicable to the analysis of different types of sections and frames as a whole.

- A more accurate estimate of the high confinement factor K_h employed in the numerical model is required. Different steel sections will encase larger areas of concrete and increased b/T ratios will provided enhanced confinement at greater displacements; thus a suitable method of predicting this value need to be established numerically.

REFERENCES

AMERICAN CONCRETE INSTITUTE 2005. Building Code Requirements for Reinforced Concrete and Commentary, Manual of Concrete Practice. *ACI-318M-05*. Michigan: American Concrete Institute.

AMERICAN INSTITUTE OF STEEL CONSTRUCTION (AISC) 1993. Load and Resistance Factor Design Specification for Structural Steel Buildings (LRFD). 2nd ed. Chicago Illinois.

ARCHITECTURAL INSTITUTE OF JAPAN 1994. Design Guidelines for Earthquake Resistant Reinforced Concrete Buildings Based on Ultimate Strength Concept. Tokyo.

BALLIO, G., CALADO, L., IORI, I. & MIRABELLA, R. 1987. I Problemi Delle Grandi Construzioni in Zona Sismica' Aicap. Rome, 33-44.

BAYRAK, O. & SHEIKH, S. A. 1998. Confinement Reinforcement Design Consideration for Ductile HSC Columns. *Journal of the Structural Engineer* ASCE, 124(9), 999-1010.

BING, L., PARK, R. & TANAKA, H. 2001. Stress-Strain Behaviour of High-Strength Concrete Confined by Ultra-High and Normal-Strength Transverse Reinforcements. *ACI Structural Journal,* 98(3), 395-406.

BOOTH, E. D. 1994. *Concrete Structures in Earthquake Regions. Design and Analysis*, Longman Scientific and Technical.

BRITISH STANDARDS INSTITUTION 1969. BS 449: Part 2. Specification for the Use of Structural Steel in Building. London.

BRITISH STANDARDS INSTITUTION 2001. BS EN 10002: Part 1. Tensile Testing of Metallic Materials. Method of Test at Ambient Temperature London.

BRITISH STANDARDS INSTITUTION 2001. EN 206: Part 1. Concrete: Specification, Performance, Production & Conformity. London.

BRITISH STANDARDS INSTITUTION 2005. BS 8666: Scheduling, Dimensioning, Bending and Cutting of Steel Reinforcement for Concrete. Specification. London.

BRODERICK, B. M. 1994. *Seismic Testing, Analysis and Design of Composite Frames.* PhD Thesis, University of London, Imperial College.

CAMPIONE, G., MIRAGLIA, N. & SCIBILIA, N. 2001. Comportamento in Compressione Di Elementi in Calcestruzzo Armato a Sezione Quadrata E Circalore Rinforzati Con FRP (in Italian). *Ingegneria Sismica.*

CHEN, C. C. & LIN, N. J. 2006. Analytical Model for Predicting Axial Capacity and Behavior of Concrete Encased Steel Composite Stub Columns. *Journal of Constructional Steel Research,* 62, 424-433.

CHEN, C. C., WENG, C. C., LIN, I. M. & LI, J. I. 1999. Seismic Behaviour and Strength of Concrete Encased Steel Stub Columns and Beam-Columns (in

Chinese). *Report No. MOIS 881012-1.* Architecture and Buliding Research Institute.

CHEN, C. C. & YEH, S. C. 1996. Ultimate Strength of Concrete Encased Steel Composite Columns (in Chinese). Proceedings of the Third National Conference on Structural Engineering, China, 2197–2206.

CHUNG, H.-S., YANG, K.-H., LEE, Y.-H. & EUN, H.-C. 2002. Stress-Strain Curve of Laterally Confined Concrete. *Engineering Structures,* 24, 1153-1163.

COMITÉ EURO-INTERNATIONAL DU BÉTON 1998. Seismic Design of Reinforced Concrete Structures for Controlled Inelastic Response. Bulletin 236.

CUSSON, D. & PAULTRE, P. 1994. High-Strength Concrete Columns Confined by Rectangular Ties. *Journal of Structural Engineering,* 120, 783-804.

CUSSON, D. & PAULTRE, P. 1995. Stress-Strain Model for Confined High-Strength Concrete. *Journal of Structural Engineering,* 121, 468-477.

DESAYI, P., IYENGAR, K. T. S. R. & REDDY, T. S. 1978. Equations for Stress-Strain Curves of Concrete Confined in Circular Steel Spirals. *Materiaux et Constructions,* September/October, 339-345.

DIERLIN, G. & NOGUCHI, H. 2000. Research on Rc/Src Column Systems. Proceedings of The Twelfth World Conference on Earthquake Engineering (12WCEE), Auckland, New Zealand, Paper No. 2621.

ELGHAZOULI, A. Y. & TREADWAY, J. 2008. Inelastic Behaviour of Composite Members under Combined Bending and Axial Loading. *Journal of Constructional Steel Research,* 64, 1008-1019.

ELGHAZOULI, A. Y. & TREADWAY, J. 2008. Inelastic Behaviour of Composite Members under Combined Bending and Axial Loading. *Journal of Constructional Steel Research,* 64, 1008-1019.

EL-TAWIL, S. & DEIERLEIN, G. G. 1999. Strength and Ductility of Concrete Encased Composite Columns. *Journal of Structural Engineering,* 125, 1009-1019.

EUROPEAN COMMITTEE FOR STANDARDISATION (CEN) 2004. Eurocode 2: Design of Concrete Structures - Part 1-1: General Rules and Rules for Buildings. *BS EN 1992-1-1:2004.* UK: British Standards Institute.

EUROPEAN COMMITTEE FOR STANDARDISATION (CEN) 2004. Eurocode 4: Design of Composite Steel and Concrete Structures - Part 1-1: General Rulea and Rules for Buildings. *BS EN 1994-1-1:2004.* UK: British Standards Institute.

EUROPEAN COMMITTEE FOR STANDARDISATION (CEN) 2004. Eurocode 8: Design of Structures for Earthquake Resistance – Part 1: General Rules, Seismic Actions and Rules for Buildings. *BS EN 1998-1:2004.* UK: British Standards Institute.

FURUKAWA, J. & KOUJI, O. 1996. Effect of Yield Strength of Longitudinal Reinforcing Bar on Ductility of R/C Beam Yield Hinge. Proceedings of the Eleventh World Conference on Earthquake Engineering (11WCEE), Acapulco, Mexico, Paper No. 1197.

GIAKOUMELIS, G. & LAM, D. 2004. Axial Capacity of Circular Concrete-Filled Tube Columns. *Journal of Constructional Steel Research,* 60, 1049-1068.

GRIFFIS, L. G. 1986. Some Design Considerations for Composite-Frame Structures. *AISC Engineering Journal,* 23(2), 59-64.

HAYES Jr, J. R., WOODSON, S. C., PEKELNICKY, R. G., POLAND, C. D., CORLEY, W. G. & SOZEN, M. 2005. Can Strengthening for Earthquake Improve Blast and Progressive Collapse Resistance? *Journal of Structural Engineering,* 131(8), 1157-1177.

HAN, B. S., SHIN, S. W. & BAHN, B. Y. 2003. A Model of Confined Concrete in High-Strength Reinforced Concrete Tied Columns. *Magazine of Concrete Research,* 55(3), 203-214.

HAN, L. H. 2002. Tests on Stub Columns of Concrete-Filled RHS Sections. *Journal of Constructional Steel Research,* 58, 353-372.

HO, J. C. M., LAM, J. Y. K. & KWAN, A. K. H. 2010. Effectiveness of Adding Confinement for Ductility Improvement of High-Strength Concrete Columns. *Engineering Structures,* 32, 714-725.

HOGNESTAD, E., HANSON, N. W. & MCHENRY, D. 1955. Concrete Stress-Strain Distribution in Ultimate Strength Design. *American Concrete Institute,* 52(12), 455-480.

HONG, K. N., AKIYAMA, S. T. & SUZUKI, M. 2006. Stress-Strain Behaviour of High-Strength Concrete Columns Confined by Low-Volumetric Ratio Rectangular Ties. *Magazine of Concrete Research,* 58(2), 101-115.

HONG, K. N., HAN, S. H. & YI, S. T. 2006. High-Strength Concrete Columns Confined by Low-Volumetric-Ratio Lateral Ties. *Engineering Structures,* 28, 1346-1353.

HSU, H. L., JAN, F. J. & JUANG, J. L. 2009. Performance of Composite Members Subjected to Axial Load and Bi-Axial Bending. *Journal of Constructional Steel Research,* 65, 869-878.

HOUSNER, G. W. & HUDSON D. E. 1966. Earthquake Research Problems of Nuclear Power Plants. *Nuclear Engineering and Design,* 3, 308-319.

HWANG, S. K. & YUN, H. D. 2004. Effects of Transverse Reinforcement on Flexural Behaviour of High-Strength Concrete Columns. *Engineering Structures,* 26, 1-12.

KENT, D. C. & PARK, R. 1971. Flexural Members with Confined Concrete. *Journal of the Structural Division,* 97(7), 1969-1990.

LEGERON, F. & PAULTRE, P. 2000. Behaviour of High-Strength Concrete Columns under Cyclic Flexure and Constant Axial Load. *ACI Structural Journal,* 97(4), 591-601.

LESLIE, P. D. 1974. Ductility of Reinforced Concrete Piers. *M.E. Report.* University of Canterbury, New Zealand.

LU, X. & HSU, C.-T. T. 2007. Stress-Strain Relations of High-Strength Concrete under Tri-axial Compression. *Journal of Materials in Civil Engineering,* 19, 261-268.

MANDER, J. B., PRIESTLEY, M. J. N. & PARK, R. 1988. Theoretical Stress-Strain Model for Confined Concrete. *Journal of Structural Engineering,* 114, 1804-1826.

MARKOVSKI, G. 2010. Have We Forgotten Skopje 1963 Earthquake? Proceedings of The Fourteenth European Earthquake Engineering Conference (14ECEE), Ohrid, Macedonia, Paper No. 1889.

MCFARLANE, A. 2007. High-Strength Concrete Columns: A Design Guidance. *The Structural Engineer,* 85(6), 31-38.

MENDIS, P. 2001. Design of High-Strength Concrete Members: State of the Art. *Engineers Australia Pty Limited,* 2(17), 4-29.

MIRZA, S. A., HYTTINEN, V. & HYTTINEN, E. 1996. Physical Tests and Analyses of Composite Steel-Concrete Beam-Columns. *Journal of Structural Engineering,* 122, 1317-1326.

MIRZA, S. A. & SKRABEK, B. W. 1992. Statistical Analysis of Slender Composite Beam-Column Strength. *Journal of Structural Engineering,* 118, 1312-1332.

MIRZA, S. A. & TIKKA, T. K. 1999. Flexural Stiffness of Composite Columns Subjected to Major Axis Bending. *American Concrete Institute,* 96(1), 19-28.

MUGURUMA, H. & WATANABE, F. 1990. Ductility Improvement of High-Strength Concrete Columns with Lateral Confinement. Proceedings of The Second International Symposium on Utilization of High-Strength Concrete, University of Berkeley, California.

NAWY, E. G. 2001. *Fundamentals of High-Performance Concrete (2nd Edition)*, John Wiley & Sons.

NEVILLE, A. M. 1995. *Properties of Concrete*, Longman Group Limited.

OH, M. H., JU, Y. K., KIM, M. H. & KIM, S. D. 2006. Structural Performance of Steel-Concrete Composite Column Subject to Axial and Flexural Loading. *Journal of Asian Architecture and Building Engineering,* 5(1), 153-160.

O'SHEA, M. D. & BRIDGE, R. Q. 2000. Design of Circular Thin-Walled Concrete Filled Steel Tubes. *Journal of Structural Engineering,* 126, 1295-1303.

PARK, R. 1992. Capacity Design of Ductile RC Building Structures for Earthquake Resistance. *The Structural Engineer,* 70(16), 279.

PARK, R. & PAULAY, T. 1975. *Reinforced Concrete Structures*, John Wiley & Sons.

POPOVICS, S. 1973. A Numerical Approach to the Complete Stress-Strain Curves of Concrete. *Cement and Concrete Research,* 3(5), 583-599.

RAZVI, R. & SAATCIOGLU, M. 1994. Strength and Deformability of Confined High-Strength Concrete Columns. *ACI Structural Journal,* 91(6), 1-10.

RAZVI, R. & SAATCIOGLU, M. 1996. Confinement of High-Strength Concrete Columns for Seismic Applications. Proceedings of The Eleventh World Conference on Earthquake Engineering (11WCEE), Acapulco, Mexico, Paper No. 1855.

RICHART, F. B., BRANDTZAEG, A. & BROWN, R. L. 1928. A Study of the Failure of Concrete under Combined Compressive Stress. *Engineering Research Station,* University of Illinois, Bulletin No. 185.

RICHART, F. B., BRANDTZAEG, A. & BROWN, R. L. 1929. The Failure of Plain and Spirally Reinforced Concrete in Compression. *Engineering Research Station,* University of Illinois, Bulletin No 190.

RICLES, J. A. & PABOOJIAN, S. A. 1992. Behaviour of Composite Columns under Seismic Conditions. Proceedings of The Tenth World Conference on Earthquake Engineering (10WCEE), Balkema, Rotterdam, 3431-3436.

RICLES, J. M. & PABOOJIAN, S. D. 1994. Seismic Performance of Steel-Encased Composite Columns. *Journal of Structural Engineering,* 120, 2474-2494.

ROY, H. E. H. & SOZEN, M. A. 1964. Ductility of Concrete. Proceedings of International Symposium on the Flexural Mechanics of Reinforced Concrete: ASCE - American Concrete Institute, 213-224.

RYAN, C. A. 2001. *Confinement in Wireball Reinforced Concrete Members.* PhD Thesis, University of Dublin, Trinity College.

SAATCIOGLU, M. & BAINGO, D. 1999. Circular High-Strength Concrete Columns under Simulated Seismic Loading. *Journal of Structural Engineering,* 125, 272-280.

SAATCIOGLU, M. & RAZVI, S. R. 1998. High-Strength Concrete Columns with Square Sections under Concentric Compression. *Journal of Structural Engineering,* 124, 1438-1447.

SAKAI, J., MATSUI, C. & MINAMI, K. 2000. Earthquake Resistant Properties of Core Steel Composite Columns. Proceedings of The Twelfth World Conference on Earthquake Engineering (12WCEE), Auckland, New Zealand, Paper No. 1280.

SAKINO, K., NAKAHARA, H., MORINO, S. & NISHIYAMA, I. 2004. Behaviour of Centrally Loaded Concrete-Filled Steel-Tube Short Columns. *Journal of Structural Engineering,* 130, 180-188.

SCHNEIDER, S. P. 1998. Axially Loaded Concrete-Filled Steel Tubes. *Journal of Structural Engineering,* 124, 1125-1138.

SCOTT, B. D., PARK, R. & PRIESTLEY, M. J. N. 1982. Stress-Strain Behaviour of Concrete Confined by Overlapping Hoops at Low and High Strain Rates. *American Concrete Institute Journal,* 79(1), 13-27.

SHEIKH, S. A., SHAH, D. V. & KHOURY, S. S. 1994. Confinement of High-Strength Concrete Columns. *ACI Structural Journal,* 91(1), 100-111.

SHEIKH, S. A. & UZUMERI, S. M. 1980. Strength and Ductility of Tied Concrete Columns. *Journal of the Structural Division,* ASCE, 106(5), 1079-1102.

SHIM, C.S., CHUNG, Y.S. & HAN, J.H. 2008. Cyclic Response of Concrete-Encased Composite Columns with Low Steel Ratio. *Structures & Buildings,* 161(2), 77-89.

SHIN, S. A., GHOSH, S. K. & MORENO, J. 1989. Flexural Ductility of Ultra-High-Strength Concrete Members. *ACI Structural Journal,* 86(4), 394-400.

SUSANTHA, K. A. S., GE, H. & USAMI, T. 2001. Uni-axial Stress-Strain Relationship of Concrete Confined by Various Shaped Steel Tubes. *Engineering Structures,* 23, 1331-1347.

TSAI, K. C., LIEN, Y. & C., C. C. 1996. Behaviour of Axially Loaded Steel Reinforced Concrete Columns. *Journal of the Chinese Institute of Civil and Hydraulic Engineering* 8(4), 535–545 (In Chinese).

VARMA, A. H., RICLES, J. M., SAUSE, R. & LU, L. W. 2002. Seismic Behaviour and Modelling of High-Strength Composite Concrete-Filled Steel Tube (CFT) Beam–Columns. *Journal of Constructional Steel Research,* 58, 725-758.

VELLENAS, J., BERTOERO, V. V. & POPOV, E. P. 1977. Concrete Confined by Rectangular Hoops Subjected to Axial Loads. *Report 77/13.* Earthquake Engineering Research Centre, University of California, Berkeley, California.

WAKABAYASHI, M. 1987. A Historical Study of Research on Composite Construction in Japan. Proceedings of The Engineering Foundation Conference, Henniker, New Hampshire: ASCE, 400-427.

WAKABAYASHI, M., SHIBATA, M., MATSUI, C. & MINAMI, K. 1974. A Study on the Behaviour of Steel-Reinforced Concrete Columns and Frames. Proceedings of The IABSE Symposium, 53-60.

WENG, C. C. & YEN, S. I. 2002. Comparisons of Concrete-Encased Composite Column Strength Provisions of ACI Code and AISC Specification. *Engineering Structures,* 24, 59-72.

Appendix A

Specimen JD1 – ID2

Stain Gauge 1 Offline

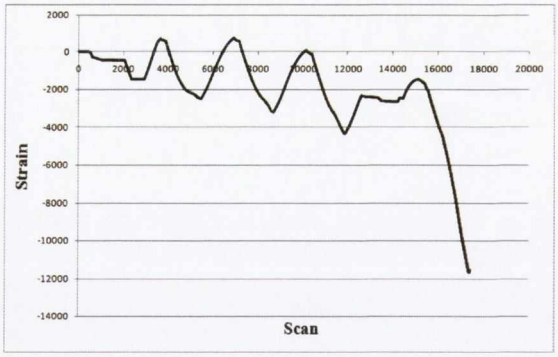

Figure A.1: Strain versus Scan Plot: Specimen JD1 – S.G. 1 (a) Run 1 (b) Run 2

Stain Gauge 3 Offline

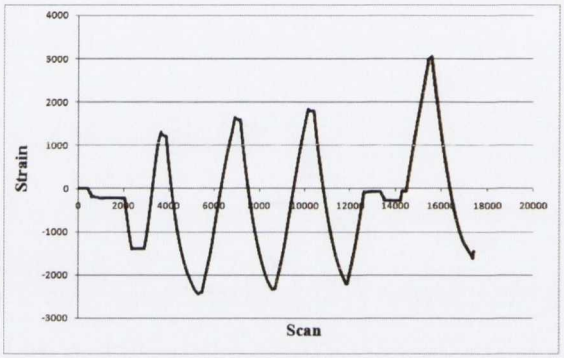

Figure A.2: Strain versus Scan Plot: Specimen JD1 – S.G. 3 (a) Run 1 (b) Run 2

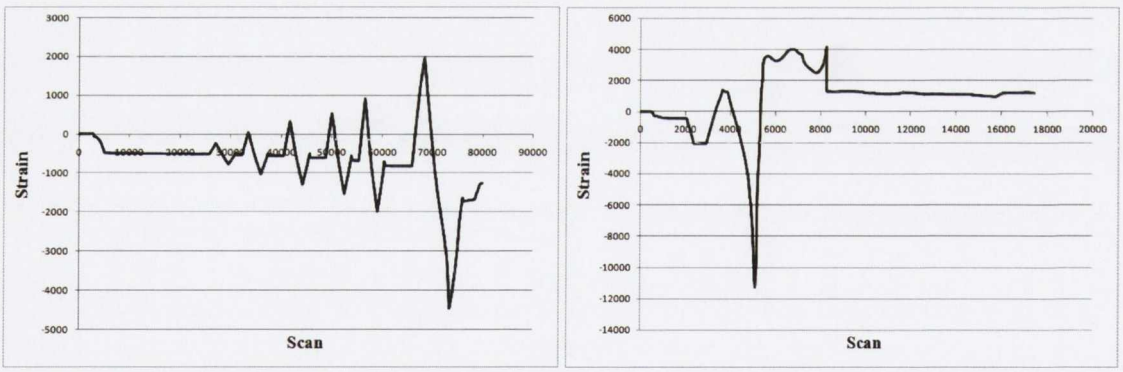

Figure A.3: Strain versus Scan Plot: Specimen JD1 – S.G. 5 (a) Run 1 (b) Run 2

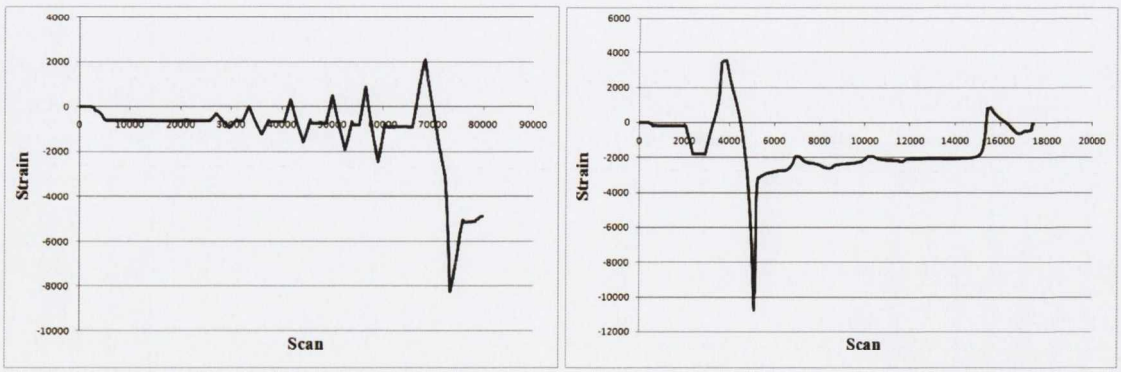

Figure A.4: Strain versus Scan Plot: Specimen JD1 – S.G. 7 (a) Run 1 (b) Run 2

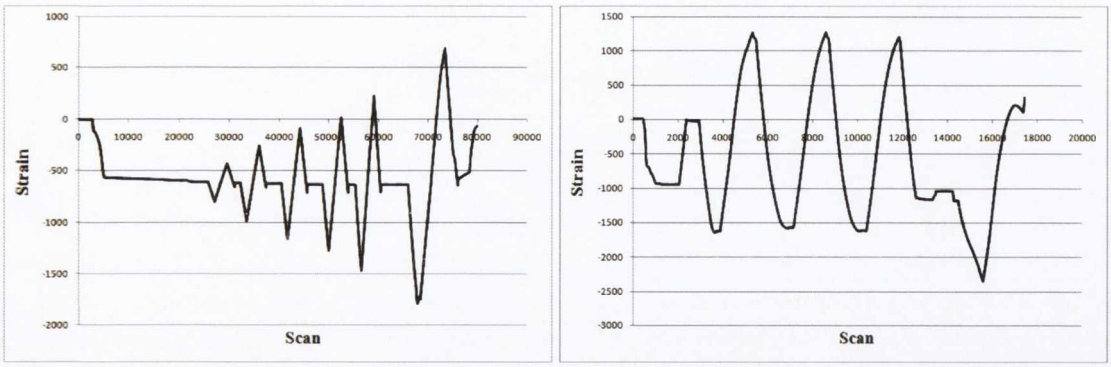

Figure A.5: Strain versus Scan Plot: Specimen JD1 – S.G. 9 (a) Run 1 (b) Run 2

Stain Gauge 11 Offline

Stain Gauge 11 Offline

Figure A.6: Strain versus Scan Plot: Specimen JD1 – S.G. 11 (a) Run 1 (b) Run 2

Stain Gauge 13 Offline

Stain Gauge 13 Offline

Figure A.7: Strain versus Scan Plot: Specimen JD1 – S.G. 13 (a) Run 1 (b) Run 2

Stain Gauge 15 Offline

Stain Gauge 15 Offline

Figure A.8: Strain versus Scan Plot: Specimen JD1 – S.G. 15 (a) Run 1 (b) Run 2

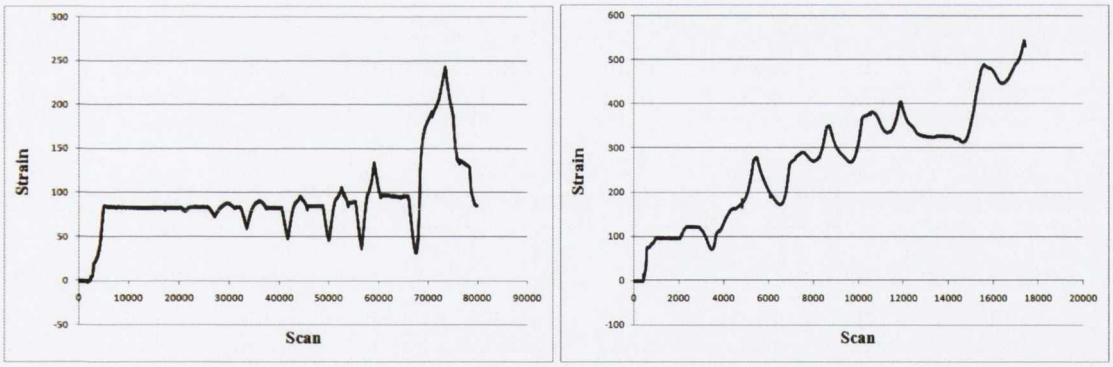

Figure A.9: Strain versus Scan Plot: Specimen JD1 – S.G. 17 (a) Run 1 (b) Run 2

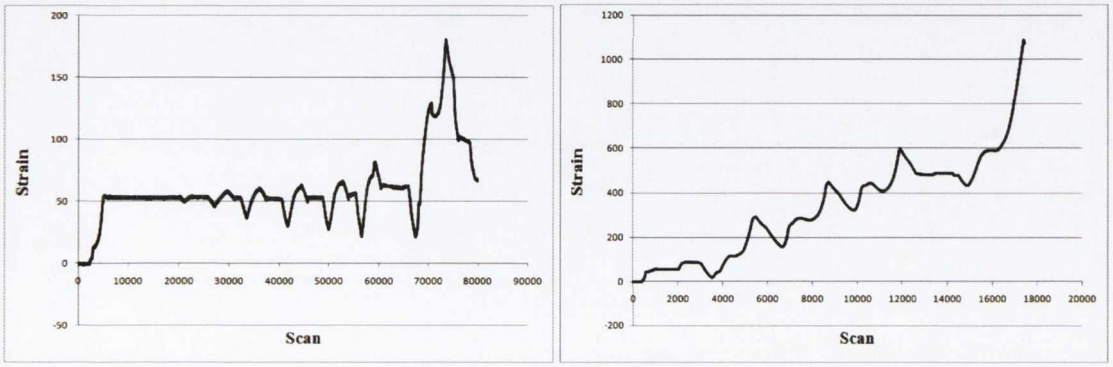

Figure A.10: Strain versus Scan Plot: Specimen JD1 – S.G. 19 (a) Run 1 (b) Run 2

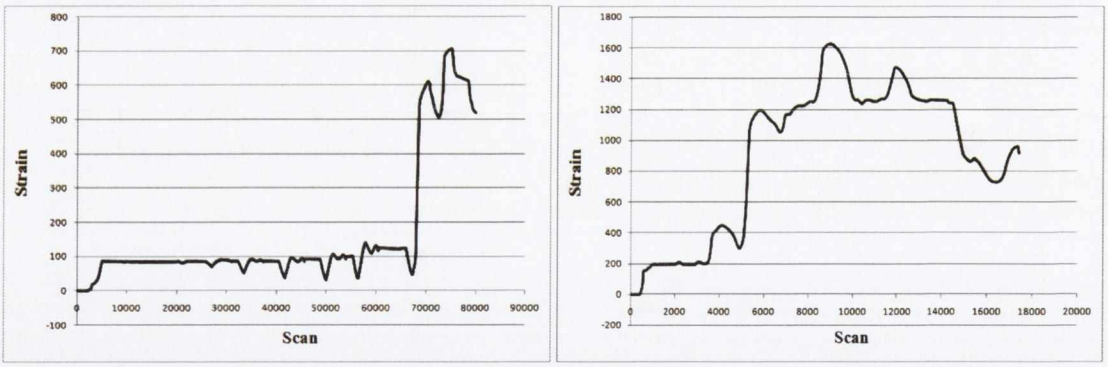

Figure A.11: Strain versus Scan Plot: Specimen JD1 – S.G. 21 (a) Run 1 (b) Run 2

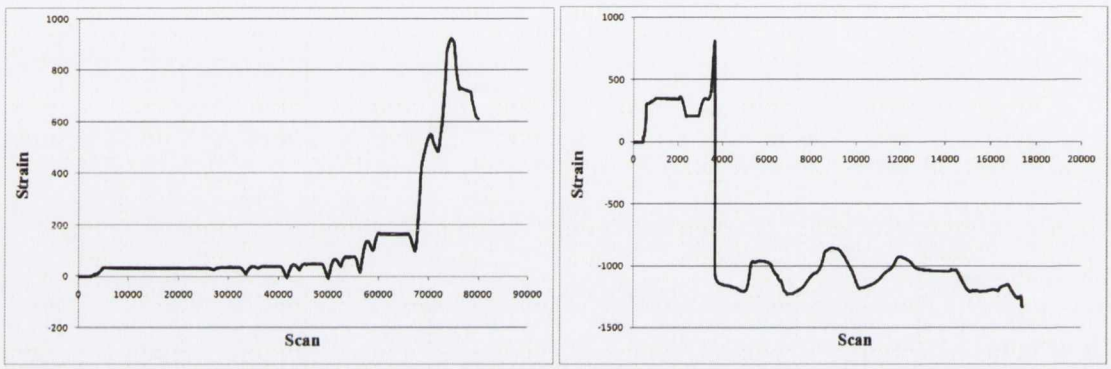

Figure A.12: Strain versus Scan Plot: Specimen JD1 – S.G. 23 (a) Run 1 (b) Run 2

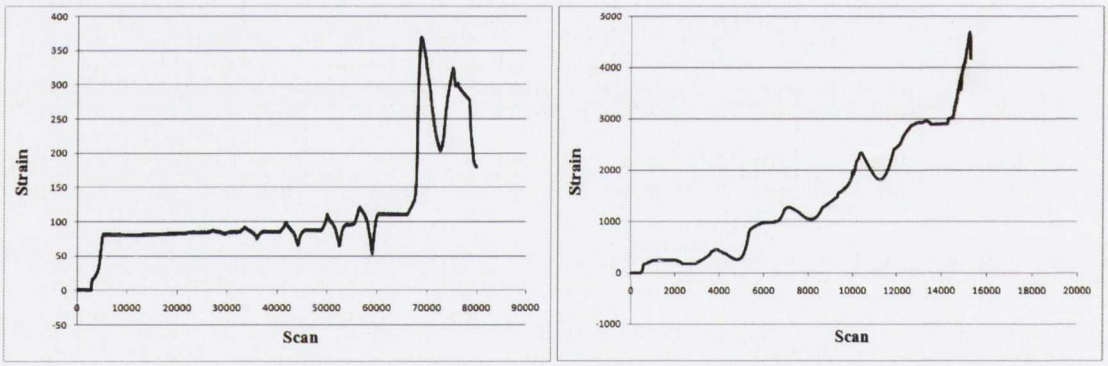

Figure A.13: Strain versus Scan Plot: Specimen JD1 – S.G. 25 (a) Run 1 (b) Run 2

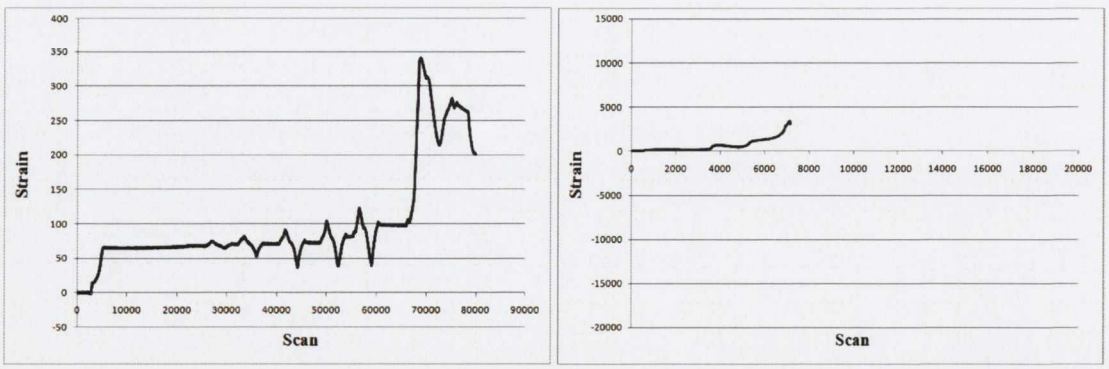

Figure A.14: Strain versus Scan Plot: Specimen JD1 – S.G. 27 (a) Run 1 (b) Run 2

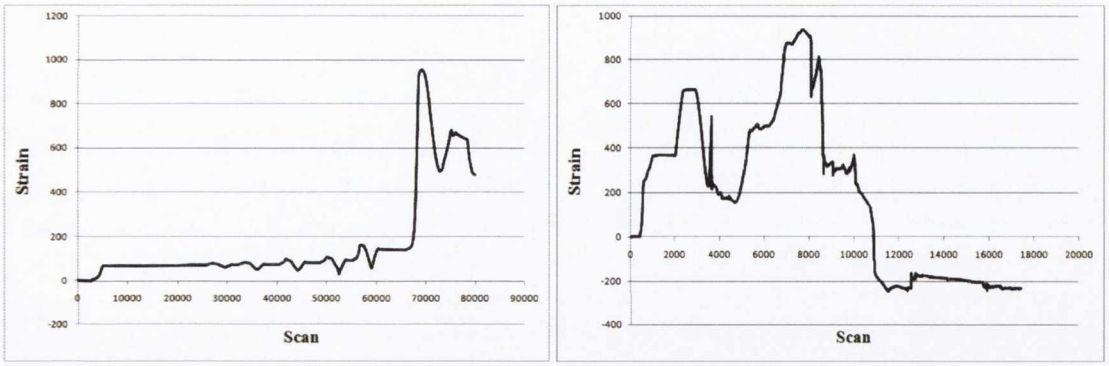

Figure A.15: Strain versus Scan Plot: Specimen JD1 – S.G. 29 (a) Run 1 (b) Run 2

Stain Gauge 2 Offline

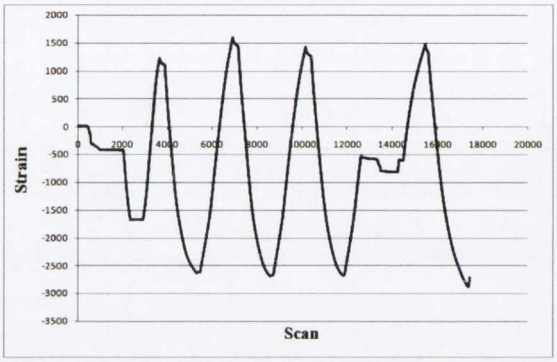

Figure A.16: Strain versus Scan Plot: Specimen JD1 – S.G. 2 (a) Run 1 (b) Run 2

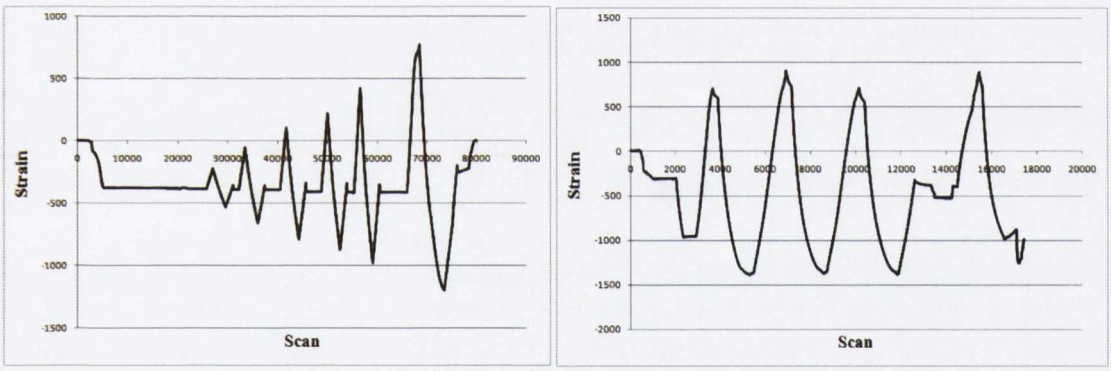

Figure A.17: Strain versus Scan Plot: Specimen JD1 – S.G. 4 (a) Run 1 (b) Run 2

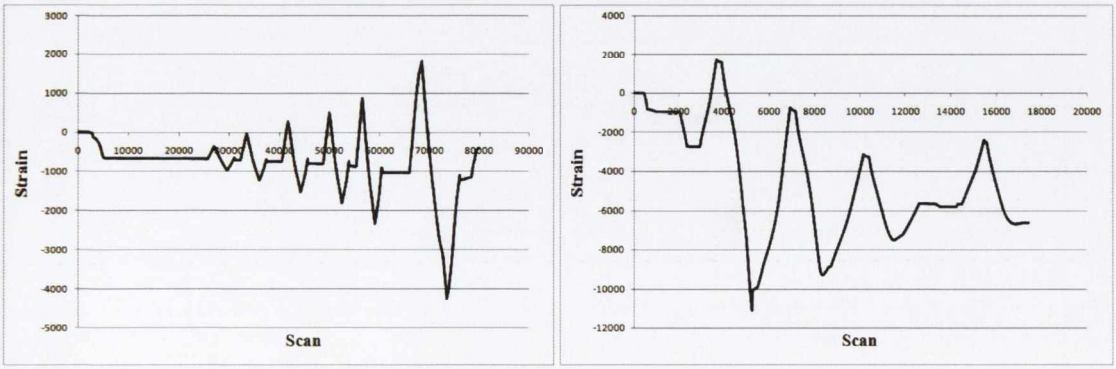

Figure A.18: Strain versus Scan Plot: Specimen JD1 – S.G. 6 (a) Run 1 (b) Run 2

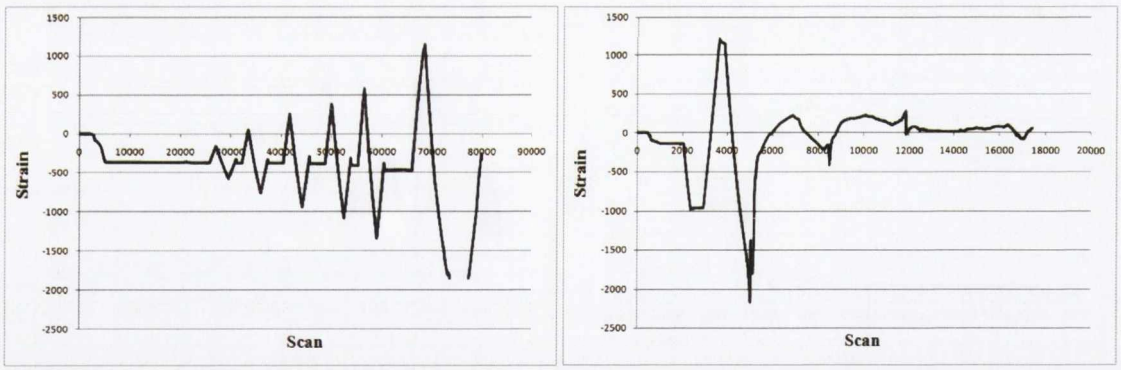

Figure A.19: Strain versus Scan Plot: Specimen JD1 – S.G. 8 (a) Run 1 (b) Run 2

Stain Gauge 10 Offline

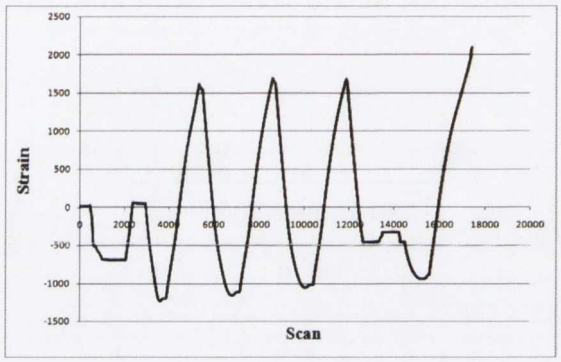

Figure A.20: Strain versus Scan Plot: Specimen JD1 – S.G. 10 (a) Run 1 (b) Run 2

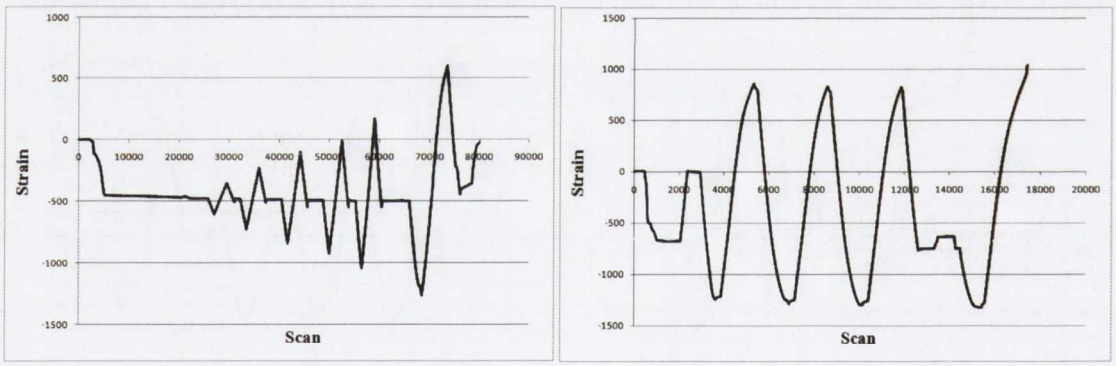

Figure A.21: Strain versus Scan Plot: Specimen JD1 – S.G. 12 (a) Run 1 (b) Run 2

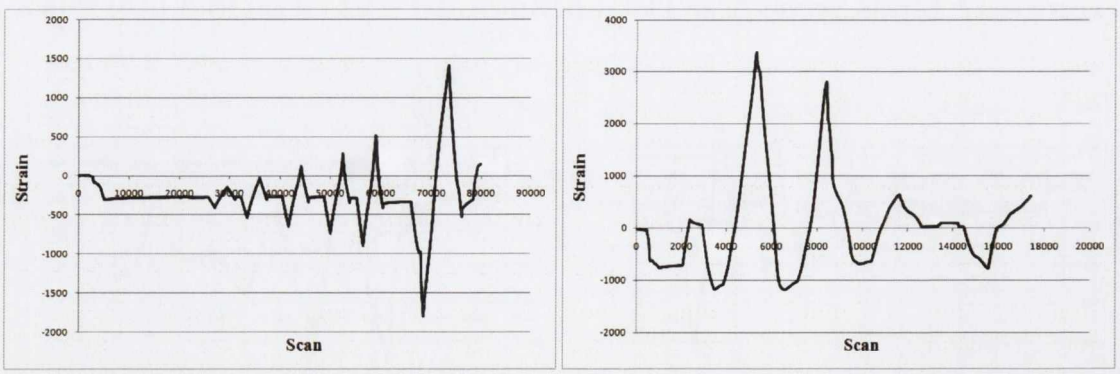

Figure A.22: Strain versus Scan Plot: Specimen JD1 – S.G. 14 (a) Run 1 (b) Run 2

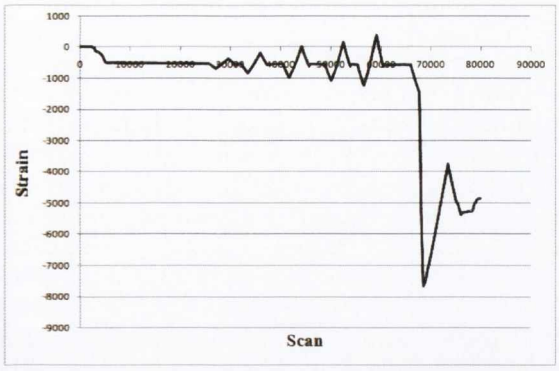

Stain Gauge 16 Offline

Figure A.23: Strain versus Scan Plot: Specimen JD1 – S.G. 16 (a) Run 1 (b) Run 2

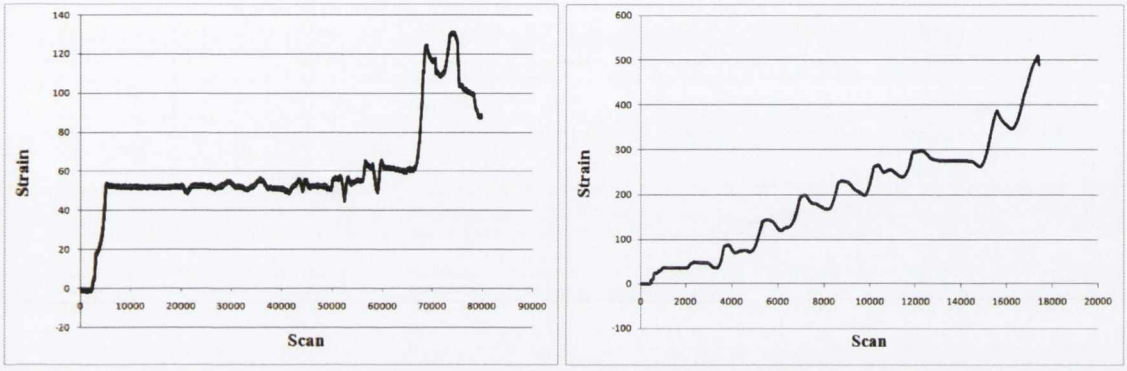

Figure A.24: Strain versus Scan Plot: Specimen JD1 – S.G. 18 (a) Run 1 (b) Run 2

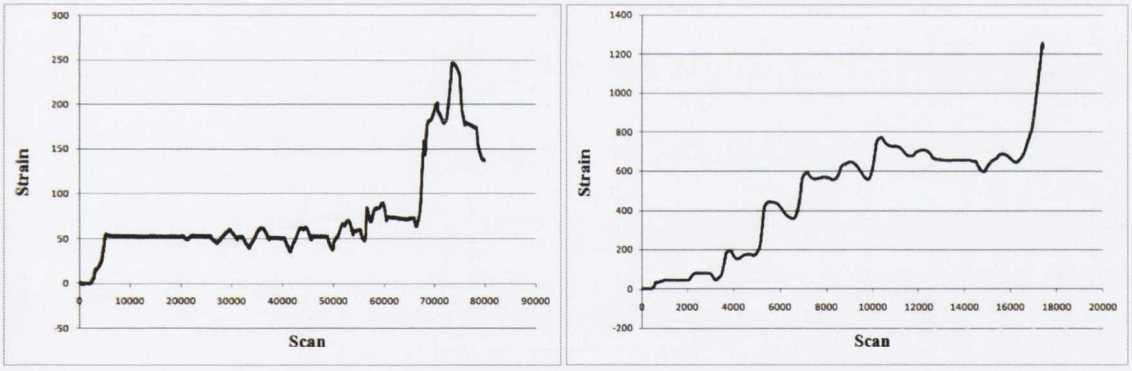

Figure A.25: Strain versus Scan Plot: Specimen JD1 – S.G. 20 (a) Run 1 (b) Run 2

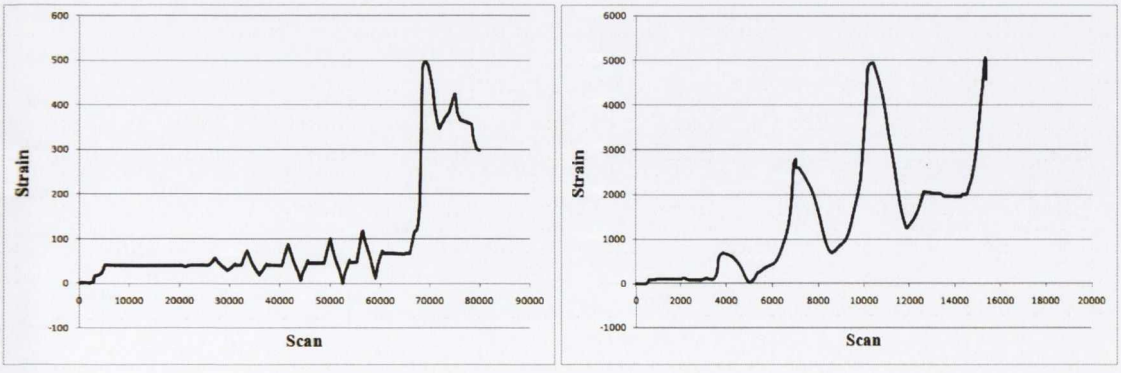

Figure A.26: Strain versus Scan Plot: Specimen JD1 – S.G. 22 (a) Run 1 (b) Run 2

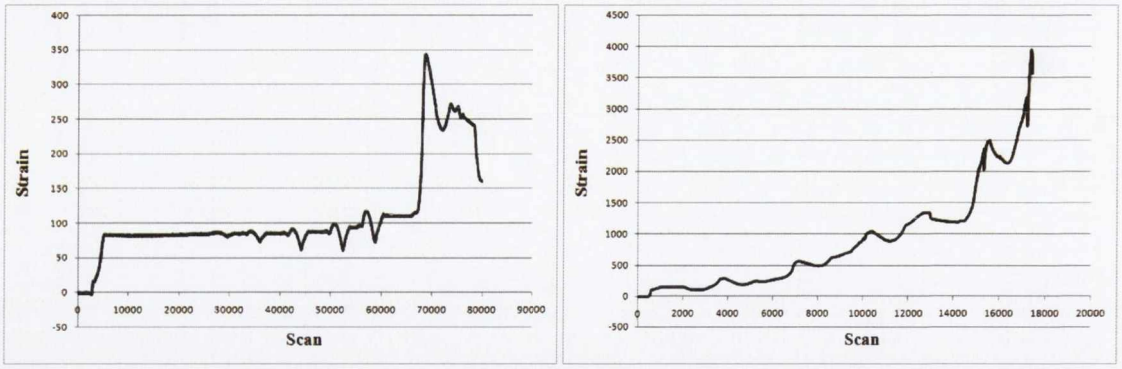

Figure A.27: Strain versus Scan Plot: Specimen JD1 – S.G. 24 (a) Run 1 (b) Run 2

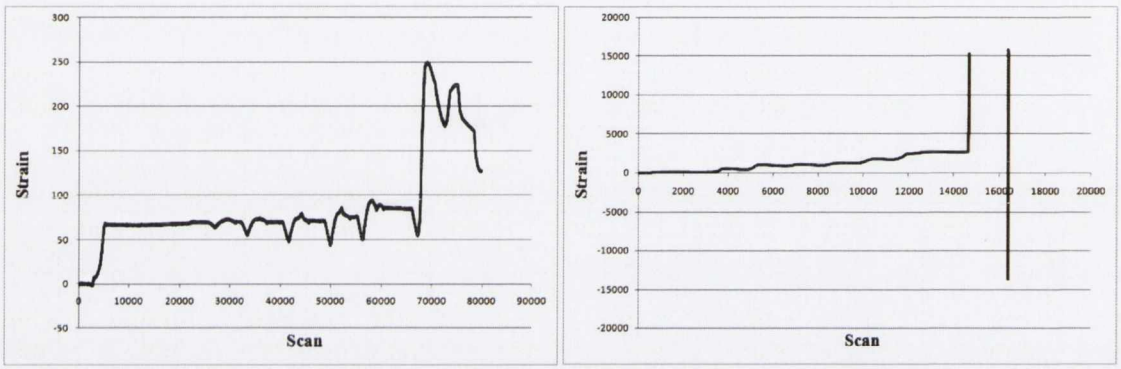

Figure A.28: Strain versus Scan Plot: Specimen JD1 – S.G. 26 (a) Run 1 (b) Run 2

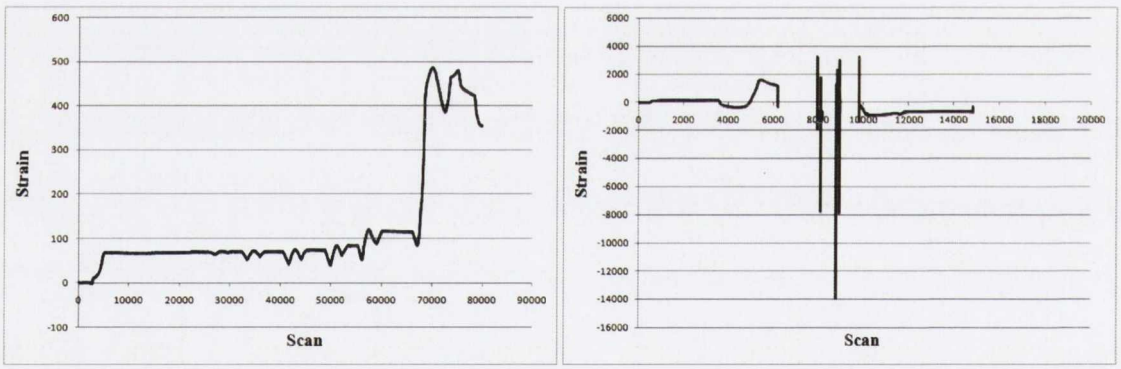

Figure A.29: Strain versus Scan Plot: Specimen JD1 – S.G. 28 (a) Run 1 (b) Run 2

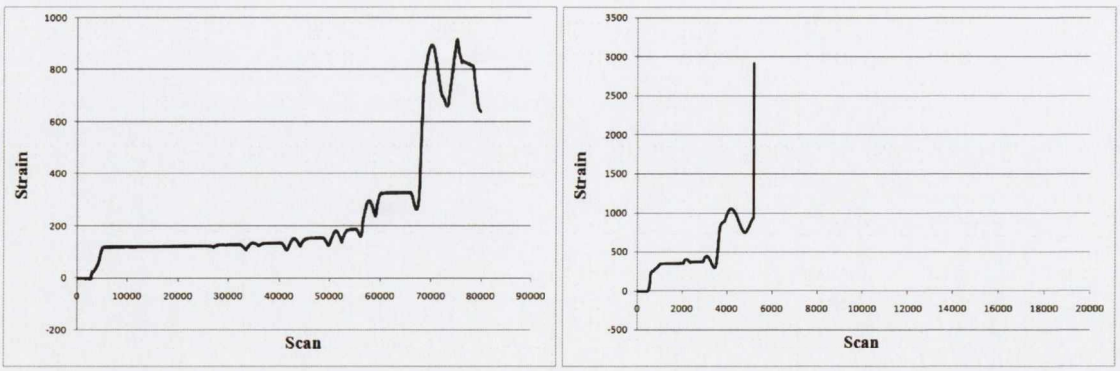

Figure A.30: Strain versus Scan Plot: Specimen JD1 – S.G. 30 (a) Run 1 (b) Run 2

Specimen JD2 – ID1

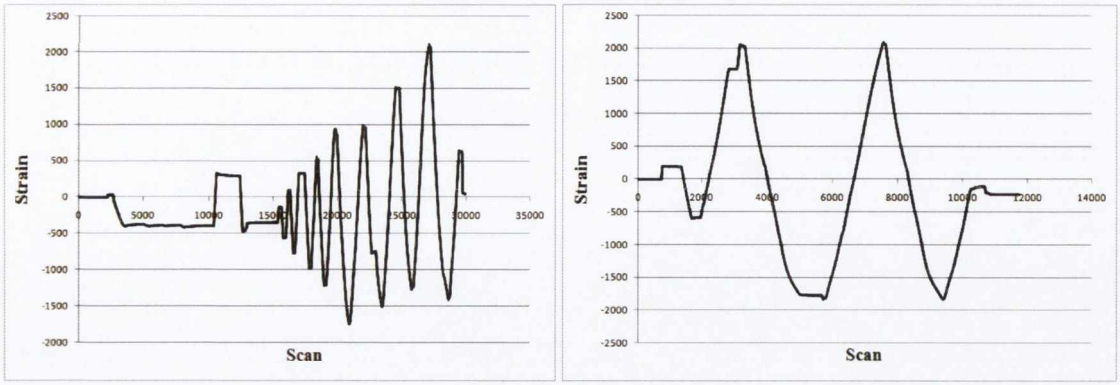

Figure A.31: Strain versus Scan Plot: Specimen JD2 – S.G. 1 (a) Run 1 (b) Run 2

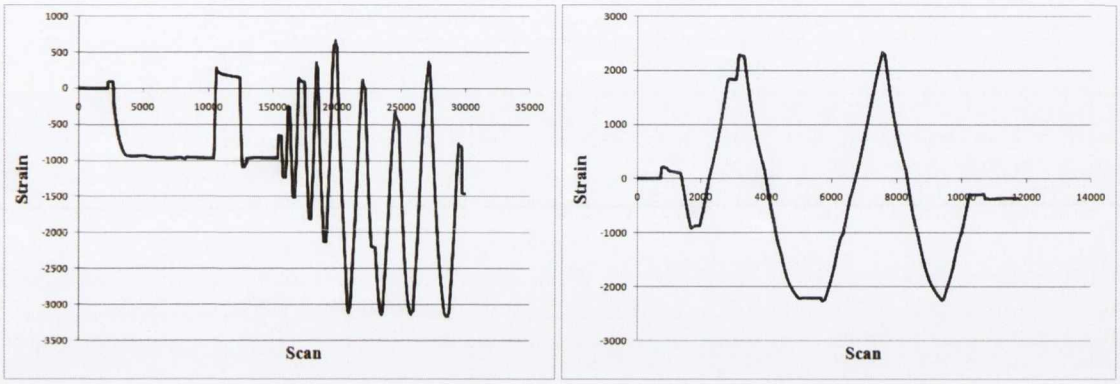

Figure A.32: Strain versus Scan Plot: Specimen JD2 – S.G. 3 (a) Run 1 (b) Run 2

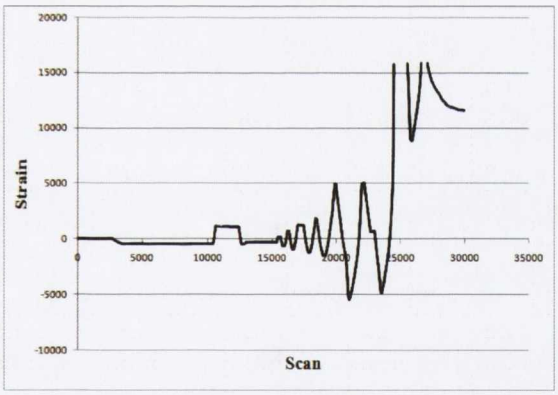

Stain Gauge 5 Offline

Figure A.33: Strain versus Scan Plot: Specimen JD2 – S.G. 5 (a) Run 1 (b) Run 2

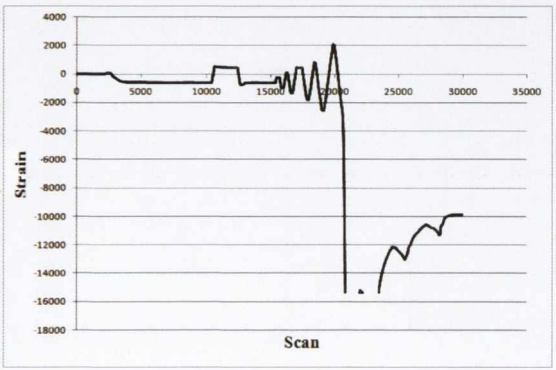

Stain Gauge 7 Offline

Figure A.34: Strain versus Scan Plot: Specimen JD2 – S.G. 7 (a) Run 1 (b) Run 2

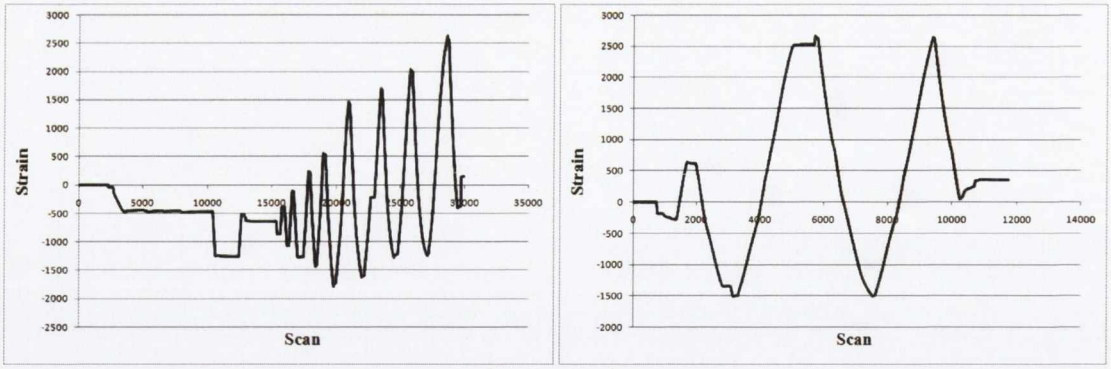

Figure A.35: Strain versus Scan Plot: Specimen JD2 – S.G. 9 (a) Run 1 (b) Run 2

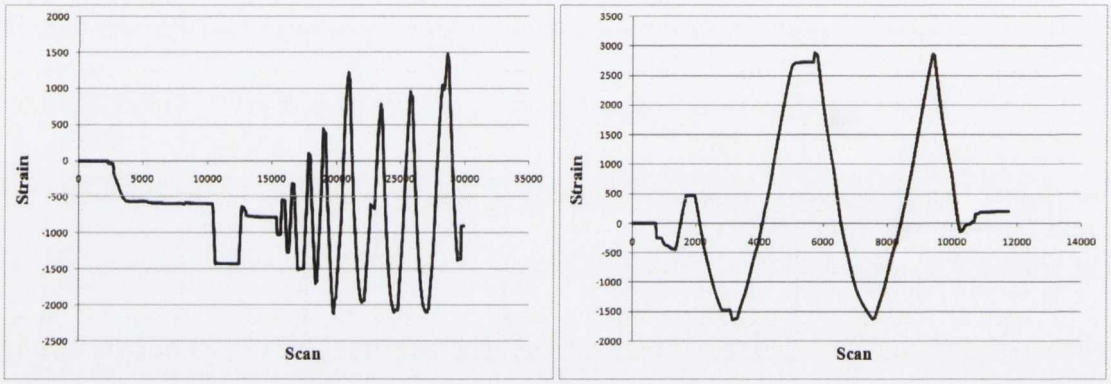

Figure A.36: Strain versus Scan Plot: Specimen JD2 – S.G. 11 (a) Run 1 (b) Run 2

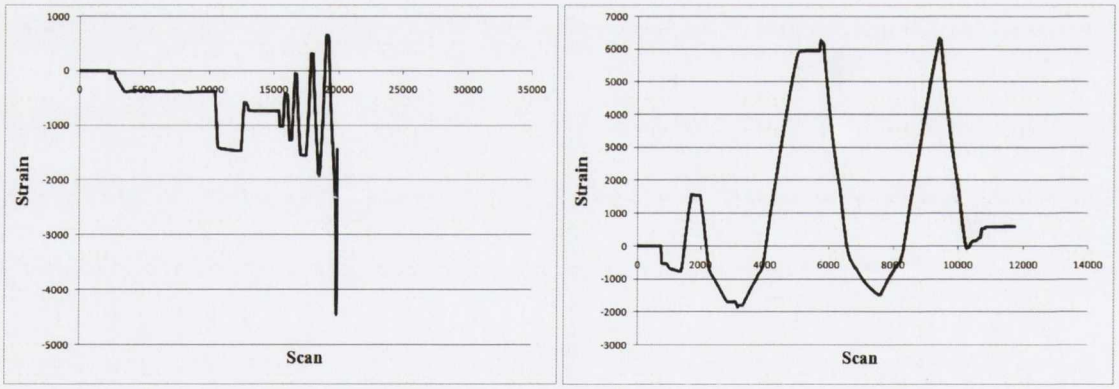

Figure A.37: Strain versus Scan Plot: Specimen JD2 – S.G. 13 (a) Run 1 (b) Run 2

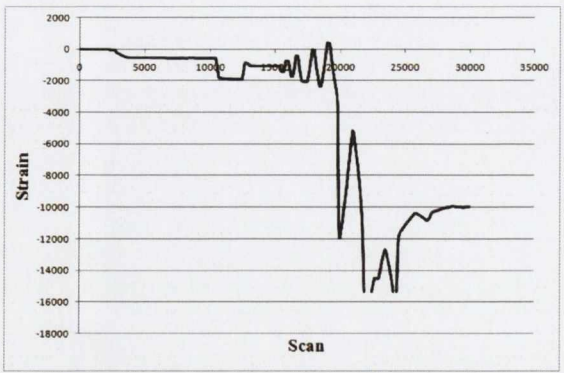

Stain Gauge 15 Offline

Figure A.38: Strain versus Scan Plot: Specimen JD2 – S.G. 15 (a) Run 1 (b) Run 2

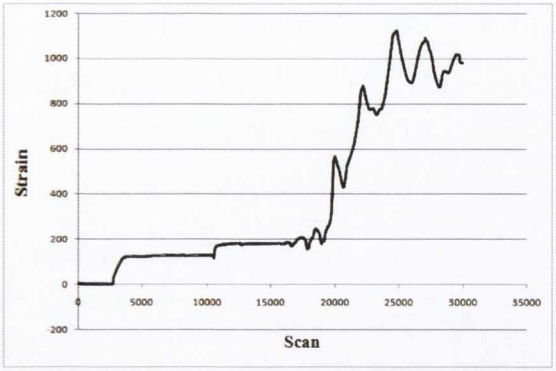

Stain Gauge 17 Offline

Figure A.39: Strain versus Scan Plot: Specimen JD2 – S.G. 17 (a) Run 1 (b) Run 2

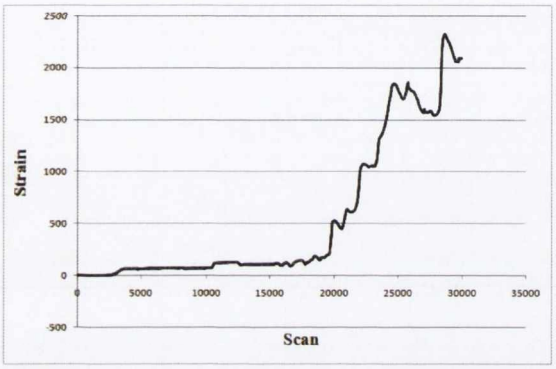

Stain Gauge 19 Offline

Figure A.40: Strain versus Scan Plot: Specimen JD2 – S.G. 19 (a) Run 1 (b) Run 2

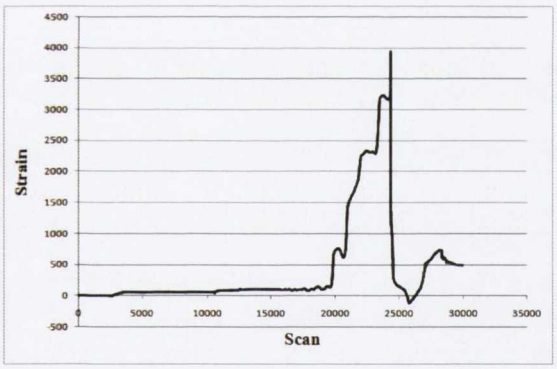

Stain Gauge 21 Offline

Figure A.41: Strain versus Scan Plot: Specimen JD2 – S.G. 21 (a) Run 1 (b) Run 2

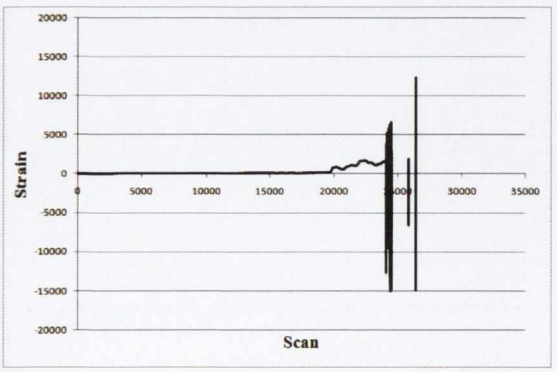

Stain Gauge 23 Offline

Figure A.42: Strain versus Scan Plot: Specimen JD2 – S.G. 23 (a) Run 1 (b) Run 2

Stain Gauge 25 Offline

Stain Gauge 25 Offline

Figure A.43: Strain versus Scan Plot: Specimen JD2 – S.G. 25 (a) Run 1 (b) Run 2

Stain Gauge 27 Offline

Stain Gauge 27 Offline

Figure A.44: Strain versus Scan Plot: Specimen JD2 – S.G. 27 (a) Run 1 (b) Run 2

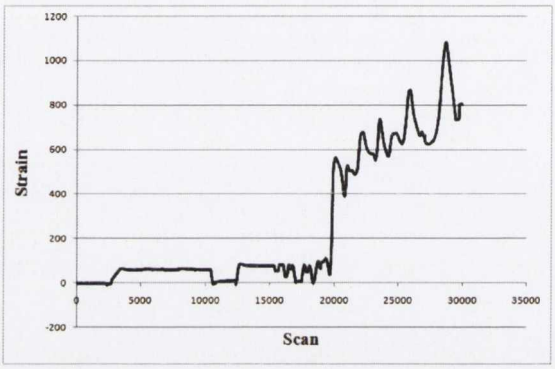

Stain Gauge 29 Offline

Figure A.45: Strain versus Scan Plot: Specimen JD2 – S.G. 29 (a) Run 1 (b) Run 2

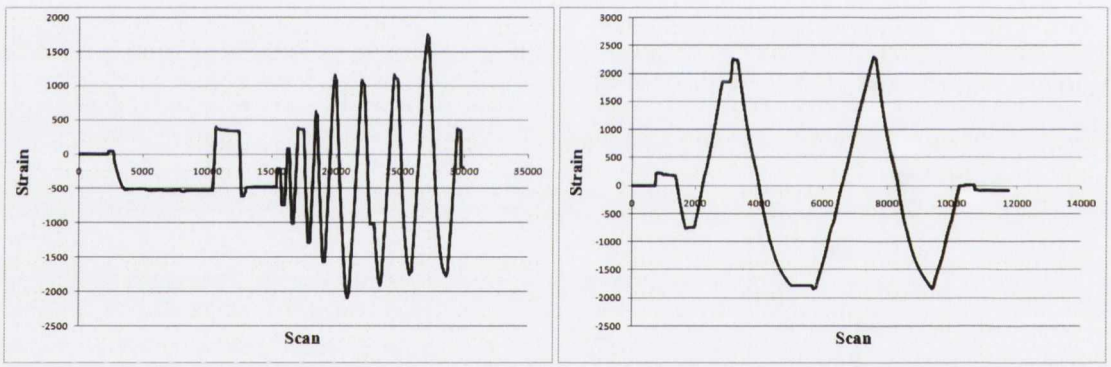

Figure A.46: Strain versus Scan Plot: Specimen JD2 – S.G. 2 (a) Run 1 (b) Run 2

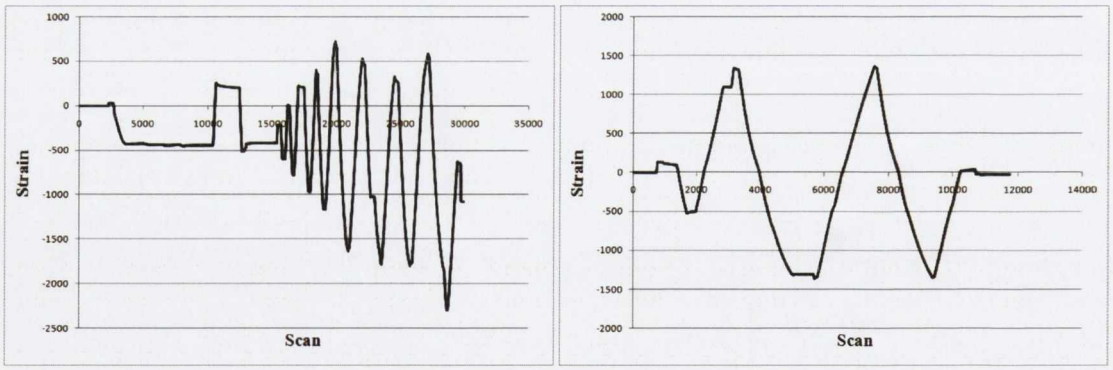

Figure A.47: Strain versus Scan Plot: Specimen JD2 – S.G. 4 (a) Run 1 (b) Run 2

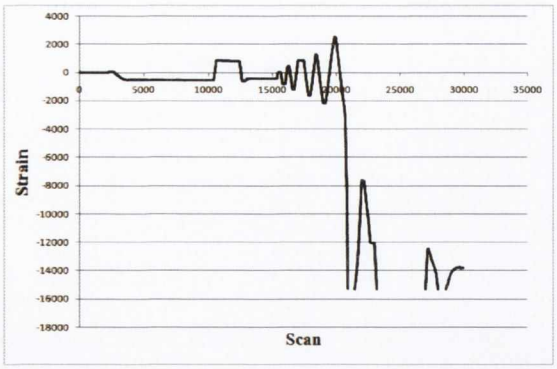

Stain Gauge 6 Offline

Figure A.48: Strain versus Scan Plot: Specimen JD2 – S.G. 6 (a) Run 1 (b) Run 2

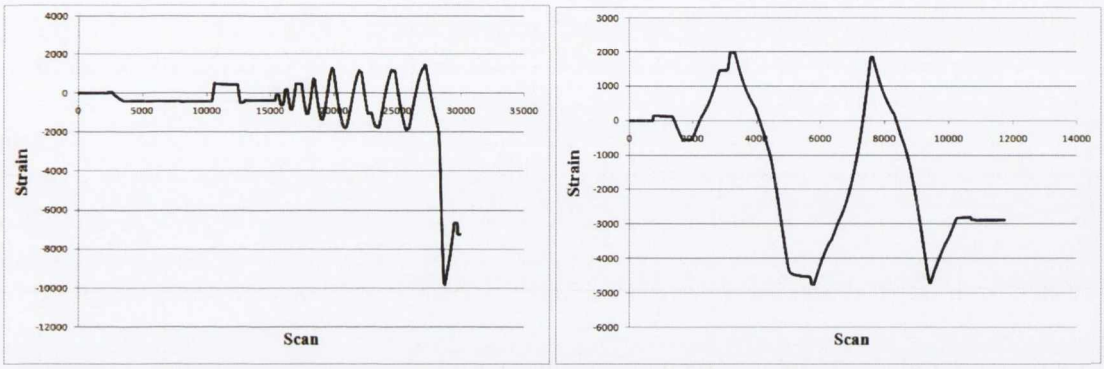

Figure A.49: Strain versus Scan Plot: Specimen JD2 – S.G. 8 (a) Run 1 (b) Run 2

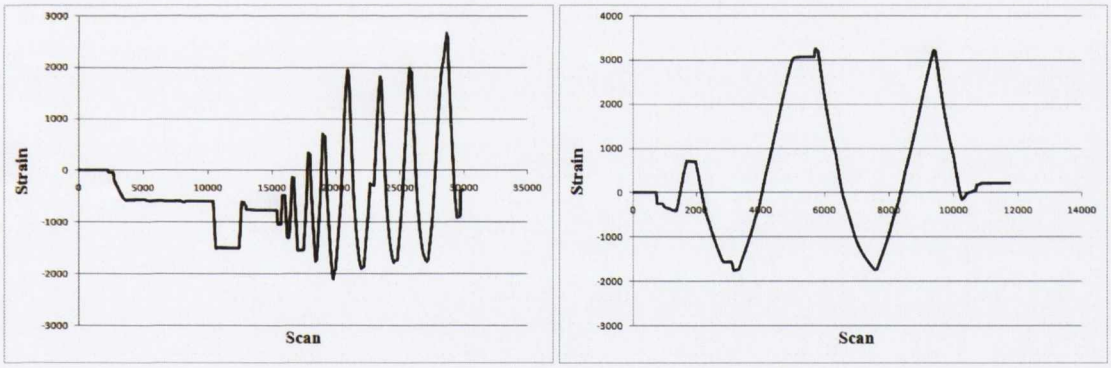

Figure A.50: Strain versus Scan Plot: Specimen JD2 – S.G. 10 (a) Run 1 (b) Run 2

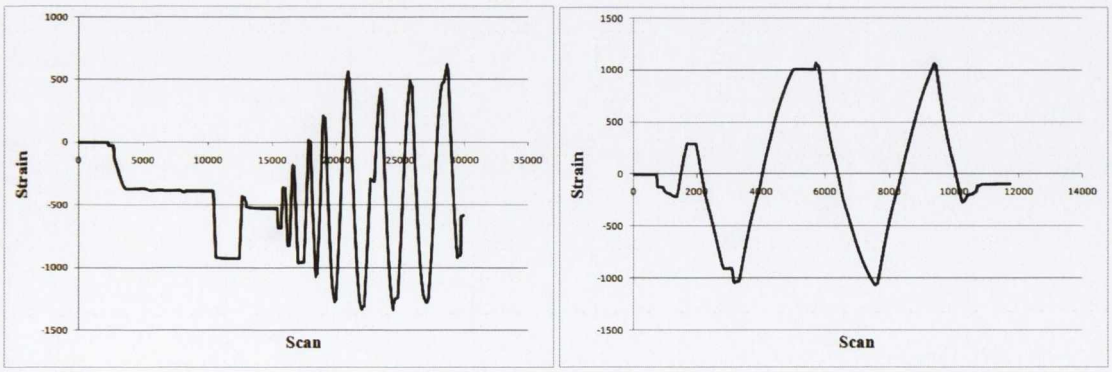

Figure A.51: Strain versus Scan Plot: Specimen JD2 – S.G. 12 (a) Run 1 (b) Run 2

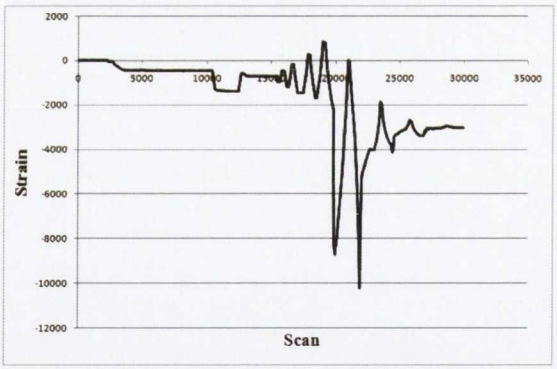

Stain Gauge 14 Offline

Figure A.52: Strain versus Scan Plot: Specimen JD2 – S.G. 14 (a) Run 1 (b) Run 2

Stain Gauge 16 Offline

Stain Gauge 16 Offline

Figure A.53: Strain versus Scan Plot: Specimen JD2 – S.G. 16 (a) Run 1 (b) Run 2

Stain Gauge 18 Offline

Figure A.54: Strain versus Scan Plot: Specimen JD2 – S.G. 18 (a) Run 1 (b) Run 2

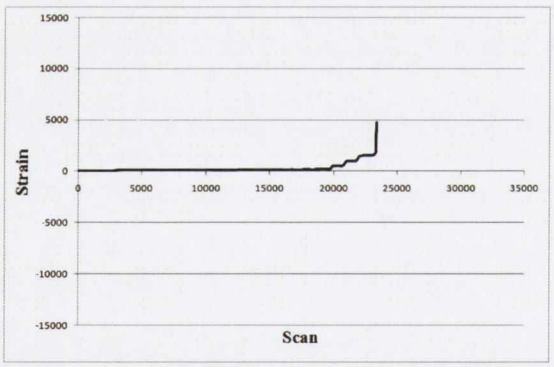

Stain Gauge 20 Offline

Figure A.55: Strain versus Scan Plot: Specimen JD2 – S.G. 20 (a) Run 1 (b) Run 2

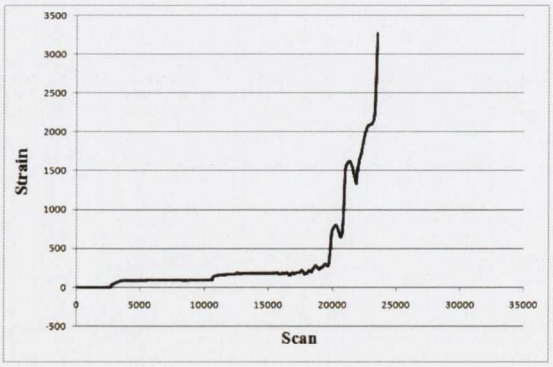

Stain Gauge 22 Offline

Figure A.56: Strain versus Scan Plot: Specimen JD2 – S.G. 22 (a) Run 1 (b) Run 2

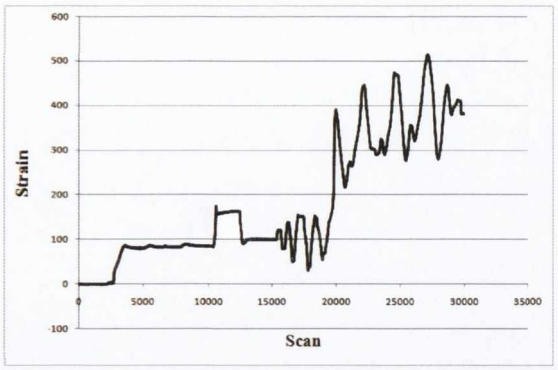

Stain Gauge 24 Offline

Figure A.57: Strain versus Scan Plot: Specimen JD2 – S.G. 24 (a) Run 1 (b) Run 2

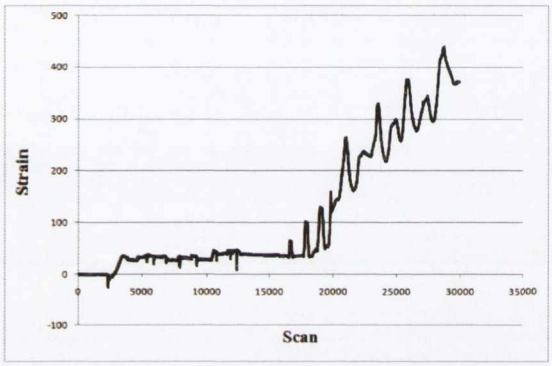

Stain Gauge 26 Offline

Figure A.58: Strain versus Scan Plot: Specimen JD2 – S.G. 26 (a) Run 1 (b) Run 2

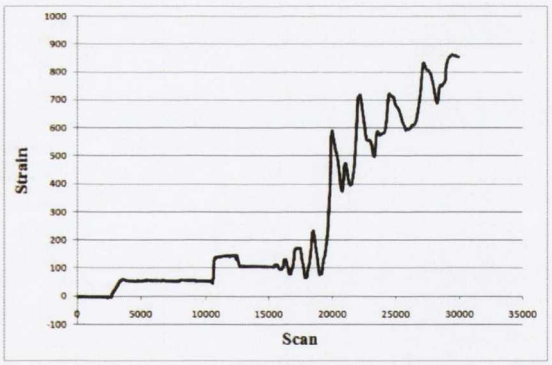

Stain Gauge 28 Offline

Figure A.59: Strain versus Scan Plot: Specimen JD2 – S.G. 28 (a) Run 1 (b) Run 2

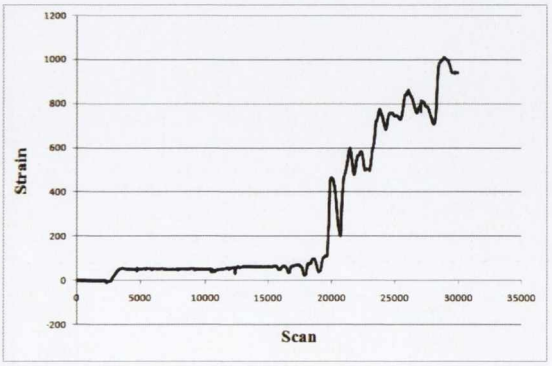

Stain Gauge 30 Offline

Figure A.60: Strain versus Scan Plot: Specimen JD2 – S.G. 30 (a) Run 1 (b) Run 2

Specimen JD3 – ID3

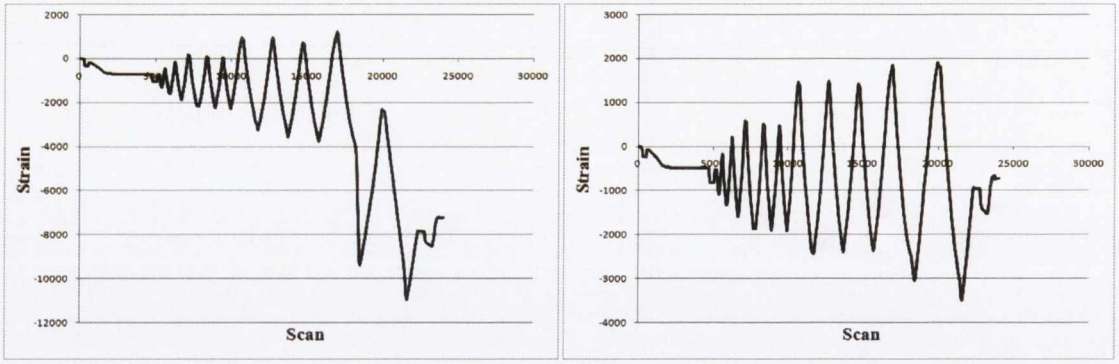

Figure A.61: Strain versus Scan Plot: Specimen JD3 – (a) S.G. 1, (b) S.G. 2

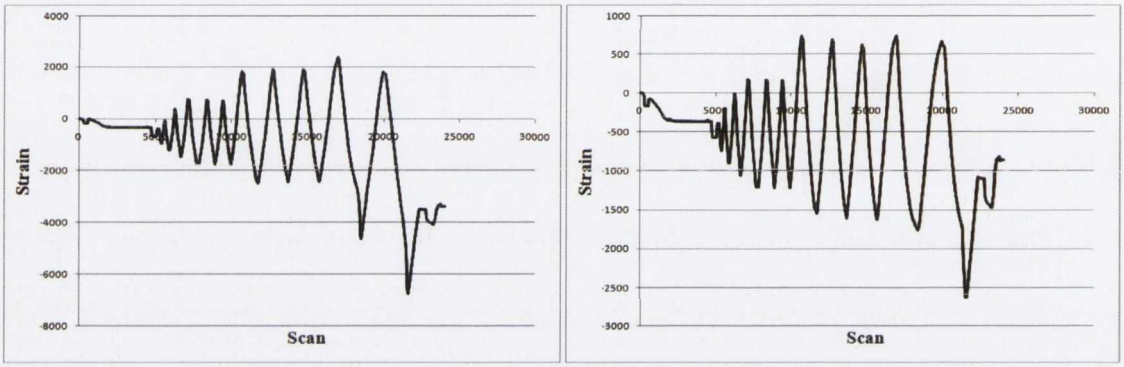

Figure A.62: Strain versus Scan Plot: Specimen JD3 – (a) S.G. 3, (b) S.G. 4

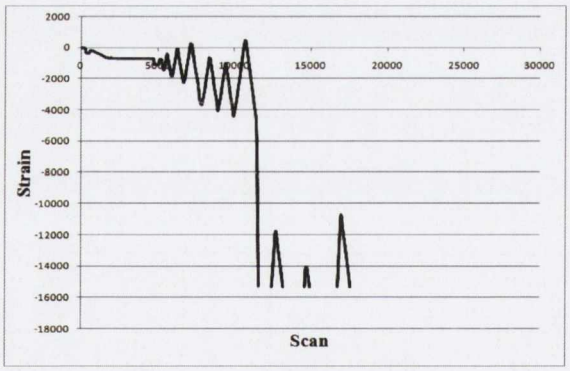

Stain Gauge 6 Offline

Figure A.63: Strain versus Scan Plot: Specimen JD3 – (a) S.G. 5, (b) S.G. 6

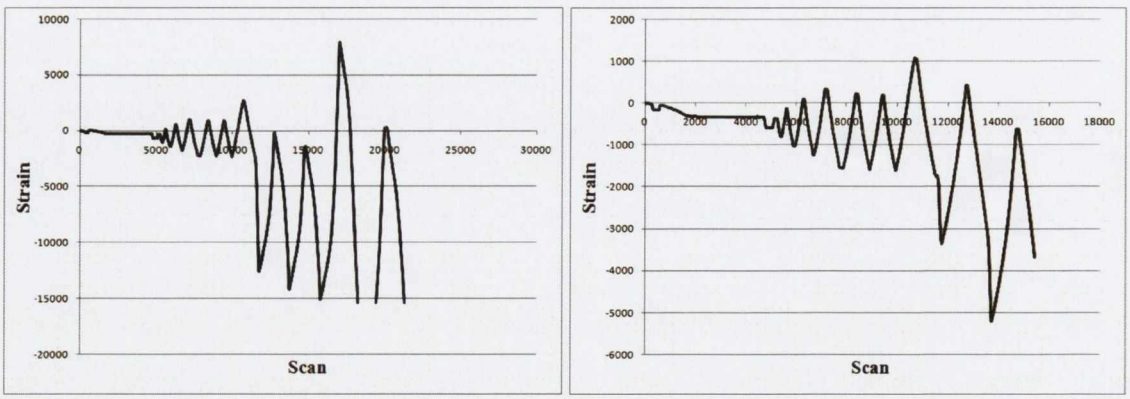

Figure A.64: Strain versus Scan Plot: Specimen JD3 – (a) S.G. 7, (b) S.G. 8

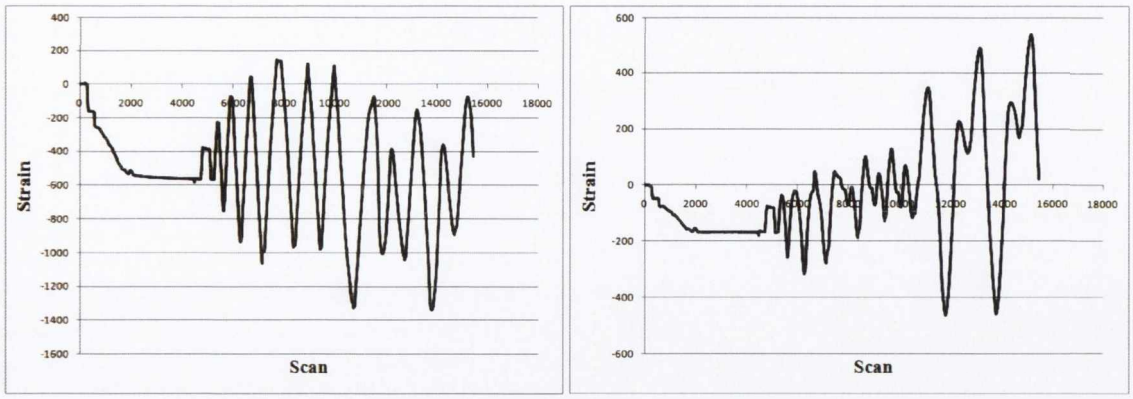

Figure A.65: Strain versus Scan Plot: Specimen JD3 – (a) S.G. 9, (b) S.G. 10

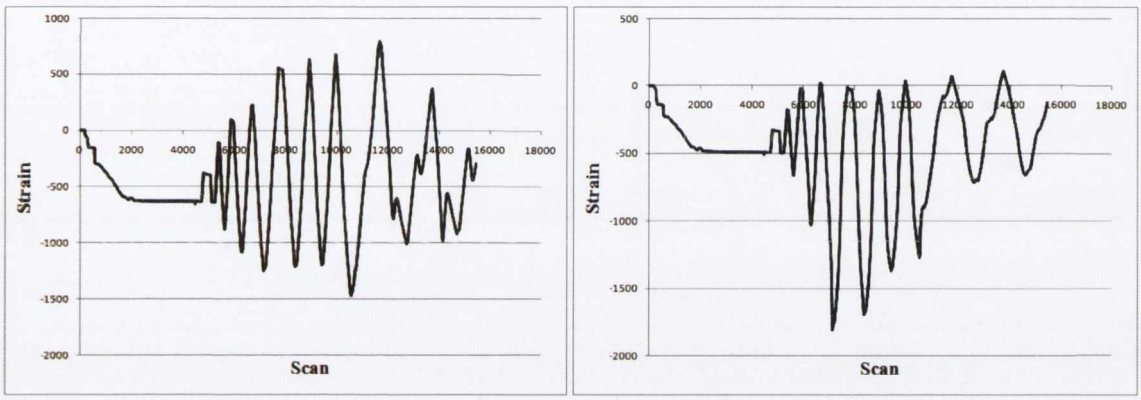

Figure A.66: Strain versus Scan Plot: Specimen JD3 – (a) S.G. 11, (b) S.G. 12

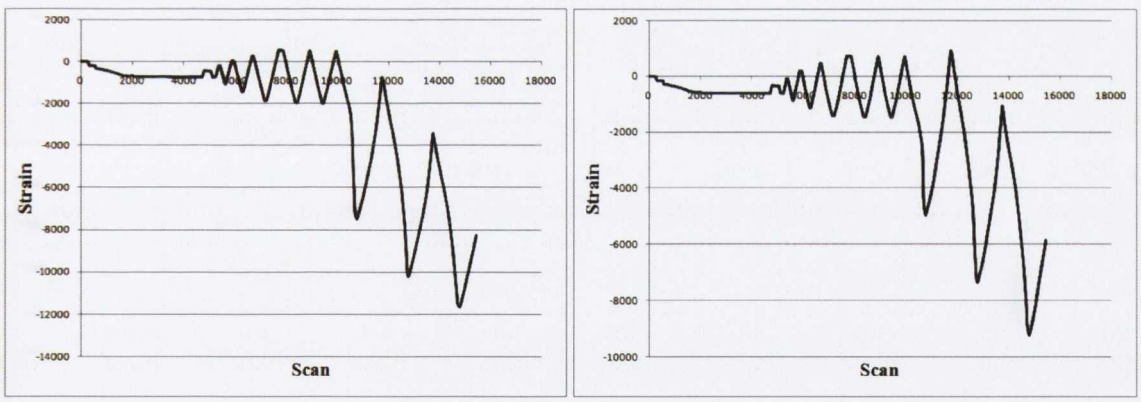

Figure A.67: Strain versus Scan Plot: Specimen JD3 – (a) S.G. 13, (b) S.G. 14

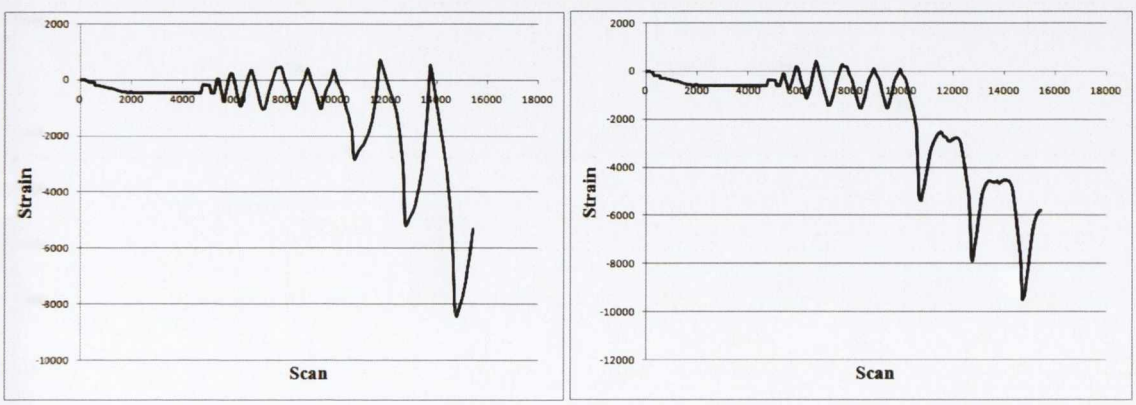

Figure A.68: Strain versus Scan Plot: Specimen JD3 – (a) S.G. 15, (b) S.G. 16

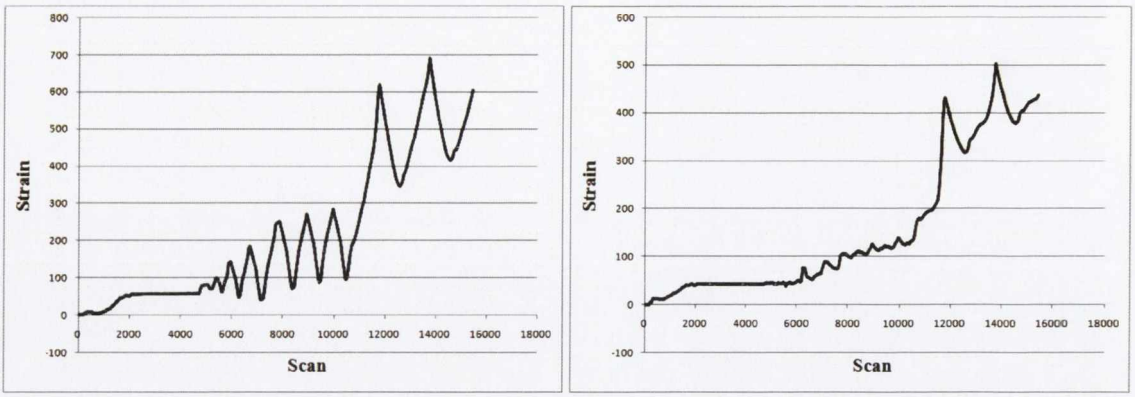

Figure A.69: Strain versus Scan Plot: Specimen JD3 – (a) S.G. 17, (b) S.G. 18

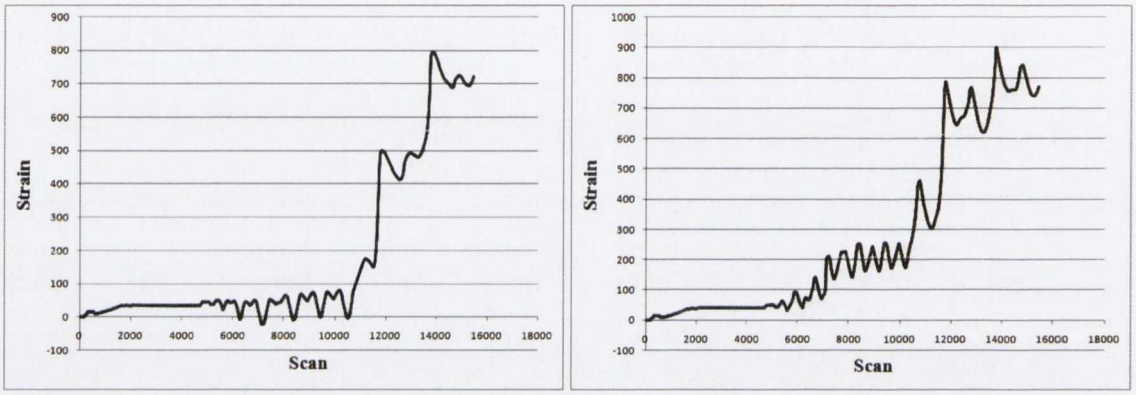

Figure A.70: Strain versus Scan Plot: Specimen JD3 – (a) S.G. 19, (b) S.G. 20

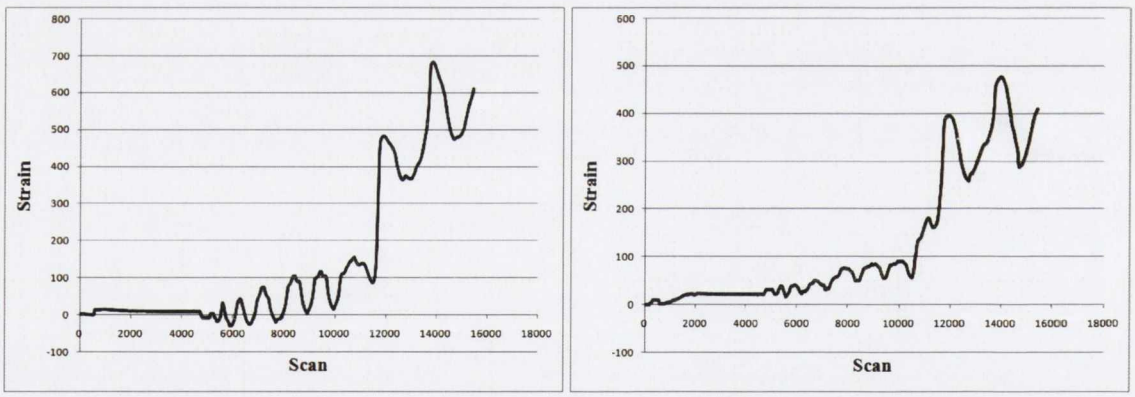

Figure A.71: Strain versus Scan Plot: Specimen JD3 – (a) S.G. 21, (b) S.G. 22

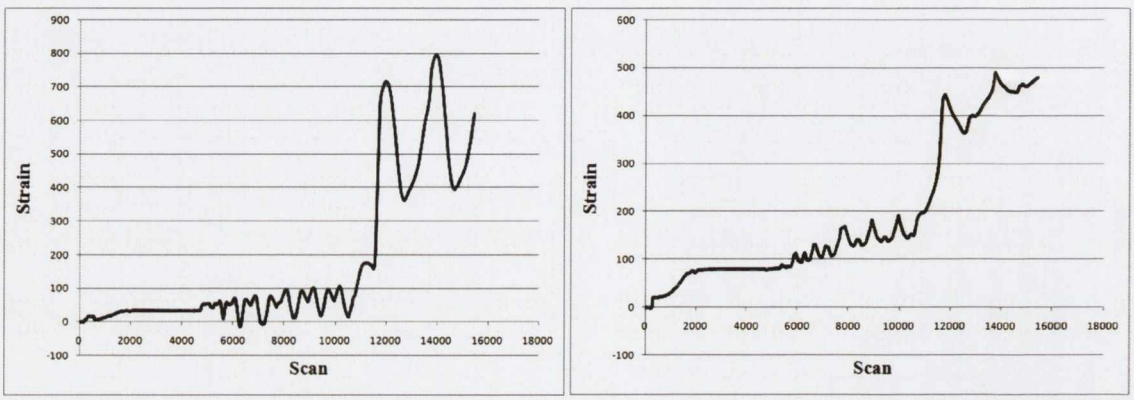

Figure A.72: Strain versus Scan Plot: Specimen JD3 – (a) S.G. 23, (b) S.G. 24

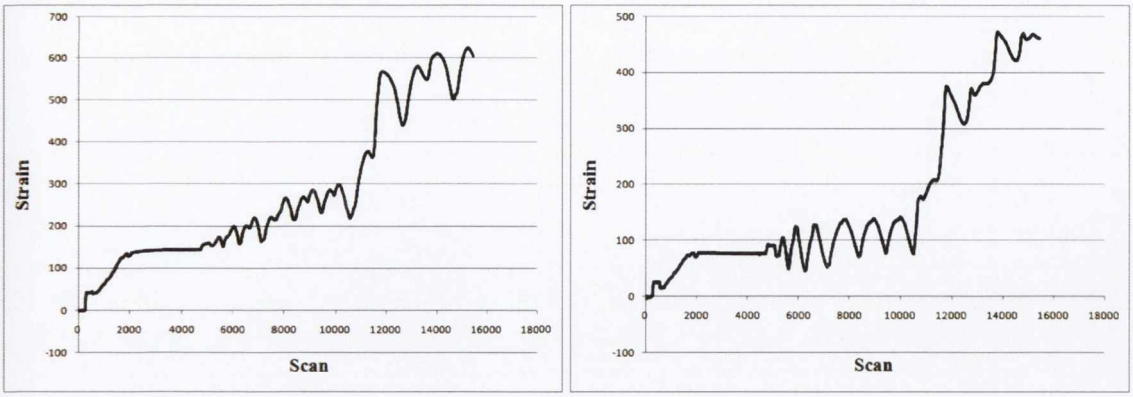

Figure A.73: Strain versus Scan Plot: Specimen JD3 – (a) S.G. 25, (b) S.G. 26

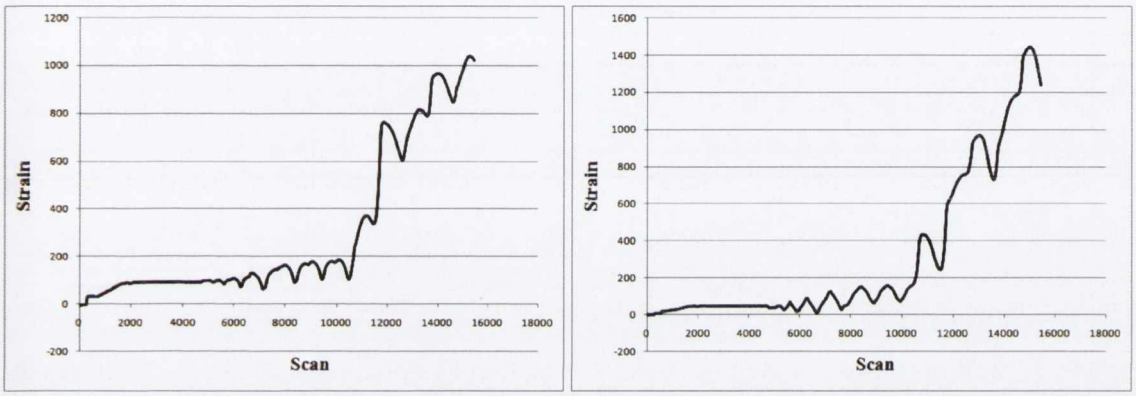

Figure A.74: Strain versus Scan Plot: Specimen JD3 – (a) S.G. 27, (b) S.G. 28

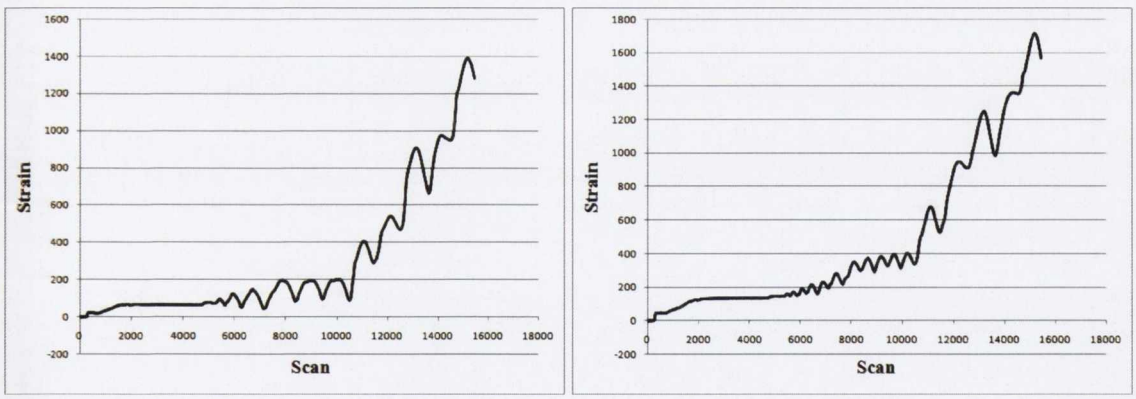

Figure A.75: Strain versus Scan Plot: Specimen JD3 – (a) S.G. 29, (b) S.G. 30

Specimen JD4 – ID5

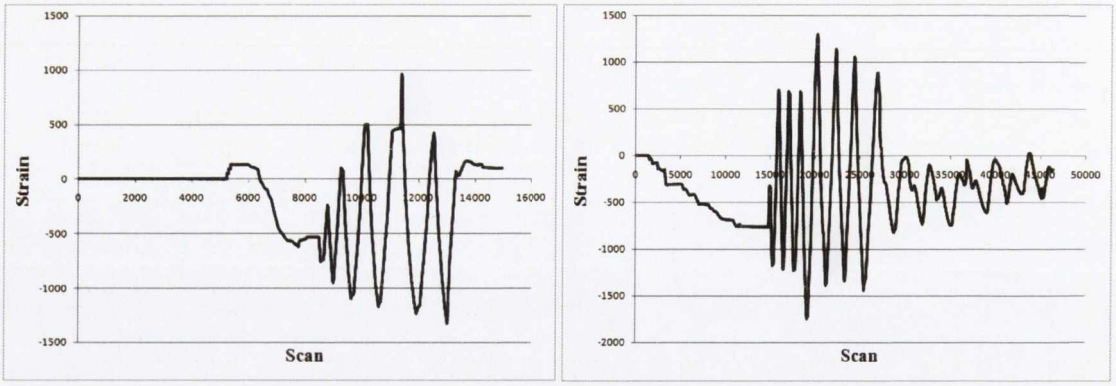

Figure A.76: Strain versus Scan Plot: Specimen JD4 – S.G. 1 (a) Run 1 (b) Run 2

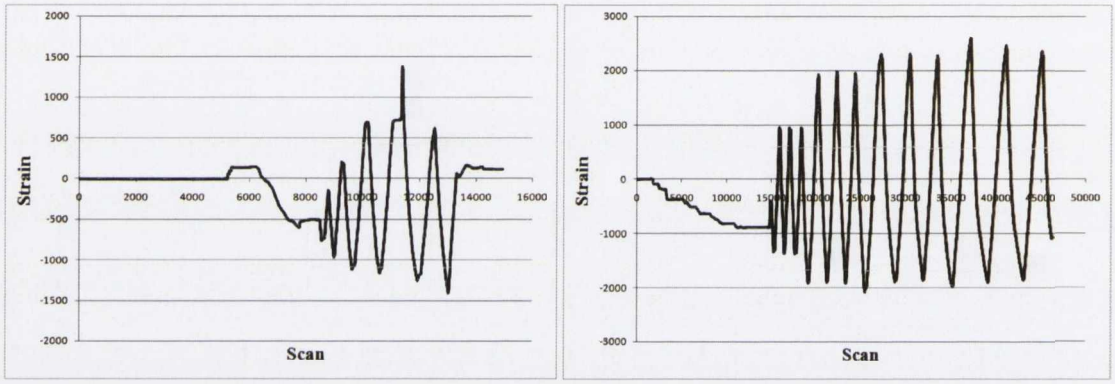

Figure A.77: Strain versus Scan Plot: Specimen JD4 – S.G. 3 (a) Run 1 (b) Run 2

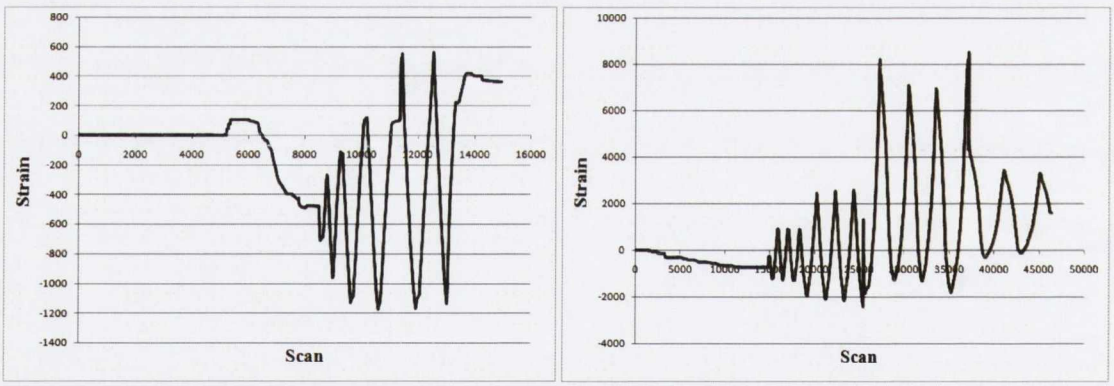

Figure A.78: Strain versus Scan Plot: Specimen JD4 – S.G. 5 (a) Run 1 (b) Run 2

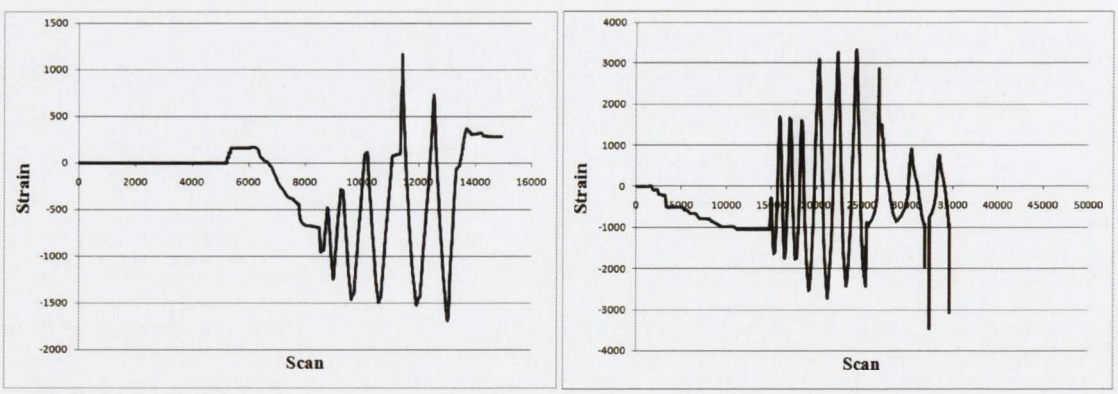

Figure A.79: Strain versus Scan Plot: Specimen JD4 – S.G. 7 (a) Run 1 (b) Run 2

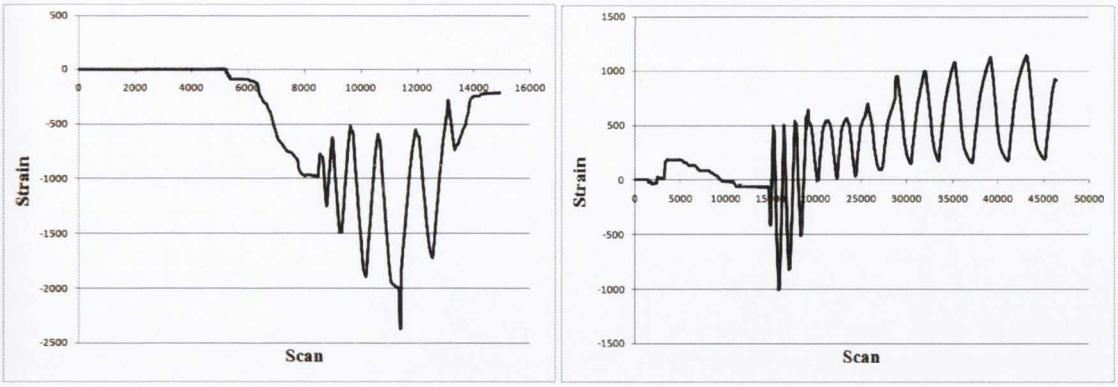

Figure A.80: Strain versus Scan Plot: Specimen JD4 – S.G. 9 (a) Run 1 (b) Run 2

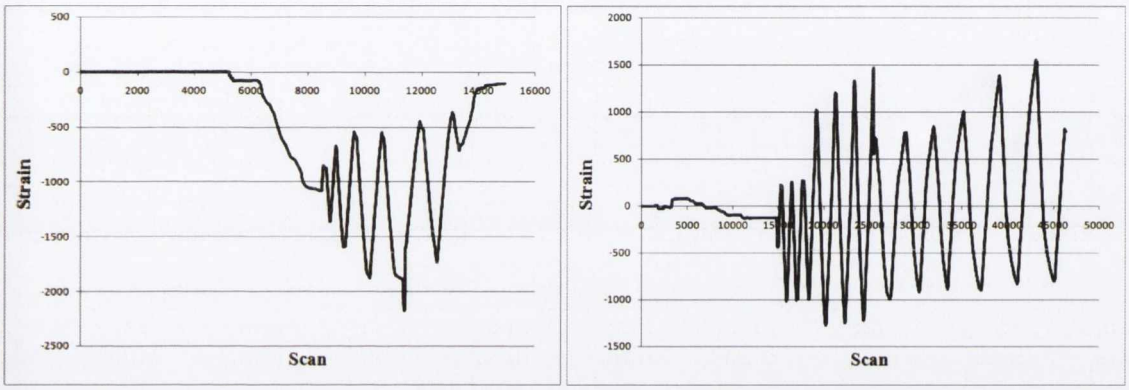

Figure A.81: Strain versus Scan Plot: Specimen JD4 – S.G. 11 (a) Run 1 (b) Run 2

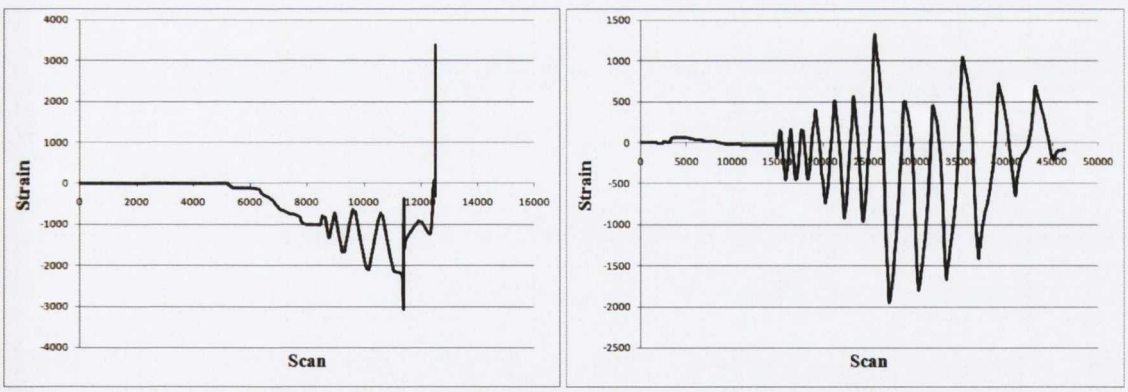

Figure A.82: Strain versus Scan Plot: Specimen JD4 – S.G. 13 (a) Run 1 (b) Run 2

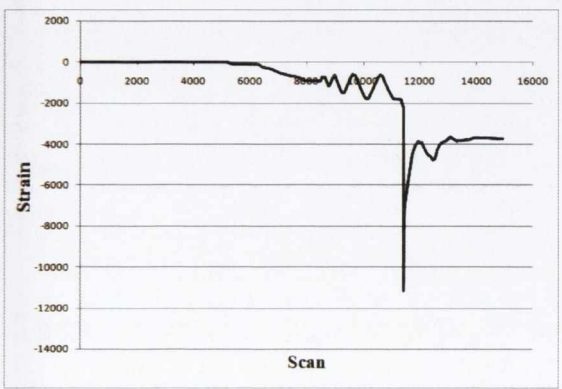

Stain Gauge 15 Offline

Figure A.83: Strain versus Scan Plot: Specimen JD4 – S.G. 15 (a) Run 1 (b) Run 2

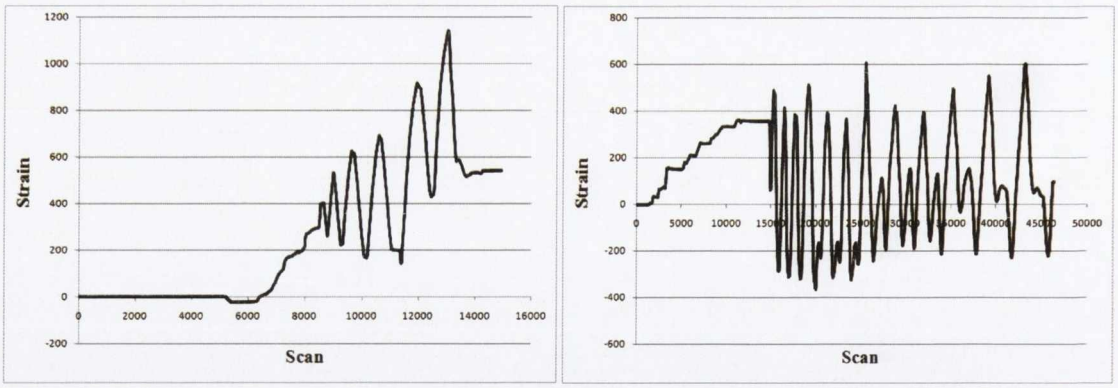

Figure A.84: Strain versus Scan Plot: Specimen JD4 – S.G. 17 (a) Run 1 (b) Run 2

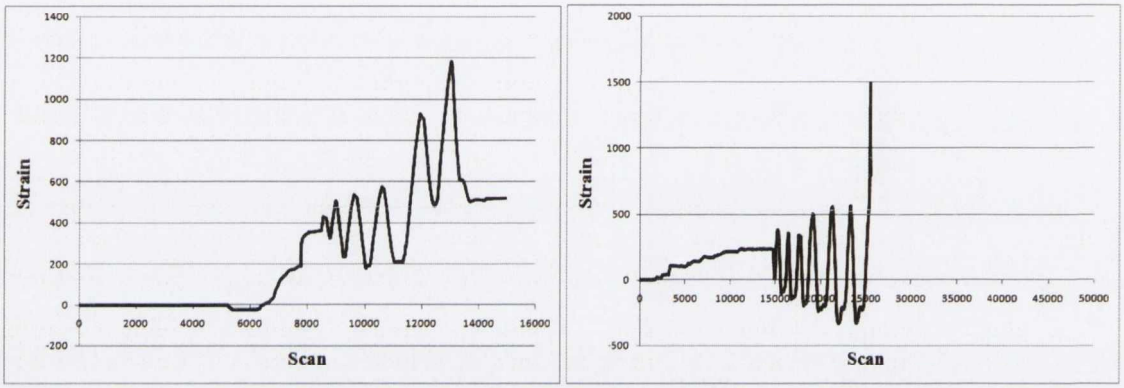

Figure A.85: Strain versus Scan Plot: Specimen JD4 – S.G. 19 (a) Run 1 (b) Run 2

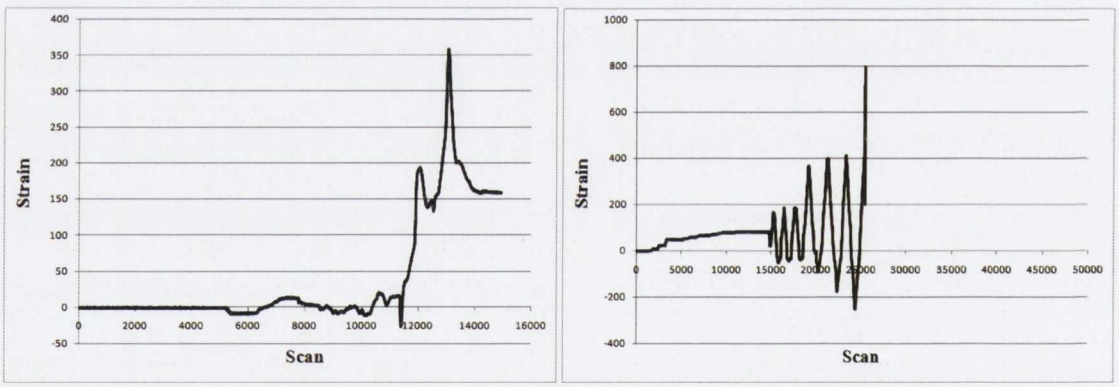

Figure A.86: Strain versus Scan Plot: Specimen JD4 – S.G. 21 (a) Run 1 (b) Run 2

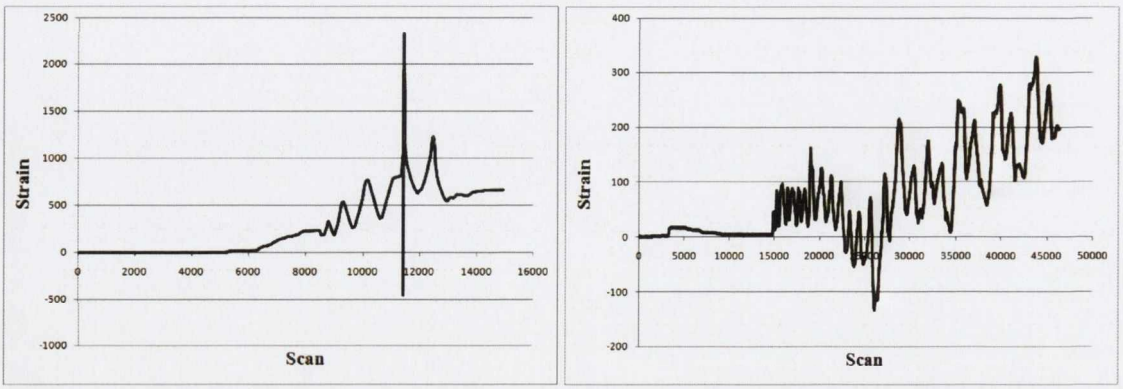

Figure A.87: Strain versus Scan Plot: Specimen JD4 – S.G. 23 (a) Run 1 (b) Run 2

Stain Gauge 25 Offline

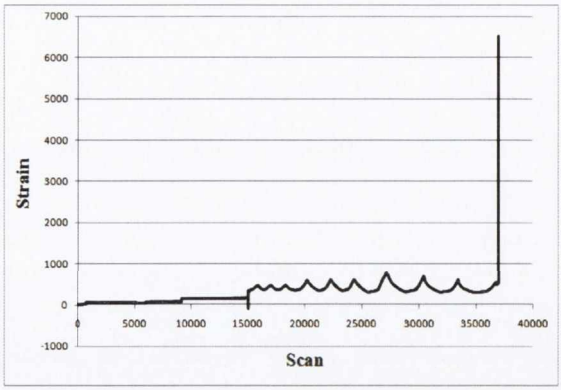

Figure A.88: Strain versus Scan Plot: Specimen JD4 – S.G. 25 (a) Run 1 (b) Run 2

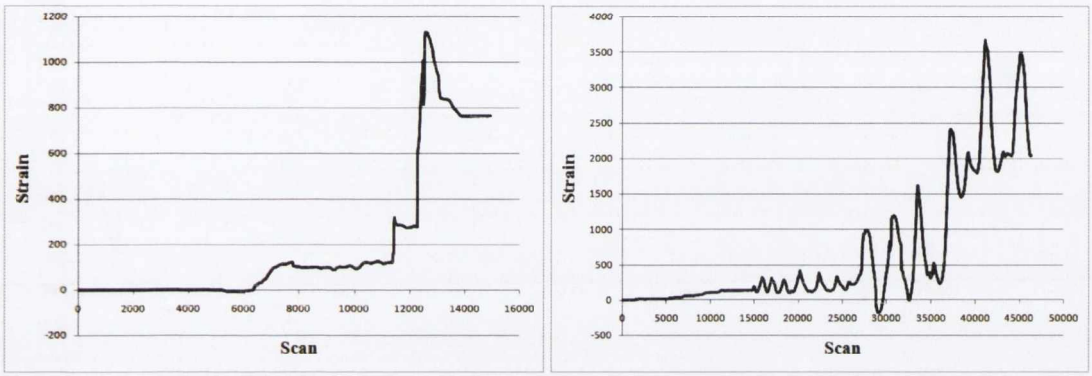

Figure A.89: Strain versus Scan Plot: Specimen JD4 – S.G. 27 (a) Run 1 (b) Run 2

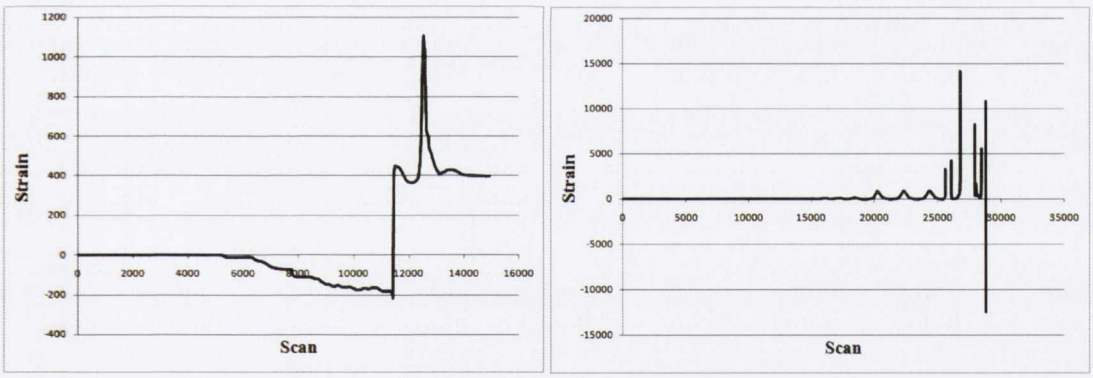

Figure A.90: Strain versus Scan Plot: Specimen JD4 – S.G. 29 (a) Run 1 (b) Run 2

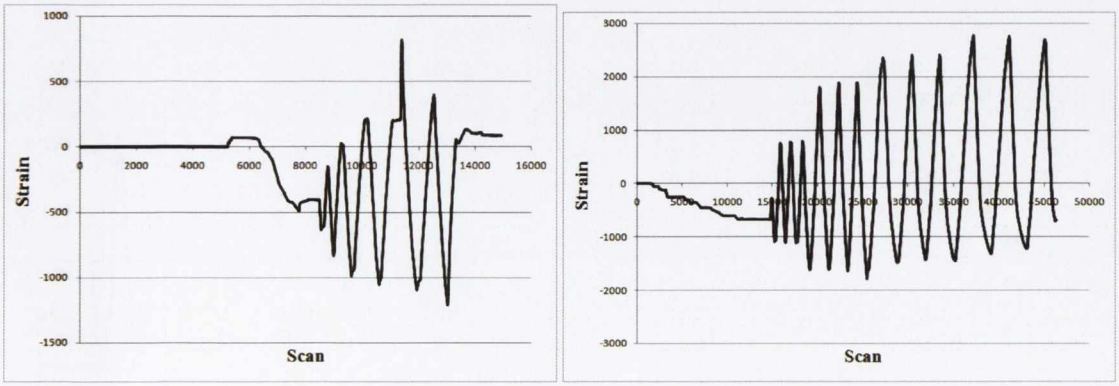

Figure A.91: Strain versus Scan Plot: Specimen JD4 – S.G. 2 (a) Run 1 (b) Run 2

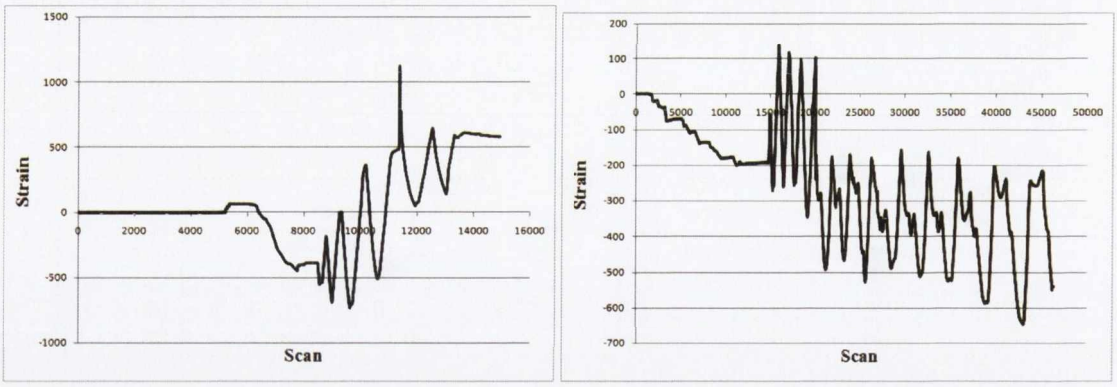

Figure A.92: Strain versus Scan Plot: Specimen JD4 – S.G. 4 (a) Run 1 (b) Run 2

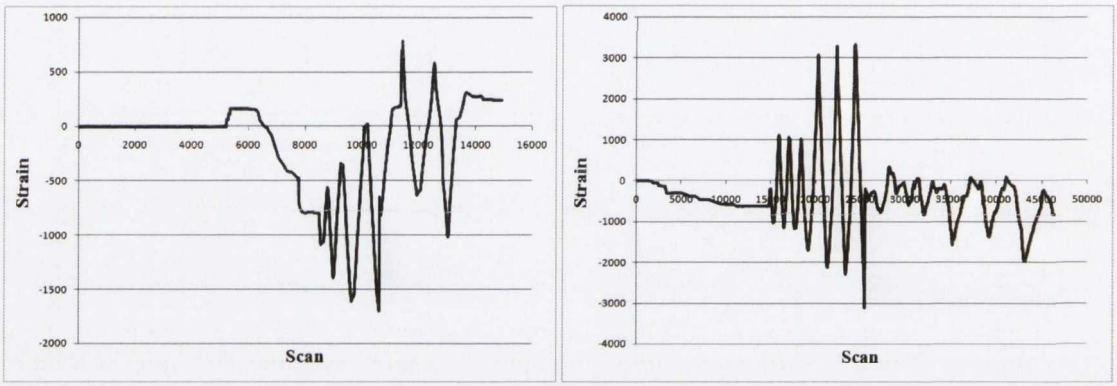

Figure A.93: Strain versus Scan Plot: Specimen JD4 – S.G. 6 (a) Run 1 (b) Run 2

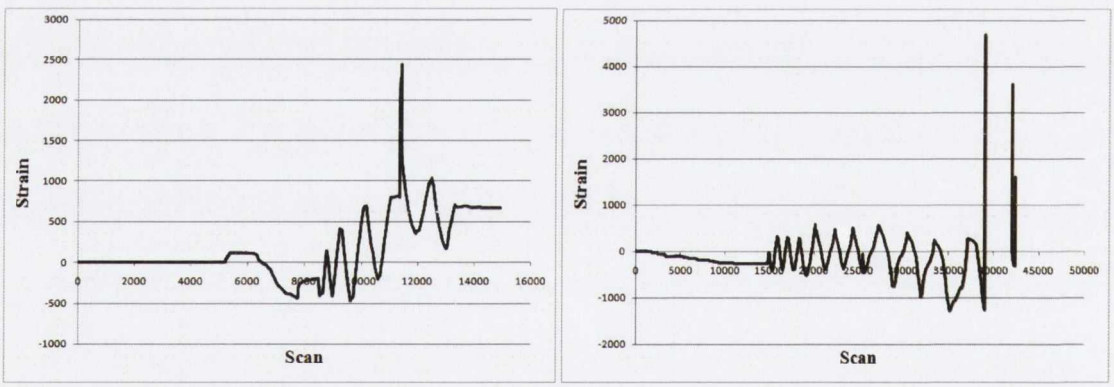

Figure A.94: Strain versus Scan Plot: Specimen JD4 – S.G. 8 (a) Run 1 (b) Run 2

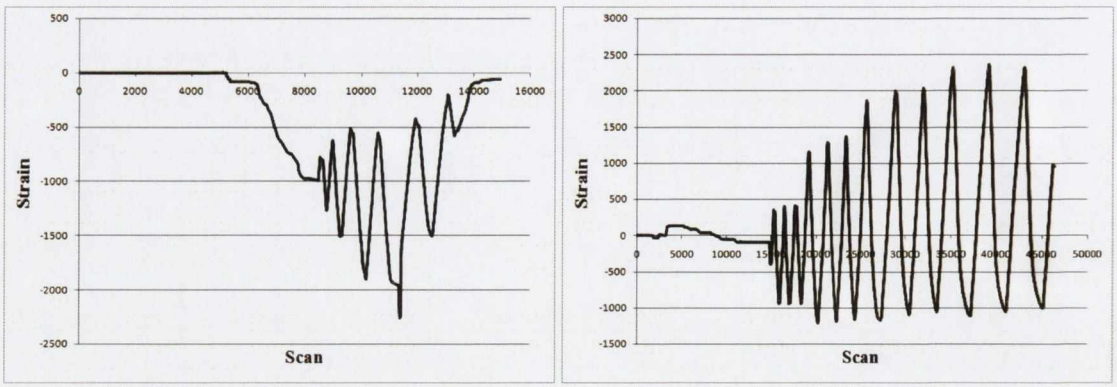

Figure A.95: Strain versus Scan Plot: Specimen JD4 – S.G. 10 (a) Run 1 (b) Run 2

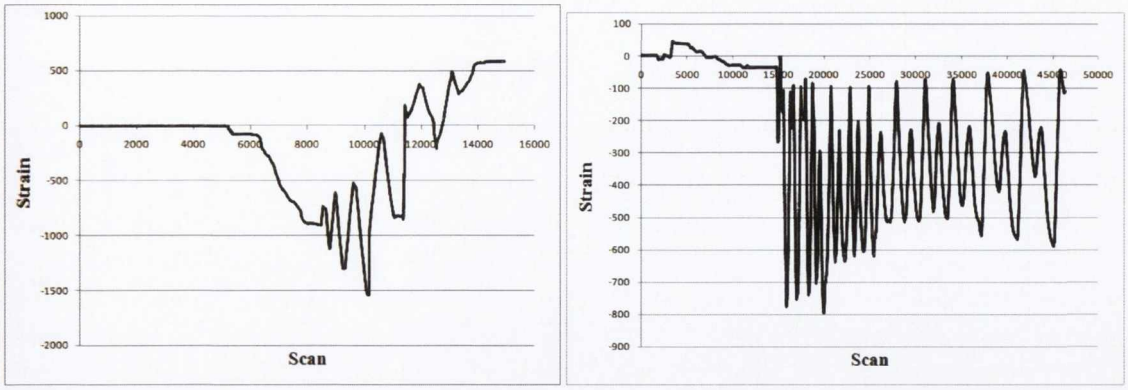

Figure A.96: Strain versus Scan Plot: Specimen JD4 – S.G. 12 (a) Run 1 (b) Run 2

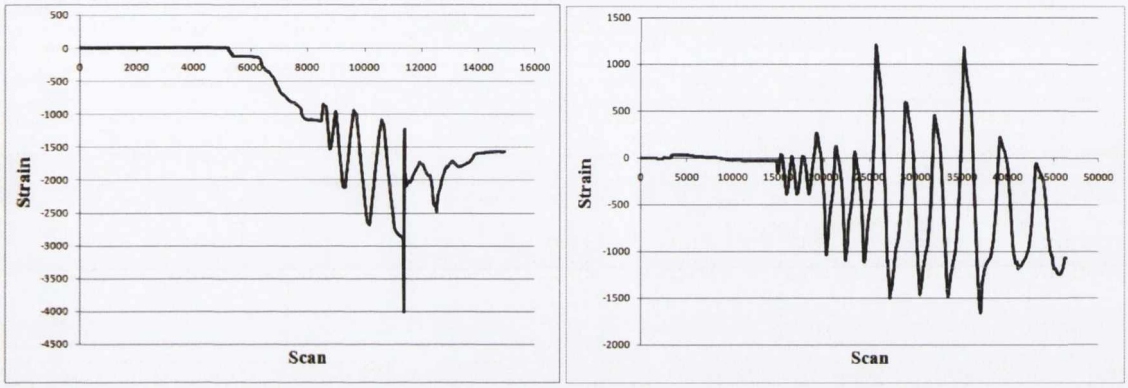

Figure A.97: Strain versus Scan Plot: Specimen JD4 – S.G. 14 (a) Run 1 (b) Run 2

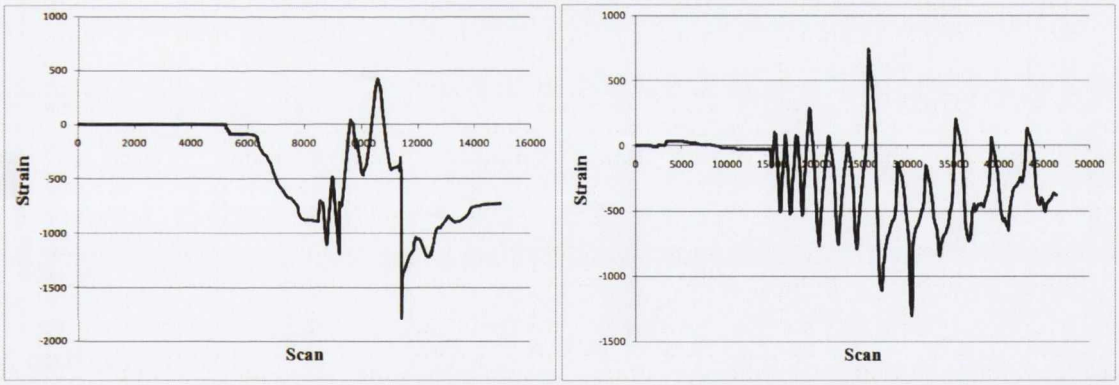

Figure A.98: Strain versus Scan Plot: Specimen JD4 – S.G. 16 (a) Run 1 (b) Run 2

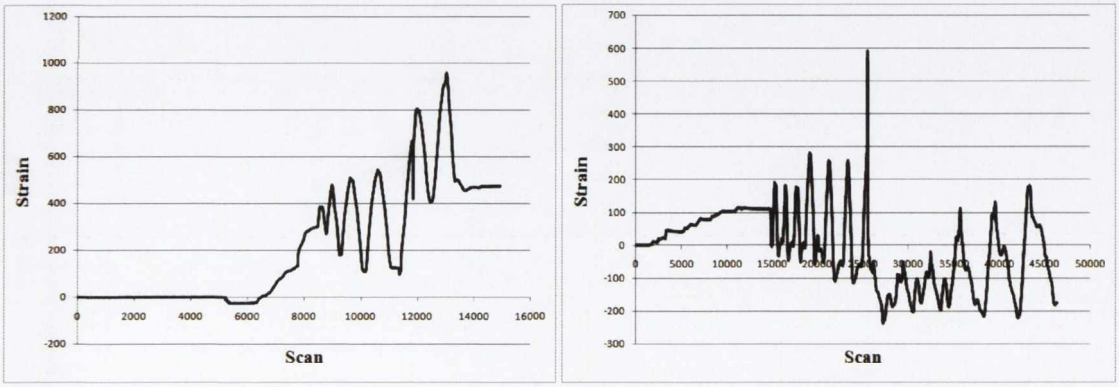

Figure A.99: Strain versus Scan Plot: Specimen JD4 – S.G. 18 (a) Run 1 (b) Run 2

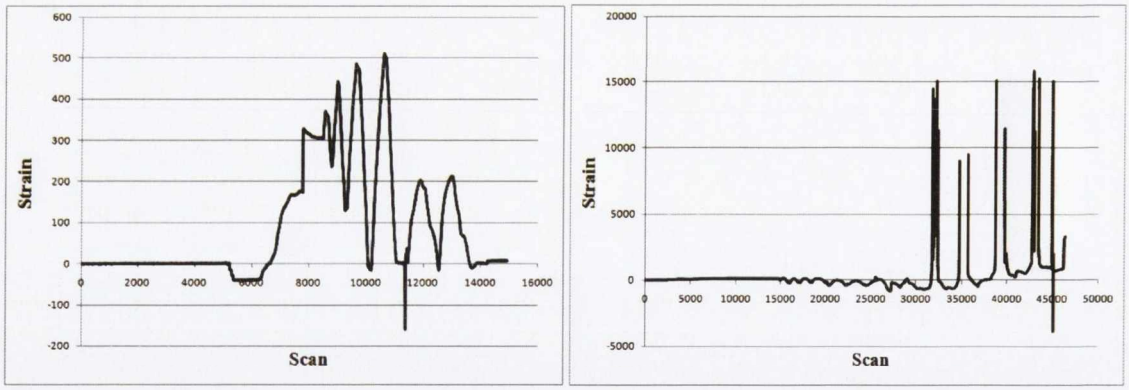

Figure A.100: Strain versus Scan Plot: Specimen JD4 – S.G. 20 (a) Run 1 (b) Run 2

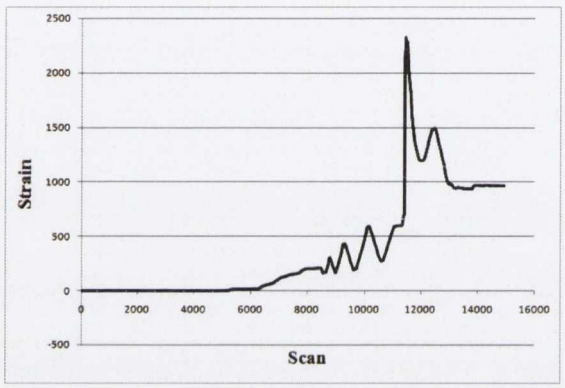

Stain Gauge 22 Offline

Figure A.101: Strain versus Scan Plot: Specimen JD4 – S.G. 22 (a) Run 1 (b) Run 2

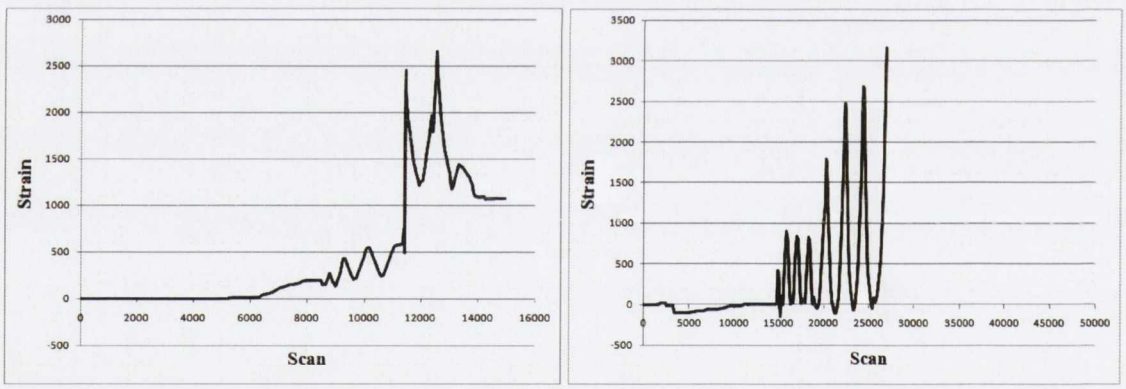

Figure A.102: Strain versus Scan Plot: Specimen JD4 – S.G. 24 (a) Run 1 (b) Run 2

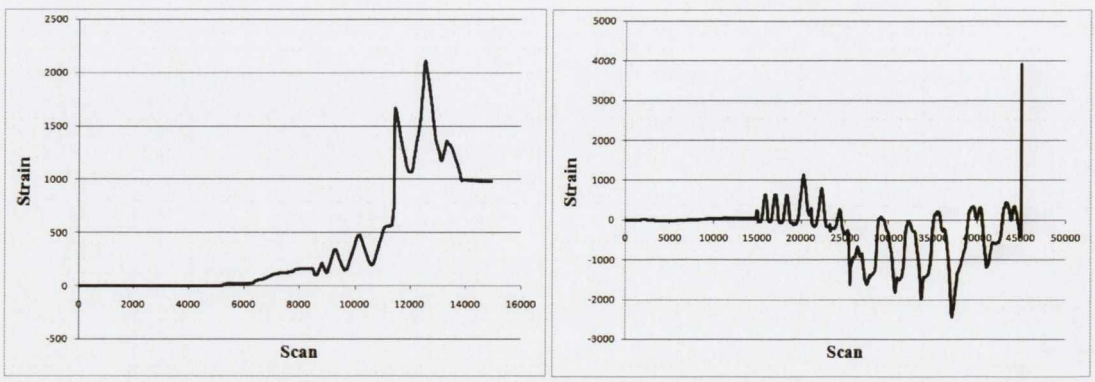

Figure A.103: Strain versus Scan Plot: Specimen JD4 – S.G. 26 (a) Run 1 (b) Run 2

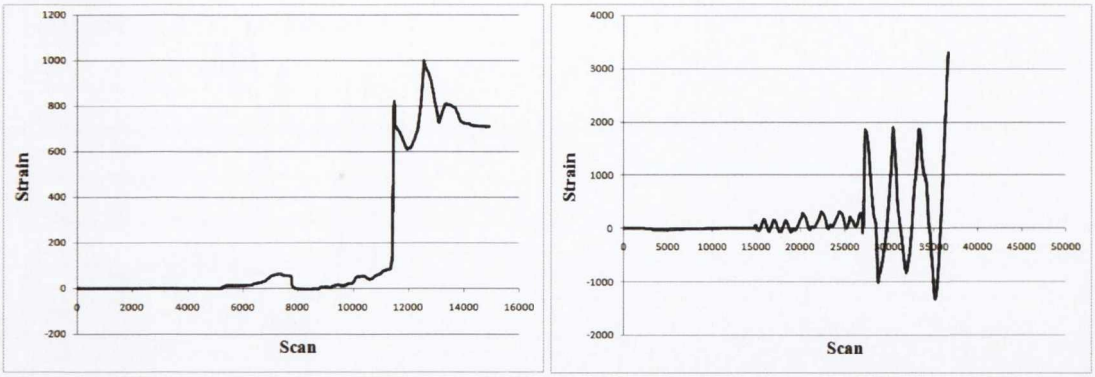

Figure A.104: Strain versus Scan Plot: Specimen JD4 – S.G. 28 (a) Run 1 (b) Run 2

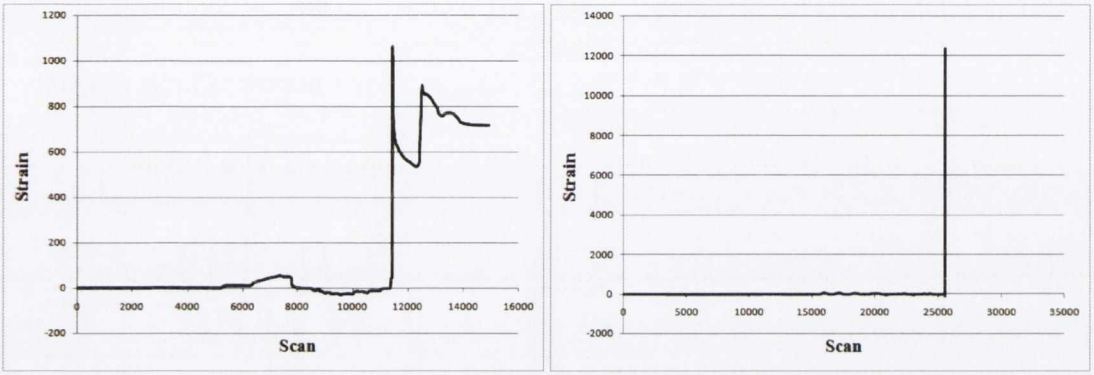

Figure A.105: Strain versus Scan Plot: Specimen JD4 – S.G. 30 (a) Run 1 (b) Run 2

Specimen JD5 – ID6

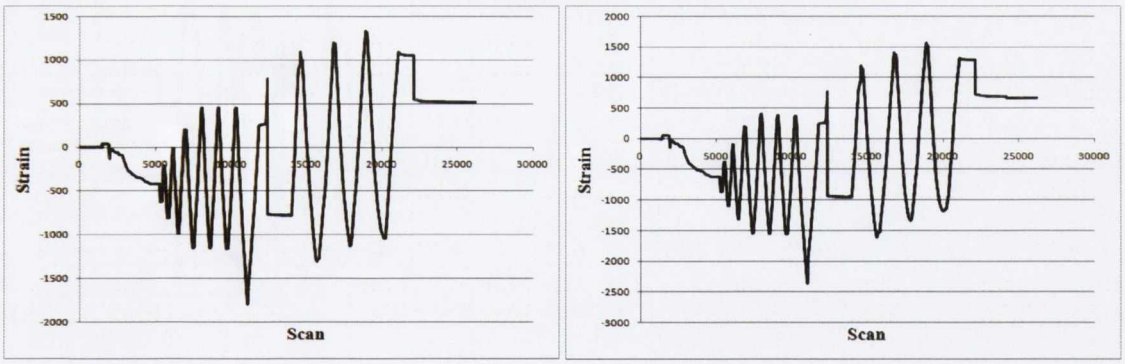

Figure A.106: Strain versus Scan Plot: Specimen JD5 – (a) S.G. 1, (b) S.G. 2

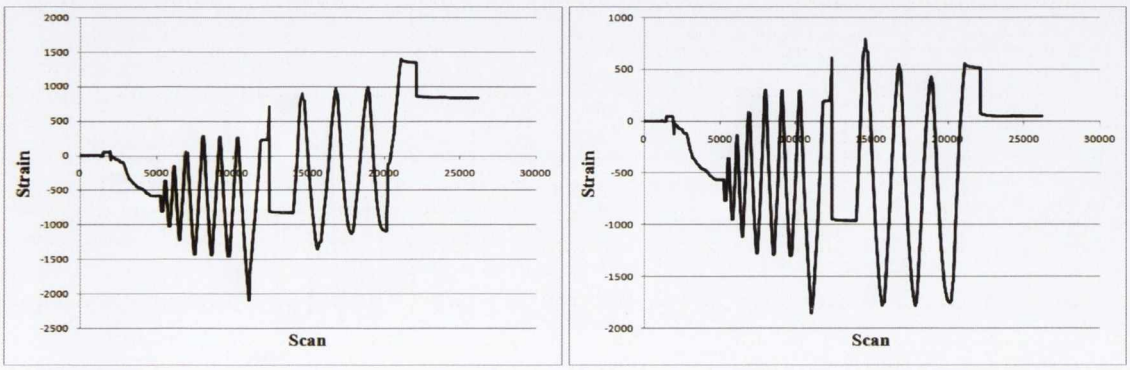

Figure A.107: Strain versus Scan Plot: Specimen JD5 – (a) S.G. 3, (b) S.G. 4

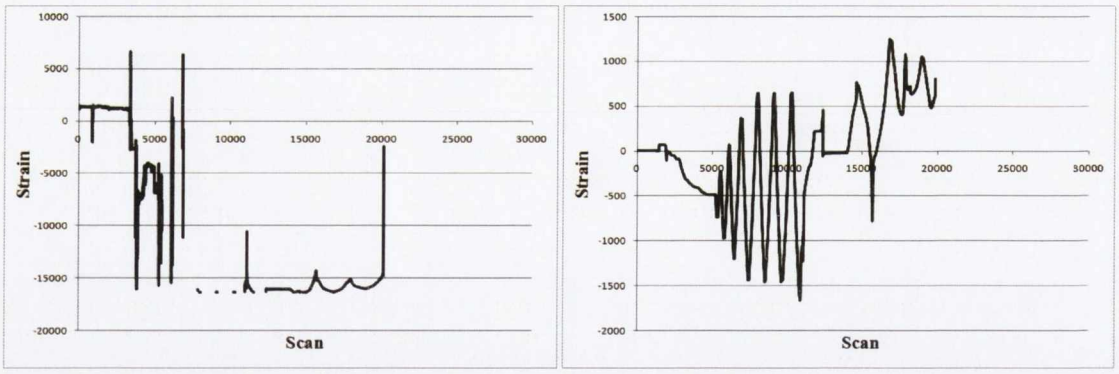

Figure A.108: Strain versus Scan Plot: Specimen JD5 – (a) S.G. 5, (b) S.G. 6

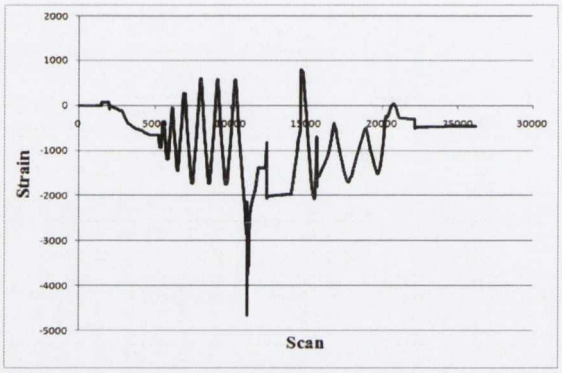

Stain Gauge 8 Offline

Figure A.109: Strain versus Scan Plot: Specimen JD5 – (a) S.G. 7, (b) S.G. 8

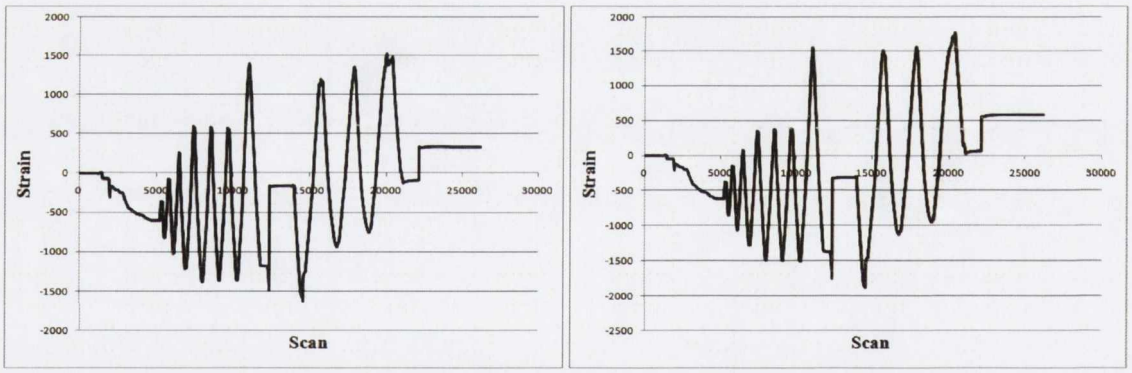

Figure A.110: Strain versus Scan Plot: Specimen JD5 – (a) S.G. 9, (b) S.G. 10

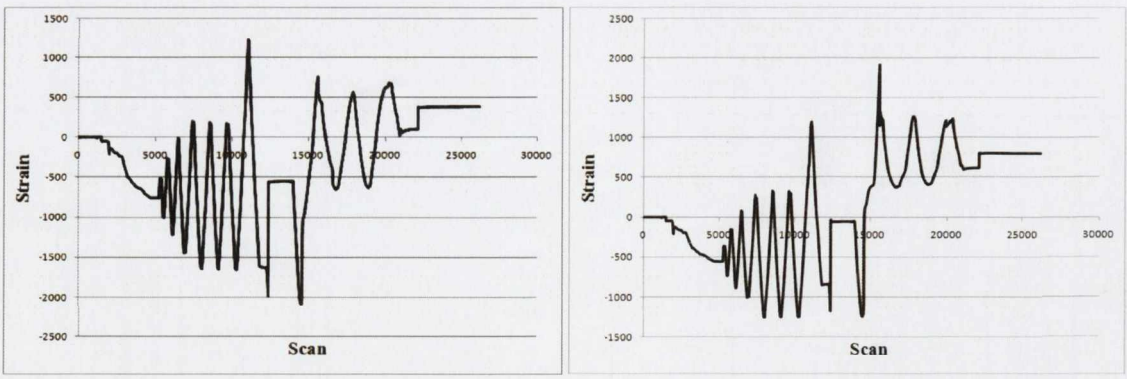

Figure A.111: Strain versus Scan Plot: Specimen JD5 – (a) S.G. 11, (b) S.G. 12

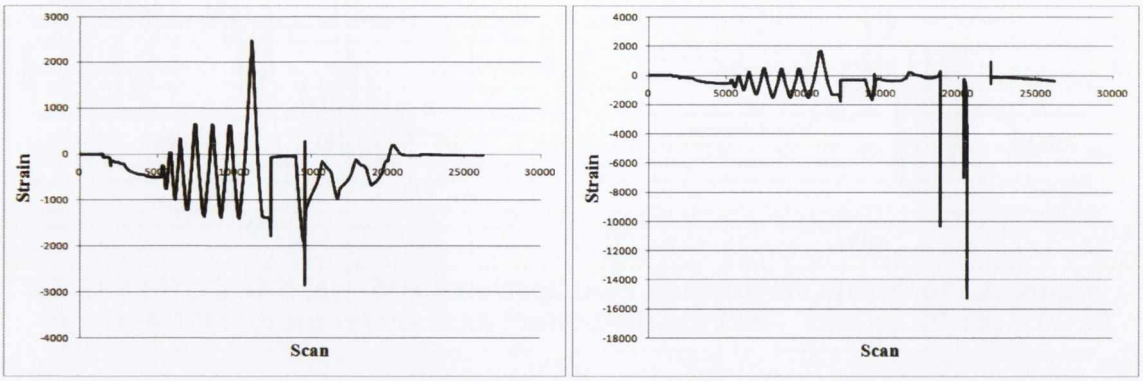

Figure A.112: Strain versus Scan Plot: Specimen JD5 – (a) S.G. 13, (b) S.G. 14

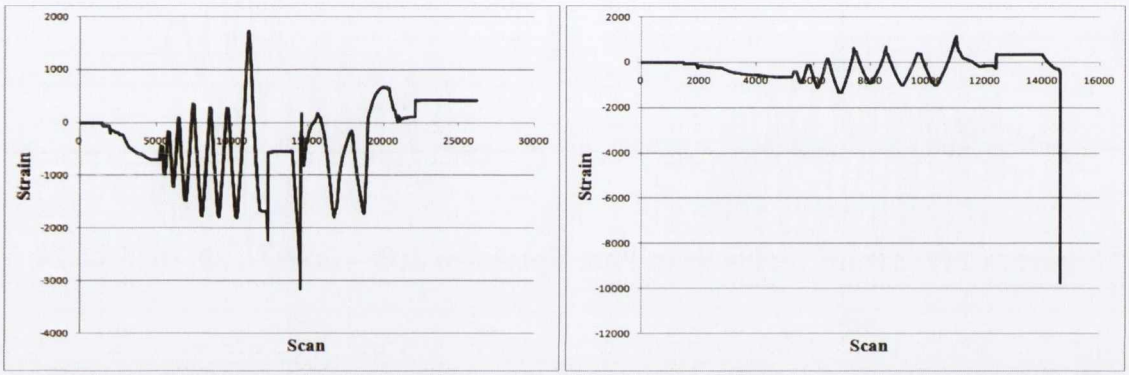

Figure A.113: Strain versus Scan Plot: Specimen JD5 – (a) S.G. 15, (b) S.G. 16

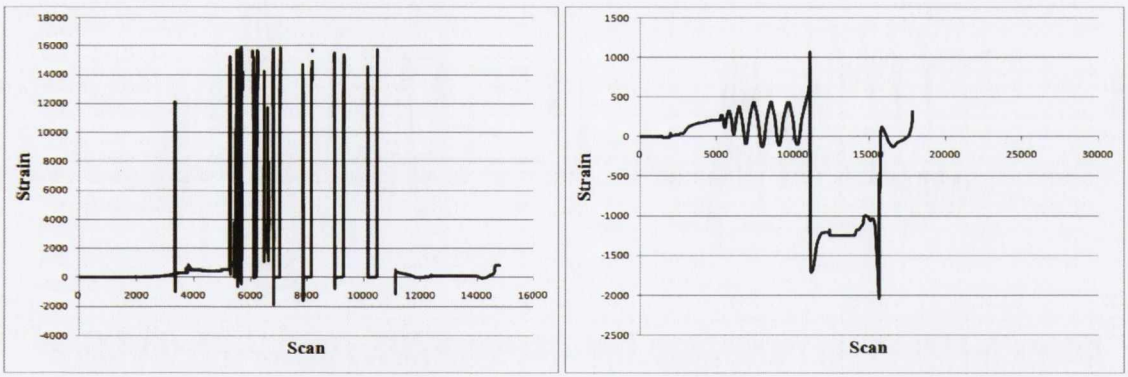

Figure A.114: Strain versus Scan Plot: Specimen JD5 – (a) S.G. 17, (b) S.G. 18

Stain Gauge 19 Offline

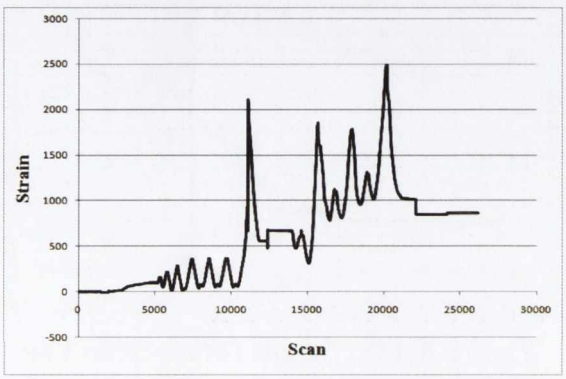

Figure A.115: Strain versus Scan Plot: Specimen JD5 – (a) S.G. 19, (b) S.G. 20

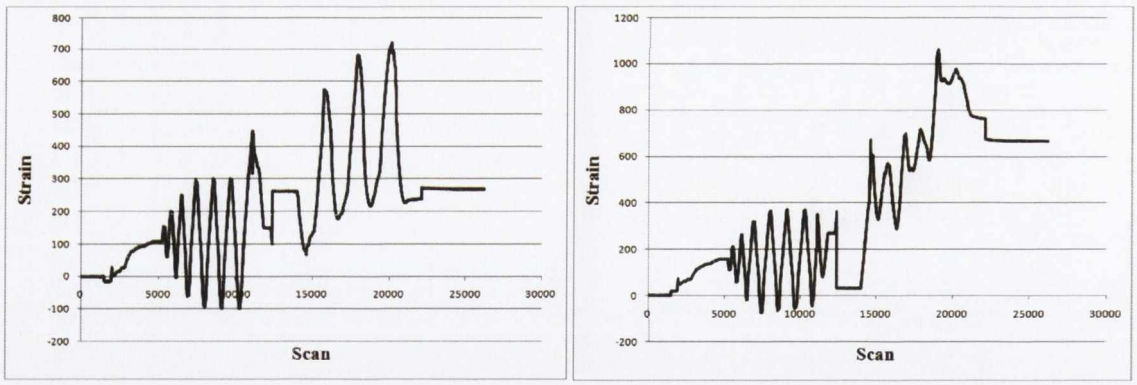

Figure A.116: Strain versus Scan Plot: Specimen JD5 – (a) S.G. 21, (b) S.G. 22

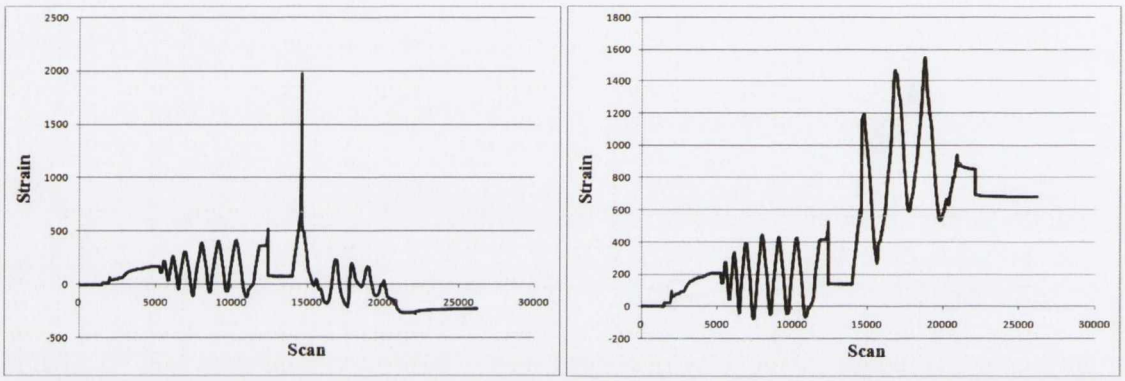

Figure A.117: Strain versus Scan Plot: Specimen JD5 – (a) S.G. 23, (b) S.G. 24

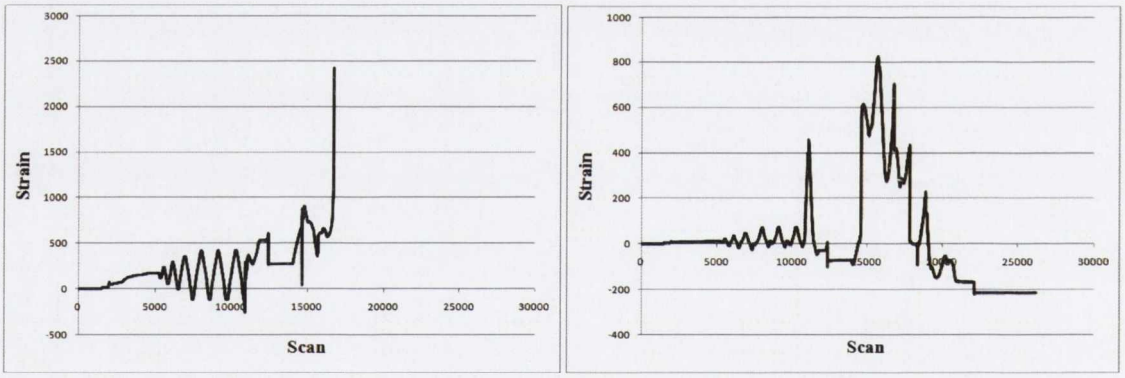

Figure A.118: Strain versus Scan Plot: Specimen JD5 – (a) S.G. 25, (b) S.G. 26

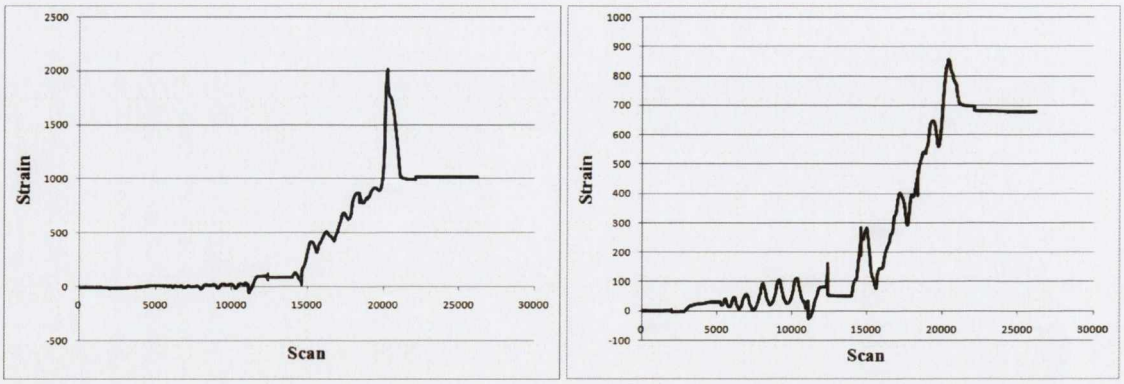

Figure A.119: Strain versus Scan Plot: Specimen JD5 – (a) S.G. 27, (b) S.G. 28

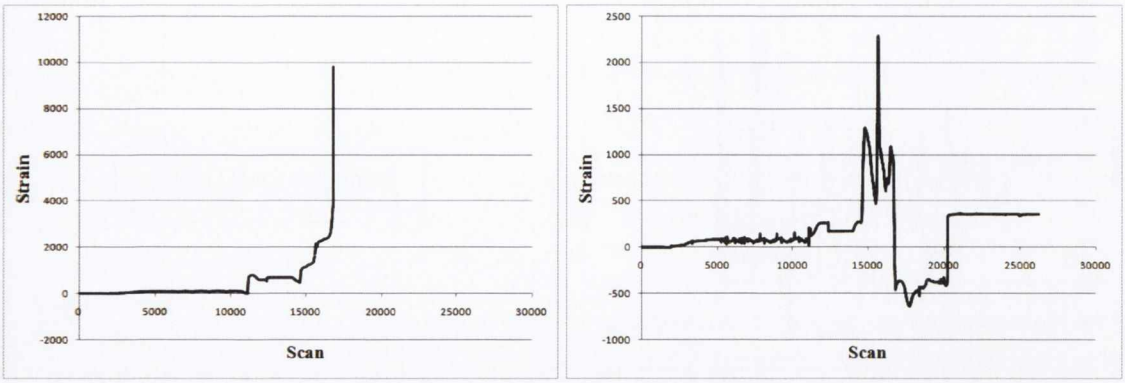

Figure A.120: Strain versus Scan Plot: Specimen JD5 – (a) S.G. 29, (b) S.G. 30

Specimen JD6 – ID4

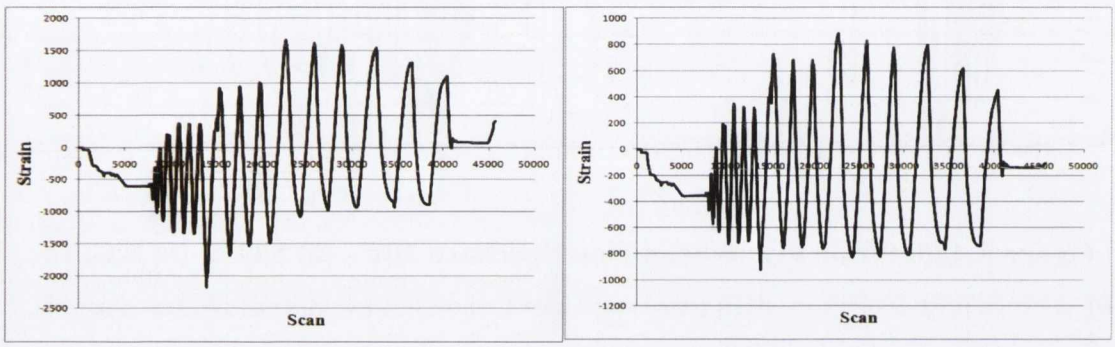

Figure A.121: Strain versus Scan Plot: Specimen JD6 – (a) S.G. 1, (b) S.G. 2

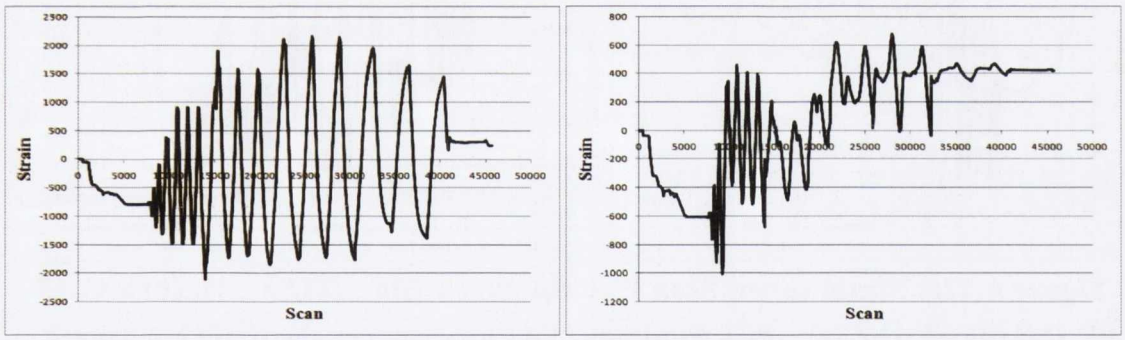

Figure A.122: Strain versus Scan Plot: Specimen JD6 – (a) S.G. 3, (b) S.G. 4

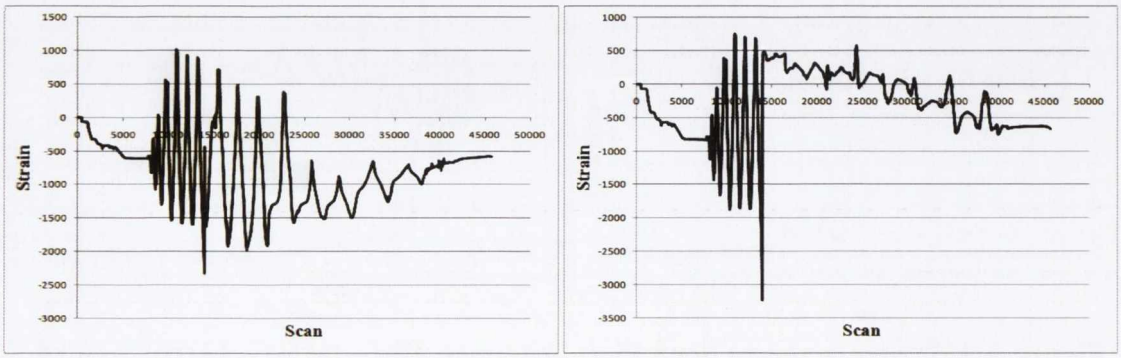

Figure A.123: Strain versus Scan Plot: Specimen JD6 – (a) S.G. 5, (b) S.G. 6

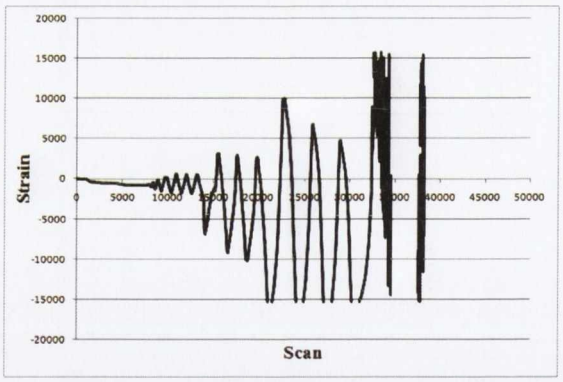

Stain Gauge 8 Offline

Figure A.124: Strain versus Scan Plot: Specimen JD6 – (a) S.G. 7, (b) S.G. 8

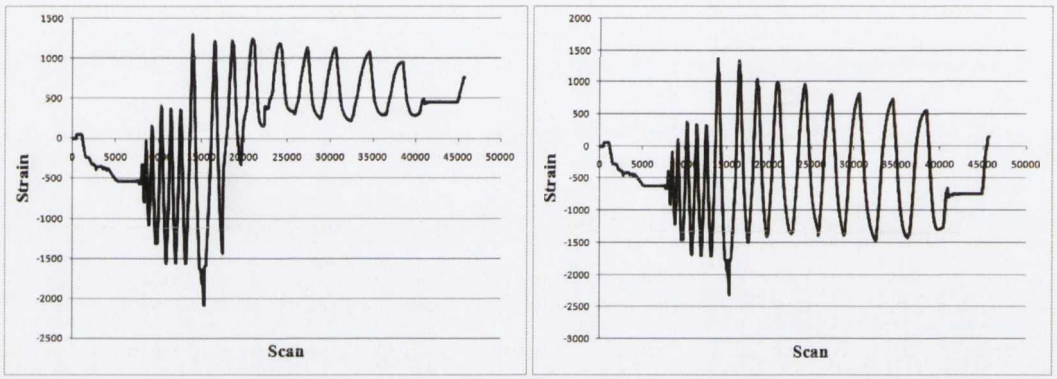

Figure A.125: Strain versus Scan Plot: Specimen JD6 – (a) S.G. 9, (b) S.G. 10

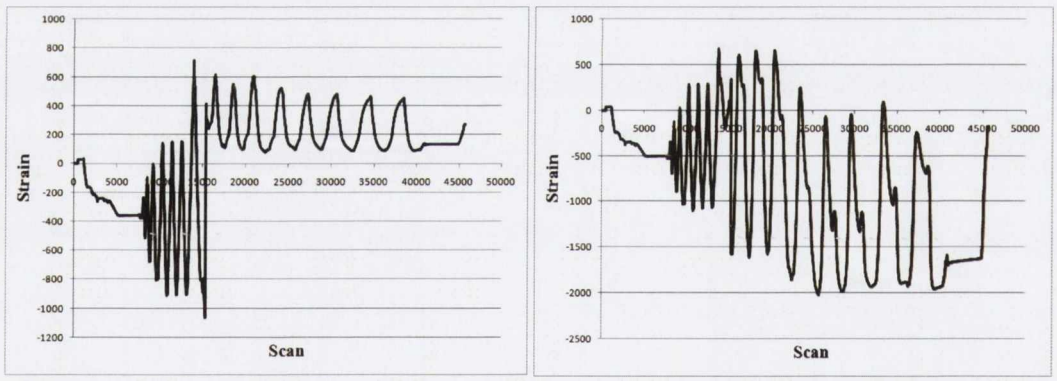

Figure A.126: Strain versus Scan Plot: Specimen JD6 – (a) S.G. 11, (b) S.G. 12

Stain Gauge 13 Offline

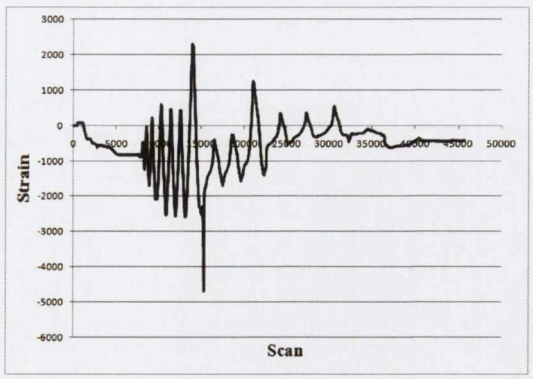

Figure A.127: Strain versus Scan Plot: Specimen JD6 – (a) S.G. 13, (b) S.G. 14

Stain Gauge 15 Offline

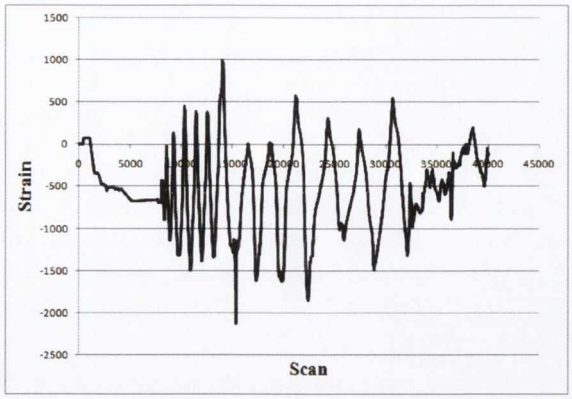

Figure A.128: Strain versus Scan Plot: Specimen JD6 – (a) S.G. 15, (b) S.G. 16

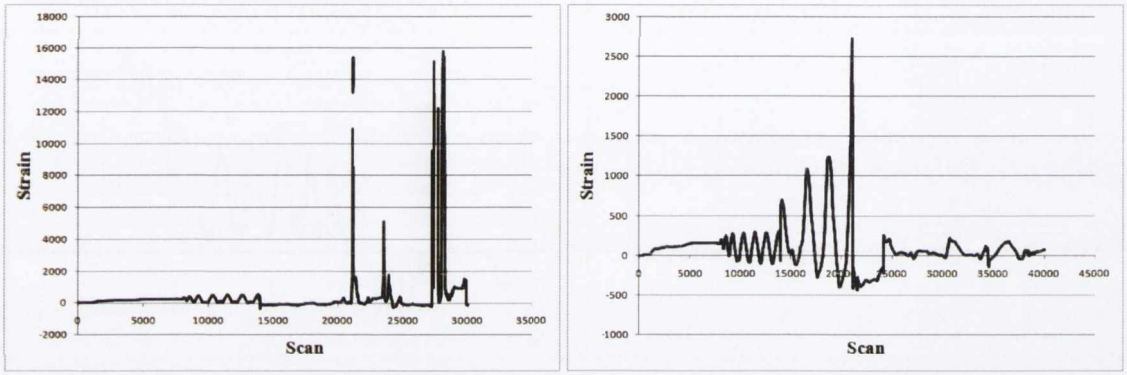

Figure A.129: Strain versus Scan Plot: Specimen JD6 – (a) S.G. 17, (b) S.G. 18

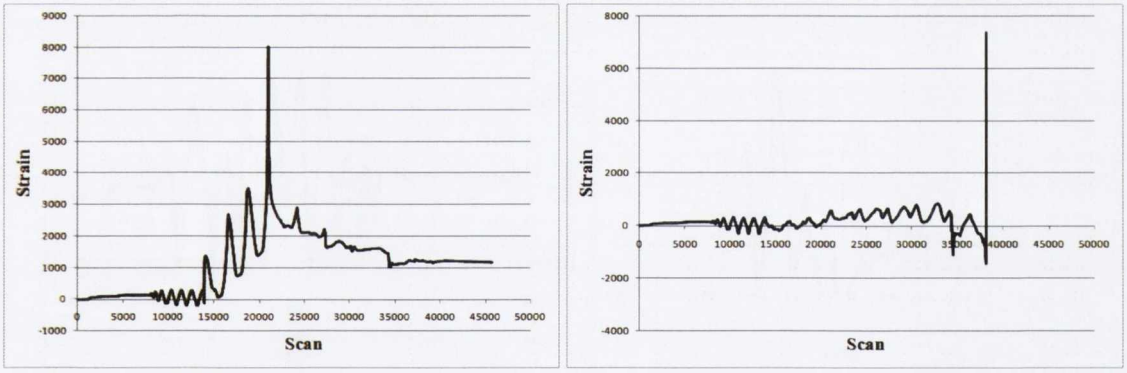

Figure A.130: Strain versus Scan Plot: Specimen JD6 – (a) S.G. 19, (b) S.G. 20

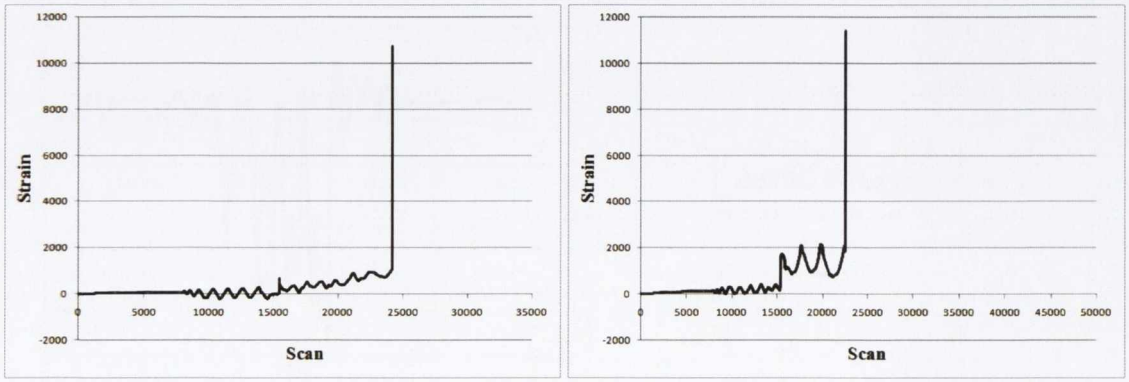

Figure A.131: Strain versus Scan Plot: Specimen JD6 – (a) S.G. 21, (b) S.G. 22

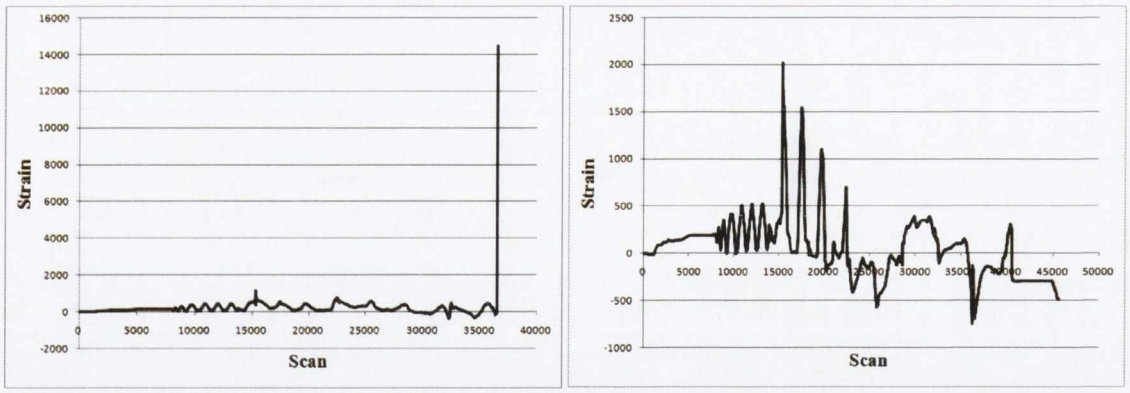

Figure A.132: Strain versus Scan Plot: Specimen JD6 – (a) S.G. 23, (b) S.G. 24

Stain Gauge 25 Offline

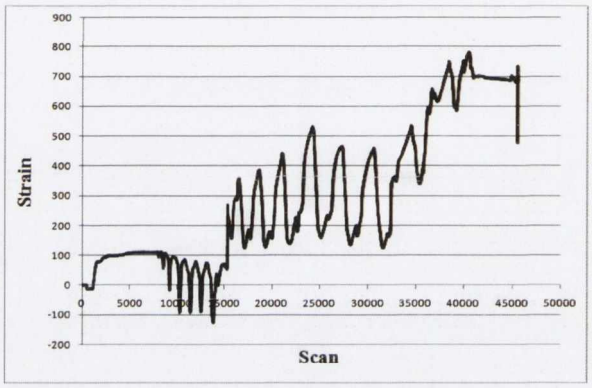

Figure A.133: Strain versus Scan Plot: Specimen JD6 – (a) S.G. 25, (b) S.G. 26

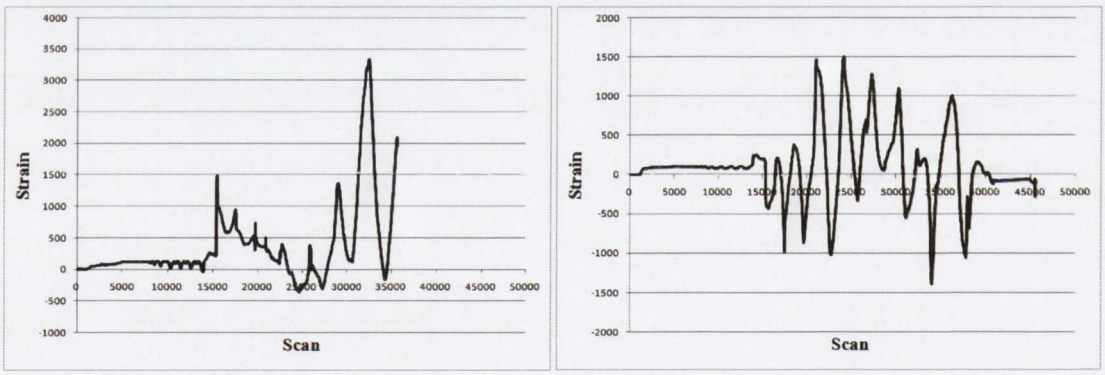

Figure A.134: Strain versus Scan Plot: Specimen JD6 – (a) S.G. 27, (b) S.G. 28

Stain Gauge 29 Offline

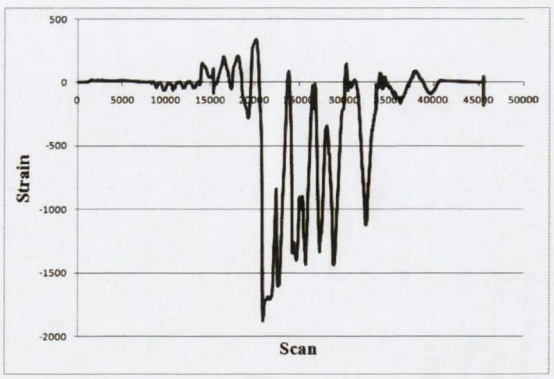

Figure A.135: Strain versus Scan Plot: Specimen JD6 – (a) S.G. 29, (b) S.G. 30